

# Enhancing membrane filtration and persulphate advanced oxidation processes for water treatment

Ikechukwu Anthony Ike

A thesis submitted in fulfilment of the requirements for the degree of  
Doctor of Philosophy

Institute for Sustainability and Innovation  
College of Engineering and Science  
Victoria University

August 2017

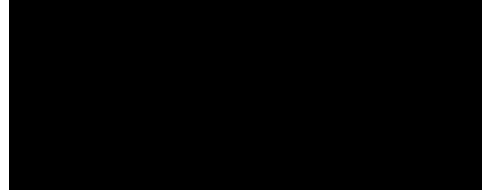
## Abstract

Membrane filtration processes (MFPs) and advanced oxidation processes (AOPs) are two highly effective water treatment techniques in common use today. Although conceptually distinct, these processes are used complementarily for efficient water treatment. The aim of this study is to provide practical enhancement of the performance of these techniques to meet growing global water demands. The specific objectives include effective control over the properties and functionalities of membranes and the development and harnessing of new materials and techniques in AOPs. Using controlled laboratory studies and critical review of the relevant literatures, this study provided a number of practical and theoretical insights towards the cost-effective and sustainable advancement of MFPs and AOPs to meet the rising global demand for safe and affordable water. Key findings include the delineation of the important effects of common membrane preparatory recipes; the possibility of a facile tailoring of the properties of polymeric membrane using the often-overlooked effects of polymer dissolution conditions; and the demonstration that activated persulphate AOP was effective in resolving the problem of membrane fouling. Other important findings include the demonstrated feasibility of the effective degradation of water pollutants such humic acid, orange G, salicylic acid and naphthylamine, using persulphate activated by either phosphate chelated zerovalent iron nanoparticles, commercially available steel wool and iron powder or waste heat. An in-depth investigation of the practical and potential benefits of nanotechnology to membrane development was presented as well as a critical review of the literature of AOPs focused on persulphate with new insights provided for a consistent understanding of reaction mechanisms. Overall, the results presented in this work may be considered significant contributions to the important fields of MFPs and AOPs with both theoretical and practical implications for the treatment of raw and wastewater.

**Declaration**

"I, Ikechukwu Anthony Ike, declare that the PhD thesis by Publication entitled 'Enhancing membrane filtration and persulphate advanced oxidation processes for water treatment' is no more than 100,000 words in length including quotes and exclusive of tables, figures, appendices, bibliography, references and footnotes. This thesis contains no material that has been submitted previously, in whole or in part, for the award of any other academic degree or diploma. Except where otherwise indicated, this thesis is my own work".

Signature:



Date: 16 August 2017

## Dedication

To St Augustine of Hippo,  
that philosophy may revive in our day and revive our day.

## Acknowledgement

### **Deo Gratias!**

This study was commenced and was completed through the support provided by Victoria University via the Victoria University International Postgraduate Scholarship. I am very grateful to Victoria University for the award, for the trust and for the opportunity.

My sincere and unqualified gratitude to Professor Mikel Duke and Professor John Orbell, my PhD supervisors and advisers. Thank you. Thank you very much.

I am especially indebted to Professor Kiyonori Suzuki, Dr Ludovic F. Dumée and Professor Stephen Gray for providing much needed access to equipment and other resources. My heartfelt gratitude to Mrs Catherine Enriquez who has been more than a great help to me. How can I fittingly thank Ms Stacey Lloyd and Mr Joseph Pelle who did more than enough to keep me going? Ms Min Nguyen, Mrs Mary Marshall, Mrs Charmaine DiQuattro were also very kind and generous to me. Thank you all.

I am also greatly indebted to Ms Anbharasi Vanangamudi and Mr Digby Wrede for their valued assistance and company. My profoundest gratitude to Mrs Manpreet Grewal, Mrs Swati Garg and Mr Robin Wilson, my very dear friends. It would have easily gone differently without you all.

I am indebted to Dr Peter Sanciolo, Dr Jianhua Zhang, Mr Noel Dow, Dr Bo Zhu and Dr Marlene Cran for their valued assistance in one way or the other. I will not fail to mention Dr and Mrs Waechter who were very supportive and to express my heartfelt gratitude for their kindness.

I certainly have not exhausted the thank-you list. Nor can I adequately put to words the depth of my gratitude for the many acts of kindness and professionalism I have been privileged to witness.

God bless you all.

## Thesis summary

Sustainable chemical processes and environmental conservation efforts rely increasingly on membrane filtration processes (MFPs) and advanced oxidation processes (AOPs). These technologies provide effective water separation, purification and waste detoxification in industries as diverse as drinking water production, chemical manufacturing, medicine and subsurface contamination remediation. Although conceptually different, MFPs and AOPs have much in common, in that they are often used complementarily so that developments in one has direct bearing on the other. For example, AOPs may be used as pre-treatments for a MFP while the product of a MFP may require further polishing by an AOP to meet established specifications. The interdependence of these processes is a key motivation to investigate them together as presented in this work with the view of making fundamental and practical contributions towards their enhancement.

One of the many important areas of research with much promise for improving the performance of MFPs is nanotechnology. This work provides an in-depth investigation of the potential and practical improvement to membrane performance derived from the incorporation of nanoparticles into membranes. However, several challenges remain unresolved. Nanoparticle aggregation during membrane synthesis, arising from the thermodynamic drive to minimise surface energy, and the inevitable and complex problems associated with membrane fouling, has greatly hampered the practical realisation of some of the potential benefits of nanoparticle incorporation into membranes.

The effects of two common steps in the production of polymeric membranes, dope ultrasonication and the addition of a hydrophilic polymer, poly (vinylpyrrolidone) (PVP), in resolving the problem of nanoparticle aggregation in poly (vinylidene fluoride) (PVDF), a well-known hydrophobic polymeric membrane forming material, were studied by controlled laboratory experiments. The results provided a number of novel fundamental insights into the nature and functionality of polymeric membranes. It showed that PVP, popularly referred to as a ‘pore former’, was surprisingly not responsible for pore formation but functioned rather as a ‘pore connector’ and as an aid to particle dispersion. While

dope ultrasonication resulted in efficient particle dispersion as may be expected, it did not improve the membrane surface wettability as the hydrophilic nanoparticles were completely locked within the hydrophobic PVDF matrix. Ultrasonication resulted in significant reduction in membrane porosity but did not change the membrane thermal stability. The addition of PVP, however, significantly reduced thermal stability as well as the PVDF  $\beta$ -phase mass fraction.

In the absence of nanoparticles and with appropriate addition of PVP, further controlled experiments were performed to advance a new route for remedying the inevitable problem of membrane fouling using the often-overlooked effects of polymer dissolution conditions. The results showed that compared to conventional PVDF dissolution procedure, ultrasonication dissolution results in a membrane with improved permeate flux during oil emulsion filtration and high flux recovery of ~63% after cleaning. As a comparison, flux recovery of only ~26% was obtained for the membrane produced from dope dissolved conventionally at 24 °C. The outstanding performance of the dope-sonicated membrane was linked to its slightly lower porosity, narrow distribution of small pores and relatively smooth skin layer. Performance parameters for all membranes showed good correlation to porosity suggesting a tool for membrane design achievable by simple variation in the mode of polymer dissolution. The polymer dissolution effect was related to the degree of unfolding of the polymer molecular chains and their entanglements.

A critical review of the literature of AOPs focused on the commercially important oxidant, persulphate (PS), was provided with novel explanations suggested for some important observations in the field, new proposals presented to explain reaction mechanisms more consistently and discrepancies and areas for further studies identified. Although PS is a very powerful oxidant, it often needs to be activated to produce more powerful oxidising radicals for rapid pollutant degradation. For the degradation of wastewater containing recalcitrant pollutants, iron was recognised as the most important PS activator due to its affordability, biocompatibility and activation effectiveness. However, whenever waste heat is available, which is often generated abundantly from most industrial processes, heat activation provide the most effective and sustainable PS activation technique. Except in justified cases, unactivated PS was recommended for in-

situ chemical oxidation of subsurface contaminations with an endorsement of base injection only for very acidic subsurface environments.

Although it has been shown that zerovalent iron nanoparticles (nZVI) are very effective in activating PS for the degradation of environmental pollutants, particles aggregation and surface oxidation lead to diminished reactivity and remain crucial challenges for nZVI application as an activator. This work evaluated for the first time the performance of three different nZVI that are each stabilised with one of three phosphonic acids, ATMP, DTPMP or HTPMP for activating PS to degrade orange G (OG), a typical azo dye. Azo dyes are known for their non-biodegradability and their direct or potential carcinogenicity. While ATMP- and DTPMP-stabilised nZVI were practically inert to OG solution in the absence of PS, HTPMP-stabilised nZVI achieved ~15% total carbon (TC) reduction under similar conditions. However, in the presence of PS, the degradation rate constants for ATMP- and DTPMP-stabilised nZVI were double the rate constant obtained for HTPMP-stabilised nZVI under similar conditions. These results highlight the important role of both stabilisers and PS in modulating nZVI activity with potential niche applications.

Controlled experiments also showed, for the first time, that commercial zerovalent iron (ZVI) - as steel wool and carbonyl iron powder - activation of PS were effective for the degradation of four important water pollutants, namely, OG, salicylic acid (SA), phenol (Ph) and 1-naphthylamine (1NA) in the presence or absence of methanol (MeOH). The addition of MeOH mimics the presence of industrial solvents and/or feedstuff in real industrial wastewater. MeOH had no effect on the nature of the degradation products but reduced the rate of degradation of the target pollutants. The alcohol had more retarding effect on the degradation of an aromatic pollutant relatively resistant to oxidation such as SA due to the presence of an electron-withdrawing group compared to a pollutant such as 1NA that has an electron-donating group. The azo bond in OG was found to constitute a structural weakness leading to a comparatively more effective degradation of the aromatic moieties. Compared to activation of PS by ionic iron, the ZVI materials were shown to be more effective in pollutant degradation. In addition, the surfaces of the ZVI were not oxidised, an advantage over ZVI

nanoparticles, and they required no prior pretreatment indicating the probable suitability of waste iron filings for PS activation.

Based on laboratory scale experiments, this research showed that waste heat from industries such as textile dyeing is adequate for the rapid degradation and mineralisation of OG solution in the absence or presence of high concentration of inorganic salts relevant to the textile industry. An important point of novelty in this study was the identification of the important role of radical kinetic energy in determining the rate and effectiveness of heat-activated PS mineralisation of pollutants. One effect of the kinetic energy of radicals is the existence of an optimal mineralisation temperature. For uncatalysed PS activation, the optimal temperature was identified as 80 °C - 90 °C and is expectedly independent of the target pollutant. Also presented are new insights on a number of themes relevant to radical oxidation such as: inhibition and enhancement of decomposition and mineralisation by background ion; radical scavengers selection and reaction quenching assessment.

This study also uniquely demonstrated the feasibility of humic acid (HA) degradation by heat-activated PS mainly at a low waste heat temperature of 40 °C, but also at 60 °C and 90 °C in which ~70% TOC loss was achieved within 168 h, 24 h and 1 h, respectively. HA as a major constituent of natural organic matter in raw water presents major challenges to drinking water production including membrane fouling and serving as a precursor for the production of disinfection by products. Heat-activated PS treatment of synthetic raw water at 40 °C was also shown to significantly reduce ultrafiltration membrane fouling. Low concentration of chloride ( $\leq 0.9$  mM) accelerated PS degradation of HA but the promotion was lost at higher concentration ( $\geq 9$  mM). HA spiked into tap water was degraded by PS even at 25 °C suggesting activation by trace minerals present within regulatory limits. These results promises an overall effective raw water treatment for drinking water production.

Taken together, the results of the studies presented in this work may be considered significant contributions to the important fields of MFPs and AOPs with both theoretical and practical implications. It provided novel insights on the effects of membrane preparatory recipes; and demonstrated a facile membrane

tailoring strategy. It explored PS activation with analytical and commercial grade iron samples for controlled pollutant degradation; and highlighted the efficiency and sustainability of heat-activated PS for wastewater and drinking water production using waste heat. Finally, it provided detailed and critical reviews of aspects of AOPs and MFPs literature to foster further practical and theoretical developments in the fields.

**PART A:**
**DETAILS OF INCLUDED PAPERS: THESIS BY PUBLICATION**

Please list details of each Paper included in the thesis submission. Copies of published Papers and submitted and/or final draft Paper manuscripts should also be included in the thesis submission

Item/ Chapter No.	Paper Title	Publication Status (e.g. published, accepted for publication, to be revised and resubmitted, currently under review, unsubmitted but proposed to be submitted )	Publication Title and Details (e.g. date published, impact factor etc.)
2	Nanoparticle incorporation into desalination and water treatment membranes - potential advantages and challenges (book chapter)	Published	<b>Chapter 7 in Desalination Sustainability, Elsevier June 2017, Pages 261–303</b>
3	Effects of dope sonication and hydrophilic polymer addition on the properties of low pressure PVDF mixed matrix membranes	Published	<b>Journal of Membrane Science, Vol 540, 15 Oct 2017, P 200-211, Impact Factor 6.035</b>
4	Effects of dissolution conditions on the properties of PVDF ultrafiltration membranes	Published	<b>Ultrasonics Sonochemistry, Vol 39, Nov 2017, P 716-726, Impact Factor 4.218</b>
5	Critical review of the science and sustainability of persulphate advanced oxidation processes	Proposed to be submitted	
6	Advanced oxidation of orange G using phosphonic acid stabilised zerovalent iron	Published	Journal of Environmental Chemical Engineering, Vol 5, Issue 4, Aug 2017, P 4014-4023, CiteScore 3.83
7	Steel wool and carbonyl iron powder activation of persulphate for pollutant degradation	Under review	Chemical Engineering Journal

xi.

Date:

Signature:

 Ikechukwu A. Ike  
 16 August 2017

PART A:

**DETAILS OF INCLUDED PAPERS: THESIS BY PUBLICATION**

Please list details of each Paper included in the thesis submission. Copies of published Papers and submitted and/or final draft Paper manuscripts should also be included in the thesis submission

Item/ Chapter No.	Paper Title	Publication Status (e.g. published, accepted for publication, to be revised and resubmitted, currently under review, unsubmitted but proposed to be submitted)	Publication Title and Details (e.g. date published, impact factor etc.)
8	Degradation of azo dye orange G by thermally activated persulphate: practical and theoretical implications	Under review	<b>Journal of Hazardous Materials</b>
9	Activation of persulphate for effective humic acid mineralisation in low energy environment	Under review	<b>ACS Sustainable Chemistry &amp; Engineering</b>

Declaration by [candidate name]:  
**Ikechukwu A. Ike**

Date:  
[Redacted]

## Table of contents

Abstract.....	ii
Declaration.....	iii
Dedication.....	iv
Acknowledgement.....	v
Thesis summary.....	vi
Details of included papers.....	xi
Table of contents.....	xiii
List of tables.....	xix
List of figures.....	xxi
List of abbreviations.....	xxvi
1. General introduction.....	1
1.1. Research background.....	1
1.1.1. Water treatment.....	2
1.1.1.1. Uncontaminated water.....	2
1.1.1.2. Contaminated water.....	3
1.1.2. Treatment techniques.....	3
1.1.2.1. Aeration.....	3
1.1.2.2. Activated carbon adsorption.....	3
1.1.2.3. Ozonation.....	4
1.1.2.4. Chlorination.....	5
1.1.2.5. UV irradiation.....	5
1.1.2.6. Ion exchange.....	5
1.1.2.7. Membrane filtration processes.....	6
1.1.2.8. Advanced oxidation processes.....	8
1.1.2.9. Combined MFPs and AOPs.....	9
1.2. Research statement.....	9
1.3. Thesis structure.....	10
2. Nanoparticles incorporation into desalination and water treatment and	

membranes - potential advantages and challenges.....	14
2.1. Membrane for water treatment: background and motivation for nanoparticle incorporation.....	14
2.2. Nanoparticles and their unique properties.....	16
2.2.1. Surface effects.....	17
2.2.2. Quantum effects.....	18
2.2.3. Summary of key nanoparticle properties and relevance to membrane technology.....	20
2.3. Nanoparticles for membrane desalination and water treatment..	20
2.3.1. Carbon nanotubes.....	21
2.3.2. Aquaporin.....	28
2.3.3. Nanozeolites.....	34
2.3.4. Nanotitania.....	41
2.3.5. Nanosilver.....	46
2.3.6. Nanosilica.....	49
2.3.7. Nanoalumina.....	52
2.3.8. Nanoclay and iron oxide nanoparticles.....	54
2.4. Conclusions and future prospects.....	56
Appendix.....	75
3. Effects of dope sonication and hydrophilic polymer addition on the properties of low pressure PVDF mixed matrix membranes.....	77
3.1. Introduction.....	77
3.2. Experimental.....	80
3.2.1. Materials.....	80
3.2.2. Particle synthesis.....	81
3.2.3. Particle characterisation.....	81
3.2.4. Membrane fabrication.....	82
3.2.5. Membrane characterisation.....	84
3.3. Results and discussion.....	86
3.3.1. Particle characterisation.....	86
3.3.2. Particle dispersion in membrane.....	87
3.3.3. Crystalline phase.....	89
3.3.4. Thermal properties.....	93
3.3.5. Porosity and pore surface area.....	94

3.3.6. Membrane wettability.....	99
3.3.7. Membrane integrity and filtration performance.....	101
3.4. Conclusions.....	106
3.5. Acknowledgments.....	107
Appendix.....	114
4. Effects of dissolution conditions on the properties of PVDF ultrafiltration membranes.....	124
4.1. Introduction.....	124
4.2. Materials and methods.....	127
4.2.1. Materials.....	127
4.2.2. Membrane fabrication and characterisation.....	128
4.2.2.1. Membrane fabrication.....	128
4.2.2.2. Membrane characterisation.....	129
4.2.2.3. Filtration experiments.....	131
4.3. Results and discussions.....	132
4.3.1. Membrane morphology.....	132
4.3.2. Crystalline phase.....	134
4.3.3. Thermal stability.....	135
4.3.4. Mechanical strength and shrinkage.....	137
4.3.5. Porosity.....	139
4.3.6. Wettability.....	140
4.3.7. Filtration performance.....	141
4.3.7.1. Flux and rejection.....	141
4.3.7.2. Cake formation and modelling.....	145
4.3.7.3. Porosity correlations.....	147
4.3.7.4. Dope dissolution environment.....	148
4.4. Conclusion.....	152
4.5. Acknowledgement.....	152
Appendix.....	158
5. Critical review of the science and sustainability of persulphate advanced oxidation processes.....	164
5.1. Introduction.....	164
5.2. A history of persulphate.....	166
5.3. Physicochemical properties of persulphate and standard reduction	

potentials.....	167
5.4. Commercial production of PS.....	168
5.5. The O-O bond.....	168
5.6. Persulphate advanced oxidation processes.....	170
5.6.1. Catalysis.....	171
5.6.1.1. Silver(I).....	171
5.6.1.2. Iron(II) and (III).....	175
5.6.1.3. Other metal catalysts.....	190
5.6.1.4. Carbon catalyst.....	192
5.6.1.5. Organic substrates as catalyst.....	194
5.6.1.6. Alkaline activation.....	196
5.6.2. Thermolysis.....	199
5.6.3. Photolysis.....	204
5.6.4. Sonolysis.....	206
5.6.5. Radiolysis.....	207
5.7. Practical applications.....	207
5.7.1. In-situ chemical oxidation.....	207
5.7.2. Waste treatment.....	209
5.7.3. Drinking water production.....	210
5.7.4. Coupling to membrane filtration.....	210
5.8. Conclusions.....	211
6. Advanced oxidation of orange G using phosphonic acid stabilised zerovalent iron.....	230
6.1. Introduction.....	231
6.2. Material and methods.....	233
6.2.1. Materials.....	233
6.2.2. Methods.....	233
6.3. Results and discussion.....	236
6.3.1. Nanoparticle characterisation.....	236
6.3.2. OG degradation kinetics.....	240
6.3.3. OG degradation mechanism and products.....	243
6.3.4. Dissolution of nZVI.....	248
6.3.5. Mineralisation of OG.....	249
6.3.6. Reaction mechanism.....	251

6.4. Conclusions.....	252
Appendix.....	258
7. Steel wool and carbonyl iron powder activation of persulphate for pollutant degradation.....	272
7.1. Introduction.....	272
7.2. Experimental procedures.....	274
7.2.1. Materials.....	274
7.2.2. Methods.....	275
7.3. Results and discussions.....	276
7.3.1. Characterisation of ZVI samples.....	276
7.3.2. Degradation of OG.....	278
7.3.3. Degradation of salicylic acid.....	289
7.3.4. Degradation of 1-naphthylamine and phenol.....	294
7.4. Conclusions.....	298
7.5. Acknowledgement.....	299
Appendix.....	304
8. Degradation of azo dye orange G by thermally activated persulphate: practical and theoretical implications.....	309
8.1. Introduction.....	309
8.2. Experimental section.....	312
8.3. Results and discussions.....	313
8.3.1. Degradation kinetics.....	313
8.3.2. Effects of ions on OG degradations by TAPS.....	315
8.3.3. Degradation mechanism.....	317
8.3.3.1. Radical scavenging.....	317
8.3.3.2. Degradation pathway.....	319
8.3.3.3. Reaction quenching.....	322
8.3.4. Mineralisation.....	323
8.4. Implications.....	325
8.5. Acknowledgement.....	326
Appendix.....	332
9. Activation of persulphate for effective humic acid degradation at waste heat temperature.....	337
9.1. Introduction.....	337

9.2.	Materials and methods.....	340
9.3.	Results and discussions.....	341
9.4.	Acknowledgment.....	356
	Appendix.....	361
10.	General conclusion and future research.....	365
10.1.	General conclusion.....	365
10.2.	Future research.....	369

## List of tables

Table 3.1. Membrane compositions	84
Table 3.2. BET surface areas and particle sizes for synthesized particles	87
Table 3.3. Surface porosity computed from ImageJ analysis of SEM	99
 Images	
Table 5.1. Basic properties of sodium persulphate	167
Table 5.2 Standard reduction potentials ( $E^\circ$ ) relevant to AOPs	167
Table 5.3. Pollutant degradation by PS activated by minerals and solids	183
Table 6.1. Basic properties of Orange G	231
Table 6.3. Computation of fraction of organic carbon contributed by fumaric acid degradation product at 60 min	248
Table S6.1. UV $\lambda_{\max}$ and $\lambda_{\min}$ for possible products from OG degradation and degraded OG at 60 min	264
Table S6.2. Retention times for the HPLC conditions specified in this work for known chemical compounds	265
Table 7.1. Reaction constants for activated PS degradation of 0.1 mM OG at 24 °C	280
Table S7.1. Retention times for known chemicals	306
Table 8.1. Typical process parameters for industrial textile dyeing	311
Table 8.2. Pseudo first order reaction constants as a function of temperatures and $CP_{S,0}$	314
Table 8.3. Pseudo first order reaction constants for OG degradation in the presence of 100 mM inorganic salt	317
Table S8.1. Retention times for known chemicals	336

Table S9.1. Retention times for selected chemicals	362
Table S9.2. Tap water chemical analysis	364

## List of figures

Figure 2.1. Various carbon materials and their relatives	22
Figure 2.2. Aquaporin protein structure	29
Figure 2.3. Schematic presentation of aquaporin (AQP) laden membranes	32
Figure 2.4. Schematic showing three types of microstructure of a high Quality polycrystalline zeolite membrane	37
Figure 2.5. Characterization of hand-cast thin film properties by TEM and EDX for (a–b) pure polyamide membrane and (c–d) nanocomposite membrane	39
Figure 2.6. Bulk structures of rutile and anatase	42
Figure 2.7. Schematic of oxidative radical generation on photoactive TiO <sub>2</sub>	43
Figure 3.1. XRD patterns (a) and FTIR spectra (b) for IO and SIO powders	87
Figure 3.2. Optical transmission microscope and SEM images of membranes	89
Figure 3.3. FTIR spectra showing characteristics peaks for $\alpha$ and $\beta$ phases of PVDF	91
Figure 3.4. TGA weight loss profiles	94
Figure 3.5. Estimations of membrane porosity	97
Figure 3.6. SEM images of the skin-layer surface of 10 wt.% membranes	98
Figure 3.7. Water contact angle CA	101
Figure 3.8. Transmembrane pressure at constant water flux	103
Figure 3.9. The effects of dope sonication and PVP addition on some of the properties of PVDF MMM	105
Figure S3.1. Optical microscope image of membranes	115
Figure S3.2. SEM images showing membrane microstructure	116

Figure S3.3. SEM cross-sectional images of membranes	117
Figure S3.4. TGA weight loss profiles for P48	118
Figure S3.5. SEM images showing skin layer pores	119
Figure S3.6. Oil emulsion droplet sizes as measured by DLS technique	120
Figure 4.1. Schematic diagram of filtration set up	132
Figure 4.2. SEM images of membrane skin layer and cross section	133
Figure 4.3. Membranes $\beta$ -phase mass fractions	135
Figure 4.4. Heat flow differential scanning calorimetry and weight loss thermogravimetric analysis	136
Figure 4.5. Mechanical strength and shrinkage property	138
Figure 4.6. Membrane bulk porosity and pore size distribution	140
Figure 4.7. Membrane water contact angles	141
Figure 4.8. Membrane performance during crossflow clean water and oil emulsion filtration	143
Figure 4.9. Image of representative membranes after fouling and cleaning	145
Figure 4.10. Permeate flux during filtration of an oil emulsion at 2 h and cake filtration model plots	146
Figure 4.11. Membranes performance correlations to bulk porosity	148
Figure 4.12. Schematic elucidation of porosity/pore size influence on key membrane performance parameters	150
Figure 4.13. Schematic representation of the effects of different dope dissolving conditions on PVDF polymer networks entanglement	151
Figure S4.1. Typical FTIR spectra for the membranes	158
Figure S4.2. Typical stress-strain curves for membranes	159

Figure S4.3. Typical water contact angles on membranes	160
Figure 5.1. Schematic illustration of the association of the H atom and –SO <sub>3</sub> - group with the lone pair electrons on the O–O bond oxygen atoms	170
Figure 5.2. Possible iron/PS reaction pathways for pollutant degradation	189
Figure 5.3. Effect of pH on PS decomposition	197
Figure 6.1. Scanning electron microscopy images of AT-nZVI, DT-nZVI, and HT-nZVI	236
Figure 6.2. XRD patterns for AT-nZVI, DT-nZVI and HT-nZVI	237
Figure 6.3. FTIR spectra for stabilising chemicals and nanoparticles	239
Figure 6.4. OG (0.1 mM) degradation at 24 °C measured by UV-Vis spectroscopy at 478 nm	243
Figure 6.5. Chromatograms for 0.1 mM OG degradation	246
Figure 6.6. Simplified major degradation pathway for optimised reaction condition	248
Figure 6.7. Dissolved iron concentration during OG degradation	249
Figure 6.8. Mineralisation at 60 min for 0.1 mM OG	251
Figure S6.1. UV-vis characteristic spectral patterns	262
Figure S6.2. HPLC DAD UV spectra for the LMWA and ND peaks	267
Figure S6.3. UV spectra for standard/known LMWA and ND	268
Figure 7.1. XRD patterns (a) and FTIR spectra (b) for SW and CIP	277
Figure 7.2. Optical image of SW (a) and CIP (b)	278
Figure 7.3. The degradation of OG by PS	281
Figure 7.4. OG simplified degradation pathway	284
Figure 7.5. The degradation and mineralisation of OG with or without MeOH	286
Figure 7.6. Total carbon reduction for 0.1 mM OG	287
Figure 7.7. Effects of initial concentration and mode of PS addition on the TC reduction	288

Figure 7.8. Degradation and mineralisation of SA	287
Figure 7.9. SA simplified degradation pathway	293
Figure 7.10. Degradation of Ph and 1NA	297
Figure 7.11. Mineralisation and remaining PS after 60 min	297
Figure S7.1. Isotherm plots for CIP and SW	304
Figure S7.2. The degradation trends for 0.1 mM OG at room temperature CPS,0 = 10 mM; [Fe] = 1.8 mM	305
Figure S7.3. DAD generated UV spectra for the LMWA peak at 60 min	307
Figure S7.4. UV spectra for relevant chemicals	307
Figure S7.5. Syringe filter colouration after filtering reacting	308
Figure 8.1. Arrhenius plot for CPS,0 = 1 mM and 10 mM	315
Figure 8.2. The effects of radical scavengers on TAPS degradation	319
Figure 8.3. Chromatograms for 0.1 mM OG degradation at various temperature	321
Figure 8.4. OG degradation for CPS,0 = 10 mM at 70 °C with quenching In either methanol or ice bath	322
Figure 8.5. TC reduction for 0.1 mM OG with CPS,0 = 1 mM and 10 mM	324
Figure S8.1. Rate of OG degradation	333
Figure S8.2. Effect of 100 mM (except where otherwise stated) salt concentrations on the rate of 0.1 mM OG degradation	334
Figure 9.1. 4 mg/L HA synthetic raw water degradation by 0.25 mM PS activated by heat at 40 °C	342
Figure 9.2. EEM contours for the degradation of 4 mg/L HA synthetic raw water	344
Figure 9.3. UV-visible spectral profile and chromatogram	345
Figure 9.4. TOC loss for 4 mg/L HA synthetic raw water	347
Figure 9.5. Degradation and flux profile	348

Figure 9.6. EEM spectra for HA 15 mg/L synthetic raw water	350
Figure 9.7. The effects of water chemistry on the degradation of HA	354
Figure S9.1. UV spectra for selected organic compounds	361
Figure S9.2. Normalised flux profile for raw water after treatment at 40 °C for 336 h without added PS	363

### List of abbreviations

- AAS – Atomic adsorption spectroscopy  
AC – Activated carbon  
AOPs - Advanced oxidation processes  
AqpZ – Aquaporin Z  
ar/R – Aromatic/arginine filter  
ATMP – Amino tri (methylene phosphonic acid)  
ATR-FTIR – Attenuated total reflectance Fourier transform infra-red  
BCP – Block copolymers  
BET – Brunauer Emmett Teller  
BSA – Bovine serum albumin  
BuOH – tert-Butanol  
CA – Contact angle  
CA-d – Rate of decrease of contact angle  
CIP – Carbonyl iron powder  
CNT – Carbon nanotube  
CVD – Chemical vapour deposition  
DAD – Diode array detector  
DBPs – Disinfection by products  
DLS – Dynamic light scattering  
DMF – Dimethylformamide  
DOS – Density of states  
DPhPC – 1,2-diphytanoyl-sn-glycero-3-phosphocholine  
DSC – Differential scanning calorimetry  
DTPMP – Diethylenetriamine penta (methylene phosphonic acid)  
EEM – Excitation-emission-matrix  
EDDS – [S,S]-ethylene-diamine-di-succinic acid  
EDTA – Ethylene-diamine-tetra-acetic acid  
ESR – Electron spin resonance  
F( $\beta$ ) – Mass fraction of beta phase

FO – Forward osmosis

FR – Flux recovery

GAC – Granular activated carbon

HA – Humic acid

HD – Hydroquinone derivative

HPLC – high performance liquid chromatography

HTPMP – Bis (hexamethylene triamine penta (methylenephosphonic acid))

IO – Iron oxide nanoparticles

ISCO – In-situ chemical oxidation

IX – Ion exchange

LMWA – low molecular weight acid

MeOH – Methanol

MDWT – Membrane desalination and water treatment

MF – Microfiltration

MFPs – Membrane filtration processes

MMM – Mixed matrix membrane

MSN – Mesoporous silica nanoparticles

MTBE – Methyl tert-butyl ether

MWCNT – Multi-wall carbon nanotube

n – Nano-

ND – Naphthalene derivative

NF – Nanofiltration

NIPS – Nonsolvent induced phase separation

NMP – 1-methyl-2-pyrrolidinone

NPA – Asparagine-proline-alanine motifs

NOM – Natural organic matter

NPOC – Nonpurgeable organic carbon

NT – 1-Naphthylamine

OG – Orange G

PAC – Powdered activated carbon

PD – Phenol derivative  
PES – Polyethersulfone  
Ph – Phenol  
PMS – Peroxymonosulphate  
PrOH – Propanol-1  
PS – persulphate  
PVDF – Poly (vinylidene fluoride)  
PVP – Poly (vinylpyrrolidone)  
R – Rejection  
RO – Reverse osmosis  
SA – Salicylic acid  
SDA – Structure directing agent  
SEM – Scanning electron microscopy  
SIO – Silica coated iron oxide nanoparticles  
SML – Supported membrane layer  
SUVA – Specific UV absorption  
SW – Steel wool  
SWCNT – Single-wall carbon nanotube  
TAPS – Thermally activated persulphate  
TEOS – Tetraethylorthosilicate  
TC – Total carbon  
TOC – Total organic carbon  
TFC – Thin film composite  
TFN – Thin film nanocomposite  
TGA – Thermal gravimetric analysis  
TMP – Transmembrane pressure  
UF – Ultrafiltration  
UV-Vis – Ultraviolet – visible spectroscopy  
VACNTs – Vertically aligned carbon nanotubes  
VEM – Vesicle encapsulated membrane

XRD – X-ray diffraction

ZVI – Zerovalent iron

## Chapter 1

### **General introduction**

#### 1.1. Research background

Water is life because it is essential to life in all its forms [1, 2]. Consequently the importance of water to every economy and society is inestimable since their very existence is tied to the availability and affordability of usable water [3]. Water use permeates and sustains the entire network of human activities as well as the environmental ecology. Unfortunately, many economic and social activities not only use up significant amount of water, they also pollute unused water thereby exerting a two prong pressure, as it were, on the availability of water [4]. Surface and ground water may be contaminated from a deliberate discharge of untreated wastewater from industries and domestic sewers onto the soil or into rivers, lakes and seas. Accidental discharges of toxic substances into the environment may also result in extensive and damaging pollution. Some of the components of the polluting substance may be recalcitrant to natural degradation processes or may be toxic to these processes and therefore persist in surface or ground water. Even when the pollutant is in itself degradable, a large amount of the material discharged within a short period may overwhelm the natural aerobic processes occasioning anaerobic decomposition with the production of harmful or unpleasant gases [4].

Water pollution may be physical, physiological, biological or chemical [1]. Physical pollution includes water colouring that may arise from the activities of dissolved iron or dyestuffs; turbidity arising from suspension of soil and clay; and relatively significant temperature increase that may result from the discharge of warm industrial water. Physiological pollution are instances of water developing unnatural taste and odour due to the presence of dissolved iron or the decomposition of biological species and organic matter in water. Excessive growth of biological organisms whether pathogenic or not are considered biological pollution and this frequently follows from chemical pollution where significant amounts of nutrient-enriching materials have been discharged. Chemical pollution commonly present the most damaging effect to the environment and normally precipitate other forms of pollution. Chemical pollution

involves the discharge of a certain amount of organic or inorganic materials into water that result in a significant disturbance of chemical and biological processes. Depending on the nature of the chemical, substantial harm may be done to the natural environment and specific remediation activity may be necessary to restore ecological balance [4].

### 1.1.1 Water treatment

To obtain water with the right quality for drinking and other domestic and industrial uses, forestall environmental pollution that may arise from the discharge of industrial and domestic effluent or abate already existing environmental contamination, water treatment may be required [1, 3]. The kind and degree of treatment required for a particular water use or remediation effort is a function of the source and nature of the water, associated contamination and the application to which the water will be put to [1, 3, 5].

#### 1.1.1.1. Uncontaminated water

Drinking water for urban communities is usually obtained from protected underground or surface sources but contaminants may still be present [5]. Water from these sources may be stored in a reservoir for some time where smaller particles in the water may sediment and aeration may be deployed to control bacterial growth or hardness correction [1, 5, 6]. Smaller particles and colloidal matter which do not sediment or settle too slowly may require the addition of a coagulant such as aluminium or iron soluble salts [1, 5]. The effect of the coagulant is to neutralise the surface negative charges, which usually develop on dispersed particles in water thereby eliminating electrostatic repulsion between particles. This results in particle aggregation and sedimentation [1, 5].

Filtration may be applied in lieu of or subsequent to a sedimentation stage to remove suspended particles [1]. Sand filtration is the traditional method for drinking water treatment by filtration but in recent times, membrane filtration especially as microfiltration and ultrafiltration is increasingly employed for the removal of entrained solids and microscopic organisms from raw water [5, 6]. Treated drinking water is often stabilised by adjusting pH to avoid corrosion of pipes used for water distribution. The final stages of treatment for drinking water

usually involve a disinfection stage where chlorine, ozone or UV irradiation may be employed to kill pathogens in the water [5, 6].

#### 1.1.1.2. Contaminated water

For contaminated raw water, other treatment techniques such as aeration, air stripping, activated carbon adsorption, ozonation, chlorination, UV-irradiation, chemical oxidation, microfiltration, ultrafiltration, nanofiltration and reverse osmosis may be deployed depending on the nature of the contaminants and the available resources [5, 6]. These techniques are also employed extensively for the treatment of wastewater streams from industrial and domestic communities before disposal or reuse [1].

### 1.1.2. Treatment techniques

#### 1.1.2.1. Aeration

Aeration is the process of increasing the amount of dissolved oxygen in water, which may be used for the oxidisation and precipitation of dissolved iron and manganese so that they could be removed by filtration. Simple aeration may sometimes be adequate for removing hydrogen sulphide, carbon dioxide and other volatile organic chemicals from water [5, 6]. However, water contaminated with volatile organic chemicals with limited solubility in water such as radon, trichloroethane, tetrachloroethane and carbon dioxide may be better treated using air stripping involving the passage of air through the water usually while the water is flowed down a tower and the air made to flow in the opposite direction [6]. Contaminants diffuse from the water to the air due to vapour pressure and concentration differences and are carried off the tower. The major limitation of this technique relates to its inability to remove significant amount of common stable water pollutants. Other challenges include possible dirt entrainment and water contamination with airborne pollutants and, conversely, air pollution from the released water pollutants [5].

#### 1.1.2.2. Activated carbon adsorption

Contaminant adsorption by activated carbon (AC) is a popular technique for water treatment [6]. AC used for water treatment has large amount of internal pore

networks that allow the entry of liquid and thus provide large surface area for the adsorption of dissolved organic matter in water [7]. The carbon adsorbent may be supplied as powdered AC (PAC) or granular AC (GAC). PAC is often dosed into water and removed during a clarification stage but it is frequently difficult to handle and reuse and increases the amount of solid waste to be disposed [5]. GAC is usually set up as a fixed bed through which water is flowed for contaminant removal. It is easier to manage and optimise a GAC system compared to a PAC treatment. However, pore blockage and the thriving of microscopic organisms may challenge the GAC pack. The later challenge arises from the reactive propensity of AC towards chlorine and other disinfectant commonly used in the control of microscopic organisms [5, 6]. Not infrequently, however, the growth of biological species within GAC structures have been found helpful in the destruction of adsorb chemicals, prolonging the lifespan of the adsorbent in what is referred to as biological AC but the control of the process may be difficult [5]. In addition, GAC systems have been found to be ineffective in the removal of small volatile organic pollutants [6] or soluble and/or hydrophilic contaminants.

#### 1.1.2.3. Ozonation

Ozonation, the application of ozone for the decomposition of impurities in water, is currently a popular method of water disinfection and contaminant degradation producing water with improved colour, taste and odour [1, 8]. Ozone is found particularly effective in the removal of many important organic pollutants such as pesticide, dissolved iron and manganese, the destruction of algae species and the removal of pathogenic bacteria and viruses from water [5]. Ozone is produced by the passage of air or oxygen through a high-voltage electric discharge. The quality of the feed gas is often very important in determining the efficiency of ozone production and is therefore a significant contributor to the cost of ozone generation. Other than the cost of ozone generation and the limited effectiveness of ozone in the degradation of certain organic pollutants, one other important challenge in the use of ozone is the potential production of bromate in water containing bromide [5, 6].

#### 1.1.2.4. Chlorination

Chlorination has remained a popular method for disinfecting and oxidising water and has been particularly instrumental in the prevention of water-borne epidemics [1, 5]. Modern large-scale chlorination of drinking water involves the dosing of water supplies with chlorine gas to kill or deactivate pathogens as well as oxidise organic and inorganic material in water. Smaller applications may utilise sodium or calcium hypochlorite. For drinking water disinfection, chlorine gas must be administered in control amounts to avoid excessive dosage of the gas which may impact a taste and odour to the water or too little which may not provide sufficient disinfection. Dissolved chlorine readily attacks the organic structures of pathogens including their toxin and other organic matter in water resulting in an efficient water disinfection and pollutant degradation [5]. The dissolved chlorine provide residual protection against reinfection by pathogen in the course of water distribution. One important disadvantage of chlorination is the danger of producing hazardous halogenated disinfection by products (DBPs).

#### 1.1.2.5. UV irradiation

UV irradiation has also been used for water disinfection for the production of drinking water and the disinfection of water for medical and industrial uses [5, 8]. UV germicidal processes are effective against a variety of pathogens, easy to maintain and energy efficient especially for the disinfection of particle-free water [5]. The high-energy electromagnetic radiation denatures the DNA in microbial organisms and consequently kills or at least deactivates them [5, 8, 9]. UV irradiation does not add to the odour or taste of water like chlorination and is less likely to produce harmful DBPs compared to chlorination and ozonation [5]. However, UV irradiation may not degrade chemical pollutants already present in water nor does it provide any protection against reinfection during water distribution or use. Suspended particles diminish the effectiveness of UV disinfection as penetration is limited and pathogens may be shielded [5].

#### 1.1.2.6 Ion exchange

Ion exchange (IX) beds may be used for water softening, arsenate and nitrate removal [5, 6]. The insoluble synthetic resin used for IX have exchangeable ion

for the removal of specific ion from water. Cation IX have exchangeable sodium ion, which may be used for replacing divalent ions of calcium and magnesium in water leading to water softening. Anion IX resins may be used for the removal of nitrate from water using chloride ion as replacement. The removal of nitrate requires the use of special anionic resin to limit the removal of sulphate ion which may compete with nitrate for space on the resin [6]. The exhausted IX bed is often regenerated using a concentrated sodium chloride solution. IX has also been used for the removal of ionic organic materials as pretreatment to membrane filtration or chlorination to reduce membrane fouling or limit the production of trihalomethanes, respectively [5, 6, 10]. A major challenge with the use of IX is the disposal of used regenerating solution which is usually strong saline solution containing the ions removed from water [5, 6]. Other challenges include the need to keep the resin bed free from chemical deposition which may seriously impair performance [5].

#### 1.1.2.7 Membrane filtration processes

Membrane filtration processes (MFPs) are relatively recent addition to the suite of technologies employed for commercial water treatment and it is projected that the role of membrane processes will increase in the future [6, 11]. The advantages of MFPs include simplicity, predictability, scalability, energy and contaminant removal efficiency and limited reliance on chemical except for cleaning purposes [5, 6]. Not only are pathogens excluded, suspended particles, colloidal matter, dissolved molecules and ions may also be effectively removed depending on the selectivity of the membrane process. Furthermore, there is no risk of DBPs. Pressure-driven MFPs including microfiltration (MF), ultrafiltration (UF), nanofiltration (NF) and reverse osmosis (RO) are increasingly employed at commercial scales for the filtration of contaminated water and the treatment of raw water for drinking water production [5]. The pore diameter of MF membranes ranging from about 0.1 µm to 10 µm is suitable for high-flux production of treated water with efficient removal of suspended particles, fines and certain microscopic organisms. The smaller pore size range of UF membranes ranging from about 0.1 µm to 0.01 µm may be employed for the removal of large organic molecules, colloids and smaller microscopic organisms from water [2, 6]. The price for better selectivity is reduced water flux, which is usually addressed by higher

transmembrane pressure to sustain economic filtration rates. MF are often operated commercially in the pressure range of 50 – 200 kPa while the imposed hydrostatic pressure on UF membranes may range from 100 – 500 kPa [2]. The filtration mechanism for MF and UF is simple straining or size exclusion.

Membranes with much smaller pores in the range 2 – 70 Å are categorised as NF membranes and may be operated at pressures above 10 bar [2]. Such membranes can reject divalent ions and many dissolved organic molecules. The surface charge of NF membranes greatly influences the rejection performance of the membrane towards ions. Consequently, the rejection mechanisms for NF membrane include both size exclusion and Donnan exclusion. The latter is the result of the electric potential developed between the membrane surface and the water medium in contact [2]. NF may be used for water softening (removal of divalent ions), nitrate removal and the exclusion of certain organic molecules that would have reacted with chlorine added for disinfection to produce halogenated DBPs. RO involves the use of a thin, dense, selective film with no discernible pore that allows the permeation of water under pressure through a solution-diffusion process [12]. The permeating water molecules is first dissolved in the membrane material and then diffuses through the thin selective side under hydrostatic pressure overcoming the natural osmotic pressure developed between the high salt concentration feed and the low salt concentration permeate. RO is used for water desalination since it can remove most dissolved ions. Dissolved organic molecules are also rejected by RO although some very small uncharged chemical species may pass through a RO membrane [6, 13, 14].

One of the most important challenges with MFPs is fouling, the accumulation and attachment of rejected impurities onto the surface of membrane [2, 6, 15]. The attached impurities may block the pores or selective surfaces of the membrane consequently impairing productivity. In practice, membranes are cleaned regularly to remove foulant and restore performance. Cleaning increases the cost of MFPs as a result of chemical cost and system down time during cleaning. In addition, membrane cleaning may deteriorate the membrane integrity leading to reduced operational lifespan [2]. In recent times, significant research effort has been directed towards producing membranes that are more resistant to fouling

and/or are more easily cleaned when fouled. Much progress has been made in this direction, as well as in improving general membrane operations but much room for development still exist. There is also the pressing need to develop high flux membranes without compromising rejection to meet the growing demand for low-cost, high quality water for domestic and industrial applications. Research in nanotechnology is considered to hold enormous promise in contributing to the resolution of the fouling and the flux enhancement problems of membranes [16, 17].

#### 1.1.2.8. Advanced oxidation processes

Another increasingly important component of modern water treatment is advanced oxidation processes (AOPs). Advanced oxidation is a term used to describe the chemical destruction of contaminants in water and waste streams using chemical radical species such as hydroxyl and sulphate radicals [18, 19]. Advanced oxidation processes are usually designed to either achieve complete destruction of organic or inorganic contaminants or their transformation to products that are more compatible with natural processes. Presently, oxidative radicals for AOPs are commonly produced from the activation of the three common peroxygen compounds, namely, hydrogen peroxide ( $H_2O_2$ ), persulphate ( $S_2O_8^{2-}$ ) and peroxymonosulphate ( $HSO_5^-$ ) [18, 19].

The earliest and the most common AOPs are hydroxyl-radical based [19]. The hydroxyl radical is a non-selective, oxidising agent with standard reduction potential ( $E^\circ$ ) of 2.76 V [18, 20]. Several pilot and full-scale water treatment projects using hydroxyl-radical AOPs have been reported [21]. The reactive radicals may be produced from oxidising agents such  $H_2O_2$  and  $O_3$ , high energy radiation such as ultraviolet (UV) and ultrasonic radiation and transition metal catalysis. The hydroxyl radical aggressively attacks polluting molecules either abstracting hydrogen from saturated organic molecules such as alkane and alcohol or adding itself to unsaturated molecules such as alkene and aromatic compound via their electron rich double bonds [21, 22]. The addition or abstraction process may result in the generation of organic radical species that could maintain a radical chain reaction [21].

Sulphate radical processes are comparatively more recent developments in the field of AOPs [19, 23, 24]. Sulphate radicals are typically generated from the persulphate or the peroxyomonosulphate anion. The persulphate anion is the most reactive species of the three common peroxygen compounds with an  $E^\circ$  of 2.01 V which is slightly less than the 2.07 V for  $O_3$  [20, 25]. The reactive potential of the persulphate anion is greatly enhanced when it is converted to the sulphate radical with an  $E^\circ$  of 2.6 V [18, 20, 23]. Persulphate activation has been achieved by heat, UV and transition metals, high pH and hydrogen peroxide [18, 20, 23]. Interest in persulphate application for wastewater treatment has been increasing rapidly but it still lags behind  $H_2O_2$ -based processes concerning the understanding of reaction mechanisms and effectiveness of activation techniques. In addition, while  $H_2O_2$  and  $O_3$  advanced oxidation processes have been used extensively as pretreatment to membrane filtration, persulphate AOPs have been much less used for this application despite the latter high reactive potential, long shelf-life and relatively low cost [26-28].

#### 1.1.2.9. Combined MFPs and AOPs

Significant synergistic benefits have been reported when AOPs are integrated with MFPs for water treatment [11, 29]. AOPs may be installed as pretreatment processes to mitigate membrane fouling; or as post-treatment processes for the polishing of permeate to remove poorly rejected contaminant or for the detoxification/mineralisation of membrane concentrate [29]. Integration of MFPs and AOPs are also favoured with the view of achieving multiple barrier treatment especially for drinking water production [5]. The complementarity of MFPs and AOPs is a key reason for studying the processes together in this work.

### 1.2. Research statement

This research is aimed at improving the performance of two highly effective water treatment techniques in current use, namely, MFPs and persulphate AOPs, to enhance their capacity to meet the rising global demand for safe and affordable water. Research in MFPs is fairly advanced so that while it remains valuable to explore new concepts to resolve challenges, it is also important to re-assess established concepts for novel developmental opportunities. The impact of the promising field of nanotechnology to advance the effectiveness of MFPs will be

investigated in this work. This study will include an exploration of how nanoparticles interact with membrane to produce functional composite membranes. With suitable modification, iron oxide nanoparticles because of their biocompatibility and affordability will be used as a typical nanoparticle in the study.

The impact of common membrane preparatory procedures are generally overlooked in the search for techniques to enhance the performance of membranes. As mentioned earlier, some unexplored opportunities may exist in these routine procedures. In this study, attention will be given to understanding the effects of two common membrane preparatory protocols, namely, ultrasonication and hydrophilic polymer addition on the performance of the hydrophobic poly (vinylidene fluoride) (PVDF) membranes with or without nanoparticles.

A critical review of the emerging field of AOPs focused on persulphate is proposed. This is to facilitate future development in the area for sustainable water treatment and to enhance integration with MFPs. Controlled experiments on the activation of persulphate by novel phosphate chelated zerovalent iron nanoparticles and commercially available steel wool and carbonyl iron powder is proposed. The activated persulphate is employed for the degradation of hazardous water pollutants including orange G, a typical azo dye, and 1-naphthylamine, a probable carcinogen. The feasibility of utilising waste heat for persulphate activation to treat industrial wastewater and to degrade NOM for drinking water production will be investigated by laboratory scale experiments. Membrane fouling reduction using heat-activated PS will also be evaluated.

### 1.3 Thesis structure

The thesis is divided into ten (10) chapters including this introduction as chapter one. An investigation of the potential benefits and challenges of nanoparticles incorporation into membranes with a focus on desalination application is presented in chapter two. This chapter highlights the fouling and permeability enhancement problems of MFPs, the roles of nanoparticles in resolving these problems and the challenge of nanoparticle aggregations among other difficulties. In chapter three, the effects of two common steps in the production of polymeric

membranes, dope ultrasonication and the addition of a hydrophilic polymer, poly (vinylpyrrolidone) (PVP), in resolving the problem of nanoparticle aggregation in polymeric membranes is investigated. This is followed in chapter four by an exploration of the effects of the often-overlooked polymer dissolution conditions on the performance of the popular poly (vinylidene fluoride) membranes including the impact on fouling reduction. In chapter five, a critical review of the science and sustainability AOPs focused on the commercially important oxidant, persulphate (PS), is presented with a view to complement the performance of MFPs and to provide more viable options for water treatment. A study of PS activation for the degradation of orange G using phosphonic acid stabilised zerovalent iron nanoparticles is presented in chapter six. A similar study using commercially available steel wool and carbonyl iron powder for the degradation of hazardous pollutants including 1-naphthylamine is presented in chapter seven. In chapter eight, heat-activation of PS is explored for pollutant degradation under conditions relevant to the textile industry. Chapter nine looks at the activation of PS in low-energy environment with implication for drinking water production and reduction of membrane fouling. The thesis is concluded in chapter ten with a presentation of the overall implication of the study and suggestions for future studies.

## References

- [1] G.V. James, Water treatment 4ed., Technical Press, United Kingdom, 1971.
- [2] A. Cipollina, G. Micale, L. Rizzuti, Seawater desalination, in: Green Energy and Technology, Springer-Verlag, Heidelberg, 2009.
- [3] M. Duke, D. Zhao, R. Semiat, Functional nanostructured materials and membranes for water treatment, Wiley-VCH, Weinheim, Germany, 2013.
- [4] A.V. Kneese, Water Pollution : Economics Aspects and Research Needs, Taylor and Francis, New York, 2015.
- [5] AWWA, Water Treatment, 4 ed., American Water Works Association, Denver, 2010.
- [6] C. Binnie, M. Kimber, Basic Water Treatment, in, ICE Publishing, London, 2013.

- [7] B. Wu, Y. An, Y. Li, F.S. Wong, Effect of adsorption/coagulation on membrane fouling in microfiltration process post-treating anaerobic digestion effluent, *Desalination*, 242 (2009) 183–192.
- [8] S.T. Summerfelt, Ozonation and UV irradiation—an introduction and examples of current applications, *Aquacultural Engineering*, 28 (2003) 21-36.
- [9] M.J. Sharrer, S.T. Summerfelt, G.L. Bullock, L.E. Gleason, J. Taeuber, Inactivation of bacteria using ultraviolet irradiation in a recirculating salmonid culture system, *Aquacultural Engineering*, 33 (2005) 135-149.
- [10] D.T. Myat, M. Mergen, O. Zhao, M.B. Stewart, J.D. Orbell, T. Merle, J.P. Croue, S. Gray, Effect of IX dosing on polypropylene and PVDF membrane fouling control, *Water Res*, 47 (2013) 3827-3834.
- [11] H.T. Madsen, Membrane Filtration in Water Treatment – Removal of Micropollutants, in: Chemistry of Advanced Environmental Purification Processes of Water, Elsevier B.V., 2014, pp. 199-248.
- [12] R.W. Baker, Membrane technology and applications, 2nd ed., John Wiley and Sons, Ltd, England, 2004.
- [13] T. Fujioka, N. Oshima, R. Suzuki, S.J. Khan, A. Roux, Y. Poussade, J.E. Drewes, L.D. Nghiem, Rejection of small and uncharged chemicals of emerging concern by reverse osmosis membranes: The role of free volume space within the active skin layer, *Separation and Purification Technology*, 116 (2013) 426-432.
- [14] T. Fujioka, S.J. Khan, Y. Poussade, J.E. Drewes, L.D. Nghiem, N-nitrosamine removal by reverse osmosis for indirect potable water reuse – A critical review based on observations from laboratory-, pilot- and full-scale studies, *Separation and Purification Technology*, 98 (2012) 503-515.
- [15] W. Guo, H.H. Ngo, J. Li, A mini-review on membrane fouling, *Bioresource technology*, 122 (2012) 27-34.
- [16] X. Qu, J. Brame, Q. Li, P.J.J. Alvarez, Nanotechnology for a Safe and Sustainable Water Supply: Enabling Integrated Water Treatment and Reuse, *Account of Chemical Research*, 46 (2013) 834 - 843.
- [17] X. Qu, P.J. Alvarez, Q. Li, Applications of nanotechnology in water and wastewater treatment, *Water Research*, 47 (2013) 3931-3946.
- [18] Y. Deng, R. Zhao, Advanced Oxidation Processes (AOPs) in Wastewater Treatment, *Current Pollution Reports*, 1 (2015) 167-176.

- [19] H. Sun, S. Wang, Catalytic oxidation of organic pollutants in aqueous solution using sulfate radicals, *Catalysis*, 27 (2015) 209-247.
- [20] L.R. Bennedsen, In situ chemical oxidation: the mechanisms and applications of chemical oxidants for remediation purposes, in: E. Sogaard (Ed.) *Chemistry of advanced environmental purification processes of water*, Elsevier Science, 2014, pp. 13-74.
- [21] R. Munter, Advanced oxidation processes - current status and prospects, *Proceedings of the Estonian Academy of Science. Chemistry*, 50 (2001) 59–80.
- [22] P. Devi, U. Das, A.K. Dalai, In-situ chemical oxidation: Principle and applications of peroxide and persulfate treatments in wastewater systems, *The Science of the total environment*, 571 (2016) 643-657.
- [23] Y. Deng, C.M. Ezyske, Sulfate radical-advanced oxidation process (SR-AOP) for simultaneous removal of refractory organic contaminants and ammonia in landfill leachate, *Water Res*, 45 (2011) 6189-6194.
- [24] S. Wacławek, H.V. Lutze, K. Grübel, V.V.T. Padil, M. Černík, D.D. Dionysiou, Chemistry of persulfates in water and wastewater treatment: A review, *Chemical Engineering Journal*, 330 (2017) 44-62.
- [25] FMC, Persulfates technical information, in, FMC Corporation, [http://www.peroxychem.com/media/90826/aod\\_brochure\\_persulfate.pdf](http://www.peroxychem.com/media/90826/aod_brochure_persulfate.pdf), 2001.
- [26] X. Zhao, C.S. Yeung, V.M. Dong, Palladium-catalyzed ortho-arylation of o-phenylcarbamates with simple arenes and sodium persulfate, *Journal of American Chemical Society*, 132 (2010) 5837–5844.
- [27] F. Corporation, Persulfates technical information, in: F. Corporation (Ed.), FMC Corporation, 2001.
- [28] T. Zhang, Y. Chen, Y. Wang, J.L. Roux, Y. Yang, J.-P. Croué, Efficient Peroxydisulfate Activation Process Not Relying on Sulfate Radical Generation for Water Pollutant Degradation, *Environmental Science & Technology*, 48 (2014) 5868–5875.
- [29] S.O. Ganiyu, E.D. van Hullebusch, M. Cretin, G. Esposito, M.A. Oturan, Coupling of membrane filtration and advanced oxidation processes for removal of pharmaceutical residues: A critical review, *Separation and Purification Technology*, 156 (2015) 891-914.

## Chapter 2

### **Nanoparticle incorporation into desalination and water treatment membranes - potential advantages and challenges\***

#### **Abstract**

The incorporation of nanoparticles into desalination and water treatment membranes is considered one of the most promising steps towards resolving two of the most important challenges of membranes: the selectivity-permeability tradeoff and the pervasive problem of fouling. The key nanoparticles for the development of next generation high flux, high selectivity membranes are carbon nanotubes, aquaporins and nanozeolites due to their molecular-size channels for superfast transport of water and solutes rejection. However, the economic production and scale up of these nanomaterials whilst retaining stable molecular-level functionalities for membrane applications have remained challenging. Nano-titania is a promising material for antifouling applications with the potential for self-cleaning, foulant degradation, antimicrobial effects and self-wettability modification. However, critical improvements in visible light photocatalysis are necessary to realize these functionalities. Other important membrane-relevant nanoparticles are nano-silver, nano-silica, nano-alumina, nanoclay and iron oxide nanoparticles. This chapter overviews the challenges, properties and prospects of these nano-materials that together constitute an exciting field of fundamental and practical research towards water sustainability.

#### **2.1. Membranes for water treatment: background and motivation for nanoparticle incorporation**

A membrane has been defined as ‘a discrete, thin interface that moderates the permeation of chemical species in contact with it’ [1]. In water treatment and desalination, where the membrane material may be polymeric, ceramic or metallic or a combination of these materials known as a composite membrane, the goal is to hinder the permeation of dissolved, dispersed and/or suspended solutes in the water while the water flows through the membrane. The membrane

\*Published as chapter 7 in Desalination Sustainability - <https://doi.org/10.1016/B978-0-12-809791-5.00007-9>. See the Appendix for list of contributors.

materials may be porous as in microfiltration (MF) and ultrafiltration (UF) membranes where largely size exclusion or molecular sieving under a pressure differential achieves separation. Alternatively, it may be dense as are the reverse osmosis (RO) and forward osmosis (FO) membranes where the separation mechanism is more commonly described by a solution-diffusion process under a pressure or concentration differential. Despite the difference in physical mechanisms, membranes may be conceptualised as composed of a number of capillary tubes per unit membrane area,  $N$ ; with an average diameter,  $d$ . In this simplified conceptual framework, assuming incompressible particles and the absence of pore bridging or clogging, impurities in the feed water larger than the capillary diameter are rejected while those smaller are permeated. It follows then, that the smaller the average capillary diameter, the greater is the membrane rejection. On the other hand, the flux of clean water through the capillary bundle is proportional to the (fourth power of the) average diameter according to the Hagen-Poissueille equation given below (Equation 2.1) [1].

$$J = \frac{N\pi d^4 \Delta P}{128\mu L} \quad 2.1$$

where  $\Delta P$  is the pressure differential,  $L$  is the pore length and  $\mu$  is the water viscosity. Generally, a larger average pore diameter results in greater flux but lower rejection; a smaller average diameter results in reduced water flux but better rejection. This observation is often referred to as the permeability-selectivity tradeoff which is a fundamental challenge in membrane performance improvement.

On the other hand, the greater the membrane rejection, the greater is the concentration of the rejected material in contact with the membrane on the feed side, a phenomenon which is commonly called concentration polarisation. The increased solute concentration may translate to a relative reduction of water concentration in direct contact with the membrane which may imply that less water permeates through the membrane's capillary pores. At the same time, some of the capillary pores may become partly or completely unavailable for water permeation due to solute clogging, a problem that is often aggravated by concentration polarisation. Furthermore, the greater concentration of solute (arising from concentration polarisation) increases the chance of chemical or

physical interaction between the solute and the membrane surface; an interaction that might be detrimental to the membrane filtration performance. The attachment of solute material onto the surface and inside the pores of the membrane, leading to productivity decline with time, is often referred to as membrane fouling. Ensuring concentration polarisation and fouling do not compromise the practical operation of the membrane system constitutes another fundamental challenge inherent in membrane processes.

Since the problems of membrane permeability-selectivity tradeoff, concentration polarisation and fouling are inherent to the membrane process [2], simple solutions to overcome them are not readily available and they have consequently been the subjects of much research over the years. Apparently, relatively more progress has been made in resolving the permeability-selectivity challenge (especially with regards to the application of thin film composite (TFC) technology to RO desalination) than in resolving the fouling problem [3]. However, there is still significant scope for improvement concerning these inherent challenges. Research in nanotechnology has been shown to hold enormous promise in contributing to the resolution of these problems. Aligned carbon nanotube, aquaporin-based biomimetic and thin film nanocomposite membrane nanotechnologies are being promoted as having the greatest promise in the advancement of membrane desalination and water treatment (MDWT) technologies for the future [2]. Nanotechnology has also shown much promise in improving other desirable membrane properties such as chemical, mechanical and thermal stability, which are crucial for membrane application under challenging conditions, as well as in the development of active functionalities such as self-cleaning, contaminant degradation and antimicrobial effects [2, 4]. Active functionalities appear to hold the key to an effective resolution of the elusive problem of membrane fouling.

## 2.2. Nanoparticles and their unique properties

All the promises of nanotechnology in resolving the problems of membrane processes rely on the unique properties of nanoparticles that are distinct from the material bulk properties. A nanoparticle is a material whose external dimensions or internal pore structure, in at least one dimension, is in the size range 1 – 100

nm resulting in unique physical or chemical properties [5]. A particle having all dimensions between 1 – 100 nm is termed a zero dimension nanoparticle. If only two dimensions are in the nano-scale range such as nanotubes or nanorods, they are referred to as a one dimensional nano-material. Materials that are in the nano-scale range only in their thickness, such as thin films, are accordingly referred to as two dimensional nano-structures [5]. Some materials such as bulk zeolites may exhibit a nano-scale dimension only in their internal pore structure though they may also be available as nano-sized crystals. However, a material may need more than one dimension in the 1 – 100 nm range to qualify as a nanoparticle; it must also be observed to exhibit novel phenomena due to its nano-size that are absent in the bulk [5]. The critical nano-size for novel phenomena varies from material to material and from property to property [5]. A material with an active diameter smaller than 1 nm or greater than 100 nm is outside the accepted range for a nanoparticle and is rather often referred to as a cluster (molecule) or a microparticle, respectively [6].

The variation of the intrinsic properties of materials with particle size as exhibited by nanoparticles is attributable to two nanoscale effects. Namely, a smoothly scaling surface/volume ratio effect which reflects the fraction of surface atoms in the nanoparticle in relation to the total atoms present; and a discontinuous quantum effect which indicates the limited spatial confinement of nanoparticles and changes in the shells of delocalised electrons in the nanoparticle due to this confinement [5, 7]. These are described in the following sections as ‘surface effects’ and ‘quantum effects’, respectively.

### 2.2.1. Surface effects

The fraction of surface atoms (ratio of surface area to volume) or dispersion of a spherical particle scales smoothly with the inverse of the diameter or radius since the particle’s surface area and volume are functions of the square and cube of the radius, respectively. Hence the smaller the particle, the greater is the fraction of surface atoms relative to the total atoms, a trend that is observed even for non-spherical materials. A surface atom can differ considerably in its properties from an otherwise similar atom located in the interior of the particle because surface atoms have fewer neighbours, possess unsatisfied bonding potentials, are more

exposed to external interactions and hence are more reactive [5, 7]. As the proportion of the surface atoms increase in a nanoparticle, their contribution to the overall behaviour of the particle becomes considerable. The overall energy of the particle increases as a consequence and its stability declines, resulting in greater chemical activities and the exhibition of unique properties that are not observed for a bulk sample of the same material [8]. An example of a proportionate scaling property due to the surface effect is the trend of the melting point of a solid with respective to the size of the material which follows the Gibbs-Thomson equation [7]:

$$\frac{T_m - T_m^*}{T_m^*} = \frac{2V_{m(l)}\gamma_{sl}}{\Delta H_m r} \quad 2.2$$

where  $T_m$  is the melting point of a particle with radius  $r$ ,  $T_m^*$  is the bulk material melting point,  $V_{m(l)}$  the molar volume of the liquid,  $\gamma_{sl}$  the solid-liquid interfacial tension and  $\Delta H_m$  the bulk latent heat of melting. The equation clearly shows that the melting temperature is directly related to the inverse of the radius of the particle. The dependence of melting point on size is commonly illustrated with gold. As a bulk material, gold melt at 1,337 K but this value gradually reduces as the size of the particle decreases, reaching a value of 600 K at a nanoparticle diameter of 3 nm [5].

### 2.2.2. Quantum effects

Not all size-dependent properties of nanoparticles scale smoothly. Discontinuous changes are explained by the quantum mechanical nature of matter which is related to the discrete electronic energy levels in systems with delocalised electrons and the effects of spatial confinement [5, 7]. The positions of electrons in an atom are restricted to quantised orbitals (energy levels) around the nucleus. The highest energy orbital occupied by an electron(s) in the ground state of an atom is referred to as the valence orbital. The atoms of different materials require different quanta of energy to excite the valence electron(s) to a higher energy level. When atoms are grouped together, their orbitals may combine giving rise to a band structure [7]. At the ground state, the highest energy occupied band is the valence band and the lowest energy unoccupied band is the conduction band and the difference between these two energy levels is called the band or Kubo

gap [7]. The properties of a solid such as conductivity and optical properties are dependent on this energy gap [6]. A band gap is absent in metals but is present in semi-conductors and insulators. Consequently, changes in the band gap have important effects on the properties of a material. Interestingly, such fundamental changes could be effected by a decrease in particle size to specific critical nanoscale dimensions [6, 8].

The energy difference between adjacent energy levels ( $\delta$ ) in a band of a metal is often expressed as the quotient of the highest occupied molecular orbital (HOMO) or Fermi level ( $E_F$ ) and the number of atoms present ( $n$ ) i.e.  $\delta \approx E_F/n$ . For a bulk material, the number of atoms is exceedingly large indicating that the energy gap is negligible so that electrons can move easily from the valence band to the conduction band whenever the thermal energy is greater than the (negligible) energy gap [7, 8]. However, as the number of atoms in the system decrease to a critical nanoscale dimension,  $\delta$  widens and becomes significant resulting in a finite difference between the valence and conduction band indicating a transition from metallic to non-metallic properties. The shrinking size of the nanoparticle and expanding band gap imposes a spatial quantum confinement effect resulting in novel physical and chemical properties. Changes in particle sizes within the nanoscale range for semiconductors such as CdSe have been shown to lead to spectacular photoluminescence due to changes in the band gap [5, 7]. Similar highly tunable optical phenomena have been reported for gold and silver nanoparticles but here the effect is due not to changes in the band gap but to the excitation of the surface free electrons. These electrons experience Plasmon surface resonance, a spatial quantum confinement effect, when the size of the nanoparticle approaches the critical free electron mean free path [5, 7].

The development of superparamagnetism at the nanoscale dimension from otherwise ferromagnetic and ferrimagnetic materials in the bulk is another example of the quantum confinement effect [5]. Due to the thermodynamic drive to reduce internal energy, the magnetisation of bulk magnetic materials are known to spontaneously divide into many small magnetic compartments called domains. The magnetisation within each domain is uniform in direction but distinct from the directions of nearby domains. The equilibrium size of the domains is reached when the energy cost in making new domain walls equals the energy

saved in creating a new domain. However, upon reduction of particle size to a characteristic nanoscale dimension, the energy saved in the formation of domain walls become insignificant and the nanoparticle thereby exists as a single domain, exhibiting the unique property of superparamagnetism [5].

### 2.2.3. Summary of key nanoparticle properties and relevance to membrane technology

The key features of nanoparticles of value to membrane technology include high surface area, increased chemical and physical activity and certain unique properties. The high surface areas of hydrophilic nanoparticles such as nanosilica and nanoalumina are employed to improve the performance of membranes by increasing membrane hydrophilicity. An example of enhanced nanoparticle activity of relevance to membrane processes is the improved biocidal effect that is associated with nanosilver when compared with bulk silver. The former when added to a membrane alleviates the challenging problem of membrane biofouling. Titania nanoparticles benefit from both quantum and surface effects to demonstrate enhanced photocatalysis which is employed for the degradation of attached foulants on the membrane as well as the expression of other active functionalities. Quantum confinement effects and the molecular level smoothness of the pores of carbon nanotubes, aquaporin proteins and nanozeolite crystals are of immense value in the development of high flux membrane for MDWT applications. These unique nanoparticle properties and their applications to membrane technology will be discussed in more detail in the next section.

## 2.3. Nanoparticles for membrane desalination and water treatment

The unique properties of nanoparticles have led to the surge in interest in the development of nanoparticle-based novel applications in many aspects of MDWT processes. Nanoparticles that have attracted significant research interest include carbon nanotubes (CNT), aquaporins and nanozeolites. They are considered the most promising materials for the development of novel and high performance membranes for RO and nanofiltration (NF) desalination and water treatment applications [2]. Other important nanoparticles, especially for MF and UF applications, include nanosilver (nAg), nanotitania ( $n\text{TiO}_2$ ), nanosilica ( $n\text{SiO}_2$ ) and nanoalumina ( $n\text{Al}_2\text{O}_3$ ) [4]. Nanoclay and iron oxide nanoparticles are also

attracting research attention in many MF and UF membrane water treatment applications. The promise and achievements of these nanoparticles in improving MDWT process form the focus of this section as well as the key challenges that must be addressed to realise their full potential.

### 2.3.1. Carbon-nanotubes

Carbon has four valence electrons, which in diamond are hybridised in the  $sp^3$  configuration resulting in the three dimensional tetrahedral structure that gives diamond its unique mechanical strength and electrical insulation. Graphite, on the other hand, exhibits  $sp^2$  hybridisation resulting in hexagonal (honeycomb) sheets joined together by a weak bonding resulting from the free and delocalised  $p_z$  orbitals on each sheet [9]. Due to the delocalisation of the electrons and the weakness of the developed inter-sheet bonds, graphite is electrically conductive and exhibits a lubricating property as graphene sheets can slip relative to each other. A CNT has been described as a cylindrical rolled up graphite sheet(s). Figure 2.1 shows various carbon materials and how they are related. When a CNT consist of a single graphene sheet, it is referred to as single wall CNT (SWCNT) and when it is composed of more than one layer of concentric cylinders held together by van der Waal attractions, it is known as multi-wall CNT (MWCNT). The diameter of a CNT is commonly between 0.8 nm to 20 nm although larger diameters are known; the length however can measure up to several centimetres. Consequently, a CNT is unique as it is both molecular and macroscopic in dimension, making it feasible for molecular properties to be directly available for macroscopic applications [10]. The molecular-macroscopic nature of a CNT is of immense importance in many potential applications deriving from its phenomenal properties. For example, mechanical strength measurements have established that the CNT is one of the strongest materials in existence, stronger than steel, with a modulus of elasticity of about 1 TPa and tensile strength of 100 GPa whilst being extraordinarily flexible. The thermal conductivity of a CNT is also extraordinary, exceeding the value for diamond, and has been given as  $3500 \text{ W m}^{-1} \text{ K}^{-1}$  for individual SWCNT. Furthermore, a CNT can exhibit metallic or semiconducting properties depending on the chirality (the orientation of the honeycomb lattice with respect to the axis of the tube) and the tube's diameter [9-11].

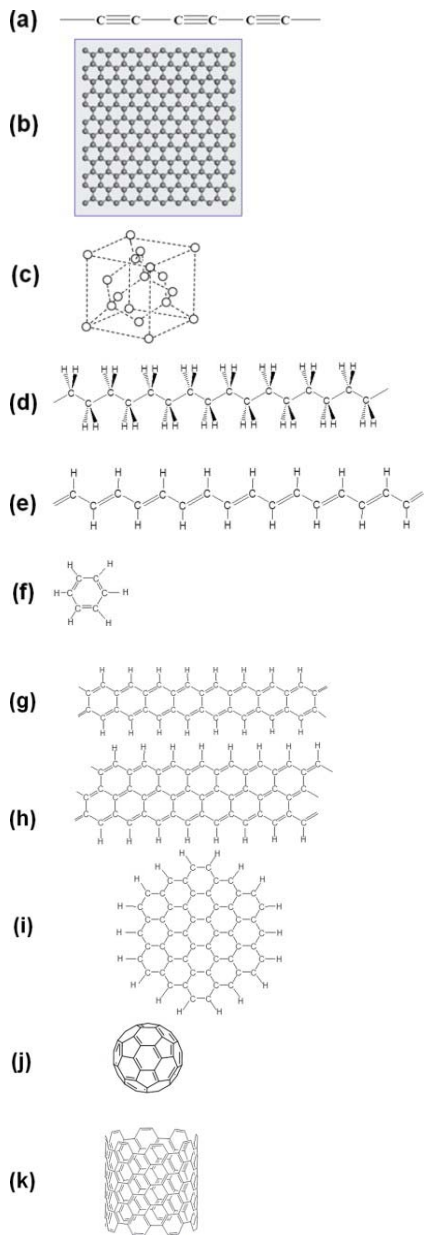


Figure 2.1. Various carbon materials and their relatives: (a) carbyne (polyyne), (b) graphene, (c) diamond, (d) polyethylene, (e) polyacetylene, (f) benzene, (g) polyacene, (h) graphene nanoribbon, (i) nanographene, (j) fullerene and (k) CNT. Reprinted from K. Tanaka, Classification of Carbon, in: K. Tanaka, S. Iijima (Eds.) Carbon Nanotubes and Graphene, pg. 3, Elsevier 2014, with permission from Elsevier.

The perfect planar arrangement of the carbon atoms constituting each graphene sheet provides the CNT with an exceptionally smooth and hydrophobic wall which has resulted in the surprising superfast flow of water due to the almost frictionless transport of water molecules [12-14]. The nanoscale confinement of the CNT channels has been reported to enhance intermolecular interaction between water molecules resulting in even less interaction with the graphitic wall of the CNT further contributing to the near frictionless flow [12, 15]. However, evidence has also been provided to show that the walls of CNT are not always hydrophobic; they may become hydrophilic with decreasing temperature. The liquid-solid interactions in the CNT have also been shown to be pressure dependent. These effects are due to changes in the spatial configurations and orientations of water molecules and the nature and number of free hydrogen bonds in nanoscale confinements [15, 16]. However, predicted rapid water flux through a CNT is not due to hydrophilicity improvement but to the narrowness (confinement effects), smoothness and hydrophobicity of the channels [14, 17]. The flux of water through CNT has been shown experimentally to be more than three orders of magnitude greater than the predictions of Hagen-Poiseuille law for bulk water flow [3, 17]. Like water, hydrated ions can also be transported through a large diameter CNT. However, for a narrow CNT with a diameter less than 0.5 nm, the transport of ion requires the stripping of the hydration layer, thus creating an unfavourable energy barrier for ion transport. For instance, the hydrated ion diameter of  $\text{Na}^+$  has been given as 0.716 nm and that of  $\text{Cl}^-$  0.664 nm [18]. It follows then that these ions would be rejected by a CNT of 0.5 nm. Even though energy is also required to break down hydrogen bonds for water to enter such a narrow CNT in single file, the stability of the water chain in the hydrophobic channel minimises the energy barrier [14, 19], providing for rapid transport of water but the complete rejection of hydrated ions. These findings suggest that small diameter CNT is a very promising material for the development of low energy, high flux membrane desalination technology for sea and brackish water [12, 13].

The charge configuration on a CNT has been shown to result in interesting flux and selectivity properties. A single external charge at a certain critical distance from the SWCNT has been reported to create a tunable influence on the

permeation of water [16] while ions were reportedly excluded and water flux enhanced when the CNTs were alternatively electrostatically charged [12]. The functionalisation of CNT tips with charged chemical groups has been reported to improve rejection of ions through electrostatic and steric exclusion [12, 13, 16, 19]. Such a gating system has been shown to allow for the use of a relatively large diameter CNT for ion rejection [19]. The potential of very high water permeability alongside very high solute selectivity for CNTs is regarded as an avenue to extend beyond the permeability-selectivity tradeoff upper boundary inherent in membrane processes as discussed earlier.

Besides selectivity and permeability, the incorporation of CNTs in membrane processes promises many other important benefits of which fouling resistance is one. CNTs possess cytotoxic properties which are valuable in the prevention of biofouling, one of the most significant problems in MDWT processes [12, 13, 20]. The mechanism of the CNT cytotoxic effect has been proposed to involve disruption of the microbial cell membrane and oxidative stress arising from the CNT's electronic configuration [2, 21]. A CNT can be readily functionalised through the generation or attachment of chemical groups such as hydroxyl, carboxylic and other hydrophilic moieties that aids in the reduction of fouling [22, 23]. The deposition or incorporation of functional nanoparticle such as Ag and TiO<sub>2</sub> on a CNT has been reported to extend the reactive properties in membrane processes [13, 24, 25]. The extraordinary mechanical strength and the high aspect ratio of CNTs have also been recognised as useful for the production of high-strength membrane suitable for application in challenging conditions. Such membranes are expected to withstand high pressure without unfavourable permeability loss and resist irreversible wearing arising from abrasive material in feed water during the long operation of a full scale membrane installation [26]. Majeed et al reported a 36% increase in compaction resistance and over 97% increase in tensile strength when 2% CNT was blended with polyacrylonitrile in the production of a mixed matrix membrane (MMM) [27].

CNTs for desalination and water treatment are available either as vertically aligned (VA) CNTs or as MMM [13]. VACNTs require an orderly arrangement of CNTs such that all the nanotubes point and open in the same direction. Filler materials impermeable to water usually hold the arranged CNTs together. The

open CNTs are arranged parallel to the direction of feed flow so that permeation is directed through the nanochannels. This arrangement ensures that the maximum flux capacity of the CNTs is harnessed. VACNTs may be produced by growing CNT forests on suitable substrates after conditioning and activation. The interstitial spaces between CNTs are then filled with filler materials to exclude water permeation except through the nanotubes. Holt et al [17] reported the successful fabrication of VACNT membrane with superfast water transport by growing VACNTs on a silicon chip and applying silicon nitride ( $\text{Si}_3\text{N}_4$ ) as filler material. Ion milling and reactive ion etching were applied to remove excess fillers and open up the CNTs respectively. Du et al [15] suggested the use of superlong (7 mm) CNTs for the production of VACNT with epoxy resin as filler material demonstrating a simple procedure for the removal of excess filler and nanotube mouth opening by cutting with a knife. They showed that while water flux was superfast; the flux of ethanol was much lower due to a possible clustering of ethanol molecules in the carbon tubes.

VACNTs have also been produced by orienting CNTs in either an electrical or magnetic field. In one of such techniques, magnetic field alignment of CNTs was achieved through the help of liquid crystal mesophase forming cylindrical micelles around the nanotubes [28]. The mesophase contained monomers which were polymerised to fix the orientation of the CNTs after the removal of the orienting magnetic field. A simple filtration procedure for producing VACNTs has also been reported whereby dispersed CNTs were filtered through a polymeric membrane such that some of the nanotubes penetrated the membrane and were fixed within the pores [16]. Since the membrane pore size can only allow the entry of CNTs in the vertical position, this method is a simple approach for vertical alignment of the nanotubes. However, the density of the CNTs may be much lower than is achievable in other VACNTs techniques.

The fabrication of CNT MMMs is much simpler and cheaper and usually involves the blending of certain amounts of CNTs either as a powder or as functionalised dispersions with a suitable polymer material. Polymers such as poly(tetrafluoroethylene), polysulfone and other polymers used for the production of water permeable membranes are commonly used as matrix materials [16, 29]. The blend is formed into a membrane following one of the usual polymeric

membrane production routes such as non-solvent induced phase inversion [30]. Consequently, in MMMs, the CNTs are oriented randomly with a limited amount of the nanotubes transporting water directly through their internal cavities. However, several experiments have shown that even at small functionalised CNT concentrations, appreciable water permeability and other filtration performance improvement could be achieved [22, 23, 27, 29, 31, 32]. A fraction of the water transportation enhancement is derived from flux through voids or defects existing between the polymeric matrix and the nanotubes as well as possible water transportation on the external surface of CNTs [12].

Brady-Estevez et al [33] reported a different kind of composite membrane where the CNTs were deposited on the surface of a polymer membrane and held together by van der Waal forces rather than dispersed within the polymer support. The authors showed that an effective water filter against bacteria and viruses could be produced by simply depositing bundles of SWCNT on a PVDF microfiltration membrane. Bacteria deactivation was reported and the authors suggested that the deposition of the nanofibres on a ceramic microfiltration membrane would allow the production of a re-generable low pressure filter suitable for point of use application. A similar kind of membrane, but this time without any polymeric membrane support, was reported by Dumee et al [34] for membrane distillation (MD) water desalination. The self-supporting bundles of CNTs were held together only by van der Waal forces and are known as Bucky-paper with very favourable properties for MD application such as high hydrophobicity (contact angles measuring up to 113 °) and high porosity (as much as 90%). In a direct contact MD process, the authors reported 99% salt rejection using this membrane at a flux rate of  $\sim 12 \text{ kgm}^{-2} \text{ h}^{-1}$  and a water vapour partial pressure difference of 22.7 kPa.

Despite the promises of CNT technology in membrane desalination and water treatment, there are still many unresolved challenges. One of the most important of these is the difficulty in producing homogenous CNTs in commercial quantity [12, 13]. The selectivity of a membrane is crucial to its use in membrane processes, unfortunately CNTs produced with the more common chemical vapour deposition (CVD) technology usually have variable diameters. Current techniques to separate out small diameter tubes have not been economically successful,

preventing the experimental realisation of the high salt rejections required for practical desalination using high flux VACNTs [3, 19]. A novel template bottom-up approach promises to overcome the problem of variable diameter [35] but the technique is still at an early stage and may not be suitable for low cost production of CNT suitable for desalination applications [13]. Apart from the general challenge of producing uniform diameter CNTs, there is the specific problem of producing small diameter MWCNTs for desalination applications. SWCNTs that are small enough to reject ions are available for desalination applications but they are much more expensive [10, 13] and are more challenging to handle in making VACNT membranes [17].

Furthermore, scale up of VACNTs still poses some challenges especially when the CNT forests are grown on chips [19]. Complete sealing of the interstitial spaces between the aligned nanotubes is still challenging, and this complicates the production process and increases cost [13]. Defects in the sealing of the interstitial spaces impair the selectivity of the membrane. There is also the lack of experimental data on the performance of a fully functional CNT system on a scale and at conditions practical to membrane desalination leaving outstanding questions such as the extent of fouling at high permeation flux supposing such a flow rate is realised [3]. Other uncertainties include health concerns and the environmental implications of a widespread application of CNT water desalination technology [12]. This later concern is compounded by the exceptional adsorptive potential of CNTs for heavy metals, their relative inertness and their well proven cytotoxic effects.

From this brief overview, it has been concluded that CNTs have enormous potential in resolving the permeability-selectivity tradeoff boundary problem and to contribute significantly towards improving membrane fouling resistance. However, major hurdles remain to be resolved including making low-cost, small-diameter CNTs, and assembling the nanotubes into compact and scalable VACNTs membranes for high flux applications. These problems call for ongoing innovation and creativity. The development of a viable VACNT based membrane may allow MDWT applications to venture into even more challenging conditions supported by the potentially superior mechanical and thermal stability of VACNT membranes.

### 2.3.2. Aquaporin

The membranes of many living cells, in simple terms, consist of a lipid bilayer that provides an efficient barrier between the content of the cell and the surroundings by restricting the flow of water and solutes into and out of the cell. The basic makeup of a lipid bilayer is two layers of lipid molecules arranged such that the hydrophilic heads are directed outward, forming the boundaries of the barrier, while the hydrophobic tails are directed towards the middle, forming the hydrophobic interior [36]. For many years, scientists have been bewildered by the mechanism of water transport across this impermeable barrier. Diffusion through the cell membrane has always been considered but that was thought insufficient to account for the volume and efficiency of water transport needed for the rapid physiological processes taking place in the cells of many plants and animals [37, 38]. Peter Agre and his co-workers in the discovery and characterisation of aquaporin addressed this confusion in 1992 [37, 39].

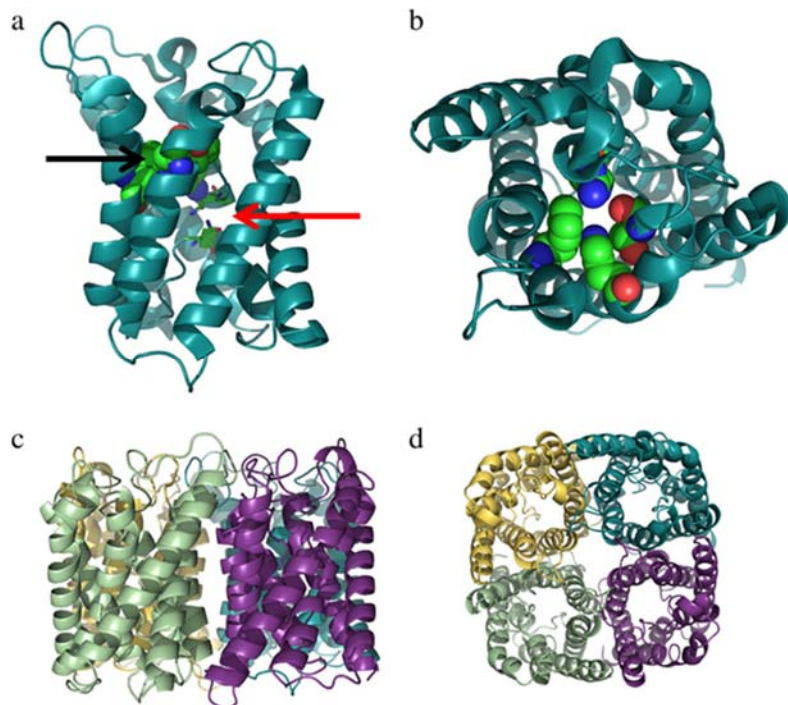


Figure 2.2. Aquaporin protein structure. (a): Sideview of *Escherichia coli* aquaporin-Z (AqpZ) monomer. Protein backbone (deep teal) with the two terminal asparagines from the NPA motifs shown in stick representation (red arrow) and the ar/R selectivity filter residues shown in spacefill representation (black arrow). For stick and spacefill representations atoms are colored as carbon (green), oxygen (red) and nitrogen (blue). (b): Top view illustrating the selectivity filter (or constriction site) created by the four amino acids: F43, H174, R189 and T183. (c-d): Side and top view of the tetrameric AqpZ complex with the four monomers shown in deep teal, violet purple, pale green, and yellow. All renderings were generated using PyMol 1.5.0.2 using AqpZ PDB coordinates 2ABM. Reprinted from C.Y. Tang, Y. Zhao, R. Wang, C. Hélix-Nielsen, A.G. Fane, Desalination by biomimetic aquaporin membranes: Review of status and prospects, Desalination, 308, pg. 35, 2013, with permission from Elsevier.

Aquaporins are pore forming proteins found on the cell membrane of many biological organisms (eubacteria, archaea and eukaryotes) and are responsible for the efficient osmotic-driven transportation of water with a remarkably efficient solute rejection [37, 40]. Similar pore forming proteins, called aquaglyceroporins,

with the capability of permeating glycerol and other small solutes, in addition to water, have been isolated from many single and multi-cell organisms [37, 41]. Aquaporins are homotetramers i.e. they are formed by the self-assembly of four identical protein subunits or monomers into an hour glass structure, with each monomer creating a pore, permeable to water in single file but restricting the permeation of protons, ions and other solutes [37, 39, 42]. The solute restriction capability of aquaporin arises from two constriction sites. One of the two regions of selectivity is formed by two asparagine-proline-alanine (NPA) motifs located on the end of two half helices and are known to provide electrostatic barrier credited for the exclusion of protons [41]. The other constriction zone is the aromatic/arginine (ar/R) filter which constitutes the narrowest part of the channel, measuring only 0.28 nm at this point, for efficient size and hydrophobicity selectivity [37, 41, 43] (see Fig. 2.2).

Since the discovery of the protein water channels, their unique properties have intrigued researchers in many fields spurring intense research efforts to understand the structure and properties of these proteins and to harness them for many applications including MDWT applications. For MDWT applications of aquaporins, the first challenge is the production of the stabilised aquaporin protein. The second major step is the reconstitution of the protein in a lipid bilayer (liposome) to form a proteoliposome. The third is the incorporation of the proteoliposome into a suitable support framework to form a robust composite membrane for MDWT applications [44, 45]. Since aquaporin is expressed in many biological cells, the protein has been harvested and purified directly from these cells [38]. However, the density of membrane protein in natural cells is so small that only very small amounts can be produced under any given condition [40]. Consequently, innovative techniques to induce overexpression of membrane proteins in simple cells such as yeast and *E. coli* with rapid replicative capability have been developed to enhance the production [38, 40, 46], purification and solubilisation of aquaporins in detergent - ready for reconstitution. Alternative cell-free methods for potential large-scale production of functional membrane proteins have attracted a lot of attention [47-49]. One of the interesting benefits of this technique is the potential to directly produce large amount of aquaporins solubilised and stabilised in detergent.

After production, solubilisation in a suitable detergent to prevent aggregation and precipitation is usually needed to keep the protein viable for reconstitution into a suitable synthetic liposome, which is the second step towards producing aquaporin-based membrane for MDWT [38]. Membrane protein reconstitution in a liposome is intended to provide the extracted aquaporin protein a synthetic functional environment similar to the natural phospholipid bilayer that constitutes the membrane of many living cells [46]. Self-assembled lipid vesicles have been used as synthetic liposomes for reconstitution of aquaporin. A commonly used lipid for this purpose is 1,2-diphytanoyl-sn-glycero-3-phosphocholine (DPhPC) which is known to support the correct folding of membrane proteins when reconstituted [50]. Unfortunately, lipids are too unstable for desalination application. Hence, there is need to source materials that can form lipid-like bilayers that can sustain the activity of aquaporin but is less biodegradable [51]. Tri block copolymers (BCP) such as polymethyloxazoline-polydimethylsilane-polymethyloxazoline (PMOXA-PDMS-PMOXA) have been shown to be such a material [50]. BCP has the additional benefit that it can be tailored for specific additional functionalities such as attaching a polymerisable group to provide even better physical support for membrane proteins without diminishing protein activity [52]. A reconstituted aquaporin in liposome or BCP bilayer (polymersome) is called a proteoliposome or proteopolymersome [36, 52]. A typical scheme for making such a system involves dissolving lipid or polymer in suitable organic solvent; evaporating the organic solvent and hydrating the lipid or polymer left behind to give a vesicle solution; and then adding detergent solubilised aquaporin to the vesicle solution. The proteins are then incorporated into the vesicle upon detergent removal, usually by means of biobeads [46, 51, 52].

The final stage in the production of an aquaporin-based biomimetic membrane is the incorporation of the proteopolymersome in a suitable support framework. Researchers attempting to produce biomimetic membranes for water treatment have generally followed one of two schemes in fabricating supported proteopolymersome - resulting in two basic kinds of supported biomimetic membranes, namely, supported membrane layer (SML) and vesicle encapsulated membrane (VEM) [45], as illustrated in Fig. 2.3. The SML is produced by the surface deposition of proteopolymersomes as vesicles or other

configurations onto a porous support to form a uniform flat layer of supported aquaporin-incorporated polymer bilayer. In this design, the proteopolymersomes form the top surface of the biomimetic composite membrane and are in direct contact with the feed stream. Recently, this method was adopted by Zhong et al [52] to produce a aquaporin-based biomimetic membrane for nanofiltration (NF).

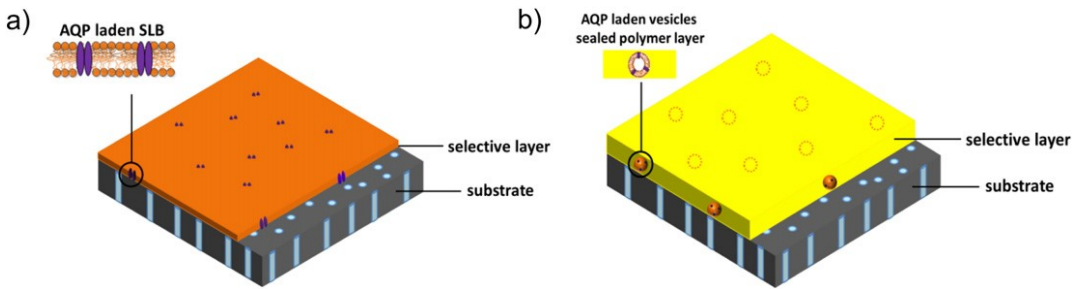


Figure 2.3. Schematic presentation of aquaporin (AQP) laden membranes (a): Supported membrane layer (SML) where AQPs (purple) is embedded in a flat bilayer (orange) deposited onto a porous support (gray). (b): and AQP laden vesicles encapsulated membrane (VEM) where vesicles (orange) are immobilized in a polymer layer (yellow) on a porous support substrate (gray). Reprinted from C. Tang, Z. Wang, I. Petrinić, A.G. Fane, C. Hélix-Nielsen, Biomimetic aquaporin membranes coming of age, Desalination, 368, pg. 94, 2015 with permission from Elsevier.

The authors deposited polymerizable vesicle proteopolymersomes onto a silanised cellulose acetate membrane to produce a hybrid NF membrane with enhanced water permeability and salt rejection when compared to an unmodified cellulose acetate membrane. Upon deposition, the amphiphilic triblock copolymer with polymerizable methacrylate end-groups was cross-linked by UV irradiation to provide suitable physical support without significantly impairing the activity of the protein. The reported 30% salt rejection was good enough for a NF process but not for desalination that is classically performed by RO. Wang et al [46] described the synthesis of a biomimetic membrane using polycarbonate tracked-etched (PTCE) as support for the vesicle proteopolymersomes. The PTCE was

first covered with a gold coating, after which the gold surface was modified with photo-reactive acrylate functional groups. Pressure was applied to force the vesicle into the pores of the porous support to close them up to flux. Thereafter the deformed vesicles were polymerised by UV irradiation leading to vesicle rupture and fusion and the formation of a uniform selective layer. The authors tested their biomimetic membrane for forward osmosis (FO) and reported salt rejections of more than 98.5% for all cases tested. The advantage of SML is that aquaporin's permeability and selectivity may be more fully harnessed due to the protein unhindered contact with the feed. The challenges include the difficulty in synthesising membrane-scale defect-free polymersome to provide a completely impermeable surface between the aquaporins; and the stability problem that might arise from the direct interaction between the feed and the delicate proteopolymersomes under real MDWT conditions.

The VEM method involves the immobilisation of the proteopolymersome vesicles within the matrix of a permeable polymer layer. Zhao et al [53] recently demonstrated the application of this method for the synthesis of a high performance biomimetic membrane where the vesicles were incorporated into the thin selective layer of a TFN membrane. The authors claimed the synthesis of a robust and viable aquaporin-based desalination membrane with an enhanced water flux when compared with commercial brackish and seawater desalination membranes, while showing comparable salt rejection of 97%. The aquaporins were incorporated into an amphiphilic lipid (1,2-dioleoyl-sn-glycero-3-phosphocholine) bilayer and then added to m-phenylene-diamine aqueous solution for interfacial polymerisation to produce an aquaporin-based TFN polyamide membrane. The produced biomimetic membrane was found to be stable under RO conditions (subjected to a pressure of up to 10 bar), showing that the proteoliposomes were well supported by the polyamide matrix. The advantages of the VEM method include better protection for membrane proteins, as the proteins are shielded from direct contact with the feed and have greater prospect for scale up since it closely follows the standard TFN fabrication procedure. Disadvantages of this method include possible deactivation of some membrane protein by being immobilised within a polymer matrix and the

additional resistance to water flux arising from the double passes of water through the polymer matrix before and after permeation through aquaporins.

Recent developments have shown the great potential of aquaporin-based biomimetic membranes to serve as the next generation of high performance membrane for MDWT applications. However, a number of challenges remain unresolved across every segment of the technology. Firstly, large-scale cost effective production of aquaporin proteins is still unrealised even though much progress have been made towards its achievement [44, 45]. Until this is attained, economically, the aquaporin-based biomimetic membrane may not compare favourably with conventional MDWT technologies. Secondly, current technologies for the incorporation of proteopolymersomes into a robust support still present important challenges for upscaling and the maintenance of the activity of membrane proteins, due to limited fundamental and experiential knowledge of protein-support interactions [44]. Thirdly, the long term viability of incorporated proteins and polymers under practical MDWT conditions of high pressure, salinity, fouling and cleaning cycles is still unknown [36, 51]. It is worth mentioning at this point that the flux enhancement observed for current aquaporin-based membranes is still significantly far below the orders of magnitude improvement predicted by computer simulation and exhibited by living cells. The use of synthetic lipid-like materials such as BCP and the development of synthetic self-assembly water channels along with advancements in supramolecular chemistry, have great potential in resolving some of the identified challenges [36, 51]. Biomimetic membranes have an interesting and promising prospect but much work is still required to realise its enormous potential.

### 2.3.3. Nanozeolites

Zeolites are three dimensional aluminosilicate tetrahedral crystalline networks with molecular lattice openings containing water molecules and cations. The cations in natural or synthesised zeolites are group I and II elements but because they are often mobile and exchangeable, they could be replaced by other polyvalent ions. Some zeolites could be dehydrated of their water of crystallisation and/or their cations exchanged, without losing their original structure. This gives rise to molecular pores and cavities functioning as molecular

sieves and/or ion exchange surfaces that lend themselves to many important applications [54-56]. Ammonium or alkyammonium ions may replace metallic cations in the zeolitic network, where their relative large sizes are known to constrain the structure of the zeolites to specific lattice networks and cavity configurations and are thereby called structure directing agents (SDA) or templates [55, 56]. In the zeolite crystal, all the oxygen atoms positioned at the end of regular tetrahedra are shared between Al and Si atoms, which are centred in separate tetrahedra. Since Al has a valence electron of three, the sharing of four oxygen atoms with Si in neighbouring tetrahedra results in one negative charge for each Al tetrahedron. Al is therefore responsible for the negative charge of the zeolite framework. Consequently, the greater the proportion of Al in a zeolite network, the greater is the structural negative charge, which must be balanced by cations. It has also been established that the hydrophilicity of zeolite crystals correlates positively with the amount of Al. Si in the zeolites may be replaced by Ge or P while Ga may take the place of Al and this may result in major structural changes [55]. From the foregoing, it may be appreciated that zeolites lends themselves to a significant degree of tailoring relevant to many important applications.

Due to their molecular cavities, negative surface charge and superhydrophilicity, zeolites have found many important applications in MDWT. Simulation results using ZK-4 zeolite with crystalline voids of 0.42 nm showed 100% rejection of  $\text{Na}^+$ . This is because the size of the void was much smaller than the diameter of hydrated  $\text{Na}^+$  which is given as 0.716 nm [18, 55, 57]. As a consequence of this result and other similar ones, there has been a lot of interest in the development of zeolite based membranes for desalination. Zeolite membranes for water treatment are often produced by the composite membrane preparation method. This involves the growth of a very thin layer of zeolite crystals on porous support materials such as alumina, zirconia, stainless steel and carbon. The zeolite layer may be produced by a hydrothermal process from a precursor solution or gel on the porous support - a method called direct in situ crystallisation. When crystals are produced from solution, it is often necessary to direct the zeolite network to specific structures by incorporating SDAs. However, due to the size of the SDA, there is need to remove it after crystallisation to open up the zeolite pores for

water permeation, a procedure that may unfortunately result in cracking of the zeolite layer. To minimise layer cracking, an alternative method called seeded secondary growth has been developed. This may involve directing the structure of the zeolite network without SDA using nano-sized zeolite seeds that are deposited on the support material, upon which the precursor solution is spread before subjecting the system to hydrothermal crystallisation [56, 58]. The use of microwaves as a heat source for the synthesis of zeolite membranes has been shown to be a very efficient means of producing different types of zeolites in less time. Moreover, microwave synthesis is also known to influence the particle size and properties of the zeolite layer resulting in enhanced water treatment capability [56].

Zhu and co-workers reported an experimental study of MFI-type zeolites with Si/Al ratios varying from 30 to >1000 using X-ray diffraction (XRD) and positron annihilation lifetime spectroscopy (PALS) [57]. They showed that in addition to the regular intracrystalline zeolitic channels between 0.27 and 0.36 nm in diameter, there also exist intercrystalline microporous and mesoporous voids and defects measuring about 1.1 nm and 8 nm respectively. Intercrystalline defects may result from insufficient intergrowth of crystals or from structural strain arising from thermal removal of template or complete material de-watering and may significantly affect the performance of zeolitic membranes for desalination applications. The study showed that increasing the concentration of alumina decreased the volume of the microporous channels, suggesting that this parameter may be used for the design of zeolitic membranes for specific MDWT applications. Other studies have shown that the adsorption of certain molecules such as p-xylene and water could lead to the expansion or contraction of zeolite crystals resulting in important changes to the size and permeability of the zeolitic pores [58-60]. Zeolite membrane permeability can also be influenced by the presence of impurities [58]. Fig. 2.4 is an illustration of some of the possible variations in zeolite membranes porous structures.

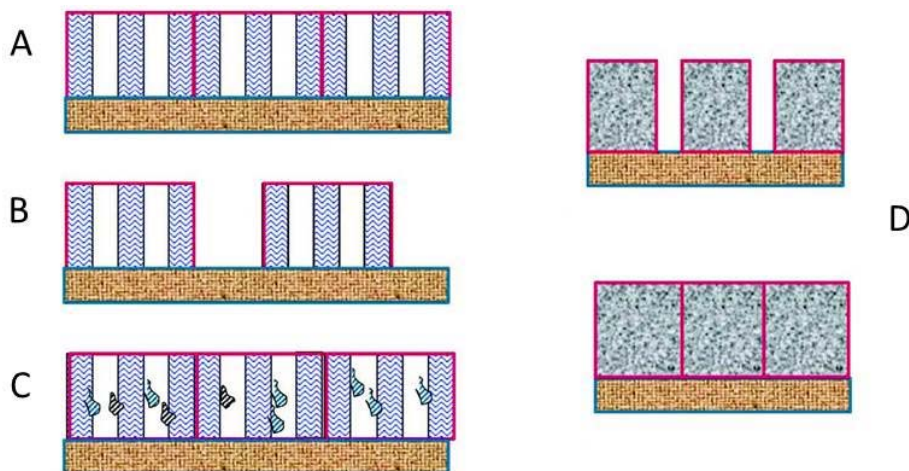


Figure 2.4. Schematic showing three types of microstructure of a high quality polycrystalline zeolite membrane: (a) perfect membranes without non-zeolitic pores,(b) membrane with microporous intercrystalline gaps or non-zeolitic pores, (c) membranes with impurity trapped in the zeolitic pores; and (d)schematic showing adsorption induced crystal expansion to seal the intercrystalline gaps of zeolite membrane. Reprinted from Y.S. Lin, M.C. Duke, Recent progress in polycrystalline zeolite membrane research, Current Opinion in Chemical Engineering, 2, pg. 211, 2013, with permission from Elsevier.

Zhu and co-workers [57, 61] demonstrated that the exposure of MFI-type zeolites to seawater and ionic solutions could result in complex interactions with ion exchange and crystal expansion. Micropores were observed to decrease while mesopores increased upon exposure to ionic solutions. Despite these observed interactions, MFI-type zeolite membranes have been successfully used for the desalination of saline recycled waste water, without costly pretreatment that would have been considered a necessity if polymeric membranes were to be used [62]. The membranes showed good resistance to organic fouling and performance was not significantly affected when the membrane was subjected to a strong hypochlorite solution for 7 days. This demonstrates the superior stability of zeolite membranes when operating under harsh process conditions.

A typical experimental set-up using an MFI-type zeolite with a pore diameter of 0.56 nm, prepared on an alumina support, showed a salt rejection of 76.7% and

a water flux of  $0.112 \text{ kg m}^{-2} \text{ h}^{-1}$ , when exposed to a single NaCl feed solution at 2.07 MPa pressure [63]. For a complex feed solution with multiple cations, the  $\text{Na}^+$  rejection reduced to 58%. Considering that the zeolitic pores are smaller than the hydrated ions, the limited ion rejection may indicate the presence of intercrystalline micropores and mesopores, as discussed earlier, or it may be indicative of structural failures and defects in the zeolite layer. Higher salt rejections have been achieved for zeolite membranes by eliminating SDA in the membrane synthesis process to minimise crystal defects and by increasing the concentration of Al, which is associated with higher surface negative charge, hydrophilicity and decreasing concentration of micropores. However, the production of defect-free zeolite film is still challenging and achieved water flux in RO applications is still lower than what is obtainable using polymeric membranes [56, 58, 62]. In addition, zeolite membranes are currently produced via batch processes which are expensive when compared to the more cost-effective continuous fabrication process employed for polymeric membranes [58].

Jeong et al [64] first suggested the incorporation of nanosized zeolite crystals into the polyamide layer of a TFC membrane to give a novel thin film nanocomposite membrane (TFN). This was intended to exploit the molecular water permeating channels, superhydrophilicity and tunable surface negative charges of zeolites in combination with the processibility and good salt rejections of polyamide membranes. The authors proposed that the nanozeolites distributed within the polyamide layer would provide a preferential flow path for water molecules while preventing the passage of hydrated ions as a consequence of both steric and Donnan exclusion arising from the negativity and nanoscale dimensions of the zeolitic channels [64]. Whilst less chemically stable, the polymer matrix eliminates the need to employ large scale defect free zeolite crystal films, which is often more challenging to produce [58]. Furthermore, the good rejection of the polymer ensures that any defect in the zeolite crystals is contained and does not impair the membrane rejection.

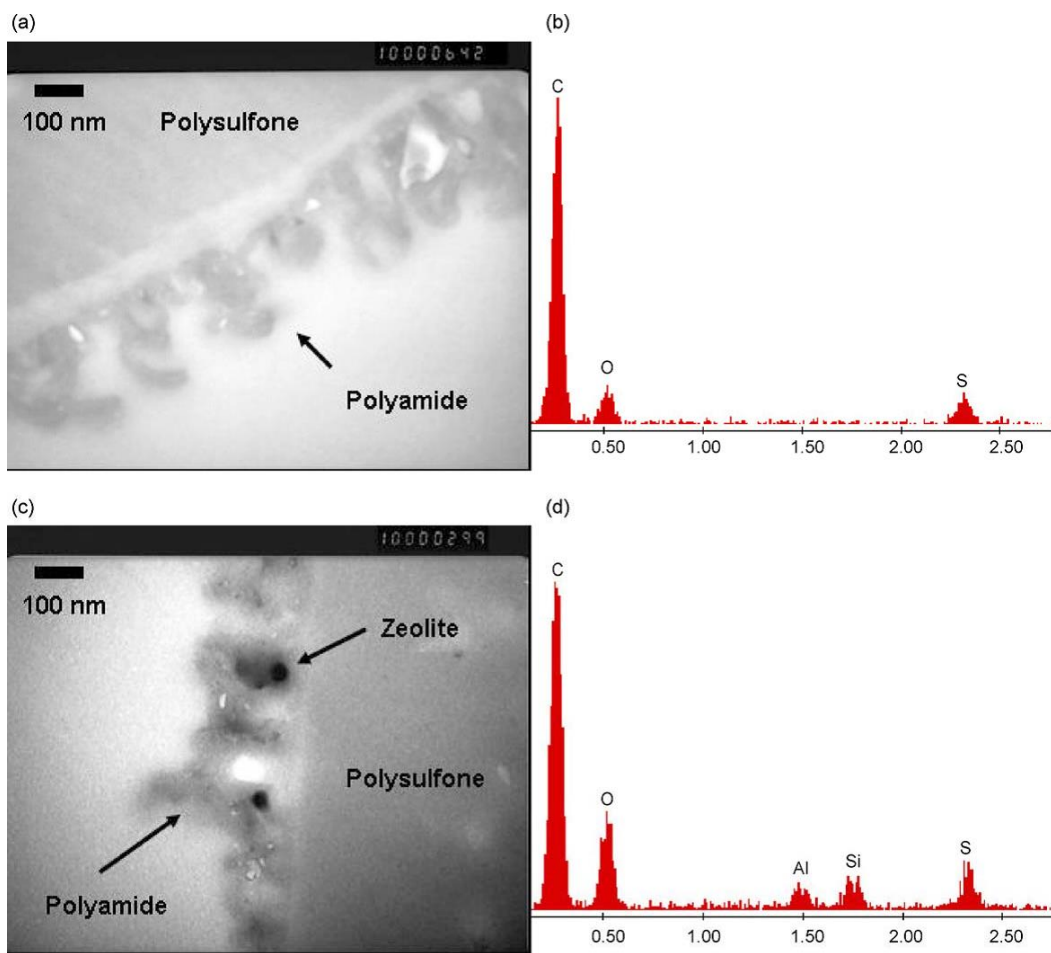


Figure 2.5. Characterization of hand-cast thin film properties by TEM and EDX for (a–b) pure polyamide membrane and (c–d) nanocomposite membrane. Magnification is 100,000 $\times$  in TEM images. Reprinted from B.-H. Jeong, E.M.V. Hoek, Y. Yan, A. Subramani, X. Huang, G. Hurwitz, A.K. Ghosh, A. Jawor, Interfacial polymerization of thin film nanocomposites: A new concept for reverse osmosis membranes, Journal of Membrane Science, 294, pg. 4, 2007 with permission from Elsevier.

Jeong and co-workers reported the synthesis of NaA zeolite nanoparticles by a hydrothermal process that employed an organic template (tetramethylammonium hydroxide). The pore-filled, as-produced, zeolite nanoparticles, because of the presence of the organic template, were subjected to calcination in air to open up the pore cavity by combusting the template. This process was assisted by a polyacrylamide hydrogel network to prevent nanoparticle aggregation during calcination, as suggested by Wang et al [65]. The zeolite nanoparticles were

dispersed in trimesoyl chloride (TMC) hexane solution via sonication and thereafter employed in interfacial polymerisation on a polysulfone support with m-phenylenediamine (MPD) to give a TFN NaA zeolite polyamide membrane. The novel zeolite TFN was shown to exhibit higher hydrophilicity, increased negative charge and improved surface smoothness, resulting in an almost doubling of the water permeability at comparable rejection with respect to pure polyamide TFC. Fig. 2.5 shows TEM images and EDX elemental analysis of the synthesised pure polyamide and zeolite nanocomposite membranes.

A number of research publications were directed towards the optimisation of zeolite TFN for enhanced stable desalination applications. Kong et al [66] showed that the direct deposition of zeolite nanoparticles onto an MPD-covered polysulfone support (called ‘pre-seeding’), before applying TMC for interfacial polymerisation, ensures that zeolite nanoparticles are well anchored but not completely submerged within the polyamide layer. This produces membranes with double the permeability, reaching  $5.8 \times 10^{-12} \text{ m Pa}^{-1} \text{ s}^{-1}$ , and a slight (1%) increase in solute rejection when compared to the membrane produced without pre-seeding. Fathizadeh et al [67] recently reported that while increasing the concentration of NaX nanozeolite fillers led to improvement in water permeability, without impairing rejection, increasing the concentration of monomers led to a water permeability increase at the cost of rejection. Lind et al [68] showed that the permeability, selectivity, morphology and surface of a TFN membrane could be tailored by the incorporation of different sizes of zeolite nanoparticles. They reported that smaller zeolite nanoparticles produced better permeability improvement and enhanced the polymer matrix surface chemistry and morphology. A recent study by Pendergast et al [69] showed that the addition of zeolite and silica nanoparticles to a polyamide TFC membrane improved compaction resistance in addition to permeability enhancement. The addition of zeolite nanoparticles to a polyamide TFN membrane designed for FO was also reported to result in up to 50% improvement in flux [70]. Flux performance and chlorine resistance improvement was also recorded for non-polyamide RO membranes such as those made from sulfonated poly(arylene ether sulfone) containing amino groups when zeolite nanoparticles were incorporated [71].

Deriving from the original work by Hoek and his group [64] and other subsequent developments and optimisations, NanoH<sub>2</sub>O (now LG Chem) took up the commercialisation of the zeolite TFN membrane for seawater RO (SWRO) applications [72]. This is considered one of the success stories in membrane performance enhancement using nanotechnology. However, the flux improvement derivable from nanozeolite-based TFN membrane bears no comparison to the order of magnitude flux enhancement that is promised by emerging materials (e.g. VACNT). The limitations of nanozeolite-based TFN membrane is common to all MMM technologies; namely, limited water channel alignment and additional flow resistance imposed by the polymer matrix. There is a limited possibility that the performance of current nanozeolite based TFN membranes can be significantly increased in the future. However, this technology still serves as one key example of the successful commercial adoption of nanotechnology in membrane desalination until the higher performing technologies can move from the laboratory environment to commercial reality.

#### 2.3.4. Nanotitania ( $n\text{TiO}_2$ )

Titanium oxide, or titania, is a crystalline solid with the molecular formula TiO<sub>2</sub>. TiO<sub>2</sub> may exist in a number of polymorphs such as rutile, anatase and brookite. The most stable phase is the rutile and, at high temperature, the anatase and brookite phases transform irreversibly to the rutile phase. The most important researched application of TiO<sub>2</sub> is in photocatalysis and since brookite shows limited photocatalytic activities, it is much less researched than anatase and rutile [73, 74] and will not be discussed further in this overview. Structurally, both anatase and rutile exist as tetragonal crystalline structures built from octahedra units where the Ti<sup>4+</sup> is coordinated to six O<sup>2-</sup> anions (see Fig. 2.6). The structural difference between the two polymorphs arises from the fact that anatase is corner sharing at the (0 0 1) planes whilst rutile shares edges at this plane [73, 75]. Anatase has a band gap of 3.2 eV that falls within the UV band while rutile has a band gap of 3.0 eV, which is just within the visible light region, indicating that rutile can be photoreactive under visible light while anatase is photoreactive under UV light [74-76]. However, anatase is the most photoactive phase of TiO<sub>2</sub> [77] and has been widely studied for its photocatalytic applications. TiO<sub>2</sub> is the most researched photocatalyst due to its efficient photoactivity, chemical and

thermal stability, low cost, limited toxicity and its diverse and important applications [73-76]. Further details on the structure, properties and applications of TiO<sub>2</sub> can be sourced in the following excellent review articles [73, 77-81].

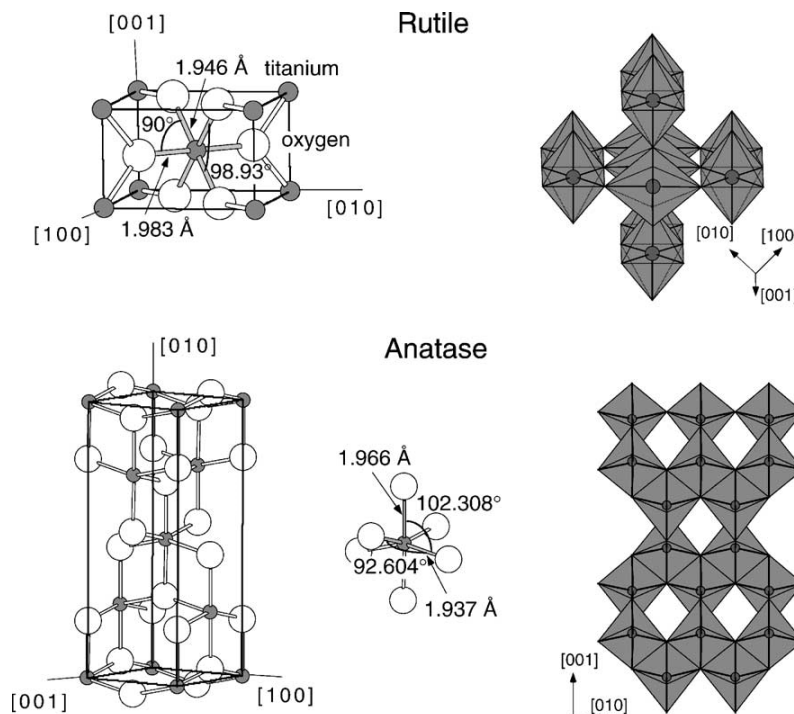


Figure 2.6. Bulk structures of rutile and anatase. The tetragonal bulk unit cell of rutile has the dimensions,  $a = b = 4.587 \text{ \AA}$ ,  $c = 2.953 \text{ \AA}$ , and the one of anatase  $a = b = 3.782 \text{ \AA}$ ,  $c = 9.502 \text{ \AA}$ . In both structures, slightly distorted octahedra are the basic building units. The bond lengths and angles of the octahedrally coordinated Ti atoms are indicated and the stacking of the octahedra in both structures is shown on the right side. Reprinted from U. Diebold, The surface science of titanium dioxide, Surface Science Reports, 48, pg. 67, 2003 with permission from Elsevier.

When light of an appropriate energy ( $h\nu$ ) heats a photoactive semiconductor like anatase and rutile TiO<sub>2</sub>, an electron-hole pair can be created if the valence electron of the semiconductor becomes excited causing it to move from its ground state in the valence band to the conduction band, as  $e^{CB^-}$  (R2.1). This movement creates a deficiency of negative charge in the valence band which is called a

hole,  $h^{VB+}$ . Within the conduction band,  $e^{CB-}$  can move along an electrical gradient to the surface of the crystal. In the same vein, when an electron within the valence band fills up the hole created by the movement of the excited electron, a vacancy is left in its former position and, in this way, the  $h^{VB+}$  can also move along an electrical gradient and can reach the surface of the crystal.

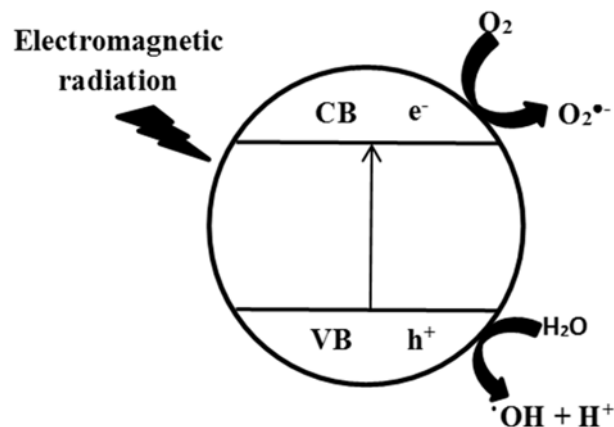
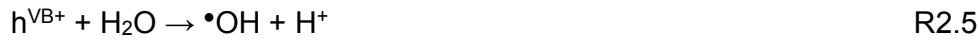


Figure 2.7. Schematic of oxidative radical generation on photoactive  $\text{TiO}_2$

However, the electron-hole pair so created may never reach the surface of the crystal if they become absorbed due to  $\text{Ti}^{3+}$  or  $\text{O}^-$  structural defects or if they recombine with a release of energy within the crystal (R2.2). But if the pair reach the crystal surface,  $e^{CB-}$  could react with adsorbed oxygen on the crystal surface to give the superoxide radical ( $\text{O}_2^{\bullet-}$ ) (R2.3). Subsequent to its formation, the superoxide radical could react with a proton to give the hydroperoxide radical ( $\cdot\text{OOH}$ ) (R2.4). On the other hand,  $h^{VB+}$  may react with adsorbed water to form the hydroxyl radical ( $\cdot\text{OH}$ ) (R2.5). These generated radicals could rapidly degrade organic and inorganic materials that are in the vicinity [75, 76]. The generation of oxidative radicals on photoactive  $\text{TiO}_2$  is illustrated in Fig. 2.7.  $\text{TiO}_2$  photocatalytic degradation of organic matter is an efficient environmental remediation technology and several excellent reviews have been published detailing the mechanisms involved and the applications [74, 76, 77, 82-84].





The efficiency of a photocatalyst is dependent on how much of the generated electron-hole pair is prevented from recombining. Recombination may occur in the bulk of the crystal or on the surface and this is greatly facilitated by structural defects and impurities. There are a number of techniques that have been suggested to decrease recombination and improve the performance of TiO<sub>2</sub> photocatalysts as well as extend performance over visible light spectrum. These include doping, surface modification and nanoscale sizing [75, 85, 86]. The reduction of recombination potential, the enhancement of surface area and the greater affinity for organic material have been recognised as some of the key benefits of nTiO<sub>2</sub> over bulk materials. The enhanced surface area in nTiO<sub>2</sub> is associated with a number of advantages such as greater surface for adsorption of energy, water and hydroxyl groups (for radicals generation) and improved photocatalytic reaction rate [74, 75, 87, 88]. Xiao et al [89] showed that doping nTiO<sub>2</sub> with carbon increased the photocatalytic degradation of methylene blue under solar irradiation. Lee et al [90] reported the synthesis of low-band graphene-wrapped anatase nTiO<sub>2</sub> with enhanced photocatalysis under visible light which was also employed for the successful degradation of methylene blue. Sayilan et al [91] reported that Sn<sup>4+</sup>-doped nTiO<sub>2</sub> showed improved antibacterial effects against gram negative *E. coli* and gram positive *S. aureus* when compared to undoped nTiO<sub>2</sub>. Lin et al [92] prepared N-doped TiO<sub>2</sub> nanotubes which were loaded with Ag to improve the photocatalytic degradation of dye Reactive Brilliant Red X-3B under visible light. The authors reported that the addition of Ag improved performance when compared with nanotubes with only nitrogen doping. Increasing concentration of surface hydroxyl groups has also been reported to lead to improved nTiO<sub>2</sub> photocatalytic degradation of methylene blue and formaldehyde [93].

A number of researchers have taken advantage of the unique photocatalytic properties of nTiO<sub>2</sub> to improve the performance of membrane filtration systems.

Rahimpour et al [94] reported that when nTiO<sub>2</sub> was incorporated into a PES ultrafiltration membrane, membrane hydrophilicity and antifouling properties were improved upon UV irradiation. This derives from the photocatalytic effects of nTiO<sub>2</sub> in increasing the amount of coordinated hydroxyl groups and the degradation of attached foulants. A similar result using PVDF was reported by Song et al [95] whereby a fraction of the original flux of a membrane fouled with natural organic matter was recovered upon UV irradiation. Unfortunately, longer UV irradiation (beyond 12 h) was found to degrade the membrane polymeric matrix. The authors suggested that a practical application of TiO<sub>2</sub> UV irradiation for foulant cleaning requires careful optimisation to ensure maximum foulant removal and minimum membrane damage when organic polymeric membranes are used.

Apart from the established photocatalytic effect of nTiO<sub>2</sub> in improving membrane performance, numerous researchers have shown that the mere presence of pure or surface modified nTiO<sub>2</sub> in polymeric membrane could increase the composite membrane hydrophilicity and could positively influence the structure of the polymer matrix towards improve porosity and filtration performance [96-106]. The addition of nTiO<sub>2</sub> in polymeric membranes has also been associated with improvement in thermal and mechanical strength up to certain blend proportions [107, 108]. Chang et al [109] showed that the hydrophilicity and performance improving effects of nTiO<sub>2</sub> is not restricted to polymeric membrane but can also be realised on a ceramic membrane. The abundant hydroxyl groups on the surface of TiO<sub>2</sub> [93, 110, 111] accounts for the hydrophilicity improvement associated with the incorporation of nTiO<sub>2</sub> in membranes. However, TiO<sub>2</sub> could become even more hydrophilic upon UV irradiation. This phenomenon is proposed to be related to the generation of electron-hole pairs when electromagnetic radiation of the appropriate energy is absorbed resulting in the ejection of structural oxide ion. The created vacancy is filled with a water molecule which coordinates with the titanium ion left behind. To maintain charge, the water molecules loses a proton resulting in the generation of a coordinated hydroxyl group that enhances the overall material hydrophilicity [81, 87]. This unique phenomenon of changing wettability with UV irradiation is potentially another

important tool in the hands of researchers that could be exploited towards developing next generation surface-active membranes.

Membrane composites containing nTiO<sub>2</sub> offer unique opportunity for the effective degradation of harmful contaminants and the disinfection of water. The use of solar energy is particularly significant in its economic advantages but, unfortunately, the efficiency of currently available visible light nTiO<sub>2</sub> photocatalyst is still low and therefore the technology cannot be used except for low contaminant concentrations in water [74, 75, 77, 81]. There is also the problem of photocatalyst inactivation which arises when partially degraded molecules block active photocatalytic sites [75]. In addition, for membrane technology and other supported applications, the immobilisation of nTiO<sub>2</sub> is said to result in about 60 -70% loss in system efficiency when compared with the use of free-standing nanoparticles [82]. There is also the problem of the generation of toxic intermediate degradation products requiring careful design of photocatalytic processes [75, 82].

### 2.3.5. Nanosilver (nAg)

Silver is a ‘noble’ metal which implies that, in the bulk, it naturally occurs in the metallic zero-valent state due to its pronounced chemical inactivity. The nobility of silver and other noble metals like gold have been explained with reference to the concepts of relativistic contraction/expansion of electron shells and the molecular orbital theory. The former, deriving from the special theory of relativity, maintains that the s and p orbitals in atoms experience a relativistic contraction but the relativistic contraction of the valence s orbitals is particularly pronounced for gold and silver making the loss of these valence electrons (oxidation) more difficult. The stability of the contracted s orbitals provides an explanation for the relative chemical inactivity and metallic nobility of Ag and Au [8, 112, 113]. According to the molecular orbital theory, the nobility of metals could be traced to the existence of anti-bonding density of states (DOS) below the Fermi level. DOS indicates the number of states available for occupation at a given energy level. Consequently, the existence of anti-bonding DOS below the Fermi energy level implies that anti-bonding orbitals could be formed. This necessarily introduces instability in potential chemical bonds thereby rendering the noble metals

chemically inactive and stable [8]. However, nAg is markedly different from bulk Ag. The large amount of surface atoms and the rapid translation of ‘free electrons’ to the surface due to the spatial confinement of the nanoparticles gives rise to novel chemical and physical characteristics [8].

The most common application of nAg in membrane water treatment processes harnesses Ag’s unique biocidal properties which have been known for centuries and have been employed for the disinfection of water and wounds both as ionic and metallic silver [8, 114]. The effectiveness of bulk Ag as a bactericidal agent relies on oxidation when the metal is in contact with moisture. The basis of the lethal effect of  $\text{Ag}^+$  is suggested to include breaching of the microorganism’s cell membrane, interfering with cell DNA biochemistry and the production of reactive oxygen species that may eventually lead to the death of the organism [8, 114-116].  $\text{Ag}^+$  is also known to increase the effectiveness of UV irradiation in bacterial disinfection, and may also enhance the antimicrobial effects of electromagnetic fields [117]. The large surface to volume ratio of nAg suggests that when they are incorporated into water treatment membranes, they could continuously ionise to leach  $\text{Ag}^+$  within and on the surface of the membrane preventing membrane colonisation by microbes [8, 116]. Also, if they become dislodged from the filtration membrane network, they could permeate the cell wall of microbial species causing their death [118]. Silver nanoparticles are generally produced by the reduction of a soluble Ag salt (commonly  $\text{AgNO}_3$ ) in the presence of a capping agent to stabilise the nanoparticles. The nature of the capping agent has recently been shown to have major influence on the bactericidal efficiency of nAg [119]. Reducing agents such as polyol [120], sodium borohydride [121, 122], sodium citrate [122] and poly(ethylene glycol) [123] have been reported in the synthesis of nAg. A review of several environmentally benign techniques for producing nAg was recently published [124]. nAg may be incorporated into the framework of a water treatment membrane as a preformed nanoparticle powder or dispersion or it may be generated *in situ* from a solution of  $\text{Ag}^+$ .

Taurozzi et al [116] studied the effect of the nAg incorporation route in a polysulfone membrane. They found that the addition of pre-formed nAg to the polymer resulted in the accumulation of the nanoparticle in the membrane skin layer which, in some instances, led to the formation of macrovoids on the

membrane skin layer resulting in reduced rejection of dextran. In situ formation of nAg resulted in an even distribution of the nanoparticles in the membrane and better biofilm growth inhibition. Sawad et al [125] reported the in situ formation of nAg in an acrylamide layer grafted onto a polyethersulfone (PES) membrane, resulting in the development of an antibacterial and antifouling membrane for water treatment. Similar improvements in both antifouling and antibacterial effects were reported by Vatanpour et al [126] when they incorporated graphene oxide Ag nanocomposite into the framework of a PES membrane. Yang et al [127] reported that the coating of the surface of an RO membrane and spacers with nAg produced by the reduction of a basic solution of  $\text{AgNO}_3$  by formaldehyde, resulted in reduced microbial activities and sustained permeate flux in a pilot desalination run. While in situ incorporation of nAg is commonly employed to produce homogenous composite membranes, Yin et al [128] showed that a stable membrane with good antibacterial properties could be fabricated by covalently attaching nAg produced ex situ to the surface of a polyamide TFC membrane via cysteamine link.

One challenge with the use of immobilised nAg for antimicrobial effects is related to the leaching, with permeate flow, of the  $\text{Ag}^+$  away from the surface of the membrane where the microorganisms are more likely to make first contact. This is expected to diminish the overall effectiveness of the antimicrobial design [116]. In this regard, surface incorporation of nAg might be more effective than uniform distribution within the membrane matrix. Noting that the antimicrobial effect of nAg depends largely on the production of  $\text{Ag}^+$ , long term studies of the antimicrobial effect of nAg incorporated in desalination and water treatment membranes is desirable. Such studies should aim at developing a method for estimating how much nAg would be needed for a particular water treatment scenario. The environmental and health implications of the widespread use of nAg is an important matter for critical evaluation [129] especially considering recent demonstrations of the significant toxicity of nAg on mammalian cells and other biological systems [130-132].

### 2.3.6. Nanosilica ( $n\text{SiO}_2$ )

Silica or Silicon (IV) oxide is a crystalline or amorphous solid with the molecular formula  $\text{SiO}_2$ . Generally, silica materials are built up from a basic tetrahedral unit composed of four oxygen atoms at the ends of a regular tetrahedron and one Si atom occupying the central position or centroid. The tetrahedral  $[\text{SiO}_4]^{4-}$  units are connected differently in a random or orderly fashion to give the various polymorphs of silica with varying densities and porosities. Silica materials are composed of the stable siloxane bond, Si-O, and the less stable silanol bond Si-OH [133]. The latter is usually found on the surface but may exist in the interior in some cases [134]. The physisorption of water molecules onto hydroxyl groups could result in a chain-reaction-type destabilisation of the silica structure through repeated chemisorptive breakdown (hydrolysis) of siloxane bonds [135]. Due to the high free surface energy of silica and the abundance of silanol group supplying hydrogen bonding, water molecules are easily adsorbed. These, in combination with the silanol groups, play key roles in silica surface chemistry [134, 136, 137] and are responsible for the hydrophilic properties of silica which, however, could be lost on heating [138, 139]. Silica nanoparticles are commonly produced by the Stober process or a modification of this process. These techniques basically involve the ammonia (base) catalysed reaction between tetraethylorthosilicate (TEOS) (silicon alkoxide) and water in a low molecular weight alcohol as the solvent. Varying the solvent and other reaction conditions have been used to produce nanoparticles of varying sizes and size distributions [140-142]. Recently, Wu et al [143] published a review of techniques for the production of mesoporous silica nanoparticles with varying porosity, morphology, uniformity and dispersity. On the other hand, microporous solids could be made by adopting an acid catalysed sol gel process, which is useful for preparing silica with pores small enough to separate light gases by size exclusion [144].

The hydrophilic properties of porous and non-porous silica nanoparticles have been employed to enhance the performance of desalination and water treatment membranes by a number of researchers in recent times. Ahmad et al [145] reported that the wettability of a polysulfone ultrafiltration membrane was improved by the addition of  $n\text{SiO}_2$ . The presence of the nanoparticles were found to not only lead to better hydrophilicity, but to have increased the surface porosity

of the membrane, resulting in an approximately 16 fold increment in permeability when compared to the unmodified membrane and to enhanced antifouling properties. However, according to the authors, the hybrid membrane suffered a slight 4% decrease in rejection. Shen et al [146] reported a similar modification of a PES polymeric ultrafiltration membrane by the addition of nSiO<sub>2</sub> during the membrane synthesis. The addition of nSiO<sub>2</sub> was associated with improvement in hydrophilicity, porosity, permeability, rejection and antifouling properties when compared to the unmodified membrane. Yu et al [147] devised a method for the production of PVDF-SiO<sub>2</sub> nanocomposite membranes that involved the direct addition of SiO<sub>2</sub> sol produced from the reaction of acidified TEOS, water and N,N-dimethylformamide (DMF) mixture to a PVDF dope to produce hybrid hollow fibre ultrafiltration membranes. The hybridisation was reported to have resulted in major structural changes in the membrane with improved thermal and mechanical properties at lower blend proportions. Hydrophilicity, permeability and antifouling properties were also enhanced. Flux increased four-fold, while rejection was reduced by about 5%. A similar technique, where cellulose acetate was used as the base membrane, was adopted by Chen et al [148] in which TEOS was directly added to a DMF-cellulose-acetate dope and then phase inverted in pure, acidic and basic water baths. The authors reported that upon phase inversion, large amounts of the in situ generated SiO<sub>2</sub> particles transferred from the skin layer into the coagulation bath resulting in enhanced surface porosity. The best flux was reported for a membrane phased inverted in acidic water, where the permeability was said to be about 256 times higher than the permeability of pure cellulose acetate membrane. Enhancement of antifouling properties at high oil rejection was reported for the modified membrane when tested against an oil emulsion.

Yin et al [149] reported that the dispersion and stability of hydrophilic nSiO<sub>2</sub> in PES was enhanced when the nanoparticles were grafted with a hydrophilic zwitterionic copolymer (poly (2 (dimethylamino) ethylmethacrylate-co-3-dimethyl (methacryloyloxyethyl) ammonium propane sulfonate)) before blending with PES. It was reported that the homogenous and stable modified membrane resulted in improved porosity, hydrophilicity, permeability and antifouling properties in comparison to a pure PES membrane. To harness both the surface hydrophilising effect of SiO<sub>2</sub> and the nanopores for enhanced water permeability, Yin et al [150]

reported the synthesis of a polyamide TFN with mesoporous SiO<sub>2</sub> nanoparticles (MSN) as the inorganic fillers. Both membrane hydrophilicity and zeta potential were said to have benefited from the addition of the porous nSiO<sub>2</sub>. By comparing the MSN modified membrane to a membrane modified by non-porous nSiO<sub>2</sub>, the authors established that the nanopores were important channels for improving water permeability without decreasing rejection. Similarly, Huang et al [151] reported that the addition of MSN to PES resulted in the production of a hybrid UF membrane with enhanced hydrophilicity, water permeability and antifouling properties. Thermal stability also benefited from the presence of nSiO<sub>2</sub>. A modification of the surface of MSN by amino groups was suggested by Wu et al [152] as a potentially viable means of improving the nanoparticles' stability due to the developed covalent bonds between the nanoparticles and the polymer framework. Long-term membrane stability, enhanced permeability and antifouling performance were reported as some of the benefits of the technique.

The incorporation of nSiO<sub>2</sub> is evidently an important route to improve the performance of membranes for desalination and water treatment applications. Particularly important are mesoporous nanoparticles where enhanced flux could be attained without sacrificing rejection. The surface of nSiO<sub>2</sub> lends itself to important modifications that could allow the development of unique hydrophilising and antifouling groups. However, many researchers are constrained to limiting the amount of the nanoparticles incorporated into the membrane due to the problem of agglomeration and the decline in desirable properties above certain blend proportions - even with advanced dispersion techniques [145-147, 149, 151, 152]. This appears to place a cap on the benefits derivable from nSiO<sub>2</sub> incorporation into membranes. However, the problem of aggregation is a general problem of nanotechnology and is not peculiar to nSiO<sub>2</sub>. Despite the rich supply of hydroxyl groups on the SiO<sub>2</sub> surface, the adsorption of organic materials is not excluded [138] and this may impact the long-term performance of SiO<sub>2</sub> modified membranes. Studies have shown that nSiO<sub>2</sub> exhibit a certain measure of cytotoxicity that must be considered in the development and deployment of nSiO<sub>2</sub> based technologies [153-155].

### 2.3.7. Nanoalumina ( $n\text{Al}_2\text{O}_3$ )

Alumina ( $\text{Al}_2\text{O}_3$ ) exists in a number of crystalline phases but perhaps the most common phase for catalytic application is gamma alumina ( $\gamma\text{-Al}_2\text{O}_3$ ) [156, 157]. However, alpha alumina ( $\alpha\text{-Al}_2\text{O}_3$ ) continues to find widespread applications in many industrial settings for its unique mechanical, electrical and optical properties [158]. The crystalline structure of  $\gamma\text{-Al}_2\text{O}_3$  is often considered to be a defective spinel type due to the absence of magnesium, as is found in the ideal spinel structure of  $\text{MgAl}_2\text{O}_4$  [157]. Like most metal oxides, the surface of  $\gamma\text{-Al}_2\text{O}_3$  is covered by OH groups which are of great importance with respect to its chemical characteristics. The properties and functionalities of the hydroxyl groups are said to depend on a number of factors such as the chemical environment, the synthesis technique, the purity of the sample and the morphology of the surface [157]. Aside from abundant surface hydroxyl groups, it has been evidenced that there is ‘excess’ molecular water strongly bonded or ‘chemisorbed’ to the surface of  $\gamma\text{-Al}_2\text{O}_3$ . The bonding of the ‘excess’ water to surface oxide ions is via hydrogen bonding [156]. The bonded water and hydroxyl groups have been explored in the production of MMM for water treatment. Usually, in membrane water applications,  $n\text{Al}_2\text{O}_3$  are used to harness the extensive surface area provided by nanoparticles by adding preformed nanoparticles to a polymer dope.  $n\text{Al}_2\text{O}_3$  have been produced by a number of techniques including ball milling, sol-gel, pyrolysis, sputtering, hydrothermal, and laser ablation [159].

Yan et al [160] reported the production of a flat sheet  $\text{Al}_2\text{O}_3$ -PVDF MMM membrane using various concentrations of nanoparticles with respect to a given mass of the polymer. They reported that the addition of  $n\text{Al}_2\text{O}_3$  resulted in the enhancement of membrane hydrophilicity, permeability, antifouling and mechanical properties for all concentrations of  $n\text{Al}_2\text{O}_3$  with respect to a pure PVDF membrane. The same group reported the production of a tubular  $n\text{Al}_2\text{O}_3$ -PVDF MMM membrane by blending PVDF with 2 wt% of  $n\text{Al}_2\text{O}_3$  with respect to the polymer [161]. The tubular membrane was used for the filtration of oily wastewater and the performance was compared to a similar membrane lacking nanoparticles. The authors reported that the addition of  $n\text{Al}_2\text{O}_3$  almost doubled the membrane flux without impairing rejection when compared with the pure PVDF membrane. The modified membrane showed better antifouling properties

and an improved cleaning response. Maximous et al [162] studied the effect of the concentrations of nAl<sub>2</sub>O<sub>3</sub> on the performance of MMM. They synthesised PES membranes into which they incorporated various amount of nAl<sub>2</sub>O<sub>3</sub>. Based on the measured mechanical strength, water permeability and antifouling performance with respect to activated sludge, they concluded that the addition of nAl<sub>2</sub>O<sub>3</sub> improved membrane performance up until 5 wt% of nAl<sub>2</sub>O<sub>3</sub> was added, after which the performance declined. To improve polymer-nAl<sub>2</sub>O<sub>3</sub> bonding, which otherwise could result in poor particle dispersion that might impair membrane performance, Liu et al [163] reported that an acid catalysed reaction between hydroxyl rich γ-Al<sub>2</sub>O<sub>3</sub> and PVDF could be used to produce novel MMM with enhanced hydrophilicity and antifouling properties. However, the authors did not show how this novel membrane compares with a Al<sub>2</sub>O<sub>3</sub>-PVDF MMM without chemical interactions as reported by other authors ( for example [160, 161]). Going beyond Al<sub>2</sub>O<sub>3</sub> modifications, the membrane literature is lacking in studies which have compared the performance of membranes modified by different inorganic nanoparticles (nAl<sub>2</sub>O<sub>3</sub>, nSiO<sub>2</sub>, etc) under similar conditions. This is important if the selection of inorganic filler materials can be optimised for different applications and operating scenarios.

Maximous et al [162] and Yi et al [164] have shown that the addition of preformed nAl<sub>2</sub>O<sub>3</sub> to polymer membranes at certain blend concentrations leads to membrane performance improvement. However, such simple blending might not be suitable for the modification of a ceramic membrane since calcination, which is often necessary to fix the nanoparticles to the membrane, may lead to the loss of the nanoparticles' surface hydroxyl groups resulting in decrease in hydrophilicity [157, 165]. Chang et al [165] showed that this problem could be overcome by an in situ formation of a γ-Al<sub>2</sub>O<sub>3</sub> ceramic membrane. In situ formation provides the additional benefit of good dispersion. The nanoparticles were produced from aluminium isopropoxide dimethyl benzene which was used to saturate the base ceramic membrane and after which the wet membrane was subjected to heat treatment [165]. Both water permeability and antifouling performance were improved by the modification.

The common applications of nAl<sub>2</sub>O<sub>3</sub> in membrane water treatment as overviewed above have attempted to harness the surface hydrophilicity of the material to

improve membrane filtration performance. However,  $\gamma$ -Al<sub>2</sub>O<sub>3</sub> is used as a catalyst and a catalyst support in many other important industrial processes [156, 157]. Recently, the toxicological impact of nAl<sub>2</sub>O<sub>3</sub> and to a lesser degree bulk Al<sub>2</sub>O<sub>3</sub> on aquatic microalgae was demonstrated [166]. A detailed study of the mechanism of the phytotoxicity of nAl<sub>2</sub>O<sub>3</sub> on plants have also been made [167]. All these suggest that there are potentials for more active nAl<sub>2</sub>O<sub>3</sub> in membrane water treatment processes, which is yet to be exploited as well as the need for caution in the use of the material.

### 2.3.8 Nanoclay and iron oxide nanoparticles

Clays are generally hydrous aluminosilicates composed of two structural units, namely, the tetrahedral silica sheets and the octahedral alumina sheets in the presence of other metallic ions [168]. They are abundant in nature and are used in many important industrial processes. One of the many applications of clays is in the catalytic degradation of organic compounds using hydrogen peroxide as oxidant in Fenton-like reactions [169, 170]. Another important practical application of nanoclays is in the improvement of the mechanical properties and thermal stability of polymer films [129]. A number of papers have documented significant improvements in mechanical strength when nanoclays were incorporated into polymeric membranes such as PVDF [171-173]. This improvement is attributed to the large surface area of nanoclays providing for enhanced energy dissipation as well as their unique crystal lattice compatibility with the PVDF  $\beta$  crystal phase [171-174]. PVDF is known to exist in at least four different crystal phases,  $\alpha$ ,  $\beta$ ,  $\gamma$ , and  $\delta$ , with the  $\beta$  phase being the most important polymorph because of its unique piezoelectric, pyroelectric and toughness enhancement properties [171-174]. The proportion of the  $\beta$  phase and consequently the toughness has been shown to be enhanced in PVDF/nanoclay composite membranes compared to the virgin PVDF films [171]. In such nanocomposites, nanoclays act as structure and morphology directors to increase the amount of metastable phases to achieve enhanced mechanical properties. Membranes with enhanced mechanical strength and more resilience to abrasive wear are desirable in water treatment, especially for seawater desalination pretreatment where abrasive wear from particles in seawater could impair the membrane physical integrity and thereby deprecate selectivity and

membrane life-span [172, 173]. The incorporation of organically modified nanoclays into PVDF membranes have also been reported to result in improvements in hydrophilicity, water flux and fouling resistance [175, 176].

Like clays, iron oxides are abundant in nature and have been used extensively for Fenton-like catalytic degradation of organic compounds [170, 177]. Huang et al [178] reported that increasing the concentration of iron (II,III) oxide ( $\text{Fe}_3\text{O}_4$ ) in a polysulfone composite membrane resulted in continuous increase in the water flux. However, the rejection of bovine serum albumin (BSA) initially increased but subsequently declined as the concentration of the inorganic fillers increased. In another work, the same authors documented that the application of a magnetic field during the phase inversion process could result in novel pore structure refinement for a membrane with a high concentration of magnetic iron oxide particles (more than two times the mass of the polymeric matrix) resulting in enhanced water flux and BSA rejection [179]. Magnetic functionalisation was also adopted by Yang and co-workers [180] to fabricate a responsive NF membrane by the attachment of magnetic nanoparticles to the ends of poly (2-hydroxyethylmethacrylate) chains that have been previously grafted onto the surface of a TFC polyamide membrane. Increased permeate flux and increased salt rejection was recorded when the modified membrane was placed within an oscillating magnetic field during the desalination of a solution of  $\text{CaCl}_2$  and  $\text{MgSO}_4$ . Ling and Chung [181] reported the use of hydrophilic magnetic nanoparticles as a draw solute in an integrated FO-UF process for water reuse and desalination. An attempt to recover the magnetic nanoparticles using a magnetic field rather than via UF was unsuccessful due to the aggregation of the nanoparticles after magnetic separation. The development of an effective technique to prevent nanoparticle aggregation is likely to advance FO using magnetic draw solutes as an important desalination procedure.

Both nanoclay and iron oxide nanoparticles could potentially play important roles towards the development of efficient pretreatments for water desalination applications. The unique magnetic property of iron oxides lends itself to many novel research options, which might potentially yield important results in the future for MDWT applications.

## 2.4. Conclusions and future prospects

In relation to the development of high flux, high rejection, low cost and long-life membranes, nanotechnology research has been shown to hold enormous promise in contributing to the resolution of the two inherent problems of membrane technology; namely, the permeability-selectivity tradeoff and membrane fouling. Carbon nanotubes, aquaporin and nanozeolites promise significant improvements in RO and NF water flux with very high and tunable rejection as a consequence of their molecular-level porosities and nano-scale surface areas, hence breaking down the permeability-selectivity tradeoff inherent in membrane processes. However, none of these molecular channels at their full capacity are currently available for MDWT applications. One common challenge relates to the technical and economic difficulties in scaling up these nano-filters to the requisite macro-dimension for MDWT applications without defects and functionality impairments. For aquaporin, and to some extent CNT, the nano-filters with the desired functionalities are still not commercially available, limiting research and development. For zeolite based systems, the production of integral crystal films is still challenging and, although much progress has been made towards understanding the complexity of the zeolitic structure, chemistry and ionic interaction, major knowledge gaps still exist and thus potential flux enhancement and rejection improvement as a consequence of zeolite molecular porosity is still unrealised. Aligned CNTs appear to be the most promising high performance membrane that could reach the market first going by the current state of the technology, the stability of the material and the versatility and ease of its functionalisation. However, much research is still needed to meet these expectations, as its high costs and challenging manufacturing are not yet competitive with the state of the art polyamide and cellulose acetate RO membranes.

Starting with nanozeolite, later CNT and recently aquaporin, enhanced water flux has been achieved by incorporating nano-filters into the thin selective layer of composite polymer membranes. Nanocomposite membranes, in particular nanozeolite, represent one of the major success stories of nanotechnology applications to MDWT. For aquaporin, nanocomposite membranes and other MDWT application of membrane proteins, there are still major stability issues that

must be resolved before these materials could compete favourably with other technologies. However, the flux enhancements currently observed for nanozeolite and CNT nanocomposite membranes are still orders of magnitude below the theoretical performance of a molecular sieve. The limited water transportation capability of present nanocomposite systems relate to the disorderly arrangement of the nanochannels and the flux limitation imposed by the polymer matrix. Innovative channel alignment and reduction of polymer flux-path-length would potentially improve the performance of these membranes.

The many important properties of nTiO<sub>2</sub> are likely to impact positively the development of next generation membranes. In addition to the flux enhancement due to the natural hydrophilic properties of nTiO<sub>2</sub>, this nano-material provides unique functionalisation in self-cleaning, contaminant degradation and self-wettability modification in response to exposure to electromagnetic radiations. These intriguing effects may provide the platform for the reduction of the elusive problem of membrane fouling and productivity decline in the future. The potentially enhanced antifouling properties of nTiO<sub>2</sub> is likely to play a critical role in the practical operation of future high performance membranes since these membranes are likely to face more challenging problems of concentration polarisation and membrane fouling. However, the practical realisation of these unique nTiO<sub>2</sub> functionalities is dependent on the success of current and future research in improving visible light photocatalysis. nAg is another important material for the reduction of the problem of membrane fouling, particularly biological fouling. Composite systems with nAg and other nanoparticles are likely to be more prevalent in the future in MDWT but questions surrounding the effects of the leaching of dissolved nanoparticles or the potential dislodgement of whole nAg or other nanoparticles into the permeate stream must be resolved. Researchers have considered leaching mostly for nAg as it is in metallic form and may become ionised in water or acidic solutions resulting in charged reactive and/or toxic species. Less attention has been paid to the issue of leaching of the other common nanoparticles such as TiO<sub>2</sub>, Al<sub>2</sub>O<sub>3</sub> and clay probably because they are considered less soluble and/or less reactive. The importance of nSiO<sub>2</sub>, nAl<sub>2</sub>O<sub>3</sub>, nanoclay and iron oxide nanoparticles are likely to be centred on low-cost enhancement in permeate flux, thermal stability and mechanical strength.

especially in UF and MF applications. However, the currently little explored cytotoxicity of nSiO<sub>2</sub> and nAl<sub>2</sub>O<sub>3</sub> might prove useful for future applications as well might the catalytic properties of nanoclay and iron oxide nanoparticles. Mesoporous nSiO<sub>2</sub> might also be of future importance in the development of high flux RO and UF membranes and the many potential magnetic applications of iron oxide nanoparticles might result in important MDWT applications.

## References

- [1] R.W. Baker, Membrane technology and application, 2nd ed., John Wiley & Sons, Ltd, West Sussex, England, 2004.
- [2] X. Qu, J. Brame, Q. Li, P.J.J. Alvarez, Nanotechnology for a Safe and Sustainable Water Supply: Enabling Integrated Water Treatment and Reuse, Account of Chemical Research, 46 (2013) 834 - 843.
- [3] M. Elimelech, W.A. Phillip, The Future of Seawater Desalination: Energy, Technology, and the Environment, Science, 333 (2011) 712-717.
- [4] X. Qu, P.J. Alvarez, Q. Li, Applications of nanotechnology in water and wastewater treatment, Water Research, 47 (2013) 3931-3946.
- [5] C.d.M. Donega, Nanoparticles, the workhorses of nanoscience, in, Springer, Heidelberg, 2014.
- [6] K. Sattler, The energy gap of clusters , nanoparticles and quantum dot, in: H.S. Nalwa (Ed.) Handbook of Thin Films, Academic Press, 2002, pp. 61 - 97.
- [7] E. Roduner, Size matters: why nanomaterials are different, Chemical Society reviews, 35 (2006) 583-592.
- [8] T. Pradeep, Anshup, Noble metal nanoparticles for water purification: A critical review, Thin Solid Films, 517 (2009) 6441-6478.
- [9] M. Terrones, Science and Technology of the Twenty-First Century: Synthesis, Properties, and Applications of Carbon Nanotubes, Annual Review of Materials Research, 33 (2003) 419-501.
- [10] M.F.L. De Volder, S.H. Tawfick, R.H. Baughman, A.J. Hart, Carbon nanotubes: present and future commercial applications, Science 339 (2013) 535-539.

- [11] M.H. Rummeli, P. Ayala, T. Pichler, Carbon nanotubes and related structures: production and formation, in: D.M. Guildi, N. Martin (Eds.) Carbon nanotubes and related structures, WILEY-VCH Verlag GmbH & Co. KGaA, Weinheim, 2010.
- [12] P.S. Goh, A.F. Ismail, B.C. Ng, Carbon nanotubes for desalination: Performance evaluation and current hurdles, *Desalination*, 308 (2013) 2-14.
- [13] R. Das, M.E. Ali, S.B.A. Hamid, S. Ramakrishna, Z.Z. Chowdhury, Carbon nanotube membranes for water purification: A bright future in water desalination, *Desalination*, 336 (2014) 97-109.
- [14] B. Corry, Designing Carbon Nanotube Membranes for Efficient Water Desalination, *Journal of Physical Chemistry B*, 112 (2008) 1427-1434.
- [15] F. Du, L. Qu, Z. Xia, L. Feng, L. Dai, Membranes of vertically aligned superlong carbon nanotubes, *Langmuir*, 27 (2011) 8437-8443.
- [16] J.K. Holt, Carbon Nanotubes and Nanofluidic Transport, *Advanced Materials*, 21 (2009) 3542-3550.
- [17] J.K. Holt, H.G. Park, Y. Wang, M. Stadermann, A.B. Artyukhin, C.P. Grigoropoulos, A. Noy, O. Bakajin, Fast Mass Transport Through Sub-2-Nanometer Carbon Nanotubes, *Science*, 312 (2006) 1034-1037.
- [18] E.R. Nightingale, Phenomenological theory of ion solvation. effective radii of hydrated ions, *The Journal of Physical Chemistry C*, 63 (1959) 1381-1387.
- [19] W.-F. Chan, H.-y. Chen, A. Surapathi, M.G. Taylor, X. Shao, E. Marand, J.K. Johnson, Zwitterion Functionalized Carbon Nanotube/Polyamide Nanocomposite Membranes for Water Desalination, *ACS Nano*, 7 (2013) 5308–5319.
- [20] J.S. Vrouwenvelder, M.C. Van Loosdrecht, J.C. Kruithof, A novel scenario for biofouling control of spiral wound membrane systems, *Water Research*, 45 (2011) 3890-3898.
- [21] Y. Baek, C. Kim, D.K. Seo, T. Kim, J.S. Lee, Y.H. Kim, K.H. Ahn, S.S. Bae, S.C. Lee, J. Lim, K. Lee, J. Yoon, High performance and antifouling vertically aligned carbon nanotube membrane for water purification, *Journal of Membrane Science*, 460 (2014) 171-177.
- [22] P. Daraei, S.S. Madaeni, N. Ghaemi, M.A. Khadivi, B. Astinchap, R. Moradian, Enhancing antifouling capability of PES membrane via mixing with various types of polymer modified multi-walled carbon nanotube, *Journal of Membrane Science*, 444 (2013) 184-191.

- [23] S. Majeed, D. Fierro, K. Buhr, J. Wind, B. Du, A. Boschetti-de-Fierro, V. Abetz, Multi-walled carbon nanotubes (MWCNTs) mixed polyacrylonitrile (PAN) ultrafiltration membranes, *Journal of Membrane Science*, 403-404 (2012) 101-109.
- [24] V. Vatanpour, S.S. Madaeni, R. Moradian, S. Zinadini, B. Astinchap, Novel antibifouling nanofiltration polyethersulfone membrane fabricated from embedding TiO<sub>2</sub> coated multiwalled carbon nanotubes, *Separation and Purification Technology*, 90 (2012) 69-82.
- [25] A. Yoosefi Booshehri, R. Wang, R. Xu, The effect of re-generable silver nanoparticles/multi-walled carbon nanotubes coating on the antibacterial performance of hollow fiber membrane, *Chemical Engineering Journal*, 230 (2013) 251-259.
- [26] C.Y. Lai, A. Groth, S. Gray, M. Duke, Nanocomposites for Improved Physical Durability of Porous PVDF Membranes, *Membranes* (Basel), 4 (2014) 55-78.
- [27] J. Yin, G. Zhu, B. Deng, Multi-walled carbon nanotubes (MWNTs)/polysulfone (PSU) mixed matrix hollow fiber membranes for enhanced water treatment, *Journal of Membrane Science*, 437 (2013) 237-248.
- [28] M.S. Mauter, M. Elimelech, C.O. Osuji, Nanocomposites of vertically aligned single-walled carbon nanotubes by Magnetic alignment and polymerization of a lyotropic precursor, *American Chemical Society Nano*, 4 (2010) 6651–6658.
- [29] C.-F. de Lannoy, E. Soyer, M.R. Wiesner, Optimizing carbon nanotube-reinforced polysulfone ultrafiltration membranes through carboxylic acid functionalization, *Journal of Membrane Science*, 447 (2013) 395-402.
- [30] F. Liu, N.A. Hashim, Y. Liu, M.R.M. Abed, K. Li, Progress in the production and modification of PVDF membranes, *Journal of Membrane Science*, 375 (2011) 1-27.
- [31] N. Phao, E.N. Nxumalo, B.B. Mamba, S.D. Mhlanga, A nitrogen-doped carbon nanotube enhanced polyethersulfone membrane system for water treatment, *Physics and Chemistry of the Earth, Parts A/B/C*, 66 (2013) 148-156.
- [32] S. Qiu, L. Wu, X. Pan, L. Zhang, H. Chen, C. Gao, Preparation and properties of functionalized carbon nanotube/PSF blend ultrafiltration membranes, *Journal of Membrane Science*, 342 (2009) 165-172.

- [33] A.S. Brady-Estevez, S. Kang, M. Elimelech, A single-walled-carbon-nanotube filter for removal of viral and bacterial pathogens, *Small*, 4 (2008) 481-484.
- [34] L.F. Dumée, K. Sears, J. Schütz, N. Finn, C. Huynh, S. Hawkins, M. Duke, S. Gray, Characterization and evaluation of carbon nanotube Bucky-Paper membranes for direct contact membrane distillation, *Journal of Membrane Science*, 351 (2010) 36-43.
- [35] H. Omachi, T. Nakayama, E. Takahashi, Y. Segawa, K. Itami, Initiation of carbon nanotube growth by well-defined carbon nanorings, *Nature Chemistry*, 5 (2013) 572–576.
- [36] Y. Kaufman, V. Freger, Supported biomimetic membranes for pressure driven water purification, *On Biomimetics*, InTech, (2011).
- [37] P. Gena, M. Pellegrini-Calace, A. Biasco, M. Svelto, G. Calamita, Aquaporin Membrane Channels: Biophysics, Classification, Functions, and Possible Biotechnological Applications, *Food Biophysics*, 6 (2010) 241-249.
- [38] M.J. Borgnia, D. Kozono, G. Calamita, P.C. Maloney, P. Agre, Functional reconstitution and characterization of AqpZ the *Ecoli* water channel protein, *Journal of Molecular Biology*, 291 (1999) 1169-1179.
- [39] P. Agre, Aquaporin water channels (Nobel Lecture), *Angewandte Chemie International Edition English*, 43 (2004) 4278-4290.
- [40] J. Bomholt, C. Helix-Nielsen, P. Scharff-Poulsen, P.A. Pedersen, Recombinant production of human Aquaporin-1 to an exceptional high membrane density in *Saccharomyces cerevisiae*, *PLoS ONE*, 8 (2013) e56431.
- [41] J.S. Hub, B.L. de Groot, Mechanism of selectivity in aquaporins and aquaglyceroporins, *Proceedings of the National Academy of Sciences of the United States of America*, 105 (2008) 1198-1203.
- [42] C.X. Zhao, H.B. Shao, L.Y. Chu, Aquaporin structure-function relationships: water flow through plant living cells, *Colloids and Surfaces B: Biointerfaces*, 62 (2008) 163-172.
- [43] J. Wang, L. Feng, Z. Zhu, M. Zheng, D. Wang, Z. Chen, H. Sun, Aquaporins as diagnostic and therapeutic targets in cancer: how far we are?, *Journal of translational medicine*, 13 (2015) 96.

- [44] C.Y. Tang, Y. Zhao, R. Wang, C. Hélix-Nielsen, A.G. Fane, Desalination by biomimetic aquaporin membranes: Review of status and prospects, *Desalination*, 308 (2013) 34-40.
- [45] C. Tang, Z. Wang, I. Petrinić, A.G. Fane, C. Hélix-Nielsen, Biomimetic aquaporin membranes coming of age, *Desalination*, 368 (2015) 89-105.
- [46] H. Wang, T.S. Chung, Y.W. Tong, K. Jeyaseelan, A. Armugam, Z. Chen, M. Hong, W. Meier, Highly permeable and selective pore-spanning biomimetic membrane embedded with aquaporin Z, *Small*, 8 (2012) 1185-1190, 1125.
- [47] L. Kai, R. Kaldenhoff, J. Lian, X. Zhu, V. Dotsch, F. Bernhard, P. Cen, Z. Xu, Preparative Scale Production of Functional Mouse Aquaporin 4 Using Different Cell-Free Expression Modes, *PLoS ONE*, 5 (2010).
- [48] D. Schwarz, C. Klammt, A. Koglin, F. Löhr, B. Schneider, V. Dötsch, F. Bernhard, Preparative scale cell-free expression systems: New tools for the large scale preparation of integral membrane proteins for functional and structural studies, *Methods*, 41 (2007) 355-369.
- [49] A. Muller-Lucks, P. Gena, D. Frascaria, N. Altamura, M. Svelto, E. Beitz, G. Calamita, Preparative scale production and functional reconstitution of a human aquaglyceroporin (AQP3) using a cell free expression system, *New biotechnology*, 30 (2013) 545-551.
- [50] M. Perry, C. Rein, J. Vogel, Large Scale Biomimetic Membrane Arrays, in: C. Hélix-Nielsen (Ed.) *Biomimetic Membranes for Sensor and Separation Applications*, Springer Science+Business Media B.V, 2012, pp. 205-231.
- [51] Y.-x. Shen, P.O. Saboe, I.T. Sines, M. Erbakan, M. Kumar, Biomimetic membranes: A review, *Journal of Membrane Science*, 454 (2014) 359-381.
- [52] P.S. Zhong, T.-S. Chung, K. Jeyaseelan, A. Armugam, Aquaporin-embedded biomimetic membranes for nanofiltration, *Journal of Membrane Science*, 407-408 (2012) 27-33.
- [53] Y. Zhao, C. Qiu, X. Li, A. Vararattanavech, W. Shen, J. Torres, C. Hélix-Nielsen, R. Wang, X. Hu, A.G. Fane, C.Y. Tang, Synthesis of robust and high-performance aquaporin-based biomimetic membranes by interfacial polymerization-membrane preparation and RO performance characterization, *Journal of Membrane Science*, 423-424 (2012) 422-428.
- [54] I.D. Rollmann, E.W. Valyocsik, R.D. Shannon, Miscellaneous solid-state compounds, in: D.W. Murphy, I.V. Leonard (Eds.) *Inorganic Syntheses*, 1995.

- [55] D.W. Breck, Zeolite molecular sieves: structure, chemistry and use, John Wiley & Sons, New York, 1974.
- [56] M. Duke, D. Zhao, R. Semiat, Functional nanostructured materials and membranes for water treatment, Wiley-VCH, 2013.
- [57] B. Zhu, C.M. Doherty, X. Hu, A.J. Hill, L. Zou, Y.S. Lin, M. Duke, Designing hierarchical porous features of ZSM-5 zeolites via Si/Al ratio and their dynamic behavior in seawater ion complexes, *Microporous and Mesoporous Materials*, 173 (2013) 78–85.
- [58] Y.S. Lin, M.C. Duke, Recent progress in polycrystalline zeolite membrane research, *Current Opinion in Chemical Engineering*, 2 (2013) 209-216.
- [59] J. O'Brien-Abraham, M. Kanezashi, Y.S. Lin, Effects of adsorption-induced microstructural changes on separation of xylene isomers through MFI-type zeolite membranes, *Journal of Membrane Science*, 320 (2008) 505–513.
- [60] S.G. Sorenson, E.A. Payzant, W.T. Gibbons, B. Soydas, H. Kita, R.D. Noble, J.L. Falconer, Influence of zeolite crystal expansion/contraction on NaA zeolite membrane separations, *Journal of Membrane Science*, 366 (2011) 413–420.
- [61] B. Zhu, L. Zou, C.M. Doherty, A.J. Hill, Y.S. Lin, X. Hu, H. Wang, M. Duke, Investigation of the effects of ion and water interaction on structure and chemistry of silicalite MFI type zeolite for its potential use as a seawater desalination membrane, *Journal of Materials Chemistry*, 20 (2010) 4675–4683.
- [62] B. Zhu, D.T. Myat, J.-W. Shin, Y.-H. Na, I.-S. Moon, G. Connor, S. Maeda, G. Morris, S. Gray, M. Duke, Application of robust MFI-type zeolite membrane for desalination of saline wastewater, *Journal of Membrane Science* 475 (2015) 167–174.
- [63] L. Li, J. Dong, T.M. Nenoff, R. Lee, Desalination by reverse osmosis using MFI zeolite membranes, *Journal of Membrane Science*, 243 (2004) 401-404.
- [64] B.-H. Jeong, E.M.V. Hoek, Y. Yan, A. Subramani, X. Huang, G. Hurwitz, A.K. Ghosh, A. Jawor, Interfacial polymerization of thin film nanocomposites: A new concept for reverse osmosis membranes, *Journal of Membrane Science*, 294 (2007) 1-7.
- [65] H. Wang, Z. Wang, Y. Yan, Colloidal suspensions of template-removed zeolite nanocrystals, *Chemical Communications*, (2000) 2333-2334.

- [66] C. Kong, T. Shintani, T. Tsuru, "Pre-seeding"-assisted synthesis of a high performance polyamide-zeolite nnaocomposite membrane for water purification, *New Journal of Chemistry*, 34 (2010) 2101-2104.
- [67] M. Fathizadeh, A. Aroujalian, A. Raisi, Effect of added NaX nano-zeolite into polyamide as a top thin layer of membrane on water flux and salt rejection in a reverse osmosis process, *Journal of Membrane Science*, 375 (2011) 88-95.
- [68] M.L. Lind, A.K. Ghosh, A. Jawor, X. Huang, W. Hou, Y. Yang, E.M. Hoek, Influence of zeolite crystal size on zeolite-polyamide thin film nanocomposite membranes, *Langmuir*, 25 (2009) 10139-10145.
- [69] M.M. Pendergast, A.K. Ghosh, E.M.V. Hoek, Separation performance and interfacial properties of nanocomposite reverse osmosis membranes, *Desalination*, 308 (2013) 180-185.
- [70] N. Ma, J. Wei, R. Liao, C.Y. Tang, Zeolite-polyamide thin film nanocomposite membranes: Towards enhanced performance for forward osmosis, *Journal of Membrane Science*, 405-406 (2012) 149-157.
- [71] S.G. Kim, D.H. Hyeon, J.H. Chun, B.-H. Chun, S.H. Kim, Nanocomposite poly(arylene ether sulfone) reverse osmosis membrane containing functional zeolite nanoparticles for seawater desalination, *Journal of Membrane Science*, 443 (2013) 10-18.
- [72] L. Chem, Leveraging Nanotechnology for Next Generation Seawater Desalination (The International Desalination & Water Reuse Quarterly), in, LG NanoH2O, Inc., 2015.
- [73] U. Diebold, The surface science of titanium dioxide, *Surface Science Reports*, 48 (2003) 53-229.
- [74] Y. Lan, Y. Lu, Z. Ren, Mini review on photocatalysis of titanium dioxide nanoparticles and their solar applications, *Nano Energy*, 2 (2013) 1031-1045.
- [75] M. Pelaez, N.T. Nolan, S.C. Pillai, M.K. Seery, P. Falaras, A.G. Kontos, P.S.M. Dunlop, J.W.J. Hamilton, J.A. Byrne, K. O'Shea, M.H. Entezari, D.D. Dionysiou, A review on the visible light active titanium dioxide photocatalysts for environmental applications, *Applied Catalysis B: Environmental*, 125 (2012) 331-349.
- [76] D. Chatterjee, S. Dasgupta, Visible light induced photocatalytic degradation of organic pollutants, *Journal of Photochemistry and Photobiology C: Photochemistry Reviews*, 6 (2005) 186-205.

- [77] A. Fujishima, X. Zhang, D. Tryk, Heterogeneous photocatalysis: From water photolysis to applications in environmental cleanup, International Journal of Hydrogen Energy, 32 (2007) 2664-2672.
- [78] O. Carp, Photoinduced reactivity of titanium dioxide, Progress in Solid State Chemistry, 32 (2004) 33-177.
- [79] A. Fujishima, T.N. Rao, D.A. Tryk, Titanium dioxide photocatalysis, Journal of Photochemistry and Photobiology C: Photochemistry Reviews 1(2000) 1-21.
- [80] A. Fujishima, X. Zhang, Titanium dioxide photocatalysis: present situation and future approaches, Comptes Rendus Chimie, 9 (2006) 750-760.
- [81] A. Fujishima, X. Zhang, D. Tryk, TiO<sub>2</sub> photocatalysis and related surface phenomena, Surface Science Reports, 63 (2008) 515-582.
- [82] U.I. Gaya, A.H. Abdullah, Heterogeneous photocatalytic degradation of organic contaminants over titanium dioxide: A review of fundamentals, progress and problems, Journal of Photochemistry and Photobiology C: Photochemistry Reviews, 9 (2008) 1-12.
- [83] J.-M. Herrmann, Heterogeneous photocatalysis: fundamentals and applications to the removal of various types of aqueous pollutants, Catalysis Today, 53 (1999) 115-129.
- [84] S. Malato, P. Fernández-Ibáñez, M.I. Maldonado, J. Blanco, W. Gernjak, Decontamination and disinfection of water by solar photocatalysis: Recent overview and trends, Catalysis Today, 147 (2009) 1-59.
- [85] Alamgir, W. Khan, S. Ahmad, M. Mehedi Hassan, A.H. Naqvi, Structural phase analysis, band gap tuning and fluorescence properties of Co doped TiO<sub>2</sub> nanoparticles, Optical Materials, 38 (2014) 278-285.
- [86] M. Anpo, The design and development of highly reactive titanium oxide photocatalysts operating under visible light irradiation, Journal of Catalysis, 216 (2003) 505-516.
- [87] K. Nakata, T. Ochiai, T. Murakami, A. Fujishima, Photoenergy conversion with TiO<sub>2</sub> photocatalysis: New materials and recent applications, Electrochimica Acta, 84 (2012) 103-111.
- [88] H. Lin, C. Huang, W. Li, C. Ni, S. Shah, Y. Tseng, Size dependency of nanocrystalline TiO<sub>2</sub> on its optical property and photocatalytic reactivity exemplified by 2-chlorophenol, Applied Catalysis B: Environmental, 68 (2006) 1-11.

- [89] Q. Xiao, J. Zhang, C. Xiao, Z. Si, X. Tan, Solar photocatalytic degradation of methylene blue in carbon-doped TiO<sub>2</sub> nanoparticles suspension, *Solar Energy*, 82 (2008) 706-713.
- [90] J.S. Lee, K.H. You, C.B. Park, Highly photoactive, low bandgap TiO<sub>2</sub> nanoparticles wrapped by graphene, *Advanced Materials*, 24 (2012) 1084-1088.
- [91] F. Sayilan, M. Asilturk, N. Kiraz, E. Burunkaya, E. Arpac, H. Sayilan, Photocatalytic antibacterial performance of Sn(4+)-doped TiO<sub>2</sub> thin films on glass substrate, *Journal of Hazardous Materials*, 162 (2009) 1309-1316.
- [92] X. Lin, F. Rong, X. Ji, D. Fu, C. Yuan, Preparation and enhanced visible light photocatalytic activity of N-doped titanate nanotubes by loaded with Ag for the degradation of X-3B, *Solid State Sciences*, 13 (2011) 1424-1428.
- [93] J. Wang, X. Liu, R. Li, P. Qiao, L. Xiao, J. Fan, TiO<sub>2</sub> nanoparticles with increased surface hydroxyl groups and their improved photocatalytic activity, *Catalysis Communications*, 19 (2012) 96-99.
- [94] A. Rahimpour, S.S. Madaeni, A.H. Taheri, Y. Mansourpanah, Coupling TiO<sub>2</sub> nanoparticles with UV irradiation for modification of polyethersulfone ultrafiltration membranes, *Journal of Membrane Science*, 313 (2008) 158-169.
- [95] H. Song, J. Shao, Y. He, B. Liu, X. Zhong, Natural organic matter removal and flux decline with PEG-TiO<sub>2</sub>-doped PVDF membranes by integration of ultrafiltration with photocatalysis, *Journal of Membrane Science*, 405-406 (2012) 48-56.
- [96] X. Cao, J. Ma, X. Shi, Z. Ren, Effect of TiO<sub>2</sub> nanoparticle size on the performance of PVDF membrane, *Applied Surface Science*, 253 (2006) 2003-2010.
- [97] T.-H. Bae, T.-M. Tak, Effect of TiO<sub>2</sub> nanoparticles on fouling mitigation of ultrafiltration membranes for activated sludge filtration, *Journal of Membrane Science*, 249 (2005) 1-8.
- [98] B. Rajaeian, A. Rahimpour, M.O. Tade, S. Liu, Fabrication and characterization of polyamide thin film nanocomposite (TFN) nanofiltration membrane impregnated with TiO<sub>2</sub> nanoparticles, *Desalination*, 313 (2013) 176-188.
- [99] M.-L. Luo, J.-Q. Zhao, W. Tang, C.-S. Pu, Hydrophilic modification of poly(ether sulfone) ultrafiltration membrane surface by self-assembly of TiO<sub>2</sub> nanoparticles, *Applied Surface Science*, 249 (2005) 76-84.

- [100] X. Zhao, Y. Su, Y. Liu, R. Zhang, Z. Jiang, Multiple antifouling capacities of hybrid membranes derived from multifunctional titania nanoparticles, *Journal of Membrane Science*, 495 (2015) 226-234.
- [101] R.-X. Zhang, L. Braeken, P. Luis, X.-L. Wang, B. Van der Bruggen, Novel binding procedure of TiO<sub>2</sub> nanoparticles to thin film composite membranes via self-polymerized polydopamine, *Journal of Membrane Science*, 437 (2013) 179-188.
- [102] H.S. Lee, S.J. Im, J.H. Kim, H.J. Kim, J.P. Kim, B.R. Min, Polyamide thin-film nanofiltration membranes containing TiO<sub>2</sub> nanoparticles, *Desalination*, 219 (2008) 48-56.
- [103] T.-H. Bae, I.-C. Kim, T.-M. Tak, Preparation and characterization of fouling-resistant TiO<sub>2</sub> self-assembled nanocomposite membranes, *Journal of Membrane Science*, 275 (2006) 1-5.
- [104] F. Shi, Y. Ma, J. Ma, P. Wang, W. Sun, Preparation and characterization of PVDF/TiO<sub>2</sub> hybrid membranes with ionic liquid modified nano-TiO<sub>2</sub> particles, *Journal of Membrane Science*, 427 (2013) 259-269.
- [105] F. Zhang, W. Zhang, Y. Yu, B. Deng, J. Li, J. Jin, Sol-gel preparation of PAA-g-PVDF/TiO<sub>2</sub> nanocomposite hollow fiber membranes with extremely high water flux and improved antifouling property, *Journal of Membrane Science*, 432 (2013) 25-32.
- [106] V. Vatanpour, S.S. Madaeni, A.R. Khataee, E. Salehi, S. Zinadini, H.A. Monfared, TiO<sub>2</sub> embedded mixed matrix PES nanocomposite membranes: Influence of different sizes and types of nanoparticles on antifouling and performance, *Desalination*, 292 (2012) 19-29.
- [107] G. Wu, S. Gan, L. Cui, Y. Xu, Preparation and characterization of PES/TiO<sub>2</sub> composite membranes, *Applied Surface Science*, 254 (2008) 7080-7086.
- [108] Y. Yang, H. Zhang, P. Wang, Q. Zheng, J. Li, The influence of nano-sized TiO<sub>2</sub> fillers on the morphologies and properties of PSF UF membrane, *Journal of Membrane Science*, 288 (2007) 231-238.
- [109] Q. Chang, J.-e. Zhou, Y. Wang, J. Liang, X. Zhang, S. Cerneaux, X. Wang, Z. Zhu, Y. Dong, Application of ceramic microfiltration membrane modified by nano-TiO<sub>2</sub> coating in separation of a stable oil-in-water emulsion, *Journal of Membrane Science*, 456 (2014) 128-133.

- [110] A.Š. Vuk, R. Ješe, B. Orel, G. Draži, The effect of surface hydroxyl groups on the adsorption properties of nanocrystalline TiO<sub>2</sub> film, International journal of photoenergy, 7 (2005).
- [111] J.-H. Kim, H.-I. Lee, Effect of Surface Hydroxyl Groups of Pure TiO<sub>2</sub> and Modified TiO<sub>2</sub> on the Photocatalytic Oxidation of Aqueous Cyanide, Korean Journal of Chemical Engineering, 21 (2004) 116-122.
- [112] J.S. Thayer, Relativistic effects and the chemistry of the heavier main group elements, in: M. Barysz, Y. Ishikawa (Eds.) Relativistic Methods for Chemists, Springer Science+Business Media B.V, 2010.
- [113] M. Jansen, Effects of relativistic motion of electrons on the chemistry of gold and platinum, Solid State Sciences, 7 (2005) 1464-1474.
- [114] M. Rai, A. Yadav, A. Gade, Silver nanoparticles as a new generation of antimicrobials, Biotechnology advances, 27 (2009) 76-83.
- [115] Q. Li, S. Mahendra, D.Y. Lyon, L. Brunet, M.V. Liga, D. Li, P.J. Alvarez, Antimicrobial nanomaterials for water disinfection and microbial control: potential applications and implications, Water Research, 42 (2008) 4591-4602.
- [116] J.S. Taurozzi, H. Arul, V.Z. Bosak, A.F. Burban, T.C. Voice, M.L. Bruening, V.V. Tarabara, Effect of filler incorporation route on the properties of polysulfone–silver nanocomposite membranes of different porosities, Journal of Membrane Science, 325 (2008) 58-68.
- [117] C. Piyadasa, H.F. Ridgway, T. Yeager, S.R. Gray, M.B. Stewart, J.D. Orbell, The application of electromagnetic fields to the control of the scaling and biofouling of reverse osmosis membranes - a review, Water Science and Technology, in press, (2016).
- [118] I. Sondi, B. Salopek-Sondi, Silver nanoparticles as antimicrobial agent: a case study on *E. coli* as a model for Gram-negative bacteria, Journal of colloid and interface science, 275 (2004) 177-182.
- [119] A.J. Kora, R. Manjusha, J. Arunachalam, Superior bactericidal activity of SDS capped silver nanoparticles: Synthesis and characterization, Materials Science and Engineering: C, 29 (2009) 2104-2109.
- [120] J.H. Byeon, Y.W. Kim, A novel polyol method to synthesize colloidal silver nanoparticles by ultrasonic irradiation, Ultrasonics sonochemistry, 19 (2012) 209-215.

- [121] I.A. Wani, S. Khatoon, A. Ganguly, J. Ahmed, A.K. Ganguli, T. Ahmad, Silver nanoparticles: Large scale solvothermal synthesis and optical properties, *Materials Research Bulletin*, 45 (2010) 1033-1038.
- [122] I.A. Wani, A. Ganguly, J. Ahmed, T. Ahmad, Silver nanoparticles: Ultrasonic wave assisted synthesis, optical characterization and surface area studies, *Materials Letters*, 65 (2011) 520-522.
- [123] C. Luo, Y. Zhang, X. Zeng, Y. Zeng, Y. Wang, The role of poly(ethylene glycol) in the formation of silver nanoparticles, *Journal of colloid and interface science*, 288 (2005) 444-448.
- [124] V.K. Sharma, R.A. Yngard, Y. Lin, Silver nanoparticles: green synthesis and their antimicrobial activities, *Advances in Colloid and Interface Science*, 145 (2009) 83-96.
- [125] I. Sawada, R. Fachrul, T. Ito, Y. Ohmukai, T. Maruyama, H. Matsuyama, Development of a hydrophilic polymer membrane containing silver nanoparticles with both organic antifouling and antibacterial properties, *Journal of Membrane Science*, 387-388 (2012) 1-6.
- [126] V. Vatanpour, A. Shockravi, H. Zarrabi, Z. Nikjavan, A. Javadi, Fabrication and characterization of anti-fouling and anti-bacterial Ag-loaded graphene oxide/polyethersulfone mixed matrix membrane, *Journal of Industrial and Engineering Chemistry*, 30 (2015) 342-352.
- [127] H.L. Yang, J.C. Lin, C. Huang, Application of nanosilver surface modification to RO membrane and spacer for mitigating biofouling in seawater desalination, *Water Research*, 43 (2009) 3777-3786.
- [128] J. Yin, Y. Yang, Z. Hu, B. Deng, Attachment of silver nanoparticles (AgNPs) onto thin-film composite (TFC) membranes through covalent bonding to reduce membrane biofouling, *Journal of Membrane Science*, 441 (2013) 73-82.
- [129] K.K. Kuorwel, M.J. Cran, J.D. Orbell, S. Buddhadasa, S.W. Bigger, Review of Mechanical Properties, Migration, and Potential Applications in Active Food Packaging Systems Containing Nanoclays and Nanosilver, *Comprehensive Reviews in Food Science and Food Safety*, 14 (2015) 411-430.
- [130] M. Ghosh, M. J, S. Sinha, A. Chakraborty, S.K. Mallick, M. Bandyopadhyay, A. Mukherjee, In vitro and in vivo genotoxicity of silver nanoparticles, *Mutation research*, 749 (2012) 60-69.

- [131] S. Grosse, L. Evje, T. Syversen, Silver nanoparticle-induced cytotoxicity in rat brain endothelial cell culture, *Toxicology in vitro : an international journal published in association with BIBRA*, 27 (2013) 305-313.
- [132] R.P. Singh, P. Ramarao, Cellular uptake, intracellular trafficking and cytotoxicity of silver nanoparticles, *Toxicology letters*, 213 (2012) 249-259.
- [133] H.E. Bergna, *Colloid Chemistry of Silica*, 234 (1994) 1-47.
- [134] L.T. Zhuravlev, The surface chemistry of amorphous silica. Zhuravlev model, *Colloids and Surfaces A: Physicochemical Engineering Aspects*, 173 (2000) 1–38.
- [135] M.C. Duke, J.C.D. da Costa, D.D. Do, P.G. Gray, G.Q. Lu, Hydrothermally Robust Molecular Sieve Silica for Wet Gas Separation, *Advanced Functional Materials*, 16 (2006) 1215-1220.
- [136] L. Peng, W. Qisui, L. Xi, Z. Chaocan, Investigation of the states of water and OH groups on the surface of silica, *Colloids and Surfaces A: Physicochemical and Engineering Aspects*, 334 (2009) 112-115.
- [137] J.T. Yates, Water interactions with silica surfaces: A big role for surface structure, *Surface Science*, 565 (2004) 103-106.
- [138] S.K. Parida, S. Dash, S. Patel, B.K. Mishra, Adsorption of organic molecules on silica surface, *Advances in Colloid and Interface Science*, 121 (2006) 77-110.
- [139] J. Yang, E. Wang, Reaction of water on silica surfaces, *Current Opinion in Solid State and Materials Science*, 10 (2006) 33-39.
- [140] K.S. Rao, K. El-Hami, T. Kodaki, K. Matsushige, K. Makino, A novel method for synthesis of silica nanoparticles, *Journal of colloid and interface science*, 289 (2005) 125-131.
- [141] D.L. Green, J.S. Lin, Y.-F. Lam, M.Z.C. Hu, D.W. Schaefer, M.T. Harris, Size, volume fraction, and nucleation of Stober silica nanoparticles, *Journal of colloid and interface science*, 266 (2003) 346-358.
- [142] S.K. Park, K.D. Kim, H.T. Kim, Preparation of silica nanoparticles: determination of the optimal synthesis conditions for small and uniform particles, *Colloids and Surfaces A: Physicochemical and Engineering Aspects*, 197 (2002) 7–17.
- [143] S.H. Wu, C.Y. Mou, H.P. Lin, Synthesis of mesoporous silica nanoparticles, *Chemical Society reviews*, 42 (2013) 3862-3875.

- [144] M. Duke, Carbonised template molecular sieve silica membranes in fuel processing systems: permeation, hydrostability and regeneration, *Journal of Membrane Science*, 241 (2004) 325-333.
- [145] A.L. Ahmad, M.A. Majid, B.S. Ooi, Functionalized PSf/SiO<sub>2</sub> nanocomposite membrane for oil-in-water emulsion separation, *Desalination*, 268 (2011) 266-269.
- [146] J.-n. Shen, H.-m. Ruan, L.-g. Wu, C.-j. Gao, Preparation and characterization of PES–SiO<sub>2</sub> organic–inorganic composite ultrafiltration membrane for raw water pretreatment, *Chemical Engineering Journal*, 168 (2011) 1272-1278.
- [147] L.-Y. Yu, Z.-L. Xu, H.-M. Shen, H. Yang, Preparation and characterization of PVDF–SiO<sub>2</sub> composite hollow fiber UF membrane by sol–gel method, *Journal of Membrane Science*, 337 (2009) 257-265.
- [148] W. Chen, Y. Su, L. Zhang, Q. Shi, J. Peng, Z. Jiang, In situ generated silica nanoparticles as pore-forming agent for enhanced permeability of cellulose acetate membranes, *Journal of Membrane Science*, 348 (2010) 75-83.
- [149] J. Yin, J. Zhou, Novel polyethersulfone hybrid ultrafiltration membrane prepared with SiO<sub>2</sub>-g-(PDMAEMA-co-PDMAPS) and its antifouling performances in oil-in-water emulsion application, *Desalination*, 365 (2015) 46-56.
- [150] J. Yin, E.-S. Kim, J. Yang, B. Deng, Fabrication of a novel thin-film nanocomposite (TFN) membrane containing MCM-41 silica nanoparticles (NPs) for water purification, *Journal of Membrane Science*, 423-424 (2012) 238-246.
- [151] J. Huang, K. Zhang, K. Wang, Z. Xie, B. Ladewig, H. Wang, Fabrication of polyethersulfone-mesoporous silica nanocomposite ultrafiltration membranes with antifouling properties, *Journal of Membrane Science*, 423-424 (2012) 362-370.
- [152] H. Wu, B. Tang, P. Wu, Optimizing polyamide thin film composite membrane covalently bonded with modified mesoporous silica nanoparticles, *Journal of Membrane Science*, 428 (2013) 341-348.
- [153] I.Y. Kim, E. Joachim, H. Choi, K. Kim, Toxicity of silica nanoparticles depends on size, dose, and cell type, *Nanomedicine : nanotechnology, biology, and medicine*, 11 (2015) 1407-1416.

- [154] W. Lin, Y.W. Huang, X.D. Zhou, Y. Ma, In vitro toxicity of silica nanoparticles in human lung cancer cells, *Toxicology and applied pharmacology*, 217 (2006) 252-259.
- [155] L. Clement, A. Zenerino, C. Hurel, S. Amigoni, E. Taffin de Givenchy, F. Guittard, N. Marmier, Toxicity assessment of silica nanoparticles, functionalised silica nanoparticles, and HASE-grafted silica nanoparticles, *The Science of the total environment*, 450-451 (2013) 120-128.
- [156] D.S. Maciver, H.H. Tobin, B.R. T., Catalytic Aluminas I. Surface Chemistry of Eta and Gamma Alumina, *Journal of Catalysis*, 2 (1963) 485-497.
- [157] M. Trueba, S.P. Trasatti,  $\gamma$ -Alumina as a Support for Catalysts: A Review of Fundamental Aspects, *European Journal of Inorganic Chemistry*, 2005 (2005) 3393-3403.
- [158] E. Yalamaç, A. Trapani, S. Akkurt, Sintering and microstructural investigation of gamma–alpha alumina powders, *Engineering Science and Technology, an International Journal*, 17 (2014) 2-7.
- [159] V. Piriyawong, V. Thongpool, P. Asanithi, P. Limsuwan, Preparation and Characterization of Alumina Nanoparticles in Deionized Water Using Laser Ablation Technique, *Journal of Nanomaterials*, 2012 (2012) 1-6.
- [160] L. Yan, Y. Li, C. Xiang, S. Xianda, Effect of nano-sized Al<sub>2</sub>O<sub>3</sub>-particle addition on PVDF ultrafiltration membrane performance, *Journal of Membrane Science*, 276 (2006) 162-167.
- [161] L. Yan, S. Hong, M.L. Li, Y.S. Li, Application of the Al<sub>2</sub>O<sub>3</sub>–PVDF nanocomposite tubular ultrafiltration (UF) membrane for oily wastewater treatment and its antifouling research, *Separation and Purification Technology*, 66 (2009) 347-352.
- [162] N. Maximous, G. Nakhla, W. Wan, K. Wong, Preparation, characterization and performance of Al<sub>2</sub>O<sub>3</sub>/PES membrane for wastewater filtration, *Journal of Membrane Science*, 341 (2009) 67-75.
- [163] F. Liu, M.R.M. Abed, K. Li, Preparation and characterization of poly(vinylidene fluoride) (PVDF) based ultrafiltration membranes using nano  $\gamma$ -Al<sub>2</sub>O<sub>3</sub>, *Journal of Membrane Science*, 366 (2011) 97-103.
- [164] X.S. Yi, S.L. Yu, W.X. Shi, N. Sun, L.M. Jin, S. Wang, B. Zhang, C. Ma, L.P. Sun, The influence of important factors on ultrafiltration of oil/water emulsion

- using PVDF membrane modified by nano-sized TiO<sub>2</sub>/Al<sub>2</sub>O<sub>3</sub>, Desalination, 281 (2011) 179-184.
- [165] Q. Chang, J.-e. Zhou, Y. Wang, J. Wang, G. Meng, Hydrophilic modification of Al<sub>2</sub>O<sub>3</sub> microfiltration membrane with nano-sized γ-Al<sub>2</sub>O<sub>3</sub> coating, Desalination, 262 (2010) 110-114.
- [166] I.M. Sadiq, S. Pakrashi, N. Chandrasekaran, A. Mukherjee, Studies on toxicity of aluminum oxide (Al<sub>2</sub>O<sub>3</sub>) nanoparticles to microalgae species: Scenedesmus sp. and Chlorella sp, Journal of Nanoparticle Research, 13 (2011) 3287-3299.
- [167] A. Eltijius, Study of mechanisms of phytotoxicity of alumina nanoparticles, in: Materials Science and Engineering, New Jersey Institute of Technology, New Jersey, 2011.
- [168] R.D. Holtz, W.D. Kovacs, An introduction to geotechnical engineering, Prentice-Hall, New Jersey, 1981.
- [169] J. Barrault, M. Abdellaoui, C. Bouchoule, A. Majesté, J.M. Tatibouët, A. Louloudi, N. Papayannakos, N.H. Gangas, Catalytic wet peroxide oxidation over mixed (Al-Fe) pillared clays, Applied Catalysis B: Environmental, 27 (2000) L225–L230.
- [170] E.G. Garrido-Ramírez, B.K.G. Theng, M.L. Mora, Clays and oxide minerals as catalysts and nanocatalysts in Fenton-like reactions — A review, Applied Clay Science, 47 (2010) 182-192.
- [171] D. Shah, P. Maiti, E. Gunn, D.F. Schmidt, D.D. Jiang, C.A. Batt, E.P. Giannelis, Dramatic enhancements in toughness of Polyvinylidene fluoride nanocomposites via nanoclay directed crystal structure and morphology, Advanced Materials, 16 (2004) 1173-1177.
- [172] C.Y. Lai, A. Groth, S. Gray, M. Duke, Enhanced abrasion resistant PVDF/nanoclay hollow fibre composite membranes for water treatment, Journal of Membrane Science, 449 (2014) 146-157.
- [173] C.Y. Lai, A. Groth, S. Gray, M. Duke, Preparation and characterization of poly(vinylidene fluoride)/nanoclay nanocomposite flat sheet membranes for abrasion resistance, Water Research, 57 (2014) 56-66.
- [174] L. Priya, J.P. Jog, Polymorphism in Intercalated Poly(vinylidene fluoride)/Clay Nanocomposites, Journal of Applied Polymer Science, 89 (2003) 2036–2040.

- [175] H. Rajabi, N. Ghaemi, S.S. Madaeni, P. Daraei, M.A. Khadivi, M. Falsafi, Nanoclay embedded mixed matrix PVDF nanocomposite membrane: Preparation, characterization and biofouling resistance, *Applied Surface Science*, 313 (2014) 207-214.
- [176] Y. Zhang, J. Zhao, H. Chu, X. Zhou, Y. Wei, Effect of modified attapulgite addition on the performance of a PVDF ultrafiltration membrane, *Desalination*, 344 (2014) 71-78.
- [177] S.-S. Lin, M.D. Gurol, Catalytic Decomposition of Hydrogen Peroxide on Iron Oxide: Kinetics, Mechanism, and Implications, *Environmental Science & Technology*, 32 (1998) 1417-1423.
- [178] Z.-Q. Huang, K. Chen, S.-N. Li, X.-T. Yin, Z. Zhang, H.-T. Xu, Effect of ferrosoferric oxide content on the performances of polysulfone–ferrosoferric oxide ultrafiltration membranes, *Journal of Membrane Science*, 315 (2008) 164-171.
- [179] Z.-Q. Huang, L. Chen, K. Chen, Z. Zhang, H.-T. Xu, A novel method for controlling the sublayer microstructure of an ultrafiltration membrane: The preparation of the PSF-Fe<sub>3</sub>O<sub>4</sub>ultrafiltration membrane in a parallel magnetic field, *Journal of Applied Polymer Science*, 117 (2010) 1960-1968.
- [180] Q. Yang, H.H. Himstedt, M. Ulbricht, X. Qian, S. Ranil Wickramasinghe, Designing magnetic field responsive nanofiltration membranes, *Journal of Membrane Science*, 430 (2013) 70-78.
- [181] M.M. Ling, T.-S. Chung, Desalination process using super hydrophilic nanoparticles via forward osmosis integrated with ultrafiltration regeneration, *Desalination*, 278 (2011) 194-202.

## GRADUATE RESEARCH CENTRE

### DECLARATION OF CO-AUTHORSHIP AND CO-CONTRIBUTION: PAPERS INCORPORATED IN THESIS BY PUBLICATION

*This declaration is to be completed for each conjointly authored publication and placed at the beginning of the thesis chapter in which the publication appears.*

#### 1. PUBLICATION DETAILS (to be completed by the candidate)

Title of Paper/Journal/Book:	Nanoparticle Incorporation into Desalination and Water Treatment Membranes—Potential Advantages and Challenges		
Surname:	Ike	First name:	Ikechukwu
College:	College of Engineering & Science	Candidate's Contribution (%):	90
Status:			
Accepted and in press:	<input type="checkbox"/>	Date:	<input type="text"/>
Published:	<input checked="" type="checkbox"/>	Date:	<input type="text"/> 15 June 2017

#### 2. CANDIDATE DECLARATION

I declare that the publication above meets the requirements to be included in the thesis as outlined in the HDR Policy and related Procedures – [policy.vu.edu.au](http://policy.vu.edu.au).

Ikechukwu Anthony Ike	Digitally signed by Ikechukwu Anthony Ike DN: cn=ikechukwu Anthony Ike, o, ou, email=tonyjamesike@yahoo.com, c=AU Date: 2017.08.11 11:18:13 +10'00'	9 August 2017
Signature	Date	

#### 3. CO-AUTHOR(S) DECLARATION

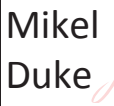
In the case of the above publication, the following authors contributed to the work as follows:

The undersigned certify that:

1. They meet criteria for authorship in that they have participated in the conception, execution or interpretation of at least that part of the publication in their field of expertise;
2. They take public responsibility for their part of the publication, except for the responsible author who accepts overall responsibility for the publication;
3. There are no other authors of the publication according to these criteria;
4. Potential conflicts of interest have been disclosed to a) granting bodies, b) the editor or publisher of journals or other publications, and c) the head of the responsible academic unit; and

5. The original data will be held for at least five years from the date indicated below and is stored at the following **location(s)**:

Institute for Sustainability and Innovation, Victoria University, Melbourne, Australia

Name(s) of Co-Author(s)	Contribution (%)	Nature of Contribution	Signature	Date
John D. Orbell	5	Review of manuscript	 Digitally signed by John Orbell John.Orbell, o=Victoria University, ou=Engineering & Science email=John.Orbell@vu.edu.au, c=AU Date: 2017.08.16 10:18:54 +10'00'	
Mikel Duke	5	Review of manuscript	 Digitally signed by Mikel Duke Date: 2017.08.11 10:41:47 +10'00'	

## Chapter 3

### **Effects of dope sonication and hydrophilic polymer addition on the properties of low pressure PVDF mixed matrix membranes\***

#### Abstract

Mixed matrix membranes (MMM) made from hydrophilic fillers incorporated into poly (vinylidene fluoride) (PVDF) are well known to have improved membrane properties and durability. However, the contributions from two key steps in MMM fabrication: dope sonication and the addition of a hydrophilic polymer like poly (vinylpyrrolidone) (PVP), have not been sufficiently highlighted. In this work, a range of MMM were made by extended dope sonication and stepwise PVP addition. The results showed that PVP, popularly referred to as a 'pore former', was surprisingly not responsible for pore formation but functioned rather as a 'pore connector' and as an aid to particle dispersion. While dope sonication resulted in efficient particle dispersion as may be expected, it did not improve membrane surface wettability as the hydrophilic nanoparticles were completely locked within the hydrophobic PVDF matrix. Sonication resulted in significant reduction in membrane porosity but did not change the membrane thermal stability. The addition of PVP, however, significantly reduced thermal stability as well as the PVDF  $\beta$ -phase mass fraction. The results of this study provide valuable insights to the effects of dope sonication and PVP addition for manufacturers and researchers developing low pressure membranes for water treatment applications.

#### 3.1. Introduction

Poly (vinylidene fluoride) (PVDF) membranes are widely used in water treatment and separation processes. The popularity of these materials derives much from their relatively good chemical, thermal and mechanical stability [1, 2]. Furthermore, these polymers could be readily processed into porous membranes for applications as diverse as membrane distillation, membrane bioreactor and for direct drinking water treatment and waste water reclamation [1]. Their wide

\*Published in Journal of Membrane Science -

<https://doi.org/10.1016/j.memsci.2017.06.056>. See the Appendix for list of contributors.

commercial fabrication and application supports ongoing research improvements [1].

PVDF is natively hydrophobic evident from its low critical surface tension (25-28.5 dynes/cm) [2] resulting in reduced water flux and higher membrane fouling [3] when applied in water treatment in comparison to less hydrophobic materials such as polyacrylonitrile (critical surface tension 44 dynes/cm [2]). Significant research efforts have been committed towards improving the filtration performance of PVDF membranes by chemical coating, plasma treatment, polymer grafting, organic and inorganic nanoparticles blending [4-6]. Direct blending of preformed inorganic nanoparticles has received significant attention in recent times as a convenient, low cost, scalable and effective means to improve the filtration performance of hydrophobic polymeric membranes [2, 4, 5, 7].

When inorganic nanoparticles are incorporated into polymeric membranes to give mixed matrix membrane (MMM), it is critical that the filler particles are properly dispersed in the polymer matrix for optimal membrane performance. One common method of achieving good particle dispersion is the application of sonication. Sonication could be applied to the solvent as well as to the dope in order to achieve good dispersion of large amount of filler in the membrane [8, 9]. Another feature of producing high quality MMMs is the addition of a hydrophilic polymer such as poly (vinylpyrrolidone) (PVP) as a pore former [9-12]. Despite the use of these two techniques for controlling performance of the PVDF membrane, a systematic investigation into their individual roles in MMM formation, rather than merely introducing them as constant preparatory recipes such as were done by Rajabi et. al [9], Liang et. al [13] and Zhang et. al [14] has not been conducted. A better understanding of the individual effects of PVP addition and dope sonication may result in the advancement of MMM design and optimisation, benefitting commercial water treatment practice.

This work explores the independent effects of dope sonication and the addition of PVP using silica coated iron oxide nanoparticles as the inorganic phase to advance knowledge in the design and fabrication of MMM for water treatment

applications. Iron oxide nanoparticle (IO) was chosen for this study because of its low cost, biocompatibility, biodegradation and magnetic properties which allows for interesting magnetic functionalisations for enhancing membrane performance [15-18]. In addition, magnetic IO could be easily and conveniently synthesised in the laboratory via the co-precipitation or reversed co-precipitation methods [19-21] with the further ease of magnetic separation from experimental suspension. However, due to IO significant absorptive capacity for natural organic matter and other common pollutants in water [22-25], the long term stability of an IO functionalised membrane under practical fouling conditions is questionable [26]. Consequently, surface coating with silica to produce more hydrophilic silica coated IO (SIO) with less affinity for pollutants was undertaken [27-29]. The hydrophilicity of silica is the result of the abundance of hydroxyl groups on the material surface. In addition, due to the high free surface energy of silica and the abundance of silanol (Si-OH) groups supplying hydrogen bonding, water molecules are easily adsorbed and these, in combination with the silanol groups, enhances the hydrophilicity of silica materials [30-32].

Although the in-situ generation of nanoparticles aimed at reducing agglomeration has been the focus of a number of recent reports [33-35], the choice of using the classical addition of preformed nanoparticles in this work stem from a number of reasons one of which is the simplicity of the latter. Another reason is the need to avoid undue interference from the complex chemical and physical interactions that may occur during in-situ nanoparticle generation. Furthermore, in-situ nanoparticles generation is more restrictive in the choice of nanoparticles, polymer and solvent that are applicable and it may be less amenable to certain hierarchical or layered nanoparticles modification such as membrane modification with silica coated iron oxide as reported in this work. Consequently, the classical addition of preformed nanoparticles remains a more general method for producing and studying MMM. Another reason, peculiar to this work, for choosing the classical method is that the addition of preformed, neat inorganic nanoparticles to a hydrophobic polymer base is prone to poor nanoparticle dispersion [33], and is therefore suitable for the study of the problem of agglomeration. Nevertheless, since addition of a pore former [34] and effective

dispersion of the polymer and the precursor in solvent media [33] are important for producing integral membranes by in-situ nanoparticles generation, the results of this study is relevant to both methods of nanoparticle incorporation.

It may be stated at this point that this research is exploratory in its aim rather than practical in the sense that the outline and extent of phenomena/processes are sought rather than their optimal performance conditions. Initial comprehensive development of the outline of phenomena is crucial for further optimisation of process conditions. The research effort so far in the field of membrane technology has been focused almost exclusively on optimising process conditions and analysing novel additives that the full independent import of certain routine recipes were left largely unexplored. This report intends to bridge this critical knowledge gap to provide more control for future optimisation.

### 3.2. Experimental

#### 3.2.1. Materials

Iron (II) chloride from Ajax Chemical, ammonia solution (25% v/v) from Merck, tetraethyl orthosilicate (TEOS) from Sigma, and analytical grade absolute ethanol were used for nanoparticle synthesis. Solef 1015 PVDF from Solvay and poly (vinylpyrrolidone) (PVP), MW 40,000 g/mol, from Sigma were dried at 60 °C for the membrane fabrications. 1-methyl-2-pyrrolidinone (NMP) from SigmaAldrich was used as solvent for the dissolution of the polymers. Analytical grade sodium chloride (NaCl) and poly (oxyethylene) (20) sorbitanmonolaurate (Tween 20), and commercial sunflower oil were used for emulsion preparation. Milli-Q™ (type 1) water was used for all chemical synthesis while oil-water emulsion production and all filtration test utilised Elix™ (type 2) water both from a commercial Merck Millipore Integrated Water Purification System. Elix water had a conductivity of 6.3 µS/cm and no particle was detected when analysed by the dynamic light scattering (DLS) technique using Malvern zetasizer nano ZS.

### 3.2.2. Particle synthesis

IO were produced by the co-precipitation method from Iron (II) chloride precursor and ammonia solution following the method of Mahmed et al [21] with a slight modification. Briefly, iron (II) chloride was transferred into vigorously boiling Milli-Q water at atmospheric pressure. The system was heated and magnetically stirred over a hot plate. After dissolution of the iron (II) chloride, ammonia solution was added drop wise resulting in the precipitation of IO which was aged for 6 hours with continuous stirring and boiling. Subsequently, the precipitate was washed in Elix water and was magnetically separated from the washing liquid to give black IO particles. For the purpose of silica coating to make SIO particles, the washed precipitate was transferred into a large conical flask holding a mixture of ethanol, TEOS, ammonia solution and Milli-Q water following a modified sol-gel process [36]. The suspension was stirred vigorously using an overhead stirrer at room temperature for 24 h. Thereafter, the magnetic nanoparticles were separated with a bar magnet, washed, dried at 60°C and then crushed to fine powder to give SIO nanoparticles.

### 3.2.3. Particle characterisation

The synthesised nanoparticles were analysed by X-ray diffraction (XRD), attenuated total reflectance Fourier transform infra-red (ATR-FTIR) spectroscopy and N<sub>2</sub> porosimetry. XRD studies were conducted using Panalytical X'pert Powder XRD diffractometer operated at 45 kV and 30 mA and was employed to define the crystalline phase of the produced particles. Based on the XRD data, the crystallite size of the IO particles was estimated using the Scherrer equation [21]:

$$\tau = \frac{0.9\lambda}{\beta \cos\theta} \quad 3.1$$

where  $\tau$  is the crystallite size,  $\lambda$  is the X-ray wavelength (1.5406 Å),  $\beta$  the line broadening at half the maximum intensity (FWHM) and  $\theta$  the Bragg angle. ATR-FTIR analysis was conducted using Perkin Elmer FTIR Spectrometer with Universal ATR Diamond/ZnSe crystals operated at an accumulation of 16 scans and at a resolution of 4 cm<sup>-1</sup> to identify the presence of the silica coating. Particle

size characterisation was conducted via N<sub>2</sub> porosimetry to determine Brunauer Emmett Teller (BET) specific surface area from which the particle size was calculated using the following expression [37, 38].

$$d = \frac{6000}{S \times \rho}$$

### 3.2

where  $d$  is the average particles diameter (nm),  $S$  the particles BET surface area (m<sup>2</sup>/g) and  $\rho$  particles' density (g/cm<sup>3</sup>). The derivation of Equation 3.2 is provided in the Appendix. BET measurements were conducted using Micrometrics TriStar Surface Area and Porosity Analyser with TriStar 3000 version 6.04 analysis software. Powders were degassed at 150 °C for 24 h for the analysis.

#### 3.2.4. Membrane fabrication

Membranes were made by the well-known nonsolvent induced phase separation (NIPS) procedure with addition of inorganic fillers following a slight modification of the procedures published by Rajabi *et al* [9] and Lai *et al.* [39]. Four sets of PVDF MMM, named P0, P21, P48 and Sonic, were fabricated by dissolving separately 3.75 g of PVDF powder in NMP. Various weight percent (wt.%) of SIO fillers with respect to the mass of the PVDF were added to the dissolved polymer after the particles were sonicated in NMP for 1 h using a probe-type sonicator (Hielscher Ultrasonic Processor UP400S) operated at an effective power of ~10 W and working frequency of 24 kHz. The compositions of the membranes for each set are given in Table 3.1. The mass of NMP used as solvent for each membrane was approximately 5 times the total mass of solids (PVDF + SIO + PVP). This scheme of variable solvent amount was adopted in view of the large variation in the amount of added solids in order to eliminate any potential effect of solvent concentration on the properties of the membranes. Using a fixed amount of solvent was such that some dope would not form membrane either due to too much solvent or too little solvent. For the P21 and P48 sets, 0.8 g and 1.8 g of PVP was added to the PVDF powder respectively, and stirred to dissolution at room temperature (~24 °C) using an overhead stirrer before the addition of the sonicated nanoparticles after which stirring was continued until the dope appeared homogenous. The dopes were degased by connecting the flask to a vacuum pump until bubbles had noticeably disappeared. The P0 membranes were subjected to a similar treatment as was P21 and P48 with the sole exception

that no PVP was added. Due to the observed significant particle aggregation that resulted in visible tear of the membrane during casting, membranes with filler >10 wt.% were not synthesised for the P0 set. For the Sonic set, no PVP was added to the PVDF powder. Fillers were sonicated in NMP for 1 h before PVDF powder was added and sonication was continued. At intervals of 45 min, sonication was stopped and the dope stirred by hand after which sonication was continued. This process was terminated when the dope appeared homogeneous and free of bubbles. Clear dopes after standing for at least 1 h were cast on glass plates and underwent phase inversion in Elix water at room temperature. After phase inversion, membranes were left in fresh Elix water for 24 h at room temperature before they were removed and stored wet at 4 °C.

Table 3.1. Membrane compositions,g (wt.% with respect to the mass of PVDF).

Membrane set	SIO	PVDF	PVP	NMP	Membrane Code
<b>P0</b>	0(0)	3.75(100)	0(0)	23(600)	P0_S0
	0.15(4)	3.75(100)	0(0)	23(600)	P0_S4
	0.38(10)	3.75(100)	0(0)	23(600)	P0_S10
<b>P21</b>	0(0)	3.75(100)	0.79(21)	23(600)	P21_S0
	0.15(4)	3.75(100)	0.79(21)	23(600)	P21_S4
	0.38(10)	3.75(100)	0.79(21)	23(600)	P21_S10
	0.75(20)	3.75(100)	0.79(21)	26(700)	P21_S20
	1.88(50)	3.75(100)	0.79(21)	30(800)	P21_S50
<b>P48</b>	0	3.75(100)	1.80(48)	26(700)	P48_S0
	0.15(4)	3.75(100)	1.80(48)	26(700)	P48_S4
	0.38(10)	3.75(100)	1.80(48)	30(800)	P48_S10
	0.75(20)	3.75(100)	1.80(48)	30(800)	P48_S20
	1.88(50)	3.75(100)	1.80(48)	34(900)	P48_S50
<b>Sonic</b>	0	3.75(100)	0(0)	23(600)	Sonic_S0
	0.15(4)	3.75(100)	0(0)	23(600)	Sonic_S4
	0.38(10)	3.75(100)	0(0)	23(600)	Sonic_S10
	0.75(20)	3.75(100)	0(0)	23(600)	Sonic_S20
	1.88(50)	3.75(100)	0(0)	30(800)	Sonic_S50

### 3.2.5. Membrane characterisation

Particle dispersion in the MMM was evaluated by optical and scanning electron microscopy (SEM). For optical microscopy a small rectangular piece of each membrane was placed on a microscope slide and imaged using Carl Zeiss Axioplan 2 optical microscope in transmission mode using a fixed scanning objective lens (4x). For SEM, a FEI Quanta 3D FEG electron microscope was used to observe the material microstructure at 20 kV. Cross-sectional images of membranes were obtained using JEOL Neoscope JCM-5000 at 10 kV after membranes were snapped following immersion in liquid nitrogen. All membranes

were gold coated before imaging. Polymer crystalline phase was studied by FTIR analysis under conditions already specified (Section 3.2.3) on samples that were dried by exposure to ambient laboratory conditions. A quantitative estimation of the mass fraction of the  $\beta$  phase with respect to the  $\alpha$  phase from the characteristic band of 763 and 840  $\text{cm}^{-1}$  for  $\alpha$  and  $\beta$  phases respectively was computed using [40]:

$$F(\beta) = \frac{A_\beta}{1.26A_\alpha + A_\beta} \quad 3.3$$

where  $F(\beta)$  is the mass fraction of  $\beta$  phase in a sample of PVDF polymer and  $A_\alpha$  and  $A_\beta$  are absorption peaks height of the  $\alpha$  and  $\beta$  phases corresponding to the characteristics wavenumbers of 763 and 840  $\text{cm}^{-1}$  respectively. Thermal gravimetric analysis (TGA) was performed with Mettler Toledo Thermal Analyser TGA/DSC 1 STARe System under nitrogen flow of 20 mL/min and steady temperature increment of 10  $^{\circ}\text{C}/\text{min}$  until a temperature of 700  $^{\circ}\text{C}$  was reached. To determine the concentration of pores on the skin layer or membrane surface porosity defined as the total area of the surface pores detectable on a membrane skin layer divided by the membrane area, the SEM images of the membrane skin layers were processed using ImageJ (<https://imagej.nih.gov/ij/>). Bulk porosities ( $\varepsilon$ ) for filler-free membranes were computed using the following expressions [41]:

$$\varepsilon = \frac{M_w - M_d}{(M_w - M_d) + \frac{M_d}{\rho_P}} \quad 3.4$$

where  $M_w$  is the mass of a wet piece of membrane (after all surface water was removed using a paper towel),  $M_d$  is the mass of the same piece of membrane after drying at 60  $^{\circ}\text{C}$  for 24 h and  $\rho_P$  is the density of PVDF (1.78 g/cm $^3$ ). The density of water was assumed to be 1 g/cm $^3$ [41]. N<sub>2</sub> porosimetry analysis was conducted as specified in Section 3.2.3 except that each sample was degassed at 90  $^{\circ}\text{C}$  for 24 h before analysis.

Membrane contact angles (CA) were measured using Krüss drop shape analyser – DSA25 under room temperature of 20  $^{\circ}\text{C}$  using PTFE needle of diameter 0.69 mm. 4.0  $\mu\text{L}$  droplet volume was placed on a membrane and the CA computed using the Young Laplace fitting method. About 10 cm long strip of each membrane was used for the wettability experiment with at least five CA measurements taken along each strip and the results averaged. A dead end

filtration test to evaluate the membrane integrity and filtration performance was conducted using Polypropylene In-Line holder (PP47) from Adventec as membrane module. A FMI “Q” pump (QG20) from Cerampump operated at a constant flux of  $96 \text{ Lm}^{-2}\text{h}^{-1}$  was used for the test. Transmembrane pressure was measured using logged TPI665 digital manometer. The filtration test cycles involve membrane compression to 180 kPa for 10 min by filtering with clean water, and then clean water ‘pre-fouling’ filtration for 40 mins, 2 h oil emulsion ‘fouling’ filtration, and ‘post-fouling’ clean water filtration for 40 min. After each emulsion filtration, the membrane was removed from the module and the membrane selective surface was rinsed under flowing tap water to remove reversible foulants. Before returning the membrane to the module for the ‘post-fouling’ water permeation, the module was rinsed with water, 0.1 M NaOH solution and water consecutively; each rinsing lasting for a period of 40 min to remove any oil residue. The oil emulsion used as fouling solution was produced by homogenising 0.5 g sunflower oil and 0.1 g Tween 20 and in 1 litre of Elix water using a Unidrive X 1000 homogeniser operated at 17,500 rpm for 30 minutes [42]. Oil droplet size was measured by the DLS technique using Malvern zetasizer nano ZS. Membrane rejection was evaluated based on turbidity reduction as measured by Hanna Instruments Turbidimeter.

### 3.3. Results and Discussion

#### 3.3.1. Particle characterisation

The XRD patterns for the IO and SIO powders are shown in Figure 3.1a. These patterns show well developed standard Bragg peaks for magnetite ( $\text{Fe}_3\text{O}_4$ ) or maghemite ( $\gamma\text{-Fe}_2\text{O}_3$ ) at  $2\theta$  values of  $30^\circ$  (220),  $35^\circ$  (311),  $37^\circ$  (222),  $43^\circ$  (400),  $53^\circ$  (422),  $57^\circ$  (511) and  $63^\circ$  (440) [21, 43, 44]. However, the black colour of the IO powder is suggestive of  $\text{Fe}_3\text{O}_4$  phase rather than  $\gamma\text{-Fe}_2\text{O}_3$  [18]. The similarity between the two patterns in Figure 3.1a without a distinct broad peak between  $2\theta 20\text{-}25^\circ$  is indicative of minimal silica influence [21] suggestive of a thin silica shell. Using the Scherrer Equation (Equation 3.1) for the (311) peak of the IO XRD pattern, the average crystallite size was calculated as 20 nm. The FTIR spectra for IO and SIO synthesised particles are given in Figure 3.1b. The major peak between  $1160\text{-}1000 \text{ cm}^{-1}$  is characteristic of the Si-O-Si bond [31, 45]

showing the presence of silica on SIO, while this peak as expected was not present for IO. The BET surface areas for IO and SIO as measured from N<sub>2</sub> porosimetry were 38 and 29 m<sup>2</sup>/g. The slightly lower surface area for the SIO may be associated to the probable silica coating of aggregated IO particles. Assuming a thin silica coating for SIO and using 5.1 g/cm<sup>3</sup>, the density of bulk magnetite, as representative density value for both powders, the computed particle size using Equation 3.2 is 31 and 41 nm for IO and SIO respectively. The BET computed particle size of 31 nm for IO compares with the XRD derived average particles crystalline size of 20 nm. The BET surface areas and calculated particles sizes are summarised in Table 3.2.

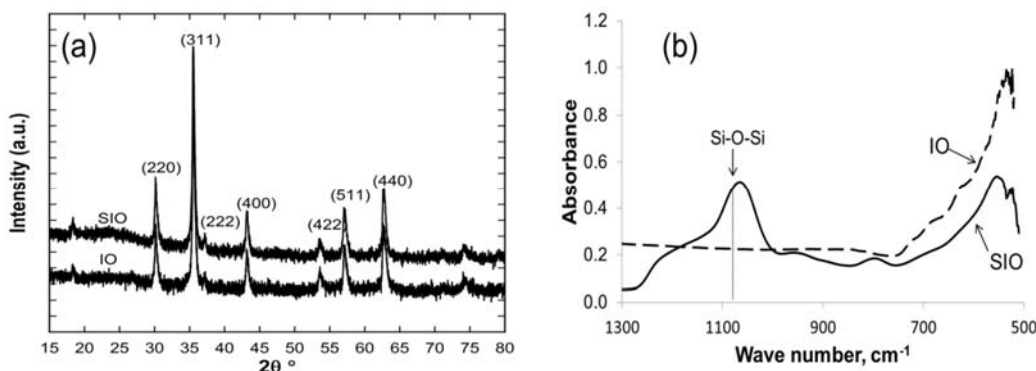


Figure 3.1. XRD patterns (a) and FTIR spectra (b) for IO and SIO powders

Table 3.2. BET surface areas and particle sizes for synthesized particles

Particle	BET specific surface area (m <sup>2</sup> /g)	BET derived particle size using Equation 2 (nm)	XRD derived crystalline size using Equation 1 (nm)
IO	38	31	20
SIO	29	41	-

### 3.3.2. Particle dispersion in membrane

Figure 3.2 shows optical transmission and SEM images of representative membranes at 4 wt.% and 50 wt.% filler as well as images for the filler free

P21\_S0 membrane. Optical and SEM images at other filler proportions are presented in the Appendix (Figures S3.1 and S3.2 respectively). Also presented in the Appendix is the SEM cross-sectional images showing typical asymmetric pore morphology of thin skin layer and spongy substructure (Figure S3.3) [39]. In Figure 3.2, significant surface inhomogeneity could be observed in the P0\_S4 membrane containing no PVP suggesting severe particle aggregations. The P21 and P48 membranes with 21 wt.% and 48wt .% PVP respectively shows a more homogeneous surface feature under the optical microscope which could be interpreted as indicating that the addition of PVP aided the dispersion of the hydrophilic nanoparticles across the PVDF matrix. The Sonic membrane (Fig. 3.2a) showed very homogenous surface features comparable with the filler-free membrane (P21\_S0) (Figure 3.2b). The inhomogeneity in the P21 and P48 membranes becomes more obvious at the higher filler proportion of 50 wt.% (Figure 3.2b). The P48\_S50 membrane appears to show better homogeneity than the P21\_S50 membrane apparently suggesting that as the concentration of PVP increased (i.e. from 21 to 48 wt.%) the hydrophilic nanoparticles were better dispersed further implying that PVP aids filler dispersion in membranes. Light could not be transmitted through the Sonic\_S50, which seems to suggest good particle dispersion. The reasoning here derives from the fact that the nanoparticles were black and opaque to light hence when well dispersed in the membrane, every portion of the membrane would be opaque/black. When poorly dispersed, some regions would be opaque while other regions would transmit light, as was the case for P21\_S50 and P48\_S50. This appears to be corroborated by the SEM image of Figure 3.2c where the homogenous feature of Sonic\_S50 is comparable to that of the filler free P21\_S0. The intense particle aggregation for the P0\_S4 membrane resulted in visible tear on the membrane during casting, thereby undermining its use as a membrane. Consequently, membranes with filler >10 wt.% were not produced for the P0 set.

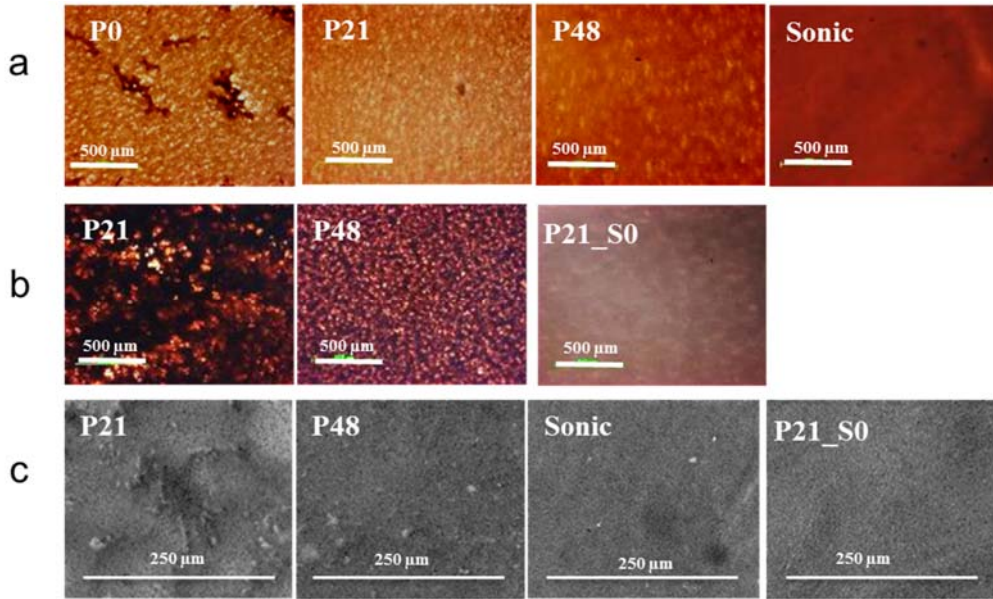


Figure 3.2. Optical transmission microscope images of membranes at filler proportion of 4 wt.% (a), 50 wt.% (b), and SEM images at 50 wt.% (c). Optical and SEM images for P21\_S0 membrane are shown in (b) and (c) respectively.

### 3.3.3. Crystalline phase

PVDF is known to exist in about four crystalline forms [46, 47]. The  $\beta$  phase appears to be the most important as it exhibits important properties such as piezo-, pyro- and ferroelectric effects and has also been associated with enhanced mechanical strength which is important for developing durable and integral membranes [39, 40, 48, 49]. The polar  $\beta$  phase has also been associated with PVDF membranes increased affinity for polar molecules [41] and hence could be valuable in the control of fouling by non-polar contaminants. A number of procedures have been shown to induce or enhance the formation of the  $\beta$  phase of PVDF including mechanical treatment and the incorporation of nanoparticles [49, 50]. Infrared spectroscopy is a common technique for characterising the crystalline phase of PVDF. FTIR peaks at 763, 796 and 976  $\text{cm}^{-1}$ , have been associated with the  $\alpha$  phase while peaks at 840 and 1175  $\text{cm}^{-1}$  have been linked to the  $\beta$  phase [41, 51]. Figure 3.3a is the FTIR spectra for filler-free membranes showing characteristics band for  $\alpha$  and  $\beta$  phases of PVDF as well as a band at

1660 cm<sup>-1</sup> that could be associated with C=O [52] indicative of the presence of PVP in P21 and P48 but not in the other two membrane sets. It may be noted that peaks for the  $\alpha$  phase are most prominent for the P48 membrane and least expressed for the P0 membrane suggesting that both PVP addition and dope sonication favoured the development of the  $\alpha$  phase of PVDF. The FTIR spectra for P0, P21, P48 and Sonic membranes are shown in Figure 3.3b, c, d, and e, respectively. It can been seen that the addition of the nanoparticles decreased the peak for the  $\alpha$  phase for all membrane sets. In fact, the peaks for the  $\alpha$  phase almost disappeared at 20 wt.% filler for P21, P48 and Sonic sets. For the P21 set,  $\alpha$  phase peak was also absent at 4 wt.%. Consequently, the SIO nanoparticles appear to direct/stabilise the PVDF crystalline structure in favour of the  $\beta$  phase as has been previously reported for silicates [39, 53]. However, at the higher filler loading of 50 wt.%, the  $\alpha$  phase peak is seen to reappear. This observation may be related to significant interference with the polymer framework with diminished polymer-polymer entanglement and altered properties due to the presence of large amount of nanoparticles [54, 55].

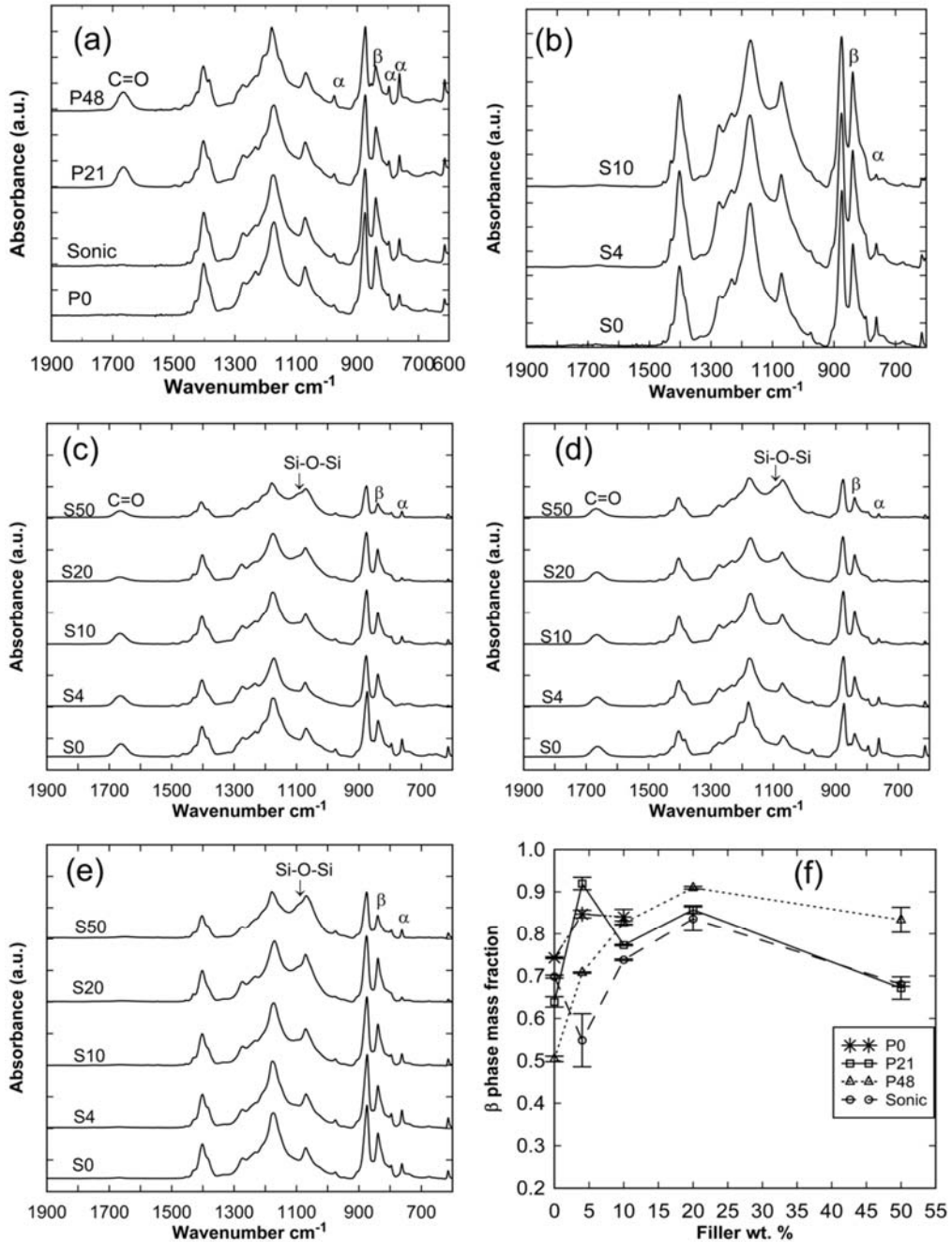


Figure 3.3. FTIR spectra showing characteristics peaks for  $\alpha$  and  $\beta$  phases of PVDF, the Si-O-Si peak for silica, and the C=O peak for PVP for membranes with no added filler nanoparticles (a) P0 membranes (b) P21 membranes (c) P48 membranes (d) Sonic membranes (e) and the mass fraction of PVDF  $\beta$  phase determined from FTIR spectra by Equation 3.3 (f).

Using Equation 3.3, the computed  $\beta$  phase mass fractions for the membranes under investigation are given in Figure 3.3f. These results suggest that in the absence of inorganic filler, both sonication and PVP addition reduced the formation of  $\beta$  phase as have been noted with the later showing a more significant reduction effect. The addition of 48 wt.% PVP reduced the  $\beta$  phase mass fraction from 0.74 to 0.50. Zhao et al. [51] has previously reported that the addition of a hydrophilic polymer, poly(methylmethacrylate) (PMMA), favoured a particular PVDF polymorph. In their work, PMMA was reported to increase the formation of the  $\beta$  phase while in this work the  $\beta$  phase was observed to decrease with the addition of the hydrophilic PVP. The difference may be associated with the nature of solvent used for phase inversion or to specific effect of the hydrophilic polymer itself [51]. However the addition of 4 wt.% inorganic filler assisted in the prevention of  $\beta$  phase reduction, where 0.71 remained. For the P0 and P21 membranes (Figure 3.3b,c), 4 wt.% filler material resulted in a polymer film with a  $\beta$  phase concentration of 0.85 and 0.92 respectively. The high value of 0.92 for  $\beta$  phase mass fraction for P21\_S4 is consistent with the absence of an  $\alpha$  phase peak in Figure 3.3c. The same amount of filler material, however, decreased the  $\beta$  phase for the Sonic membrane from 0.70 to 0.55. Further filler addition to 20 wt% increased the  $\beta$  phase for the Sonic membrane to 0.84. The  $\beta$  phase fraction declined at the highest filler composition of 50 wt.%, settling to between 0.67 and 0.83 for P21, P48 and Sonic. The P48 membrane maintained the highest  $\beta$  phase of 0.83 at the maximum filler composition of 50 wt% indicating its crystalline phase was least affected by the presence of significant amount of inorganic filler interfering with the PVDF polymer framework probably due to its higher PVP content.

Figure 3.3f shows relatively complicated trends in the  $\beta$  phase mass fraction with respect to dope sonication, nanoparticles and PVP addition demonstrating the complex interaction of the PVDF polymer crystalline phase to membrane fabrication processes and additives. However, the complex trends of the  $\beta$  phase mass fraction are not limited to membrane relevant processes [49]. In fact, the trends in Figure 3.3f is similar to those published by Sajkiewicz et al [50] for the effects of drawing temperatures on the proportion of  $\beta$  phase in PVDF samples

from different suppliers and under different rate of drawing. The  $\beta$  phase mass fraction was seen to increase with increasing drawing temperature at diverse rates for these samples, peaked at some point and subsequently began to decrease at dissimilar rates at higher drawing temperatures.

### 3.3.4. Thermal properties

Several articles published on MMM have shown that the addition of silica nanoparticles and nanoparticle of other materials could lead to substantial improvement in thermal stability [29, 56, 57]. The results of the thermal stability measured by TGA are given in Figure 3.4. It can be seen that the addition 21 wt.% PVP (Figure 3.4a) led to a significant loss in thermal stability, reducing the onset of thermal induced weight loss for the filler-free membrane from 440 °C for P0\_S0 to 310 °C for P21\_S0. Initial addition of 4 wt.% filler to P21 increased the thermal degradation temperature from about 310 °C to about 350 °C while the stability improvement for P48 (Figure S3.4) was from about 295 °C to 340 °C. No significant change in thermal stability was observed for the P0 set upon filler addition up to 10 wt.%. This may be the consequence of the limited integration of the filler material with the polymer network due to the significant filler aggregation observed earlier (Section 3.3.2). The observed improvement in thermal stability for the P21 membrane due to filler addition appears to correlate with the increase in the proportion of the  $\beta$  phases as identified in Figure 3.3. However, unlike the  $\beta$  phase mass fraction trend, after the initial improvement in thermal stability with the addition of 4 wt.% inorganic filler, subsequent increase in the amount of the inorganic particles does not appear to have significant effect on MMM thermal stability. Nevertheless, it appears that increasing amount of filler may have had a slight negative effect on thermal stability. However, the lower profile for the 50 wt.% membrane may be due partly to the filler nanoparticles dehydration since it is composed of the greatest proportion of filler material. For the Sonic membranes (Figure 3.4b), the highest temperature of about 440 °C for the initial onset of thermal weight loss was measured for the filler-free membrane identical to the P0\_S0 membrane. There appears to be a gradual but consistent reduction in thermal stability with increase in the amount of filler unlike the P0 set suggesting

better integration of the particles in the polymer network. Decreasing thermal stability of MMM with increasing particle loading has been previously reported [39] suggesting that the presence of the filler materials are probably physically interfering with the polymer structural networks or are catalysing the decomposition of the composite membrane [39, 54, 55].

It seems that while higher  $\beta$  phase mass fraction favours improved thermal stability based on literature data [39, 48], the amount of the filler nanoparticles when considered in isolation seems to impair thermal stability. Consequently, membranes with high filler fractions even when they possess appreciable amount of  $\beta$  phase shows relatively lower thermal stability. The addition of PVP appears to weaken the membrane thermal stability, which can be seen by comparing the temperature for the initial onset of thermal degradation for P0\_S0 of 440 °C to the reduced values of 310 °C and 295 °C for P21\_S0 and P48\_S0 respectively. Since the profile for P0\_S0 closely matches the profile for Sonic\_S0, it may be concluded that dope sonication had no significant effect on thermal stability.

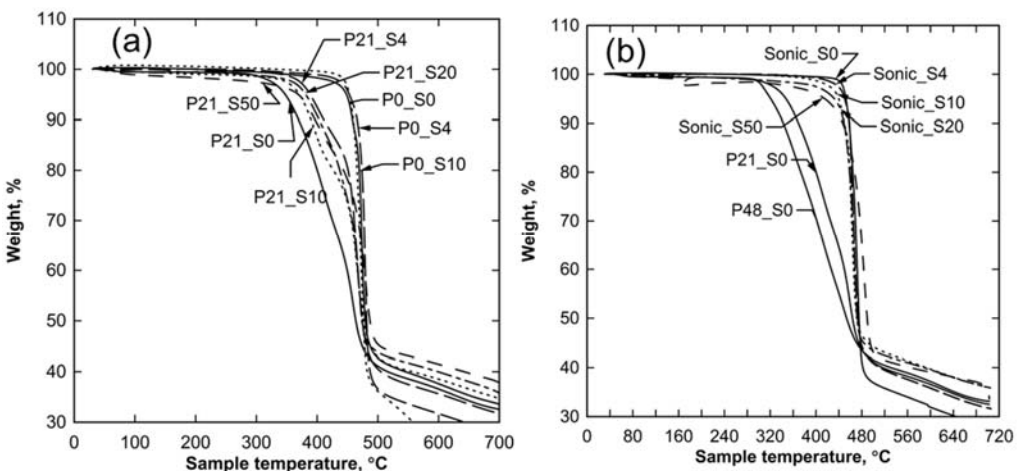


Figure 3.4. TGA weight loss profiles for P21 and P0 (a) Sonic (b) membranes. The weight loss profile for P21\_S0 and P48\_S0 are included in (b).

### 3.3.5. Porosity and pore surface area

Figure 3.5a shows that the bulk porosity for filler-free membranes computed using Equation 3.4 ranged from 68% to 90%. Since the matrix density was assumed to be the density of PVDF ( $1.78 \text{ g/cm}^3$ ), this equation was only applied to the filler-

free membranes. From Figure 3.5a, P0\_S0, with no added PVP, showed a bulk porosity of 86% indicative of a porous membrane and suggestive of rapid demixing during phase inversion [12]. The addition of 21% PVP only provided a marginal increase in porosity to 90%. For the higher PVP content of 48%, the porosity appears to shrink to 85%. The limited beneficial effect of the addition of PVP to the bulk porosity of membranes produced in this work may be associated with a possible increase in dope viscosity due to the high PVP content [12]. At a high PVP concentration, the increased dope viscosity has been reported to reduce the rate of demixing or solvent/non-solvent inter-diffusion during the phase inversion process resulting in a less porous membrane [12]. In addition, during the demixing process, hydrophilic PVP polymer has been reported to separate from the hydrophobic polymer (PVDF) and to accumulate in developing pores and channels (PVDF-lean regions) [58], a process that is expected to reduce the overall porosity of the membrane as was the case for P48. Sonication, in the absence of PVP, evidently resulted in the reduction of membrane bulk porosity as the Sonic\_S0 showed the lowest porosity of 68%. The result may also be associated to the effect of dope viscosity increase due to local high temperature developed in the dope during the sonication process [59, 60] that may have increased the rate of solvent evaporation. In addition, the intense energy of the ultrasonic energy [59] may result in better dissolution of the PVDF polymer due to greater unfolding of the polymer molecular chains [47]. Well dissolved PVDF has been reported to result in higher dope viscosity [47]. The higher viscosity of the casting dope from sonication is expected to result in limited demixing and therefore less porous membranes [12].

BET specific surface areas for all membranes studied in this work are shown in Figure 3.5b. The specific surface area ranged from 10 m<sup>2</sup>/g to 30 m<sup>2</sup>/g showing the degree of porosity within the PVDF that is accessible by N<sub>2</sub> molecules. Specifically, the Sonic membranes showed the least pore surface area at all filler proportions. These results are consistent with the bulk porosity results discussed in the previous section where sonication was seen to result in less porous membrane. In the absence of fillers, the P0 membrane is seen to exhibit a higher BET specific surface area than P21 and P48 membranes but in the presence of

filler materials, the effect was reversed and the P0 membranes showed lower pore surface areas than the PVP containing membranes. The lower BET surface area for P21 and P48 membranes in the absence of fillers may be explained by a possible trapping of PVP chains in PVDF pores [58] thereby reducing the surface for N<sub>2</sub> absorption. The subsequent higher BET specific surface area for the PVP containing membranes in the presence of fillers may have resulted from the contribution to the total surface area provided by the fillers due to their relatively better dispersion in the presence of PVP (Section 3.3.2). However, since the fillers also fill up matrix pores, higher filler amounts did not result in further improvement in the BET specific surface area except for the Sonic membranes. The addition of nanoparticles could lead to higher membrane specific surface area due to the contribution to the total surface area provided by the nanoparticles (SIO BET specific surface area was 29 m<sup>2</sup>/g ) or it could lead to reduction in the net surface area if the particles substantially fill up the pores of the polymer matrix [3, 61]. These two contrary tendencies appear to influence the trend of the membrane pore surface with increasing amounts of filler. The contribution to the specific surface area from SIO particles for the Sonic sample may explain its sudden rise in BET specific surface area at 50 wt% filler, especially considering that the Sonic membranes uniquely had lower surface area compared to membranes with PVP.

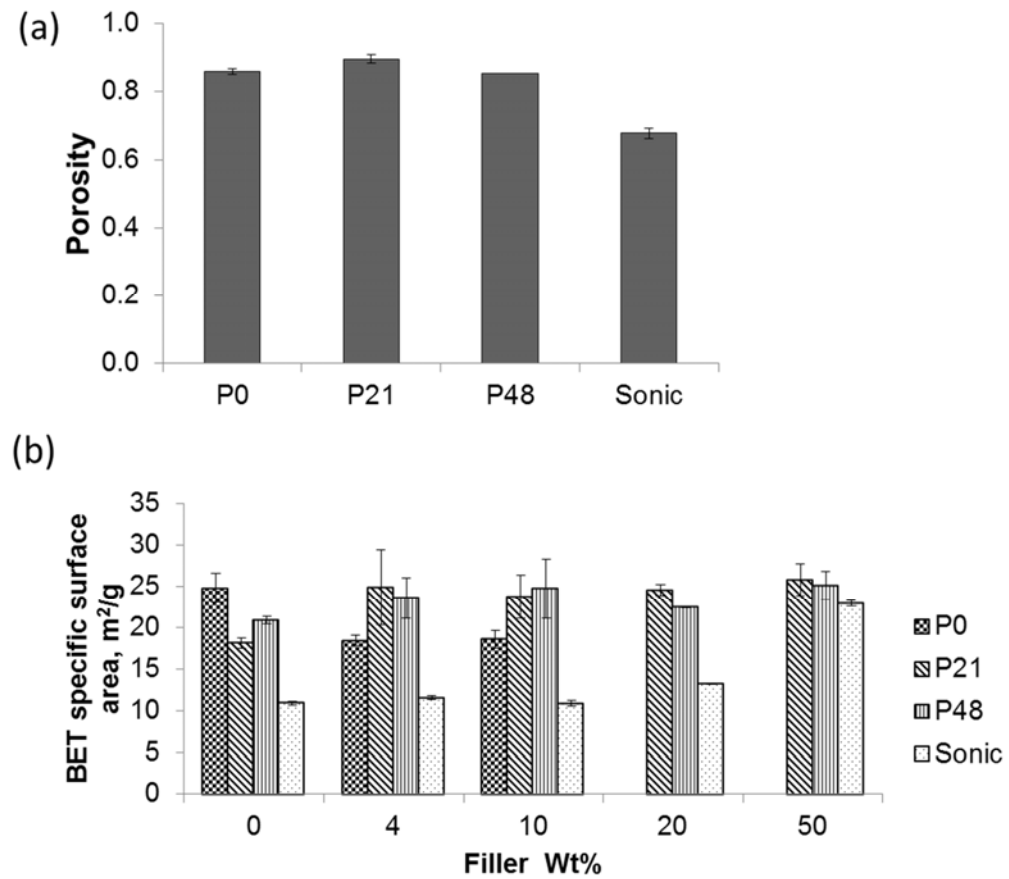


Figure 3.5. Estimations of membrane porosity by the gravimetric technique for filler free membranes (a), BET specific surface area as a function of filler amounts (b)

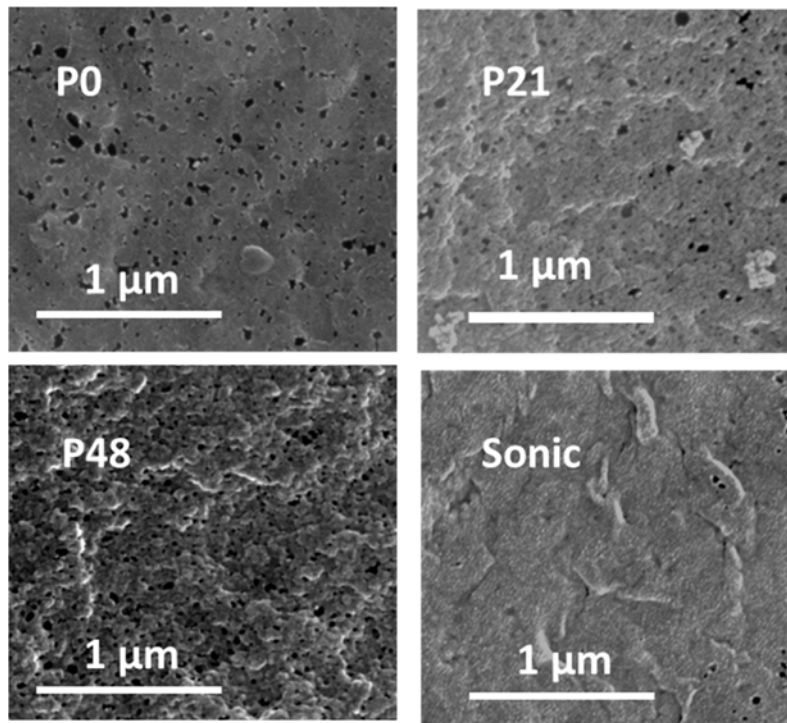


Figure 3.6. SEM images of the skin-layer surface of 10 wt.% membranes

The close-up SEM image of the selective surfaces of the membranes at 10 wt.% filler is given in Figure 3.6. Images at other filler proportions are provided in Figure S3.5. The number of visible pores on the surface of the Sonic membrane is much lower than those of the other three membranes further indicating that sonication results in reduced membrane porosity. Consistent with the bulk porosity and the BET specific surface areas, the SEM image indicates that significant amount of pores could develop in a PVDF membrane in the absence of a pore former like PVP. The surface porosity for membrane skin layer computed from SEM images is shown in Table 3.3 as detected and analysed by ImageJ. The surface porosity values appear to roughly follow a trend similar to the bulk porosity of Figure 3.5a. However, the porosity is an order of magnitude lower than the bulk PVDF, which is expected considering the skin layer has a more dense structure to provide the membrane with its selective function. The Sonic membrane is shown to have the lowest surface porosity indicative of a less porous membrane while the P21 membrane appears to show the highest surface porosity except at 20 wt.% filler. The slightly lower surface porosity value of the P48 membrane even with respect to the P0 membrane except at 20 wt% filler once again indicates that high PVP

concentration results in less porous membrane probably due to increase in dope viscosity [12] or due to pore filling by trapped PVP [58]. The relatively high surface porosity for the P0 membrane could be taken to imply that in the absence of a pore former, significant amount of pores could still develop in a PVDF membrane. However, it can be observed from Figure 3.6 that the presence of PVP appears to result in the development of skin layers with distinct nodular structures [58] and round pores though with apparently rougher surface morphology. From Table 3.3, it appears that the surface porosity for all membranes appear to increase with added filler with the P48\_S20 membrane being the sole exception to this trend. A possible explanation for the positive correlation between filler amount and surface porosity is that the presence of fillers provides rigidity for the membrane such that pore collapse or shrinkage is reduced. Another possible explanation may be the loss of more surface hydrophilic fillers into the coagulating bath during the phase inversion process as the amount of initial filler increased resulting in more pores in the membrane structure [62].

Table 3.3. Surface porosity computed from ImageJ analysis of SEM images

<b>Membrane</b>	<b>Surface porosity (%) for various filler concentrations</b>			
	<b>4 wt.%</b>	<b>10 wt.%</b>	<b>20 wt.%</b>	<b>50 wt.%</b>
<b>P0</b>	3.3	5.4	-	-
<b>P21</b>	3.8	5.8	6.7	11.3
<b>P48</b>	2.4	4.5	8.4	6.8
<b>Sonic</b>	0.7	1.1	1.5	3.0

### 3.3.6. Membrane wettability

The water CA of the membranes is shown in Figure 3.7a. Significant fluctuations in measured CA ranging from about 70 to 90 ° were observed for the membrane at varying filler amounts. Filler additions appear not to have any discernable effect on the membrane CA, likely because of interference from membrane roughness and limited filler dispersion as discussed in Section 3.3.2. Particle aggregation reduces the effective amount of hydroxyl groups in direct contact with the water drop [29, 61] and also provide an uneven and rough surface so that part of the

water drop makes no contact with the membrane but is suspended in air resulting in high CA [63]. Overall, it can be said that the CA for all the membranes based on Figure 3.7a are similar irrespective of the amount of hydrophilic additive or ultrasonic treatment. However, during the CA measurement, a record was kept of the rate of decrease of the CA (CA-d) with time for the membranes. The trends for this dynamic behavior are presented in Figure 3.7b. This result shows there is significant difference in the interactions between the different membrane sets and water, which is indicative of varying wettability properties not captured by static CA results of Figure 3.7a. The P48 showed CA-d of up to about 2 °/s while the values for the P0 membranes were <0.05 °/s. The CA-d is related to the rate of water penetration into the membrane via capillary action which have been shown to be dependent on the effective water CA with the substrate [64]. Consequently, it can be said that the membrane wettability or affinity for water improved considerably with the addition of PVP and hydrophilic inorganic particles. The relative decrease in the CA-d for the P21\_S50 membrane may be related to poor particle dispersion as shown in Figure 3.2b. It is likely that the specific effect of PVP is to connect the hydrophilic inorganic particles so that water molecules are attracted to particles further away from the membrane surface [65]. Since the demixing process during phase inversion result in an interconnected PVDF-lean and PVP-rich regions forming the membrane pore network [58] it can be expected that the hydrophilic nanoparticles are more likely to be associated with this PVP interconnected network [65]. In this system, water molecules on the membrane surface could be rapidly adsorbed into the membrane, being transferred from one particle to the other with the help of the hydrophilic connectivity provided by PVP polymer chains resulting in the great water affinity shown by the P21 and P48 membranes but not by P0 and Sonic membranes. For the Sonic membranes, the powerful dispersing effect of ultrasonication locked much of the hydrophilic particles within the hydrophobic polymeric matrix restricting contact with water. During the phase inversion process for the Sonic membranes, well dispersed hydrophilic particles on the dope interface migrated more readily into the non-solvent polar water phase [62] and away from the hydrophobic PVDF matrix thereby depleting surface hydrophilic particles while well-secured or “locked” particles remained within the hydrophobic PVDF matrix. The overall effect is that

the Sonic membranes showed limited affinity for water. However, the Sonic membranes showed a slightly higher CA-d than the P0 membranes suggesting that the better particle dispersion for the Sonic membranes allowed for slightly more water penetration and that some amount of hydrophilic particles remained on the membrane surface while severe particle aggregation meant that water penetration was very low for the P0 membranes.

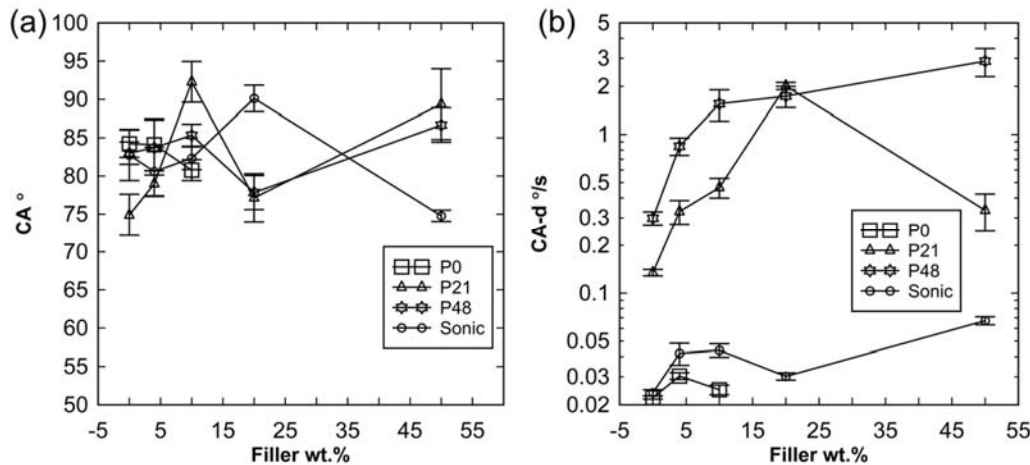


Figure 3.7. Water contact angle (CA) on membrane taken as the first stable angle before percolation induced decrease (a) and water contact angle rate of decrease with time due to water penetration into membrane under capillary action (CA-d) (b). Standard errors for at least five measurements are specified.

### 3.3.7. Membrane integrity and filtration performance

Operating under constant fluid flux of 96 L/m<sup>2</sup>/h, the transmembrane pressure (TMP) was recorded for the evaluation of the membrane filtration performance under dead-end mode. The Sonic membranes all resulted in very high 'pre-fouling' clean water filtration TMP with some TMPs rising almost instantaneously to over 600 kPa and the tests were consequently terminated as it exceeded the capacity of the experimental setup. Due to the already mentioned visible tear on the P0\_S4 and P0\_S10, these membranes were excluded from the filtration tests. Although the P0\_S0 membrane showed reasonable 'pre-fouling' clean water TMP of 140 kPa, it failed to achieve a stable emulsion filtration as its TMP rose

rapidly to more than 600 kPa and the filtration test had to be discontinued. Only the P21 and P48 membranes sustained emulsion and water flux below 600 kPa. These outcomes were not unexpected as integral membranes usually benefit from both sonication and PVP addition that were eliminated or isolated in this work. The ‘pre-fouling’ and ‘post-fouling’ water flux for the P21 and P48 membranes are shown in Figure 3.8. It can be seen that the P21 and P48 membranes permeated clean water at TMP less than 30 kPa underscoring the positive effect of PVP addition in improving water permeation consistent with their higher CA-d values. It has also been reported that the presence of PVP results in high interconnectivity of pores [58] as a consequence of the migration of PVP molecules to PVDF-lean water interface regions during the phase inversion process and subsequent loss of some of the PVP molecules into the coagulating bath leaving behind channels connecting membrane pores. The lower TMP for the P21 and P48 membranes may have benefitted from both higher pore connectivity and more hydrophilic property due to the presence of PVP.

The average TMP for the ‘post-fouling’ constant flux of clean water for oil-emulsion fouled P21 and P48 membranes is given in Figure 3.8b. The greater proportion of the emulsion oil droplet sizes ranged from about 10 to 1000 nm (Figure S3.6). It can be seen in Figure 3.8 that the addition of inorganic fillers resulted in an overall significant reduction in the TMP when compared to the filler-free membrane, a trend that may be associated to the hydrophilic effect of the inorganic fillers. Improved membrane hydrophilicity due to the presence of inorganic particles resulted in decreased capillary resistance to water flow [66]. However, the TMPs appear not to reveal a discernable trend with regards to increasing amount of filler. Nevertheless, a consideration of the turbidity rejection (Figure 3.8c) indicates that higher filler fractions seem to result in better membrane rejection. Increasing MMM rejection with increasing inorganic amount of filler have been previously reported [17, 57]. It was suggested that such a trend benefits from improving hydrophilicity arising from increasing amount of filler [57]. Hydrophobic impurities in water such as emulsified oil permeate the membrane pores less readily as hydrophilicity increases thus improving rejection. The rejection results may also be indicative that large pores and defects in the MMM

were apparently more effectively blocked by the inorganic particles at higher filler fractions. The standard error for the P21 membranes were generally very large which may be attributed to the limited homogeneity of the membranes as previously noted in section 3.3.2.

Better membrane performance for the PVP containing membranes may potentially result if the polymer were dissolved at higher temperature as a consequence of a lower viscosity dope rather than at room temperature as was done in this work. However, one of the specific interests of this study was to explore the particular effects of PVP addition; future work may study how temperature enhances the PVP contribution to the membrane integrity. The rejection values for the filler-free membranes were not given because only limited permeate could be collected as the membrane fouled extensively and the test had to be terminated.

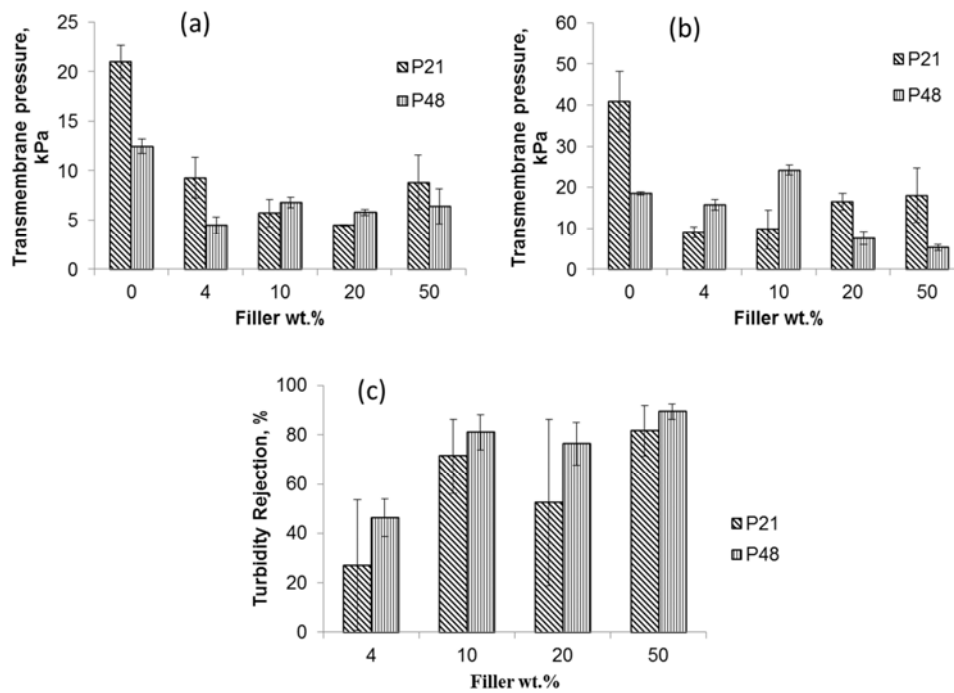


Figure 3.8. Transmembrane pressure at constant water flux of 96 L/m<sup>2</sup>/h for clean membranes (a), oil emulsion fouled membrane (b), and membrane turbidity rejection (c)

The effects of PVP addition and dope ultrasonication on hydrophilic nanoparticles dispersion, pore development and pore connectivity which ultimately determine the membrane wettability and water permeability are summarised in Figure 3.9.

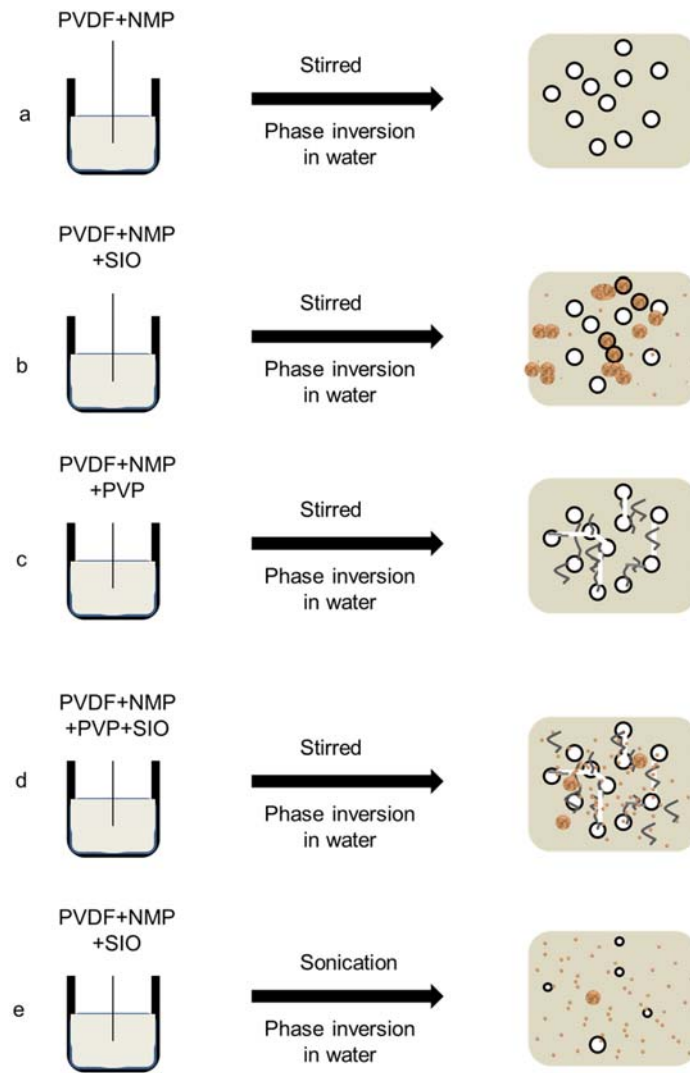


Figure 3.9. The effects of dope sonication and PVP addition on some of the properties of PVDF MMM showing pore developments due to nucleation of the polymer lean phase but limited connectivity (a); severe nanoparticle aggregation due to the hydrophilic nanoparticles incompatibility with the hydrophobic PVDF (b); pore connectivity arising from PVP migration to the polymer lean phase during phase inversion and subsequent loss of some of the PVP molecules into the coagulating bath leaving behind connecting channels (c); limited hydrophilic nanoparticle dispersion arising from the bridging effect of the hydrophilic PVP (d); good nanoparticle dispersion but limited interconnection between particles and diminished pore development as a consequence of dope sonication (e).

### 3.4. Conclusions

Based on the results of this study, the following conclusions have been drawn on the effect of PVP addition and dope sonication on the properties of PVDF MMM:

1. Membrane pores arise mainly from solvent/polymer demixing during the phase inversion process. The main function of a hydrophilic polymer is to connect membranes pores rather than form them.
2. Dope sonication is a very effective means of dispersing hydrophilic fillers within hydrophobic polymer matrix although limited particles dispersion could be achieved by the addition of a hydrophilic polymer like PVP.
3. In the absence of inorganic fillers, the PVDF  $\beta$ -phase decreased by 6% upon sonication and by 32% when 48 wt.% of PVP was added. However, at 4 wt.% filler, the highest  $\beta$ -phase mass fraction of 0.92 was recorded for the P21 membrane while the  $\beta$ -phase for the Sonic membrane reduced to its lowest value of 0.55 demonstrating membrane crystallinity dependence on dope treatment.
4. PVP addition is shown to result in significant reduction in temperature for the initial onset of membrane thermal degradation from 440 °C to 295 °C upon addition of 48 wt.% PVP. For PVP containing membranes, the initial addition of inorganic filler led to substantial improvement in thermal stability. Sonication did not appear to affect the thermal stability of the membrane but the addition of fillers to the Sonic membranes resulted in a steady but gradual reduction in the temperature for the onset of initial thermal degradation.
5. In the absence of PVP, the addition of even large amount of inorganic filler material provided only minimal improvement in membrane hydrophilicity for the Sonic membrane. However, in the presence of PVP, the membrane water affinity was enhanced considerably resulting in rapid water adsorption into the membrane. It is seen that dynamic CA, which relates to the rate of CA decrease rather than static CA is a good measure of membrane wettability.
6. Dope sonication in the absence of PVP results in tight membranes with very low permeation for water. The presence of both PVP and inorganic filler resulted in the constant flux permeation of water at low TMP. Increasing filler amount was seen to result in better turbidity rejection.

Consequently, dope sonication and PVP addition are useful methods to provide more control over PVDF MMM integrity, homogeneity, crystallinity, thermal stability, porosity and permeability for water treatment applications. The results of this study provide new data for optimising MMM design for water treatment applications.

### 3.5. Acknowledgments

The authors acknowledge the financial support provided by Victoria University to Ike Ikechukwu through the Victoria University International Postgraduate Research Scholarship. Sincere thanks to Bao Lin at Deakin University for his assistance in acquiring the SEM images. Thanks also to Dr Jianhua Zhang and Dr Marlene Cran from Victoria University for their kind suggestions.

### References

- [1] G.-d. Kang, Y.-m. Cao, Application and modification of poly(vinylidene fluoride) (PVDF) membranes – A review, *Journal of Membrane Science*, 463 (2014) 145-165.
- [2] F. Liu, N.A. Hashim, Y. Liu, M.R.M. Abed, K. Li, Progress in the production and modification of PVDF membranes, *Journal of Membrane Science*, 375 (2011) 1-27.
- [3] S.J. Oh, N. Kim, Y.T. Lee, Preparation and characterization of PVDF/TiO<sub>2</sub> organic–inorganic composite membranes for fouling resistance improvement, *Journal of Membrane Science*, 345 (2009) 13-20.
- [4] C. Zhao, X. Xu, J. Chen, F. Yang, Effect of graphene oxide concentration on the morphologies and antifouling properties of PVDF ultrafiltration membranes, *Journal of Environmental Chemical Engineering*, 1 (2013) 349-354.
- [5] X. Zhang, Y. Wang, Y. You, H. Meng, J. Zhang, X. Xu, Preparation, performance and adsorption activity of TiO<sub>2</sub> nanoparticles entrapped PVDF hybrid membranes, *Applied Surface Science*, 263 (2012) 660-665.
- [6] A. Cui, Z. Liu, C. Xiao, Y. Zhang, Effect of micro-sized SiO<sub>2</sub>-particle on the performance of PVDF blend membranes via TIPS, *Journal of Membrane Science*, 360 (2010) 259-264.

- [7] L. Yan, S. Hong, M.L. Li, Y.S. Li, Application of the Al<sub>2</sub>O<sub>3</sub>–PVDF nanocomposite tubular ultrafiltration (UF) membrane for oily wastewater treatment and its antifouling research, *Separation and Purification Technology*, 66 (2009) 347-352.
- [8] A. Bottino, G. Capannelli, A. Comite, Preparation and characterization of novel porous PVDF-ZrO<sub>2</sub> composite membranes, *Desalination*, 146 (2002) 35-40.
- [9] H. Rajabi, N. Ghaemi, S.S. Madaeni, P. Daraei, M.A. Khadivi, M. Falsafi, Nanoclay embedded mixed matrix PVDF nanocomposite membrane: Preparation, characterization and biofouling resistance, *Applied Surface Science*, 313 (2014) 207-214.
- [10] A. Pagidi, R. Saranya, G. Arthanareeswaran, A.F. Ismail, T. Matsuura, Enhanced oil–water separation using polysulfone membranes modified with polymeric additives, *Desalination*, 344 (2014) 280-288.
- [11] H. Basri, A.F. Ismail, M. Aziz, Polyethersulfone (PES)–silver composite UF membrane: Effect of silver loading and PVP molecular weight on membrane morphology and antibacterial activity, *Desalination*, 273 (2011) 72-80.
- [12] E. Saljoughi, T. Mohammadi, Cellulose acetate (CA)/polyvinylpyrrolidone (PVP) blend asymmetric membranes: Preparation, morphology and performance, *Desalination*, 249 (2009) 850-854.
- [13] S. Liang, K. Xiao, Y. Mo, X. Huang, A novel ZnO nanoparticle blended polyvinylidene fluoride membrane for anti-irreversible fouling, *Journal of Membrane Science*, 394-395 (2012) 184-192.
- [14] S. Zhang, R. Wang, S. Zhang, G. Li, Y. Zhang, Treatment of wastewater containing oil using phosphorylated silica nanotubes (PSNTs)/polyvinylidene fluoride (PVDF) composite membrane, *Desalination*, 332 (2014) 109-116.
- [15] Z.-Q. Huang, F. Zheng, Z. Zhang, H.-T. Xu, K.-M. Zhou, The performance of the PVDF-Fe<sub>3</sub>O<sub>4</sub> ultrafiltration membrane and the effect of a parallel magnetic field used during the membrane formation, *Desalination*, 292 (2012) 64-72.
- [16] Z.-Q. Huang, L. Chen, K. Chen, Z. Zhang, H.-T. Xu, A novel method for controlling the sublayer microstructure of an ultrafiltration membrane: The preparation of the PSF-Fe<sub>3</sub>O<sub>4</sub>ultrafiltration membrane in a parallel magnetic field, *Journal of Applied Polymer Science*, 117 (2010) 1960-1968.

- [17] Z.-Q. Huang, K. Chen, S.-N. Li, X.-T. Yin, Z. Zhang, H.-T. Xu, Effect of ferrosoferric oxide content on the performances of polysulfone–ferrosoferric oxide ultrafiltration membranes, *Journal of Membrane Science*, 315 (2008) 164-171.
- [18] R.M. Cornell, U. Schwerdtmann, *The Iron Oxides: Structures, Properties, Reactions, Occurrences and Uses*, 2nd Edition ed., WILEY-VCH Verlag GmbH & Co. KGaA, Weinheim, 2003.
- [19] A.P.A. Faiyas, E.M. Vinoda, J. Joseph, R. Ganesan, R.K. Pandey, Dependence of pH and surfactant effect in the synthesis of magnetite ( $\text{Fe}_3\text{O}_4$ ) nanoparticles and its properties, *Journal of Magnetism and Magnetic Materials*, 322 (2010) 400 - 404.
- [20] T. Ahn, J.H. Kim, H.-M. Yang, J.W. Lee, J.-D. Kim, Formation Pathways of Magnetite Nanoparticles by Coprecipitation Method, *The Journal of Physical Chemistry C*, 116 (2012) 6069–6076.
- [21] N. Mahmed, O. Heczko, A. Lancok, S.-P. Hannula, The magnetic and oxidation behavior of bare and silica-coated iron oxide nanoparticles synthesized by reverse co-precipitation of ferrous ion ( $\text{Fe}^{2+}$ ) in ambient atmosphere, *Journal of Magnetism and Magnetic Materials*, 353 (2014) 15 - 22.
- [22] G.U. Semblante, S.D.R. Tampubolon, S.-J. You, Y.-F. Lin, T.-C. Chang, F.-C. Yen, Fouling reduction in membrane reactor through magnetic particles, *Journal of Membrane Science*, 435 (2013) 62-70.
- [23] S.D.R. Tampubolon, G.U. Semblante, S.-J. You, Y.-F. Lin, Application of magnetic  $\gamma\text{-Fe}_2\text{O}_3$  to reduce membrane fouling, *Journal of the Taiwan Institute of Chemical Engineers*, (2013).
- [24] B.I. Harman, H. Koseoglu, N.O. Yigit, M. Beyhan, M. Kitis, The use of iron oxide-coated ceramic membranes in removing natural organic matter and phenol from waters, *Desalination*, 261 (2010) 27-33.
- [25] P. Sabbatini, F. Yrazu, F. Rossi, G. Thern, A. Marajofsky, M.M. Fidalgo de Cortalezzi, Fabrication and characterization of iron oxide ceramic membranes for arsenic removal, *Water Research*, 44 (2010) 5702-5712.
- [26] L. De Angelis, M.M.F. de Cortalezzi, Ceramic membrane filtration of organic compounds: Effect of concentration, pH, and mixtures interactions on fouling, *Separation and Purification Technology*, 118 (2013) 762-775.

- [27] A.L. Ahmad, M.A. Majid, B.S. Ooi, Functionalized PSf/SiO<sub>2</sub> nanocomposite membrane for oil-in-water emulsion separation, *Desalination*, 268 (2011) 266-269.
- [28] H. Wu, B. Tang, P. Wu, Optimizing polyamide thin film composite membrane covalently bonded with modified mesoporous silica nanoparticles, *Journal of Membrane Science*, 428 (2013) 341-348.
- [29] L.-Y. Yu, Z.-L. Xu, H.-M. Shen, H. Yang, Preparation and characterization of PVDF–SiO<sub>2</sub> composite hollow fiber UF membrane by sol–gel method, *Journal of Membrane Science*, 337 (2009) 257-265.
- [30] L.T. Zhuravlev, The surface chemistry of amorphous silica. Zhuravlev model, *Colloids and Surfaces A: Physicochemical Engineering Aspects*, 173 (2000) 1–38.
- [31] L. Peng, W. Qisui, L. Xi, Z. Chaocan, Investigation of the states of water and OH groups on the surface of silica, *Colloids and Surfaces A: Physicochemical and Engineering Aspects*, 334 (2009) 112-115.
- [32] J.T. Yates, Water interactions with silica surfaces: A big role for surface structure, *Surface Science*, 565 (2004) 103-106.
- [33] X. Li, A. Sotto, J. Li, B. Van der Bruggen, Progress and perspectives for synthesis of sustainable antifouling composite membranes containing *in situ* generated nanoparticles, *Journal of Membrane Science*, 524 (2017) 502-528.
- [34] J.S. Taurozzi, H. Arul, V.Z. Bosak, A.F. Burban, T.C. Voice, M.L. Bruening, V.V. Tarabara, Effect of filler incorporation route on the properties of polysulfone–silver nanocomposite membranes of different porosities, *Journal of Membrane Science*, 325 (2008) 58-68.
- [35] X. Li, R. Pang, J. Li, X. Sun, J. Shen, W. Han, L. Wang, In situ formation of Ag nanoparticles in PVDF ultrafiltration membrane to mitigate organic and bacterial fouling, *Desalination*, 324 (2013) 48-56.
- [36] H. Xu, N. Tong, L. Cui, Y. Lu, H. Gu, Preparation of hydrophilic magnetic nanospheres with high saturation magnetization, *Journal of Magnetism and Magnetic Materials*, 311 (2007) 125-130.
- [37] AZoNano, Sizing Nanoparticles - Determining the Particle Size of Nanomaterials by Micromeritics, in: M.I. Corporation (Ed.), 2013.

- [38] S.A. Kirillov, Surface area and pore volume of a system of particles as a function of their size and packing, *Microporous and Mesoporous Materials*, 122 (2009) 234-239.
- [39] C.Y. Lai, A. Groth, S. Gray, M. Duke, Preparation and characterization of poly(vinylidene fluoride)/nanoclay nanocomposite flat sheet membranes for abrasion resistance, *Water Research*, 57 (2014) 56-66.
- [40] B. Mohammadi, A.A. Yousefi, S.M. Bellah, Effect of tensile strain rate and elongation on crystalline structure and piezoelectric properties of PVDF thin films, *Polymer Testing*, 26 (2007) 42-50.
- [41] A.L. Ahmad, N. Ideris, B.S. Ooi, S.C. Low, A. Ismail, Morphology and polymorph study of a polyvinylidene fluoride (PVDF) membrane for protein binding: Effect of the dissolving temperature, *Desalination*, 278 (2011) 318-324.
- [42] H. Ju, B.D. McCloskey, A.C. Sagle, Y.-H. Wu, V.A. Kusuma, B.D. Freeman, Crosslinked poly(ethylene oxide) fouling resistant coating materials for oil/water separation, *Journal of Membrane Science*, 307 (2008) 260-267.
- [43] W. Kim, C.Y. Suh, S.W. Cho, K.M. Roh, H. Kwon, K. Song, I.J. Shon, A new method for the identification and quantification of magnetite-maghemit mixture using conventional X-ray diffraction technique, *Talanta*, 94 (2012) 348-352.
- [44] F. Yazdania, M. Edrissia, Effect of pressure on the size of magnetite nanoparticles in the coprecipitation synthesis, *Materials Science and Engineering B*, 171 (2010) 86 - 89.
- [45] R. Hofman, J.G.F. Westheim, I. Pouwel, T. Fransen, P.J. Gellings, FTIR and XPS Studies on Corrosion-resistant SiO<sub>2</sub> Coatings as a Function of the Humidity during Deposition, *Surface and interface analysis*, 24 (1996) 1-6.
- [46] L. Priya, J.P. Jog, Polymorphism in Intercalated Poly(vinylidene fluoride)/Clay Nanocomposites, *Journal of Applied Polymer Science*, 89 (2003) 2036–2040.
- [47] X. Wang, X. Wang, L. Zhang, Q. An, H. Chen, Morphology and Formation Mechanism of Poly(Vinylidene Fluoride) Membranes Prepared with Immersion Precipitation: Effect of Dissolving Temperature, *Journal of Macromolecular Science, Part B*, 48 (2009) 696-709.

- [48] C.Y. Lai, A. Groth, S. Gray, M. Duke, Enhanced abrasion resistant PVDF/nanoclay hollow fibre composite membranes for water treatment, *Journal of Membrane Science*, 449 (2014) 146-157.
- [49] D.R. Dillon, K.K. Tenneti, C.Y. Li, F.K. Ko, I. Sics, B.S. Hsiao, On the structure and morphology of polyvinylidene fluoride–nanoclay nanocomposites, *Polymer*, 47 (2006) 1678-1688.
- [50] P. Sajkiewicz, A. Wasiak, Z. Gocłowski, Phase transitions during stretching of poly(vinylidenefluoride), *European Polymer Journal*, 35 (1999) 423-429.
- [51] X. Zhao, S. Chen, J. Zhang, W. Zhang, X. Wang, Crystallization of PVDF in the PVDF/PMMA blends precipitated from their non-solvents: Special “orientation” behavior, morphology, and thermal properties, *Journal of Crystal Growth*, 328 (2011) 74-80.
- [52] M. Avram, *Infrared Spectroscopy: Applications in Organic Chemistry*, Robert E. Krieger Publishing Co., Inc, New York, 1978.
- [53] D. Shah, P. Maiti, E. Gunn, D.F. Schmidt, D.D. Jiang, C.A. Batt, E.P. Giannelis, Dramatic enhancements in toughness of Polyvinylidene fluoride nanocomposites via nanoclay directed crystal structure and morphology, *Advanced Materials*, 16 (2004) 1173-1177.
- [54] A. Karatrantos, N. Clarke, R.J. Composto, K.I. Winey, Entanglements in polymer nanocomposites containing spherical nanoparticles, *Soft Matter*, 12 (2016) 2567--2574.
- [55] R. Mangal, S. Srivastava, L.A. Archer, Phase stability and dynamics of entangled polymer-nanoparticle composites, *Nature communications*, 6 (2015) 7198.
- [56] G.L. Jadav, P.S. Singh, Synthesis of novel silica-polyamide nanocomposite membrane with enhanced properties, *Journal of Membrane Science*, 328 (2009) 257-267.
- [57] Y. Zhang, J. Zhao, H. Chu, X. Zhou, Y. Wei, Effect of modified attapulgite addition on the performance of a PVDF ultrafiltration membrane, *Desalination*, 344 (2014) 71-78.
- [58] I.M. Wienk, R.M. Boom, M.A.M. Beerlage, A.M.W. Bulte, C.A. Smolders, H. Strathmann, Recent advances in the formation of phase inversion membranes

- made from amorphous or semi-crystalline polymers, *Journal of Membrane Science*, 113 (1996) 361-371.
- [59] N. Pokhrel, P.K. Vabbina, N. Pala, *Sonochemistry: Science and Engineering*, *Ultrasonics sonochemistry*, 29 (2016) 104-128.
- [60] B. Banerjee, Recent developments on ultrasound assisted catalyst-free organic synthesis, *Ultrasonics sonochemistry*, 35 (2017) 1-14.
- [61] R.A. Damodar, S.J. You, H.H. Chou, Study the self cleaning, antibacterial and photocatalytic properties of TiO<sub>2</sub> entrapped PVDF membranes, *J Hazard Mater*, 172 (2009) 1321-1328.
- [62] W. Chen, Y. Su, L. Zhang, Q. Shi, J. Peng, Z. Jiang, In situ generated silica nanoparticles as pore-forming agent for enhanced permeability of cellulose acetate membranes, *Journal of Membrane Science*, 348 (2010) 75-83.
- [63] D.J. Shaw, *Introduction to colloid and surface chemistry*, Butterworth & Co. (Publishers) Ltd, London, 1980.
- [64] E.W. Washburn, The dynamics of capillary flow, *The Physical Review*, 17 (1921) 273-283.
- [65] S. Bonyadi, T.S. Chung, Flux enhancement in membrane distillation by fabrication of dual layer hydrophilic–hydrophobic hollow fiber membranes, *Journal of Membrane Science*, 306 (2007) 134-146.
- [66] Y. Liu, X. Chen, High permeability and salt rejection reverse osmosis by a zeolite nano-membrane, *Physical Chemistry Chemical Physics*, 15 (2013) 6817-6824.

## Appendix

### S.3.1. Relating BET surface area to particle diameter

Let the surface area of a unit mass of the material composed of N nanoparticles  
 $= S = \text{BET surface area (m}^2/\text{g})$

Assuming spherical particles with average diameter d,

$$S = N \times 4\pi(d^2/4) \quad \text{S3.1}$$

The volume of N nanoparticles, V, is given by

$$V = N \times (4/3)\pi(d^3/8) \quad \text{S3.2}$$

Rearranging S3.2 gives

$$V = (d/6) \times N \times 4\pi(d^2/4) = (d/6)S \quad \text{S3.3}$$

Since the N nanoparticles have a unit mass, the density of the material,  $\rho$  (g/cm<sup>3</sup>) can be expressed as

$$\rho = \text{mass}/V = 1/V = 6/dS \quad \text{S3.4}$$

From equation S3.4, the diameter of the particles can be written as

$$d = 6/\rho S \quad \text{S3.5}$$

Making necessary unit adjustments to obtain d in nm gives

$$d = \frac{6000}{S \times \rho} \quad \text{S3.6}$$

Equation S3.6 is cited in the manuscript as Equation 3.2.



Figure S3.1. Optical microscope image of membranes

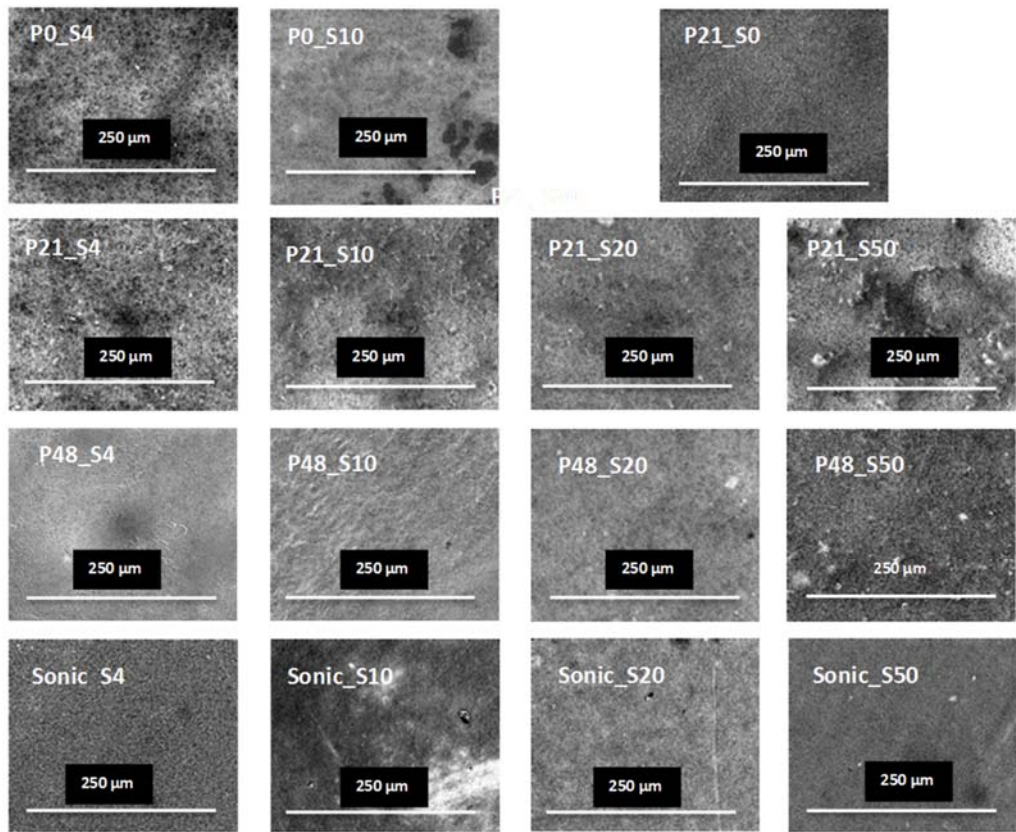


Figure S3.2. SEM images showing membrane microstructure

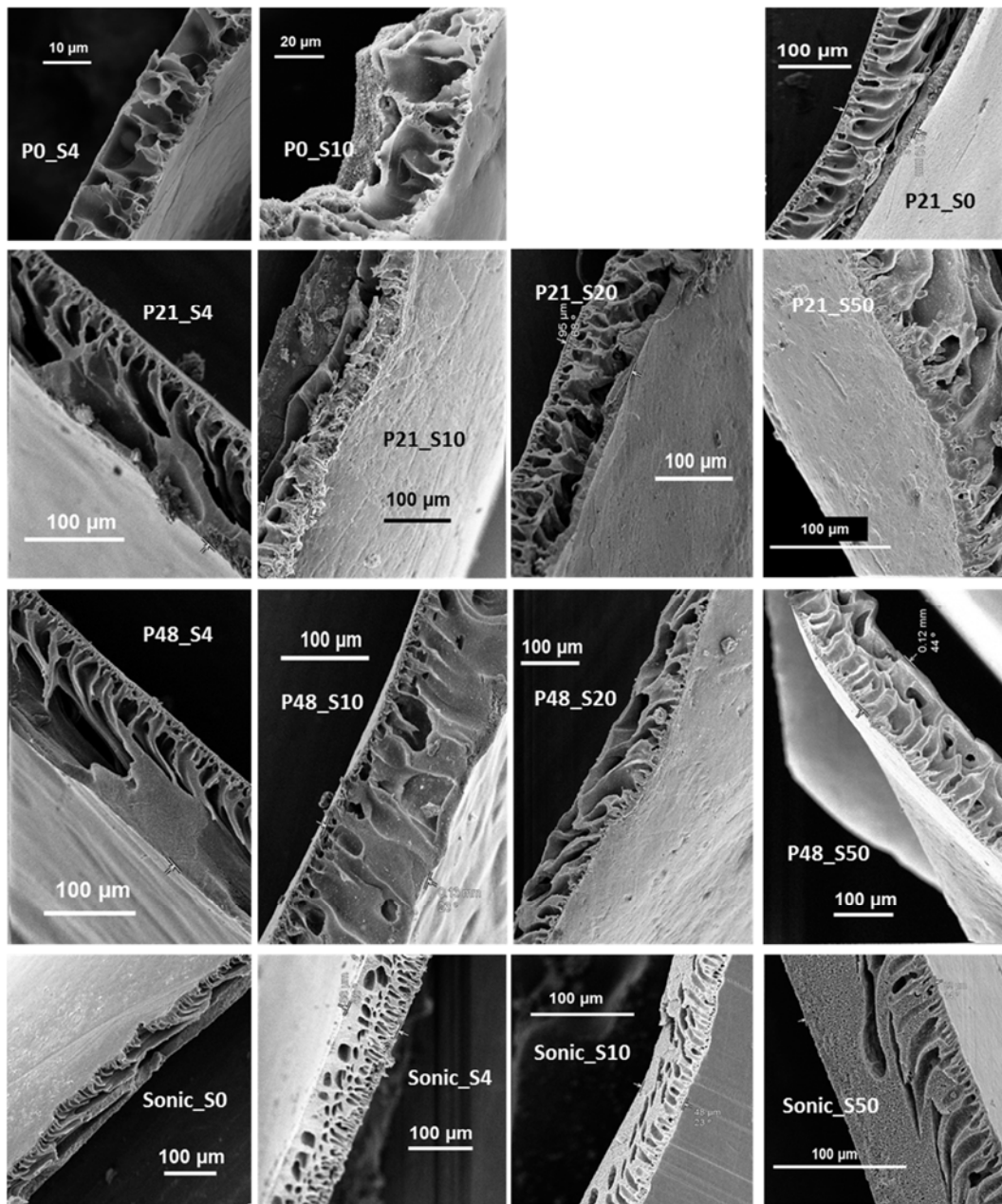


Figure S3.3. SEM cross-sectional images of membranes

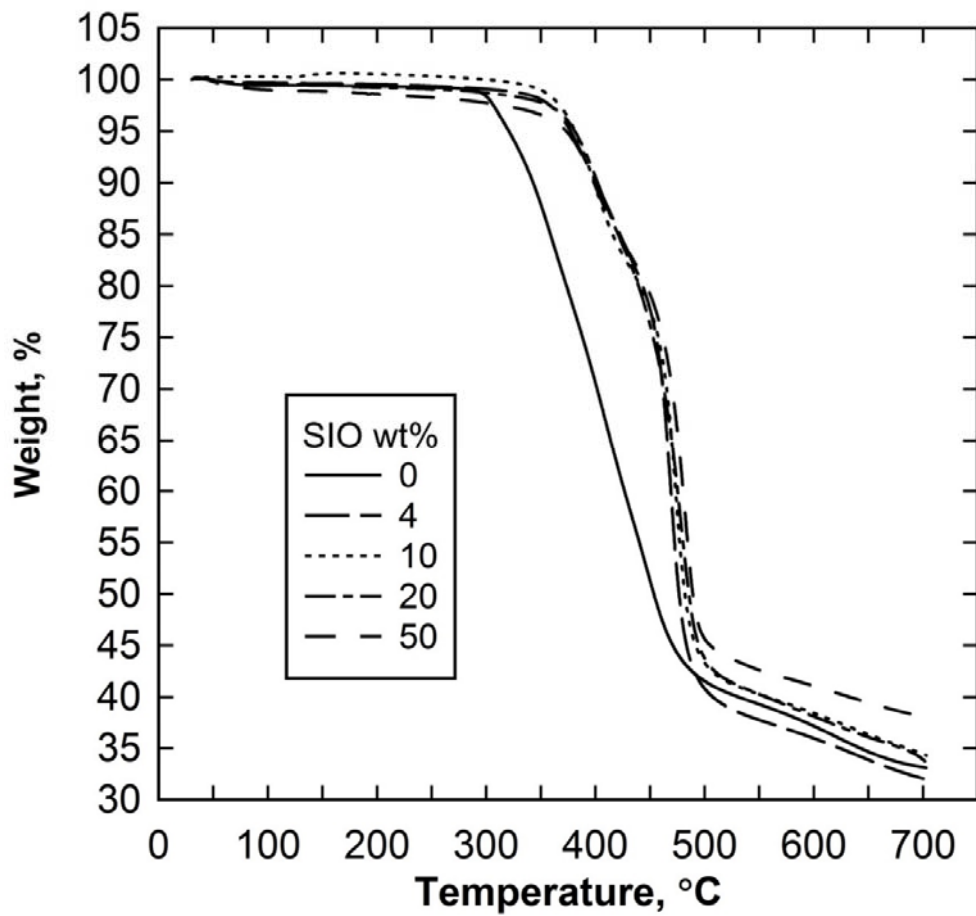


Figure S3.4. TGA weight loss profiles for P48

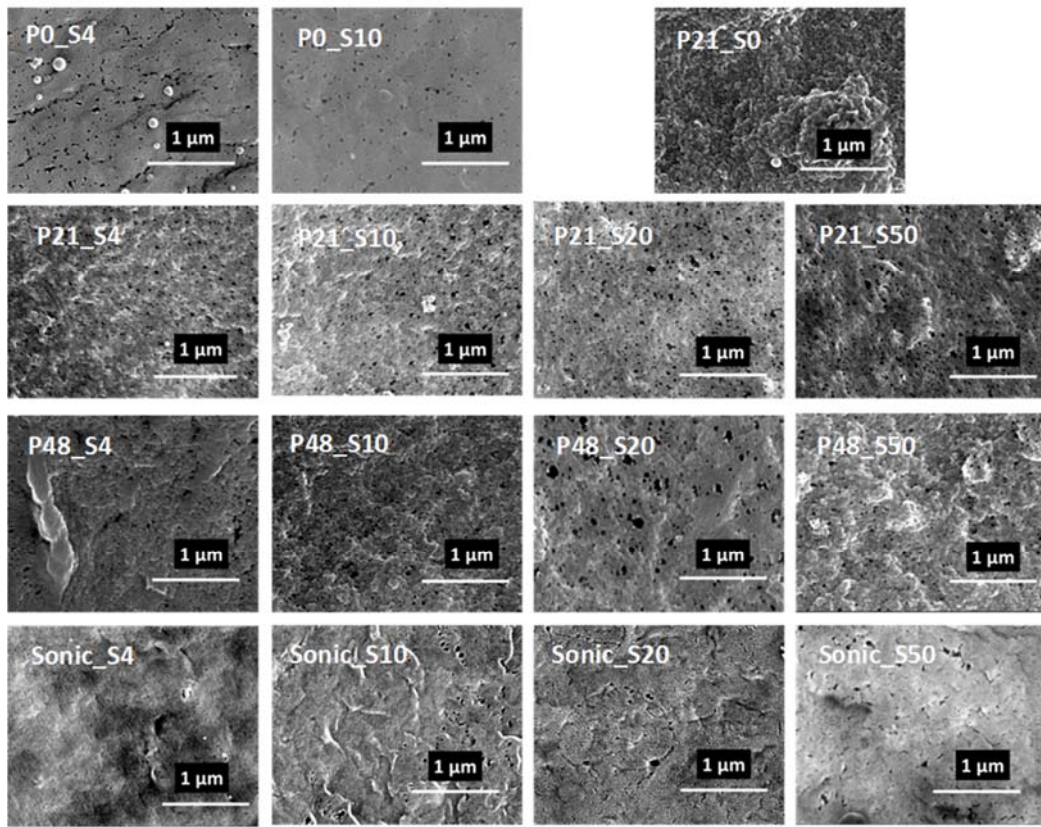


Figure S3.5. SEM images showing skin layer pores

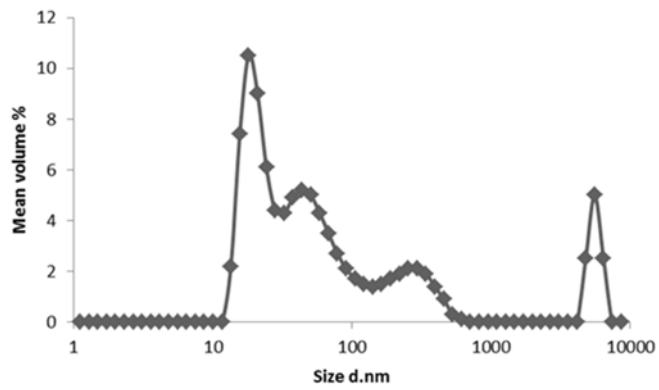


Figure S3.6. Oil emulsion droplet sizes as measured by DLS technique

## GRADUATE RESEARCH CENTRE

### DECLARATION OF CO-AUTHORSHIP AND CO-CONTRIBUTION: PAPERS INCORPORATED IN THESIS BY PUBLICATION

*This declaration is to be completed for each conjointly authored publication and placed at the beginning of the thesis chapter in which the publication appears.*

#### 1. PUBLICATION DETAILS (to be completed by the candidate)

Title of Paper/Journal/Book:	Effects of dope sonication and hydrophilic polymer addition on the properties of low pressure PVDF mixed matrix membranes		
Surname:	Ike	First name:	Ikechukwu
College:	College	Candidate's Contribution (%):	86
Status:			
Accepted and in press:	<input type="checkbox"/>	Date:	<input type="text"/>
Published:	<input checked="" type="checkbox"/>	Date:	<input type="text"/> 24 June 2017

#### 2. CANDIDATE DECLARATION

I declare that the publication above meets the requirements to be included in the thesis as outlined in the HDR Policy and related Procedures – [policy.vu.edu.au](http://policy.vu.edu.au).

Ikechukwu Anthony Ike	Digitally signed by Ikechukwu Anthony Ike DN: cn=ikechukwu Anthony Ike, o, ou, email=tonyjamesike@yahoo.com, c=AU Date: 2017.08.11 11:12:35 +10'00'	9 August 2017
Signature	Date	

#### 3. CO-AUTHOR(S) DECLARATION

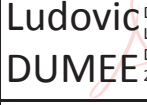
In the case of the above publication, the following authors contributed to the work as follows:

The undersigned certify that:

1. They meet criteria for authorship in that they have participated in the conception, execution or interpretation of at least that part of the publication in their field of expertise;
2. They take public responsibility for their part of the publication, except for the responsible author who accepts overall responsibility for the publication;
3. There are no other authors of the publication according to these criteria;
4. Potential conflicts of interest have been disclosed to a) granting bodies, b) the editor or publisher of journals or other publications, and c) the head of the responsible academic unit; and

5. The original data will be held for at least five years from the date indicated below and is stored at the following location(s):

Institute for Sustainability and Innovation, Victoria University, Melbourne, Australia

Name(s) of Co-Author(s)	Contribution (%)	Nature of Contribution	Signature	Date
Ludovic F. Dumée	3	Manuscript revision	 Digitally signed by Ludovic DUMEE Date: 2017.08.14 21:00:08 +10'00'	
Andrew Groth	3	Manuscript revision		
John D. Orbell	3	Manuscript revision	 Digitally signed by John Orbell DNI:John.Orbell, o=Victoria University, ou=Engineerng & Science email=John.Orbell@vu.edu.au, c=AU Date: 2017.08.16 10:12:50 +10'00'	
Mikel Duke	5	Manuscript revision	 Digitally signed by Mikel Duke Date: 2017.08.11 10:44:15 +10'00'	

5. The original data will be held for at least five years from the date indicated below and is stored at the following location(s):

Institute for Sustainability and Innovation, Victoria University, Melbourne, Australia

Name(s) of Co-Author(s)	Contribution (%)	Nature of Contribution	Signature	Date
Ludovic F. Dumée	3	Manuscript revision		
Andrew Groth	3	Manuscript revision		14.8.17
John D. Orbell	3	Manuscript revision		
Mikel Duke	5	Manuscript revision	 Digitally signed by Mikel Duke Date: 2017.08.11 10:44:15 +10'00'	

Chapter 4  
**Effects of dissolution conditions on the properties of PVDF ultrafiltration membranes\***

Abstract

Poly (vinylidene fluoride) (PVDF) is an important membrane forming material for water treatment. Earlier works have shown that major morphological changes could be achieved when PVDF is dissolved under different conditions with practical applications in membrane distillation and protein attachment. However, no previous report has discussed the effects of dissolution conditions on the performance of PVDF under ultrafiltration, which is one of the most important applications of the polymer. In this work, four different PVDF ultrafiltration membranes were produced from dopes dissolved either by stirring at 24 °C, 90 °C, 120 °C or by sonication. It is shown that dope sonication results in membrane with enhanced thermal and mechanical stability, improved permeate flux during oil emulsion filtration and high flux recovery of ~63% after cleaning. As a comparison, flux recovery of only ~26% was obtained for the membrane produced from dope dissolved at 24 °C. The outstanding performance of the dope-sonicated membrane was linked to its slightly lower porosity, narrow distribution of small pores and relatively smooth skin layer. Performance parameters for all membranes showed good correlation to porosity suggesting a tool for membrane design achievable by simple variation in the mode of polymer dissolution. The polymer dissolution effect was related to the degree of unfolding of the polymer molecular chains and their entanglements.

#### 4.1. Introduction

Poly (vinylidene fluoride) (PVDF) membranes find application in a number of water treatment and separation processes and are an ongoing subject of much research due to their recognised beneficial properties such as high mechanical and thermal stability, and resistance to chemical degradation [1, 2]. There are many routes that have been developed to synthesise PVDF membranes for

\*Published in Ultrasonics Sonochemistry -  
<https://doi.org/10.1016/j.ulsonch.2017.05.041>. See the Appendix for list of contributors.

various applications, with non-solvent induced phase separation (NIPS) being one of the more common techniques. Several research reports have shown that the final properties of the membranes produced during a NIPS process is dependent on a number of factors such as the type of dissolving solvent, the duration of dope exposure to evaporation, and the type, temperature and impurities present in the coagulating bath [2-5]. While significant attention has been paid to properties influenced by coagulation, research is still emerging on the equally important conditions of polymer dissolution [1, 6-8]. For example, Lin et al. [7] showed that varying the temperature of dissolution of the PVDF polymer from 50 °C to 110 °C resulted in an order of magnitude change in the size of the membrane semicrystalline particles from 0.5 to 15 µm. Several other researchers have confirmed the strong effect of pre-coagulation dope preparation route on the morphological and surface properties of PVDF membranes such as porosity, crystallinity, surface energy, etc. [1, 6, 8, 9]. The lasting effect of polymer dissolution temperature has been attributed to differences in the degree of dissolution of polymer crystals in the dopes [7] as well as to differences in the extent of unfolding of the polymer molecular chains [1] prior to the membrane forming stage.

These changes to the polymer ultimately affect the practical properties of the membranes which also need to be analysed. For example, Wang et al. [1] demonstrated that the significant morphological effects arising from variations in the dissolution temperature of PVDF polymer have great impact on membrane distillation performance with flux decreasing as a result of decreasing membrane porosity as the temperature of polymer dissolution increased from 50 to 120 °C. However, the results reported by Gugliuzza and Drioli [6] for membrane produced with dopes treated to lower pre-coagulation temperatures between 30 °C and 60 °C showed increasing membrane distillation flux with increasing dope treatment temperature. Gugliuzza and Drioli related the positive effect of temperature on flux to the observed positive correlation between temperature and membrane pore sizes. The difference in the flux trends with dissolution temperature in these two reports may have resulted from difference in the temperature range for the two sets of experiments or it may relate to the use of different solvents for phase inversion. Wang et al. [1] used water for the phase inversion of their membranes

while Gugliuzza and Drioli [6] used propanol. The important point for our purpose, however, is the demonstrated strong effect of dope dissolution condition on membrane performance. Recently, Ahmad et al. [8] showed that the morphological impact and crystalline re-structuring arising from changes in the dope dissolution temperature has significant effects on the membrane protein binding ability for immunological analytical application. They showed that the protein binding properties of membranes produced from dopes dissolved above a critical temperature value of 40 °C were governed by the membrane porosity but when produced from dopes dissolved at lower temperature, the binding properties were governed by the membrane crystalline structure. Higher surface area for protein binding due to higher porosity and greater electrostatic attraction of the more polar β phase to protein were advanced to explain the results.

Although the most common applications of PVDF in membrane processes is in microfiltration (MF) and ultrafiltration (UF) [2], there are no studies known to the authors that have evaluated the effect of polymer dissolution conditions on the properties of membranes for these two important applications. In these applications, surface hydrophilicity, pore size distribution and water flux are important as well as mechanical properties [2]. Since the proposed variation in the degree of polymer crystal dissolution and chain elongation [1, 7] are dependent on the amount of energy received during polymer dissolution, it is interesting to know how variations in energy during polymer dissolution could be utilised for designing membranes with optimal properties for MF and UF applications. It is the aim of this work to address this research need by studying the performance of PVDF UF membranes produced under four different energy environments taking particular note of the effects of the different energy environments on the membrane mechanical properties, hydrophilicity, porosity, pore size distribution and filtration performance. Three membranes were produced from dopes dissolved separately by stirring at 24 °C, 90 °C and 120 °C. The choice of the dissolution temperatures was to explore the effects over practical production temperature range. The temperatures of 90 °C and 120 °C falls well within and at the upper limit, respectively, of the common dissolution range for PVDF of 50 – 120 °C [1, 7] while the temperature of 24 °C is outside this range and also below the critical dissolution temperature of 40 °C [8]. If the

environment of dope dissolution has a lasting effect on the properties of the PVDF membrane as have been advanced in the preceding discussion, high intensity radiations such as ultrasonication may impact unique properties to the membrane [10]. Consequently, a fourth membrane was produced from dope dissolved by the novel application of ultrasonication. Although sonication has been employed routinely for the dispersion of particles in polymer solution for making membranes [11-14], it is rarely reported as a tool for polymer dissolution without the aid of mechanical stirring nor has its unique impact recognised beyond particle dispersion. This fourth method of polymer dissolution takes advantage of the highly energised environment of localised high temperature and pressure for chemical and physical changes produced as a result of the collapse of cavitation bubbles as well as other physicochemical effects arising from ultrasonication [10, 15]. All membranes were produced by the NIPS method under identical conditions except the conditions of polymer dissolution. Since every parameter and procedure were the same in the fabrication of the four membranes except the energy of the dissolution environment, it seems logical that any observed difference in the properties of the membranes could systematically be related to the effects of the different dissolution environments. To explore the effect of the dissolution conditions on the membrane properties relevant to low pressure water filtration, the membranes produced were characterised by scanning electron microscopy (SEM) for morphology, attenuated total reflectance Fourier transform infrared spectroscopy (ATR-FTIR) for crystallinity, thermal gravimetric analysis (TGA) and differential scanning calorimetry (DSC) for thermal stability and water contact angle (CA) analysis for wettability. Furthermore, mechanical strength stability and filtration performance using clean water and oil emulsion were also evaluated.

## 4.2. Materials and methods

### 4.2.1. Materials

PVDF, Solef 1015 brand from Solvay, poly (vinylpyrrolidone) (PVP), MW 40,000 g/mol, from Sigma and 1-methyl-2-pyrrolidinone (NMP) from SigmaAldrich were used for membrane fabrication. Commercial Sunflower oil and analytical grade poly (oxyethylene) (20) sorbitanmonolaurate (Tween 20) added as a surfactant

were used for emulsion preparation. Elix<sup>TM</sup> (type 2) water from a commercial Merck Millipore Integrated Water Purification System was used throughout this study. Elix water had a conductivity of 6.3 µS/cm and no particle was detected when analysed by the dynamic light scattering (DLS) technique using Malvern zetasizer nano ZS with size measurement range of 0.3 nm to 10 µm.

#### 4.2.3. Membrane fabrication and characterisation

##### 4.2.3.1. Membrane fabrication

All membranes were made by NIPS following a common procedure reported elsewhere [12, 13]. Membranes were cast from dopes prepared from 3.75 g PVDF, 0.8 g PVP and 24 g NMP and dissolved by stirring using an overhead stirrer operated at an average speed of 200 rpm at either a temperature of 24 °C, 90 °C or 120 °C and will hereafter be referred to as M24, M90 and M120 membranes. During stirring dissolution, the dopes were maintained at their respective temperature values using an oil bath set at the required temperature. The fourth dope, with the same composition as those dissolved by stirring, was prepared by ultrasonication of the polymer powders mixed in the solvent with intermittent hand mixing to move undissolved powder away from the wall of the container until the dope was clear and homogeneous. Ultrasonication usually goes on for 40 min between hand mixing. A probe-type sonicator (Hielscher Ultrasonic Processor UP400S) operated at an effective power of ~10 W, sonic irradiation pulsing of 30% and a working frequency of 24 kHz was used. During ultrasonication, the dope, contained in a 100 ml glass beaker, was cooled by an oil bath immersed in an ice bath to reduce the possibility of water contamination. The dope average temperature during ultrasonication resulting from the conversion of the dissipated sonic energy to heat energy was ~ 110 °C. The average temperature of the ultrasonication environment was defined by the ultrasonication conditions and the efficiency of the cooling system. The membrane made from the sonicated dope will hereafter be referred to simply as Sonic. After complete PVDF dissolution, which was assessed visually by noting when the dope was wholly homogeneous and clear, each dope was allowed to stand for at least 1 h to equilibrate with the ambient condition. Typically, complete PVDF dissolution was achieved between 2 to 3 h for M90, M120 and Sonic while

8 h or more were needed for M24. Similar dependence of PVDF dissolution time on the energy of dope dissolution environment has been previously reported [1, 7]. The dopes were not maintained at their dissolution environment for the same length of time (>8 h) because increasing ultrasonication time well beyond 3 h significantly impaired the Sonic membrane properties while the other membranes were not affected. This informed the decision to standardise the dope by ending dissolution once the dope was visually clear and homogeneous. Previous works have demonstrated that the specific effects of variable temperature dissolution environments are observed when dopes were maintained for the same extended duration in different dissolution environments [1, 8] or when they were subjected to dissimilar dissolution times [7]. Ahmad et al. [8] specifically reported that PVDF membrane properties were independent of practical dissolution time but dependent on dissolution environment. After clear polymer solutions have equilibrated to room temperature conditions, they were hand cast on glass plates using an Elcometer adjustable doctor blade set to a nominal opening of 300 µm before phase inversion in room temperature Elix water. The membranes were placed in the Elix water for at least 24 h at room temperature and subsequently were stored wet at 4 °C.

#### 4.2.3.2. Membrane characterisation

Samples for SEM, ATR-FTIR spectroscopy, TGA and DSC, CA analysis and mechanical strength tests were dried at room temperature prior to analysis while wet membranes were used for other characterisations. Surface SEM images were acquired on a Zeiss Supra 55VP FEG SEM. Cross section SEMs were acquired using a FEI Quanta 3D FEG Scanning Electron Microscope - gallium dual beam. The membrane cross sectioning was made by ion milling. Milling with the Gallium Focus Ion Beam (Ga FIB-SEM) was performed at 20 keV and in three steps, including a rough milling step at 3 nA and two cleaning steps at 1 nA and 0.3 nA. To determine the average size of the pores on the selective surfaces of the membranes, the SEM images of the membrane skin layers were processed using ImageJ (<https://imagej.nih.gov/ij/>). ATR-FTIR was used to study the crystalline phase of the PVDF membranes. The crystalline mass fraction of the β-phase was computed using Equation 4.1 [16]

$$F(\beta) = \frac{P_\beta}{1.26P_\alpha + P_\beta} \quad 4.1$$

where  $F(\beta)$  is the mass fraction of the  $\beta$  phase in a sample of PVDF polymer and  $P_\alpha$  and  $P_\beta$  are absorption peaks of the  $\alpha$  and  $\beta$  phases corresponding to the characteristics wavenumbers of 763 and 840 cm<sup>-1</sup> respectively. TGA and DSC studies were simultaneously conducted using a Mettler Toledo Thermal Analyser TGA/DSC 1 STAR<sup>e</sup> system under nitrogen flow of 20 mL/min and steady temperature increment of 10 °C/min until a temperature of 700 °C was reached. Membrane water CA was measured using an Attension Theta Optical Tensiometer operated at room temperature. The bulk porosity,  $\epsilon$ , for each membrane was computed gravimetrically by first measuring the mass of a membrane piece wet with water [17, 18]. Loose water on the membrane surface was wiped off with paper towel before weighing [8]. The membrane piece was then dried in an oven at 60 °C for at least 24 h and was re-weighed subsequently. Porosity was computed using the following equations [8, 17, 18]:

$$\epsilon = \frac{(M_w - M_d)/\rho_w}{(M_w - M_d)/\rho_w + M_d/\rho_P} \quad 4.2$$

where  $M_w$  is the mass of the wet piece of membrane,  $M_d$  is the mass of the dry piece of membrane,  $\rho_P$  and  $\rho_w$  are the density of PVDF (1.78 g/cm<sup>3</sup>) and water (1 g/cm<sup>3</sup>), respectively [8]. Mechanical strength tests were conducted using an Instron Materials Testing Instrument, with a 5 kN load cell. Dry samples were cut into 10 cm x 1 cm strips for mechanical strength test conducted by sample extension at a constant speed of 10 cm/min at room temperature [12, 17]. A shrinkage test was performed to better understand the mechanical strength properties of the dry membranes. The shrinkage test involved measuring the area of a piece of membrane when wet ( $A_w$ ) and after drying ( $A_d$ ) at room temperature. Observed reduction in membrane thickness was negligible compared to contraction in area. Consequently, the shrinkage ( $S$ ) was defined as the percentage reduction in membrane area due to drying:

$$S = \frac{A_w - A_d}{A_w} \times 100 \quad 4.3$$

#### 4.2.3.3. Filtration experiments

Fresh oil-in-water emulsions were produced for filtration experiments by homogenising 1.5 g sunflower oil and 0.5 g Tween 20 in 1 L Elix water using a Unidrive X 1000 homogeniser operated at 17,500 rpm for 30 min. The droplet size distribution of the resulting white emulsion was characterised by the DLS technique using a Malvern zetasizer nano ZS. The emulsion remained stable for several days with no change in the milky appearance and thus suitable for membrane tests conducted over a period of a few hours each. The filtration experiment involved the measurement of three sequential fluxes on wet membranes: membrane clean water flux ( $J_0$ ) determined from 30 min of water filtration; emulsion flux ( $J_1$ ) obtained from 2 h emulsion filtration; and membrane after-fouling clean water flux ( $J_2$ ) determined from 30 min of water filtration after emulsion fouling and membrane cleaning. The  $J_2$  flux measurements were preceded by 20 min of water filtration to remove foulant cake; a 30 min chemical flush using 0.1 M NaOH solution as a mild cleaning agent; and another 20 min of water filtration to rinse the NaOH solution. The average membrane flux recovery, ( $FR$ ) defined as [13]:

$$FR(\%) = \frac{J_2}{J_0} \times 100 \quad 4.4$$

was computed for each membrane using average clean water flux values  $J_0$  and  $J_2$ . Each series of flux measurements for a clean membrane were preceded by an initial membrane compaction by water filtration at 50 kPa transmembrane pressure (TMP) for 30 min. Flux measurements were conducted under a constant TMP of 30 kPa and cross flow velocity of 13 cm/s (volumetric flow rate of 10 cm<sup>3</sup>/s) using a crossflow acrylic module from Sterlitech®. Figure 4.1 is the schematic of the filtration setup. The permeate mass was constantly measured over a balance and logged to a computer every minute. The feed and permeate total carbon (TC) were measured using a Shimadzu TOC-V<sub>CSH</sub> Total Organic Carbon Analyzer. These values were used in evaluating the membrane rejection ( $R$ ) computed using the expression:

$$R(\%) = (1 - C_p/C_f) \times 100 \quad 4.5$$

where  $C_p$  and  $C_f$  denote permeate and feed TC concentrations (mg/L), respectively.

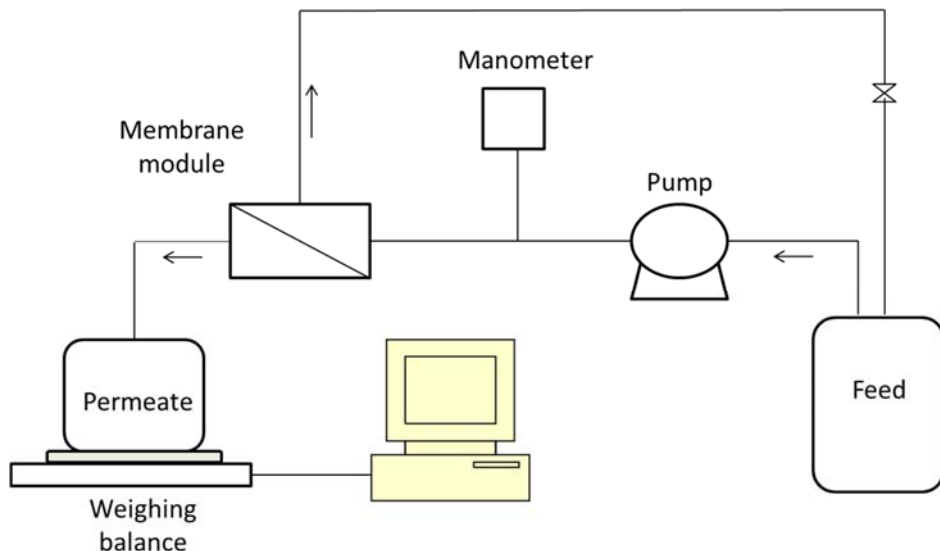


Figure 4.1. Schematic diagram of filtration set up.

### 4.3. Results and discussions

#### 4.3.1. Membrane morphology

The morphological features of the membranes were examined by SEM. Figure 4.2 is the skin layer and cross section images of the membranes. The membrane cross sections clearly shows typical asymmetric structural features characteristic of phase inversion in a strong non-solvent such as water with a thin selective skin layer of relatively smaller pore sizes resting on larger macrovoids [2]. Relative to Sonic, the membrane skin layer surface and cross sections for M24, M90 and M120 appeared reasonably similar, with a rough and nodular appearance. The roughness appears to develop from scattered and irregular depressions in which most of the membrane pores are formed. This unique structural arrangement seems to create the impression of very large skin layer pores in the cross section images. However, some of the impressions of large pores observed in the cross sections especially those closer to the line of ion milling may be real and are

believed to have developed from stray ion beam during ion milling. Uniquely, the M120 showed slightly larger pore openings compared to M24 and M90. Figure 4.2 shows that Sonic is markedly different from the other membranes. Its relatively smooth surface and lack of apparent pore openings at the resolution of the figure are contrasted by the roughness and large pores of the other three membranes made without sonication. In addition, the relatively dense skin layer resting on slightly more ordered macrovoids of the Sonic creates the impression of a sturdy membrane framework and further distinguishes it from the other membranes.

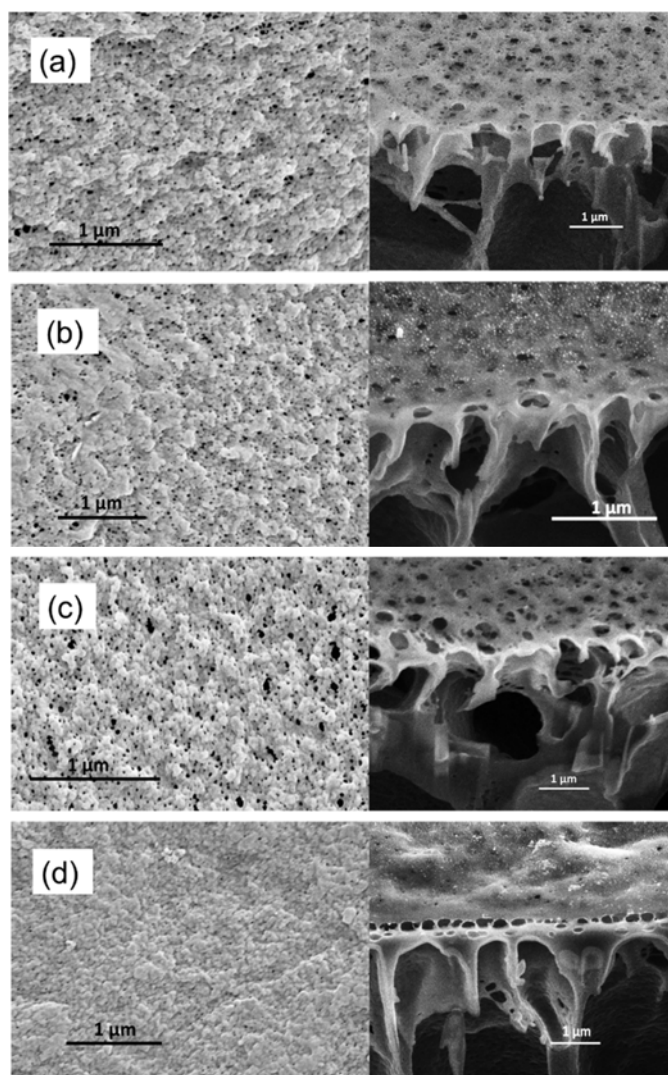


Figure 4.2. SEM images of membrane skin layer (left) and cross section (right) for M24 (a) M90 (b) M120 (c) and Sonic (d).

#### 4.3.2. Crystalline phase

Typical FTIR spectra for the membranes are shown in the Appendix (Figure S4.1). The similarity of the spectra is an indication that physical differences in the membranes cannot be explained by chemical changes during the various polymer dissolution processes. The computed  $F(\beta)$  using Equation 4.1 based on FTIR data is given in Figure 4.3. It is evident that  $F(\beta)$  increased steadily with the dissolution temperature of the polymer. PVDF has been reported to crystallise in at least four different polymorphs under various conditions [1, 2, 19]. The most common polymorphs are the  $\alpha$  and  $\beta$  phases. The  $\beta$  phase has been associated with a number of interesting properties such as piezo-, pyro- and ferroelectric effects and has also been connected with enhanced mechanical strength of the polymer [16, 20, 21]. The all *trans* conformation of the polar  $\beta$  phase are known to be favoured when PVDF is crystallised from solution while the *trans-gauche trans-gauche* conformation of the non-polar  $\alpha$  phase are known to crystallise readily from the melt [19, 22]. The maximum  $F(\beta)$  of 68% was recorded for M120 while the Sonic followed closely with a mass fraction of 66%. The lowest  $F(\beta)$  of 56% was computed for M24 suggesting strong dependence of crystal phase on temperature of dope dissolution. Ahmad et al. [8] documented significant influence of dissolution temperature on the crystallinity of PVDF membranes as measured by FTIR. However, in their work, the  $\beta$  phase was reported to decrease with temperature of dope dissolution from a value of ~70% at 20 °C to ~45% at 100 °C. This is a reversal to the trend observed in this work. The divergence in trend may be linked to differences in coagulating solvent. Ahmad et al [8] used 2-propanol (a soft non-solvent) as their coagulating solvent while water (a harsh non-solvent) [2] was used in this work. Since the  $\beta$  phase is the polar form of PVDF [19], the polarity of the coagulating solvent might influence the crystalline structure of the polymer during the phase inversion process. However, Lai et al [12] reported a low  $\beta$  phase of only 17% for PVDF membrane produced by stirring at 90 °C with phase inversion in 60 °C deionised water. Furthermore, Wang et al. [1] and Lin et al. [7] reported that the temperature of dope dissolution had no effect on membrane crystalline phase with only the  $\alpha$  phase of PVDF identified. It is worthy of note that the two last groups assessed crystalline phase by the X-ray diffraction (XRD) method. It appears that the XRD technique is a less

sensitive method for characterising PVDF crystalline phases probably due to the limited crystallinity of PVDF. XRD is more suitable for characterising long range order crystallinity since it averages the properties of materials over the entire structure while FTIR probe material properties over a short range [23, 24]. Lekgoathi and Kock [24] recently showed that Raman spectroscopy was more sensitive than XRD analysis in characterising the short range order crystalline structure of LiPF<sub>6</sub>. Since Raman scattering is a vibrational spectroscopic technique like FTIR, the report by Lekgoathi and Kock [24] supports the proposal that FTIR is probably more sensitive than XRD in characterising PVDF crystalline phases.

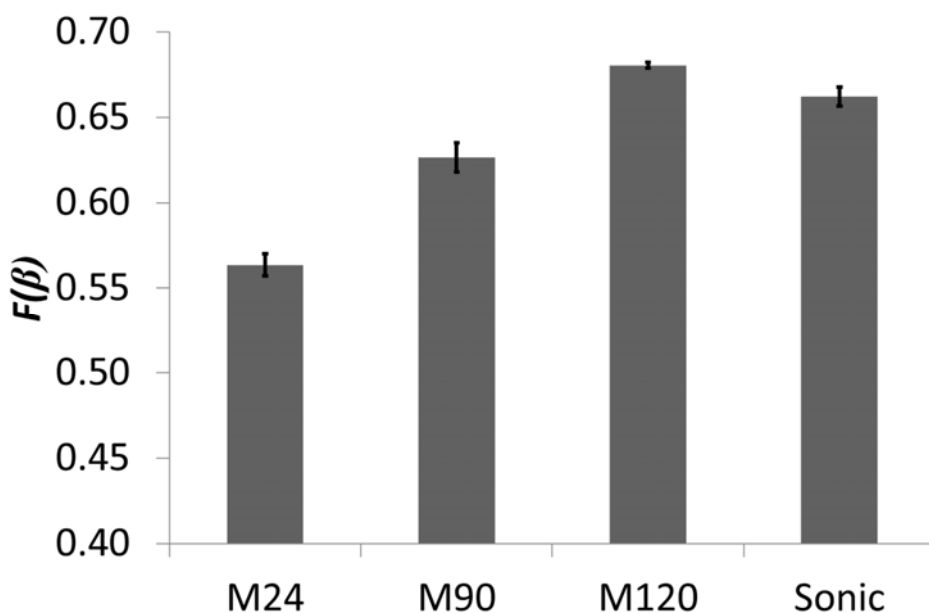


Figure 4.3. Membranes  $\beta$ -phase mass fractions,  $F(\beta)$ , from FTIR data using Equation 4.1. Error bars indicate computed standard error.

#### 4.3.3. Thermal stability

The results of the DSC and TGA performed on the membranes are given in Figure 4.4. The DSC results shows that the four membranes have similar glass transition temperature ( $T_g$ ) of about 36 °C which is close to the PVDF literature value of 40 °C [25] as well as similar melting point ( $T_m$ ) of 172 °C which closely matches both the PVDF supplier data and literature values [25, 26]. These results

indicate that the pre-melt properties of the membranes, namely, chain alignment and crystallinity [25], were practically unchanged by the dope dissolution techniques. Ahmad et al. [8] also reported unchanged pre-melt thermal properties for PVDF membranes produced from dopes dissolved by stirring under different temperature conditions between 20 °C and 100 °C despite significant morphological differences between the membranes. However, it can be seen in the TGA results that the initial onset of thermal degradation ( $T_d$ ), defined as the temperature at 1.5 % thermally induced weight loss [27], was significantly influenced by the polymer dissolution conditions. Sonic showed the highest  $T_d$  of about 350 °C. Decomposition temperatures for M24, M90 and M120 were 300 °C, 340 °C, and 315 °C respectively. The minimum  $T_d$  for pure PVDF has been given as approx. 330 °C [25]. The  $T_d$  values reported in this work are similar to the  $T_d$  of 320 °C reported by Zhang et al. [27] for PVDF membrane with incorporated PVP (for hydrophilicity enhancement) as was the case in this work.

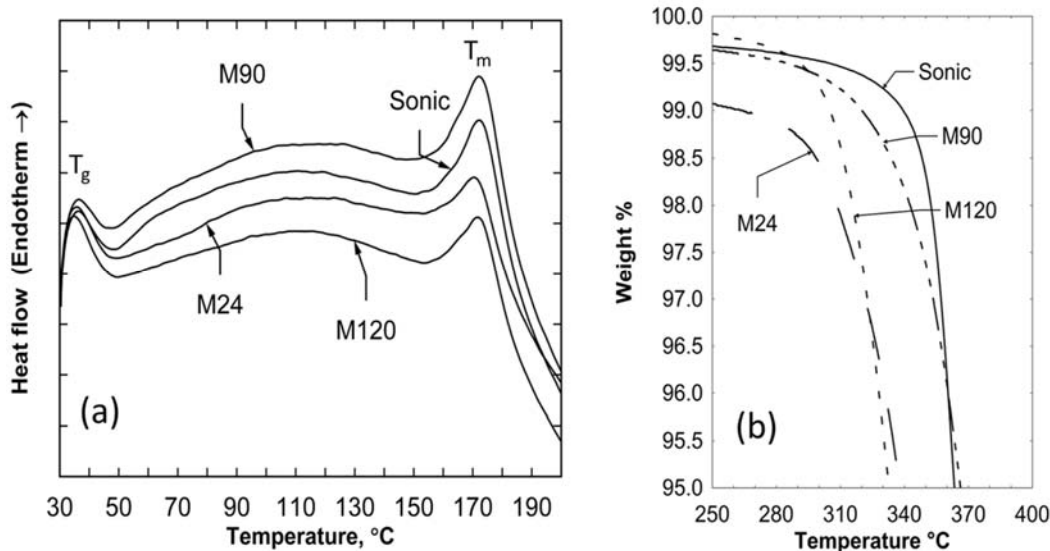


Figure 4.4. Heat flow differential scanning calorimetry (a) and weight loss thermogravimetric analysis (b) of membranes under nitrogen atmosphere and steady temperature increment of 10 °C/min.

The TGA results in this work indicate that while sonication improved thermal stability, low temperature (24 °C) and high temperature (120 °C) dissolution

conditions impaired membrane thermal stability. Improvement in resistance to thermal decomposition has been associated with higher molecular weight and more cross linking due to reduced number of end groups and restrained molecular movement [25]. Reduction in the number of end groups and restrained molecular movement may also develop from higher degree of polymer chain entanglement in the melt [28, 29] resulting from high energy dissolution environments [1, 7] thus increasing the polymer  $T_d$ . This proposal may explain the higher  $T_d$  for Sonic and M90 and the lower value for M24. The lower  $T_d$  for M120 may suggest the initiation of some degree of polymer chain scission [25] at the dissolution temperature of 120 °C which reduced chain entanglement and consequently  $T_d$ . Structurally weak PVDF membrane at higher dissolution temperature has been previously reported [7].

#### 4.3.4. Mechanical strength and shrinkage

The tensile strength and elastic modulus for each membrane is given in Figure 4.5 as well as the areal shrinkage when the membranes were dried prior to the mechanical tests. The maximum tensile strengths at break were 1.51, 1.31, 1.26 and 1.47 MPa for M24, M90, M120 and Sonic respectively. These values were close to the 1.61 MPa maximum tensile strength value reported by Yu et al. [17] for their PVDF hollow fibre membranes. However, in the absence of a hydrophilic polymer such as the PVP used in this work, a much higher maximum tensile strength of 4.5 MPa was reported by Lai et al. [12] for flat sheet PVDF membrane but at the cost of low water permeability. The high tensile strength of M24 seems to have been influenced by the membrane's very high shrinkage of about 50 %. The significant shrinkage of M24 is thought to be due to the limited unfolding or coupling of the polymer molecular chains as a consequence of the dope dissolution at the low temperature of 24 °C [1, 8, 9]. This proposal is apparently corroborated by the uniquely limited ductility of M24 in the stress-strain curves shown in Figure S4.2. The other three membranes produced from dopes dissolved in higher energy environments showed shrinkage of ~10%. When M24 was annealed at 90 °C for 1 h before drying, however, the tensile strength and elastic modulus was found to have dropped significantly from 1.51 MPa to 0.90 MPa and from 10.4 MPa to 3.7 MPa, respectively. The areal shrinkage was found to decline correspondingly from 50% to 9%, clearly demonstrating that the high

areal shrinkage of M24 is due to the low temperature of dope dissolution. Consequently, membranes produced at room temperature should be annealed at higher temperature if they are to be stored dried. Sonic with a tensile strength of 1.47 MPa and elastic modulus of 5.99 MPa is therefore seen to exhibit the highest load bearing capacity and stiffness for the stable membranes. The elastic modulus for M90 and M120 were 4.67 MPa and 4.42 MPa respectively. The mechanical strength results appear to follow the trend observed for the thermal stability tests with Sonic showing the highest thermal and mechanical stability and M24 (when the effect of shrinkage is excluded) showing the least.

The shrinkage results presented in Figure 4.5 sheds some light on the observed relative membrane skin layer pores in the SEM images of Figure 4.2. Since M24 experienced a 50% areal shrinkage, it can be argued that the membranes pores observed in Figure 4.2 may be half of the actual pore areas for the wet membranes. Consequently, wet M24 may have similar pore sizes as M120.

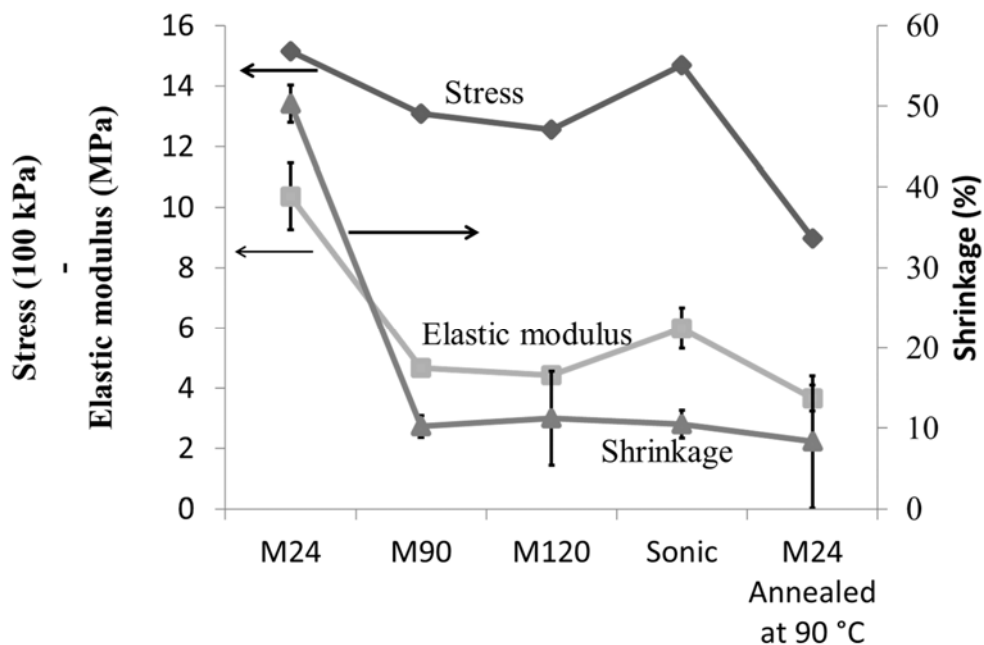


Figure 4.5. Mechanical strength and shrinkage property results. Error bars indicate computed standard error. Standard errors in the tensile stress values were <1%.

#### 4.3.5 Porosity

The membrane bulk porosity determined using Equation 4.2 is shown in Figure 4.6a. The porosity values obtained ranged from 86 to 90%. M24 had the highest bulk porosity of 90% while Sonic had the least bulk porosity of 86%. Consequently, dope sonication appears to result in less porous and dense membrane consistent with the SEM image of Figure 4.2. Although these values are very close, they seem to be important performance determinant as they appear to correspond with the trend of the membrane thermal and mechanical stability results discussed in Sections 4.3.3 and 4.3.4, respectively, as well as other performance parameter discussed in subsequent sections. The pore size distribution obtained by analysing skin layer SEM surface images using ImageJ is shown in Figure 4.6b. Membrane pore size distribution determination from SEM images as performed in this work is a favoured technique for membrane pore analysis [30, 31]. Sonic shows an approximate bimodal normal pore size distribution while lognormal distribution better describes the pore size distribution for the other three membranes. UF membranes have been more commonly described by the lognormal distribution [31, 32] which further underscores the unique effect of dope sonication on membrane properties. The pores of dry Sonic are seen to range from about 2.5 nm to 25 nm with sharp cut-offs suggesting a relatively narrow pore distribution for the UF membrane. The other three membranes showed a large spread in pore sizes ranging from about 2.5 nm to about 80 nm indicating wider pore distribution UF membranes [33, 34]. Large pores contribute more to permeability but may result in reduced rejection [30, 31].

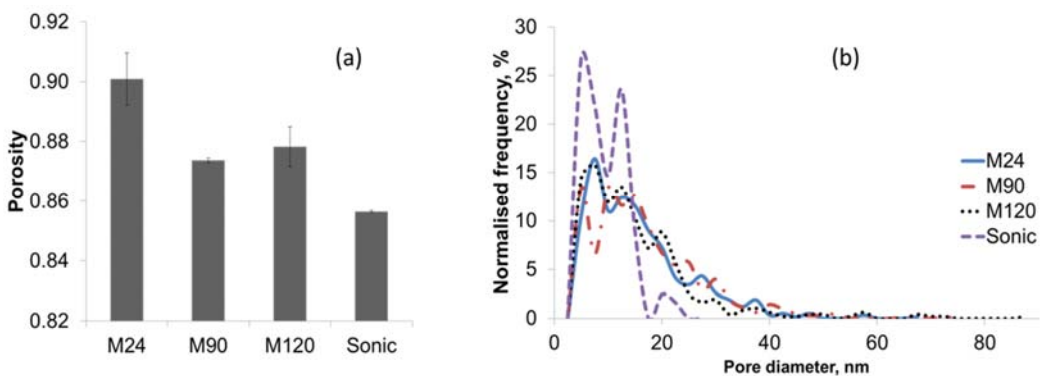


Figure 4.6. Membrane bulk porosity obtained gravimetrically (a) and pore size distribution on skin layer as obtained from image analysis of the SEM images of membrane selective surfaces (b). Error bars indicate computed standard error.

#### 4.3.6. Wettability

The membrane wettability as measured by water CA is presented in Figure 4.7 showing that CAs for the membranes were between  $76^\circ$  and  $95^\circ$ . Images of typical water contact angles on the membranes are shown in Figure S4.3. From Figure 4.7, M120 is seen to have the largest water CA of  $95^\circ$  while M90 had the lowest water CA of  $76^\circ$ . Although the difference between these results is significant with respect to the computed standard error, there appears to be no consistent pattern in the results. Considering that roughness (not quantified in this work) can greatly influence the outcome of water CA [35], the CA values for these membrane may be said to be practically similar and thus not a strong function of dissolution condition. The water CA for PVDF membranes with added pore former has been reported variously as  $74.4^\circ$  [27],  $82.9^\circ$  [17],  $76^\circ$  and  $93^\circ$  [36]. This shows that the results of this study are within the expected range of previously reported wettability values for PVDF membranes.

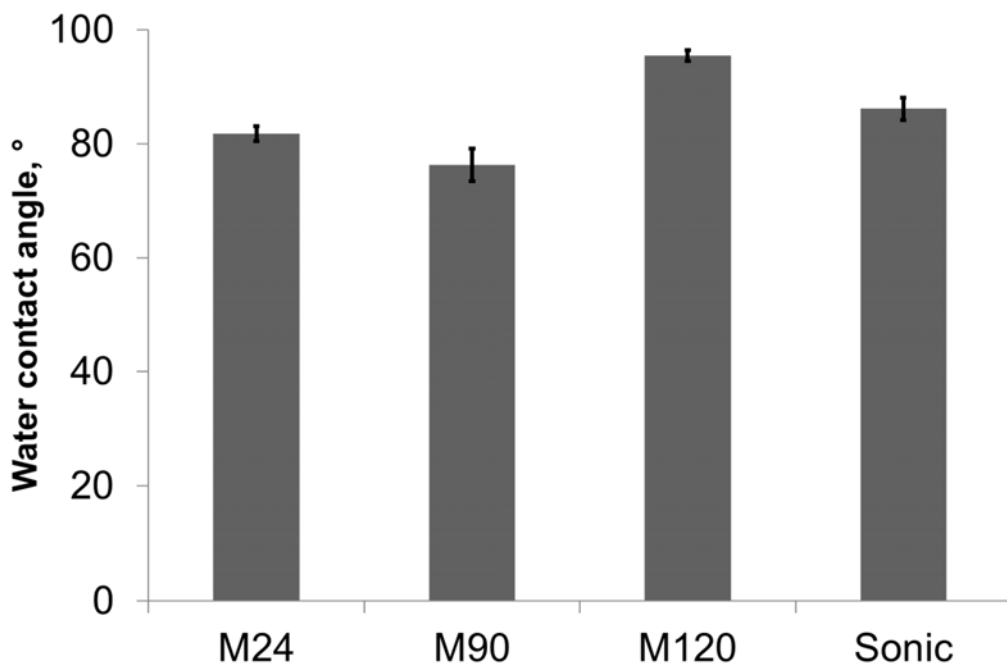


Figure 4.7. Membrane water contact angles measured using optical tensiometer operated at room temperature. Error bars indicate computed standard error.

#### 4.3.7. Filtration performance

##### 4.3.7.1. Flux and rejection

The membrane crossflow filtration performance at a TMP of 30 kPa is shown in Figure 4.8. The clean water flux results (Figure 4.8a) shows that very high  $J_0$  of more than  $600 \text{ Lm}^{-2}\text{h}^{-1}$  was obtained for M24 and M120. The similarity in  $J_0$  for M24 and M120 strongly suggest similar skin layer pore sizes for the wet membranes as reasoned previously (Section 4.3.4). The lowest  $J_0$  of about  $180 \text{ Lm}^{-2}\text{h}^{-1}$  resulted for Sonic. The clean water flux results can be explained by the membrane porosity and surface pore size distribution shown in Figure 4.6. The larger surface pores and higher bulk porosity of M24, M90 and M120 allowed for higher permeation of water through the membrane while the denser morphology of small pores and lower porosity means that only a relatively limited amount of water can be permeated through Sonic [30]. It may be noted that the clean water flux values observed in this work are significantly higher than the value of  $5 \text{ Lm}^{-2}\text{h}^{-1}$  at a TMP of 175 kPa reported by Lai et al [12] for their PVDF membrane

which was produced without the addition of a hydrophilic polymer such as the PVP used in this work. The addition of hydrophilic polymers to hydrophobic membrane materials is credited to increase hydrophilicity and pore formation [13, 37, 38].

The oil emulsion droplet sizes for the feed used to evaluate the fouling and rejection performance of the produced membranes ranged from 20 nm to 500 nm as shown in Figure 4.8e. Since the SEM-observed pore sizes for the dry membranes are between 0 and 100 nm, it can be expected that both pore blocking and cake formation are possible fouling mechanism for the filtration systems [39]. The average permeate flux during the oil emulsion filtration,  $J_1$ , is shown in Figure 4.8b. The sample trend is an almost reversal of  $J_0$  with the Sonic showing the highest flux value of  $37 \text{ Lm}^{-2}\text{h}^{-1}$  while M24 had the lowest flux of  $20 \text{ Lm}^{-2}\text{h}^{-1}$ . The  $J_1$  for M90 and M120 were both approx.  $26 \text{ Lm}^{-2}\text{h}^{-1}$ . The rejection of TC by the membranes during the oil emulsion filtration is shown in Figure 4.8c. It can be seen that the rejection value for all the membranes are similar at a value of 92% despite the lower pore size observed for the Sonic. An explanation for the rejection results may be advanced along the line that the larger pores in M24, M90 and M120 were rapidly blocked by foulants thereby giving the effect of similar TC rejection. If this reasoning is correct, it is expected that Sonic will have the better *FR*. The *FR*, after oil emulsion fouling and cleaning with a 0.1 M NaOH solution for the membranes, is shown in Figure 4.8d. As expected, Sonic exhibited the best *FR* of 63% while M24 had the lowest *FR* of 26%. The *FR* for M90 and M120 were 46% and 43% respectively. Overall, the Sonic can be said to be suitable for the filtration of more challenging feed while the stable M120 with high  $J_0$  is more suitable for the high flux filtration of low fouling feeds.

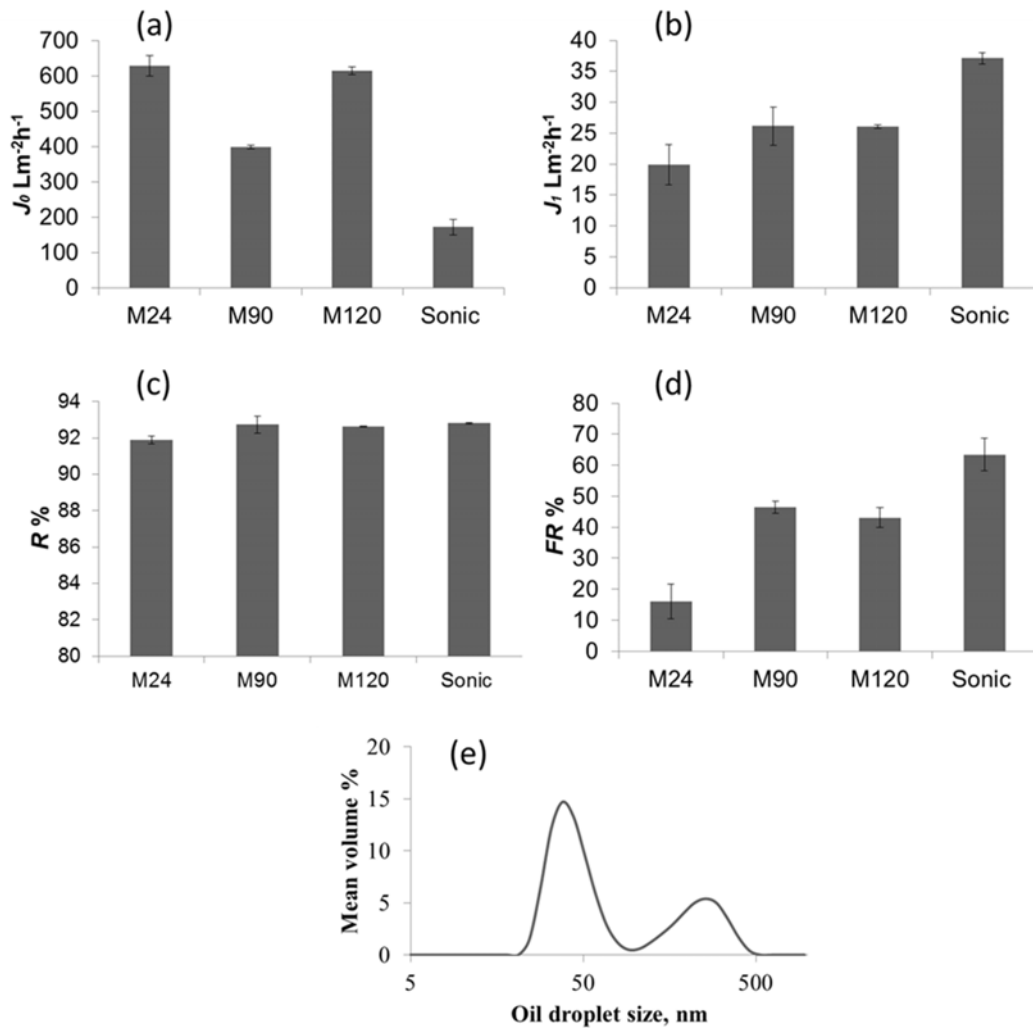


Figure 4.8. Membrane performance during crossflow clean water and oil emulsion filtration at TMP of 30 kPa. Clean water flux,  $J_0$  (a), average permeate flux during oil emulsion filtration,  $J_1$  (b), membrane TC rejections,  $R$  (c), membrane flux recovery after oil emulsion fouling and cleaning with 0.1 M NaOH solutions,  $FR$  (d) and droplet size distribution for oil emulsion used as feed (e). Error bars indicate computed standard error.

Although high permeate flux under severe fouling conditions and enhanced flux recovery is often associated with hydrophilicity improvement [40], membrane wettability differences cannot explain the flux results obtained in this work since the average CA for Sonic with the best flux recovery was 86° while M24 with the

lowest flux recovery had a slightly lower water CA of 82°. The wettability values are practically alike as discussed earlier but a lower CA for Sonic would have been expected to explain the filtration results obtained. As pointed out earlier, a consideration of the skin layer pore size distributions for the membranes (Figure 4.6b) may suggest that Sonic with lower pore sizes and narrow pore size distribution should provide better rejection [30, 31]. But as that was not the case (Figure 4.8c), a reasonable explanation of the filtration results will emphasise the role of skin layer pore size where larger pores were extensively and rapidly blocked [39, 41] and de-emphasise the influence of surface hydrophilicity. Although the deformable property of oil droplets have been reported to allow the squeezing of large droplet particles into much smaller membrane pores at operating pressure of 150 kPa [42], the low TMP value of 30 kPa used in this work is thought to be insufficient to cause significant oil droplet deformation so that only large pores were effectively blocked. The implication here would be that Sonic with smaller pores will experience more cake fouling and limited pore blocking [39]. The proposed rapid pore blocking for M24, M90 and M120 due to their larger pore sizes also explain their observed lower  $J_1$ . This can be seen by considering that a significant amount of the pores in these membranes are greater than the minimum oil droplet size of 20 nm while only a small fraction of the pores in Sonic have sizes greater than 20 nm. Consequently, the rapid blockage of large pores would affect the  $J_1$  more for M24, M90 and M120 compared to Sonic. The limited *FR* for M24, M90 and M120 relative to Sonic is also consistent with this explanation in which pore blocking increased the problem of irreversible fouling [43]. It may therefore be concluded that the narrow pore diameter range (<25 nm) for Sonic allowed for adequate percolation of water molecules but was less accessible to the oil droplets (>20 nm) in the emulsion resulting in sustained high water permeation and low pore blocking as oil droplets were substantially excluded from the membrane pores.

In addition, the relatively smooth surface for Sonic with limited surface depressions as was shown in the SEM images of Figure 4.2 may have contributed significantly to its better flux recovery as foulants are less likely attached onto a smooth surface when compared to a rough surface [44].

#### 4.3.7.2. Cake formation and modelling

After the filtration tests, significant differences in the membranes were clearly seen upon visual inspection. Images of representative fouled membranes after cleaning are shown in Figure 4.9. The Sonic showed the most colouring followed by M24 while M120 seems to show the least colouring. The more intense yellowish colouring of Sonic may be indicative of more surface or cake fouling. The intense surface colouring on Sonic is expected since with smaller pores and higher permeate flux during the oil emulsion filtration, more rejected foulant may deposit on the membrane surface as cake. Surprisingly, the instantaneous  $J_1$  taken at the 2 h mark (Figure 4.10a) shows that despite the more intense surface colouring indicative of more surface fouling, Sonic sustained not only a higher overall  $J_1$ , but also maintained higher permeate flux to the last moment of the fouling test.



Figure 4.9. Image of representative membranes after fouling and cleaning with 0.1 M NaOH, from left to right M24, M90, M120 and Sonic.

To elucidate the fouling mechanism responsible for the varied colouring of the membranes and their filtration behaviour, simple filtration modelling was employed. A linear relation when filtration-time/filtrate-volume ( $t/v$ ) is plotted against filtrate-volume ( $v$ ) has been shown to be indicative of cake fouling [39, 41, 45]. These plots are presented in Figure 4.10b. The four membranes show an early non-linear trend which is indicative of pore blocking [39, 41, 43, 45]. The

non-linear trend was continued for almost the entire filtration volume for M24 suggestive of minimal cake fouling but extensive pore blocking. That M24 had the lowest  $J_1$  supports the claim that the principal fouling for this membrane was pore blocking. However, it has to be considered that some amount of cake deposition did occur on M24 after the pores were sufficiently blocked giving rise to the observed colouring. The limited colouring of M120 may be due to its limited permeate volume when compared to M90 and Sonic (Figure 4.10b). In addition, M120 showed the highest polar  $F(\beta)$  (Figure 4.3) which is likely to reduce its attachment to the non-polar oil droplets [8]. In the same vein, M24 with the least  $F(\beta)$  is expected to show greater affinity to the non-polar oil.

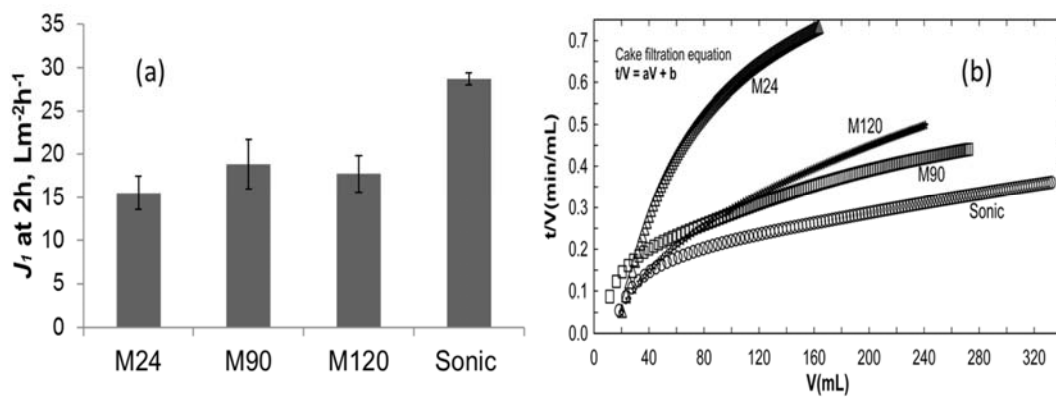


Figure 4.10. Permeate flux during filtration of an oil emulsion at 2 h (a), cake filtration model plots (b). Error bars indicate computed standard error.

The initial non-linear trend for Sonic in Figure 4.10b was seen to give way after only a small filtration volume to an extended linear relationship indicative of extensive cake fouling which is consistent with the cake fouling mechanism advanced in this work for this membrane. The filtration experiment in this work is set up such that the concentration of the feed increased as permeate is removed (see Figure 4.1). As shown in Figure 4.10b, for the 2 h duration of the filtration test, more permeate volume was removed from the feed by Sonic than the other membranes implying that the former was charged with more concentrated feed towards the end of the 2 h filtration tests. This fact is probably partly responsible for the increased surface colouring observed for this membrane arising from increased cake deposition due to higher feed concentration. It is interesting that

despite the significant surface colouring indicative of more cake formation and the more concentrated feed towards the end of the filtration, Sonic retained the highest  $J_1$  at 2 h (Figure 4.10a) which highlights its superior filtration performance. It is also important to note that no deviation from a straight line was observed for any of the membrane towards the end of the filtration period which suggests that cake compression was minimal or absent [45]. This observation corroborate the earlier proposal that although oil droplets are deformable and can penetrate much smaller pores than their diameters, the TMP of 30 kPa at which the experiment in this work were perform was probably too low for such deformation to occur so that only pores bigger than the oil droplets were blocked.

#### 4.3.7.3. Porosity correlations

The results presented so far highlight major differences in membrane properties and performance as a result of altering the conditions of the dope dissolution. To more fully comprehend the basis for the changes in performance and properties, the results were analysed more closely to determine whether there is a primary parameter directly altered by the dissolution conditions and which then impacted other membrane properties. An overview of the performance evaluations conducted seems to suggest a consistent pattern in which M24 and Sonic appear to occupy opposite extremes while M90 and M120 take the middle place following approximately the bulk porosity trend of Figure 6b. To quantify this apparent relationship, linear regressions of the performance data against the bulk porosity were made and presented in Figure 4.11.

Interestingly, all the performance data show reasonable to strong correlations to the bulk porosity as measured by the coefficient of determination ( $R^2$ ). The minimum  $R^2$  observed was for  $J_0$ , which however was a reasonable  $R^2$  of 0.7668, while the largest  $R^2$  was for mechanical strength, which showed a strong correlation of 0.9951. A schematic elucidation of how porosity/pore size could influence such varying key membrane performance parameters is presented in Figure 4.12. Figure 4.12 assumes that the pore distribution, pore shape and number of pores for the membranes are alike. The probable implications are that membrane porosity/pore size is an important tool for the design of membrane for specific applications and that such tailored design could be achieved by simply

altering the condition of the initial PVDF polymer dissolution. Further research on the parameters affecting membrane properties using diverse membrane forming materials, preparation conditions and advanced statistical analysis seems a natural extension of this study.

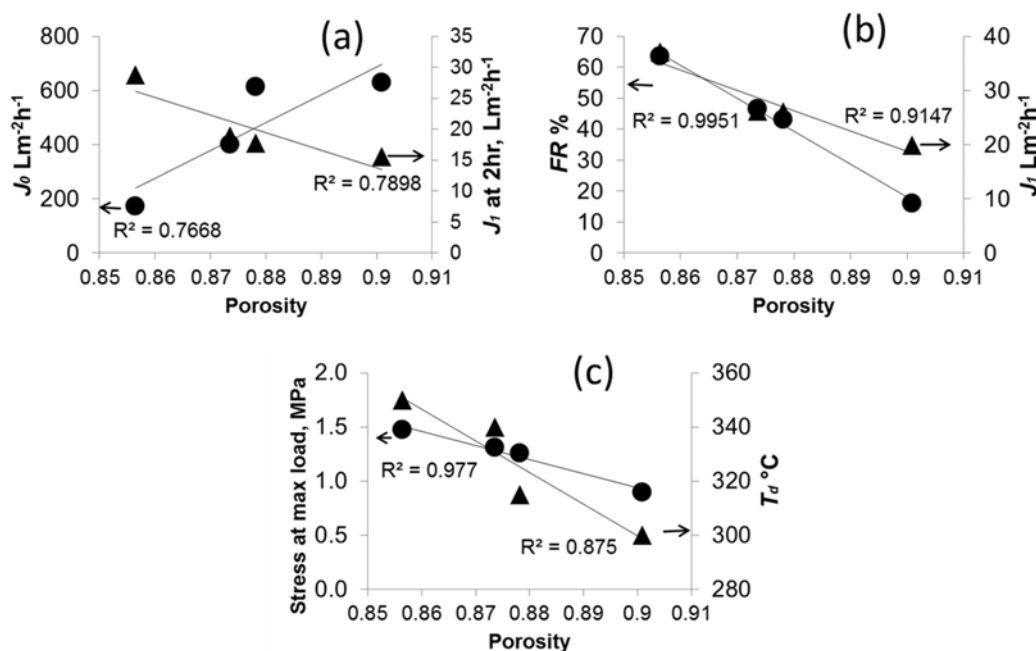


Figure 4.11. Membranes performance correlations to bulk porosity for water flux,  $J_0$ , and emulsion permeate flux at 2 h,  $J_1$  (a) flux recovery, RF, and average emulsion permeate flux,  $J_1$  (b) tensile stress at maximum load and temperature for the onset of thermal degradation  $T_d$  (c). Inserted arrows point to the axis relevant to each set of triangular or circular symbols

#### 4.3.7.4. Dope dissolution environment

Previous studies on the effects of physical dissolution conditions on the properties of PVDF membranes have focused exclusively on temperature which results in gradual and predictable changes in the properties of the synthesised membrane [1, 7, 8]. The properties of the Sonic membrane in this work is starkly different from the other membranes suggesting that a mere temperature effect cannot

explain the unique properties. Since several physical mechanisms develop from ultrasonication such as heating, structural effects, compression and rarefaction, turbulence and cavitation [10, 15], it appears that the unique properties of the Sonic membrane is due to the combined effects of several physical processes. These physical processes can be simply referred to as providing a more energetic dissolution environment.

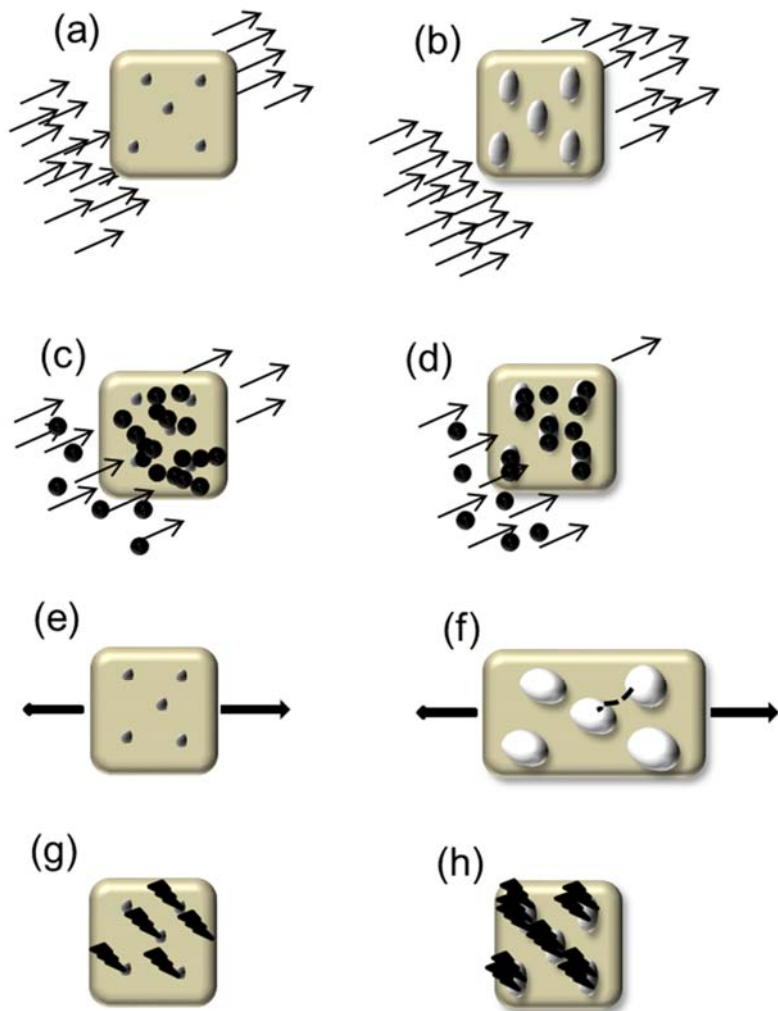


Figure 4.12. Schematic elucidation of porosity/pore size influence on key membrane performance parameters assuming similar number of pores. Low water flux – small flow area (Poiseuille's Law) [46] (a); high water flux – large flow area (Poiseuille's Law) [46] (b); good emulsion permeation/flux recovery – less pore blocking and more cake deposition [39, 41, 43] (c); poor emulsion permeation/flux recovery – extensive pore blocking and limited cake deposition [39, 41] (d); good mechanical stability – more membrane material supporting load (less effective stress) [47] (e); poor mechanical stability – less load bearing material (more effective stress) [47] (f); good thermal stability – limited thermal attack fronts or end chains [25] (g); poor thermal stability – large area for thermal attack or end chains [25] (h).

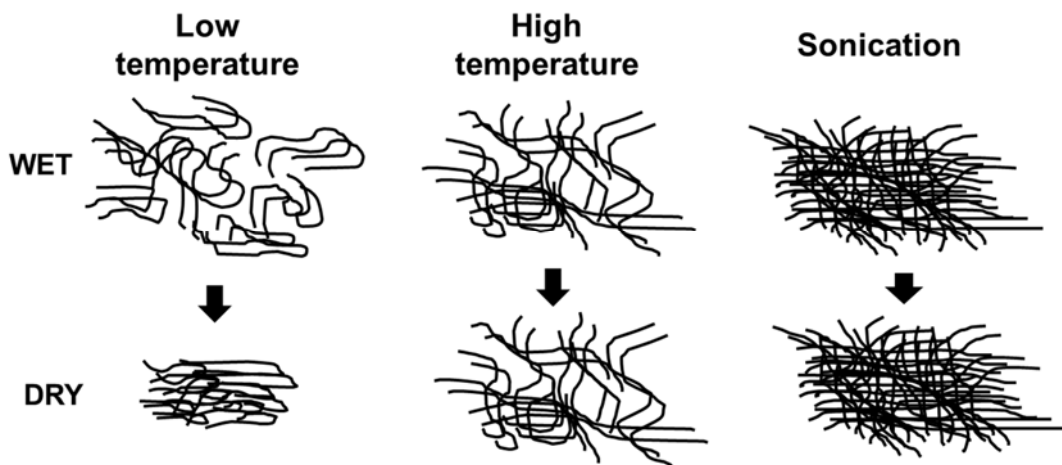


Figure 4.13. Schematic representation of the effects of different dope dissolving conditions on PVDF polymer networks entanglement [1] as wet and dry membranes.

The observed effects of dissolution environments in terms of their energy level could be related to the degree of unfolding of the polymer molecular chains and their entanglements following Wang et al. [1]. As discussed in earlier sections, the energy of the PVDF dissolution environment defines to what extent the polymer molecular chains could unfold/dissolve and to what extent the unfolded chains are entangled or resist gelation [1, 7, 8]. In a low temperature environment, the chains are folded [1, 8] or partially dissolved even though visually clear [7, 8] and therefore achieve limited permanent entanglement resulting in an unstable polymer framework. This is observed as the large shrinkage of M24 upon drying highlighting that its loose framework allowed for the presence of significant amount of water and when the embedded water was dried out, the membrane structure was too weak to maintain its original volume and therefore collapsed. However, as the temperature of dope dissolution increased, the kinetic energy of the polymer allowed for greater unfolding and therefore greater entanglement [1] resulting in a permanent structure when the membrane was dried of water. The highly energised environment provided by ultrasonication resulted in significant unfolding of the polymer chains and their extensive entanglement. The extensive entanglement is hypothesised to cause a permanent grid system with uniform pores of small size and enhanced mechanical properties. Consequently, dope

sonication provides a unique technique to achieve comparatively small pore size membrane with narrow pore size distribution and strong physical properties. A conceptualisation of the effects of different dope dissolving conditions on PVDF polymer networks as wet and dry membranes following Wang et al. [1] is shown in Figure 4.13.

#### 4.4. Conclusion

This study contributes to a growing body of research that demonstrates the important effects of PVDF dissolution conditions on the properties of the membranes. It is shown that not only the specific temperature of dope dissolution but other physical forms of energy inputs such as are generated via ultrasonication have significant effects on the performance of UF membranes and therefore may be employed for specific membrane design. Dope dissolved by ultrasonication was shown to result in a membrane with dense structure and reduced porosity, narrow size distribution of small pores and reasonably smooth skin layer relative to the other membranes produced under identical conditions excepting the polymer dissolution process. Even though this membrane suffered from reduced clean water flux when compared to the other membranes produced without sonication, its unique properties were shown to result in enhanced thermal stability, improved mechanical strength and outstanding oil emulsion filtration performance of high permeate flux and high *FR*. Consequently, Sonic may be suitable for filtration under more practical conditions of challenging feed while the high clean water flux of M120 may allow for high productivity under less challenging conditions. The performances of the membranes evaluated in this work irrespective of the mode of original polymer dissolution showed strong correlations to the membrane porosity suggesting a possible convenient means for UF membrane design achievable by simply altering the mode of polymer dissolution. The observed difference in the properties of membranes due to dope dissolution in different energy environment was related to the degree of unfolding/dissolution of the polymer molecular chains and their entanglements.

#### 4.5. Acknowledgement

The financial support provided by Victoria University to Ikechukwu A. Ike through the Victoria University International Postgraduate Research Scholarship is

gratefully acknowledged. Sincere gratitude to Ludovic F. Dumée, Deakin University, for his many insightful suggestions and for acquiring the SEM cross section images. Anbharasi Vanangamudi, Victoria University, is also gratefully acknowledged for acquiring the surface SEM images.

## References

- [1] X. Wang, X. Wang, L. Zhang, Q. An, H. Chen, Morphology and Formation Mechanism of Poly(Vinylidene Fluoride) Membranes Prepared with Immersion Precipitation: Effect of Dissolving Temperature, *Journal of Macromolecular Science, Part B*, 48 (2009) 696-709.
- [2] F. Liu, N.A. Hashim, Y. Liu, M.R.M. Abed, K. Li, Progress in the production and modification of PVDF membranes, *Journal of Membrane Science*, 375 (2011) 1-27.
- [3] G.-d. Kang, Y.-m. Cao, Application and modification of poly(vinylidene fluoride) (PVDF) membranes – A review, *Journal of Membrane Science*, 463 (2014) 145-165.
- [4] B. Wu, K. Li, W.K. Teo, Preparation and characterization of poly(vinylidene fluoride) hollow fiber membranes for vacuum membrane distillation, *Journal of Applied Polymer Science*, 106 (2007) 1482-1495.
- [5] A. Bottino, G. Camera-Roda, G. Capannelli, S. Munari, The formation of microporous polyvinylidene difluoride membrane by phase separation, *Journal of Membrane Science*, 57 (1991) 1-20.
- [6] A. Gugliuzza, E. Drioli, New performance of hydrophobic fluorinated porous membranes exhibiting particulate-like morphology, *Desalination* 240 (2009) 14 - 20.
- [7] D.-J. Lin, K. Beltsios, T.-H. Young, Y.-S. Jeng, L.-P. Cheng, Strong effect of precursor preparation on the morphology of semicrystalline phase inversion poly(vinylidene fluoride) membranes, *Journal of Membrane Science*, 274 (2006) 64-72.
- [8] A.L. Ahmad, N. Ideris, B.S. Ooi, S.C. Low, A. Ismail, Morphology and polymorph study of a polyvinylidene fluoride (PVDF) membrane for protein binding: Effect of the dissolving temperature, *Desalination*, 278 (2011) 318-324.

- [9] M. Li, I. Katsouras, C. Piliego, G. Glasser, I. Lieberwirth, P.W.M. Blom, D.M. de Leeuw, Controlling the microstructure of poly(vinylidenefluoride) (PVDF) thin films for microelectronics, *Journal Material Chemistry C*, 1 (2013) 7695–7702.
- [10] I. Masselin, X. Chasseray, L. Durand-Bourlier, J.-M. Lainé, P.-Y. Syzaret, D. Lemordant, Effect of sonication on polymeric membranes, *Journal of Membrane Science*, (2001) 213-220.
- [11] A. Bottino, G. Capannelli, A. Comite, Preparation and characterization of novel porous PVDF-ZrO<sub>2</sub> composite membranes, *Desalination*, 146 (2002) 35-40.
- [12] C.Y. Lai, A. Groth, S. Gray, M. Duke, Preparation and characterization of poly(vinylidene fluoride)/nanoclay nanocomposite flat sheet membranes for abrasion resistance, *Water Research*, 57 (2014) 56-66.
- [13] H. Rajabi, N. Ghaemi, S.S. Madaeni, P. Daraei, M.A. Khadivi, M. Falsafi, Nanoclay embedded mixed matrix PVDF nanocomposite membrane: Preparation, characterization and biofouling resistance, *Applied Surface Science*, 313 (2014) 207-214.
- [14] S. Liang, K. Xiao, Y. Mo, X. Huang, A novel ZnO nanoparticle blended polyvinylidene fluoride membrane for anti-irreversible fouling, *Journal of Membrane Science*, 394-395 (2012) 184-192.
- [15] B. Banerjee, Recent developments on ultrasound assisted catalyst-free organic synthesis, *Ultrasonics sonochemistry*, 35 (2017) 1-14.
- [16] B. Mohammadi, A.A. Yousefi, S.M. Bellah, Effect of tensile strain rate and elongation on crystalline structure and piezoelectric properties of PVDF thin films, *Polymer Testing*, 26 (2007) 42-50.
- [17] L.-Y. Yu, Z.-L. Xu, H.-M. Shen, H. Yang, Preparation and characterization of PVDF–SiO<sub>2</sub> composite hollow fiber UF membrane by sol–gel method, *Journal of Membrane Science*, 337 (2009) 257-265.
- [18] J.-F. Li, Z.-L. Xu, H. Yang, Microporous polyethersulfone membranes prepared under the combined precipitation conditions with non-solvent additives, *Polymers for Advanced Technologies*, 19 (2008) 251-257.
- [19] L. Priya, J.P. Jog, Polymorphism in Intercalated Poly(vinylidene fluoride)/Clay Nanocomposites, *Journal of Applied Polymer Science*, 89 (2003) 2036–2040.

- [20] C.Y. Lai, A. Groth, S. Gray, M. Duke, Enhanced abrasion resistant PVDF/nanoclay hollow fibre composite membranes for water treatment, *Journal of Membrane Science*, 449 (2014) 146-157.
- [21] D.R. Dillon, K.K. Tenneti, C.Y. Li, F.K. Ko, I. Sics, B.S. Hsiao, On the structure and morphology of polyvinylidene fluoride–nanoclay nanocomposites, *Polymer*, 47 (2006) 1678-1688.
- [22] D. Shah, P. Maiti, E. Gunn, D.F. Schmidt, D.D. Jiang, C.A. Batt, E.P. Giannelis, Dramatic enhancements in toughness of Polyvinylidene fluoride nanocomposites via nanoclay directed crystal structure and morphology, *Advanced Materials*, 16 (2004) 1173-1177.
- [23] R.M. Cornell, U. Schwertmann, *The Iron Oxides: Structures, Properties, Reactions, Occurrences and Uses*, 2nd Edition ed., WILEY-VCH Verlag GmbH & Co. KGaA, Weinheim, 2003.
- [24] M.D. Lekgoathi, L.D. Kock, Effect of short and long range order on crystal structure interpretation: Raman and powder X-ray diffraction of LiPF(6), *Spectrochimica acta. Part A, Molecular and biomolecular spectroscopy*, 153 (2016) 651-654.
- [25] C.L. Beyler, M.M. Hirschler, Thermal Decomposition of Polymers, in: P.J. DiNenno (Ed.) *SFPE Handbook of Fire Protection Engineering* National Fire Protection Association, 2002.
- [26] Solvay, Solef PVDF Design & Processing Guide, in, *Solvay Specialty Polymers*, 2015.
- [27] Y. Zhang, J. Zhao, H. Chu, X. Zhou, Y. Wei, Effect of modified attapulgite addition on the performance of a PVDF ultrafiltration membrane, *Desalination*, 344 (2014) 71-78.
- [28] A. Karatrantos, N. Clarke, R.J. Composto, K.I. Winey, Entanglements in polymer nanocomposites containing spherical nanoparticles, *Soft Matter*, 12 (2016) 2567--2574.
- [29] R. Mangal, S. Srivastava, L.A. Archer, Phase stability and dynamics of entangled polymer-nanoparticle composites, *Nature communications*, 6 (2015) 7198.
- [30] S. Mochizuki, A.L. Zydny, Theoretical analysis of pore size distribution effects on membrane transport, *Journal of Membrane Science*, 82 (1993) 211-227.

- [31] S.R. Wickramasinghe, S.E. Bower, Z. Chen, A. Mukherjee, S.M. Husson, Relating the pore size distribution of ultrafiltration membranes to dextran rejection, *Journal of Membrane Science*, 340 (2009) 1-8.
- [32] W.R. Bowen, J.S. Welfoot, Modelling of membrane nanofiltration—pore size distribution effects, *Chemical Engineering Science*, (2002) 1393–1407.
- [33] C. Binnie, M. Kimber, *Basic Water Treatment*, in, ICE Publishing, London, 2013.
- [34] A. Cipollina, G. Micale, L. Rizzuti, Seawater desalination, in: *Green Energy and Technology*, Springer-Verlag, Heidelberg, 2009.
- [35] D.J. Shaw, *Introduction to colloid and surface chemistry*, Butterworth & Co. (Publishers) Ltd, London, 1980.
- [36] E. Fontananova, J.C. Jansen, A. Cristiano, E. Curcio, E. Drioli, Effect of additives in the casting solution on the formation of PVDF membranes, *Desalination*, 192 (2006) 190-197.
- [37] A. Pagidi, R. Saranya, G. Arthanareeswaran, A.F. Ismail, T. Matsuura, Enhanced oil–water separation using polysulfone membranes modified with polymeric additives, *Desalination*, 344 (2014) 280-288.
- [38] H. Basri, A.F. Ismail, M. Aziz, Polyethersulfone (PES)–silver composite UF membrane: Effect of silver loading and PVP molecular weight on membrane morphology and antibacterial activity, *Desalination*, 273 (2011) 72-80.
- [39] T. Mohammadi, A. Kohpeyma, M. Sadrzadeh, Mathematical modeling of flux decline in ultrafiltration, *Desalination*, 184 (2005) 367-375.
- [40] L. Yan, S. Hong, M.L. Li, Y.S. Li, Application of the Al<sub>2</sub>O<sub>3</sub>–PVDF nanocomposite tubular ultrafiltration (UF) membrane for oily wastewater treatment and its antifouling research, *Separation and Purification Technology*, 66 (2009) 347-352.
- [41] Y. Ye, P. Le Clech, V. Chen, A.G. Fane, B. Jefferson, Fouling mechanisms of alginate solutions as model extracellular polymeric substances, *Desalination*, 175 (2005) 7-20.
- [42] A. Hong, A.G. Fane, R. Burford, Factors affecting membrane coalescence of stable oil-in-water emulsions, *Journal of Membrane Science*, 222 (2003) 19-39.
- [43] L. De Angelis, M.M.F. de Cortalezzi, Ceramic membrane filtration of organic compounds: Effect of concentration, pH, and mixtures interactions on fouling, *Separation and Purification Technology*, 118 (2013) 762-775.

- [44] X. Cao, J. Ma, X. Shi, Z. Ren, Effect of TiO<sub>2</sub> nanoparticle size on the performance of PVDF membrane, *Applied Surface Science*, 253 (2006) 2003-2010.
- [45] H.T. Madsen, Membrane Filtration in Water Treatment – Removal of Micropollutants, in: Chemistry of Advanced Environmental Purification Processes of Water, Elsevier B.V., 2014, pp. 199-248.
- [46] R.W. Baker, Membrane technology and application, 2nd ed., John Wiley & Sons, Ltd, West Sussex, England, 2004.
- [47] P. Ghavami, Stress and strain, in: P. Ghavami (Ed.) *Mechanics of Materials*, Springer International Publishing, Switzerland, 2015, pp. 143-162.

## Appendix

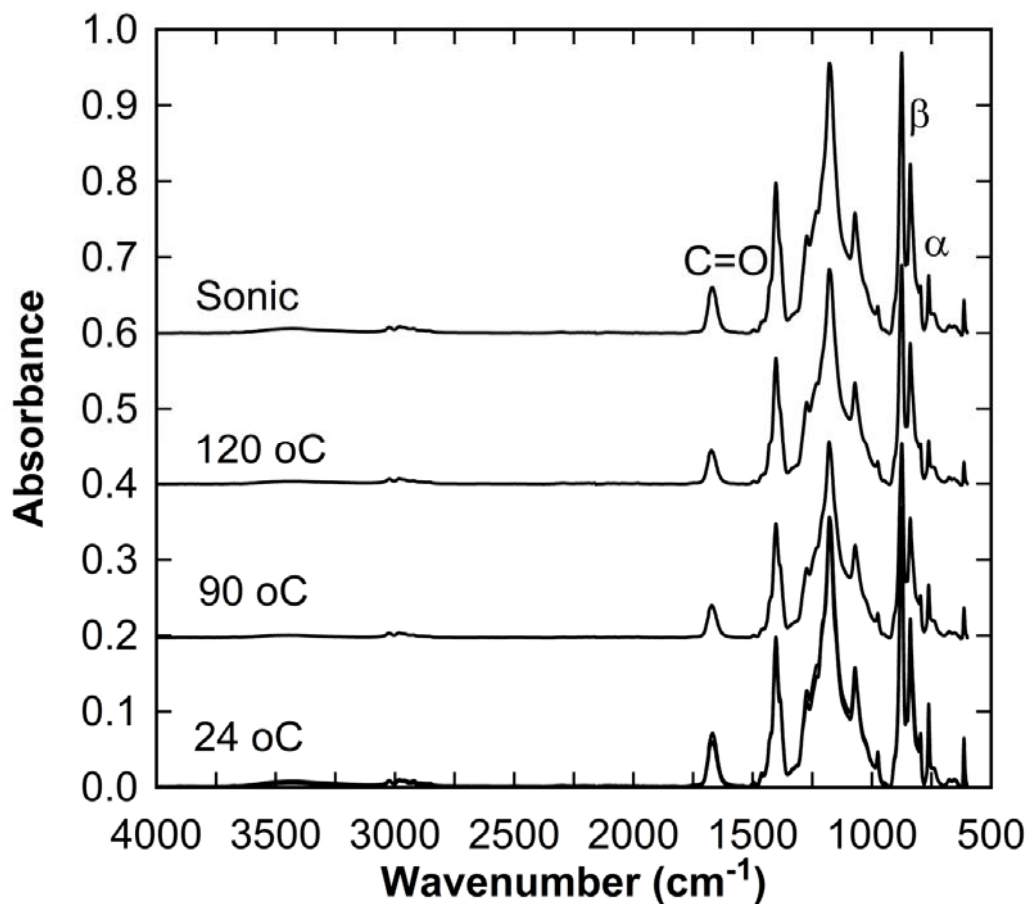


Figure S4.1. Typical FTIR spectra for the membranes

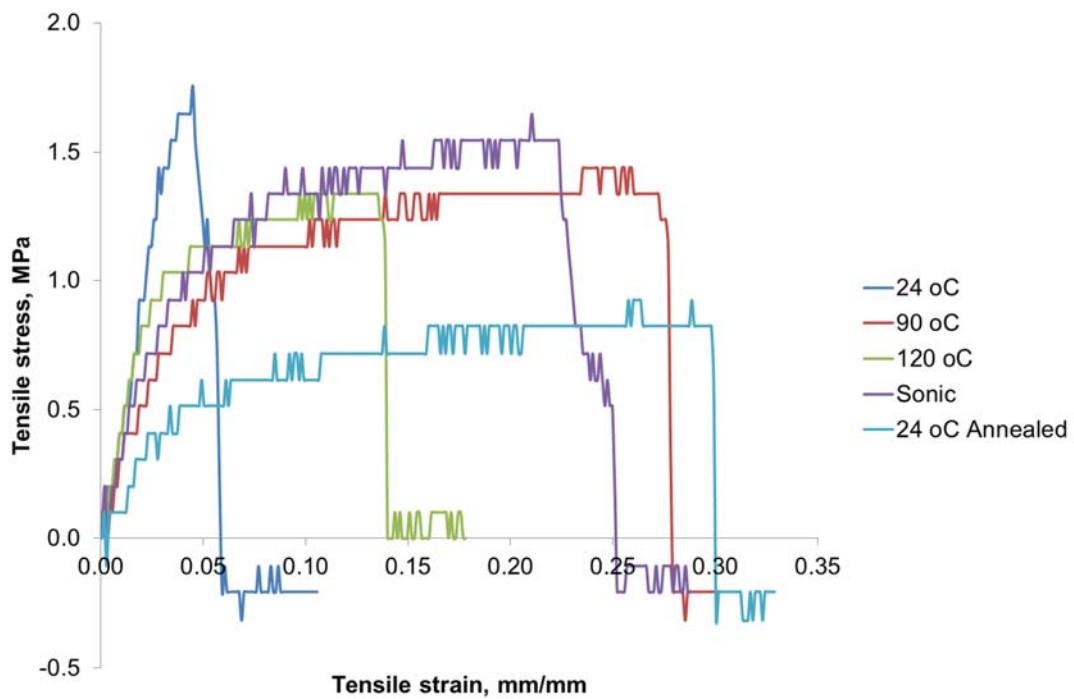


Figure S4.2. Typical stress-strain curves for membranes

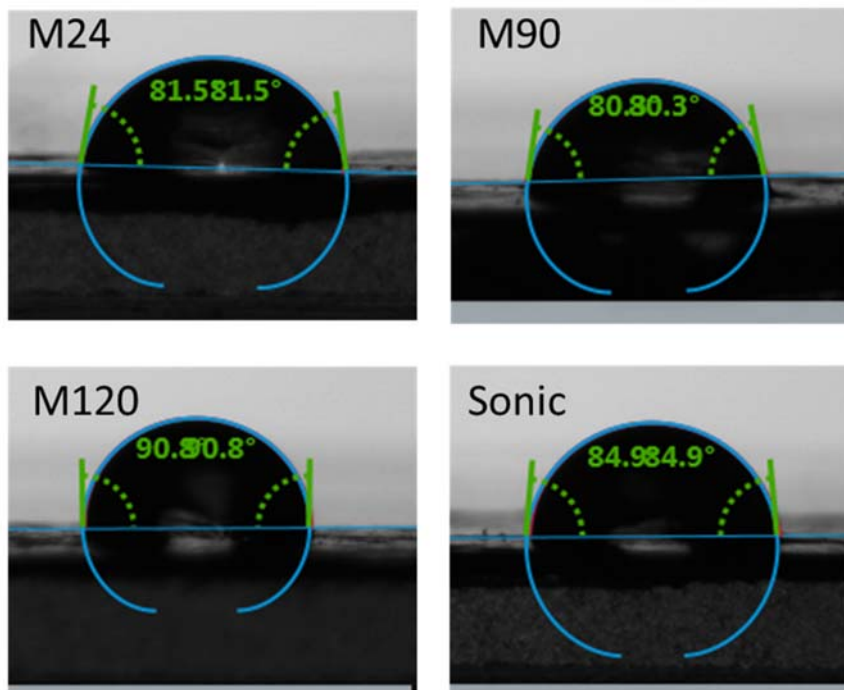


Figure S4.3. Typical water contact angles on membranes. Images obtained using Krüss drop shape analyser – DSA25 under room temperature of 20 °C using PTFE needle of diameter 0.69 mm. 4.0  $\mu$ L droplet volume was placed on a membrane and the CA computed using the Young Laplace fitting method.

## GRADUATE RESEARCH CENTRE

### DECLARATION OF CO-AUTHORSHIP AND CO-CONTRIBUTION: PAPERS INCORPORATED IN THESIS BY PUBLICATION

*This declaration is to be completed for each conjointly authored publication and placed at the beginning of the thesis chapter in which the publication appears.*

#### 1. PUBLICATION DETAILS (to be completed by the candidate)

Title of Paper/Journal/Book:	Effects of dissolution conditions on the properties of PVDF ultrafiltration membranes	
------------------------------	---	--

Surname:	Ike	First name:	Ikechukwu
College:	College	Candidate's Contribution (%):	90

Status:

Accepted and in press:

Date:

Published:

Date:  01 June 2017

#### 2. CANDIDATE DECLARATION

I declare that the publication above meets the requirements to be included in the thesis as outlined in the HDR Policy and related Procedures – [policy.vu.edu.au](http://policy.vu.edu.au).

Ikechukwu Anthony Ike	Digitally signed by Ikechukwu Anthony Ike DN: cn=ikechukwu Anthony Ike, o, ou, email=tonyjamesike@yahoo.com, c=AU Date: 2017.08.11 11:13:20 +10'00'	9 August 2017
--------------------------	---	---------------

Signature

Date

#### 3. CO-AUTHOR(S) DECLARATION

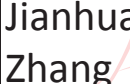
In the case of the above publication, the following authors contributed to the work as follows:

The undersigned certify that:

1. They meet criteria for authorship in that they have participated in the conception, execution or interpretation of at least that part of the publication in their field of expertise;
2. They take public responsibility for their part of the publication, except for the responsible author who accepts overall responsibility for the publication;
3. There are no other authors of the publication according to these criteria;
4. Potential conflicts of interest have been disclosed to a) granting bodies, b) the editor or publisher of journals or other publications, and c) the head of the responsible academic unit; and

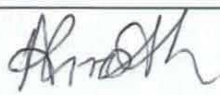
5. The original data will be held for at least five years from the date indicated below and is stored at the following location(s):

Institute for Sustainability and Innovation, Victoria University, Melbourne, Australia

Name(s) of Co-Author(s)	Contribution (%)	Nature of Contribution	Signature	Date
Jianhua Zhang	2	Manuscript revision	 Digitally signed by Jianhua Zhang Date: 2017.08.15 09:39:36 +10'00'	
Andrew Groth	2	Manuscript revision		
John D. Orbell	3	Manuscript revision	 Digitally signed by John Orbell Date: 2017.08.16 10:15:35 +10'00'	
Mikel Duke	3	Manuscript revision	 Digitally signed by Mikel Duke Date: 2017.08.11 10:43:31 +10'00'	

5. The original data will be held for at least five years from the date indicated below and is stored at the following location(s):

Institute for Sustainability and Innovation, Victoria University, Melbourne, Australia

Name(s) of Co-Author(s)	Contribution (%)	Nature of Contribution	Signature	Date
Jianhua Zhang	2	Manuscript revision		
Andrew Groth	2	Manuscript revision		14.8.17
John D. Orbell	3	Manuscript revision		
Mikel Duke	3	Manuscript revision	 Digitally signed by Mikel Duke Date: 2017.08.11 10:43:31 +10'00'	

## Chapter 5

### **Critical review of the science and sustainability of persulphate advanced oxidation processes\***

#### **Abstract**

A critical review of the literature of AOPs focused on the commercially important oxidant, persulphate (PS), is provided with novel explanations suggested for some important observations in the field, new proposals presented to explain reaction mechanisms more consistently and discrepancies and areas for further studies identified. Although PS is a very powerful oxidant, it often needs to be activated to produce more powerful oxidising radicals for rapid pollutant degradation. For the degradation of wastewater containing recalcitrant pollutants, iron was recognised as the most important PS activator due to its affordability, biocompatibility and activation effectiveness. However, reusable catalysts based on nanocarbon materials and transition metal (hydro) oxides may become more important in the future. Nevertheless, whenever waste heat is available, which is often generated abundantly from most industrial processes, heat activation provide the most effective and sustainable PS activation technique. Except in justified cases, unactivated PS was recommended for in-situ chemical oxidation of subsurface contaminations with an endorsement of base injection only for very acidic subsurface environments.

#### **5.1. Introduction**

Increasing industrialisation, urbanisation and commercialisation are resulting in the discharge of substantial amount of waste material into the environment. A significant proportion of these discharges are composed of synthetic materials with limited biodegradability while some, although biodegradable, are discharged in such a large quantity that the natural process of oxidation and recycling are overwhelmed. Practical consequences include compromised human health, disturbed ecological balance and unsustainable operating conditions. To secure human health, maintain ecological balance and improve sustainability, a number

\*Published in Chemical Engineering Journal - <https://doi.org/10.1016/j.cej.2018.01.034>

of technologies have been developed in recent decades to treat industrial and domestic wastes before discharge into the environment as well as to remediate contaminated sites. Some of the most important developments in this direction are advanced oxidation processes (AOPs), which typically involve the treatment of wastes and contaminants in the environment using highly reactive radical species. For many years, hydroxyl-radical-based processes such as Fenton and Fenton-like processes, UV-photolysis, ozonation, and heterogeneous photocatalysis were the principal AOPs for the treatment of wastes and contaminants [1-3].

However, within the last two decades, significant attention has been paid to sulphate radical AOPs typically generated from persulphate (peroxodisulphate) (PS), usually supplied as a sodium salt ( $\text{Na}_2\text{S}_2\text{O}_8$ ), or peroxymonosulphate (PMS), usually available as a triple salt of potassium ( $2\text{KHSO}_5 \cdot \text{KHSO}_4 \cdot \text{K}_2\text{SO}_4$ ) with the trade name of oxone [4]. Although PMS-AOPs constitute an important field of research with significant potential for practical applications, signified by the numerous research articles and reviews on the subject [5, 6], PS has been used almost exclusively in commercial applications as a precursor for the sulphate radical [4, 7]. Perhaps one reason for this is that PMS has two “dead” sulphate salts in its structure that cannot be activated. Other reason that have been given are that PS as sodium salt is very stable and soluble in water [4], properties that are desirable for many practical applications. Also of significant importance is the lower cost of PS compared to PMS [8].

Several excellent reviews of PS-AOPs alongside other processes have been recently published [1, 3-5, 9-13]. However, a number of key aspects and sometimes inconsistencies in the PS-AOPs literature have not been sufficiently highlighted or have been overlooked. It is the aim of the authors by this critical review to close the knowledge gap in an attempt to harmonise the science of the rapidly expanding field of PS-AOPs. Conceptual consistency is necessary in any field of knowledge if its theories are to be practicable. In addition, since the primary purpose of AOPs is to eliminate pollution and minimise negative environmental impacts of industrial and domestic activities, environmental sustainability must be the hallmark of every AOPs. Consequently, special attention will be paid to the environmental impacts of the processes reviewed.

## 5.2 A history of persulphate

The discovery of the persulphate ion ( $S_2O_8^{2-}$ ) and its realisation as an important precursor for the powerful sulphate oxidative radical ( $SO_4^{\bullet-}$ ) for AOP applications were overshadowed by hydrogen peroxide ( $H_2O_2$ ) and the associated hydroxyl radical ( $HO^{\bullet}$ ).  $H_2O_2$  has been known as a powerful oxidising agent for several decades before the first claim of the synthesis of persulphuric acid was made by Berthelot in 1878 [14]. The discovery was disputed on the ground that the observed oxidising properties of the new compound were due to  $H_2O_2$ . However, the detailed work by Hugh Marshall [14] established the new compound as persulphuric acid and its associated salt as persulphate i.e. a sulphur oxyanion with one more oxygen than a regular sulphate.

In some parallel sense,  $H_2O_2$  overshadowed PS as a powerful oxidant for AOPs. For many years, AOPs were defined as processes that generate  $HO^{\bullet}$  such as Fenton and Fenton-like processes, photolysis and heterogeneous catalysis for the treatment of wastewater and contaminated sites. Other similar processes such as ozonation (which is often combined with  $H_2O_2$ ) and permanganate oxidation processes were included in this definition [2, 13]. However, the recognition as AOPs has only been given in recent times to processes that generate  $SO_4^{\bullet-}$  [13]. Similarly, in-situ chemical oxidation (ISCO) processes for the remediation of contaminated subsurface sites were initially associated with  $H_2O_2$ , later ozone and permanganate processes were included. Persulphate was only the latest addition to the list [15]. In fact, in a 1939 review of analytical quantification of peroxygen compounds, PS was not recognised as having any commercial importance [16]. Moreover, even within the present decade, a review of AOPs may be found with no reference to the sulphate radical [17]. Nevertheless, as signified by exponentially increasing research publications, technical reviews and successful field applications, the place of PS in AOPs is firmly established.

### 5.3. Physicochemical properties of persulphate and standard reduction potentials

Some physicochemical properties of the sodium salt of PS, the more common form in which PS is used in AOPs, is presented in Table 1. Table 2 lists the standard reduction potentials ( $E^\circ$ ) of some half-cell reactions relevant to AOPs.

Table 5.1. Basic properties of sodium persulphate [18, 19].

<b>IUPAC Name</b>	Disodium sulfonatoxy sulphate
<b>Other names</b>	Sodium persulphate; sodium peroxodisulphate
<b>Molecular formula</b>	$\text{Na}_2\text{S}_2\text{O}_8$
<b>Structural formula</b>	
<b>Solubility (g/100g of H<sub>2</sub>O) at 25 °C [18]</b>	73
<b>Physical description</b>	White crystalline (monoclinic) solid
<b>Bulk density (g/cm<sup>3</sup>)</b>	1.12

Table 5.2 Standard reduction potentials ( $E^\circ$ ) relevant to AOPs

<b>Half reactions</b>	<b><math>E^\circ, \text{V}</math></b>	<b>Reference</b>
$\text{Cu}^{2+} + \text{e}^- \rightleftharpoons \text{Cu}^+$	+0.153	[20]
$\text{Fe}^{3+} + \text{e}^- \rightleftharpoons \text{Fe}^{2+}$	+0.771	[20]
$\text{FeO}^{2+} + \text{e}^- \rightleftharpoons \text{Fe}^{3+} + 1/2\text{O}_2$	+1.2	[21]
$\text{MnO}_4^- + 4\text{H}^+ + 3\text{e}^- \rightleftharpoons \text{MnO}_2 + 2\text{H}_2\text{O}$	+1.69	[21, 22]
$\text{H}_2\text{O}_2 + 2\text{H}^+ + 2\text{e}^- \rightleftharpoons 2\text{H}_2\text{O}$	+1.76	[21]
$\text{Co}^{3+} + \text{e}^- \rightleftharpoons \text{Co}^{2+}$	+1.82	[20]
$\text{Ag}^{2+} + \text{e}^- \rightleftharpoons \text{Ag}^+$	+1.98	[20]
$\text{S}_2\text{O}_8^{2-} + 2\text{e}^- \rightleftharpoons 2\text{SO}_4^{2-}$	+2.01	[23, 24]
$\text{O}_3 + 2\text{H}^+ + 2\text{e}^- \rightleftharpoons \text{O}_2 + \text{H}_2\text{O}$	+2.08	[21]
$\text{HO}^\bullet + \text{H}^+ + \text{e}^- \rightleftharpoons \text{H}_2\text{O}$	+(2.0 – 2.8)	[13]
$\text{SO}_4^{\bullet-} + \text{e}^- \rightleftharpoons \text{SO}_4^{2-}$	+(2.5 – 3.1)	[25]

#### 5.4. Commercial production of PS

Like the first production of PS by H. Marshall in the nineteenth century [14], today PS is produced commercially by the anodic oxidation of an acidic solution of sulphates at a high current density [24]. The basic chemical process is:



Low temperature electrolysis is required to limit thermal decomposition of the produced PS. Consequently, access to large amount of water for cooling and hydroelectricity is an important asset for sustainable and low-cost production of PS. Since PS is a powder under normal environmental conditions and has good shelf-life if stored properly [18], production could be centralised where ample water for cooling and hydroelectricity are available and distribution to end users could be made conveniently and affordably. In this way, the overall carbon footprint and energy consumption of PS production and distribution is relatively low. Compared to PS, the advantage for centralised production of H<sub>2</sub>O<sub>2</sub> is less favourable because H<sub>2</sub>O<sub>2</sub> is supplied as solution in water and its stability decreases as its concentration increases [26]. The prospect for centralised production is most unfavourable for O<sub>3</sub> as onsite production using local electricity is usually required [27]. Consequently, the environmental impact of O<sub>3</sub> production is directly dependent on local electricity supply and its energy consumption and carbon footprint may be significant.

#### 5.5. The O-O bond

The chemistry of PS like other peroxygens are characterised by the properties of the O-O bond. The O-O bond length in PS has been given as 1.497 Å; that in PMS as 1.460 Å and for H<sub>2</sub>O<sub>2</sub>, the length is 1.453 Å [3]. These figures show that as the -SO<sub>3</sub> group replaces hydrogen atom, the bond is lengthened. The O-O bond dissociation energy in solvated PS ion has been given as 140.2 kJ mol<sup>-1</sup> [28] while the corresponding dissociation energy for H<sub>2</sub>O<sub>2</sub> in aqueous solution has been given as 195.4 kJ mol<sup>-1</sup> [29] although this value has frequently been incorrectly reported as 232.6 kJ mol<sup>-1</sup>. The latter value is the O-O bond dissociation energy for H<sub>2</sub>O<sub>2</sub> in the gas phase [29]. However, no data is available for the O-O bond dissociation energy for PMS [3].

Although a correlation may be seen between the O-O bond length and bond dissociation energy for PS and H<sub>2</sub>O<sub>2</sub>, Uri [29] considered the 140.2 kJ mol<sup>-1</sup> dissociation energy for PS to be surprisingly low and asked if the result had not been influenced by impurities in the reacting media. Considering that such effects have been previously identified for other reactions, a ready example being the enhanced decomposition of H<sub>2</sub>O<sub>2</sub> due to impurities [30], there is good ground for the doubt.

However, the 140.2 kJ mol<sup>-1</sup> dissociation energy for PS have so far remained unchallenged. A number of reasons may be given for the relatively low dissociation energy of the O-O bond in PS compared to H<sub>2</sub>O<sub>2</sub>. Oxygen is a first period element with two unshared electron pairs on its valence shell. Repulsion between the lone pairs of electrons in the oxygen atoms in the O-O bond are known to lower the bond strength [24]. The partial positive charge on the hydrogen atoms attached singly to the oxygen atoms of the O-O bond in H<sub>2</sub>O<sub>2</sub> introduces a positive electrostatic field, which is expected to exert an attractive force on the lone pair electrons thereby stabilising the O-O bond. This stabilising effect is absent in PS, a situation that is further exacerbated by the formal negative charge on the ionised –SO<sub>3</sub><sup>-</sup> group. The repulsion between the lone pairs of electron in the –SO<sub>3</sub><sup>-</sup> also exert ‘steric pressure’ on the O-O bond, further weakening it. Steric interference has been advanced to explain the relatively low C-C bond in benzopinacol and other tetraarylethane [31]. The same explanation may be given for the low O-O bond energy in diacyl peroxides such as benzoyl and acetyl peroxide as well as isopropyl peroxydicarbonate, radical precursors that have been extensively studied [32]. The stabilising effect of the partially positively charged hydrogen atoms and the steric pressure of –SO<sub>3</sub><sup>-</sup> groups on the O-O bond is illustrated in Figure 5.1.

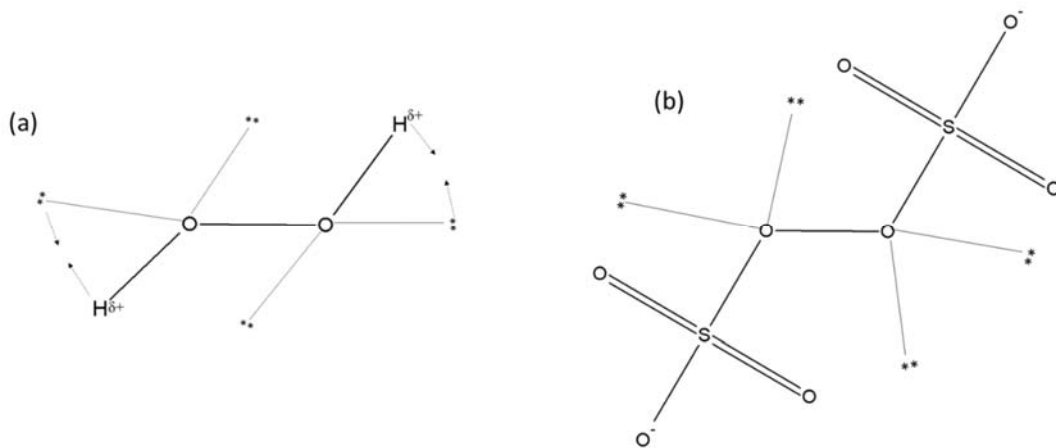
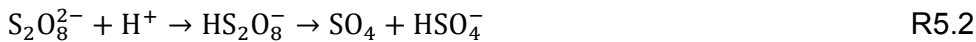


Figure 5.1. Schematic illustration of the association of the H atom and  $\text{--SO}_3^-$  group with the lone pair electrons on the O-O bond oxygen atoms.  $\text{H}_2\text{O}_2$  (a)  $\text{S}_2\text{O}_8^{2-}$  (b). Stabilising attractive forces shown by arrows while other bond interactions are repulsive.

The influence of the partially positively charged hydrogen atom attached to the oxygen of the O-O bond may be further appreciated by considering the following acid catalysed decomposition of PS [28]:



In strong acid, the reaction may proceed thus [23]:



House [23] explained that due to the influence of the incorporated hydrogen ion, the protonated PS anion ( $\text{HS}_2\text{O}_8^-$ ) decomposes unsymmetrically involving the break of the S-O bond rather than the O-O bond.

## 5.6. Persulphate advanced oxidation processes

The chemistry of PS is characterised by its oxidising properties with  $E^\circ$  second only to  $\text{O}_3$  for the commonly used oxidants in AOPs (Table 5.2). However, at room

temperature and in the absence of a catalyst, PS oxidative reactions are usually slow. The activation of PS, which involves the homolytic cleavage of the O-O bond, produces the highly oxidising  $\text{SO}_4^{\bullet-}$ . The energy for the cleavage may be derived from heat (thermolysis), UV irradiation (photolysis), ionising irradiation (radiolysis) or by chemical electron transfer (catalysis) [31]. For practical AOPs, activation of PS by radiolysis has been given the least attention. Significant amount of publications are available on catalytic, photolytic and thermal activation of PS.

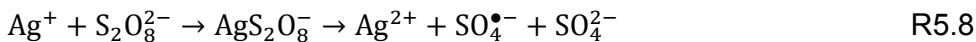
### 5.6.1. Catalysis

#### 5.6.1.1. Silver(I)

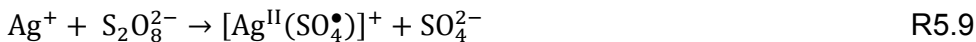
Before the advent of environmental PS-AOPs aimed at pollutant degradation, the catalytic role of Ag(I) in activating PS has been well established. D. A. House in his 1961 review [23], discussed a number of research reports that showed that Ag(I) activation of PS can result in the oxidation of a variety of inorganic and organic molecules/ions including  $\text{NH}_4^+$ ,  $\text{Mn}^{2+}$ , and acetone. Gallopo and Edwards in 1971 [33] published a study of the oxidation of ethanol by PS where the catalytic effects of several metal ions were evaluated including Cu(II), Fe(II), Mn(II), Cr(III), Co(III), Mg(II), Sn(II) and Ag(I) among others. Ag(I) alone at a concentration of 0.1 mM was reported to have significantly enhanced the rate of ethanol oxidation. In a 2004 publication, Anipsitakis and Dionysiou [34] evaluated the rate of oxidation of PS, PMS and  $\text{H}_2\text{O}_2$  by nine transition metal ions: Ag(I), Ce(III), Co(II), Fe(II), Fe(III), Mn(II), Ni(II), Ru(III), and V(III). From this study, they concluded that the most efficient catalyst for the activation of PS as measured by the rate of degradation of an organic probe molecule, 2,4-dichlorophenol, was Ag(I). However, the degradation rate for the Ag(I)/PS couple were lower than those reported for the Co(II)/PMS and Fe(II)/ $\text{H}_2\text{O}_2$  couples. From the foregoing, it seems Ag(I) activation of PS may find important application in AOPs. The activation of PS by Ag(I) may be expressed simply as [23, 34]:



Ag(I) association with PS has been proposed as a probable mechanism for the effective Ag(I) catalytic decomposition of PS as follows [23]:



From an alcohol scavenging study, Anipsitakis and Dionysiou [34], concluded that the principal oxidising species for the Ag(I)/PS couple was  $\text{SO}_4^{\bullet-}$ . However, they noted that the Ag(I)/PS couple behaved differently to tertiary butanol alcohol (TBA) and ethanol compared to the Co(II)/PMS couple whose major oxidising species was also said to be  $\text{SO}_4^{\bullet-}$ . For the Co(II)/PMS couple, the presence of TBA provided only 1% inhibition to the oxidation of the substrate while the addition of ethanol resulted in 84% inhibition. Since  $\text{SO}_4^{\bullet-}$  shows limited reaction with TBA ( $k = 4 \times 10^5 - 9.1 \times 10^5 \text{ M}^{-1} \text{ s}^{-1}$ ) compared to ethanol ( $k = 1.6 \times 10^7 - 7.7 \times 10^7 \text{ M}^{-1} \text{ s}^{-1}$ ) [34], the inhibition results for the Co(II)/PMS was expected if  $\text{SO}_4^{\bullet-}$  is the principal oxidising species. For the Ag(I)/PS system, however, 18% inhibition to oxidation was provided by TBA while 53% inhibition resulted from the addition of ethanol. The authors explained the unique behaviour of the Ag(I)/PS couple by suggesting the generation of a radical ion pair as follows:



The indication was that the ion pair was less inhibited by ethanol in the degradation of the target substrate compared to the freely diffusible  $\text{SO}_4^{\bullet-}$ . The concept of metal bound radical is well recognised and constitute a rapidly developing field of research with significant practical potentials for the tailoring of radical reactions along predefined pathway [35]. Hence, R9 is plausible.

In a subsequent study, with varying concentration of Ag(I) for Ag(I)/PS couples, Anipsitakis and Dionysious [36] showed that the degradation rate of 2,4-dichlorophenol increased with the concentration of Ag(I). However even at the highest Ag(I) concentration of 50 ppm, the Ag(I)/PS couple was shown to be less effective in the degradation of the target pollutant compared to Co(II)/PMS, Fe(II)/ $\text{H}_2\text{O}_2$  and Fe(III)/ $\text{H}_2\text{O}_2$  couples in which the metal ion concentrations was only 1 ppm. UV-activated PS was also shown to be more effective in the degradation and mineralisation of the probe molecule compared to Ag(I) activation. For example, in 4 h, ~80% mineralisation was reported for the UV/PS system while < 20% mineralisation was reported for Ag(I)/PS.

Further study of Ag(I) activation of PS for the degradation of a water pollutant, microcystin-LR, was reported by Antoniou et al. [37]. Their results also showed

that the Ag(I)/PS couple is ineffective for the oxidation of the target pollutant. In fact, under similar condition, the authors showed that practically no degradation of the pollutant was achieved by the Ag(I)/PS couple in 1 h while complete pollutant degradation was achieved by the Co/PMS system in < 10 min. They advanced an explanation for the limited oxidative power of the Ag(I)/PS couple on the basis of the high reaction rate between Ag(I) and the generated  $\text{SO}_4^{\bullet-}$  ( $k = 3.6 \times 10^9 \text{ M}^{-1} \text{ s}^{-1}$  [25]) as follows:



The authors suggested that higher Ag(I) concentration will be required for the Ag(I)/PS system to achieve measurable degradation of the pollutant in reasonable time [37]. This suggestion is consistent with the work of Anipsitakis and Dionysious [36] cited above where it was shown that increasing Ag(I) concentration resulted in increasing rate of pollutant degradation. However, if indeed Ag(I) is an effective scavenger for  $\text{SO}_4^{\bullet-}$  as expressed in R5.10 and R5.11, will higher Ag(I) concentration not result in greater scavenging and thereby less pollutant degradation? Since increasing Ag(I) concentration did improve pollutant degradation [36], it follows that the explanation proposed by Antoniou et al. [37] is not comprehensive enough. It may be pointed out that the rate constant for Fe(II) reaction with  $\text{SO}_4^{\bullet-}$ ,  $k = 1 \times 10^9$  [25], is of the same order as Ag(I) reaction with  $\text{SO}_4^{\bullet-}$  yet Fe(II) activation of PS is known to result in rapid and significant degradation of a variety of pollutants as will be discussed in Section 5.6.1.2.

At this point, it is well to recall that nothing so far has been said about the fate of the produced oxidised silver ions. Ag(II) and Ag(III) generated from the oxidation of Ag(I) by PS are powerful oxidants able to oxidise a variety of chemical species as follows [20, 23, 38]:



The  $E^\circ$  of the Ag(II)/Ag(I) couple has been said to be higher than the  $E^\circ$  for most organic redox couples [39]. Therefore, Ag(II) can oxidise alcohol, carboxylic acid and olefinic bonds [20]. It has also been demonstrated that Ag(II) can oxidise a

number of saturated alcohols through the cleavage of the C-C bond ( $k = 2 - 3 \times 10^3 \text{ s}^{-1}$ ) [40, 41] although initial complexation of the substrates to Ag(II) is probably a prerequisite for the reactions [41].

On the basis of the established significant oxidative capacity of Ag(II) generated from a Ag(I)/PS couple, the limited degradation of the aromatic pollutants in some of the reports reviewed [36, 37] is counterintuitive. Could it be Ag(II) was not significantly produced implying that Ag(I) reaction with PS was too low under the conditions of the AOPs? If it is supposed that much of the generated  $\text{SO}_4^{\bullet-}$  were scavenged by Ag(I) as suggested by Antoniou et al. [37], that would only produce more Ag(II). Could Ag(II), as a strongly oxidising ion, remain stable in a solution with unsaturated molecules or were these molecules uniquely resistant to Ag(II) oxidation under the specific reaction conditions? Kalb and Allen [38] showed that Ag(I)-activated PS degradation of oxalate can be significantly inhibited by oxygen. They illustrated this point by stating that in an oxygen environment, the half-life of PS during Ag(I)-catalysed PS oxidation of oxalate was 90 h at a temperature of 39.7 °C. Under comparable condition except that oxygen was excluded and the reaction temperature reduced to 25 °C, the half-life of PS was 1 h [38]. It should be noted that the oxidation of oxalate was positively correlated to temperature like most PS reactions. This potential significant inhibitory effect of oxygen has not been highlighted in the AOPs literature.

Xu et al. [42] described the oxidation of gaseous Hg(0) in an aqueous medium by PS with Ag(I) and Cu(II) serving as activators. The authors reported a more effective oxidation with Ag(I) compared to Cu(II). It was suggested that Ag(II) and Ag(III) derived from PS oxidation of Ag(I) may react with water to generate  $\text{HO}^{\bullet}$  as follows:



The generated  $\text{HO}^{\bullet}$  participated in the oxidation of Hg(0). However, the possibility of Ag(II) and Ag(III) directly oxidising Hg(0) was not advanced even with the significantly favourable electrochemical potential ( $\text{Hg(II)/Hg(0)} = 0.85 \text{ V}$  [42]) although the possibility of Cu(III) oxidation of Hg(0) was recognised. Cu(III) was proposed to be produced from PS oxidation of Cu(II).

A number of patents were filed in the 1990s that harnessed the oxidative properties of Ag(II). One such patent related the degradation of organic material in water in which Ag(II) was generated by the electrolysis of Ag(I) [43]. Another described the dissolution of radioactive waste in which the oxidative Ag(II) species was also generated by the electrolysis of Ag(I) [44]. Two other patents described the disinfection of water for use in swimming pool and industrial cooling [45, 46]. In both cases, stable compounds of Ag(II) were the source of the oxidative ion. In one of the two patents on disinfection, PMS was added to the system and its role described as a stabiliser for Ag(II) [46].

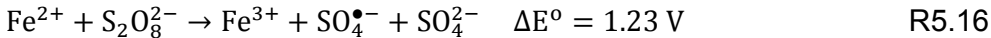
At this stage, one may ask: is Ag(I) indeed the best metal ion for the activation of PS for pollutant degradation under relevant AOP conditions? Is the efficiency of the activation and subsequent pollutant degradation limited by the nature of the pollutant or reaction conditions? Under what circumstance is Ag(I) a good activator and under what circumstance is it not? What is the value of Ag(II) and Ag(III) in practical AOPs? Is the Ag(I)/PS couple able to yield the Ag(II)/ $\text{SO}_4^{\bullet-}$  oxidative couple quantitatively under regular AOP conditions? Is Ag(II)/ $\text{SO}_4^{\bullet-}$  couple able to act synergistically as positive and negative oxidative radical ions? Is dissolved oxygen the problem of these systems? An effective Ag(II)/ $\text{SO}_4^{\bullet-}$  system, if developed, may potentially provide a sustainable treatment and safe disinfection of water for both potable use and other applications with limited energy demand and limited risk of production of disinfection by products (DBPs).

#### 5.6.1.2. Iron(II) and (III)

Although the original work by Anipsitakis and Dionysious consider Ag(I) the best activator for PS compared to other commonly available transition metals [34], there have been more published reports of AOPs using Fe(0)/Fe(II)/Fe(III) than Ag(I). Reasons for this trend may include the affordability of iron, its biocompatibility and its capacity for the rapid activation of PS [4, 47]. Iron in its various oxidation states and iron-based minerals have been used to activate PS, achieving rapid degradation of a range of pollutants such as trichloroethylene [47, 48], norfloxacin [49], 4-tert-butylphenol [50], polycyclic aromatic hydrocarbons [51], p-chloroaniline [52], dibutyl phthalate [53], propachlor [54], benzene [55] and

azo dyes [56-60]. Iron-activated PS has also be used for disinfection purposes [61] and for the dewatering of waste activated sludge [62, 63].

The use of Fe(II) has been shown to result in rapid activation of PS [47] as follows:



The  $\text{SO}_4^{\bullet-}$  generated may react with the target pollutant or with Fe(II) ( $k = 1 \times 10^9 \text{ M}^{-1} \text{ s}^{-1}$  [25]) as follows:



Consequently, for effective pollutant degradation, R5.17 must be minimised. One way that has been achieved was by gradually adding Fe(II) so that at any given instant, only a limited amount of Fe(II), with respect to the pollutant concentration, is available to react with  $\text{SO}_4^{\bullet-}$  [47]. A second technique is to start with a small amount of Fe(II) for PS activation while a reducing agent such as a thiosulphate ( $\text{S}_2\text{O}_3^{2-}$ ) is added to reduce Fe(III) and keep up the concentration of Fe(II) as follows [47]:



A third technique is similar to the second technique just described except that Fe(II) is regenerated by electrolysis [48, 64]. The current supplied can be adjusted to optimise the concentration of Fe(II) for effective pollutant degradation [48, 64]. This technique may be very effective and may be competitive where sustainably generated electricity is abundant and cheap. For ISCO applications, it was suggested that continuing electrolysis after pollutant degradation may be useful in adjusting the pH and oxidation-reduction potential of the aquifer to limit certain undesirable effects such as mobilisation of heavy metal ions [48].

Chelation of Fe(II) has been shown to be an effective technique to control the amount of Fe(II) available to react with PS or  $\text{SO}_4^{\bullet-}$  [65, 66]. An important consideration in the use of organic chelators to control the reaction of Fe(II) is the possible interference of the chelator with the pollutant degradation process and/or the chelator proving a secondary contaminant. Yan and Lo [66] compared the effectiveness of naphthalene removal using ethylene-diamine-tetra-acetic acid (EDTA) and [S,S]-ethylene-diamine-di-succinic acid (EDDS) chelated Fe(II)

activation of PS. They reported better pollutant removal by the EDTA-Fe(II) system compared to EDDS-Fe(II) on the ground that EDDS competed with the pollutant for PS oxidation. Unfortunately, EDTA is less biodegradable than EDDS and poses a risk of secondary contamination when used in pollution remediation [66]. In the report published by Liang et al. [65], it was concluded that citric-acid chelated Fe(II) provided the most effective activation of PS for pollutant removal when compared to sodium triphosphate (STPP), 1-hydroxyethane-1, 1-diphosphonic acid (HEDPA) or EDTA chelated Fe(II). It has also been shown that citric acid is more rapidly degraded in soil compared to EDTA [67] which implies that citric acid chelated Fe(II) is both relatively environmentally friendly and effective in activating PS for pollutant degradation.

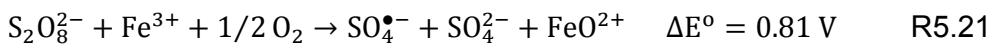
Under practical environmental conditions especially for surface water, dissolved oxygen can oxidise Fe(II) to Fe(III) according to the following reactions [29]:



Although the  $E^\circ$  for the Fe(III)/Fe(II) couple is positive, PS reaction with ionic iron is more often by oxidation than by reduction as is evident from the studies already reviewed. Consequently, R5.19 may result in the loss of oxidation capacity for a Fe(II)/PS couple. However, reaction of PS with Fe(III) is also recognised and is commonly expressed in the AOPs literature as [55, 68]:



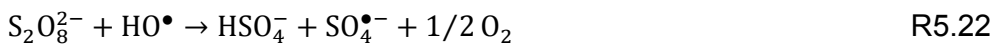
R20 appears problematic because of its unfavourable redox potential as it suggests Fe(III) oxidation of PS without any apparent catalytic influence. A more likely reaction considering the  $E^\circ$  in Table 5.2 may involve Fe(III) oxidation to higher valence iron as recently suggested by Ike et al. [69]:



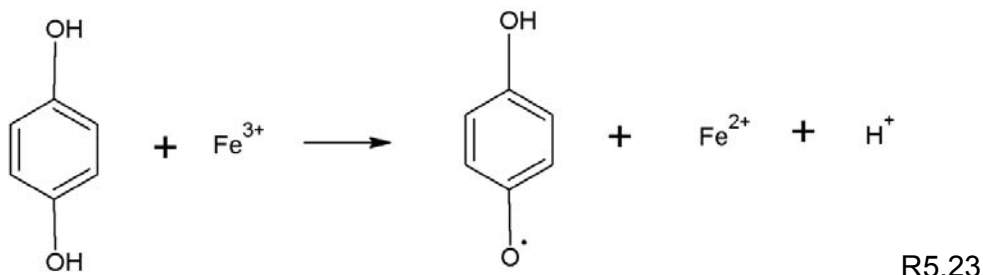
The Fe(IV) generated may also contribute towards pollutant oxidation [70, 71]. Fe(III) activation of PS as expressed in R5.21 may result in an efficient degradation process as scavenging of  $\text{SO}_4^{\bullet-}$  is limited compared to a process where the principal activator of PS is Fe(II) [72]. Furthermore, an additional oxidiser as Fe(IV) is probably introduced into the system. Although R5.21 can be considered slower than R5.16, the activation of PS by Fe(III) for pollutant

degradation is not necessarily a slow process. For example, Rodriguez et al. [56] showed that under identical conditions both Fe(II) and Fe(III) activation of PS could result in the complete removal of orange G within 30 min. However, the removal of the pollutant was slightly faster for the Fe(II) system compared to Fe(III).

The objection to R5.20 is even stronger when one considers that PS reaction with the strong oxidant HO<sup>•</sup> is expressed as producing SO<sub>4</sub><sup>•-</sup> rather than S<sub>2</sub>O<sub>8</sub><sup>•-</sup> as follows [23, 73]:



Apparently in an effort to avoid invoking R5.20, Rodriguez et al. [56] seems to suggest that the principal mode of production of SO<sub>4</sub><sup>•-</sup> from PS for any ionic iron system is always by R5.16 whether the initial iron species is Fe(II) or Fe(III). Consequently, when Fe(III) is employed to activate PS, according to these authors, it must first be reduced to Fe(II). The generated Fe(II) subsequently activates PS. Similar view was expressed by Oh et al. [5] for PMS activation by Fe(III). Fe(III) reduction may proceed according to the following reaction [56]:

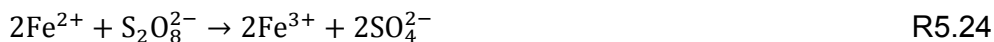


Since it has been independently verified that quinones can donate electrons directly to PS [74], the generation of Fe(II) through quinones reduction of Fe(III) as expressed in R23 seems very plausible. However, it does not exclude other contributory reactions such as R5.21. In fact, for the particular case that Rodriguez et al. [56] discussed – the oxidation of orange G – the quinone molecules were products of the degradation process implying that other than R5.23, some other form of PS activation, possibly R5.21, was active. Perhaps R5.20 is excluded for the reasons already given.

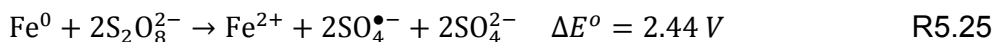
One major challenge with the Fe(III)/PS process is the low solubility of Fe(III) in the absence of organic or inorganic complexation [75]. Literature data indicates

that in aerated water with pH > 5, the concentration of Fe(III) in solution is ≤ 0.01 mg/L [76]. This is because of the strong tendency of Fe(III) to hydrolyse and form limited solubility hydroxide complexes [75]. Consequently, some form of stabilisation is required to keep Fe(III) in solution. The use of EDTA as a chelating and stabilising agent for Fe(III) to sustain PS activation has been reported [72]. It was shown that with EDTA complexation, Fe(III) can effectively activate PS to degrade trichloroethylene even at relatively high pH of 10. However, due to the limited biodegradability of EDTA, more environmentally friendly alternative chelating agent like citric acid is preferable.

The applicability of Fe(0) for the activation of PS has received significant research attention [53, 57, 59, 60, 77-81]. It has been shown that Fe(0) provide a more effective activation of PS compared to Fe(II) activation both in terms of pollutant degradation effectiveness and the applicable pH range [59, 77, 79, 81]. The reason advanced relates to the slow production of Fe(II) from Fe(0) either through acid, dissolved oxygen, PS or Fe(III) oxidation [59, 77, 82]. However, the contribution of heterogeneous chemistry to the efficiency of PS activation by Fe(0) has also been highlighted [53, 81]. The heterogeneous reaction argument rest on the limited surface area of Fe(0) compared to Fe(II). Since Fe(II) may be completely dissolved in water, it reacts readily and rapidly with PS in solution to completion as follows:



The availability of Fe(0) is limited by its surface area so that at the early stage of the reaction, PS is relatively in excess so that the principal reaction may be expressed as:

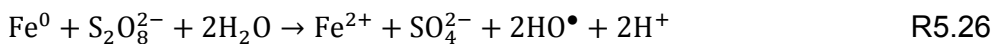


The produced Fe(II) being in short supply are likely to react according to R5.16 than R5.24. In this way, Fe(0) provide a more effective activation of PS compared to Fe(II).

The comparison of  $\Delta E^\circ$  for R5.25 and R5.16 shows that the electrochemical driving force for R5.25 is almost double the driving force for R5.16 indicating that the former is a thermodynamically more favourable reaction than the latter. The

liberated energy may be available to the associated radical as kinetic energy [83] which may probably enhance its oxidative capacity. Another obvious and by no means unimportant advantage of Fe(0) over Fe(II) is that the former is oxidised to Fe(III) by the donation of three electrons while only an electron is available to the latter for donation. Hence, Fe(0) has two more electrons to activate PS compared to Fe(II).

On the basis of electron paramagnetic resonance (ESR) analysis, Duan et al. [84] suggested the following reaction for the production of HO<sup>•</sup> from a Fe(0) system without the prior production of SO<sub>4</sub><sup>•-</sup>



One difficulty with R5.26 is the requirement of a high frequency of effective termolecular collisions compared to the bimolecular collisions required for R5.25. It may be argued that an initial association between Fe(0) and PS may imply an apparent bimolecular collision between the association and water. However, the very favourable  $\Delta E^\circ$  for R5.25 should precipitate a reaction when Fe(0) is associated with PS. Fe(0) is too reactive towards PS for R5.26 to occur rather than R5.25. R5.26 may hold for substrates less reactive towards PS. It seems more likely that SO<sub>4</sub><sup>•-</sup> is produced first (R5.25) and afterwards, HO<sup>•</sup> is generated from SO<sub>4</sub><sup>•-</sup> as is usually denoted [25, 28, 29]:



Despite the advantages enumerated for Fe(0) over Fe(II) and by extension over Fe(III), Rodriguez et al. [56] showed in their study of the oxidation of orange G by PS activated by Fe(0), Fe(II) and Fe(III) that Fe(0) activated PS was slowest in degrading the pollutant. The authors reported a particle size of 0.74 mm for their Fe(0) sample which amount to a surface area of  $1.03 \times 10^{-3} \text{ m}^2\text{g}^{-1}$  assuming a density of  $7.87 \text{ g cm}^{-3}$  for iron and using the following expression  $d = 6000/S \times \rho$  [85].  $d$  is the average particles diameter (nm),  $S$  the particles surface area ( $\text{m}^2 \text{ g}^{-1}$ ) and  $\rho$  particles' density ( $\text{g cm}^{-3}$ ). It can be seen that the very low surface area for the particles limits interaction with the solution which would explain the slow activation of PS. Li et al. [57] showed that the reactivity of Fe(0) with PS measured by the degradation of acid orange 7 increased with decreasing particle size. This result is expected since nanoparticles are typically more reactive than larger

particles due to their higher surface area and the greater proportion of surface atoms [86, 87]. Nonetheless, Fe(0) as nanoparticles may also suffer surface oxidation when exposed to air due to their greater reactivity. For example, Li et al. [57] reported that the analytical grade Fe(0) nanoparticles used in their study showed no measurable reaction with PS without acid washing - suggesting significant oxide passivation. However, Ike et al. [69] showed that if Fe(0) nanoparticles are stabilised with phosphonic acid chelators, even after significant surface oxidation following air exposure, no acid washing is required for the nanoparticles to effectively activate PS. Nevertheless, size optimisation may be the preferred route to achieve effective PS activation by Fe(0) especially where particle stabilisation with organic chelators is not considered cost effective and fast activation of PS is desired. Iron based bimetallic nanoparticles have been shown to provide better activation of PS for pollutant degradation compared to pure Fe(0) nanoparticles [88]. However, cost and environmental concern may limit the practical use of these nanoparticles to certain niche applications.

Iron oxides and oxohydroxides artificially synthesised or occurring naturally have also been used for the activation of PS. Table 5.3 summarises the application of iron oxides, oxohydroxides and hydroxides as well as a few other minerals and solids for the activation of PS aimed at pollutant degradation. There appear to be significant variation in the published data on heterogeneous activation of PS even for the same mineral. For example, Liu et al. [55] reported that only 10% of benzene (1 mM) was degraded in 768 h by 1 mM PS in the presence of ferrihydrite (BET = 180.1 m<sup>2</sup>/g). However, Wu et al. [50] showed that 60% of 4-tert-butylphenol (50 µm) was degraded in 5 h by PS (1 mM) activated by ferrihydrite (BET = 245 m<sup>2</sup>/g). Although there are clear differences in the BET values and pollutant concentrations in favour of the short time degradation reported by Wu et al. [50] compared to the work of Liu et al. [55], it seems those differences cannot completely account for the significant difference in relative degradation period. This argument, particularly for the concentration effect, rest on the notion that the rates of pollutants degradation by AOPs frequently follow the exponential decline of the pseudo-first order reaction kinetics. For a first order process, the half-life of the target pollutant is constant and independent of concentration [89].

Other inconsistencies between published reports regarding the degradation of pollutants due to mineral activation of PS can be identified in Table 5.3 such as the obvious difference in magnetite activation effectiveness as reported by Yan et al. [90] compared to Li et al. [80]. It is uncertain if these differences are due to experimental conditions, pollutant specific resistance to degradation and/or the uniqueness of a given mineral sample. The report by Liu et al. [55] showed that not only was the pollutant slowly degraded, PS decomposition was similarly slow. This observation indicates that potential differences in pollutant resistance to degradation may not provide a satisfactory explanation for the discrepancies in Table 5.3. If the local features of a sample rather than its basic chemical makeup influence activation effectiveness more, further research is required to identify these influential features before these minerals and solids can find practical use.

The rapid degradation of 4-tert-butylphenol achieved using ferrihydrite and akaganeite in relatively short time as reported by Wu et al. [50] is worth highlighting. The authors attributed the effective activation of PS by akaganeite to the high isoelectric point/point-of-zero charge (PZC) of akaganeite (9.6–10) which ensures good interaction with the negatively charged PS anion. Also important is the unique surface complexation capacity of the mineral following Marsac et al. [91]. This explanation, however, may not serve for ferrihydrite with a lower PZC (8.2) compared to goethite (9.1) [50]. It seems the surface area of the minerals has some role to play in deciding the effectiveness of pollutant degradation. However, a comparison of surface area normalised rate constant between akaganeite and ferrihydrite showed this was not the case [50]. Another unique feature of akaganeite activation of PS for 4-tert-butylphenol degradation was that the degradation rate did not decrease with increasing pH (up to 7.8). This result, among other things, may be taken as an evidence that dissolved Fe(III) played a minimal role in the activation. No data on the reusability of the minerals were presented. A reusable catalytic activator with negligible leaching of metal is attractive for the development of sustainable and environmentally friendly AOPs.

Table 5.3. Pollutant degradation by PS activated by minerals and solids

Mineral	Surface area (m <sup>2</sup> /g)	Concen-tration (g/L)	Pollutant	Oxidant	Duration (h)	pH	Degrad-a-tion (%)	Refer-ence
Natural soil	-	170	Diesel (4.2 ml in 700 mg of solid)	PS:Fe(II) = 100:1 (molar ratio)	12	3	40	[89]
Sand	"	"					20	
Magnetite (5%) + sand	"	"					30	
Hematite (5%) + sand	"	"					20	
Goethite (5%) + sand	"	"					25	
MnO <sub>2</sub> (5%) + sand	233	100	Nitrobenzene (1 mM)	PS (500 mM)	168	6 - 3	35	[90]
Ferrhydrite	37	400			168		40	
Goethite	28	400			168		40	
Hematite	44	200			144		100	
Bimessite	-	-			108		30	
Montmorillonite	-	-			108		40	
Kaolinite	-	500			168		50	
Soil	-	-			168		40	
PS alone	-	-			144		40	
Ferrhydrite	233	100	Nitrobenzene (1 mM)	PS (500 mM)	72	13 - 12	20	[90]
Goethite	37	400			72		60	
Hematite	28	400			72		40	
Bimessite	44	200			72		90	
Montmorillonite	-	-			108		90	
Kaolinite	-	-			108		80	
Soil	-	500			168		80	
PS alone	-	-			72		60	

Table 5.3. Pollutant degradation by PS activated by minerals and solids cont'd

Mineral	Surface area ( $\text{m}^2/\text{g}$ )	Pollutant concentration (g/L)	Oxidant	Duration (h)	pH	Degradation (%)	Reference
Ferrihydrate	233	100	Hexachloroethane (2 $\mu\text{M}$ )	48	6 – 3	20	[90]
Goethite	37	400	"	48	"	80	
Hematite	28	400	"	48	"	20	
Birnessite	44	200	"	48	"	10	
Montmorillonite	-	-	"	48	"	5	
Kaolinite	-	-	"	48	"	20	
Soil	-	500	"	48	"	40	
PS alone	-	-	Hexachloroethane (2 $\mu\text{M}$ )	48	"	10	
Ferrihydrate	233	100	PS (500 mM)	48	13 – 12	25	[90]
Goethite	37	400	"	48	"	95	
Hematite	28	400	"	48	"	25	
Birnessite	44	200	"	48	"	20	
Montmorillonite	-	-	"	48	"	20	
Kaolinite	-	-	"	48	"	20	
Soil	-	500	"	5	"	100	
PS alone	-	-	"	48	"	20	
Anatase	11.7	400	Anisole (1 mM)	24	4 – 5	49	[91]
Bauxite	28.8	"	"	"	"	52	
Calcite	38.0	"	"	"	"	40	
Cobaltite	2.21	"	"	"	"	40	
Cuprite	49.5	"	"	"	"	57	
Hematite	28.2	"	"	"	"	67	
Ilmenite	1.70	"	"	"	"	43	
Pyrolusite	1.39	"	"	"	"	49	
Pyrite	2.12	"	"	"	"	100	

Table 5.3. Pollutant degradation by PS activated by minerals and solids cont'd

Mineral	Surface area ( $\text{m}^2/\text{g}$ )	Concen-tration (g/L)	Pollutant	Oxidant	Duration (h)	pH	Degrad-ation (%)	Refer-ence
Malachite	3.65	400	Anisole (1 mM)	PS (500 mM)	24	4 – 5	83	[91]
Magnesite	38.0	"	"	"	"	"	51	
Siderite	6.80	"	"	"	"	"	51	
Willemite	1.80	"	"	"	"	"	44	
PS alone	-	-	"	"	"	"	45	
Anatase	11.7	400	Nitrobenzene (1 mM)	PS (500 mM)	24	4 – 5	37	[91]
Bauxite	28.8	"	"	"	"	"	30	
Calcite	38.0	"	"	"	"	"	26	
Cobaltite	2.21	"	"	"	"	"	44	
Cuprite	49.5	"	"	"	"	"	36	
Hematite	28.2	"	"	"	"	"	48	
Ilmenite	1.70	"	"	"	"	"	48	
Pyrolusite	1.39	"	"	"	"	"	23	
Pyrite	2.12	"	"	"	"	"	100	
Malachite	3.65	"	"	"	"	"	43	
Magnesite	38.0	"	"	"	"	"	63	
Siderite	6.80	"	"	"	"	"	35	
Willemite	1.80	"	"	"	"	"	51	
PS alone	-	-	"	"	"	"	37	
Anatase	11.7	400	Hexachloro-ethane (1 mM)	PS (500 mM)	24	4 – 5	22	[91]
Bauxite	28.8	"	"	"	"	"	24	
Calcite	38.0	"	"	"	"	"	19	
Cobaltite	2.21	"	"	"	"	"	29	
Cuprite	49.5	"	"	"	"	"	22	

Table 5.3. Pollutant degradation by PS activated by minerals and solids cont'd

Mineral	Surface area ( $\text{m}^2/\text{g}$ )	Concen-tration (g/L)	Pollutant	Oxidant	Duration (h)	pH	Degrad-ation (%)	Refer-ence
Hematite	28.2	400	Hexachloro-ethane (1 mM)	PS (500 mM)	24	4 – 5	21	[91]
Ilmenite	1.70	"	"	"	"	"	24	
Pyrolusite	1.39	"	"	"	"	"	25	
Pyrite	2.12	"	"	"	"	"	24	
Malachite	3.65	"	"	"	"	"	20	
Magnesite	38.0	"	"	"	"	"	26	
Siderite	6.80	"	"	"	"	"	20	
Willemite	1.80	"	"	"	"	"	19	
PS alone	-	-	"	"	"	"	18	
Magnetite	78	0.56	Sulfamono-methoxine (0.06 mM)	PS (1.20 mM)	0.25	6.4	100	[87]
Magnetite	-	-	Fluorenone (0.4 g/L spiked on quartz)	1:1 (PS:Fe <sub>3</sub> O <sub>4</sub> )	48	7 <sup>a</sup>	90	[50]
Magnetite rich soil	-	-	Hydrocarbon (0.4 g/L spiked on sand)	1:1 (PS:Fe)	168	7 <sup>a</sup>	80	[92]
Hematite	16	1	4-tert-butylphenol (50 µm)	PS (1 mM)	6	4.7	15	[49]
Goethite	49	1	"	"	"	"	15	
Lepidocrocite	59	1	"	"	"	"	10	
Ferrhydrite	245	1	"	"	"	"	60	
Akaganeite	239	1	"	"	"	"	90	

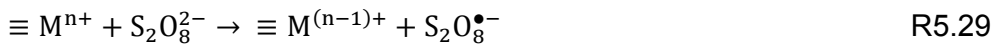
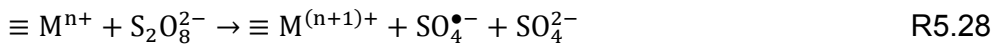
Table 5.3. Pollutant degradation by PS activated by minerals and solids cont'd

Mineral	Surface area (m <sup>2</sup> /g)	Pollutant concentration (gL) (Fe = 1.2 mM)	Oxidant	Duration (h)	pH	Degradation (%)	Reference
Ferrous hydroxide colloid		Sulfamono-methoxine	PS (1.2 mM)	0.25	6	100	[93]
Ferrihydrite	180.1	50	Benzene (1 mM)	768	8	10	[54]
Goethite	37.1	50	"	768	"	25	
Pyrolusite	0.11	50	"	768	"	15	
Silica	27.0	50	"	-	"	"	<sup>b</sup>
Nontronite	69.0	50	"	768	"	20	
Montmorillonite	32.0	50	"	768	"	25	
Aquifer solid - AFTCS	-	50	"	720	"	25	
Aquifer solid - CADOU	-	50	"	720	"	40	
Aquifer solid - AWBPH	-	50	"	720	"	45	
Aquifer solid - CAROL	-	50	"	720	"	40	
Ferruginous oxisol	-	-	Gasoline/ethanol (10% v/v) + ground water	600	4 - 2	40 (DOC)	[67]
Magnetite	50-70	1	2,4-dichlorophenol (0.18 mM)	PS (12.5 mM)	3	3	[78]
CuO	-	0.5	p-chloroaniline (0.5 mM)	PS (2.5 mM)	5	7	[94]
CuO	0.96	0.2	2,4-dichlorophenol (5 µM)	PS (0.04 mM)	0.7	5.8	100 [8]

<sup>a</sup> pH described as circumneutral. <sup>b</sup> No data shown but described as the only mineral that did not degrade benzene.

The rapid degradation of Sulfamonomethoxine within 0.25 h by PS activated by magnetite [90] and ferrous hydroxide colloids [96] is evidently unique in Table 5.3. Yan et al. [90, 96] argued that their activation of PS was entirely heterogeneous and their methods represent unique AOPs for the degradation of pollutants whose effectiveness is little affected by pH variation. Typically, in these studies,  $\geq 80\%$  of the degradation observed for the 15 min experiment occurred within the first 3 min. Thereafter, the rate of pollutant removal is significantly diminished. This trend suggests the reaction reaches a near completion within a very short time either due to the exhaustion of Fe(II) species or PS. Soluble Fe(II) produced similar pollutant degradation pattern but with limited removal effectiveness [77, 90, 96]. It seems the synthesised magnetite [90] and ferrous hydroxide [96] are effectively aggregations of Fe(II) similar to organic molecule complexed Fe(II) such that the reaction with PS is “controlled” to limit scavenging of generated reactive radicals.

The mechanism of PS catalytic activation on minerals surface ( $\equiv M^{n+}$ ) has been generalised as [55]:



However, the objections raised concerning R5.20 still holds against R5.29. Even when R5.28 involves oxidation to high valency, it probably remains the correct expression of the reaction mechanism.

From the sheer volume of the publication and the interest shown in the application of iron based catalyst for the activation of PS both for laboratory studies and field applications, there is no doubt that iron based activators hold an important place in PS-AOPs. Affordability and biocompatibility as well as effective and controllable activation are some of the important features of iron-based activators. Challenges in the use of iron-based catalyst include scavenging of radical (especially for Fe(II)); oxidation by dissolved oxygen (also particular to Fe(II)); limited solubility under neutral and alkaline conditions, sludge formation tendency and limited activating capacity of many iron based minerals towards PS. Although significant advances have been made towards resolving some of

these problems using method such as organic molecule chelation, stepwise addition and electrolytic regeneration of Fe(II), the additional cost, increased organic load or limited success means that more research is needed to improve environmental sustainability. Large surface area heterogeneous and reusable catalysts based on Fe(III) are particularly promising. Appreciably fast pollutant degradation by PS activated by Fe(III) in solution has already been demonstrated [56]. Mobilising these cations on a suitable large surface area substrate or as oxides or hydroxides such as akaganeite [50] might provide for reusable effective PS activation with the benefit of limited Fe(II) radical scavenging. To further the transfer of zerovalent iron-based activation methods to full-scale applications, commercially available samples of iron should be evaluated in addition to the use of analytical grade samples. In this regard, it is of interest to explore the performance of low cost and commercially available Fe(0) such as steelwool and iron powder. Contrary to the opinion of Oh et al. [5], iron activation of PS for pollutant degradation may be rightly regarded as catalytic as iron in its various oxidation states may participate in the processes although some oxidations states are slower or less available than others are. For example, oxidation of Fe(0) to Fe(III) does not end the activation capacity as Fe(III) can also activate PS at an appreciably high rate as have been mentioned in an earlier portion of this section. Possible iron/PS reaction pathways are shown in Figure 5.2.

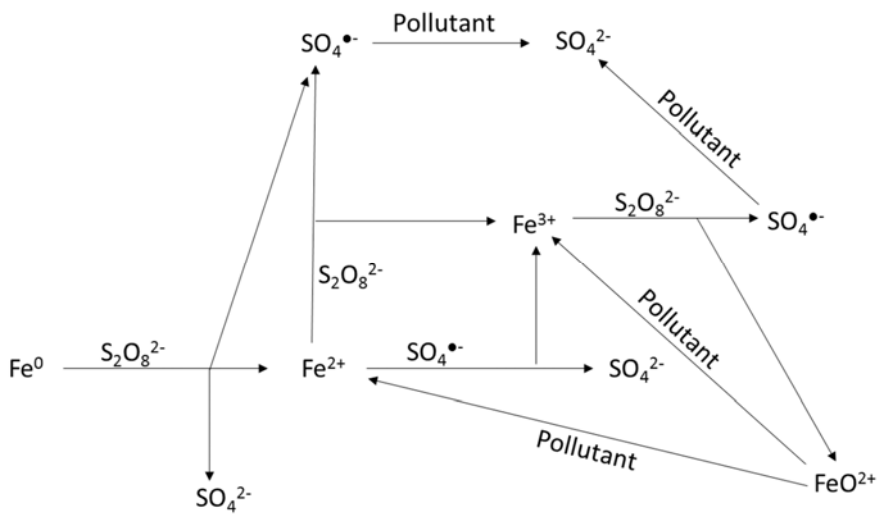
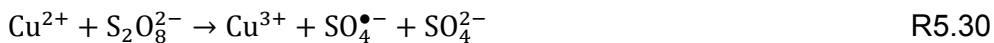


Figure 5.2. Possible iron/PS reaction pathways for pollutant degradation

### 5.6.1.3. Other metal catalysts

Compared to iron, much less research attention has been paid to the application of other transition metals for the activation of PS for pollutant oxidation. Liang et al. [97] reported the use of CuO in activating PS for the degradation of p-chloroaniline. A neutral pH was said to be most conducive for the pollutant degradation through the heterogeneous activation of PS. Although the activation was described as involving PS abstraction of an electron from CuO, Cu(II) in solution was shown to provide poorer degradation of the target pollutant. The authors suggested the generation and participation of Cu(III) in the oxidation process although no evidence was provided to substantiate the claim.

The application of Cu(II) in activating PS for the oxidation of Hg(0) as published by Xu et al. [42] has already been mentioned in Section 5.6.1.1. Xu et al. [42] also suggested the direct participation of Cu(III) in the oxidation of the target pollutant. The proposed generation of Cu(III) from Cu(II) reaction with PS was expressed as [42]:



However, Gallopo and Edwards [33] provided evidence to show that Cu(III) was not generated from Cu(II) reaction with PS. They suggested that Cu(II) interaction with PS is preceded by its reduction to Cu(I) upon reaction with a radical as follows:



$\text{R}^\bullet$  was generated from an organic substrate reaction with  $\text{SO}_4^{\bullet-}$ . The sulphate radical was produced from the spontaneous homolytic decomposition of PS. It is uncertain if the organic substrate influenced the mode of Cu(II) reaction.

Zhang et al. [8] reported a unique activation of PS by CuO which does not involve the oxidation of copper or the production of any radical. The proposed mechanism is first a loose electrostatic association of CuO to PS, which effectively “activates” PS without radical generation. Second, contact between this association and a pollutant molecule induces electron transfer from pollutant to PS resulting in

pollutant oxidation. Although copper leaching was reported at acidic conditions, the authors indicated that at neutral conditions where the activity of the CuO catalyst is optimal, copper leaching is limited. The authors held that the proposed non-radical reaction mechanism implies that the formation of halogenated intermediates from halogen ions in natural water is eliminated. The CuO/PS couple was reported to be effective in the degradation of trichloroethylene, phenol and chlorophenols but not p-chlorobenzoic acid and iopromide. It will be interesting to see the range of pollutants that may be effectively degraded using this unique AOP. However, it is uncertain what are the essential difference between Zhang et al. [8] “unique” CuO and Liang et al. [97] “regular” CuO. (See Table 3 for some parametric comparison).

Manganese compound as MnO<sub>2</sub> [92] and birnessite [93] have been shown to provide better activation of PS for the degradation of diesel and nitrobenzene, respectively, compared to commonly occurring iron oxides and hydroxides. Jo et al. [98] showed that an iron oxide/manganese oxide composite material was on the average more effective than the pure manganese oxide in activating PS for the degradation of carbon tetrachloride and benzene tested over acidic, neutral and basic conditions. The optimum pH for the activation of PS by the composite material was pH 9 with a rate constant much greater than PS alone and PS activated by pure manganese oxide.

Clays such as montmorillonite and kaolinite are less effective in activating PS for pollutant degradation compared to common iron-based minerals as shown in Table 5.3. Silica is apparently also a poor activator of PS [55]. The limited activation by clays and silica may explain the limited ability of the inorganic fraction of soil to activate PS [93]. Ahmad et al. [93] showed that the effectiveness of PS activation by the inorganic fraction of soil may remain low even when minerals with appreciable activation capacity are present due to their limited concentration.

Compared to iron that is affordable and biocompatible, manganese, copper and other transition metals have been much less studied for application in practical AOPs. However, the unique performance of the CuO catalyst as reported by Zhang et al. [8] may increase interest in the non-iron transition metals. For these

transition metal catalysts to compete favourably with iron, they must be reusable and show limited leaching of ion into the treated water.

#### 5.6.1.4. Carbon catalyst

Carbon may exist in one of many allotropic forms such as diamond, graphite or amorphous carbon. Carbon nanotubes have been described as rolled up graphite sheet(s) [99]. The properties of a particular allotrope of carbon may differ diametrically from another. For example, diamond is a good insulator while graphite is a good conductor. Carbon material show particularly good capacity to activate PS for the degradation of pollutants. An interesting suite of nanocarbon catalysts has been shown in recent times to be effective in the activation of PS for the degradation of pollutants in water [100, 101].

Duan et al. [84] studied the activation of PS by different allotropes and forms of carbon, namely, single walled carbon nanotubes, reduced graphene oxide, mesoporous carbon, fullerene, nanodiamonds, graphitic carbon nitride and activated carbon. They reported that the first three carbon materials showed good heterogeneous catalytic effect in activating PS for the degradation of phenol compared to the other carbon materials. The authors associated the capacity of a carbon material to activate PS to the presence of delocalised  $\pi$  electrons, structural defects, carbonyl functional groups and large surface area to promote mass transfer and greater exposure of active sites. Data presented also showed that the best performing carbon material, reduced graphene oxide, significantly outperformed  $\text{Fe}_3\text{O}_4$ ,  $\text{CuO}$ ,  $\text{Co}_3\text{O}_4$ ,  $\text{MnO}_2$  and vied with  $\text{Fe}(0)$  in fast activation of PS to degrade phenol. But since the carbon materials were shown to be reusable and regenerable through heat treatment, they may be considered more sustainable activators than  $\text{Fe}(0)$ . The authors also reported that UV and heat (70 °C) activation of PS (6.5 mM) under the same condition as the carbon catalyst resulted in < 30% phenol (0.2 mM) degradation in 2 h whereas reduced graphene oxide resulted in 100% phenol degradation in < 0.5 h. It is uncertain how UV and heat activation would be that poor.

Sun et al. [102] reported the use of carbon nanotubes with or without N-doping (0.2 g/L) for the activation of PS (6.2 mM) aimed at phenol (0.2 mM) degradation. The authors reported complete degradation of phenol under a temperature of 25

°C in 1.5 h and 2 h for the pristine and N-doped CNT, respectively. The authors concluded that CNT activation of PS resulting in radical generation is due primarily to the delocalised electrons and carbonyl functional groups on the CNTs with no contribution from the nitrogen functional group. They showed, however, that nitrogen functional group enhanced the activation of PMS.

Lee et al. [103] reported on the application of unmodified single and multi-walled CNTs for the degradation of a number of phenolic and pharmaceutical compounds. The CNTs were shown to significantly outperform samples of activated carbon and graphite in activating PS to degrade phenol. Citing evidences from radical scavenging test, ESR analysis and linear sweep voltammetry, the authors argued that the degradation of the organic compounds proceeded via a non-radical mechanism. They proposed a complex between PS and the CNT that subsequently degraded organic molecules to a degree determined by the affinity of the molecule toward the CNT surface without the prior production of a radical.

Carbon catalysts are potentially sustainable activators of PS for the practical degradation of environmental contaminants. More studies are however needed to fully evaluate the functionality and possible selectivity of these catalysts considering that unique reaction mechanisms have been proposed to explain their interaction with PS and the degradation of pollutants. Data on mineralisation are also needed to more fully compare the performance of the nanocarbon catalysts to other activators. Uncertainties about the fate of nanocarbon materials in the environment as well as the proven toxicity of some of these materials [99, 104] require that suitable control measures be developed such as loading in secured packed column for practical application in contaminant degradation.

Activated carbon (AC) has also been used to activate PS for the degradation of perfluorooctanoic acid [105], acid orange 7 [106], orange G and diethyl phthalate [107] and trichloroethylene [108]. Lee et al. [105] showed that for a PS/pollutant ratio of 500/1, optimum pH of 2.5, AC of 10 g/L and temperature of 25 °C, the degradation and mineralisation of perfluorooctanoic acid was about 80% and 70%, respectively, for a 12 h test. The almost equal degradation and mineralisation values indicate that the decomposition of the fluorinated acid was

the rate-determining step in the degradation. For a PS/pollutant ratio of 100/1, Yang et al.[106] reported about 80% degradation of acid orange 7 and 50% mineralisation in 5 h using AC of 1 g/L, pH of 5.1 and temperature of 25 °C. The author indicated that adsorption of the pollutant on the catalyst decreased the activation effectiveness.

Adsorption leading to limited pollutant degradation was also reported by Pu et al. [107] for Fe/S doped AC. Diethyl phthalate significantly adsorbed on the catalyst while orange G did not. For PS/pollutant ratio of 1/1, 1 g/L of Fe/S doped AC, temperature of 25 °C and reaction time of 3 h, 100% orange G degradation was recorded compared to 30% adsorption in the absence of PS, while for diethyl phthalate, degradation was 80% and adsorption 90%. The results indicate that the adsorptive capacity of the AC declined with PS activation. Similar loss in AC adsorptive capacity due to PS oxidation was reported by Liang et al. [108] which was shown to amount to poorer pollutant removal by combined PS/AC treatment compared to AC treatment alone. However, the author remarked that even with the limited PS/AC removal of pollutant, the PS/AC treatment provide pollutant degradation while for AC alone, pollutants are only adsorbed.

Fang et al. [109] reported on the degradation of a polychlorinated biphenyl by biochar produced from the pyrolysis of biomass. For 8 mM PS, 70 – 100% pollutant degradation was achieved in 4 h by the biochar/PS system. The authors showed that the persistent free radicals in biochar responsible for PS activation may be manipulated by the introduction of metal ions and phenolic compounds.

Although the structural nanocarbon in association with PS provide an interesting pollutant degradation capacity with significant potential for practical application, amorphous carbon material especially when produced from biomass remain attractive for the development of low-cost and sustainable schemes for the degradation of environmental contaminants.

#### 5.6.1.5. Organic substrates as catalyst

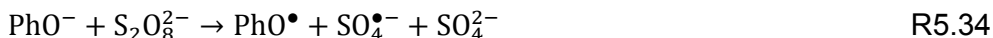
It has been shown that a number of organic molecules and substrates may decompose PS and generate  $\text{SO}_4^{\bullet-}$ . Fang et al. [74] demonstrated that quinone molecules and quinone moieties on natural organic matter can donate electron to PS in the course of self-redox cycles that generate semiquinone, the electron

transfer agent. The interaction between quinone (Q) and hydroquinone ( $\text{H}_2\text{Q}$ ) reversibly producing semiquinone ( $\text{SQ}\bullet^-$ ) has been expressed as [74]:



The author showed that 2,4,4'-trichlorobiphenyl may be degraded by  $\text{SO}_4\bullet^-$  produced from quinone interaction with PS at a pH of 7.4.

Ahmad et al. [110] showed that ionised phenol and its derivatives could activate PS to degrade nitrobenzene by electron transfer:

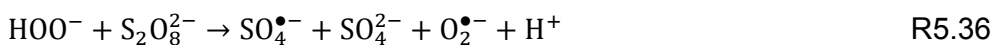
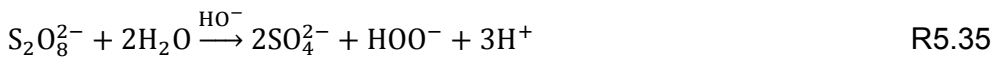


Since only phenoxides activate PS quantitatively, the reaction is pH dependent in relation to the  $\text{pK}_a$  of the phenol compound available and would proceed principally at high pH under conditions relevant to AOPs [110]. Ocampo [111] reached the same conclusion as to the requirement of ionisation provided by high pH for effective activation of PS by phenol. Experiments conducted at alkaline pH designed to evaluate the effectiveness of common organic functional groups to activate PS for the degradation of nitrobenzene and hexachloroethane showed that ketone, primary alcohol and low carbon chain aldehydes were relatively good activators. PS activation by carboxylic acids were insignificant although the acids were completely ionised. From this it may be surmised that carboxylate ion were stable to PS oxidation. However, when other functional groups such as ketone and alcohol were combined with the carboxylic acid group to give keto acid and alcohol acid, respectively, the rate of PS activation were enhanced compared to ketone or alcohol alone.

Several studies have shown that soil and aquifer solid samples activate PS more readily than most naturally existing minerals as may be seen in Table 5.3. The activating effect of organic molecules and moieties associated with soil organic matter has been identified as the reason for the greater PS activation rate achieved by soil compared to most commonly existing inorganic minerals [110]. However, soil organic matter may compete with target pollutant for degradation by PS thereby reducing the efficiency of AOPs [112, 113].

### 5.6.1.6. Alkaline activation

PS is also known to be activated by alkaline solutions which has been the basis of a number of ISCO applications [10]. A proposed reaction pathway for alkaline activation of PS has been simplified as [114]:



R36 suggests that  $\text{O}_2^{\bullet-}$  is produced at the same rate as  $\text{SO}_4^{\bullet-}$ . Under alkaline conditions,  $\text{SO}_4^{\bullet-}$  reacts with  $\text{HO}^-$  at a significantly high rate ( $k = 4.6 - 8.3 \times 10^7 \text{ M}^{-1} \text{ s}^{-1}$ ) as follows [25]:



Consequently, if R5.36 and R5.37 hold, the amount of  $\text{O}_2^{\bullet-}$  may equal the sum of  $\text{HO}^{\bullet}$  and  $\text{SO}_4^{\bullet-}$ . However, Furman et al. [115] reported that under alkaline condition of pH 12,  $\text{HO}^{\bullet}$  and  $\text{SO}_4^{\bullet-}$  were significantly generated while only minimal amount of reductant [ $\text{O}_2^{\bullet-}$ ] was produced. They reach this conclusion based on the observed substantial degradation of anisole and nitrobenzene but limited degradation of hexachloroethane.  $\text{HO}^{\bullet}$  was found to be dominant with respect to  $\text{SO}_4^{\bullet-}$ , which is consistent with R5.37. The authors showed that the degradation of hexachloroethane, which is associated with the production  $\text{O}_2^{\bullet-}$ , only became significant at base/PS ratio  $> 3:1$ . These results do not corroborate R5.35 and R5.36 at base/PS ratio  $< 3:1$ .

Molecular oxygen may be generated from superoxide reaction with sulphate or hydroxyl radicals as follows [114]:

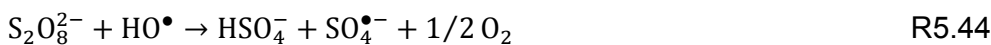
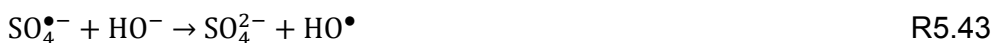


Even granted that  $\text{O}_2^{\bullet-}$  generated by R5.36 were lost as  $\text{O}_2$ , the difficulty with harmonising R5.35 and R5.36 with the results of Furman et al. [115] is not thereby removed as the significant presence of  $\text{HO}^{\bullet}$  and  $\text{SO}_4^{\bullet-}$  are still unaccounted for. The alternative reaction pathway for alkaline-catalysed decomposition of PS as

formulated by Chandra Singh and Venkataraao [116] (R5.40 and R5.41) does not resolve the problem either as they suggest non-radical degradation products.



The following sequence of reactions are therefore proposed as probable mechanism for alkaline decomposition of PS resulting in the production of oxidative radicals:



The removal of  $\text{SO}_4^{\bullet-}$  by R5.43 favours the forward reaction in R5.42, which together with R5.44 enhances the decomposition of PS while the high rate constant of R5.43 ensures the predominance of  $\text{HO}^\bullet$ . At much higher concentration of  $\text{HO}^-$ , R5.35 and R5.36 may become important leading to the production of  $\text{O}_2^{\bullet-}$ . At lower  $\text{HO}^-$ , the production of radicals are limited to R5.42, the spontaneous homolytic dissociation of PS. This formulation completely explains the results of Furman et al. [115] and is consistent with the established chemistry of PS [28, 116, 117]. A simplified representation of PS decomposition as a function of pH is given in Figure 5.3

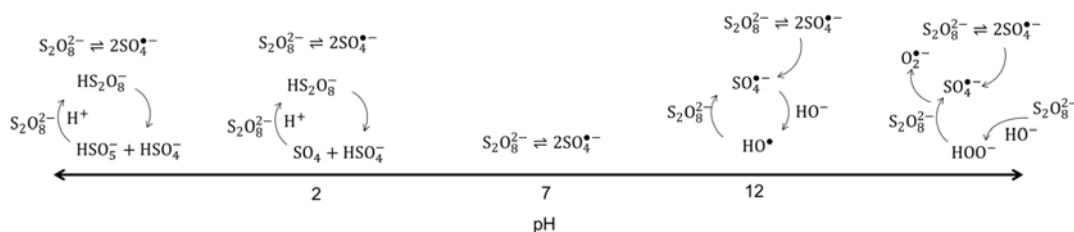


Figure 5.3. Effect of pH on PS decomposition.

Alkaline activation of PS has been widely used for ISCO applications where the basic pH provide for PS activation by  $\text{HO}^-$ , soil organic matter and inorganic solids and ions to yield  $\text{SO}_4^{\bullet-}$ ,  $\text{HO}^\bullet$  and  $\text{O}_2^{\bullet-}$  for the degradation of a range of subsurface

pollutant including highly reduced or oxidised organic molecules [10, 114]. At very high pH when R5.35 and R5.36 are important, for every mole of  $\text{SO}_4^{\bullet-}$  and  $\text{O}_2^{\bullet-}$  produced, four moles of  $\text{H}^+$  is generated which may constitute a significant demand on  $\text{HO}^\bullet$  to maintain the alkaline condition of the reactions. Considering that the natural buffering capacity of the subsurface must also be overridden, it follows that significant amount of alkaline may be required to maintain a basic condition [10]. It has been suggested that the injection of large amount of alkaline may disturb the subsurface chemical balance with potentially undesirable consequences [118].

It should be noted that  $\text{HO}^\bullet$  produced according to R5.43 is less oxidising in alkaline condition ( $\text{HO}^\bullet/\text{H}_2\text{O} = +1.55 \text{ V}$  [21]) compared to acidic conditions ( $\text{HO}^\bullet/\text{H}_2\text{O} = +2.34 \text{ V}$  [21]). While it is evident that an alkaline solution can activate PS, it may be asked if the basic condition is optimal for oxidative degradation of pollutants. Goulden and Anthony [119] studied the heat-activated PS degradation of nicotinic acid and a number of natural water samples over the pH range of 1.2 to 12 at a temperature of 100 °C. They reported the maximum rate of oxidation to be between pH 3 to 6. They remarked that phosphate buffer was used to maintain  $\text{pH} \geq 4$ . The absence of phosphate buffer at the acidic condition may have contributed to the better oxidation under this condition since phosphate may act as a radical scavenger when present [78]. Lee et al. [120] also reported that the highest rate constant at a temperature of 90 °C for the degradation of perfluorocarboxylic acids was observed under acidic conditions. Deng and Ezyske [121] reported that their investigation of heat-activated PS degradation of landfill leachate showed a more effective removal of chemical oxygen demand and ammonia at a pH of 4 compared to a pH of 8.3. They explained this result by a reference to the reduction of carbonate and bicarbonate concentration in solution at acidic conditions, which reduced radical scavenging and allowed for more effective pollutant oxidation.

Liang et al. [122] studied the rate of degradation of trichloroethylene under temperature values of 10 °C, 20 °C and 30 °C that may be considered relevant to ISCO applications with solution pH phosphate-buffered at 4, 7 or 9. Their results showed that the maximum pollutant degradation is observed at pH of 7 and the least at a pH of 4. The report by Liang et al. [122] showed that the

degradation rate at pH 9 was slightly lower than at pH 7. The authors explained that the limited degradation of the organic pollutant at pH 4 is due to backward R5.42, R5.43 and the following reactions [122]:



However, these reactions, except backward R5.42, are radical propagating reactions rather than terminating reactions and therefore may not sufficiently explain the limited pollutant degradation observed. In fact, Yu et al. [123] expressed R5.45 as a reversible reaction so that  $\text{SO}_4^{\bullet-}$  is regenerated. It is recognised that backward R5.42 reduces the amount of the active  $\text{SO}_4^{\bullet-}$  but since these reaction is premised on the excessive concentration of this radical [122], the reduction may not be considered overly deleterious to the AOP. The limited pollutant degradation observed under acidic conditions may be explained by the classical  $\text{H}^+$  catalysed unsymmetrical degradation of PS (R5.2 and R5.3) [28]. In acid catalysed decomposition of PS, the products are non-radicals [28] and therefore do not contribute to oxidative radical reactions. Liang et al. [122] also associated the limited degradation at pH 9 to  $\text{SO}_4^{\bullet-}$  conversion to  $\text{HO}^\bullet$ . This is plausible considering that  $\text{HO}^\bullet$  is less oxidising in basic conditions.

From this discussion, it appears that the optimal pH condition for radical oxidation may not be the alkaline condition although specific pollutant and experimental conditions may influence the optimal pH position for a specific AOP. Hence, the major reaction benefit, beyond PS activation, provided by the alkaline condition for ISCO applications is the increased interaction between PS and organic moieties and molecules [110, 111].

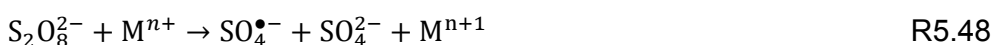
### 5.6.2. Thermolysis

The thermal homolytic cleavage of the O-O bond of PS has been a subject of increasing research interest over the last two decades for the degradation of environmental contaminants. Huang et al. [124] studied the degradation of 59 volatile organic compounds listed in the EPA SW-846 Method 8260B by thermally activated PS at relatively low temperature of 20 °C, 30 °C, and 40 °C. They reported that aromatic and unsaturated compounds were generally degraded

more readily than saturated hydrocarbon and halogenated alkanes. This result reflect the greater tendency of  $\text{SO}_4^{\bullet-}$  to abstract electron rather than the hydrogen atom [25]. Heat-activated PS has been applied successfully for the treatment of many environmental pollutants including methyl tert-butyl ether (MTBE) [125, 126], antipyrine [112], diuron [127], Ibuprofen [128], methylene blue [129], polyvinyl alcohol [79], bisoprolol [130], p-nitrophenol [113], polycyclic aromatic hydrocarbons [131], and landfill leachate [121].

Few studies that compared PS-AOPs based on thermolysis to catalysis have reported a more effective pollutant degradation by the former compared to the later. Oh et al. [79] reported that complete polyvinyl alcohol degradation was achieved in 30 min and 10 min by heat activated PS at temperatures of 60 °C and 80 °C, respectively. However, operating under optimal concentration, PS activation by Fe(0) achieved complete target pollutant degradation only after 2 h while complete degradation was not achieved with Fe(II)-activated PS even after 2 h. Similarly, Deng et al. [126] compared the heat activation of PS at modest temperatures of 25 °C and 40 °C to Fe(III)-EDTA and alkaline activation of PS aimed at the degradation of MTBE. They reported a half-life of 82 h, 0.7 h, 20 h and 235 h for MTBE under oxidising conditions of 25 °C, 40 °C, Fe(III)-EDTA and alkaline activation of PS, respectively. Similarly, Zhao et al. [131] showed that heat activation of PS at 60 °C is a more effective route for the degradation of polycyclic aromatic hydrocarbons compared to citrate-chelated Fe(II),  $\text{H}_2\text{O}_2$  and alkaline activation. This result clearly shows the superiority of heat-activated PS treatment over common PS activation methods.

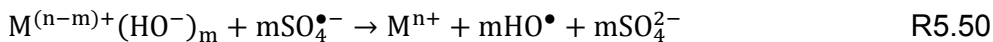
There are two major reasons why heat activation of PS yields better pollutant degradation than other common activation techniques including metal ion activation. One of these is that compared to the one mole of  $\text{SO}_4^{\bullet-}$  generated following regular transition metal ion ( $\text{M}^{2+}$ ) activation of PS, thermal/radiation activation yields stoichiometrically two moles of  $\text{SO}_4^{\bullet-}$  for each mole of PS activated.



The second is that unreacted metal ion usually compete with the target pollutant for  $\text{SO}_4^{\bullet-}$  thereby reducing the amount of pollutants oxidised for a given amount of PS [56, 79].



Liang and Su [117] showed that the predominant radical during PS thermolysis is determined by the solution pH. At a pH < 7,  $\text{SO}_4^{\bullet-}$  is the predominant radical, while both  $\text{SO}_4^{\bullet-}$  and  $\text{HO}^{\bullet}$  are formed at pH 9. When the pH is about 12, the  $\text{HO}^{\bullet}$  radical predominates. This result is consistent with the description given in Section 5.6.1.6.  $\text{SO}_4^{\bullet-}$  may react with  $\text{H}_2\text{O}$  or  $\text{OH}^-$  according to R5.45 and R5.43, respectively, to produce  $\text{HO}^{\bullet}$ . The rate constant for R5.43 given as  $4.6 - 8.3 \times 10^7 \text{ M}^{-1}\text{s}^{-1}$  [25] is significantly greater than the rate constant for R5.45 given as  $< 3 \times 10^3 \text{ s}^{-1}$  [132]. Considering that R5.45 requires the dissociation of the H-OH bond in water with a bond dissociation energy of  $502 \text{ kJ mol}^{-1}$  [29] and R5.43 requires the abstraction of an electron from  $\text{HO}^-$  with an electron affinity of  $\sim 570 \text{ kJ mol}^{-1}$  [29], the much higher rate constant for R5.43 compared to R5.45 appears counterintuitive. This is more so because  $\text{SO}_4^{\bullet-}$  is formally negatively charged and so is  $\text{OH}^-$  but not  $\text{H}_2\text{O}$  so that Coulombic repulsion [123] would have been expected to reduce the rate constant of R5.43 compared to R5.45. A possible reason for the much higher rate constant for R5.43 may relate to the effect of ion pairing between  $\text{OH}^-$  and the cation present in solution under alkaline conditions as follows:



The ion pairing may serve to not only reduce or remove charge repulsion but it may also facilitate the transfer of electron from  $\text{OH}^-$  to  $\text{SO}_4^{\bullet-}$ . This concept has been used to explain the catalytic effect of metal ions on PS oxidation of iodide [23]. The concept of ion pairing similar to R5.50 has also been used to explain important observation in Fenton and Fenton-like reactions [29]. Since ion pairs are more likely to form with 1:2 or 2:1 electrolytes or higher and at higher temperature where the permittivity of water is considerably reduced [133], it is expected that the rate of generation of  $\text{HO}^{\bullet}$  from  $\text{SO}_4^{\bullet-}$  will be dependent on temperature and electrolytes if R5.50 holds. Consequently, an experimental verification of the proposed R5.50 reaction may involve quantifying  $\text{HO}^{\bullet}$ .

dependence on temperature and electrolytes after due consideration has been given to the effect of Arrhenius-type rate increase with temperature.

Typically, the rate of degradation of organic pollutant increases with temperature which is usually linked to the higher rate of production of  $\text{SO}_4^{\bullet-}$  from the homolytic cleavage of the O-O bond in PS [28, 119]. From a study of the oxidation of a number of organic material of varying complexity, Goulden and Anthony [119] reported that the mineralisation trends were all similar. For up to 70% mineralisation,  $\text{CO}_2$  production, which was used as a measure of mineralisation, was first order with respect to PS i.e.

$$\frac{d(\text{CO}_2)}{dt} = k[\text{S}_2\text{O}_8^{2-}] \quad \text{R5.51}$$

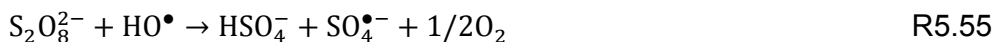
Thereafter, the reaction was second order as follows:

$$\frac{d(\text{CO}_2)}{dt} = k[\text{S}_2\text{O}_8^{2-}][\text{organic material}] \quad \text{R5.52}$$

The authors expressed surprise that such a simple expression can model the mineralisation of a variety of complex organic material. The simple model may suggest that the behaviour of PS dictates the mineralisation trend and therefore may apply for most uncatalysed PS oxidation of organic materials. Experimental and model study of nicotinic acid mineralisation by Goulden and Anthony [119] between 90 °C to 130 °C under varying pH showed that the highest mineralisation was always achieved at the temperature of 90 °C. The result was explained on the basis of the rate of PS decomposition increasing more rapidly than the rate of organic substrates oxidation as temperature increased [119]. The authors concluded that faster organic material mineralisation can be achieved more effectively with higher PS concentration than higher temperature [119].

Hori et al. [134] reported more effective mineralisation of perfluorocarboxylic acids at 80 °C compared to 150 °C for heat activated PS. Mineralisation, also measured by  $\text{CO}_2$  production, was 37% after 6 h for PS activated at 150 °C while the corresponding mineralisation was 70% at 80 °C. For this study, samples were heated in an oven to the required reaction temperature. Hori et al. [134] explained that the limited mineralisation at high temperature was due to the possible increased production of  $\text{HO}^{\bullet}$  from  $\text{SO}_4^{\bullet-}$  and to gasification of the pollutant and intermediates.

Using microwave heating for the activation of PS, Lee et al. [120] studied the degradation and mineralisation of perfluorocarboxylic acids at temperatures of 60 °C, 90 °C, and 130 °C. Like Hori et al. [134], these authors reported limited mineralisation at 130 °C compared to the pollutant oxidation at 90 °C. After 4 h of oxidation, mineralisation at 130 °C was only 40% while about 60% and about 70% mineralisation was achieved at 60 °C and 90 °C, respectively. After 12 h, mineralisation remained 40% at 130 °C while about 80% mineralisation was achieved at both 60 °C and 90 °C. These authors explained the limited mineralisation at 130 °C using backward R5.42 and R5.46. It has already been remarked that R5.42 and R5.46 are not comprehensive explanation for a limited pollutant degradation nor will they adequately explain the significant PS consumption observed at 130 °C [120]. A simplified but more complete account of the observed limited mineralisation by heat-activated PS at higher temperatures may be expressed thus [23, 29, 135]:



The generation of O<sub>2</sub> may be considered a true consumption of the oxidative capacity of PS since the oxidative capacity of O<sub>2</sub> is much lower than PS and a more oxidative radical cannot be generated from the homolytic cleavage of O<sub>2</sub> at the ordinary conditions of the reactions. It may be noted that the evolution of O<sub>2</sub> as described in R5.53 – R5.58 involve the breakage of HO-H bond of water that has a bond-dissociation energy of 502 kJ mol<sup>-1</sup> [29]. The high bond dissociation energy presents significant activation energy barrier for the reaction. Since the rate of cleavage of these bond increased with temperature as inferred from the increase in the rate of decomposition of PS and evolution of O<sub>2</sub> [28], the kinetic energy of the associated radical may be said to increase with temperature like other chemical species [83]. Radical reaction like other chemical reactions may

be limited by activation energy barrier that may be overcome with temperature increase [32, 123]. The effect of the kinetic energy of radical are rarely highlighted in the description and explanation of AOPs. For example, radical quenching in ice bath [117, 130] operates on the principle of diminished kinetic energy at low temperature, which favours radical termination reactions such as combination and disproportionation over radical propagating reactions like electron or hydrogen atom abstraction [32]. These kinetic effects are not usually emphasised in the AOPs literature although their practical import may be extensive.

In contrast to the papers so far reviewed that showed decreasing mineralisation effectiveness for temperature  $> 100$  °C, Xu et al. [136] reported steady increase in mineralisation as reaction temperature increased from 90 °C to 170 °C for a PS oxidation study in which activated carbon was used as a catalyst. The presence of activated carbon may be responsible for the unique result.

Although heat-activated PS-AOPs may be energy intensive, the economy of the process may be significantly improved if waste heat is harnessed. This is particularly important since many industries routinely discharge significant amount of waste heat [137-139]. The textile industry afford a good example where dye-contaminated wastewater may be discharged with temperature between 30 °C to 96 °C with a volumetric average of 71 °C [140]. These temperatures are significant considering that several studies on heat-activated PS degradation of pollutants have been conducted at temperatures  $\leq 70$  °C [112, 125, 127-131]. It has been shown that at a modest temperature of 40 °C; PS can be effectively activated for pollutant degradation [126]. Consequently, heat-activated PS is potentially a low-cost, effective, sustainable and environmentally friendly technique to treat wastewater wherever waste heat is generated.

### 5.6.3. Photolysis

Significant amount of research publications are available employing UV activation of PS for the degradation of environmental pollutant as well as for fundamental study of radical reactions. Like heat-activation, UV activation of PS theoretically produces two moles of the sulphate radical for each mole of PS activated. Since UV treatment is a principal component of many water treatment and disinfection processes, it was natural that application of UV for the activation of PS for

pollutant degradation will be given significant research attention. UV-activated PS has been used successfully for the laboratory study of the degradation of a variety of water pollutants including tetrafluoro-1-propanol [141], phenol [142], trichloroanisole [143], tetramethylammonium hydroxide [144], and sulfamethazine [145]. The application of UV-activated PS also include the regeneration of organic matter saturated granular activated carbon [146] and the improvement of algae coagulation to control algal blooms [147]. Chu et al. [148] showed that UV-activated PS oxidation is an effective method for the removal of disinfection by product precursors from drinking water. Compared to UV/H<sub>2</sub>O<sub>2</sub> and UV/PMS, UV/PS was shown to achieve complete destruction of the cyanobacterial toxin cylindrospermopsin at lower UV fluence [149]. Wang et al. [150] demonstrated that PS can be incorporated into an ultrafiltration membrane and UV-activated to achieve simultaneous filtration and oxidation of water contaminants. Although SO<sub>4</sub><sup>•-</sup> react readily with bromide which poses the risk of bromate generation when bromide-rich water is treated by activated PS, Lutze et al. [151] showed that in the presence of natural organic matter (NOM) at concentrations commonly found in water, bromate formation is suppressed. This accords an advantage to activated PS over ozonation where bromate formation is an important challenge [151].

An important consideration for UV/PS application is the choice of wavelength for the UV irradiation. Lin and Wu [152] showed that for the oxidation of polyvinyl alcohol (PVA), UV-254 nm radiation provided a more efficient degradation of PVA in the presence of PS especially at neutral conditions compared to UV-365 nm.

The pH of the solution also appears to be an important factor for consideration. A number of studies have reported more efficient pollutant degradation during UV/PS treatment under acidic conditions compared to neutral and alkaline conditions [143, 144, 152]. Reasons given for the observation include limited radical scavenging effect of protonated phosphate ions added as buffer compared to the deprotonated forms [143] and specific contaminant resistance to HO<sup>•</sup> degradation produced under alkaline conditions [144]. On the other hand, Gao et al. [145] reported more efficient degradation of sulfamethazine at a pH of 6.5 when compared to acidic and alkaline conditions. The authors explained their result on the ground that SO<sub>4</sub><sup>•-</sup> is most active in degrading the target pollutant

and neutral condition is most suitable for the production of this radical. As tetrabromobisphenol A has limited solubility in water with pH < 7, Guo et al.[153] showed that the degradation of the pollutant is more effective under alkaline conditions in which the  $\text{SO}_4^{\bullet-}$  was produced by UV activation of PS.

For the UV-activated PS degradation processes, similar to the heat-activated PS systems, it seems that the properties of the target pollutant has significant influence on what pH is conducive for optimal pollutant degradation.

Despite the effectiveness and elegance of UV-activated PS, its dependence on electricity, a *high-grade* form of energy, implies it may be considered adverse to the water energy nexus [154] and is less sustainable compared to waste heat activation of PS. When the contaminant load is significant or significant mineralisation is desired, the cost implication may be substantial [155]. Other challenges may include limited penetration of irradiation under certain conditions and energy lost due to absorption by organic matter and other species in water other than PS.

#### 5.6.4. Sonolysis

The application of ultrasonic energy for the activation of PS has received some amount of research attention where the significantly high local temperature and pressure generated in solution through the collapse of cavitation bubbles provide effective PS activation. Wei et al. [156] reported that during sonochemical activation of PS, the amount of generated  $\text{HO}^{\bullet}$  was up to 1 order of magnitude greater than the amount of  $\text{SO}_4^{\bullet-}$  produced. They attributed this result to cavitation bubble enhanced reaction between  $\text{SO}_4^{\bullet-}$  and water molecules. Sonic irradiation has been used successfully to activate PS for the degradation of carbamazepine [157], bisphenol A [158], trichloroethane and dioxane [159] with or without the contribution of thermal activation. Sonochemical activation of PS has also been combined with other activating techniques such as Fe(II) and UV irradiation for enhanced pollutant degradation [160]. However, due to the dependence on electricity, sono-activated PS may be considered a less cost effective and sustainable technique compared to heat-activated PS especially where waste heat can be harnessed.

### 5.6.5. Radiolysis

The generation of radicals from the activation of PS by energising radiations has been employed for fundamental studies of the chemistry of sulphate and associated radicals [132, 161]. Paul (Guin) et al. [162] showed that ibuprofen can be effectively degraded and mineralised by the activation of PS through gamma irradiation. With practical AOP in view, safety concerns and cost may be considered important disadvantages of PS activation by radiolysis.

## 5.7. Practical applications

### 5.7.1. In-situ chemical oxidation

PS has been described as the latest addition to the suite of oxidants that are used for the remediation of subsurface contaminated sites [10]. Both activated and unactivated PS have been employed for this purpose. For ISCO application, PS has certain advantages over the more commonly used oxidants. It is more stable than  $H_2O_2$  and  $O_3$  under subsurface conditions; more reactive and less affected by soil organic matter than  $KMnO_4$ , more soluble and so achieve more uniform distribution than ozone and leaves behind no insoluble precipitate like  $KMnO_4$  [1, 4]. Data derived from bench-scale experiments have also shown that activated PS oxidation is less deleterious to soil microorganisms compared to  $H_2O_2$  processes [163].

Restrained diffusion [113] in the subsurface may be considered a common challenge of ISCO applications which may exacerbate the problem of radical scavenging compared to aqueous treatments on the surface. Consequently, slow activation may be preferable under subsurface condition to extend the region of activity of the AOP. In this respect, unactivated PS relying on slow activation from subsurface materials may provide a more effective pollutant degradation outcome than activated-PS where the rapidly generated radicals may be quickly consumed. Therefore, activated-PS for ISCO applications are most desirable where rapid detoxification of underground water or soil is required. Some discussion of alkaline activation of PS for ISCO has already been presented (Section 5.6.1.6). Although alkaline activation is a popular method in practice, controlled laboratory study of this technique is rather limited [118] and opinions on its effectiveness in field applications are divided [10].

Instances of field application of heat-activated PS remediation of subsurface contamination was cited by Tsitonaki et al. [10]. A laboratory study of heat-activated PS with implication for ISCO was presented by Johnson et al. [164]. They concluded that for temperatures  $\geq 50$  °C, the half-life of PS is very short (< 1 d) so that its practical region of activity within the subsurface is significantly limited. At ~20 °C (i.e. unactivated), the half-lives of PS were reported to range from 2 d to 600 d [15].

Iron activation is potentially an effective method for PS activation for ISCO but the problem of scavenging and longevity needs to be properly addressed. Ranc et al. [12] catalogued controlled laboratory studies of real and artificially contaminated soil subjected to PS treatment with activation by various forms of iron and other oxidants. Actual field applications of iron activated PS treatment are not readily available in the peer-reviewed literature.

It has already been mentioned that natural soil systems can effectively activate PS for ISCO of subsurface contaminants. The soil organic matter was identified as a more potent activator than soil inorganic solids [93]. Nevertheless, activation due to inorganic solid can also be significant. Bench scale study by Feng et al. [165] showed that red mud composed principally of hematite, perovskite, andradite, cancrinite, diaspore, gibbsite, and calcite can effectively activate PS for the degradation of sulfadiazine. A bench-scale comparison of the effectiveness of unactivated PS and chelated-iron activated PS for the treatment of anthracene-contaminated oxisol was presented by Ferreira et al. [166]. They reported 96% pollutant degradation after 90 d for the unactivated PS while chelated-iron activated PS resulted in 70% pollutant degradation over the same period. These results indicate that unactivated PS may provide effective pollutant degradation for ISCO applications outside an emergency.

Bench-scale studies as discussed by Bennedsen [1] to determine the most suitable AOP to be implemented for the remediation of an underground contaminated site showed that unactivated PS was a very competitive technique. Unactivated PS outperformed base-activated PS treatment in pollutant degradation and can be said to outperform all other techniques evaluated in the study in consuming the least amount of oxidant. Sra et al. [167] reported the

treatment of a gasoline source zone by the injection of unactivated PS which was monitored for more than 10 months. The results showed maximum reduction in gasoline components of 52 – 86% as observed from monitoring wells between 60 to 80 d from the start of the remediation. Cumulative reduction in target pollutants over 315 d was much smaller - between 19% and 58%. The earlier higher pollutant reductions were ascribed partly to dilution arising from the injection of the PS solution. PS was practically consumed after about 100 d. Replenishing PS at set intervals is recommended for effective pollutant degradation [166].

#### 5.7.2. Waste treatment

The vast proportion of the published reports on AOPs are suited or designed for the treatment of wastewater generated from domestic and industrial activities. Activated PS achieves effective degradation and mineralisation in relatively short-term. The effectiveness of the various activation techniques for pollutant degradation were highlighted in the appropriate sections. Wherever waste heat is available, heat-activated PS is recommended as an effective and environmentally friendly treatment approach.

Solid waste management application of activated PS include sewage sludge dewatering and landfill leachate treatment. PS has been applied successfully for enhancing the dewaterability of sewage sludge with PS activated either by Fe(II) [62, 63] or by heat [168]. Successful treatment of landfill leachate by activated PS to degrade refractory organic contaminants and other associated pollutants has been reported for bench-scale experiments [121, 169, 170].

Activated PS has also been shown to be effective in the treatment of gaseous pollutants, a result that is promising for the maintenance of clean air in industrial and urban centres. The absorption and oxidation of nitric acid with or without the simultaneous adsorption of sulphur dioxide have been demonstrated using heat-activated PS [171, 172]. Waste heat from industrial processes can readily be harnessed [137, 139, 173] to supply the energy for the thermal activation of PS to achieve a cost-effective and sustainable emission reduction. Similar system may be deployed for commercial and domestic air sanitisation and cleaning.

### 5.7.3. Drinking water production

The removal of NOM and other micropollutants for drinking water production from raw water using AOPs such as ozonation, heterogeneous photocatalysis, Fenton and Fenton-like processes and other H<sub>2</sub>O<sub>2</sub>-based processes have received significant amount of research attention over the last two decades with full-scale application in many parts of the world [17, 174]. However, interest in PS processes for drinking water production have been limited even at the laboratory scale although PS has certain advantages for drinking water treatment over other oxidants. Some of this favourable properties include the greater stability of PS compared to H<sub>2</sub>O<sub>2</sub> [4, 126]; limited tendency of SO<sub>4</sub><sup>•-</sup> to form bromate compared to O<sub>3</sub> [151], moderate cost, and the ease of transportation, handling and storage of PS [126].

Few laboratory studies have demonstrated the feasibility of bacterial disinfection using PS activated by Fe(II) [61], Fe(0) [175] or natural occurring magnetic pyrrhotite [176]. The use of pyrrhotite is particularly attractive as it was shown to be reusable and due to its magnetic properties, may be readily separated from the treated water. Activated-PS disinfection technique is potentially safer compared to chlorination as it poses less risk for the formation of halomethanes and other halogenated DBPs commonly associated with chlorination. Since drinking water may contain some amount of dissolved metal ions within acceptable limits [177-180], these metal ions as well as ambient temperature depending on location/season may provide effective activation of PS for drinking water disinfection as well as the removal of NOM and micropollutants. This scheme is potentially more sustainable, safe and environmentally friendly than current disinfection and AOPs used for the production of potable water. Since the addition of 0.25 mM PS amount to the introduction of 70 mg/L sulphate, care should be taken not to exceed the thirst threshold for Na<sub>2</sub>SO<sub>4</sub> in drinking water, which has been given as 350 mg/L [181].

### 5.7.4 Coupling to membrane filtration

Membrane filtration is considered one of the most effective techniques for wastewater treatment with the potential for increased utilisation of reclaimed wastewater [182-185]. However, membrane fouling remains a major challenge

with significant cost and performance implication [186]. In addition, the widespread adoption of direct and indirect potable reuse of wastewater is significantly limited by the poor rejection of small, uncharged molecules by reverse osmosis membranes [182, 187]. Some of the molecules that are poorly rejected such as the N-nitrosamines have been identified as probable human carcinogens [182, 187]. It will be important to evaluate the feasibility of employing activated persulphate AOPs as effective and safe feed pre-treatment to reduce the problem of fouling and as a post-treatment to degrade poorly rejected molecules in the permeate. Such coupling of AOPs to membrane filtration have been reported for non-PS AOPs [188]. Harnessing waste heat for PS activation may potentially improve the sustainability and affordability of the integrated water treatment process.

### 5.8. Conclusions

The literature of PS-AOPs have been critically reviewed with important area for further studies identified and new proposals presented to explain reaction mechanisms more consistently. The still unexplained role of silver ion in PS-AOPs was discussed at some length and area for further studies identified. Since Ag(I) is commonly used as a biocide, understanding its reaction mechanism with PS may provide more effective disinfection options. Iron-based catalysis are likely to continue to dominate the scene of the catalytic activation of PS but more work is required to improve reusability and minimise radical scavenging without diminishing reactivity. In this respect, heterogeneous Fe(III)-based catalyst with large surface and limited metal leaching property are particularly promising. Recent development in CuO activation of PS present a new opportunity for the development of transition metal catalysts other than iron catalyst for PS-AOPs. Also particularly promising is the increasingly active research in metal-free activation of PS using nanocarbon materials.

However, irradiation is considered by the authors as the most effective technique for PS activation as it can theoretically produce 2 moles of radicals from each mole of PS and can provide easy control of the kinetic energy of radicals whose impact has been little explored to date. Whenever waste heat is available, heat-activation of PS is considered the most sustainable and environmentally friendly

option for pollutant degradation. Since PS may be effectively activated at temperatures as low as 40 °C and considering that substantial amount of waste heat is generated industrially, commercially and domestically, there is significant opportunity to adopt heat-activated PS-AOP for waste treatment on a wider scale. Drinking water treatment and disinfection including wastewater reuse can also benefit from heat-activated PS treatment. Activation of PS by metal ions naturally occurring or added for disinfection in drinking water may also be important in certain regions. For ISCO application, except for cases requiring prompt detoxification, unactivated PS is recommended as the most effective route for sustainably and economically treating subsurface contaminated sites. Alkaline injection should only be considered in cases where the subsurface pH is too acidic such that the risk of acid-catalysed decomposition of PS is significant.

## References

- [1] L.R. Bennedsen, In situ chemical oxidation: the mechanisms and applications of chemical oxidants for remediation purposes, in: E. Sogaard (Ed.) Chemistry of advanced environmental purification processes of water, Elsevier Science, 2014, pp. 13-74.
- [2] R. Munter, Advanced oxidation processes - current status and prospects, Proceedings of the Estonian Academy of Science. Chemistry, 50 (2001) 59–80.
- [3] H. Sun, S. Wang, Catalytic oxidation of organic pollutants in aqueous solution using sulfate radicals, Catalysis, 27 (2015) 209-247.
- [4] B.-T. Zhang, Y. Zhang, Y. Teng, M. Fan, Sulfate radical and its application in decontamination technologies, Critical Reviews in Environmental Science and Technology, 45 (2015) 1756-1800.
- [5] W.-D. Oh, Z. Dong, T.-T. Lim, Generation of sulfate radical through heterogeneous catalysis for organic contaminants removal: Current development, challenges and prospects, Applied Catalysis B: Environmental, 194 (2016) 169-201.
- [6] F. Ghanbari, M. Moradi, Application of peroxymonosulfate and its activation methods for degradation of environmental organic pollutants: Review, Chemical Engineering Journal 310 (2017) 41–62.

- [7] Hach, Phosphonates, Persulfate UV Oxidation Method (125.0 mg/L), in: H.C.H.L. GmbH (Ed.), Hach Company/Hach Lange GmbH, 2014.
- [8] T. Zhang, Y. Chen, Y. Wang, J.L. Roux, Y. Yang, J.-P. Croue, Efficient Peroxydisulfate Activation Process Not Relying on Sulfate Radical Generation for Water Pollutant Degradation, *Environmental Science & Technology*, 48 (2014) 5868–5875.
- [9] S. Wacławek, H.V. Lutze, K. Grübel, V.V.T. Padil, M. Černík, D.D. Dionysiou, Chemistry of persulfates in water and wastewater treatment: A review, *Chemical Engineering Journal*, 330 (2017) 44-62.
- [10] A. Tsitonaki, B. Petri, M. Crimi, H. MosbÆK, R.L. Siegrist, P.L. Bjerg, In Situ Chemical Oxidation of Contaminated Soil and Groundwater Using Persulfate: A Review, *Critical Reviews in Environmental Science and Technology*, 40 (2010) 55-91.
- [11] P. Devi, U. Das, A.K. Dalai, In-situ chemical oxidation: Principle and applications of peroxide and persulfate treatments in wastewater systems, *The Science of the total environment*, 571 (2016) 643-657.
- [12] B. Ranc, P. Faure, V. Croze, M.O. Simonnot, Selection of oxidant doses for in situ chemical oxidation of soils contaminated by polycyclic aromatic hydrocarbons (PAHs): A review, *J Hazard Mater*, 312 (2016) 280-297.
- [13] Y. Deng, R. Zhao, Advanced Oxidation Processes (AOPs) in Wastewater Treatment, *Current Pollution Reports*, 1 (2015) 167-176.
- [14] H. Marshall, LXXIV.—Contributions from the Chemical Laboratory of the University of Edinburgh. No. V. The persulphates, *Journal of the Chemical Society, Transactions* 59 (1891) 771-786.
- [15] K.S. Sra, N.R. Thomson, J.F. Barker, Persistence of Persulfate in Uncontaminated Aquifer Materials, *Environmental Science & Technology*, 44 (2010) 3098–3104.
- [16] J.S. Reichert, S.A. Mcneight, H.W. Rudel, Determination of Hydrogen Peroxide and Some Related Peroxygen Compounds, *Industrial & Engineering Chemistry*, 11 (1939) 194 - 197.
- [17] A. Matilainen, M. Sillanpaa, Removal of natural organic matter from drinking water by advanced oxidation processes, *Chemosphere*, 80 (2010) 351-365.
- [18] FMC, Persulfates technical information, in, FMC Corporation, [http://www.peroxycchem.com/media/90826/aod\\_brochure\\_persulfate.pdf](http://www.peroxycchem.com/media/90826/aod_brochure_persulfate.pdf), 2001.

- [19] NCBI, Sodium Persulfate in, National Center for Biotechnology Information. PubChem Compound Database; CID=62655, <https://pubchem.ncbi.nlm.nih.gov/compound/62655> (accessed July 18, 2017).
- [20] F. Minisci, A. Citterio, C. Giordano, Electron-transfer processes: peroxydisulfate, a useful and versatile reagent in organic chemistry, Accounts of Chemical Research, 16 (2002) 27-32.
- [21] P. Atkins, T. Overton, J. Rourke, M. Weller, F. Armstrong, M. Hagerman, Shriver & Atkins' inorganic chemistry, 5 ed., Oxford University Press, Great Britain, 2010.
- [22] T.W. Swaddle, Inorganic chemistry, in: An industrial and environmental perspective, Elsevier Science, 1997.
- [23] D.A. House, Kinetics and Mechanism of Oxidations by Peroxydisulfate, Chemical reviews, 62 (1962) 185-203.
- [24] A.G. Sharpe, Inorganic Chemistry, 3 ed., Longman Scientific & Technical, England, 1992.
- [25] P. Neta, R.E. Huie, A.B. Ross, Rate constants for reactions of inorganic radicals in aqueous solution, Journal of Physical and Chemical Reference Data 17, (1988), 17 (1988) 1027 - 1284.
- [26] A. Asghar, A.A. Abdul Raman, W.M.A. Wan Daud, Advanced oxidation processes for in-situ production of hydrogen peroxide/hydroxyl radical for textile wastewater treatment: a review, Journal of Cleaner Production, 87 (2015) 826-838.
- [27] AWWA, Water Treatment, 4 ed., American Water Works Association, Denver, 2010.
- [28] I.M. Kolthoff, I.K. Miller, The chemistry of persulfate. I. The kinetics and mechanism of the decomposition of the persulfate ion in aqueous medium, journal of American Chemical Society, 73 (1951) 3055–3059.
- [29] N. Uri, Inorganic free radicals in solution, Chemical Review, 50 (1952) 375–454.
- [30] F.O. Rice, O.M. Reiff, The Thermal Decomposition of Hydrogen Peroxide, Journal of Physical Chemistry, 31 (1927) 1352–1356.
- [31] D. Braun, Initiation of free radical polymerization by thermal cleavage of carbon-carbon bonds, Macromolecular Symposia, 111 (1996) 63-71.

- [32] C.J.M. Stirling, Radicals in organic chemistry, Oldbourne Press, London, 1965.
- [33] A.R. Gallopo, J.O. Edwards, Kinetics and Mechanisms of the Spontaneous and Metal-Modified Oxidations of Ethanol by Peroxydisulfate Ion, Journal of Organic Chemistry, 36 (1971) 4089 - 4096.
- [34] G.P. Anipsitakis, D.D. Dionysiou, Radical generation by the interaction of transition metals with common oxidants, Environmental Science & Technology, 38 (2004) 3705-3712.
- [35] A. Gansauer, H. Bluhm, Reagent-controlled transition-metal-catalyzed radical reactions, Chemical Review, 100 ( 2000) 2771–2788.
- [36] G.P. Anipsitakis, D.D. Dionysiou, Transition metal/UV-based advanced oxidation technologies for water decontamination, Applied Catalysis B: Environmental, 54 (2004) 155-163.
- [37] M.G. Antoniou, A.A. de la Cruz, D.D. Dionysiou, Degradation of microcystin-LR using sulfate radicals generated through photolysis, thermolysis and e- transfer mechanisms, Applied Catalysis B: Environmental, 96 (2010) 290-298.
- [38] A.J. Kalb, T.L. Allen, The Oxidation of Oxalate Ion by Peroxodisulfate. III. The Kinetics and Mechanism of the Catalysis by Silver(I), Journal of American Chemical Society, 86 (1964 ) 5107–5112.
- [39] P. Połczyński, R. Jurczakowski, W. Grochala, Strong and Long-Lived Free-Radical Oxidizer Based on Silver(II). Mechanism of Ag(I) Electrooxidation in Concentrated H<sub>2</sub>SO<sub>4</sub>, The Journal of Physical Chemistry C, 117 (2013) 20689-20696.
- [40] A. Kumar, Oxidative C-C bond cleavage of 1,2-diols by silver( II), Journal of American Chemical Society, 103 (1981) 5179-5182.
- [41] A. Kumar, Kinetics of complexation and oxidation of ethanolamine and diols by silver(II), Journal of Physical Chemistry, 86 (1982 ) 1674–1678.
- [42] X. Xu, Q. Ye, T. Tang, D. Wang, Hg(0) oxidative absorption by K(2)S(2)O(8) solution catalyzed by Ag(+) and Cu(2+), J Hazard Mater, 158 (2008) 410-416.
- [43] I. Conlin, N.D.E. Warren, D.F. Steele, Electrochemical oxidation of matter, in, Google Patents, US, 1999.
- [44] M.H. Mouliney, C. Bernard, Process and apparatus for dissolving a mixture of oxides of uranium and of plutonium, in, Google Patents, 1998.

- [45] M.S. Antelman, Divalent silver bactericide for water treatment, in, Google Patents, 1991.
- [46] M.S. Antelman, Divalent silver halide bactericide, in, Google Patents, 1992.
- [47] C. Liang, C.J. Bruell, M.C. Marley, K.L. Sperry, Persulfate oxidation for in situ remediation of TCE. I. Activated by ferrous ion with and without a persulfate-thiosulfate redox couple, *Chemosphere*, 55 (2004) 1213-1223.
- [48] S. Yuan, P. Liao, A.N. Alshawabkeh, Electrolytic manipulation of persulfate reactivity by iron electrodes for trichloroethylene degradation in groundwater, *Environmental Science & Technology*, 48 (2014) 656–663.
- [49] D. Ding, C. Liu, Y. Ji, Q. Yang, L. Chen, C. Jiang, T. Cai, Mechanism insight of degradation of norfloxacin by magnetite nanoparticles activated persulfate: Identification of radicals and degradation pathway, *Chemical Engineering Journal*, 308 (2017) 330-339.
- [50] Y. Wu, R. Prulho, M. Brigante, W. Dong, K. Hanna, G. Mailhot, Activation of persulfate by Fe(III) species: Implications for 4-tert-butylphenol degradation, *J Hazard Mater*, 322 (2017) 380-386.
- [51] M. Usman, P. Faure, C. Ruby, K. Hanna, Application of magnetite-activated persulfate oxidation for the degradation of PAHs in contaminated soils, *Chemosphere*, 87 (2012) 234-240.
- [52] I. Hussain, Y. Zhang, S. Huang, X. Du, Degradation of p-chloroaniline by persulfate activated with zero-valent iron, *Chemical Engineering Journal*, 203 (2012) 269-276.
- [53] H. Li, J. Wan, Y. Ma, M. Huang, Y. Wang, Y. Chen, New insights into the role of zero-valent iron surface oxidation layers in persulfate oxidation of dibutyl phthalate solutions, *Chemical Engineering Journal*, 250 (2014) 137-147.
- [54] C.S. Liu, K. Shih, C.X. Sun, F. Wang, Oxidative degradation of propachlor by ferrous and copper ion activated persulfate, *Science of The Total Environment*, 416 (2012) 507-512.
- [55] H. Liu, T.A. Bruton, W. Li, J.V. Buren, C. Prasse, F.M. Doyle, D.L. Sedlak, Oxidation of Benzene by Persulfate in the Presence of Fe(III)- and Mn(IV)-Containing Oxides: Stoichiometric Efficiency and Transformation Products, *Environmental Science & Technology*, 50 (2016) 890-898.

- [56] S. Rodriguez, L. Vasquez, D. Costa, A. Romero, A. Santos, Oxidation of Orange G by persulfate activated by Fe(II), Fe(III) and zero valent iron (ZVI), *Chemosphere*, 101 (2014) 86-92.
- [57] H. Li, J. Wan, Y. Ma, Y. Wang, M. Huang, Influence of particle size of zero-valent iron and dissolved silica on the reactivity of activated persulfate for degradation of acid orange 7, *Chemical Engineering Journal*, 237 (2014) 487-496.
- [58] X.-R. Xu, X.-Z. Li, Degradation of azo dye Orange G in aqueous solutions by persulfate with ferrous ion, *Separation and Purification Technology*, 72 (2010) 105-111.
- [59] H. Kusic, I. Peternel, N. Koprivanac, A.L. Bozic, Iron-activated persulfate oxidation of an azo dye in model wastewater: influence of iron activator type on process optimization, *Journal of Environmental Engineering*, 137 (2011) 454-463.
- [60] L. Zhu, Z. Ai, W. Ho, L. Zhang, Core–shell Fe–Fe<sub>2</sub>O<sub>3</sub> nanostructures as effective persulfate activator for degradation of methyl orange, *Separation and Purification Technology*, 108 (2013) 159-165.
- [61] D.N. Wordofa, S.L. Walker, H. Liu, Sulfate Radical-Induced Disinfection of PathogenicEscherichia coliO157:H7 via Iron-Activated Persulfate, *Environmental Science & Technology Letters*, 4 (2017) 154-160.
- [62] G. Zhen, X. Lu, Y. Zhao, X. Chai, D. Niu, Enhanced dewaterability of sewage sludge in the presence of Fe(II)-activated persulfate oxidation, *Bioresource technology*, 116 (2012) 259-265.
- [63] G. Zhen, X. Lu, Y. Li, Y. Zhao, B. Wang, Y. Song, X. Chai, D. Niu, X. Cao, Novel insights into enhanced dewaterability of waste activated sludge by Fe(II)-activated persulfate oxidation, *Bioresource technology*, 119 (2012) 7-14.
- [64] S. Akbari, F. Ghanbari, M. Moradi, Bisphenol A degradation in aqueous solutions by electrogenerated ferrous ion activated ozone, hydrogen peroxide and persulfate: Applying low current density for oxidation mechanism, *Chemical Engineering Journal*, 294 (2016) 298-307.
- [65] C. Liang, C.J. Bruell, M.C. Marley, K.L. Sperry, Persulfate oxidation for in situ remediation of TCE. II. Activated by chelated ferrous ion, *Chemosphere*, 55 (2004) 1225-1233.

- [66] D.Y. Yan, I.M. Lo, Removal effectiveness and mechanisms of naphthalene and heavy metals from artificially contaminated soil by iron chelate-activated persulfate, *Environ Pollut*, 178 (2013) 15-22.
- [67] J. Wen, S.P. Stacey, M.J. McLaughlin, J.K. Kirby, Biodegradation of rhamnolipid, EDTA and citric acid in cadmium and zinc contaminated soils, *Soil Biology and Biochemistry*, 41 (2009) 2214-2221.
- [68] L.N. Andrade, S.F. Araujo, A.T. Matos, A.B. Henriques, L.C. Oliveira, P.P. Souza, P. Chagas, M.M.D. Leão, C.C. Amorim, Performance of different oxidants in the presence of oxisol: Remediation of groundwater contaminated by gasoline/ethanol blend, *Chemical Engineering Journal*, 308 (2017) 428-437.
- [69] I.A. Ike, S.L. Foster, S.R. Shinn, S.T. Watson, J.D. Orbell, L.F. Greenlee, M.C. Duke, Advanced oxidation of orange G using phosphonic acid stabilised zerovalent iron, *Journal of Environmental Chemical Engineering*, 5 (2017) 4014-4023.
- [70] K. Manoli, G. Nakhla, A.K. Ray, V.K. Sharma, Enhanced oxidative transformation of organic contaminants by activation of ferrate(VI): Possible involvement of Fe V /Fe IV species, *Chemical Engineering Journal*, 307 (2017) 513-517.
- [71] V.K. Sharma, R. Zboril, R.S. Varma, Ferrates: greener oxidants with multimodal action in water treatment technologies, *Acc Chem Res*, 48 (2015) 182-191.
- [72] C. Liang, C.-P. Liang, C.-C. Chen, pH dependence of persulfate activation by EDTA/Fe(III) for degradation of trichloroethylene, *Journal of Contaminant Hydrology*, 106 (2009) 173-182.
- [73] P.D. Bartlett, J.D. Cotman, The Kinetics of the Decomposition of Potassium Persulfate in Aqueous Solutions of Methanol, *Journal of American Chemical Society*, 71 (1949) 1419–1422.
- [74] G. Fang, J. Gao, D.D. Dionysiou, C. Liu, D. Zhou, Activation of persulfate by quinones: free radical reactions and implication for the degradation of PCBs, *Environmental Science & Technology*, 47 (2013) 4605–4611.
- [75] A. Stefansson, Iron(III) Hydrolysis and Solubility at 25 °C, *Environmental Science & Technology*, 41 (2007) 6117-6123.
- [76] J.D. Hem, W.H. Cropper, Survey of ferrous-ferric chemical equilibria and redox potentials, United States Government Printing Office, Washington, (1959).

- [77] J. Deng, Y. Shao, N. Gao, Y. Deng, C. Tan, S. Zhou, Zero-valent iron/persulfate(Fe0/PS) oxidation acetaminophen in water, International Journal of Environmental Science and Technology, 11 (2013) 881-890.
- [78] X. Wei, N. Gao, C. Li, Y. Deng, S. Zhou, L. Li, Zero-valent iron (ZVI) activation of persulfate (PS) for oxidation of bentazon in water, Chemical Engineering Journal, 285 (2016) 660-670.
- [79] S.Y. Oh, H.W. Kim, J.M. Park, H.S. Park, C. Yoon, Oxidation of polyvinyl alcohol by persulfate activated with heat, Fe<sup>2+</sup>, and zero-valent iron, J Hazard Mater, 168 (2009) 346-351.
- [80] R. Li, X. Jin, M. Megharaj, R. Naidu, Z. Chen, Heterogeneous Fenton oxidation of 2,4-dichlorophenol using iron-based nanoparticles and persulfate system, Chemical Engineering Journal, 264 (2015) 587-594.
- [81] S.Y. Oh, S.G. Kang, P.C. Chiu, Degradation of 2,4-dinitrotoluene by persulfate activated with zero-valent iron, The Science of the total environment, 408 (2010) 3464-3468.
- [82] S. Rodriguez, A. Santos, A. Romero, Oxidation of priority and emerging pollutants with persulfate activated by iron: Effect of iron valence and particle size, Chemical Engineering Journal, 318 (2017) 197-205.
- [83] C.K. Law, Combustion physics, Cambridge University Press, Cambridge, 2006.
- [84] X. Duan, H. Sun, J. Kang, Y. Wang, S. Indrawirawan, S. Wang, Insights into Heterogeneous Catalysis of Persulfate Activation on Dimensional-Structured Nanocarbons, ACS Catalysis, 5 (2015) 4629-4636.
- [85] I.A. Ike, L.F. Dumée, A. Groth, J.D. Orbell, M. Duke, Effects of dope sonication and hydrophilic polymer addition on the properties of low pressure PVDF mixed matrix membranes, Journal of Membrane Science, 540 (2017) 200-211.
- [86] R.A. Crane, T.B. Scott, Nanoscale zero-valent iron: future prospects for an emerging water treatment technology, J Hazard Mater, 211-212 (2012) 112-125.
- [87] C.d.M. Donega, Nanoparticles, the workhorses of nanoscience, Springer, Heidelberg, 2014.
- [88] M.A. Al-Shamsi, N.R. Thomson, S.P. Forsey, Iron based bimetallic nanoparticles to activate peroxygens, Chemical Engineering Journal, 232 (2013) 555-563.

- [89] H.T. Madsen, Membrane Filtration in Water Treatment – Removal of Micropollutants, in: Chemistry of Advanced Environmental Purification Processes of Water, Elsevier B.V., 2014, pp. 199-248.
- [90] J. Yan, M. Lei, L. Zhu, M.N. Anjum, J. Zou, H. Tang, Degradation of sulfamonomethoxine with Fe<sub>3</sub>O<sub>4</sub> magnetic nanoparticles as heterogeneous activator of persulfate, *Journal of Hazardous Materials*, 186 (2011) 1398–1404.
- [91] R. Marsac, S. Martin, J.-F. Boily, K. Hanna, Oxolinic acid binding at goethite and akaganéite surfaces: experimental study and modeling, *Environmental Science & Technology*, 50 (2016) 660–668.
- [92] S.H. Do, Y.J. Kwon, S.H. Kong, Effect of metal oxides on the reactivity of persulfate/Fe(II) in the remediation of diesel-contaminated soil and sand, *J Hazard Mater*, 182 (2010) 933-936.
- [93] M. Ahmad, A.L. Teel, R.J. Watts, Persulfate activation by subsurface minerals, *J Contam Hydrol*, 115 (2010) 34-45.
- [94] A.L. Teel, M. Ahmad, R.J. Watts, Persulfate activation by naturally occurring trace minerals, *J Hazard Mater*, 196 (2011) 153-159.
- [95] M. Usman, P. Faure, K. Hanna, M. Abdelmoula, C. Ruby, Application of magnetite catalyzed chemical oxidation (Fenton-like and persulfate) for the remediation of oil hydrocarbon contamination, *Fuel*, 96 (2012) 270-276.
- [96] J. Yan, L. Zhu, Z. Luo, Y. Huang, H. Tang, M. Chen, Oxidative decomposition of organic pollutants by using persulfate with ferrous hydroxide colloids as efficient heterogeneous activator, *Separation and Purification Technology*, 106 (2013) 8-14.
- [97] H.-y. Liang, Y.-q. Zhang, S.-b. Huang, I. Hussain, Oxidative degradation of p-chloroaniline by copper oxide activated persulfate, *Chemical Engineering Journal*, 218 (2013) 384-391.
- [98] Y.H. Jo, S.H. Do, S.H. Kong, Persulfate activation by iron oxide-immobilized MnO<sub>2</sub> composite: identification of iron oxide and the optimum pH for degradations, *Chemosphere*, 95 (2014) 550-555.
- [99] I.A. Ike, J.D. Orbell, M. Duke, Nanoparticle incorporation into desalination and water treatment membranes—potential advantages and challenges, in: H.A. Arafat (Ed.) *Desalination Sustainability - A Technical, Socioeconomic, and Environmental Approach*, Elsevier, Netherlands, 2017, pp. 261 - 303.

- [100] H. Lee, H.-i. Kim, S. Weon, W. Choi, Y.S. Hwang, J. Seo, C. Lee, J.-H. Kim, Activation of Persulfates by Graphitized Nanodiamonds for Removal of Organic Compounds, *Environmental Science & Technology*, 50 (2016) 10134–10142.
- [101] X. Duan, C. Su, L. Zhou, H. Sun, A. Suvorova, T. Odedairo, Z. Zhu, Z. Shao, S. Wang, Surface controlled generation of reactive radicals from persulfate by carbocatalysis on nanodiamonds, *Applied Catalysis B: Environmental*, 194 (2016) 7–15.
- [102] H. Sun, C. Kwan, A. Suvorova, H.M. Ang, M.O. Tadé, S. Wang, Catalytic oxidation of organic pollutants on pristine and surface nitrogen-modified carbon nanotubes with sulfate radicals, *Applied Catalysis B: Environmental*, 154-155 (2014) 134-141.
- [103] H. Lee, H.-J. Lee, J. Jeong, J. Lee, N.-B. Park, C. Lee, Activation of persulfates by carbon nanotubes: Oxidation of organic compounds by nonradical mechanism, *Chemical Engineering Journal*, 266 (2015) 28-33.
- [104] R. Girardello, S. Tasselli, N. Baranzini, R. Valvassori, M. de Eguileor, A. Grimaldi, Effects of Carbon Nanotube Environmental Dispersion on an Aquatic Invertebrate, *Hirudo medicinalis*, PLoS One, 10 (2015) e0144361.
- [105] Y.C. Lee, S.L. Lo, J. Kuo, C.P. Huang, Promoted degradation of perfluorooctanic acid by persulfate when adding activated carbon, *J Hazard Mater*, 261 (2013) 463-469.
- [106] S. Yang, X. Yang, X. Shao, R. Niu, L. Wang, Activated carbon catalyzed persulfate oxidation of Azo dye acid orange 7 at ambient temperature, *J Hazard Mater*, 186 (2011) 659-666.
- [107] M. Pu, Y. Ma, J. Wan, Y. Wang, M. Huang, Y. Chen, Fe/S doped granular activated carbon as a highly active heterogeneous persulfate catalyst toward the degradation of Orange G and diethyl phthalate, *Journal of colloid and interface science*, 418 (2014) 330-337.
- [108] C. Liang, Y.-T. Lin, W.-H. Shih, Treatment of Trichloroethylene by Adsorption and Persulfate Oxidation in Batch Studies, *Industrial & Engineering Chemistry Research*, 48 (2009) 8373–8380.
- [109] G. Fang, C. Liu, J. Gao, D.D. Dionysiou, D. Zhou, Manipulation of Persistent Free Radicals in Biochar To Activate Persulfate for Contaminant Degradation, *Environmental Science & Technology*, 49 (2015 ) 5645–5653.

- [110] M. Ahmad, A.L. Teel, R.J. Watts, Mechanism of persulfate activation by phenols, *Environ Sci Technol*, 47 (2013) 5864-5871.
- [111] A.M. Ocampo, Persulfate Activation by Organic Compounds, in: Department of Civil and Environmental Engineering, Washington State University, 2009.
- [112] C. Tan, N. Gao, Y. Deng, W. Rong, S. Zhou, N. Lu, Degradation of antipyrine by heat activated persulfate, *Separation and Purification Technology*, 109 (2013) 122-128.
- [113] X. Chen, M. Murugananthan, Y. Zhang, Degradation of p-Nitrophenol by thermally activated persulfate in soil system, *Chemical Engineering Journal*, 283 (2016) 1357-1365.
- [114] O.S. Furman, A.L. Teel, R.J. Watts, Mechanism of Base Activation of Persulfate, *Environmental Science & Technology*, (2010) 6423–6428.
- [115] O.S. Furman, A.L. Teel, M. Ahmad, M.C. Merker, R.J. Watts, Effect of Basicity on Persulfate Reactivity, *Journal of Environmental Engineering*, 137 (2011) 241-247.
- [116] U. Chandra Singh, K. Venkataraao, Decomposition of peroxodisulphate in aqueous alkaline solution, *Journal of Inorganic & Nuclear Chemistry*, 38 (1976) 541-543.
- [117] C. Liang, H.-W. Su, Identification of sulfate and hydroxyl radicals in thermally activated persulfate, *Industrial & Engineering Chemistry*, 48 (2009) 5558–5562.
- [118] L.W. Matzek, K.E. Carter, Activated persulfate for organic chemical degradation: A review, *Chemosphere*, 151 (2016) 178-188.
- [119] P.D. Goulden, D.H.J. Anthony, Kinetics of uncatalyzed peroxydisulfate oxidation of organic material in fresh water, *Analytical Chemistry*, 50 (2002) 953-958.
- [120] Y.C. Lee, S.L. Lo, P.T. Chiueh, D.G. Chang, Efficient decomposition of perfluorocarboxylic acids in aqueous solution using microwave-induced persulfate, *Water Res*, 43 (2009) 2811-2816.
- [121] Y. Deng, C.M. Ezyske, Sulfate radical-advanced oxidation process (SR-AOP) for simultaneous removal of refractory organic contaminants and ammonia in landfill leachate, *Water Res*, 45 (2011) 6189-6194.

- [122] C. Liang, Z.S. Wang, C.J. Bruell, Influence of pH on persulfate oxidation of TCE at ambient temperatures, *Chemosphere*, 66 (2007) 106-113.
- [123] X.-Y. Yu, Z.-C. Bao, J.R. Barker, Free Radical Reactions Involving Cl<sup>•</sup>, Cl<sub>2</sub><sup>•</sup>, and SO<sub>4</sub><sup>2-</sup> in the 248 nm Photolysis of Aqueous Solutions Containing S<sub>2</sub>O<sub>8</sub><sup>2-</sup> and Cl<sup>-</sup>, *Journal of Physical Chemistry A*, 108 (2004) 295–308.
- [124] K.C. Huang, Z. Zhao, G.E. Hoag, A. Dahmani, P.A. Block, Degradation of volatile organic compounds with thermally activated persulfate oxidation, *Chemosphere*, 61 (2005) 551-560.
- [125] K.-C. Huang, R.A. Couttenye, G.E. Hoag, Kinetics of heat-assisted persulfate oxidation of methyl tert-butyl ether (MTBE), *Chemosphere*, 49 (2002) 413–420.
- [126] D. Deng, L. Peng, M. Guan, Y. Kang, Impact of activation methods on persulfate oxidation of methyl tert-butyl ether, *J Hazard Mater*, 264 (2014) 521-528.
- [127] C. Tan, N. Gao, Y. Deng, N. An, J. Deng, Heat-activated persulfate oxidation of diuron in water, *Chemical Engineering Journal*, 203 (2012) 294-300.
- [128] A. Ghauch, A.M. Tuqan, N. Kibbi, Ibuprofen removal by heated persulfate in aqueous solution: A kinetics study, *Chemical Engineering Journal*, 197 (2012) 483-492.
- [129] A. Ghauch, A.M. Tuqan, N. Kibbi, S. Geryes, Methylene blue discoloration by heated persulfate in aqueous solution, *Chemical Engineering Journal*, 213 (2012) 259-271.
- [130] A. Ghauch, A.M. Tuqan, Oxidation of bisoprolol in heated persulfate/H<sub>2</sub>O systems: Kinetics and products, *Chemical Engineering Journal*, 183 (2012) 162-171.
- [131] D. Zhao, X. Liao, X. Yan, S.G. Huling, T. Chai, H. Tao, Effect and mechanism of persulfate activated by different methods for PAHs removal in soil, *J Hazard Mater*, 254-255 (2013) 228-235.
- [132] E. Hayon, A. Treinin, J. Wilf, Electronic Spectra, Photochemistry, and Autoxidation Mechanism of the Sulfite-Bisulfite-Pyrosulfite Systems. The SO<sub>2</sub><sup>+</sup>, SO<sub>3</sub><sup>2-</sup>, SO<sub>4</sub><sup>2-</sup>, and SO<sub>5</sub><sup>2-</sup> Radicals, *Journal of American Chemical Society*, 94 (1972) 47–57.
- [133] Y. Marcus, G. Hefter, Ion Pairing, *Chemical Review*, 106 (2006) 4585–4621.

- [134] H. Hori, Y. Nagaoka, M. Murayama, S. Kutsuna, Efficient Decomposition of Perfluorocarboxylic Acids and Alternative Fluorochemical Surfactants in Hot Water, *Environmental Science & Technology*, 42 (2008) 7438–7443.
- [135] M.-S. Tsao, W.K. Wilmarth, The Aqueous Chemistry of Inorganic Free Radicals. I. The Mechanism of the Photolytic Decomposition of Aqueous Persulfate Ion and Evidence Regarding the Sulfate–Hydroxyl Radical Interconversion Equilibrium, *Journal of Physical Chemistry*, 63 (1959) 346–353.
- [136] X.-Y. Xu, G.-M. Zeng, Y.-R. Peng, Z. Zeng, Potassium persulfate promoted catalytic wet oxidation of fulvic acid as a model organic compound in landfill leachate with activated carbon, *Chemical Engineering Journal*, 200–202 (2012) 25–31.
- [137] M.Z. Stijepovic, P. Linke, Optimal waste heat recovery and reuse in industrial zones, *Energy* 36 (2011) 4019-4031.
- [138] R. Law, A. Harvey, D. Reay, Opportunities for low-grade heat recovery in the UK food processing industry, *Applied Thermal Engineering*, 53 (2013) 188-196.
- [139] S. Garimella, Low-grade waste heat recovery for simultaneous chilled and hot water generation, *Applied Thermal Engineering*, 42 (2012) 191-198.
- [140] E. Pulat, A.B. Etemoglu, M. Can, Waste-heat recovery potential in Turkish textile industry: Case study for city of Bursa, *Renewable and Sustainable Energy Reviews*, 13 (2009) 663-672.
- [141] Y.-J. Shih, Y.-C. Li, Y.-H. Huang, Application of UV/persulfate oxidation process for mineralization of 2,2,3,3-tetrafluoro-1-propanol, *Journal of the Taiwan Institute of Chemical Engineers*, 44 (2013) 287-290.
- [142] Y.T. Lin, C. Liang, J.H. Chen, Feasibility study of ultraviolet activated persulfate oxidation of phenol, *Chemosphere*, 82 (2011) 1168-1172.
- [143] C. Luo, J. Jiang, J. Ma, S. Pang, Y. Liu, Y. Song, C. Guan, J. Li, Y. Jin, D. Wu, Oxidation of the odorous compound 2,4,6-trichloroanisole by UV activated persulfate: Kinetics, products, and pathways, *Water Res*, 96 (2016) 12-21.
- [144] C.-W. Wang, C. Liang, Oxidative degradation of TMAH solution with UV persulfate activation, *Chemical Engineering Journal*, 254 (2014) 472-478.
- [145] Y.-q. Gao, N.-y. Gao, Y. Deng, Y.-q. Yang, Y. Ma, Ultraviolet (UV) light-activated persulfate oxidation of sulfamethazine in water, *Chemical Engineering Journal*, 195-196 (2012) 248-253.

- [146] D. An, P. Westerhoff, M. Zheng, M. Wu, Y. Yang, C.A. Chiu, UV-activated persulfate oxidation and regeneration of NOM-Saturated granular activated carbon, *Water Res.*, 73 (2015) 304-310.
- [147] Y. Chen, P. Xie, Z. Wang, R. Shang, S. Wang, UV/persulfate preoxidation to improve coagulation efficiency of *Microcystis aeruginosa*, *J Hazard Mater.*, 322 (2017) 508-515.
- [148] W. Chu, D. Li, N. Gao, M.R. Templeton, C. Tan, Y. Gao, The control of emerging haloacetamide DBP precursors with UV/persulfate treatment, *Water Res.*, 72 (2015) 340-348.
- [149] X. He, A.A. de la Cruz, D.D. Dionysiou, Destruction of cyanobacterial toxin cylindrospermopsin by hydroxyl radicals and sulfate radicals using UV-254nm activation of hydrogen peroxide, persulfate and peroxymonosulfate, *Journal of Photochemistry and Photobiology A: Chemistry*, 251 (2013) 160-166.
- [150] G. Wang, D. Wang, X. Dong, X. Zhang, H. Ma, Sodium persulfate based PVDF membrane for concurrent advanced oxidation and ultrafiltration of ofloxacin in water, *Chemical Engineering Journal* 315 (2017) 509–515.
- [151] H.V. Lutze, R. Bakkour, N. Kerlin, C. von Sonntag, T.C. Schmidt, Formation of bromate in sulfate radical based oxidation: mechanistic aspects and suppression by dissolved organic matter, *Water Res.*, 53 (2014) 370-377.
- [152] C.-C. Lin, M.-S. Wu, UV/S<sub>2</sub>O<sub>8</sub>2- process for degrading polyvinyl alcohol in aqueous solutions, *Chemical Engineering and Processing: Process Intensification*, 85 (2014) 209-215.
- [153] Y. Guo, J. Zhou, X. Lou, R. Liu, D. Xiao, C. Fang, Z. Wang, J. Liu, Enhanced degradation of Tetrabromobisphenol A in water by a UV/base/persulfate system: Kinetics and intermediates, *Chemical Engineering Journal*, 254 (2014) 538-544.
- [154] B.R. Scanlon, B.L. Ruddell, P.M. Reed, R.I. Hook, C. Zheng, V.C. Tidwell, S. Siebert, The food-energy-water nexus: Transforming science for society, *Water Resources Research*, 53 (2017) 3550-3556.
- [155] R. Toor, M. Mohseni, UV-H<sub>2</sub>O<sub>2</sub> based AOP and its integration with biological activated carbon treatment for DBP reduction in drinking water, *Chemosphere*, 66 (2007) 2087-2095.
- [156] Z. Wei, F.A. Villamena, L.K. Weavers, Kinetics and Mechanism of Ultrasonic Activation of Persulfate: An in Situ EPR Spin Trapping Study, *Environmental Science & Technology*, 51 (2017) 3410–3417.

- [157] S. Wang, N. Zhou, Removal of carbamazepine from aqueous solution using sono-activated persulfate process, *Ultrasonics sonochemistry*, 29 (2016) 156-162.
- [158] B. Darsinou, Z. Frontistis, M. Antonopoulou, I. Konstantinou, D. Mantzavinos, Sono-activated persulfate oxidation of bisphenol A: Kinetics, pathways and the controversial role of temperature, *Chemical Engineering Journal*, 280 (2015) 623-633.
- [159] B. Li, J. Zhu, Simultaneous degradation of 1,1,1-trichloroethane and solvent stabilizer 1,4-dioxane by a sono-activated persulfate process, *Chemical Engineering Journal*, 284 (2016) 750-763.
- [160] S. Chakma, S. Praneeth, V.S. Moholkar, Mechanistic investigations in sono-hybrid (ultrasound/Fe<sup>2+</sup>/UVC) techniques of persulfate activation for degradation of Azorubine, *Ultrasonics sonochemistry*, 38 (2017) 652-663.
- [161] P. Neta, V. Madhavan, H. Zemel, R.W. Fessenden, Rate constants and mechanism of reaction of SO<sub>4</sub><sup>2-</sup> with aromatic compounds, *Journal of American Chemical Society*, 99 (1977) 163–164.
- [162] J. Paul (Guin), D.B. Naik, Y.K. Bhardwaj, L. Varshney, Studies on oxidative radiolysis of ibuprofen in presence of potassium persulfate, *Radiation Physics and Chemistry*, 100 (2014) 38-44.
- [163] A. Tsitonaki, B.F. Smets, P.L. Bjerg, Effects of heat-activated persulfate oxidation on soil microorganisms, *Water Res*, 42 (2008) 1013-1022.
- [164] R.L. Johnson, P.G. Tratnyek, R.O.b. Johnson, Persulfate Persistence under Thermal Activation Conditions, *Environmental Science & Technology*, 42 (2008) 9350–9356.
- [165] Y. Feng, D. Wu, C. Liao, Y. Deng, T. Zhang, K. Shih, Red mud powders as low-cost and efficient catalysts for persulfate activation: Pathways and reusability of mineralizing sulfadiazine, *Separation and Purification Technology*, 167 (2016) 136-145.
- [166] I.D. Ferreira, T. Prieto, J.G. Freitas, N.R. Thomson, I.L. Nantes, E.J.H. Bechara, Natural Persulfate Activation for Anthracene Remediation in Tropical Environments, *Water, Air, & Soil Pollution*, 228 (2017).
- [167] K.S. Sra, N.R. Thomson, J.F. Barker, Persulfate injection into a gasoline source zone, *Journal of Contaminant Hydrology* 150 (2013) 35–44.

- [168] S. Waclawek, K. Grubel, M. Cernik, The impact of peroxydisulphate and peroxymonosulphate on disintegration and settleability of activated sludge, Environ Technol, 37 (2016) 1296-1304.
- [169] H. Zhang, Z. Wang, C. Liu, Y. Guo, N. Shan, C. Meng, L. Sun, Removal of COD from landfill leachate by an electro/Fe<sup>2+</sup>/peroxydisulfate process, Chemical Engineering Journal, 250 (2014) 76-82.
- [170] S.S.A. Amra, H.A. Aziz, M.N. Adlan, M.J.K. Bashir, Pretreatment of stabilized leachate using ozone/persulfate oxidation process, Chemical Engineering Journal, 221 (2013) 492-499.
- [171] N.E. Khan, Y.G. Adewuyi, Absorption and Oxidation of Nitric Oxide (NO) by Aqueous Solutions of Sodium Persulfate in a Bubble Column Reactor, Industrial & Engineering Chemistry Research, 49 (2010) 8749–8760.
- [172] Y.G. Adewuyi, N.Y. Sakyi, Simultaneous Absorption and Oxidation of Nitric Oxide and Sulfur Dioxide by Aqueous Solutions of Sodium Persulfate Activated by Temperature, Industrial & Engineering Chemistry Research, 52 (2013) 11702-11711.
- [173] A.B. Little, S. Garimella, Comparative assessment of alternative cycles for waste heat recovery and upgrade, Energy, 36 (2011) 4492-4504.
- [174] C. Binnie, M. Kimber, Basic Water Treatment, in, ICE Publishing, London, 2013.
- [175] S. Ahn, T.D. Peterson, J. Righter, D.M. Miles, P.G. Tratnyek, Disinfection of ballast water with iron activated persulfate, Environ Sci Technol, 47 (2013) 11717-11725.
- [176] D. Xia, Y. Li, G. Huang, R. Yin, T. An, G. Li, H. Zhao, A. Lu, P.K. Wong, Activation of persulfates by natural magnetic pyrrhotite for water disinfection: Efficiency, mechanisms, and stability, Water Res, 112 (2017) 236-247.
- [177] WHO, Iron in drinking-water, in: Background document for development of WHO Guidelines for Drinking-water Quality, World Health Organization, [http://www.who.int/water\\_sanitation\\_health/dwq/chemicals/iron.pdf](http://www.who.int/water_sanitation_health/dwq/chemicals/iron.pdf), 2003.
- [178] WHO, Silver in drinking-water, in: Background document for development of WHO Guidelines for Drinking-water Quality, World Health Organization, [http://www.who.int/water\\_sanitation\\_health/dwq/chemicals/silver.pdf](http://www.who.int/water_sanitation_health/dwq/chemicals/silver.pdf), 2003.
- [179] WHO, Copper in Drinking-water, in: Background document for development of WHO Guidelines for Drinking-water Quality, World Health

Organization,

[http://www.who.int/water\\_sanitation\\_health/dwq/chemicals/copper.pdf](http://www.who.int/water_sanitation_health/dwq/chemicals/copper.pdf), 2004.

[180] WHO, Manganese in Drinking-water, in: Background document for development of WHO Guidelines for Drinking-water Quality, World Health Organization,

[http://www.who.int/water\\_sanitation\\_health/dwq/chemicals/manganese.pdf](http://www.who.int/water_sanitation_health/dwq/chemicals/manganese.pdf),

2011.

[181] WHO, Sulfate in drinking-water, in: Background document for development of WHO Guidelines for Drinking-water Quality, World Health Organization,

[http://www.who.int/water\\_sanitation\\_health/dwq/chemicals/sulfate.pdf](http://www.who.int/water_sanitation_health/dwq/chemicals/sulfate.pdf)

2004.

[182] T. Fujioka, S.J. Khan, Y. Poussade, J.E. Drewes, L.D. Nghiem, N-nitrosamine removal by reverse osmosis for indirect potable water reuse – A critical review based on observations from laboratory-, pilot- and full-scale studies, *Separation and Purification Technology*, 98 (2012) 503-515.

[183] T. Wintgens, T. Melin, A. Schäfer, S. Khan, M. Muston, D. Bixio, C. Thoeye, The role of membrane processes in municipal wastewater reclamation and reuse, *Desalination*, 178 (2005) 1-11.

[184] A.A. Alturki, N. Tadkaew, J.A. McDonald, S.J. Khan, W.E. Price, L.D. Nghiem, Combining MBR and NF/RO membrane filtration for the removal of trace organics in indirect potable water reuse applications, *Journal of Membrane Science*, 365 (2010) 206-215.

[185] D. Bixio, C. Thoeye, J. De Koning, D. Joksimovic, D. Savic, T. Wintgens, T. Melin, *Wastewater reuse in Europe*, *Desalination*, 187 (2006) 89-101.

[186] W. Guo, H.H. Ngo, J. Li, A mini-review on membrane fouling, *Bioresource technology*, 122 (2012) 27-34.

[187] T. Fujioka, N. Oshima, R. Suzuki, S.J. Khan, A. Roux, Y. Poussade, J.E. Drewes, L.D. Nghiem, Rejection of small and uncharged chemicals of emerging concern by reverse osmosis membranes: The role of free volume space within the active skin layer, *Separation and Purification Technology*, 116 (2013) 426-432.

[188] S.O. Ganiyu, E.D. van Hullebusch, M. Cretin, G. Esposito, M.A. Oturan, Coupling of membrane filtration and advanced oxidation processes for removal

of pharmaceutical residues: A critical review, Separation and Purification Technology, 156 (2015) 891-914.

## Chapter 6

**Advanced oxidation of orange G using phosphonic acid stabilised zerovalent iron\*****Abstract**

Orange G (OG) is an important chemical for the textile industry but also a major water contaminant. It is also a model compound representing more toxic azo dyes and degradation products. Activation of persulphate (PS) by zerovalent iron nanoparticles (nZVI) has been proposed as an effective technique to degrade OG even at neutral pH conditions. However, particle agglomeration leads to diminished reactivity and remains a crucial challenge for nZVI applications. This work evaluates the performance of three different nZVI that are each stabilised with one of three phosphonic acids, ATMP, DTPMP or HTPMP. While ATMP- and DTPMP-stabilised nZVI were practically inert to OG solution in the absence of PS, HTPMP-stabilised nZVI achieved ~15% total carbon (TC) reduction under similar conditions. However, in the presence of PS, ATMP- and DTPMP-stabilised nZVI resulted in degradation rate constants that were double the rate constant obtained for HTPMP-stabilised nZVI under similar conditions. These results highlight the important role of both stabilisers and PS in modulating nZVI activity with potential niche application. A desirable feature of the PS-nZVI degradation mechanism is the rapid destruction of both the azo bond and benzene ring in OG, resulting in fewer, and less toxic, degradation products than have been previously reported. Significant mineralisation was recorded in longer term experiments, where 90% organic carbon reduction was achieved in 48 h for the three stabilised nZVI. Hence, phosphonate-stabilised nZVI activation of PS is an effective means to achieve complete OG degradation and significant mineralisation with non-toxic major degradation product.

\*Published in Journal of Environmental Chemical Engineering -  
<https://doi.org/10.1016/j.jece.2017.07.069>. See the Appendix for list of contributors.

## 6.1. Introduction

One of the major challenges of industrialisation in many parts of the world is the attendant release of waste streams containing non-biodegradable and potentially dangerous chemicals into water bodies or waste management systems. In the textile industry, azo dyes such as Orange G (OG) which are popular for their stability and versatility but are non-biodegradable, toxic and potentially carcinogenic [1, 2], are common examples of water contaminants. To protect water resources, effective treatment systems should be deployed before such waste streams are discharged into the environment or reused [2]. The basic properties of OG are presented in Table 6.1. It can be seen that, structurally, OG is representative of other more toxic dyes such as o-aminoazotoluene [3] and may potentially produce other toxic aromatic compounds such as 2-naphthylamine and benzidine [3] upon degradation. Consequently, OG serves as a useful model compound for studying the fate of variant toxic azo dyes and intermediate degradation products during wastewater treatment.

Table 6.1. Basic properties of Orange G

Common names	Molar mass (g/mol)	Molecular formula	Structural formula	$\lambda_{\text{max}}$ (nm)
Orange G, Acid orange 10	452.4	C <sub>16</sub> H <sub>10</sub> N <sub>2</sub> Na <sub>2</sub> O <sub>7</sub> S <sub>2</sub>		478

In the last two decades, the persulphate (PS)-based advanced oxidation process (AOP) has been widely studied as an effective technique for the degradation of OG in water [1, 2, 4-7]. The relatively high redox potential of 2.01 V reported for PS ( $S_2O_8^{2-}$ ) makes it a valuable oxidant for micropollutant degradation [2]. In addition, PS can be readily activated chemically [2] or by irradiation using heat [8], sonication and/or UV [7, 9] to yield the reactive sulphate radical ( $SO_4^{\cdot-}$ ), with

a standard redox potential of 2.6 V [6]. Homogenous activation of persulphate using Fe(II) has been shown to provide rapid degradation of OG [1]. However, Fe(II) activation is short-lived and requires repeated supply to sustain reactions [7] and such reactions can only be effectively maintained under low pH (e.g. pH 3.5) which may not be feasible in many practical conditions [6, 10]. Furthermore, Fe(II) inactivation, which results from oxidation to insoluble Fe(III), is also an important process challenge as well as the addition of accompanying anion which may inhibit the radical reaction and/or constitute secondary pollution [1, 7, 10, 11]. An alternative fast and sustainable activation of PS for OG degradation under neutral or close to neutral conditions and without the inclusion of additional anion has been achieved using zerovalent iron (ZVI) [7, 10]. It has been shown that as the size of the ZVI decreases, the rate of the surface-mediated chemical reactions increases [12, 13]. Consequently, nano ZVI (nZVI) provides an effective route for PS-activated degradation of OG [10]. However, the high surface energy and polydispersity of commonly synthesised nZVI using borohydride reduction of ferrous salts predisposes the nanoparticles to significant aggregation and leads to a loss of reactivity [12-15]. To prevent aggregation, surface stabilisation is often employed via polymers such as soluble starch and carboxymethyl cellulose [12, 13, 15]. The strong coordinating power of phosphate functional groups for ionised Fe has recently been identified as an effective means of producing stabilised nZVI [15]. In particular, the effectiveness of the stabilisation, measured by average particle size, appears to depend on the particular phosphonic acid used [15]. Greenlee and Hooker [15] presented nZVI stabilisation results using three different organophosphorus compounds, amino tri (methylene phosphonic acid) (ATMP), diethylenetriamine penta (methylene phosphonic acid) (DTPMP), and bis (hexamethylene triamine penta (methylenephosphonic acid)) (HTPMP). The results showed that although all three compounds resulted in bimodal particle distributions as measured by dynamic light scattering (DLS), a large fraction of the nZVI stabilised by ATMP or DTPMP were between 10-20 nm, while the majority of the HTPMP-stabilised nZVI were >100 nm. Hereafter ATMP-, DTPMP- and HTPMP-stabilised nZVI are referred to as AT-nZVI, DT-nZVI and HT-nZVI, respectively. In addition to the important effect of particle surface area on reactivity, it has been shown that the degree of surface oxidation [16], and possibly the nature of the stabilising agent [12], may greatly influence the

performance of stabilised nZVI for pollutant degradation. The focus of this work was thus to explore for the first time the performance of AT-nZVI, DT-nZVI and HT-nZVI towards the activation of PS for OG degradation. The stabilised nZVI were characterised by scanning electron microscopy (SEM), Fourier transform infrared (FTIR) spectroscopy, x-ray diffraction (XRD), and N<sub>2</sub> porosimetry. Batch degradation results were conducted with and without PS. The degradation processes were monitored by UV-Visible (UV-Vis) spectroscopy, high performance liquid chromatography (HPLC) and carbon content analysis. The amount of dissolved Fe was measured by atomic adsorption spectroscopy (AAS).

## 6.2. Material and methods

### 6.2.1. Materials

OG, sodium salt, from Sigma and disodium peroxodisulphate (sodium persulphate) from BDH (99%) were used for the batch degradation experiments. Water from MerckMillipore Water Purification System (hereafter referred to as MilliQ water) was used throughout the study. ACS grade ferrous sulphate heptahydrate and sodium borohydride were used for nZVI synthesis. ATMP, DTPMP and HTPMP were obtained as samples from Dequest Water Management Additives. ACS grade methanol from HoneyWell (99.9%) and propanol-1 from BDH (99%) were used as radical inhibitors [17].

### 6.2.2. Methods

nZVI were synthesised as previously reported [18-20]. Briefly, nanoparticles were synthesised in an aqueous batch process using a borosilicate glass three-neck flask. ATMP, DTPMP or HTPMP was added to purified water, and then ferrous sulphate heptahydrate was premixed with purified water and added for a final solution of 1 g/L as Fe and a phosphonate to Fe ratio of 0.05:1 (mol:mol). This solution was mixed under argon for 15 min with an orbital shaker. After mixing, sodium borohydride was premixed with purified water and added to the synthesis solution dropwise via a syringe. The target ratio of borohydride to Fe was 2.2:1 (mol:mol). After complete addition of the borohydride solution, the synthesis solution was mixed under vacuum for 15 min. Upon addition of the sodium borohydride, the solution became black, indicating Fe reduction and nanoparticle

formation. After 15 min under vacuum, the nanoparticle solution was transferred to centrifuge tubes and centrifuged at 7,000 rcf to separate the particles from the remaining synthesis salts. The particles were resuspended in Ar-bubbled water and lyophilised. Nanoparticles were deposited onto conductive carbon tabs attached to aluminium stubs and imaged with a field emission SEM, FEI Nova Nanolab 200 Dual-Beam Workstation.

Lyophilised stabilised nZVI were characterised by FTIR spectroscopy to evaluate the predominant surface functional groups of the particles. FTIR scans from 4000 to 600 cm<sup>-1</sup> at 32 accumulations and a resolution of 4 cm<sup>-1</sup> were collected for the stabilised nZVI and the respective stabilising phosphonic acid compounds using a Perkin Elmer FTIR Spectrometer with Universal ATR Diamond/ZnSe crystals. XRD peak pattern was obtained using a Rigaku Miniflex 600 diffractometer, with Cu K $\alpha$  X-ray (1.541862 Å wavelength) operated at 40 kV and 15 mA at a step size of 0.02° and speed of 1.5 °/min from 2θ 20° to 70° with Ni K $\beta$ -filter (x2) and a D/tex detector. PDXL version 2 software was used for crystallite size calculation. N<sub>2</sub> porosimetry for particle surface area determination using the Brunauer–Emmett–Teller (BET) model was conducted using a Micrometrics TriStar Surface Area and Porosity Analyser with TriStar 3000 version 6.04 analysis software.

Batch degradation experiments were conducted at ~24 °C with unbuffered 0.1 mM OG solutions having an inherent pH of 6. In the absence of PS, 0.05g AT-nZVI, DT-nZVI and HT-nZVI were individually added to 100 ml OG solutions and stirred magnetically in a 250 ml glass conical flask. 1 ml samples of the reacting suspensions were taken at designated intervals using a syringe and filtered through a 0.2 µm syringe filter into a 1.7 ml microtube containing 0.5 ml methanol to quench the reactions [4]. At the end of the 60 min for this particular set of experiments, the particulate reactants were washed several times with MilliQ water and magnetically separated after which they were dried at 60 °C. The surface functional groups as identified by FTIR before and after these reactions were compared. The effect of PS on the rate of OG degradation was evaluated by adding 1ml or 0.1 ml of 1 mole PS solution to the OG solution to give a PS concentration of 10 mM or 1 mM respectively after which a designated mass,

0.05g or 0.01g, of stabilized nZVI was immediately added. The reacting suspensions were sampled as previously described.

The rates of OG degradation were measured spectrophotometrically at the azo bond characteristic absorption wavelength of 478 nm [1] using a Biochrom Libra S22 UV/Visible Spectrophotometer. UV-visible spectral studies of OG degradation were conducted using a Shimadzu UV-1800 UV spectrophotometer between wavelengths of 200 nm and 600 nm. Care was taken to ensure that absorbance values were less than 2 as recommended in the literature [21] by diluting dissolved samples in MilliQ water as required. A HPLC study of OG degradation was conducted using a Shimadzu Prominence-i LC 2030C Liquid Chromatograph with a UV detector at 280 nm. The column used was Kinetex C18 5 $\mu$  100 Å, size 100 x 4.6 mm, and maintained at 25 °C. Binary solvent linear gradient flow at 0.8 ml/min was employed in which the concentration of solvent A, methanol, was increased from 30% to 90% in 10 min, maintained at 90% for 2.50 min and then rapidly decreased to 30% in 0.30 min. At this composition (A 30%), the column was equilibrated for 7.30 min. Solvent B was 50 mM ammonium phosphate at a pH of 6.8. Further peak analysis was conducted with a Shimadzu LC-20AT Liquid Chromatography equipped with diode array detector (DAD) under LC conditions already described. An exception was the column temperature, which was ambient in the DAD analysis. Total carbon (TC) and non-purgeable organic carbon (NPOC) were determined using a Shimadzu TOC-V<sub>CSH</sub> Total Organic Carbon Analyzer. Samples for TC/NPOC analysis were filtered through a 0.2  $\mu$ m filter immediately after collection. The samples were not quenched in methanol to avoid introduction of additional large amount of carbon that may diminish analysis sensitivity. Instead, such samples were immediately stored at 4 °C to halt or minimize further PS reactions [22] and TC/NPOC analyses were conducted and completed a few hours after samples were collected. Dissolved Fe was measured using a Shimadzu atomic adsorption spectroscopy AA-6300 with Fe flame at a wavelength of 372 nm after samples were filtered through a 0.2  $\mu$ m syringe filter.

### 6.3. Results and discussion

#### 6.3.1. Nanoparticle characterisation

Field emission SEM was used to obtain images of the nanoparticles and confirm synthesis. Representative images of AT-nZVI, DT-nZVI, and HT-nZVI are shown in Figure 6.1. The results in the images suggest agglomerates of small nanoparticles surrounded by a visible film, which is assumed to be the stabiliser coating. From these images, it is difficult to evaluate particle size in detail due to the stabiliser coating; similar results in a previous work [15] motivated the use of DLS as a supplemental tool to investigate nanoparticle size. However, these images confirm the formation of nano-sized particles which are distinctly spherical for AT-nZVI but less so for HT-nZVI.

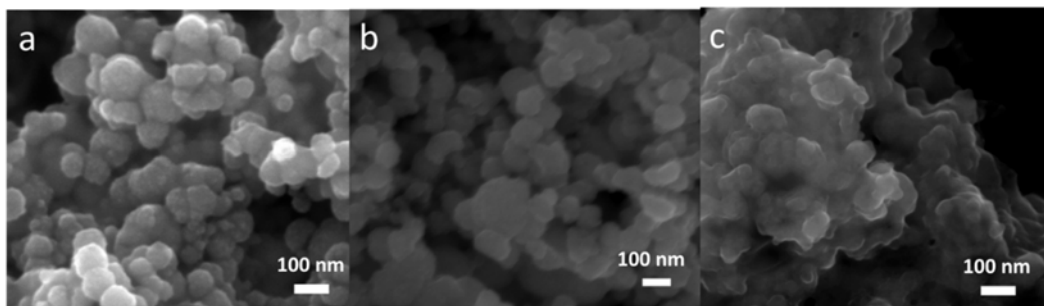


Figure 6.1. Scanning electron microscopy images of AT-nZVI (a), DT-nZVI (b), and HT-nZVI (c).

The XRD patterns for the stabilised nZVI after lyophilisation are shown in Figure 6.2. The characteristic peak for  $\text{Fe}^0$  at  $2\theta$  of  $45^\circ$  [23, 24] can be recognised as a broad peak in AT-nZVI but is less evident in DT-nZVI and much less evident in HT-nZVI suggesting decreasing crystallinity in the order AT-nZVI > DT-nZVI > HT-nZVI. The broad peak for  $\text{Fe}^0$  is suggestive of nanosize crystals [25, 26]. The peak analysis software returned a crystallite size of 2.3 nm using the  $45^\circ$   $2\theta$  peak for AT-nZVI. This result is also consistent with the nanosize particles observed by Greenlee and Hooker [15] and as shown in Figure 6.1, even though these particles were aggregated to form larger particles as determined by DLS [15]. The other well developed peaks in the XRD patterns may be indicative of a significant amount of surface oxidation, as is commonly reported for nZVI [10, 14, 24]. There appears to be specific similarities between the XRD patterns for the three

stabilized nZVI although the AT-nZVI pattern is clearly different. Tentative assignments of the peaks as shown in Figure 6.2 indicate the presence of at least bernalite, green rust, haematite, iron phosphate hydroxide, iron carbonate and oxalate [27-29]. These assignments suggest that the stabilising phosphonic acids participated in the formation of the oxidised surface layer. Further discussion of the XRD patterns is provided in the Appendix (Section S6.1).

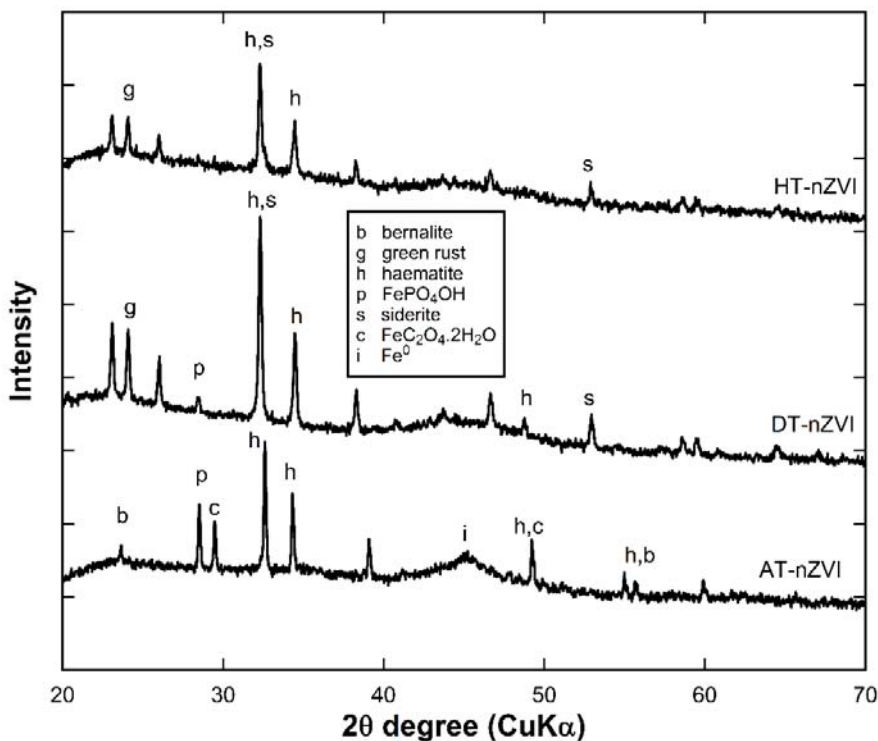


Figure 6.2. XRD patterns for AT-nZVI, DT-nZVI and HT-nZVI with markers where Bragg peaks have been reported previously for various iron compounds.

The FTIR spectra are presented in Figure 6.3a for the stabilising chemicals (ATMP, DTPMP and HTPMP) as solutions in water and the stabilised nZVI (AT-nZVI, DT-nZVI, HT-nZVI) after lyophilisation and exposure to air. Tentative assignment of major peaks is shown. Detailed discussion of Figure 6.3a is provided in Section S6.2. However, attention may be drawn to the two broad bands at  $1330\text{ cm}^{-1}$  and  $1630\text{ cm}^{-1}$  present only in the stabilised nZVI which may be assigned to C-O and  $\text{COO}^-$ , respectively, or to the symmetric and asymmetric stretching of  $\text{COO}^-$ , respectively [30, 31]. The source of the C-O and  $\text{COO}^-$  bonds

may be traced either to the possible degradation of the methylene group on the stabilising chemical during the oxidation of the nZVI upon exposure to air or the possible direct fixation of atmospheric CO<sub>2</sub> onto the particle surface in a process of Fe carbonation [32, 33].

FTIR spectra for the stabilised nanoparticles before and after (\*) batch reactions with 0.1 mM OG solution in the absence of PS are compared in Figure 6.3b. A consistent difference between the particles before and after reaction may be noted at specific peaks. The phosphate broad peak changed its apex from 1100 cm<sup>-1</sup> to 1000 cm<sup>-1</sup> which may be interpreted as an increase in the effect of the  $\nu_{\text{as}}\text{P-O}$  of PO<sub>3</sub><sup>2-</sup> over the  $\nu_{\text{as}}\text{P-O}$  of HPO<sub>3</sub><sup>-</sup>. This peak change suggests additional deprotonation during the batch reaction. On the other hand, the reduction in the 1300 cm<sup>-1</sup> peak and the corresponding increase in the 1630 cm<sup>-1</sup> peak may be interpreted as protonation of the COO<sup>-</sup>, which would result in an electron withdrawing (-I) effect in comparison to the electron donating effect of iron. Such -I effects are known to increase the wavenumber of the carboxylate group [30]. An alternative explanation for the increase in the 1630 cm<sup>-1</sup> peak might be related to the dissolution of surface carbonate during the batch reaction, which would increase the relative concentration of anchored protonated carboxylate groups. The increase in the 3100 – 3400 cm<sup>-1</sup> band linked to the OH vibration could be related to inclusion of more adsorbed water on the particle surface after the batch reaction.

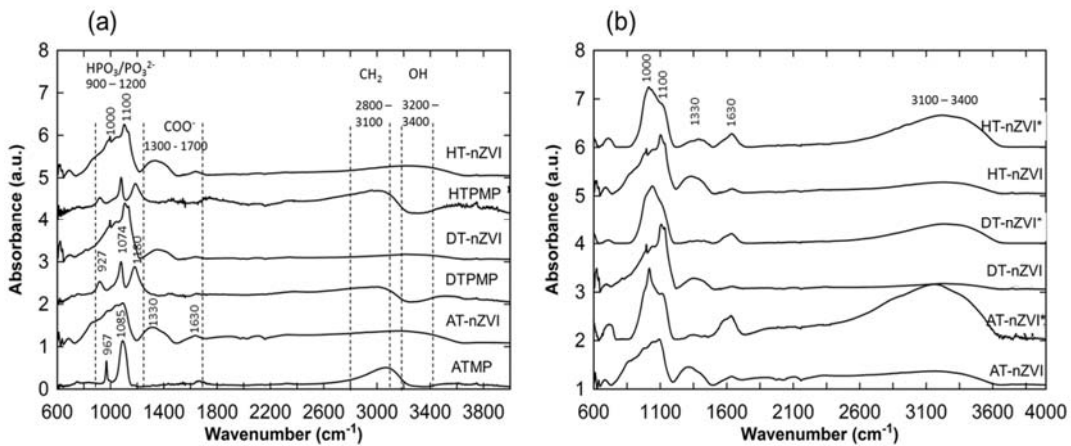


Figure 6.3. (a) FTIR spectra for stabilising chemicals, ATMP, DTPMP and HTPMP and the stabilised nZVI, AT-nZVI, DT-nZVI and HT-nZVI, respectively, obtained after lyophilisation and exposure to air. Stabilising chemicals were dissolved in water for spectra measurement. (b) FTIR spectra comparing the stabilized nZVI before and after (\*) batch reaction with 0.1 mM OG solution in the absence of PS for 60 min.

The results of surface area measurement from N<sub>2</sub> porosimetry using the BET model revealed that AT-nZVI had the lowest surface area of only 8.2 m<sup>2</sup>/g, while HT-nZVI has a greater surface area of 12.2 m<sup>2</sup>/g, and DT-nZVI has the largest measured surface area of 19.9 m<sup>2</sup>/g. The low surface area of AT-nZVI might be linked to the comparatively low molecular weight of the ATMP molecule, which might have provided only limited steric repulsion upon lyophilisation and expulsion of water, accompanied by possible charge neutralisation and close packing of particles. The relatively high surface area of DT-nZVI might have resulted both from the initial small particle size before lyophilisation [15] and the longer chain length of the DTPMP molecular structure. A larger stabiliser molecule such as DTPMP might be better able to resist the thermodynamic driving force for particle aggregation after lyophilisation. While HT-nZVI might have benefited from the long chain stabilising HTPMP molecules, the original large nanoparticle size before lyophilisation [15] might explain the lower BET surface area in comparison to DT-nZVI.

### 6.3.2. OG degradation kinetics

Results for nZVI and PS removal/degradation of OG are presented in Figure 6.4. In this figure,  $C_{OG,t}/C_{OG,0}$  is the normalized OG solution concentration with  $C_{OG,t}$  designating OG solution concentration at a given time and  $C_{OG,0}$  the concentration at time 0. In Figure 6.4a, 0.5 g/L AT-nZVI, 0.5 g/L DT-nZVI and 10 mM PS applied separately did not result in a significant OG removal/degradation. The application of PS for pollutant removal requires activation for rapid degradation [6, 10, 16]; hence, in the absence of chemical or electromagnetic activation, the limited degradation of OG by PS was expected. The poor removal/degradation results for AT-nZVI and DT-nZVI might be linked to surface passivation arising from phosphonate surface binding [34] as well as particle oxidation upon exposure to air [10, 14]. Iron phosphate layers on steel have been credited to result in increased corrosion resistance [28, 34] and similar passivating effects of iron oxide surfaces have been reported for nZVI [10, 14, 16]. That the HT-nZVI resulted in comparatively better removal/degradation results might suggest a correlation between its reactivity and its amorphous structure as indicated by the XRD results.

The addition of 10 mM PS to the various 0.5 g/L nZVI suspensions, as shown in Figure 6.4a, resulted in rapid and significant reduction in  $C_{OG,t}/C_{OG,0}$ . The major reductions in  $C_{OG,t}/C_{OG,0}$  upon PS addition is thought to indicate OG degradation rather than merely adsorption onto the nZVI surfaces since much less significant OG removal was observed in the absence of PS. The rapid degradation of OG by AT-nZVI and DT-nZVI contrasts significantly with the observed inactivity of the nanoparticles towards OG in the absence of PS. This result suggests that the surface passivation was rapidly disrupted by PS to expose the highly reactive Fe interiors of these nanoparticles. The activation of PS by UV for phosphonate oxidation is an established method to test for the presence of phosphonates in water [35, 36]. It is possible that similar reaction between activated PS and the passivating surface phosphonates occurred, paving the way for exposure of the surface and further reaction with the nanoparticles. PS was probably activated by iron oxide on the nanoparticle surface [11, 37].

The higher rate of OG degradation for AT-nZVI and DT-nZVI compared to HT-nZVI is repeated in Figure 6.4b. The results in the inset of Figure 6.4b suggest a pseudo first order degradation reaction as follows:

$$\ln C_{OG,t}/C_{OG,0} = -k_{obs}t \quad 6.1$$

where  $k_{obs}$  is the observed pseudo first order reaction constant ( $\text{min}^{-1}$ ) and  $t$  is the reaction time in minutes. The  $k_{obs}$  for AT-nZVI, DT-nZVI and HT-nZVI (Figure 6.4b inset) were  $0.78 \text{ min}^{-1}$  ( $R^2 = 0.990$ ),  $0.36 \text{ min}^{-1}$  ( $R^2 = 0.972$ ) and  $0.07 \text{ min}^{-1}$  ( $R^2 = 0.978$ ) respectively. The trend in reaction rate constants inversely follows the trend of association constant strength between the phosphonates and Fe(II) [38-40], with ATMP complexing the weakest with Fe(II) and HTPMP forming the strongest complex. The complexation strength thus may play a role in the overall degradation kinetics of OG (and other potential water contaminants). However, the type of phosphonate used does not seem to affect the overall extent of OG degradation. This result suggests that the chemistry of the surface stabiliser might be used advantageously to control nZVI reactivity and stability in solution while not affecting the overall utility of the nanoparticles as a reactive water treatment material. It is noted that the high performance of the AT-nZVI in comparison to the other two nZVI appears to be uncorrelated with the BET surface area results presented earlier. An explanation of this might be developed such that each particle, although aggregated after lyophilisation, retained individual particulate properties as a consequence of the stabilising effect of the phosphonic acid stabilisers.

The degradation trend for 1 mM PS and 0.1 g/L nZVI is presented in Figure 6.4c. The degradation pattern is similar to those of Figure 6.4a and b, underscoring HT-nZVI slower degradation rate. The  $k_{obs}$  as shown in the Figure 6.4c inset were  $0.36 \text{ min}^{-1}$  ( $R^2 = 0.922$ ),  $0.44 \text{ min}^{-1}$  ( $R^2 = 0.929$ ) and  $0.06 \text{ min}^{-1}$  ( $R^2 = 0.830$ ) for AT-nZVI, DT-nZVI and HT-nZVI, respectively. The fits are relatively poor which may be due to the limiting effect of the low PS concentration. While the  $k_{obs}$  for AT-nZVI was approximately halved for PS reduction from 10 mM to 1 mM, the  $k_{obs}$  for DT-nZVI and HT-nZVI were practically unchanged suggesting that in short term, 1 mM PS saturated DT-nZVI and HT-nZVI but not AT-nZVI. This further confirms the comparatively high reactivity of AT-nZVI.

It should be noted that despite the lower rates of OG degradation consistently recorded for HT-nZVI in the presence of PS, the nanoparticles still could be said to outperform the commercial nZVI employed by Li et al. [10]. This is so since in the degradation study reported by Li et al. [10], nZVI was reportedly only capable of activating PS after acid washing. The oxide layer on the commercial nanoparticles was said to result in complete surface passivation [10]. This report further supports the argument that the role of the phosphonate stabiliser is critical to how the phosphonate-stabilised nZVI react with PS. Further, the comparison to studies such as Li et al. [10] supports the hypothesis that the principal nanoparticle passivating agent in this work was the phosphonates. Phosphonate passivation was apparently readily removed by PS but the same is not expected for a surface completely passivated by iron oxide as reported by Li et al [10]. The unique properties of the phosphonic stabilised nZVI with and without PS point to a new class of nZVI materials with controllable surface chemistry for fast pollutant degradation with potential niche application such as for emergency contaminant containment.

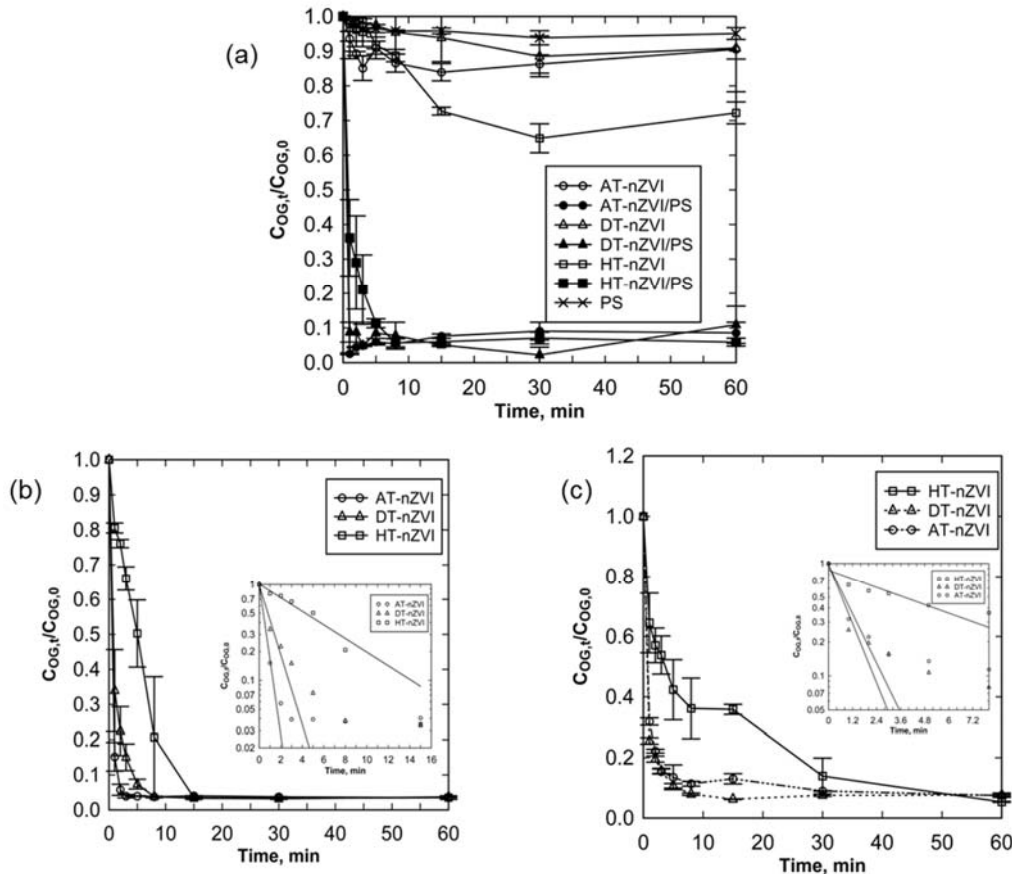


Figure 6.4. OG (0.1 mM) degradation at 24 °C measured by UV-Vis spectroscopy at 478 nm for 0.5 g/L nZVI with and without PS (10 mM) (a) 0.1 g/L nZVI and 10 mM PS (semi-log scale inset) (b) 0.1 g/L nZVI and 1 mM PS (semi-log scale inset) (c).

### 6.3.3. OG degradation mechanism and products

The UV-vis spectral patterns between 200 nm and 600 nm at specific intervals during the degradation experiments are shown in Figure S6.1. Detailed discussion of the spectra is provided in Section S6.3. In summary, it is seen that for  $[n\text{ZVI}] = 0.5 \text{ g/L}$  and  $[\text{PS}] = 10 \text{ mM}$  while the azo-bond 478 nm peak disappeared almost instantly, a new  $\lambda_{\text{max}}$  at  $\sim 290 \text{ nm}$  with very high absorptivity is seen to develop. However, for the reactions conditions of  $[n\text{ZVI}] = 0.1 \text{ g/L}$  and  $[\text{PS}] = 10 \text{ mM}$  or 1 mM, both the azo bond peak at 478 nm and the aromatic ring peak at 259 nm and 328 nm were degraded in tandem during the 60 min batch reaction without significant development of a new peak. The UV-vis spectral

patterns published by Xu and Li [1] for  $\text{Fe}^{2+}$  activated PS degradation of OG ( $[\text{OG}] = 0.1 \text{ mM}$ ,  $[\text{Fe}^{2+}] = 4\text{mM}$ ,  $[\text{PS}]=4\text{mM}$ , pH 3.5) showed that while the azo bond 478 nm  $\lambda_{\max}$  was completely degraded in 60 min, the benzene ring  $\lambda_{\max}$  at 259 and 328 nm were only slightly decreased for the same duration [1]. The authors interpreted this to imply the persistence of the benzene structure during their AOP. In contrast, the results in this work suggest that N=N was rapidly degraded and the aromatic structure was attacked as readily, resulting in new chemical species depending on the initial concentrations of nZVI and PS. Practical design of AOP should aim at optimising degradation kinetics alongside minimising the aromaticity of degradation products. Unfortunately, optimising the nature of OG degradation intermediates has received far less attention in the literature compared to improving degradation kinetics.

Rodriquez et al. [2] identified phenol and benzoquinone as the major degradation products during  $\text{Fe}^{3+}$  activated PS degradation of OG. However, analysis of the  $\lambda_{\max}$  and  $\lambda_{\min}$  (absorbance minima) derived from the spectral patterns of possible OG degradation products as identified by Rodriguez et al. [2] or as can be expected from the structure of OG showed that neither phenol nor benzoquinone can be considered the major degradation products in this work (Section S6.4.). It is noteworthy that both benzoquinone and phenol are considered toxic and their absence as degradation products is desirable from an environmental viewpoint.

To explore the nature of the degradation products obtained in this work, the results of HPLC analysis on the samples are presented in Figure 6.5. The retention times for known chemicals under the HPLC conditions defined earlier are presented in Table S6.2 (Section S6.5.) and were used in interpreting Figure 6.5. In the chromatograms of Figure 6.5a, three peaks can be identified across the treatment with three types of nanoparticles at 1.23, 3.18 and 7.63 min. The 3.18 min peak is designated as the OG peak and is observed to disappear almost instantaneously (before 1 min) in the AT-nZVI and DT-nZVI and after approximately 5 min for HT-nZVI. The peak at 7.63 min is close to the naphthylamine and  $\alpha$ -naphthol peaks and is therefore considered a naphthalene derivative (ND). The peak at 1.23 min matches the retention times for fumaric and oxalic acid and other low molecular weight acids (LMWAs) such as maleic

acid. Another peak at 1.80 min, which may be assigned to hydroquinone or a variant quinone, may be observed most clearly in HT-nZVI but less so in DT-nZVI and AT-nZVI.

The chromatograms shown in Figure 6.5b for  $[n\text{ZVI}] = 0.1 \text{ g/L}$  and  $[\text{PS}] = 10 \text{ mM}$  are similar to those presented in Figure 6.5a but with few major differences. In Figure 6.5b, degradation peaks other than the LMWA peak are almost non-identifiable, suggesting more optimised degradation conditions. As expected due to the reduction in nZVI concentration, the rate of disappearance of the OG peak is slightly slowed. However, for AT-nZVI, the difference is almost negligible. The three chromatograms presented in Figure 6.5c for  $[\text{PS}] = 1\text{mM}$  show very small degradation peaks at 1.74, 3.95 and 7.65 min in addition to the large LMWA peak at 1.23 min. The 1.74 min peak may be assigned to hydroquinone or hydroquinone derivative (HD), the 3.95 min to phenol or phenol derivative (PD) and the 7.65 min to ND. These results suggest that when the PS concentration is limiting, unfavourable partial oxidation products may form, which demonstrates the need for concerted optimisation of both the nZVI and PS concentrations.

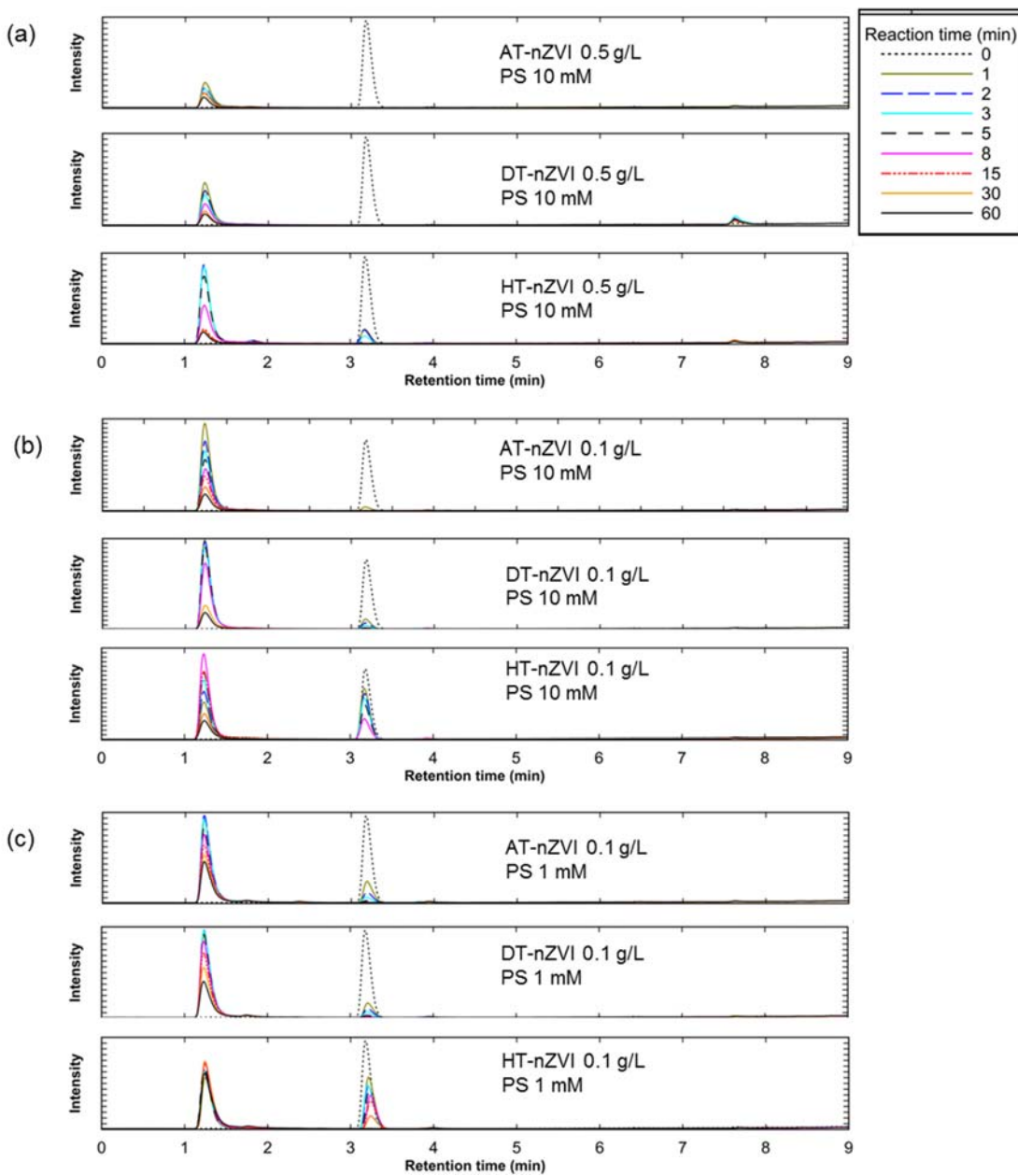


Figure 6.5. Chromatograms for 0.1 mM OG degradation for  $[n\text{ZVI}] = 0.5 \text{ g/L}$ ,  $[\text{PS}] = 10 \text{ mM}$  (a),  $[n\text{ZVI}] = 0.1 \text{ g/L}$ ,  $[\text{PS}] = 10 \text{ mM}$  (b),  $[n\text{ZVI}] = 0.1 \text{ g/L}$ ,  $[\text{PS}] = 1 \text{ mM}$  (c).

Further analysis of the degradation products using a DAD-equipped HPLC for the experimental condition:  $[\text{OG}] = 0.1 \text{ mM}$ ,  $[\text{PS}] = 10 \text{ mM}$  and  $[n\text{ZVI}] = 0.1 \text{ g/L}$  identified two major peaks with noise-free, well-developed UV spectra. These were the LMWA and the ND peaks. Other peaks appear to be below detection limits. The DAD-derived UV spectra for the LMWA and ND peaks are shown in

Figure S6.2. It can be seen in Figure S6.2 that the UV spectra for the LMWA peak is similar for the three stabilised nZVI. At 1 min, two  $\lambda_{\text{max}}$  can be clearly seen at 278 nm and at 205 nm. However, the 205 nm peak is absent at 1 min for HT-nZVI but this peak is seen to develop as the degradation experiment progressed. For the three nZVIs, the 278 nm peak practically disappeared at 60 min and the lower wavelength  $\lambda_{\text{max}}$  moved to 207 nm. These changes in the  $\lambda_{\text{max}}$  indicate chemical transformation of the LMWA peak. In Figure S6.3, the UV spectra for standard/known LMWAs and NDs are shown. Also presented in Figure S6.3 are the spectra for benzoquinone and phenol. Based on further discussion presented in Section S6.5., the LMWA degradation product is practically only fumaric acid at 60 min for the three stabilised nZVIs. Degradation products other than LMWA and ND appear to occur only in trace amounts. Compared to a previous result published for  $\text{Fe}^{3+}$  activated PS degradation of OG [2], much fewer toxic degradation products are identified in this work. This is considered a good outcome as it is desirable to minimise the amount of toxic degradation products released into the environment.

On the basis of the evidence that at 60 min for the  $[\text{PS}] = 10 \text{ mM}$ ,  $[\text{nZVI}] = 0.1 \text{ g/L}$  experiments, the LMWA peak is due entirely to fumaric acid, an attempt was made to compute the fraction of fumaric acid remaining in solution at 60 min using the HPLC peak area of Figure 6.5. The result of the computation is shown in Table 6.3. The computed moles of fumaric acid at 60 min were converted to equivalent mass concentration of carbon and were compared to the organic carbon for the degraded OG solution measured as NPOC. Within the limit of experimental error, the results show that fumaric acid as the principal degradation product accounts for practically all of the carbon present in solution at 60 min. The major degradation pathway for the optimised condition of  $[\text{PS}] = 10 \text{ mM}$  and  $[\text{nZVI}] = 0.1 \text{ g/L}$  can be simplified as shown in Figure 6.6.

Table 6.3. Computation of fraction of organic carbon contributed by fumaric acid degradation product at 60 min for  $[PS] = 10 \text{ mM}$ ,  $[nZVI] = 0.1 \text{ g/L}$  experiments using LMWA peak area

Nanoparticle	Fumaric acid (mmol/L)	Carbon content of fumaric acid (mg-C/L)	NPOC at 60 min (mg-C/L)	Fraction of carbon contributed by fumaric acid to solution NPOC (%)
AT-nZVI	0.37	18	16	110
DT-nZVI	0.36	17	17	100
HT-nZVI	0.43	21	17	120

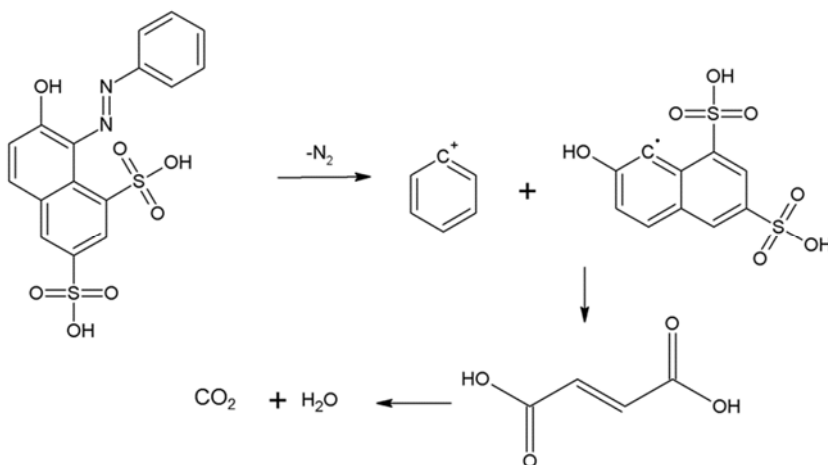


Figure 6.6. Simplified major degradation pathway for optimised reaction condition of  $[PS] = 10 \text{ mM}$  and  $[nZVI] = 0.1 \text{ g/L}$

#### 6.3.4 Dissolution of nZVI

The dissolved Fe concentrations at the end of the degradation reactions are shown in Figure 6.7. It can be seen from Figure 6.7a that Fe in solution during the 60 min experiments decreased for all types of stabilised nZVI as the concentrations of particles and/or PS reduced, as may be expected. However, at

every concentration, AT-nZVI shows the highest Fe concentration suggesting a fast reaction with PS, while HT-nZVI showed the least dissolved Fe concentration indicating lower rate of reaction with PS. This set of results is consistent with the experimental results discussed in previous sections. When the reaction time was extended to 48 h (Figure 6.7b), the Fe concentration for HT-nZVI became comparable to the Fe concentration for the other two nZVIs. The implication is that for a short duration, the amount of Fe dissolved is very different between the stabilised nZVI materials. However, at longer time, the difference diminishes as surface properties become less important and the nZVI is consumed. The presence of high Fe concentration in treated water may be considered a secondary water pollution for certain applications. However, removal of Fe can be readily achieved by aeration or by other established treatment processes [41].

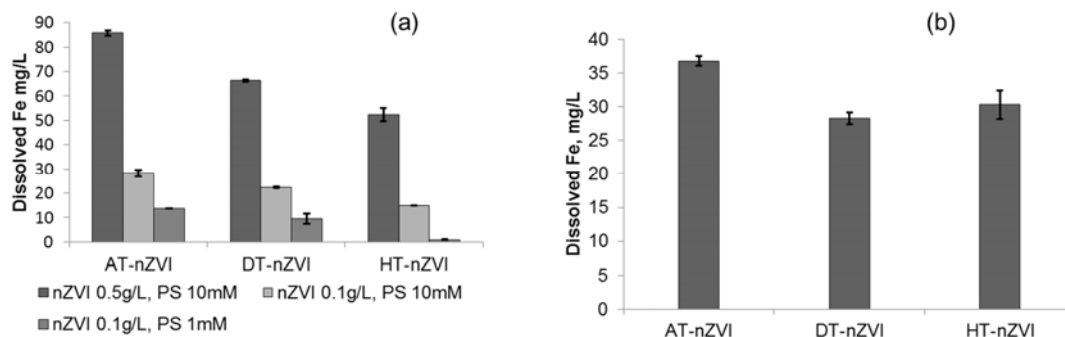


Figure 6.7. Dissolved iron concentration during OG degradation at 24 °C at the end of 60 min (a) and at the end of 48 h for [nZVI] = 0.1 g/L and [PS] = 10 mM (b).

### 6.3.5. Mineralisation of OG

The degrees of OG mineralisation at the end of 60 min batch reactions experiments were measured by TC and by NPOC and are shown in Figure 6.8a and 6.8b. The results in Figure 6.8a show the reduction in TC for 0.5 g/L nZVI with and without 10 mM PS. In the presence of 10 mM PS, similar TC reduction of ~20% was recorded for the three types of stabilised nZVI. It is evident that while PS added to nZVI resulted in almost instantaneous degradation of OG as observed previously, the mineralisation of the dye was incomplete. Similar fast OG degradation and incomplete mineralisation have been previously reported for

PS AOP [1, 2, 42]. However, in the absence of PS, while HT-nZVI still maintained a relatively high TC reduction, AT-nZVI showed a negative TC reduction, indicating TC increase during the batch reaction. To underpin the possible cause for the negative TC reduction, NPOC was measured for all samples as shown in Figure 6.8b. It is seen that AT-nZVI ( $[PS] = 0 \text{ mM}$ ) shows a slight NPOC reduction which may suggest that the large negative TC reduction is probably due to inorganic carbon (IC). It is possible that the IC responsible for the large negative TC reduction was due to the dissolution of inorganic carbon from the particle surface during the batch experiment. This explanation is consistent with the observed FTIR changes at the  $1330$  and  $1630 \text{ cm}^{-1}$  peaks as discussed previously (Section 6.3.1). It is also worth noting that the greatest relative change in the FTIR spectra at these peaks is shown by the AT-nZVI with the most significant IC effect.

Apart from the  $0 \text{ mM}$  PS case, which appears to proceed by a unique activation process, Figure 6.8b seems to suggest that NPOC reduction for AT-nZVI is relatively independent of the concentration of PS and/or nZVI. However, for both DT-nZVI and HT-nZVI, PS and/or nZVI concentrations appear to be very important. An explanation for this trend may follow the already developed hypothesis that AT-nZVI shows more effective PS activation so that only a small amount of PS is needed to achieve OG degradation and further increases in PS and/or AT-nZVI do not improve NPOC reduction significantly, as the PS is rapidly consumed [1]. However, the relatively less reactive DT-nZVI and HT-nZVI seem to benefit more in NPOC reduction from increasing PS and/or nZVI concentrations.

48 h mineralisation, as shown in Figure 6.8c, demonstrates similar 90% NPOC reduction for the different nanoparticles. The overall mineralisation trend is similar for the different nanoparticles because mineralisation was limited during the first 60 min when differences in surface chemistry were important. This result supports the conclusion that the basic performance difference for the nanoparticles is dictated by the surface chemistry, which is short-lived due to reaction with PS. Usually, the black colour of the nZVI disappears during the first 60 min of the degradation reactions as oxidised Fe species are formed [16, 43]. It follows then

that the longer term reactions were determined by the oxidised Fe species rather than by the stabilised nanoparticles.

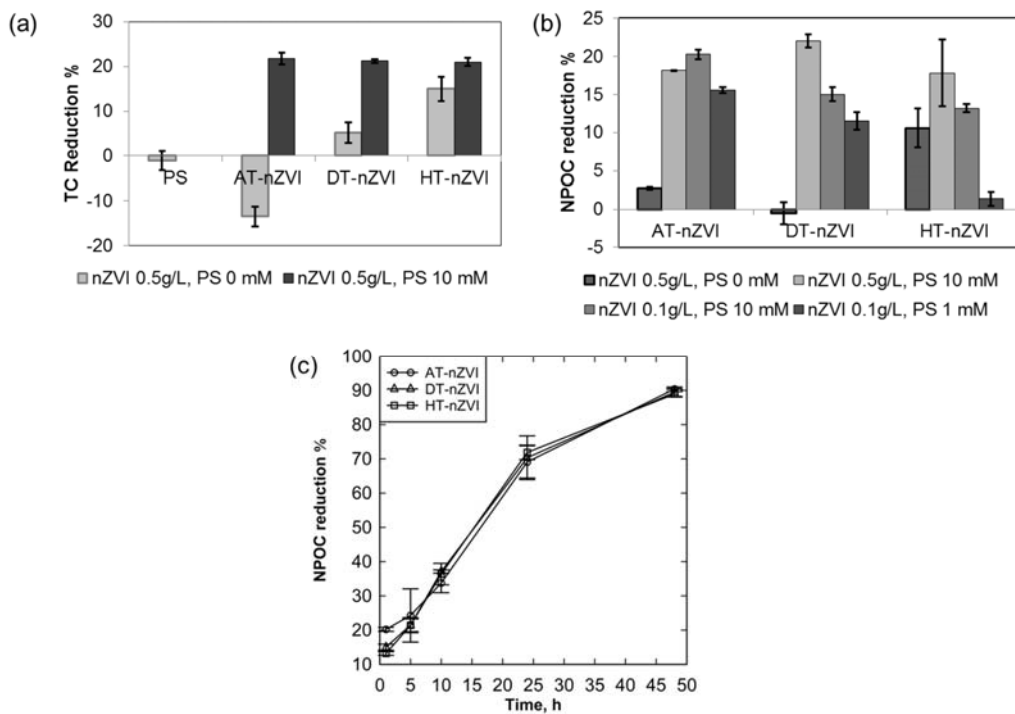
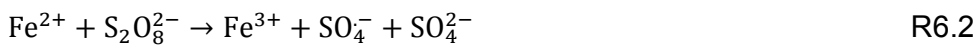
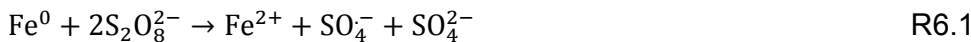


Figure 6.8. Mineralisation at 60 min for 0.1 mM OG at 24 °C, measured by TC (a) and NPOC (b). Extended mineralisation for 48 h measured by NPOC for [nZVI] = 0.1 g/L, [PS] = 10 mM (c)

### 6.3.6. Reaction mechanism

In the presence of 4000 mM propanal-1, a common radical scavenger [17], no decolourisation of OG was observed after several hours by any of the three nanoparticles at [nZVI] = 0.5 g/L and [PS] = 10 mM. This demonstrates a radical mechanism for OG degradation. Radicals were generated from PS as follows [7]:



Reaction R6.1 dominated in short term (<6 0 min) which amounted to a heterogeneous process while R6.2 and probably R6.3 became gradually more important as homogeneous processes.

#### 6.4. Conclusions

Phosphonic acid stabilised nZVI have been applied for the degradation of OG, an important azo dye, with very interesting results for practical wastewater treatment as follows:

- i. In the absence of PS, AT-nZVI and DT-nZVI showed limited chemical reaction with OG suggesting phosphonate induced surface passivation, while HT-nZVI achieved ~15% TC reduction under similar conditions without PS.
- ii. The surface passivation for AT-nZVI and DT-nZVI were disrupted by PS without acid wash, resulting in rapid degradation of OG.
- iii. Although fast reactions between PS and HT-nZVI leading to OG degradation were also observed, the  $k_{obs}$  were consistently less than or equal to half the value obtained for the corresponding AT-nZVI and DT-nZVI.
- iv. These results indicate that the nature of the stabiliser significantly impacted the chemical properties of stabilised nanoparticles and therefore lends itself to the design and control of nanoparticle functionalities for specific applications.
- v. Fewer degradation products were identified in this work during 60 min short term experiments compared to available literature report on OG degradation.
- vi. Extended mineralisation experiment showed that 90% organic carbon reduction was achieved over 48 h for the three nZVI materials.
- vii. During short term experiments, the major degradation product identified was fumaric acid rather than toxic aromatic compounds like phenol and benzoquinone which have been previously reported as the principal intermediates.

- viii. Hence, not only was the azo bond degraded during the AOP described in this work, the benzene ring was also rapidly degraded representing an overall effective pollutant removal process.
- ix. The phosphonic acid stabilised nanoparticles activation of PS is therefore an effective method for complete transformation of pollutant into non-toxic intermediates particularly for underground in-situ chemical remediation where rapid and permanent detoxification is needed and particle recycling is not feasible.

### 6.5. Acknowledgement

The financial support provided by Victoria University to Ikechukwu A. Ike through the Victoria University International Postgraduate Research Scholarship is gratefully acknowledged.

### References

- [1] X.-R. Xu, X.-Z. Li, Degradation of azo dye Orange G in aqueous solutions by persulfate with ferrous ion, *Separation and Purification Technology*, 72 (2010) 105-111.
- [2] S. Rodriguez, L. Vasquez, D. Costa, A. Romero, A. Santos, Oxidation of Orange G by persulfate activated by Fe(II), Fe(III) and zero valent iron (ZVI), *Chemosphere*, 101 (2014) 86-92.
- [3] ECHA, Appendix 8: Entry 43 - Azocolourants - List of aromatic amines, in, European Chemical Agency.
- [4] J. Deng, Y. Shao, N. Gao, Y. Deng, C. Tan, S. Zhou, Zero-valent iron/persulfate(Fe0/PS) oxidation acetaminophen in water, *International Journal of Environmental Science and Technology*, 11 (2013) 881-890.
- [5] X. Wei, N. Gao, C. Li, Y. Deng, S. Zhou, L. Li, Zero-valent iron (ZVI) activation of persulfate (PS) for oxidation of bentazon in water, *Chemical Engineering Journal*, 285 (2016) 660-670.
- [6] Y. Deng, R. Zhao, Advanced Oxidation Processes (AOPs) in Wastewater Treatment, *Current Pollution Reports*, 1 (2015) 167-176.

- [7] P. Devi, U. Das, A.K. Dalai, In-situ chemical oxidation: Principle and applications of peroxide and persulfate treatments in wastewater systems, *The Science of the total environment*, 571 (2016) 643-657.
- [8] C. Tan, N. Gao, Y. Deng, W. Rong, S. Zhou, N. Lu, Degradation of antipyrine by heat activated persulfate, *Separation and Purification Technology*, 109 (2013) 122-128.
- [9] S. Chakma, S. Praneeth, V.S. Moholkar, Mechanistic investigations in sono-hybrid (ultrasound/Fe<sup>2+</sup>/UVC) techniques of persulfate activation for degradation of Azorubine, *Ultrasonics Sonochemistry*, <http://dx.doi.org/10.1016/j.ultsonch.2016.08.015>, (2016).
- [10] H. Li, J. Wan, Y. Ma, Y. Wang, M. Huang, Influence of particle size of zero-valent iron and dissolved silica on the reactivity of activated persulfate for degradation of acid orange 7, *Chemical Engineering Journal*, 237 (2014) 487-496.
- [11] M. Usman, P. Faure, C. Ruby, K. Hanna, Application of magnetite-activated persulfate oxidation for the degradation of PAHs in contaminated soils, *Chemosphere*, 87 (2012) 234-240.
- [12] Z. Jiang, L. Lv, W. Zhang, Q. Du, B. Pan, L. Yang, Q. Zhang, Nitrate reduction using nanosized zero-valent iron supported by polystyrene resins: role of surface functional groups, *Water Res*, 45 (2011) 2191-2198.
- [13] Z. Xiong, D. Zhao, G. Pan, Rapid and complete destruction of perchlorate in water and ion-exchange brine using stabilized zero-valent iron nanoparticles, *Water Res*, 41 (2007) 3497-3505.
- [14] R.A. Crane, T.B. Scott, Nanoscale zero-valent iron: future prospects for an emerging water treatment technology, *J Hazard Mater*, 211-212 (2012) 112-125.
- [15] L.F. Greenlee, S. Hooker, Characterization of stabilized zero valent iron nanoparticles, in: T. Boellinghaus, J. Lexow, T. Kishi, M. Kitagawa (Eds.) *Materials Challenges and Testing for Supply of Energy and Resources*, Springer-Verlag Berlin Heidelberg, 2012, pp. 173-188.
- [16] H. Li, J. Wan, Y. Ma, M. Huang, Y. Wang, Y. Chen, New insights into the role of zero-valent iron surface oxidation layers in persulfate oxidation of dibutyl phthalate solutions, *Chemical Engineering Journal*, 250 (2014) 137-147.

- [17] G.P. Anipsitakis, D.D. Dionysiou, Radical generation by the interaction of transition metals with common oxidants, *Environmental Science & Technology*, 38 (2004) 3705-3712.
- [18] N. Goldstein, L.F. Greenlee, Influence of synthesis parameters on iron nanoparticle size and zeta potential, *J. Nanopart. Res.*, 14 (2012) 760.
- [19] L.F. Greenlee, S.A. Hooker, Development of stabilized zero valent iron nanoparticles, *Desalin. Water Treat.*, 37 (2012) 114-121.
- [20] L.F. Greenlee, N.S. Rentz, ATMP-stabilized iron nanoparticles: chelator-controlled nanoparticle synthesis, *Journal of Nanoparticle Research*, 16 (2014) 2712.
- [21] A.A. Edwards, B.D. Alexander, Organic applications of UV-visible absorption spectroscopy, in: J.C. Lindon, G.E. Tranter, D.W. Koppenaal (Eds.) *Encyclopedia of spectroscopy and spectrometry*, Elsevier Ltd, 2010, pp. 2030-2039.
- [22] A. Ghauch, A.M. Tuqan, Oxidation of bisoprolol in heated persulfate/H<sub>2</sub>O systems: Kinetics and products, *Chemical Engineering Journal*, 183 (2012) 162-171.
- [23] Ç. Üzüm, T. Shahwan, A.E. Eroğlu, I. Lieberwirth, T.B. Scott, K.R. Hallam, Application of zero-valent iron nanoparticles for the removal of aqueous Co<sup>2+</sup> ions under various experimental conditions, *Chemical Engineering Journal*, 144 (2008) 213-220.
- [24] Y.P. Sun, X.Q. Li, J. Cao, W.X. Zhang, H.P. Wang, Characterization of zero-valent iron nanoparticles, *Adv Colloid Interface Sci*, 120 (2006) 47-56.
- [25] A.P.A. Faiyas, E.M. Vinoda, J. Joseph, R. Ganesan, R.K. Pandey, Dependence of pH and surfactant effect in the synthesis of magnetite (Fe<sub>3</sub>O<sub>4</sub>) nanoparticles and its properties, *Journal of Magnetism and Magnetic Materials*, 322 (2010) 400 - 404.
- [26] K. Norrish, R.M. Taylor, Quantitative analysis by X-ray diffraction, *Mineralogical Society, Archive-CM*, 5 (1962) 98-109.
- [27] JCPDS, Selected powder diffraction data for minerals in: M-1-23 (Ed.), Joint Committee on Powder Diffraction Standards.
- [28] E. Dudrová, M. Kabátová, P. Hvízdoš, R. Oriňáková, Sintered composite materials on the basis of Fe/FePO<sub>4</sub>-coated powders, *Surface and interface analysis*, 47 (2015) 350-356.

- [29] M.L. Kiss, M. Chirita, R. Banica, A. Ieta, C. Savii, I. Grozescu, Transition from single crystalline FeCO<sub>3</sub> to layered and ordered nanostructured α-Fe<sub>2</sub>O<sub>3</sub>, *Materials Letters*, 158 (2015) 214-217.
- [30] M. Avram, *Infrared Spectroscopy: Applications in Organic Chemistry*, Robert E. Krieger Publishing Co., Inc, New York, 1978.
- [31] D. Yu, C. Wu, Y. Kong, N. Xue, X. Guo, W. Ding, Structural and catalytic investigation of mesoporous iron phosphate, *Journal of Physical Chemistry C*, 111 (2007) 14394-14399.
- [32] S. Das, B. Souliman, D. Stone, N. Neithalath, Synthesis and properties of a novel structural binder utilizing the chemistry of iron carbonation, *ACS applied materials & interfaces*, 6 (2014) 8295-8304.
- [33] S. Das, A.B. Kizilkanat, S. Chowdhury, D. Stone, N. Neithalath, Temperature-induced phase and microstructural transformations in a synthesized iron carbonate (siderite) complex, *Materials & Design*, 92 (2016) 189-199.
- [34] A.T. Kan, G. Fu, M.B. Tomson, Adsorption and precipitation of an aminoalkylphosphonate onto calcite, *Journal of colloid and interface science*, 281 (2005) 275-284.
- [35] Hach, Phosphonates, Persulfate UV Oxidation Method (125.0 mg/L), in: H.C.H.L. GmbH (Ed.), Hach Company/Hach Lange GmbH, 2014.
- [36] A.T. Kan, K. Varughese, M.B. Tomson, Determination of low concentrations of phosphonate in brines, in: SPE International Symposium on Oilfield Chemistry, California, 1991.
- [37] M. Usman, P. Faure, K. Hanna, M. Abdelmoula, C. Ruby, Application of magnetite catalyzed chemical oxidation (Fenton-like and persulfate) for the remediation of oil hydrocarbon contamination, *Fuel*, 96 (2012) 270-276.
- [38] K. Sawada, W.B. Duan, M. Ono, K. Satoh, Stability and structure of nitrilo(acetate-methylphosphonate) complexes of the alkaline-earth and divalent transition metal ions in aqueous solution, *J. Chem. Soc.-Dalton Trans.*, (2000) 919-924.
- [39] K. Sawada, T. Kanda, Y. Naganuma, T. Suzuki, Formation and protonation of aminopolyphosphonate complexes of alkaline-earth and divalent transition-metal ions in aqueous solution, *J. Chem. Soc. Dalton Trans.*, 17 (1993) 2557-2562.

- [40] K. Popov, H. Ronkkomaki, L.H.J. Lajunen, Critical evaluation of stability constants of phosphonic acids (IUPAC technical report), *Pure Appl. Chem.*, 73 (2001) 1641-1677.
- [41] E.G. Søgaard, D.A. Ankrah, Advanced iron oxidation at drinking water treatment plants, in: E.G. Søgaard (Ed.) *Chemistry of Advanced Environmental Purification Processes of Water: Fundamentals and Applications*, Elsevier, Amsterdam, 2014, pp. 249-283.
- [42] J. Madhavan, F. Grieser, M. Ashokkumar, Degradation of orange-G by advanced oxidation processes, *Ultrasonics sonochemistry*, 17 (2010) 338-343.
- [43] L.F. Greenlee, J.D. Torrey, R.L. Amaro, J.M. Shaw, Kinetics of zero valent iron nanoparticle oxidation in oxygenated water, *Environ Sci Technol*, 46 (2012) 12913-12920.

## Appendix

### S6.1. Extended discussion of XRD patterns

Kan et al. [1] reported that ATMP effectively adsorbed onto calcite, especially on the crystal growth steps and defects. While calcite is a different material system than nZVI, correlations can be drawn between the two materials with regards to how phosphonate stabilisers can affect crystallization and precipitate growth. In the work of Kan, Fu and Tomson [1], calcite crystal growth was inhibited as a consequence of phosphonate adsorption, and the authors observed that calcite growth was overtaken by calcium phosphonate crystal development. Similar results were reached by Nygren et al. [2] via molecular modelling. Nygren et al. [2] proposed that phosphonate binding to a crystal may result in complete or partial inhibition of native crystal growth. The latter may slow crystal growth and/or alter the native crystal morphology [2]. The size of the phosphonate molecule as well as whether the ligand shows a binding preference to crystal defects, which are usually sources for crystal growth steps, determine the effectiveness of crystal growth inhibition [2].

Several other reports have documented phosphonate/phosphate binding to, or complexation with, other cations and surfaces, including iron cations and iron oxide surfaces [3-9]. It is thus hypothesised that AT-nZVI crystal growth was effectively inhibited by ATMP without significantly modifying the native Fe<sup>0</sup> crystalline structure which resulted in the formation of small particles [10] with relatively good Fe<sup>0</sup> crystallinity. On the other hand, the more extended molecular structure of HTPMP interfered with Fe<sup>0</sup> crystallinity resulting in poorly developed Fe<sup>0</sup> peak at 45° 2θ for HT-nZVI. The molecular complexity of DTPMP falls mid-way between those of ATMP and HTPMP and consequently, the crystalline feature of the Fe<sup>0</sup> peak is mid-way between those of AT-nZVI and HT-nZVI.

### S6.2. Extended discussion of FTIR spectra (Figure 6.3a)

The pH values of the respective nanoparticle-free stabilising chemicals were 11.03, 1.13 and 1.59 for ATMP, DTPMP and HTPMP, respectively. Even though the pH values of the commercial stabiliser solutions are quite different (particularly to ATMP), these compounds are typically diluted by ~1000x from the

commercial stock solutions, and the final pH of the synthesized nanoparticles was consistently measured at 9. Thus, it is not believed that the initial pH of the stabiliser affects the synthesis of the nanoparticles. If the phosphonate pH did affect the synthesis, one impact might be on the oxidation state of the ferrous sulfate precursor, where high pH will cause the ferrous iron to oxidise relatively quickly. Iron oxidation in solution was not visually observed during any nanoparticle synthesis.

The high pH of ATMP provides for the deprotonation of the acid as compared to the low pH for the other two stabiliser chemicals, where protonation is more likely to prevail at low pH. The strong peaks between  $900 - 1200\text{ cm}^{-1}$  are characteristic of the spectra for compounds that contain phosphonic acid groups, where these peaks are known to be greatly influenced by the degree of protonation or deprotonation [11]. The sharp ATMP peak at  $967\text{ cm}^{-1}$  has been assigned to symmetric vibration ( $\nu_s$ ) of the P-O bond of  $\text{PO}_3^{2-}$ , while the prominent peak at  $1085\text{ cm}^{-1}$  has been assigned to asymmetric vibration ( $\nu_{as}$ ) of the P-O bond of  $\text{PO}_3^{2-}$ , indicating significant acid deprotonation [11]. Three peaks are recognisable for the DTPMP and HTPMP samples at  $927$ ,  $1074$  and  $1180\text{ cm}^{-1}$  which may be assigned to  $\nu_{as}\text{P-OH}$  of  $\text{HPO}_3^{2-}$ ,  $\nu_{as}\text{P-O}$  of  $\text{PO}_3^{2-}$  and  $\nu_{as}\text{P-O}$  of  $\text{HPO}_3^{2-}$ , respectively, suggesting significant protonation [11].

The phosphonic acid active region for the stabilised nZVI provides a different pattern as compared to the dissolved stabilising chemicals in the absence of nanoparticles. Here, the distinct peaks for the dissolved phosphonic acid, which are indicative of the existence of distinct but limited phosphonic species, are replaced by broad bands for the stabilised nZVI. This change in the peak behaviour, and in particular, the broadening of the peaks, is suggestive of a more varied chemical coordination with Fe and H. The slightly distinct peak at approximately  $1000\text{ cm}^{-1}$  can be assigned to vibrations of the P-O of  $\text{PO}_3^{2-}$ , while the apex of the broad band at approximately  $1100\text{ cm}^{-1}$  may be assigned to vibrations of the  $\text{HPO}_3^{2-}$  group [11-13]. The broad peak at  $2800 - 3100\text{ cm}^{-1}$  is more evident for the dissolved stabilising chemicals and is assigned to the vibration from the methylene group ( $\text{CH}_2$ ) [13, 14]. The  $\text{CH}_2$  band appears to have been affected by the broad associated OH band arising from water, which was background subtracted for samples scanned as solutions in water. The  $\text{CH}_2$

vibration is not pronounced on the stabilised nZVI, suggesting possible degradation or modification of this functional group when the particles were exposed to air. A broad band for associated OH groups at  $3200 - 3400 \text{ cm}^{-1}$  appears to be recognisable in the spectra for the stabilised particles.

### S6.3. UV spectral study of degradation products

The UV-vis spectral patterns between 200 nm and 600 nm at specific intervals during the degradation experiments are shown in Figure S6.1. The results in Figure S6.1a ( $[n\text{ZVI}] = 0.5 \text{ g/L}$  and  $[\text{PS}] = 10 \text{ mM}$ ) reveal an almost instantaneous disappearance of the 478 nm characteristic absorbance maxima ( $\lambda_{\max}$ ) of OG for the three nZVI under study, indicating rapid degradation of the N=N chromophore. However, a new  $\lambda_{\max}$  at  $\sim 290 \text{ nm}$  with very high absorptivity is seen to develop in the course of the degradation suggesting that while the azo chromophore was degraded, the dye was not completely mineralized but was transformed into new chemical species. The new  $\lambda_{\max}$  developed from the 1st min for AT-nZVI and DT-nZVI but was only observed for HT-nZVI after 2 min, further supporting the conclusion that there is a slower degradation rate for HT-nZVI. The development of new  $\lambda_{\max}$  from the beginning of the reaction is further proof that OG is being degraded rather than merely adsorbed. Due to the intensity of the new  $\lambda_{\max}$ , it is not clear what happened to the other two OG  $\lambda_{\max}$  at 259 nm and 328 nm, which have been assigned to the benzene rings of the OG molecular structure [15]. The UV-vis spectral patterns published by Xu and Li [15] for  $\text{Fe}^{2+}$  activated PS degradation of OG ( $[\text{OG}] = 0.1 \text{ mM}$ ,  $[\text{Fe}^{2+}] = 4\text{mM}$ ,  $[\text{PS}]=4\text{mM}$ , pH 3.5) showed that while the azo bond 478 nm  $\lambda_{\max}$  was completely degraded in 60 min, the benzene ring  $\lambda_{\max}$  at 259 and 328 nm were only slightly decreased for the same duration [15]. The authors interpreted this to imply the persistence of the benzene ring during their AOP.

The UV spectral patterns at  $[n\text{ZVI}] = 0.1 \text{ g/L}$  and  $[\text{PS}] = 10 \text{ mM}$  are presented in Figure S6.1b. This result shows an almost instantaneous disappearance of the 478 nm  $\lambda_{\max}$  for AT-nZVI, a slightly slower rate of disappearance for DT-nZVI, and an evidently slower rate of disappearance for HT-nZVI. These kinetics are all in keeping with the established reactivity of the three different phosphonate-stabilised nZVI particles. Consequently, the reduction of  $[n\text{ZVI}]$  from 0.5 g/L to 0.1

g/L had no effect on the rate of AT-nZVI/PS decolourisation of OG, slightly impacted the rate for DT-nZVI, but showed a definite retarding effect on the rate of HT-nZVI/PS removal of OG. The more interesting observation in Figure 6.5b with respect to Figure S6.1a is the minimal development of the new  $\lambda_{\max}$  at ~290 nm. As a consequence, it is possible to observe the fate of the aromatic ring  $\lambda_{\max}$  for OG. It is clear that not only was the 478 nm  $\lambda_{\max}$  degraded, the 259 and 328 nm  $\lambda_{\max}$  also rapidly disappeared in the course of the degradation experiments. The new  $\lambda_{\max}$  at ~290 nm was also observed but the intensity is much less in Figure S6.1b, compared to the results shown in Figure S6.1a. The results presented in Figure S6.1c for reduced PS concentration ([PS] = 1 mM and [nZVI] = 0.1 g/L) also showed the elimination of the three major OG  $\lambda_{\max}$  but without the clear development of a new  $\lambda_{\max}$ . These results suggest that the AOP in this work degraded the N=N rapidly and also attacked the benzene ring as readily, resulting in new chemical species depending on the initial concentrations of nZVI and PS.

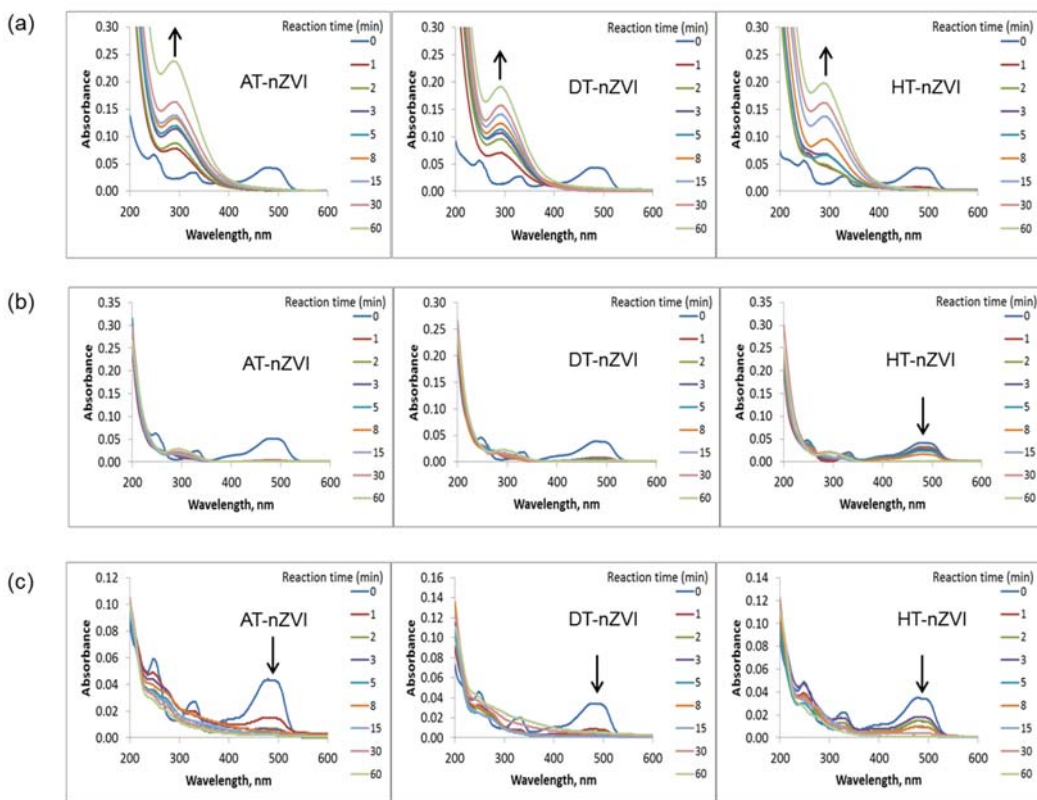


Figure S6.1. UV-vis characteristic spectral patterns between wavelengths 200 nm and 600 nm for OG degradation at 0.5 g/L nZVI and 10 mM PS (a) 0.1 g/L nZVI and 10 mM PS (b) 0.1 g/L nZVI and 1 mM PS. Arrows show the direction of increasing time at specific peaks.

#### S6.4. Analysis of UV absorbance maxima and minima

The  $\lambda_{\max}$  and  $\lambda_{\min}$  (absorbance minima) derived from the spectral patterns of possible OG degradation products as identified by Rodriguez et al. [16] or as can be expected from the structure of OG are shown in Table 6.1. Also tabulated are the  $\lambda_{\max}$  and  $\lambda_{\min}$  for the degraded OG in this work at the end of the 60 min. Rodriguez et al. [16] identified phenol and benzoquinone as the major degradation products during Fe<sup>3+</sup> activated PS degradation of OG. From Table S6.1, it can be seen that  $\lambda_{\max}$  and  $\lambda_{\min}$  for phenol does not match the observed values for the degradation products in this work. The benzoquinone  $\lambda_{\max}$  at 286 nm corresponds to some of the  $\lambda_{\max}$  observed for the degraded OG but the absence of the major 255  $\lambda_{\max}$  for benzoquinone and the mismatch between the  $\lambda_{\min}$  suggest that benzoquinone was not the major degradation product in this

work. A similar argument may be used to exclude naphthylamine, 1-naphthol and 4-aminophenol as major degradation products. Consequently, unlike the reported  $\text{Fe}^{3+}$  activated PS degradation of OG [16], neither phenol nor benzoquinone can be considered the major degradation products in this work. It is noteworthy that both benzoquinone and phenol are considered toxic and their absence as degradation products is desirable from an environmental view point. From Table S6.1, it can be seen that compounds with benzene rings have one or more  $\lambda_{\max} > 210 \text{ nm}$ . Consequently, the large intensity  $\lambda_{\max}$  at approx. 290nm for  $[\text{nZVI}] = 0.5 \text{ g/L}$  and  $[\text{PS}] = 10 \text{ mM}$  developed during OG degradation (Figure S6.1a) may indicate the production of new benzene derivative(s) as the principal degradation product(s). For the degradation experiments performed at  $[\text{nZVI}] = 0.1 \text{ g/L}$ , the complete absence of  $\lambda_{\max} > 210 \text{ nm}$  or the low intensity of such peaks is an indication that the major degradation products are not aromatic. Overall, it appears that very rapid rates of degradation favour the production of intermediates with more aromatic characteristics compared to slower rates of degradation. Consequently, practical design of AOP should aim at optimising degradation kinetics alongside minimising the aromaticity of degradation products. Unfortunately, optimising the nature of OG degradation intermediates has received far less attention in the literature compared to improving degradation kinetics.

Table S6.1. UV  $\lambda_{\text{max}}$  and  $\lambda_{\text{min}}$  for possible products from OG degradation and degraded OG at 60 min

Chemical name	UV Absorbance (nm)	
	$\lambda_{\text{max}}$	$\lambda_{\text{min}}$
Naphthylamine	211, 236, 308	229, 260
1-Naphthol	213, 294, 308, 322	250, 304, 318
Phthalic acid	230, 280	265, 320
4-Aminophenol	224, 389, 295,	218, 287, 346
4-Nitroaniline	228, 380	212, 278
Aniline	230, 281	212, 258
Phenol	209, 270	205, 241
Hydroquinone	221, 288	209, 250
Benzoquinone	221, 255, 275, 286	217, 234
Maleic acid	-	-
Fumaric acid	205	-
Oxalic acid	-	-
AT(0.5 g/L, [PS]=10 mM)	288	262
DT(0.5 g/L, [PS]=10 mM)	295	261
HT(0.5 g/L, [PS]=10 mM)	288	263
AT(0.1 g/L, [PS]=10 mM)	295	264
DT(0.1 g/L, [PS]=10 mM)	295	265
HT(0.1 g/L, [PS]=10 mM)	295	267
AT(0.1 g/L, [PS]=1 mM)	-	-
DT(0.1 g/L, [PS]=1 mM)	-	-
HT(0.1 g/L, [PS]=1 mM)	-	-

### S6.5. HPLC retention times for known chemicals

The retention times for known chemicals under the HPLC conditions defined earlier in this work are presented in Table S6.2. to aid the interpretation of the chromatograms. From Table S6.2., it can be concluded that the low molecular weight hydrophilic organic acids (LMWA), oxalic, fumaric and maleic acid, as well as phthalic acid, all eluted quickly in less than 1.5 min through the hydrophobic

C18 column. Benzene ring molecules with two hydrophilic functional groups eluted next, after 1.5 min and before the 3.15 elution time for OG. Subsequently, one hydrophilic group modified benzene ring molecules eluted from 3.25 min. Finally, naphthalene derivatives were eluted after 6.30 min.

Table S6.2. Retention times for the HPLC conditions specified in this work for known chemical compounds

<b>Chemicals</b>	<b>Retention time, min</b>
Ferrous oxalate	1.21
Sodium oxalate	1.22
Oxalic acid	1.22
Fumaric acid	1.23
Pthalic acid	1.30
Maleic acid	1.31
Hydroquinone	1.68
Benzoquinone	2.30
Resorcinol	2.09
2-hydroxybenzoic acid	2.17
4-nitrobenzoic acid	2.18
Orange G	3.15
Aniline	3.25
4-Nitroaniline	3.75
Phenol	4.01
Benzaldehyde	4.94
Nitrobenzene	6.16
Naphthylamine	6.43
$\alpha$ -Naphthol	7.45

### S6.6. Extended discussion of DAD results

With reference to Figure S6.3, the LMWA 205 nm  $\lambda_{\max}$  at 1 min in Figure S6.2 for AT-nZVI and DT-nZVI can be taken as an indication of the presence of fumaric acid and the 278 nm suggests the presence of phthalic acid. The absence of the 205 nm  $\lambda_{\max}$  and the slight inflection at 224 nm for the HT-nZVI at 1 min suggest phthalic acid as the principal degradation product at this condition and time. The disappearance of the 278 nm  $\lambda_{\max}$  and the prominence of the 207 nm  $\lambda_{\max}$  at 60 min for the three stabilised nZVIs provide evidence that the LMWA degradation product is practically only fumaric acid at 60 min.

The UV spectra for the ND peak derived from OG degradation using DT-nZVI and HT-nZVI are similar but appear to be different from the spectra for AT-nZVI (Figure S6.2). However, the  $\lambda_{\max}$  positions for the three nZVIs are alike at approx. 210 nm and 260 nm. The major difference appears to be in the relative intensities of the two  $\lambda_{\max}$ . The 260 nm  $\lambda_{\max}$  for DT-nZVI and HT-nZVI are much lower than the 210 nm peak and the former disappeared in the course of the degradation experiment. The ND pattern for AT-nZVI appears to be more stable with the intensities for the two  $\lambda_{\max}$  not differing significantly. The stability of the pattern for AT-nZVI may suggest a more recalcitrant chemical species. Since the HPLC retention times for naphthylamine and  $\alpha$ -naphthol (Table S6.2) are slightly lower than the retention time for the ND degradation product in Figure 6.5, it is not surprising that the UV patterns do not match. However, there is still good similarity in the patterns to suggest that the compounds are related. It can be concluded from the HPLC analyses for the experimental condition of  $[PS] = 10 \text{ mM}$  and  $[nZVI] = 0.1 \text{ g/L}$  that at the end of 60 min, the major stable degradation product was the non-toxic fumaric acid. Some amount of a naphthalene-like compound was also stable at the end of 60 min. Other degradation products appear to occur only in trace amounts.

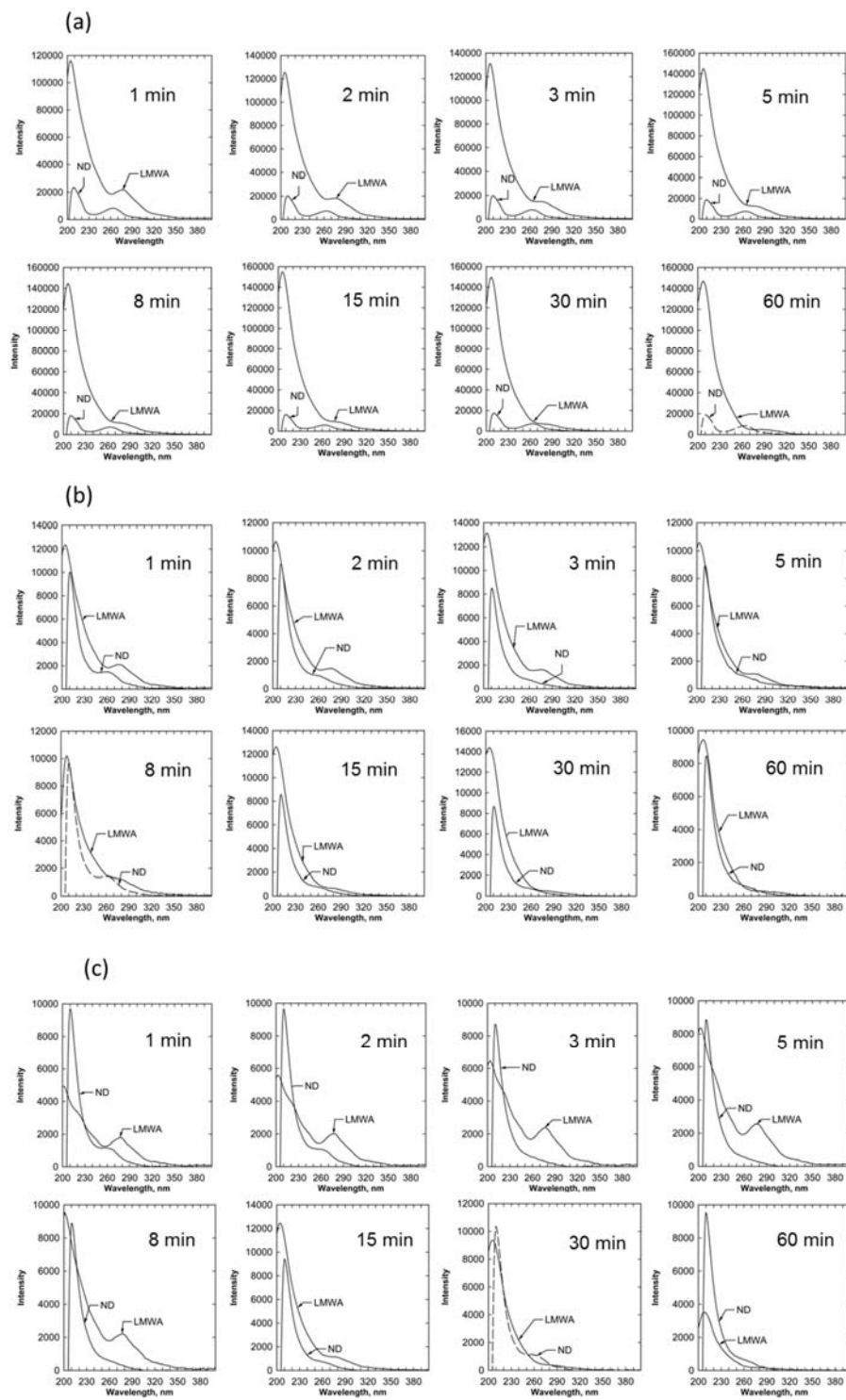


Figure S6.2. HPLC DAD UV spectra for the LMWA and ND peaks obtained from OG PS-degradation activated by AT-nZVI (a), DT-nZVI (b) and HT-nZVI (c). [OG] = 0.1 mM, [PS] = 10 mM, [nZVI] = 0.1 g/L.

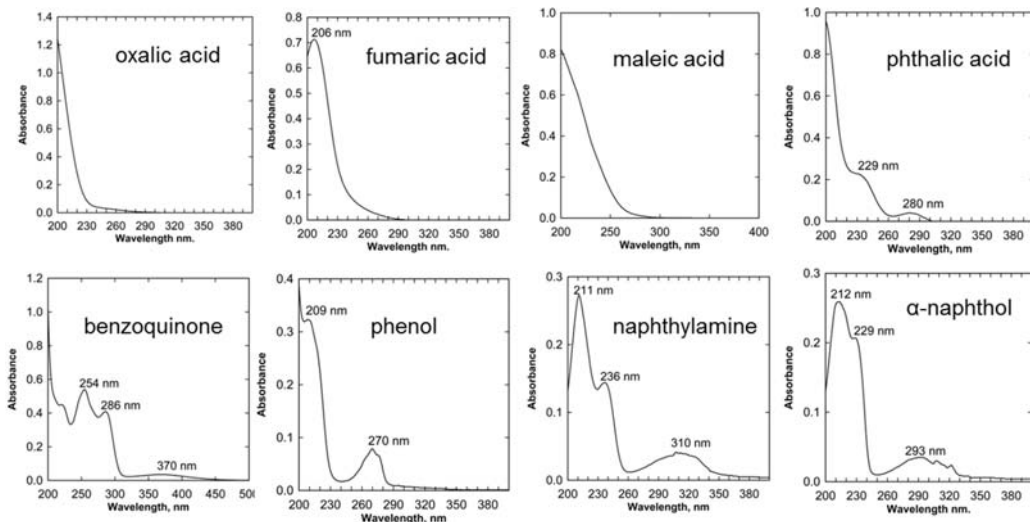


Figure S6.3. UV spectra for standard/known LMWA and ND. Spectra for benzoquinone and phenol are also shown.

## References

- [1] A.T. Kan, G. Fu, M.B. Tomson, Adsorption and precipitation of an aminoalkylphosphonate onto calcite, *Journal of colloid and interface science*, 281 (2005) 275-284.
- [2] M.A. Nygren, D.H. Gay, C.R.A. Catlow, M.P. Wilson, A.L. Rohl, Incorporation of growth-inhibiting diphosphonates into steps on the calcite cleavage plane surface, *ournal of the Chemical Society, Faraday Transactions*, 94 (1998) 3685–3693.
- [3] K. Popov, H. Ronkkomaki, L.H.J. Lajunen, Critical evaluation of stability constants of phosphonic acids (IUPAC Technical Report), *Pure and Applied Chemistry*, 73 (2001) 1641–1677.
- [4] S. Lacour, V.r. Deluchat, J.-C. Bollinger, B. Serpaud, Complexation of trivalent cations (Al(III), Cr(III), Fe(III)) with two phosphonic acids in the pH range of fresh waters, *Talanta*, 46 (1998) 999–1009.
- [5] V. Deluchat, J.-C. Bollinger, B. Serpaud, C. Caullet, Divalent cations speciation with three phosphonate ligands in the pH-range of natural waters, *Talanta*, 44 (1997) 897 907.

- [6] B. Nowack, Environmental chemistry of phosphonates, *Water Research*, 37 (2003) 2533-2546.
- [7] M. Mitra, R. Ghosh, Iron phosphonate clusters: From magnetism to biological mimics, *Inorganic Chemistry Communications*, 24 (2012) 95-103.
- [8] B.C. Barja, J. Herszage, M.d.S. Afonso, Iron(III)-phosphonate complexes, *Polyhedron* 20 (2001) 20 (2001) 1821–1830.
- [9] C. Luengo, M. Brigante, J. Antelo, M. Avena, Kinetics of phosphate adsorption on goethite: comparing batch adsorption and ATR-IR measurements, *Journal of colloid and interface science*, 300 (2006) 511-518.
- [10] L.F. Greenlee, S. Hooker, Characterization of stabilized zero valent iron nanoparticles, in: T. Boellinghaus, J. Lexow, T. Kishi, M. Kitagawa (Eds.) *Materials Challenges and Testing for Supply of Energy and Resources*, Springer-Verlag Berlin Heidelberg, 2012, pp. 173-188.
- [11] M.C. Zenobi, C.V. Luengo, M.J. Avena, E.H. Rueda, An ATR-FTIR study of different phosphonic acids in aqueous solution, *Spectrochimica acta. Part A, Molecular and biomolecular spectroscopy*, 70 (2008) 270-276.
- [12] E. Palacios, P. Leret, J.F. Fernández, A.H. De Aza, M.A. Rodríguez, Synthesis of amorphous acid iron phosphate nanoparticles, *Journal of Nanoparticle Research*, 14 (2012).
- [13] D. Yu, C. Wu, Y. Kong, N. Xue, X. Guo, W. Ding, Structural and catalytic investigation of mesoporous iron phosphate, *Journal of Physical Chemistry C*, 111 (2007) 14394-14399.
- [14] M. Avram, *Infrared Spectroscopy: Applications in Organic Chemistry*, Robert E. Krieger Publishing Co., Inc, New York, 1978.
- [15] X.-R. Xu, X.-Z. Li, Degradation of azo dye Orange G in aqueous solutions by persulfate with ferrous ion, *Separation and Purification Technology*, 72 (2010) 105-111.
- [16] S. Rodriguez, L. Vasquez, D. Costa, A. Romero, A. Santos, Oxidation of Orange G by persulfate activated by Fe(II), Fe(III) and zero valent iron (ZVI), *Chemosphere*, 101 (2014) 86-92.

## GRADUATE RESEARCH CENTRE

### DECLARATION OF CO-AUTHORSHIP AND CO-CONTRIBUTION: PAPERS INCORPORATED IN THESIS BY PUBLICATION

*This declaration is to be completed for each conjointly authored publication and placed at the beginning of the thesis chapter in which the publication appears.*

#### 1. PUBLICATION DETAILS (to be completed by the candidate)

Title of Paper/Journal/Book:	Advanced oxidation of orange G using phosphonic acid stabilised zerovalent iron	
------------------------------	---	--

Surname:	Ike	First name:	Ikechukwu
College:	College	Candidate's Contribution (%):	76

Status:			
Accepted and in press:	<input type="checkbox"/>	Date:	
Published:	<input checked="" type="checkbox"/>	Date:	30 July 2017

#### 2. CANDIDATE DECLARATION

I declare that the publication above meets the requirements to be included in the thesis as outlined in the HDR Policy and related Procedures – [policy.vu.edu.au](http://policy.vu.edu.au).

Ikechukwu Anthony Ike	Digitally signed by Ikechukwu Anthony Ike DN: cn=Ikechukwu Anthony Ike, o, ou, email=tonyjamesike@yahoo.com, c=AU Date: 2017.08.11 11:09:03 +10'00'	9 August 2017
--------------------------	--	---------------

Signature

Date

#### 3. CO-AUTHOR(S) DECLARATION

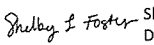
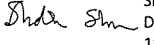
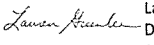
In the case of the above publication, the following authors contributed to the work as follows:

The undersigned certify that:

1. They meet criteria for authorship in that they have participated in the conception, execution or interpretation of at least that part of the publication in their field of expertise;
2. They take public responsibility for their part of the publication, except for the responsible author who accepts overall responsibility for the publication;
3. There are no other authors of the publication according to these criteria;
4. Potential conflicts of interest have been disclosed to a) granting bodies, b) the editor or publisher of journals or other publications, and c) the head of the responsible academic unit; and

5. The original data will be held for at least five years from the date indicated below and is stored at the following **location(s)**:

Institute for Sustainability and Innovation, Victoria University, Melbourne, Australia
--

Name(s) of Co-Author(s)	Contribution (%)	Nature of Contribution	Signature	Date
Shelby L. Foster	4	Synthesis and imaging of particles used for the study	 Digitally signed by Shelby L. Foster Date: 2017.08.14 13:44:29 -05'00'	
Sheldon R. Shinn	4	Synthesis and imaging of particles used for the study	 Digitally signed by Sheldon R. Shinn Date: 2017.08.14 18:07:53 -05'00'	
Skylar T. Watson	4	Synthesis and imaging of particles used for the study	 Digitally signed by Skylar Watson Date: 2017.08.16 19:02:28 -05'00'	
John D. Orbell	1	Manuscript revision		17/8/17
Lauren F. Greenlee	9	Manuscript revision	 Digitally signed by Lauren Greenlee Date: 2017.08.11 06:48:43 -05'00'	
Mikel C. Duke	2	Manuscript revision	 Digitally signed by Mikel Duke Date: 2017.08.11 10:42:49 +10'00'	

## Chapter 7

### **Steel wool and carbonyl iron powder activation of persulphate for pollutant degradation\***

#### **Abstract**

Commercial zerovalent iron (ZVI) - as steel wool and carbonyl iron powder - activation of persulphate (PS) has been demonstrated to be effective in the degradation of four important water pollutants, namely, orange G (OG), salicylic acid (SA), phenol (Ph) and 1-naphthylamine (1NA) in the presence or absence of methanol (MeOH). The addition of MeOH mimics the presence of industrial solvents and/or feedstuff in real industrial wastewater. MeOH had no effect on the nature of the degradation products but reduced the rate of degradation of the target pollutants. The alcohol had more retarding effect on the degradation of an aromatic pollutant relatively resistant to oxidation such as SA due to the presence of an electron-withdrawing group compared to a pollutant such as 1NA that has an electron-donating group. The azo bond in OG was found to constitute a structural weakness leading to a comparatively more effective degradation of the aromatic moieties. Compared to activation of PS by ionic Fe, the ZVI is shown to be more effective in the degradation of pollutants. In addition, the surfaces of the ZVI were not oxidised, an advantage over ZVI nanoparticles, and they required no prior pretreatment indicating the probable suitability of waste iron filings for PS activation. It was shown that gradual addition of PS achieves more effective pollutant degradation and mineralisation than sudden addition (except for SA) and always with less consumption of PS. These results are important for the development of affordable and effective schemes for the treatment of industrial wastewater.

#### **7.1. Introduction**

The activation of persulphate (PS) by Fe in its three common oxidation states has been the focus of numerous scientific investigations over the last two decades. Scavenging or depletion of PS, a short-lived activation requiring repeated resupply and introduction of additional anion are some of the challenges inherent

\*Under review for publication by Chemical Engineering Journal.

in the use of ionic Fe for PS activation [1, 2]. However, the use of zerovalent iron (ZVI) has been shown to overcome these challenges for efficient PS activation for the purpose of degrading a range of pollutants such as dibutyl phthalate [3], bentazon [4], p-chloroaniline [5], acetaminophen [6] and acid orange 7 [2]. ZVI as nanoparticles (nZVI) are more reactive than larger particles due to their higher surface area and the greater proportion of surface atoms [7, 8]. However, the problem of passivation due to surface oxidation upon exposure to air increases as particle size decreases. For example, Li et al [2] reported that an analytical grade of nZVI showed no measurable reaction with PS without acid washing - suggesting significant oxide passivation. Particle aggregation with attendant reduction in reactivity is another common problem implicit in the use of nZVI for pollutant degradation [7, 9, 10]. Consequently, size optimisation is critical for real-life application of ZVI activation of PS with the aim being that the particles are small enough to ensure rapid PS activation but large enough to minimise or eliminate surface passivation. Another important disadvantage of nZVI activation of PS relative to bulk ZVI is the high cost of the nanoparticles [7].

To advance the implementation of ZVI activation of PS for practical pollutant degradation, the performances of two ZVI materials that are low-cost, commercially available and with a size (at least in one dimension) <100 µm for rapid PS activation [2, 11] and >1 µm to eliminate surface oxidation [7], have been evaluated. One of the ZVI materials evaluated is industrial grade carbonyl iron powder (CIP) and the other is domestic grade steel wool (SW). The ultimate purpose was to promote the use of iron filings, which are widely available as by-products of iron processing and finishing, for environmental remediation applications. To highlight the practicality of ZVI/PS treatment of wastewater the degradation of a number of pollutants were evaluated, namely, orange G (OG), salicylic acid (SA), phenol (Ph) and 1-naphthylamine (1NA). The well-studied OG as a typical azo dye [11-13], was chosen to facilitate comparison to previous publications and because azo dyes constitute between 60-70% of global production of synthetic dyes [12-14] with about 20% lost to effluent in the textile industry, amounting to substantial water pollution [14, 15]. SA is one of the first pharmaceuticals to be detected in sewage effluent [16]. Due to its widespread use as an important pharmaceutical, either directly or in its acylated form as

acetylsalicylic acid (aspirin), SA is ubiquitous in the environment including drinking water and is considered an eco-risk [16, 17]. 1NA is described as a top priority, potentially carcinogenic pollutant, discharged from many industries such as the pharmaceutical and agrochemical industries [18]. Ph and its derivatives find important use in many chemical processes and are therefore ubiquitous at toxic concentrations in wastewater effluent [19, 20].

A number of researchers have reported on how coexisting inorganic ions and organic materials, usually natural organic matter (NOM), influence the degradation of environmental pollutants [12, 21, 22]. However, for industrial wastewater, NOM may be less important compared to industrial organic solvents and feedstuffs [23]. Since wastewater from industries and hospitals are known to be major contributors to environmental contamination [16, 23, 24], it is important that degradation studies should analyse the effect of commonly used industrial solvents and feedstuff on the degradation of target pollutants. Alcohols such as methanol (MeOH) are widely used industrial solvents and feedstuffs and have been identified in industrial wastewater [23, 25, 26]. Although MeOH and other alcohols are commonly used in the laboratory as radical scavengers and reactions quenchers [27], the systematic investigation of their effects on the radical degradation of target pollutants are uncommon. While it may be expected that the presence of MeOH like NOM [21, 22] may reduce the degradation of the target pollutant, it is not known if MeOH will influence the nature of the degradation products or whether different pollutants will be differently affected. This study includes an evaluation of the effect of MeOH on the degradation of the aforementioned target pollutants.

## 7.2. Experimental procedures

### 7.2.1. Materials

CIP of the CEP OM grade ( $\geq 98\%$  Fe,  $\leq 0.9\%$  C) from BASF (Germany) and SW of the 0000 grade from SIFA Pty. Ltd. (Australia) were used as received for PS activation. The following analytical grade chemicals were used as received: OG, sodium salt, from Sigma; PS, sodium salt ( $\geq 99\%$ ) from BDH, 1NA ( $\geq 99\%$ ) from BDH, Ph ( $\geq 99\%$ ) from Ajax Chemical, SA from Sigma. Others include MeOH ( $\geq 99.9\%$ ) from HoneyWell, tert-butanol (BuOH) ( $\geq 99.5\%$ ) from Sigma-

Aldrich, propanol-1 (PrOH) ( $\geq 99\%$ ) from BDH, sodium dihydrogen phosphate ( $\geq 99\%$ ) and disodium hydrogen phosphate ( $> 99\%$ ) from Rowe Scientific. MilliQ<sup>TM</sup> water from MerckMillipore Water Purification System was used throughout the study.

### 7.2.2. Methods

The ZVI samples were analysed using X-ray diffraction (XRD), Fourier transform infrared (FTIR) spectroscopy, N<sub>2</sub> porosimetry and optical imaging. XRD patterns for the samples were obtained using a Rigaku Miniflex 600 diffractometer, with Cu K $\alpha$  X-ray (1.541862 Å wavelength) operated at 40 kV and 15 mA at a step size of 0.02° and speed of 1.5 °/min from 2θ 20° to 120° with Ni K $\beta$ -filter (x2) and a D/tex detector. FTIR scans from 4000 to 600 cm<sup>-1</sup> at 32 accumulations and a resolution of 4 cm<sup>-1</sup> were collected using Perkin Elmer FTIR Spectrometer with Universal ATR Diamond/ZnSe crystals. N<sub>2</sub> porosimetry for surface area determination using Brunauer–Emmett–Teller (BET) model was conducted using Micrometrics TriStar Surface Area and Porosity Analyser with TriStar 3000 version 6.04 analysis software. Optical images of the ZVI samples were taken using Motic BA310 Advanced Upright Microscope with Motic Live Imaging Module.

Batch degradation experiments were conducted at  $\sim 24$  °C, for a fixed ZVI concentration of 0.1 g/L (1.8 mM) with or without a background MeOH of 25 mM to determine the effect of MeOH on the target pollutant degradation. Experiments with OG (0.1 mM) were conducted at varying initial PS concentration (C<sub>PS,0</sub>) of 1 mM, 2 mM, 5m and 10 mM to determine the effect of PS concentration on the effectiveness of the target pollutant degradation. To determine the effect of pH on PS activation by ZVI, degradation experiments with SA (0.1 mM) were conducted with and without pH modification. 10 mM phosphate buffer composed of 5 mM of NaH<sub>2</sub>PO<sub>4</sub> and 5 mM of Na<sub>2</sub>HPO<sub>4</sub> was used to stabilise the reaction pH for pH-modified reactions [21]. Experiments with 1NA and Ph (0.2 mM) were conducted in the presence of background MeOH (25 mM) except where otherwise stated. PrOH (2000 mM) and BuOH (2100 mM) [27], were used as radical scavengers in evaluating pollutant degradation mechanism. At designated intervals during the degradation experiments, 1 ml samples of the reacting

suspensions were withdrawn using a syringe and filtered through a 0.2 µm syringe filter into 0.5 ml methanol to quench the reactions [6]. The concentrations of PS in solution were determined by the iodometric method [28].

The rates of OG degradation were measured spectrophotometrically at the azo bond characteristic absorption wavelength of 478 nm [12] using Biochrom Libra S22 UV/Visible Spectrophotometer. High performance liquid chromatography (HPLC) study of OG, 1NA, SA and Ph degradations were conducted using a Shimadzu Prominence-i LC 2030C Liquid Chromatograph with UV detector at 280 nm. The column used was Kinetex C18 5µ 100 Å, size 100 x 4.6 mm maintained at 25 °C and preceded by a column guard. Binary solvent linear gradient flow at 0.8 mL/min was employed in which the concentration of solvent A, methanol, was increased from 30% to 90% in 10 min, maintained at 90% for 2.50 min and then rapidly decreased to 30% in 0.30 min. At this composition (A 30%), the column was equilibrated for 7.30 min. Solvent B was 50 mM ammonium phosphate at a pH of 6.8. Further peak analysis was conducted with a Shimadzu LC-20AT Liquid Chromatograph equipped with diode array detector (DAD) under LC conditions already described. An exception was the column temperature which was ambient in the DAD analysis. Total carbon (TC) was determined using Shimadzu TOC-V<sub>CSH</sub>Total Organic Carbon Analyzer. Samples for TC analysis were filtered through a 0.2 µm syringe filter and quenched in an ice bath [29] with TC analyses typically conducted and completed few hours after samples collection. Dissolved Fe was measured using Shimadzu atomic adsorption spectroscopy AA-6300 with Fe flame at a wavelength of 372 nm.

### 7.3. Results and discussions

#### 7.3.1. Characterisation of ZVI samples

The XRD patterns for the two ZVI samples are presented in Figure 7.1a showing peaks for Fe indexed to ICCDD 6-696. The shift in peak position for SW is believed to be due to inadequate height positioning arising from the woollen nature of the sample. The absence of any detectable oxidized Fe peak shows that the Fe samples are stable in air and are consequently unpassivated unlike nZVI [7]. The FTIR spectra for the samples are shown in Figure 7.1b. Unlike the XRD patterns which reveal the long range order of atoms or overall crystalline

properties of the samples, the FTIR spectra highlight short range order structures and therefore could better identify features restricted to the material surface [30-32]. Important difference in surface properties can be clearly seen for the SW and CIP spectra. The SW spectra show peaks that are assignable to C-H from alkane [33] which is indicative of surface coating probably by hydrocarbon. No such organic peaks were developed in the CIP spectra suggestive of cleaner surfaces. However, peaks that are assignable to iron carbonyls are developed in CIP but not in SW, which clearly confirm the carbonyl nature of the former but not the latter. The absorbance in Figure 7.1a is significantly low, which is suggestive of low concentration of non-Fe components consistent with CIP specifications, provided earlier.

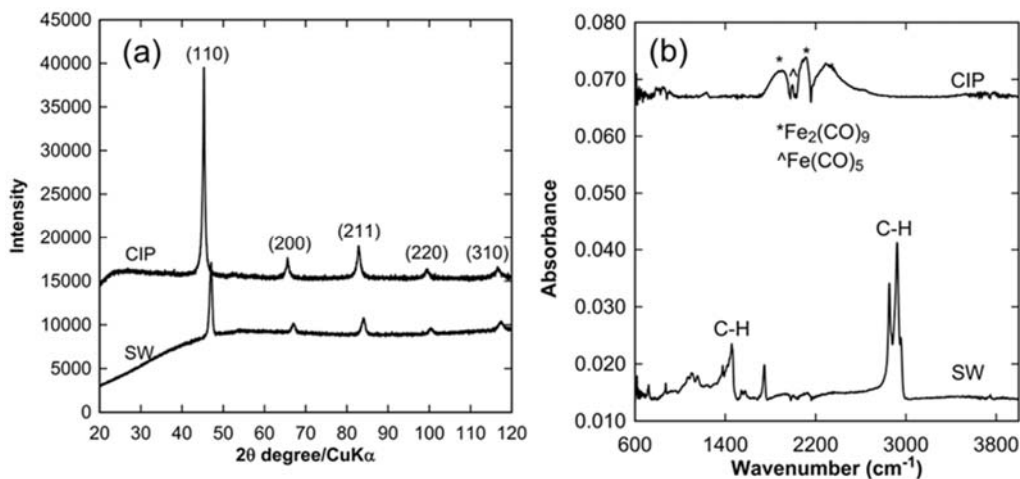


Figure 7.1. XRD patterns (a) and FTIR spectra (b) for SW and CIP.

The isotherm plot for SW and CIP are shown in Figure S7.1 in the Appendix. The isotherm for CIP could be described as a regular Type II isotherm for a non-porous or macroporous adsorbent whose surface area can be described by BET [34]. The measured BET for CIP was  $0.54 \text{ m}^2/\text{g}$ . Using  $7.86 \text{ g}/\text{cm}^3$  as the density of iron and the expression given in Equation 7.1 [35], the average diameter for the CIP particles is calculated as  $1.4 \mu\text{m}$ . Unfortunately, the isotherm plot for SW is irregular as shown in Figure S7.1 and thus the obtained BET value is not valid.

$$d = \frac{6000}{S \times \rho}$$

The optical images for the samples are shown in Figure 7.2. It can be seen that the CIP sample is composed of spherical particles with some degree of particle aggregation. The CIP particles as observed in the optical image, as computed by BET and as specified by the supplier of the particles are  $< 10 \mu\text{m}$ . The SW material is made up of sparsely arranged cylindrical fibres. The diameters of the fibres are  $< 30 \mu\text{m}$ . In addition, fibres generally have surface chippings or irregularities which may be linked to the manufacturing process. This unevenness in the surface morphology or projections may contribute towards enhancing the chemical reactivity of the ZVI fibres as it provides comparatively higher surface area to volume with respect to the overall fibre size [7].

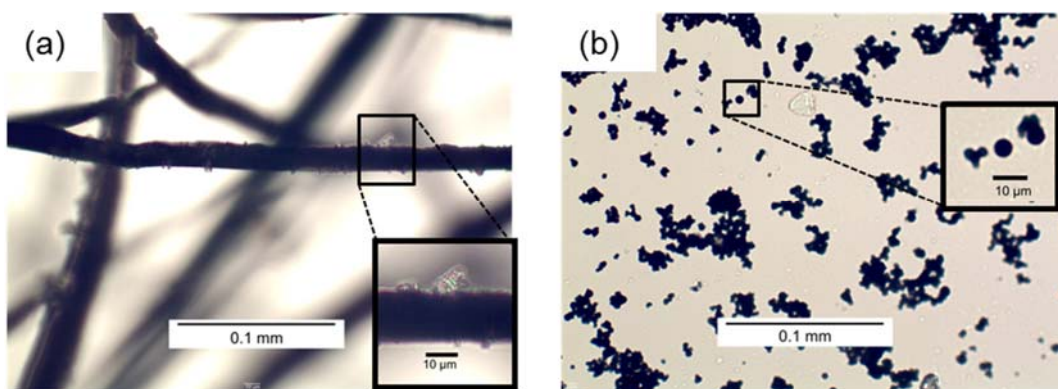
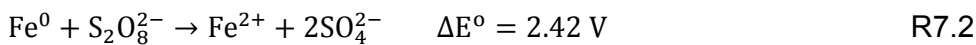


Figure 7.2. Optical image of SW (a) and CIP (b)

### 7.3.2. Degradation of OG

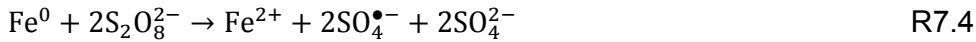
The results of the OG batch degradation experiments for  $C_{\text{PS},0} = 1 \text{ mM}$  is presented in Figure 7.3a where the normalised OG concentration,  $C_{\text{OG},t}/C_{\text{OG},0}$ , is plotted against the reaction time,  $t$ .  $C_{\text{OG},t}$  represents the OG concentration at a given time and  $C_{\text{OG},0}$  concentration at time 0. For  $C_{\text{PS},0} = 1 \text{ mM}$ , the degradation trends for  $\text{Fe}^{2+}$  ( $1.8 \text{ mM}$ ) is also shown. It can be seen that relative to the ZVI, the  $\text{Fe}^{2+}$  resulted in an early rapid degradation of OG but the rate quickly declined suggesting exhaustion of reactive species with limited pollutant removal. This is a characteristic shortcoming in the use of  $\text{Fe}^{2+}$  for PS activation [1].  $\text{Fe}^{3+}$ , the other common ionic form of Fe used in PS activation, typically achieves a slower pollutant degradation rate than  $\text{Fe}^{2+}$  [11] and therefore was not evaluated in this

work. The reason for the poorer activation of PS by  $\text{Fe}^{3+}$  relate to the fact that the standard reduction potential ( $E^\circ$ ) of PS is highly positive (+1.98 V) [36]; hence PS will react more readily as an oxidiser than as a reducer. The observed early rapid degradation of OG achieved by  $\text{Fe}^{2+}$  does not relate to higher specific  $\text{Fe}^{2+}$  reaction with PS compared to ZVI since the  $E^\circ$  for  $\text{Fe}^{3+}/\text{Fe}^{2+}$  couple is +0.771 V [36] while the  $E^\circ$  for  $\text{Fe}^{2+}/\text{Fe}^0$  couple is -0.44 V [36]. Consequently, the electrochemical potential gradient ( $\Delta E^\circ$ ) driving the redox reactions between PS and the Fe species are:



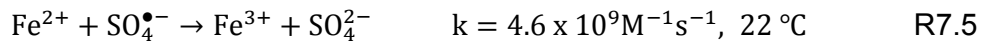
From these expressions, it can be seen that the  $\Delta E^\circ$  for the oxidation of ZVI is almost double the driving force for the oxidation of  $\text{Fe}^{2+}$ . Consequently, the higher initial degradation rate observed for  $\text{Fe}^{2+}$  does not indicate faster reaction between PS and  $\text{Fe}^{2+}$  compared to ZVI. An explanation for the initial higher rate for  $\text{Fe}^{2+}$  may be related to  $\text{Fe}^{2+}$  greater reacting surface as a solution compared to the limited surface area of the ZVI.

The radical generating reactions between PS and the Fe species have been expressed as [2, 12]:



The rate constant for R7.4 is not readily available in the literature probably due to the strong dependence of the reaction rate on the size of the ZVI [2]. Comparing R7.3 and R7.4 to R7.1 and R7.2, it could be said that radicals are formed when the Fe species are in short supply. Hence, when  $\text{Fe}^{2+}$  is abundant, R7.1 is favoured relative to R7.3. Since  $\text{Fe}^{2+}$  in solution are available almost at the same time compared to ZVI particles with limited surface area, it could be said that the non-radical producing reaction (R7.1 or R7.2) is more likely to occur with  $\text{Fe}^{2+}$  than with  $\text{Fe}^0$  when both are available at the same concentration. This partly explains the early decline in the reaction shown by  $\text{Fe}^{2+}$  in Figure 7.3 due to the possible production of more non-radical  $\text{SO}_4^{2-}$ . It may also be pointed out that the

large electrochemical driving force for ZVI activation of PS may result in more energetic radicals for pollutant degradation compared to radicals produced by Fe<sup>2+</sup>. Furthermore, Fe<sup>2+</sup> reaction with the sulphate radical is very rapid (R7.5) compared to the radical generating reaction (R7.3) which is often implicated for the limited pollutant degradation performance of Fe<sup>2+</sup> activation [2].



Finally, since R7.4 results in the production of Fe<sup>2+</sup> which could take part in R7.3, it may be said that there are two distinct PS activators when ZVI is used (Fe<sup>0</sup> and Fe<sup>2+</sup>) but only one activator when Fe<sup>2+</sup> is used. Consequently, ZVI activation of PS is a more effective route for pollutant degradation.

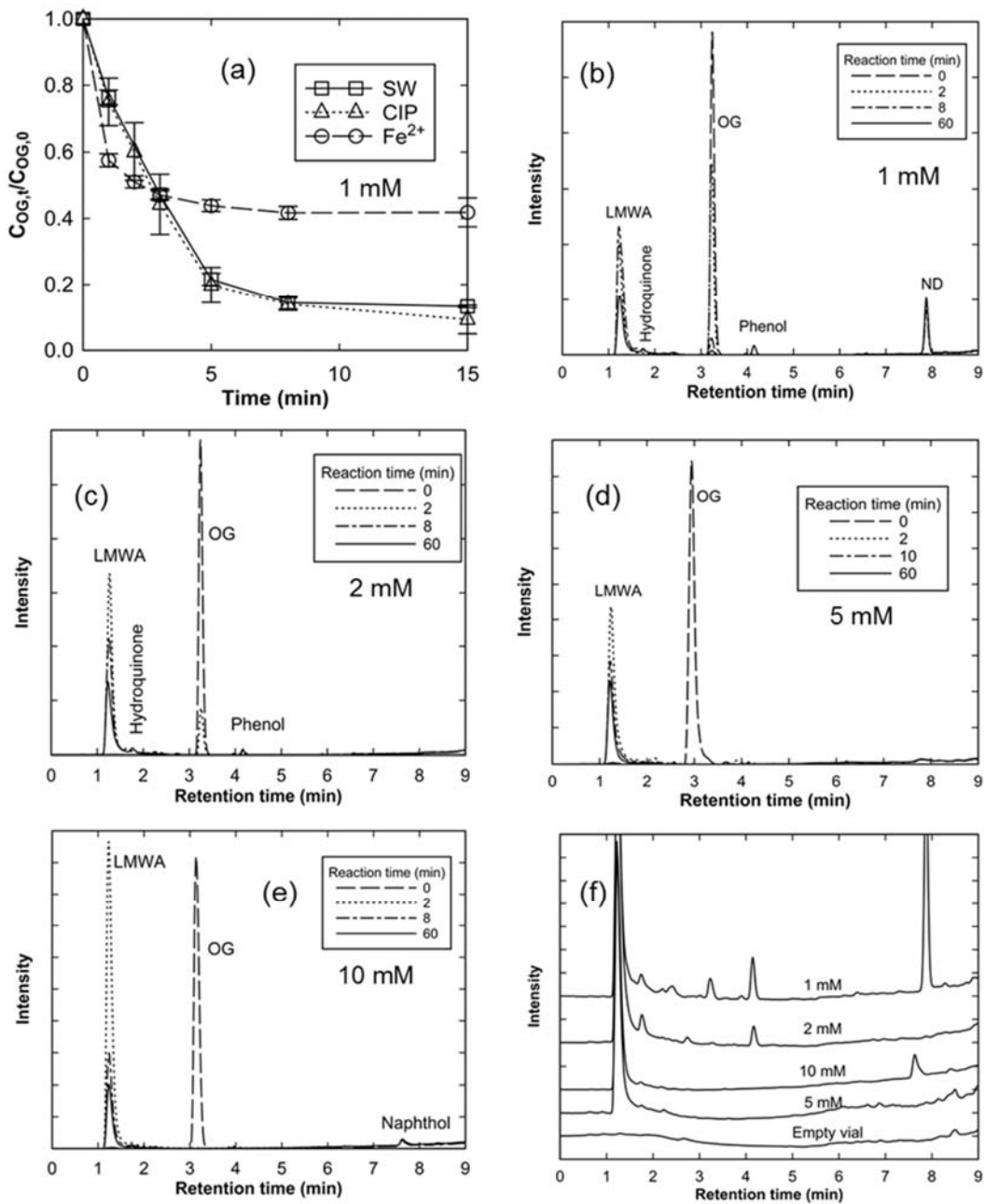


Figure 7.3. The degradation of OG by PS. Degradation trends for  $C_{PS,0} = 1 \text{ mM}$  activated by SW, CIP and  $\text{Fe}^{2+}$  (a); chromatograms for OG degradation by SW activated PS for  $C_{PS,0} = 1 \text{ mM}$  (b); 2 mM (c); 5 mM (d); and 10 mM (e). Comparison of degradation chromatograms at 60 min for various initial concentration of PS (f). Experiments conducted at room temperature (24 °C);  $C_{OG,0} = 0.1 \text{ mM}$ ; concentrations of iron species fixed at 0.1 g/L (1.8 mM);  $\text{Fe}^{2+}$  present as  $\text{FeCl}_2$ ; pH unmodified and no buffer was added.

The degradation trends in Figure 7.3a may be described by a pseudo first order reaction as expressed in Equation 7.2.

$$\ln C_{OG,t}/C_{OG,0} = -k_{obs}t \quad 7.2$$

where  $k_{obs}$  is the observed pseudo first order reaction constant ( $\text{min}^{-1}$ ) and t is the reaction time in minutes. The  $k_{obs}$  for SW, CIP and  $\text{Fe}^{2+}$  activated PS degradation of OG were  $0.117 \text{ min}^{-1}$  ( $R^2 = 0.9934$ ),  $0.121 \text{ min}^{-1}$  ( $R^2 = 0.9918$ ) and  $0.089 \text{ min}^{-1}$  ( $R^2 = 0.7402$ ), respectively. The relatively poor  $R^2$  for  $\text{Fe}^{2+}$  suggests that the early burst in activation and subsequent exhaustion did not fit very well an exponential decline. However, the exponential model was maintained to facilitate comparison to the other activators. The  $k_{obs}$  for CIP and SW are similar which is suggestive of similar chemical behaviour despite their different physical forms and surface features.

Rodriguez et al. [11] showed that OG was not completely degraded after 100 min for an experiment with  $0.1 \text{ mM OG}$ ,  $C_{PS,0} = 1 \text{ mM}$  and ZVI activation, while almost complete degradation was achieved in this study under 10 min. Although  $1 \text{ mM ZVI}$  was used in the study by Rodriguez et al. [11] versus the  $1.8 \text{ mM}$  used in this study, the difference cannot explain the dissimilarity in the degradation times. Particle size difference appears to be a better explanation [37] since the average particle size of the ZVI used by Rodriguez et al. [11] was  $740 \mu\text{m}$ , which is 500 times larger than the computed average particle size ( $1.4 \mu\text{m}$ ) of the CIP ZVI used in this study. In a recent study by Ike et al. [38] of PS degradation of OG under the same condition as reported in this study but using as PS activators three nZVI samples with different phosphonic-acid stabilisation, the reported  $k_{obs}$  for OG degradation were  $0.44 \text{ min}^{-1}$ ,  $0.36 \text{ min}^{-1}$  and  $0.06 \text{ min}^{-1}$ . Hence, the commercial ZVI used in this study with  $k_{obs}$  of  $0.12 \text{ min}^{-1}$  outperformed one of the nZVI samples. The three nZVI synthesised by Ike et al. [38] showed significant surface oxidation although the phosphonic acid stabilisation were said to prevent outright passivation in contrast to the complete passivation of the unstabilised nZVI reported by Li et al. [2], which required prior acid washing to be able to activate PS. From the foregoing, it is evident that ZVI with average diameter of particles in the size range,  $1 \mu\text{m} < d > 100 \mu\text{m}$ , as were SW and CIP in this study or available as iron filings generated as by-products of iron processing and finishing

can provide for effective and fast PS activation without the need of surface stabilisation or pretreatment.

The HPLC chromatograms for SW activated PS degradation of OG is given in Figure 7.3b-f. The chromatograms for CIP are similar to those of SW and are given in Figure S7.2, which corroborates the assertion that the behavior of SW and CIP in activating PS is similar, at least for short-term experiments. Tentative assignment of the degradation products has been provided based on the retention times of known chemicals as presented in Table S7.1 under the same chromatographic conditions as the degraded pollutant solutions. The general trend of the retention times reveals short retention times for more oxidised chemicals (relatively hydrophilic) and longer retention times for more reduced chemicals (relatively hydrophobic).

From Figure 7.3b for  $C_{PS,0} = 1 \text{ mM}$  under ZVI activation, it can be seen that degradation products identified as LMWA (low molecular weight acid), hydroquinone, phenol and ND (naphthalene derivatives) persisted after 60 min. When  $C_{PS,0} = 2 \text{ mM}$ , the ND peak disappeared but the phenol and hydroquinone peaks alongside the LMWA peak remained.  $C_{PS,0} = 5 \text{ mM}$  saw the disappearance of all degradation peaks at the end of 60 min except the LMWA peak. However, for  $C_{PS,0} = 10 \text{ mM}$ , a naphthol peak persisted after 60 min indicating that  $C_{PS,0} = 5 \text{ mM}$  is optimised for the degradation of OG under the conditions of this study. Similar optimisation is important for efficient pollutant degradation in field application of activated PS treatment of pollutants.

Based on the degradation products, OG degradation possibly progressed by a rapid radical attack on the azo bond resulting in the removal of  $N_2$  [39] and the formation of a one ring and two rings aromatic chemical species [11]. Further radical attacks transformed the radical species through hydroquinone to LMWA, which was subsequently mineralised to  $CO_2$  and  $H_2O$ . The DAD generated spectra shown in Figure S7.3 when compared with spectra for known chemicals shown in Figure S7.4 indicate that the LMWA is fumaric acid with the possibility of the presence of oxalic and/or maleic acid. A simplified reaction mechanism is shown in Figure 7.4.

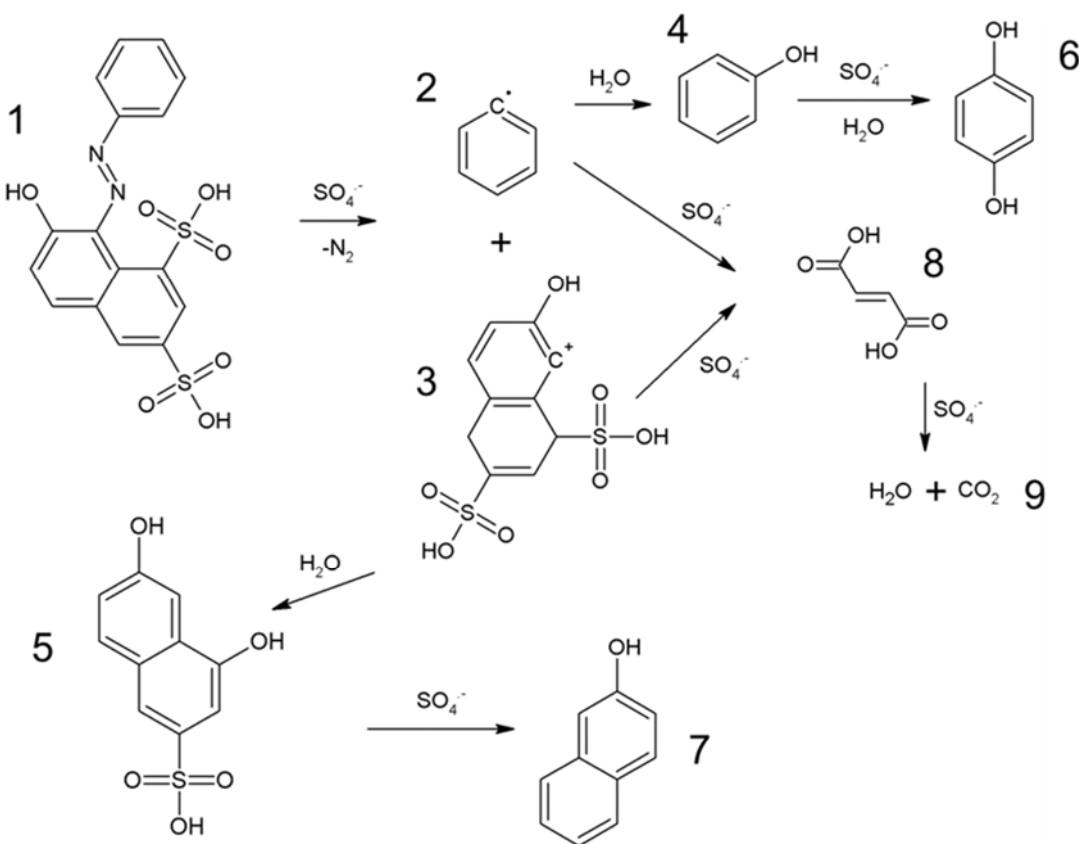


Figure 7.4. OG simplified degradation pathway

The effect of the presence of MeOH on the degradation of OG for a PS/Fe/OG/MeOH molar ratio of 5/1.8/0.1/25 is presented in Figure 7.5a. The  $k_{obs}$  for OG degradation by  $\text{C}_{\text{PS},0} = 5 \text{ mM}$  activated by SW was  $1.428 \text{ min}^{-1}$  ( $R^2 = 0.9832$ ) but in the presence of MeOH, the  $k_{obs}$  was  $0.631 \text{ min}^{-1}$  ( $R^2 = 0.9891$ ) indicating a 56 % reduction. When  $\text{Fe}^{2+}$  was used for PS activation in the presence of MeOH,  $k_{obs}$  was only  $0.020 \text{ min}^{-1}$  ( $R^2 = 0.6612$ ) which amounts to 99% reduction in degradation rates with respect to SW activation in the absence of MeOH. As expected, MeOH slowed the rate of degradation of OG but the effect was more drastic when  $\text{Fe}^{2+}$  was used as PS activator. Once again, this shows that ZVI is a better PS activator than  $\text{Fe}^{2+}$ . Figure 7.5b and 7.5c are chromatograms of OG degradation in the presence of MeOH. Compared to Figure 7.3, the presence of MeOH did not appear to have influenced the nature of the degradation products. At the end of 60 min, while only LMWA can be

identified for SW activation, for  $\text{Fe}^{2+}$  activation, two other degradation peaks persisted in addition to undecomposed OG.

For  $C_{\text{PS},0} = 5 \text{ mM}$ , the  $k_{\text{obs}}$  for OG degradation in the presence of excess BuOH (Figure 5d) was  $0.0855 \text{ min}^{-1}$  ( $R^2 = 0.9414$ ) while in the presence of excess PrOH, it was  $0.004 \text{ min}^{-1}$  ( $R^2 = 0.8407$ ). OG degradation rate in the presence of BuOH is therefore 21 times the rate in the presence of PrOH. Since  $\text{SO}_4^{\bullet-}$  reaction with BuOH is limited compared to its reaction with  $\alpha$ -hydrogen containing alcohol such as PrOH, it may be said that the principal oxidising radical for OG degradation in this study was  $\text{SO}_4^{\bullet-}$  [27].

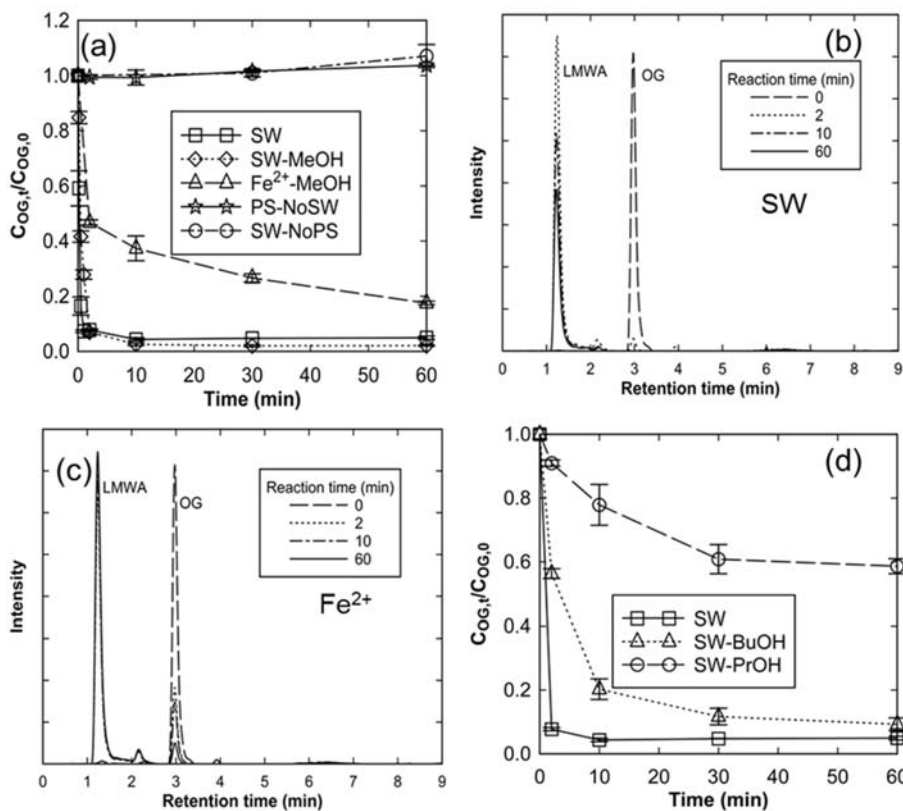


Figure 7.5. The degradation and mineralisation of OG by PS with or without MeOH. OG degradation trends for PS activated by SW and  $\text{Fe}^{2+}$  with or without 25 mM MeOH (a); chromatograms for OG degradation by PS activated by SW for PS/Fe/OG/MeOH of 5/1.8/0.1/25 (b); chromatograms for OG degradation by PS activated by  $\text{Fe}^{2+}$  for PS/Fe/OG/MeOH of 5/1.8/0.1/25 (c); OG degradation trends in the presence of 2000 mM PrOH or 2100 mM BuOH (d). Experiments conducted at room temperature (24 °C) with 0.1 mM OG solution;  $C_{PS,0} = 5 \text{ mM}$  (except where otherwise indicated); concentrations of iron species fixed at 0.1 g/L (1.8 mM);  $\text{Fe}^{2+}$  present as  $\text{FeCl}_2$ ; pH unmodified and no buffer was added.

The degree of mineralisation was measured by TC at  $C_{PS,0} = 10 \text{ mM}$ . The result is shown in Figure 7.6. Experiment at lower  $C_{PS,0}$  did not result in significantly better mineralisation in short term. The mineralisation trend shown in Figure 7.6 is typical of dye degradation experiments as previously reported [11, 12]. While OG decolourisation was accomplished in few minutes, mineralisation is seen to proceed at a much slower pace. From the previous section, it was shown that OG

degradation was rapid and was succeeded by the transformation of the aromatic degradation products to LMWA. The relatively slow conversion of the LMWA may be due to exhaustion of the reacting species or to a reduced reaction rate between the generated radical and the LMWA. The ZVI were typically dissolved in the first hour of the reaction so that the mineralisation proceeding for several hours is due to ionic Fe. Compared to previous results where the difference in the chemical behavior between SW and CIP are minimal, the extended mineralisation result shows a marked difference in behavior between the two forms of ZVI. The oxidised SW solution was found to be cloudy as the reaction extended over several hours while the oxidised CIP solution remained relatively clear suggesting the formation of colloidal  $\text{Fe}^{3+}$  species in the former. At the end of the 48 h mineralisation experiment, the amount of dissolved Fe in filtered solution of CIP compared to SW was higher by 25% confirming the formation of limited solubility ionic Fe species in SW. Mineralisation recorded for CIP at 48 h was found to be 29% higher than for SW. This result appears to indicate that the difference in soluble Fe explains the difference in the degree of mineralisation between the two ZVI samples. It is plausible that the carbonyl structures in CIP helped to prevent Fe precipitation.

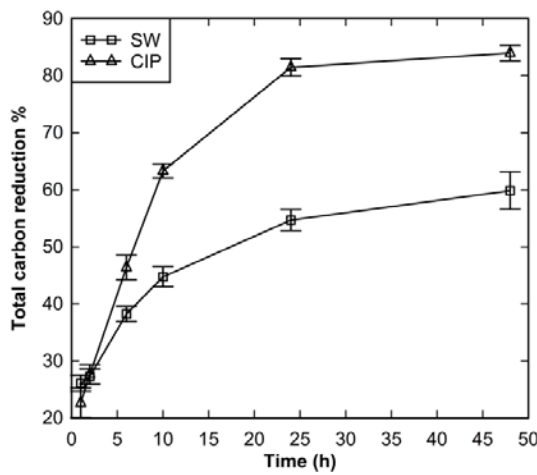


Figure 7.6. Total carbon reduction for 0.1 mM OG at 24 °C.  $C_{\text{PS},0} = 10 \text{ mM}$ ,  $[\text{Fe}] = 1.8 \text{ mM}$

The effect of the mode of PS addition to ZVI activated reactions was studied by recording the TC reduction achieved in 60 min for 5 mM PS added at once or gradually to 1.8 mM SW. The first mode (hereafter referred to as E1) was the

addition of the 5 mM PS all at once to start the radical reaction. The second mode (E2) involve the addition of 1 mM PS every 10 min for five times. The third mode involves the addition of 2 mM PS to start the reaction, another 2 mM PS after the first 10 min and an additional 1 mM PS at the end of 20 min. A fourth experiment, E4, was performed in which 50 mM PS was added suddenly to start the reaction. The mineralisation achieved at the end of 60 min is shown in Figure 7.7.

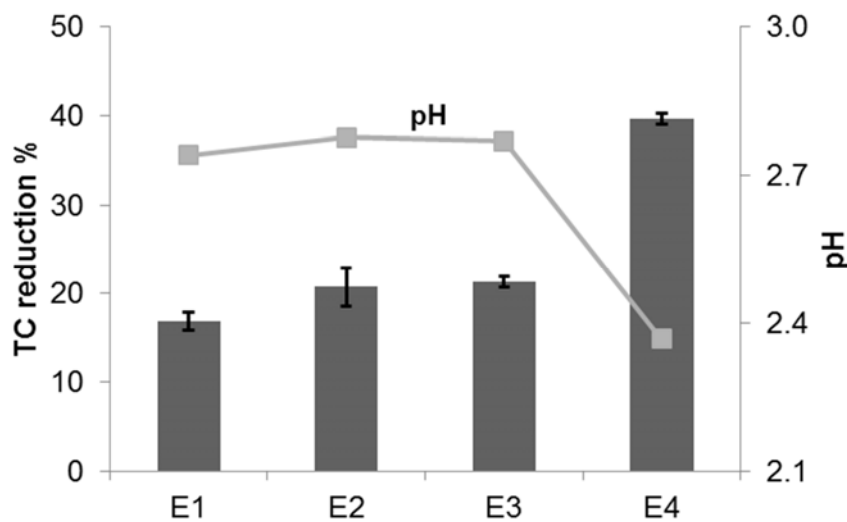


Figure 7.7. Effects of initial concentration and mode of PS addition on the TC reduction for 0.1 mM OG at 24 °C. [Fe] = 1.8 mM. No buffering or pH modification.

The greatest mineralisation observed was for E4 due to its higher  $C_{PS,0}$ . However, although the  $C_{PS,0}$  for E4 is 10 times the value used in E1, the TC reduction for the latter is only slightly more than two times the TC reduction in E1 showing that mere increase in the PS concentration does not lead to proportionally higher mineralisation. It can also be seen that the TC reduction for E2 and E3 are slightly higher than for E1 although the same overall amount of PS were added. The slightly poorer mineralisation achieved by E1 compared to E2 and E3 may be linked to more radical scavenging due to the possible profusion of radicals following the sudden addition of 5 mM PS.

However, it was also noticed that the appearance of the solution were very different: E2 was particularly cloudy while E1 and E4 were clear solution. The syringe filter used to filter E2 was significantly coloured yellow (see Figure S7.5) suggesting the formation of insoluble Fe<sup>3+</sup> species while the E1 filter was uncoloured. Since E1 was relatively clear but with a pH value close those of E2 and E3, which were both relatively cloudy, and different from that of E4, which was clear, it follows that pH does not explain the precipitate formation observed. Consequently, the mode of PS addition significantly influenced oxidised Fe speciation. A possible explanation for the difference in Fe speciation might be advanced as follows. The addition of 1 mM PS gradually oxidised some Fe<sup>0</sup> to Fe<sup>2+</sup>, producing some SO<sub>4</sub><sup>•-</sup> (R7.4) leading to the gradual degradation of OG. In addition to SO<sub>4</sub><sup>•-</sup> oxidation of Fe<sup>2+</sup> (R7.5), Fe<sup>2+</sup> may be oxidised by dissolved O<sub>2</sub> to low solubility Fe<sup>3+</sup> species to give a cloudy solution by a process that is credited to produce perhydroxy radical (HOO<sup>•</sup>) and hydroxyl radical (HO<sup>•</sup>) [40, 41]. The additional radical species may have contributed to the better mineralisation recorded for E2 and E3 compared to E1. On the other hand, addition of relatively large amount of PS results in rapid Fe oxidation as well as OG degradation producing intermediates with more complexing ability than OG which prevents ionic Fe precipitation. Difference in Fe speciation arising from the mode of PS addition might be useful in controlling the amount of dissolved Fe in treated water.

### 7.3.3. Degradation of salicylic acid

The degradation of SA was investigated considering E1 and E2 modes of PS addition as shown in Figure 7.8a. The chromatograms for E1 and E2 degradation of SA is given in Figures 7.8b and 7.8c, respectively, showing complete degradation of SA for E1 mode with LMWA being the sole degradation product at 60 min. For E2 mode, SA degradation was incomplete at 60 min and a small hydroquinone peak could be identified. The  $k_{obs}$  for E1 was 0.228 min<sup>-1</sup> ( $R^2 = 0.9955$ ) and that for E2 was only 0.0231 min<sup>-1</sup> ( $R^2 = 0.9964$ ). As shown in Figure 7.8g, E1 achieved 40% mineralisation of SA while 37% mineralisation resulted from E2. From these, it may be said that for a degradation period of 60 min under the conditions of this study, sudden addition of PS is more effective for the degradation of SA than gradual addition. However, it can be seen that leftover

PS was 34% for E1 but it was 50% for E2. Hence, there is more possibility for further pollutant degradation by E2 if the experimental time were lengthened.

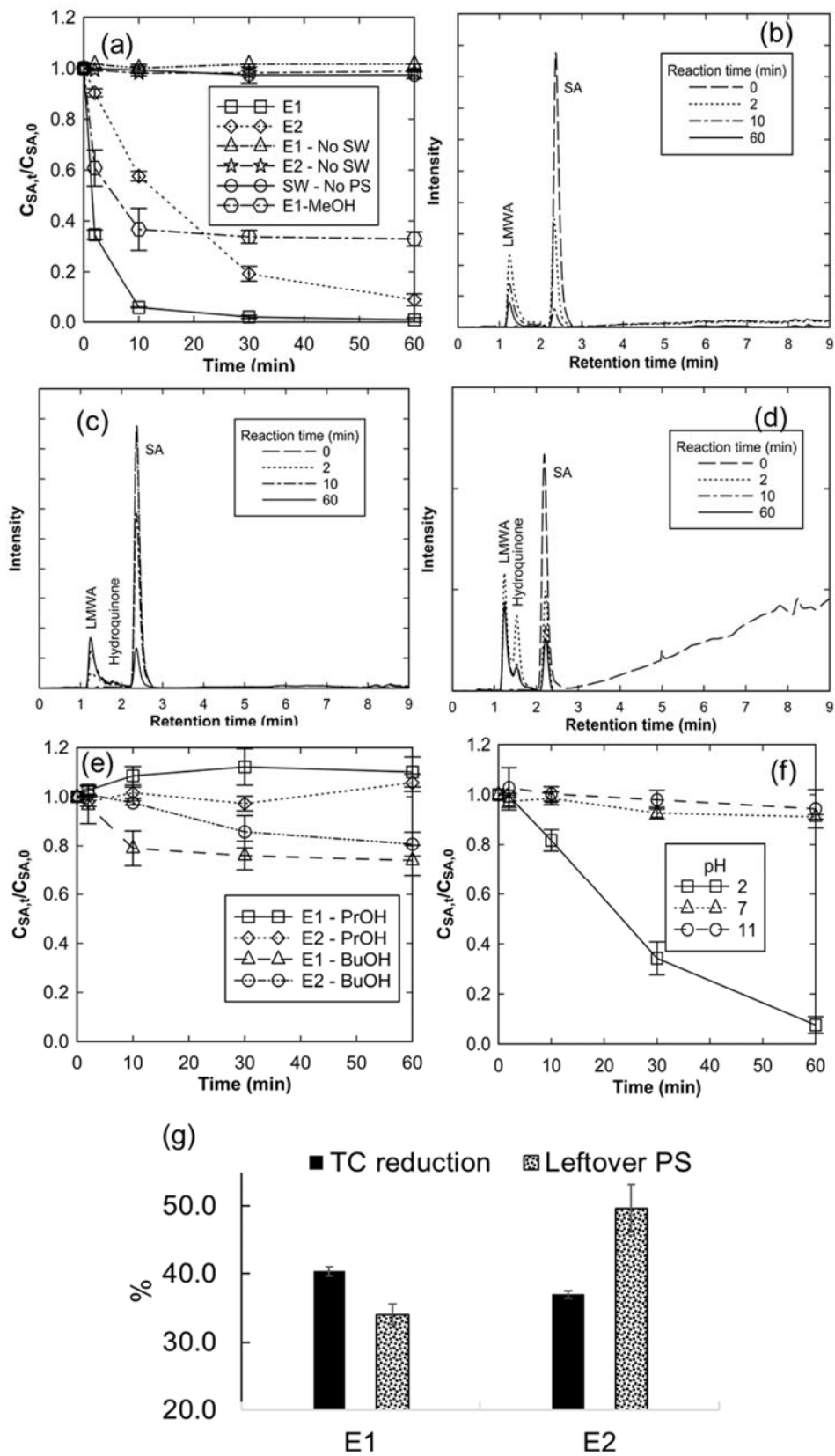


Figure 7.8. Degradation and mineralisation of SA. E1 and E2 degradation trends for SA decomposition (a); chromatograms for E1 mode of SA degradation (b); chromatograms for E2 mode of SA degradation (c); chromatograms for E1 mode of SA degradation in the presence of 25 mM MeOH (d); degradation trends in the presence of 2000 mM PrOH and 2100 mM BuOH (e); degradation trends under 10 mM phosphate-buffer controlled pH (f); TC reduction and leftover PS at 60 min (g). Experiments conducted at room temperature (24 °C); initial concentration of SA 0.1 mM; concentrations of iron species fixed at 0.1 g/L (1.8 mM).

In the presence of 25 mM MeOH, the  $k_{obs}$  for E1 mode of SA degradation was  $0.048 \text{ min}^{-1}$  ( $R^2 = 0.8671$ ) which represents a 79% reduction with respect to E1 mode of SA degradation in the absence of MeOH. The chromatogram in Figure 7.8d shows that no change in the degradation products resulted from the presence of MeOH only that the transformation to LMWA was slower due to radical consumption by MeOH. In the presence of 2000 mM PrOH, practically no degradation of SA was observed over 60 min and with 2100 mM BuOH a slight SA degradation of about 20% was observed in the course of 60 min. The results can be interpreted to mean that the major oxidising radical for SA degradation, like OG degradation, was  $\text{SO}_4^{\bullet-}$ . However, it is evident that SA degradation in the presence of PrOH and BuOH was much poorer compared to OG degradation. The results reflect the relative ease with which an oxidising radical can successfully attack the electron-rich azo bond in OG compared to a successful attack on the resonance-stabilised benzene ring. Although OG contains three benzene rings compared to the one benzene ring of SA, it can be seen that in the presence of MeOH, the benzene rings in OG were completely converted to LMWA within 60 min (Figure 7.5b). In contrast, for SA degradation in the presence of MeOH, benzene rings as SA and hydroquinone persisted after 60 min. The results can be explained as follows. The comparatively fast oxidation of the azo bond in OG resulted in relatively fast production of aromatic radical species as shown in Figure 7.4. These aromatic radicals were expectedly more reactive than a regular benzene ring [39] and were therefore readily transformed to LMWA. Hence, the azo bond is a weak link for oxidative attack on OG. Such a point of weakness is absent in SA requiring an attack on the resonance-stabilised

ring structure to begin the oxidative transformation to LMWA. The degradation of SA is summarised in Figure 7.9 showing the transformation to hydroquinone (2) and then to LMWA (3) before mineralisation.

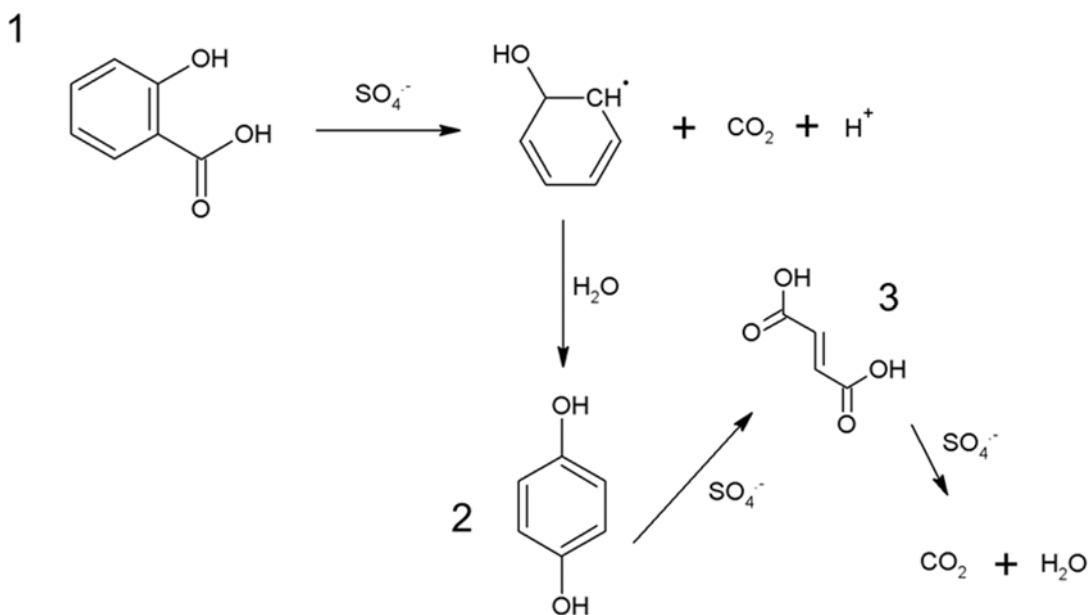
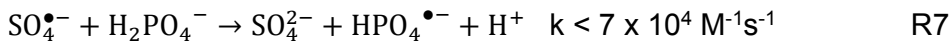


Figure 7.9 SA simplified degradation pathway

The results of the study of the effect of phosphate-stabilised pH on SW activation of PS for the degradation of SA is given in Figure 7.8f. Scarcely any degradation was achieved within 60 min at the neutral and basic conditions –  $k_{obs} = 6.51 \times 10^{-4} \text{ min}^{-1}$  ( $R^2 = 0.8595$ ) and  $5.24 \times 10^{-4} \text{ min}^{-1}$  ( $R^2 = 0.8830$ ), respectively – while 92% degradation was achieved at the acidic pH of 2 with a  $k_{obs}$  of  $0.015 \text{ min}^{-1}$  ( $R^2 = 0.9826$ ). From the results, it may be said that SW activation of PS under neutral and basic conditions is practically negligible. However, when the results of the acidic pH degradation of SA is compared to similar degradation experiment in the absence of the phosphate buffer, it is seen that the rate of SA degradation decreased by 93% due to the radical scavenging effect of phosphate. Consequently, the phosphate buffer may also have contributed to the poor degradation observed at the neutral and alkaline conditions as well. It has been reported that the rate of reaction of  $\text{SO}_4^{\bullet-}$  with the phosphate ion depends on the degree of phosphate ion protonation as follows [4, 42]:





The pKa1, pKa2, and pKa3 of the phosphate ion was computed as 1.80, 6.95 and 12.90, respectively ([www.chemicalize.com](http://www.chemicalize.com)). From these, it may be surmised that at a neutral pH, one-half of the phosphate ion exist as  $\text{HPO}_4^{2-}$ , i.e. 5 mM of the phosphate ion exist in the more reactive form with  $k = 1.2 \times 10^6 \text{ M}^{-1}\text{s}^{-1}$ , which is only one order of magnitude less reactive than methanol ( $k = 2.5 \times 10^7 \text{ M}^{-1}\text{s}^{-1}$  [43]). At a pH of 11, most of the phosphate ions exist in the more reactive form. Under these conditions, significant radical scavenging may result from the presence of the phosphate buffer, which may account, at least partly, for the poor SA degradation observed. At a pH of 2, the greater proportion of phosphate ions exist in the protonated and less reactive form of  $\text{H}_2\text{PO}_4^-$ . Consequently, it may be said that SA degradation at neutral and alkaline are substantially underestimated due to the strong radical scavenging effect of the phosphate buffer [4].

#### 7.3.4. Degradation of 1-naphthylamine and phenol (Ph)

The degradation of Ph and 1NA in the presence of 25 mM MeOH is presented in Figure 7.10. Compared to SA degradation in the presence of MeOH which was only ~60% after 60 min, significantly more Ph degradation of ~90% was achieved at the end of 60 min for both E1 and E2 modes of PS addition. The relative resistance of SA to oxidation compared to Ph can be attributed to the presence of the carbonyl group in the former but not in the latter [44]. The resonance electron withdrawing effect of the carbonyl group in SA deactivates the molecule towards electrophilic oxidation by  $\text{SO}_4^{\bullet-}$  [44]. Although the E2 degradation of Ph was slower at the earlier part of the experiment (Figure 7.10a), it attained the same degradation at the end of the experiment as E1 and the chromatograms for the two degradations (Figure 7.10b and 7.10c) are similar. In both Figure 7.10b and 7.10c, it can be seen that degradation products with much longer retention times than Ph developed. The observations suggest the possible combination of radicals derived from Ph, and possibly from MeOH, to generate a more hydrophobic degradation products [39, 45]. To determine whether MeOH participated in the generation of the possibly more hydrophobic degradation products, Ph degradation was repeated in the absence of MeOH and the

chromatogram presented as Figure 7.10d. Degradation peaks greater than Ph could still be seen which can be taken as a confirmation that MeOH was not responsible for the higher-retention-time degradation products.

From the trends shown in Figure 7.10e for the degradation of 1NA, it can be seen that both E1 and E2 attained a relatively fast degradation of the pollutant in the presence of MeOH compared to the degradation of the other pollutants studied in this work. The rapid degradation of 1NA points to the strongly electron-donating effect of NH<sub>2</sub> attached to a fused benzene rings due to resonance [44] combined with the strongly electron abstracting property of SO<sub>4</sub><sup>•-</sup> [42]. The apparent general rule therefore is that pollutants that are readily oxidised by SO<sub>4</sub><sup>•-</sup> such as 1NA are preferentially degraded over MeOH while for pollutants resistant to oxidation such as SA, MeOH is preferentially oxidised. This generalisation should be taken into account when considering radical oxidation of industrial pollutants in wastewater. As far as is known to the authors of this paper, the interestingly rapid oxidation of 1NA by activated PS under a radical scavenging condition has not been previously reported despite the significant challenge posed by the widespread use of 1NA as industrial intermediate and its designation as a priority contaminant [46]. The limited number of previous studies on the treatment of wastewater contaminated with 1NA have focused on adsorption [46, 47] and electrochemical oxidation [18]. The chromatograms for E1 and E2 degradation of 1NA as presented in Figure 7.10f and 7.10g, respectively, are largely similar. However, a short-lived peak at higher retention time was observed for E2. Due to the limited identification of the peaks in the chromatograms of Ph and 1NA degradation (Figure 7.10) using Table S7.1, further study are required to develop a degradation pathway for the pollutants.

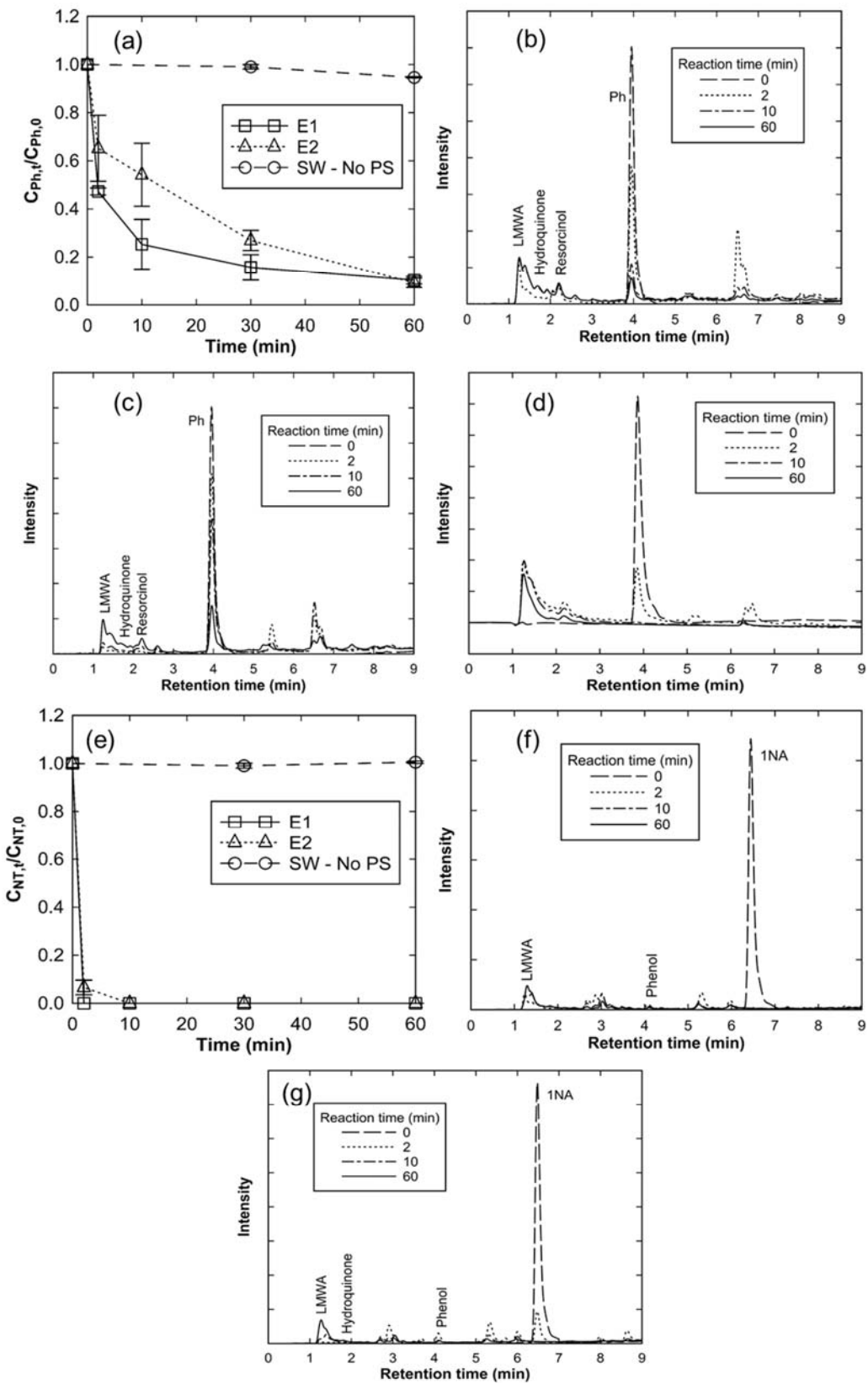


Figure 7.10. Degradation of Ph and 1NA. Trends of E1 and E2 modes of Ph degradation (a); chromatograms of E1 mode of Ph degradation (b); chromatograms of E2 mode of Ph degradation (c); chromatograms for E1 mode of Ph degradation in the absence of MeOH (d); Trends of E1 and E2 modes of 1NA degradation (e); chromatograms for E1 mode of 1NA degradation (f); chromatograms for E2 mode of 1NA degradation (g). Experiments conducted at room temperature (24 °C) in the presence of 25 mM MeOH except where otherwise stated; initial pollutant concentration was 0.2 mM; concentrations of iron species fixed at 0.1 g/L (1.8 mM).

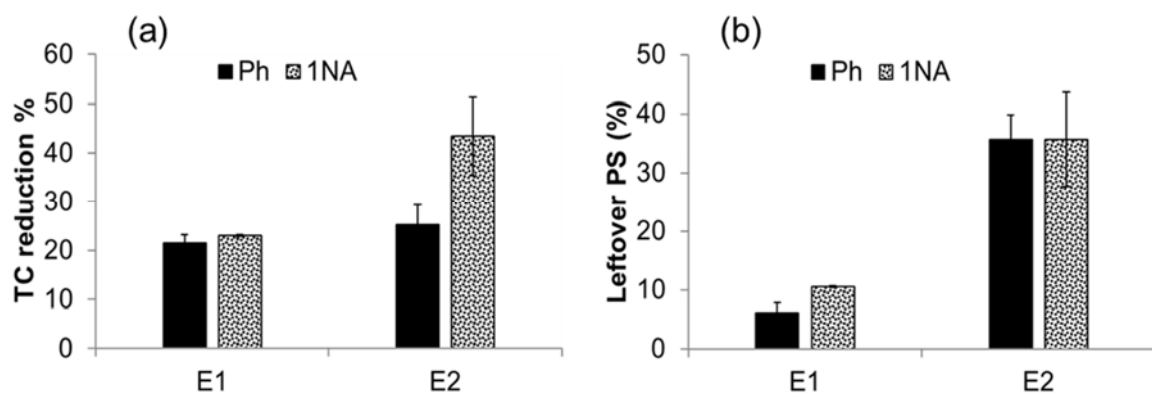


Figure 7.11. Mineralisation and remaining PS after 60 min. Experiments conducted at room temperature (24 °C) in the presence of 25 mM MeOH; initial pollutant concentration was 0.2 mM; concentrations of iron species fixed at 0.1 g/L (1.8 mM).

The degree of mineralisation and the remaining PS at the end of 60 min for Ph and 1NA degradation in the presence of 25 MeOH is presented in Figure 7.11. It can be seen from Figure 7.11a that the mineralisation obtained from E2 mode of degradation of both Ph and 1NA were greater than the mineralisation achieved by E1. Hence, except for SA degradation, E2 mode appears to achieve more effective mineralisation than E1. This can readily be interpreted to imply that the sudden addition of PS under E1 mode resulted in PS-SW mutual exhaustion. The

much higher concentrations of PS remaining after 60 min for E2 mode of addition of PS compared to E1 (Figure 7.11b) clearly support this proposal.

#### 7.4. Conclusions

This study has demonstrated that commercial ZVI is an effective activator of PS for the degradation of four important environmental pollutants, namely, OG, SA, Ph and 1NA in the presence or absence of an alcohol radical scavenger, MeOH. The addition of MeOH mimics the presence of industrial solvents and/or feedstuff in real industrial wastewater, which may influence the degradation of target environmental pollutants. The results from this study indicates that the presence of MeOH had no effect on the nature of the degradation products generated from PS oxidation but the degradation rates of the target pollutants were reduced. The alcohol had more retarding effect on the degradation of the pollutant SA, which is relatively resistant to radical oxidation due to the presence of an electron-withdrawing group on its benzene ring, compared to a pollutant such as 1NA that has an electron-donating group. The azo bond in OG was found to be a structural point of weakness leading to a comparatively more effective degradation of the aromatic moieties. An apparent general rule whereby pollutants that are readily oxidised by  $\text{SO}_4^{\bullet-}$  were preferentially degraded over MeOH while for pollutants resistant to oxidation, MeOH was preferentially oxidised, can be said to be operational. The activation of PS by the commercial ZVI samples studied in this work was found to be more effective in the degradation of pollutants compared to PS activation by  $\text{Fe}^{2+}$ . In addition, the ZVI materials required no prior acid washing (to remove oxidised surface layer that develops on nZVI) nor any other form of pretreatment. Hence, the results open up the possibility for the direct use of waste iron filings (generated as by-products of iron processing and finishing) for PS activation. An optimal PS concentration for effective pollutant degradation to suppress the persistence of aromatic degradation products was demonstrated. It was also demonstrated that the gradual addition of PS compared to a sudden addition always consumed less PS and provided for more effective mineralisation of pollutants (except SA due to its greater resistance to oxidation and therefore required longer reaction time).

## 7.5. Acknowledgement

The financial support provided by Victoria University to Ikechukwu A. Ike through the Victoria University International Postgraduate Research Scholarship is gratefully acknowledged.

## References

- [1] P. Devi, U. Das, A.K. Dalai, In-situ chemical oxidation: Principle and applications of peroxide and persulfate treatments in wastewater systems, *The Science of the total environment*, 571 (2016) 643-657.
- [2] H. Li, J. Wan, Y. Ma, Y. Wang, M. Huang, Influence of particle size of zero-valent iron and dissolved silica on the reactivity of activated persulfate for degradation of acid orange 7, *Chemical Engineering Journal*, 237 (2014) 487-496.
- [3] H. Li, J. Wan, Y. Ma, M. Huang, Y. Wang, Y. Chen, New insights into the role of zero-valent iron surface oxidation layers in persulfate oxidation of dibutyl phthalate solutions, *Chemical Engineering Journal*, 250 (2014) 137-147.
- [4] X. Wei, N. Gao, C. Li, Y. Deng, S. Zhou, L. Li, Zero-valent iron (ZVI) activation of persulfate (PS) for oxidation of bentazon in water, *Chemical Engineering Journal*, 285 (2016) 660-670.
- [5] I. Hussain, Y. Zhang, S. Huang, X. Du, Degradation of p-chloroaniline by persulfate activated with zero-valent iron, *Chemical Engineering Journal*, 203 (2012) 269-276.
- [6] J. Deng, Y. Shao, N. Gao, Y. Deng, C. Tan, S. Zhou, Zero-valent iron/persulfate(Fe0/PS) oxidation acetaminophen in water, *International Journal of Environmental Science and Technology*, 11 (2013) 881-890.
- [7] R.A. Crane, T.B. Scott, Nanoscale zero-valent iron: future prospects for an emerging water treatment technology, *J Hazard Mater*, 211-212 (2012) 112-125.
- [8] C.d.M. Donega, *Nanoparticles, the workhorses of nanoscience*, Springer, Heidelberg, 2014.
- [9] L.F. Greenlee, S. Hooker, Characterization of stabilized zero valent iron nanoparticles, in: T. Boellinghaus, J. Lexow, T. Kishi, M. Kitagawa (Eds.)

Materials Challenges and Testing for Supply of Energy and Resources, Springer-Verlag Berlin Heidelberg, 2012, pp. 173-188.

[10] Z. Xiong, D. Zhao, G. Pan, Rapid and complete destruction of perchlorate in water and ion-exchange brine using stabilized zero-valent iron nanoparticles, *Water Res.*, 41 (2007) 3497-3505.

[11] S. Rodriguez, L. Vasquez, D. Costa, A. Romero, A. Santos, Oxidation of Orange G by persulfate activated by Fe(II), Fe(III) and zero valent iron (ZVI), *Chemosphere*, 101 (2014) 86-92.

[12] X.-R. Xu, X.-Z. Li, Degradation of azo dye Orange G in aqueous solutions by persulfate with ferrous ion, *Separation and Purification Technology*, 72 (2010) 105-111.

[13] J. Madhavan, F. Grieser, M. Ashokkumar, Degradation of orange-G by advanced oxidation processes, *Ultrasonics sonochemistry*, 17 (2010) 338-343.

[14] F.M. Drumond Chequer, G.A.R. de Oliveira, E.R. Anastacio Ferraz, J. Carvalho, M.V. Boldrin Zanoni, D.P. de Oliveir, *Textile Dyes: Dyeing Process and Environmental Impact*, in: *Eco-Friendly Textile Dyeing and Finishing*, InTech, 2013.

[15] H. Kusic, I. Peternel, N. Koprivanac, A.L. Bozic, Iron-activated persulfate oxidation of an azo dye in model wastewater: influence of iron activator type on process optimization, *Journal of Environmental Engineering*, 137 (2011) 454-463.

[16] B.W. Brooks, D.B. Huggett, Human pharmaceuticals in the environment: current and future perspectives, in: L.R. Shugart (Ed.) *Emerging topics in ecotoxicology principles, approaches and perspectives*, Springer, New York, 2012.

[17] K. Fent, A.A. Weston, D. Caminada, Ecotoxicology of human pharmaceuticals, *Aquat Toxicol*, 76 (2006) 122-159.

[18] F. Chen, S. Yu, X. Dong, S. Zhang, High-efficient treatment of wastewater contained the carcinogen naphthylamine by electrochemical oxidation with  $\text{Al}_2\text{O}_3$  supported MnO<sub>2</sub> and Sb-doped SnO<sub>2</sub> catalyst, *Journal of Hazardous Materials*, 227– 228 (2012) 474– 479.

[19] S.B. Hammouda, F. Zhao, Z. Safaei, V. Srivastava, D.L. Ramasamy, S. Iftekhar, S. kalliola, M. Sillanpää, Degradation and mineralization of phenol in aqueous medium by heterogeneous monopersulfate activation on nanostructured cobalt based-perovskite catalysts ACoO<sub>3</sub> (A = La, Ba, Sr and

- Ce): Characterization, kinetics and mechanism study, *Applied Catalysis B: Environmental* 215 (2017) 60–73.
- [20] Y.T. Lin, C. Liang, J.H. Chen, Feasibility study of ultraviolet activated persulfate oxidation of phenol, *Chemosphere*, 82 (2011) 1168-1172.
- [21] H.V. Lutze, N. Kerlin, T.C. Schmidt, Sulfate radical-based water treatment in presence of chloride: Formation of chlorate, inter-conversion of sulfate radicals into hydroxyl radicals and influence of bicarbonate, *Water Research*, 72 (2015 ) 349-360.
- [22] S. Wacławek, H.V. Lutze, K. Grübel, V.V.T. Padil, M. Černík, D.D. Dionysiou, Chemistry of persulfates in water and wastewater treatment: A review, *Chemical Engineering Journal*, 330 (2017) 44-62.
- [23] L. Dsikowitzky, J. Schwarzbauer, Organic Contaminants from Industrial Wastewaters: Identification, Toxicity and Fate in the Environment, in: Pollutant Diseases, Remediation and Recycling, 2013, pp. 45-101.
- [24] C. Gadipelly, A. Pérez-González, G.D. Yadav, I. Ortiz, R. Ibáñez, V.K. Rathod, K.V. Marathe, Pharmaceutical industry wastewater: Review of the technologies for water treatment and reuse, *Industrial & Engineering Chemistry Research*, 53 (2014) 11571–11592.
- [25] EPA, Toxicological review of methanol (noncancer), in, U.S. Environmental Protection Agency, 2013.
- [26] E. Terzis, Anaerobic treatment of industrial wastewater containing organic solvents, *Water Science and Technology*, 29 (1994) 321-329.
- [27] G.P. Anipsitakis, D.D. Dionysiou, Radical generation by the interaction of transition metals with common oxidants, *Environmental Science & Technology*, 38 (2004) 3705-3712.
- [28] N.A. Frigerio, An iodometric method for the macro- and microdetermination of peroxydisulfate, *Analytical Chemistry*, 35 (1963) 412-413.
- [29] A. Ghauch, A.M. Tuqan, Oxidation of bisoprolol in heated persulfate/H<sub>2</sub>O systems: Kinetics and products, *Chemical Engineering Journal*, 183 (2012) 162-171.
- [30] R.M. Cornell, U. Schwertmann, The Iron Oxides: Structures, Properties, Reactions, Occurrences and Uses, 2nd Edition ed., WILEY-VCH Verlag GmbH & Co. KGaA, Weinheim, 2003.

- [31] I.A. Ike, J. Zhang, A. Groth, J.D. Orbell, M. Duke, Effects of dissolution conditions on the properties of PVDF ultrafiltration membranes, *Ultrasonics sonochemistry*, 39 (2017) 716-726.
- [32] M.D. Lekgoathi, L.D. Kock, Effect of short and long range order on crystal structure interpretation: Raman and powder X-ray diffraction of LiPF(6), *Spectrochimica acta. Part A, Molecular and biomolecular spectroscopy*, 153 (2016) 651-654.
- [33] M. Avram, *Infrared Spectroscopy: Applications in Organic Chemistry*, Robert E. Krieger Publishing Co., Inc, New York, 1978.
- [34] K.S.W. Sing, D.H. Everett, R.A.W. Haul, L. Moscou, R.A. Pierotti, J. Rouquerol, T. Siemieniewska, Reporting physisorption data for gas/solid systems with special reference to the determination of surface area and porosity *Pure and Applied Chemistry*, 57 (1985) 603-619.
- [35] S.A. Kirillov, Surface area and pore volume of a system of particles as a function of their size and packing, *Microporous and Mesoporous Materials*, 122 (2009) 234-239.
- [36] T.W. Swaddle, Inorganic chemistry, in: An industrial and environmental perspective, Elsevier Science, 1997.
- [37] I.A. Ike, K. Linden, J.D. Orbell, M. Duke, Critical review of the science and sustainability of persulphate advanced oxidation processes, *Chemical Engineering Journal*, 338 (2018) 651-669.
- [38] I.A. Ike, S.L. Foster, S.R. Shinn, S.T. Watson, J.D. Orbell, L.F. Greenlee, M.C. Duke, Advanced oxidation of orange G using phosphonic acid stabilised zerovalent iron, *Journal of Environmental Chemical Engineering*, 5 (2017) 4014-4023.
- [39] C.J.M. Stirling, Radicals in organic chemistry, Oldbourne Press, London, 1965.
- [40] W. Stumm, G.F. Lee, Oxygenation of ferrous iron, *Industrial & Engineering Chemistry*, 53 (1961) 143-146.
- [41] N. Uri, Inorganic free radicals in solution, *Chemical Review*, 50 (1952) 375-454.
- [42] P. Neta, R.E. Huie, A.B. Ross, Rate constants for reactions of inorganic radicals in aqueous solution, *Journal of Physical and Chemical Reference Data* 17, (1988), 17 (1988) 1027 - 1284.

- [43] L. Dogliotti, E. Hayon, Flash photolysis of persulfate ions in aqueous solutions. Study of the sulfate and ozonide radical anions, *Journal of Physical Chemistry*, 71 (1967) 2511–2516.
- [44] E.M. John, *Organic Chemistry*, in, Cengage Learning, Boston, USA, 2015.
- [45] T.K. Lau, W. Chu, N.J.D. Graham, The aqueous degradation of butylated hydroxyanisole by UV/S<sub>2</sub>O<sub>8</sub><sup>2-</sup>: study of reaction mechanisms via dimerization and mineralization, *Environmental Science & Technology*, 41 (2007) 613–619.
- [46] W. Zhang, C. Hong, B. Pan, Z. Xu, Q. Zhang, L. Lv, Removal enhancement of 1-naphthol and 1-naphthylamine in single and binary aqueous phase by acid-basic interactions with polymer adsorbents, *J Hazard Mater*, 158 (2008) 293-299.
- [47] W. Zhang, C. Hong, B. Pan, Z. Xu, Q. Zhang, Q. Zhang, A comparative study of the adsorption properties of 1-naphthylamine by XAD-4 and NDA-150 polymer resins, *Colloids and Surfaces A: Physicochemical and Engineering Aspects*, 331 (2008) 257-262.

## Appendix

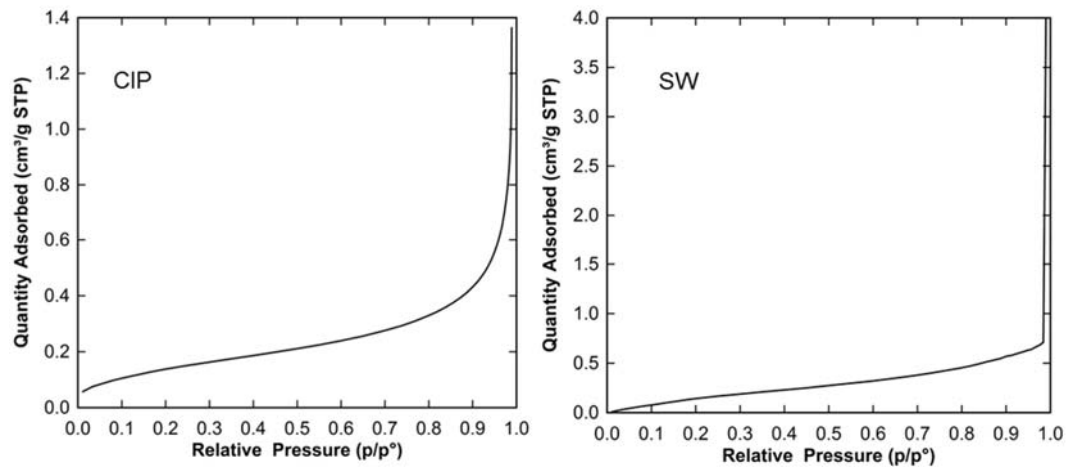


Figure S7.1. Isotherm plots for CIP and SW

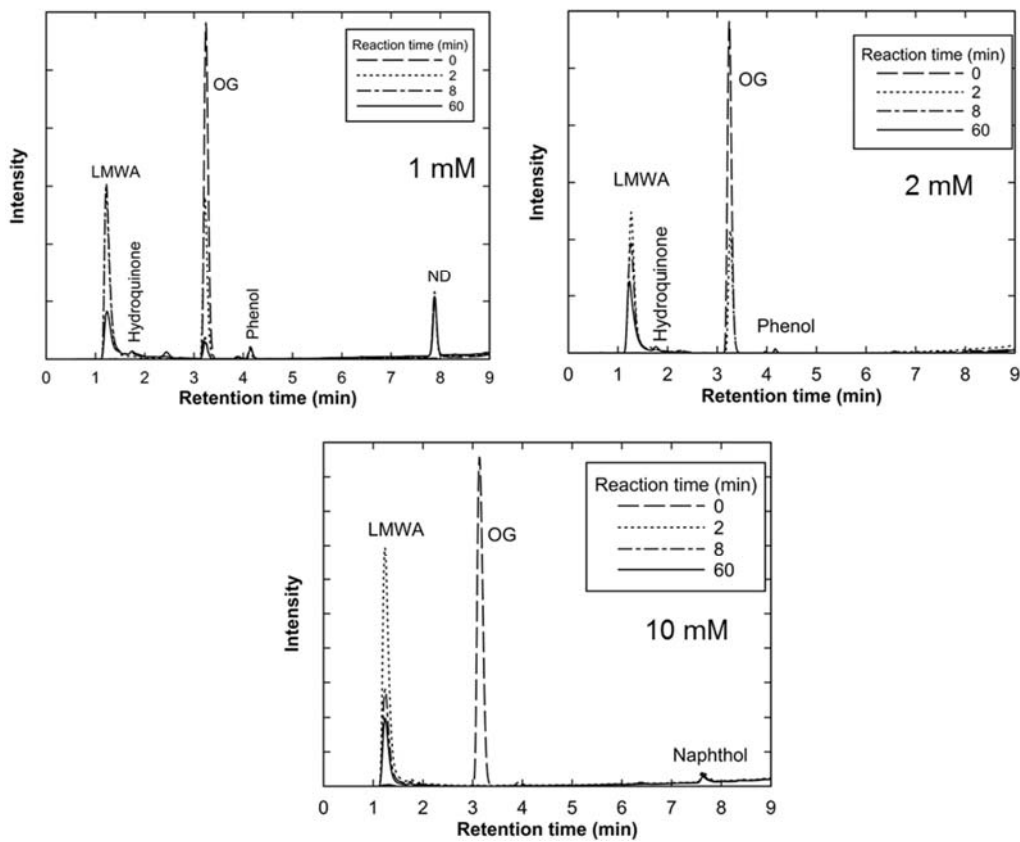


Figure S7.2. Chromatograms for 0.1 mM OG solution degradation by CIP activated PS.  $C_{PS,0} = 1\text{ mM}$  (a),  $C_{PS,0} = 2\text{ mM}$  (b) and  $C_{PS,0} = 10\text{ mM}$  (c).

Table S7.1. Retention times for known chemicals

<b>Chemicals</b>	<b>Retention time, min</b>
<b>Fumaric acid</b>	1.24
<b>Oxalic acid</b>	1.26
<b>4-aminobenzoic acid</b>	1.30
<b>Pthalic anhydride</b>	1.30
<b>Pthalic acid</b>	1.31
<b>Maleic acid</b>	1.33
<b>3-hydroxybenzoic acid</b>	1.33
<b>2-Furoic acid</b>	1.33
<b>Hydroquinone</b>	1.73
<b>Resorcinol</b>	2.20
<b>Benzoquinone</b>	2.24
<b>Salicylic acid</b>	2.32
<b>4-nitrobenzoic acid</b>	2.33
<b>2-hydroxy-5-nitrobenzaldehyde</b>	2.82
<b>Orcinol</b>	3.07
<b>Orange G</b>	3.21
<b>Aniline</b>	3.24
<b>2,4, Dinitrophenol</b>	3.39
<b>4-Nitroaniline</b>	3.82
<b>Phenol</b>	4.11
<b>3,5 Dinitrosalicylic acid</b>	4.81
<b>Benzaldehyde</b>	4.95
<b>2-nitrophenol</b>	4.95
<b>1-hydroxy-2-naphthoic acid</b>	5.53
<b>Acetophenone</b>	5.61
<b>Nitrobenzene</b>	6.21
<b>2-nitroso-1-naphthol</b>	6.27
<b>Naphthylamine</b>	6.64
<b>α-Naphthol</b>	7.68
<b>2-hydroxy-1-naphthaldehyde</b>	8.00
<b>Bisphenol A</b>	8.12

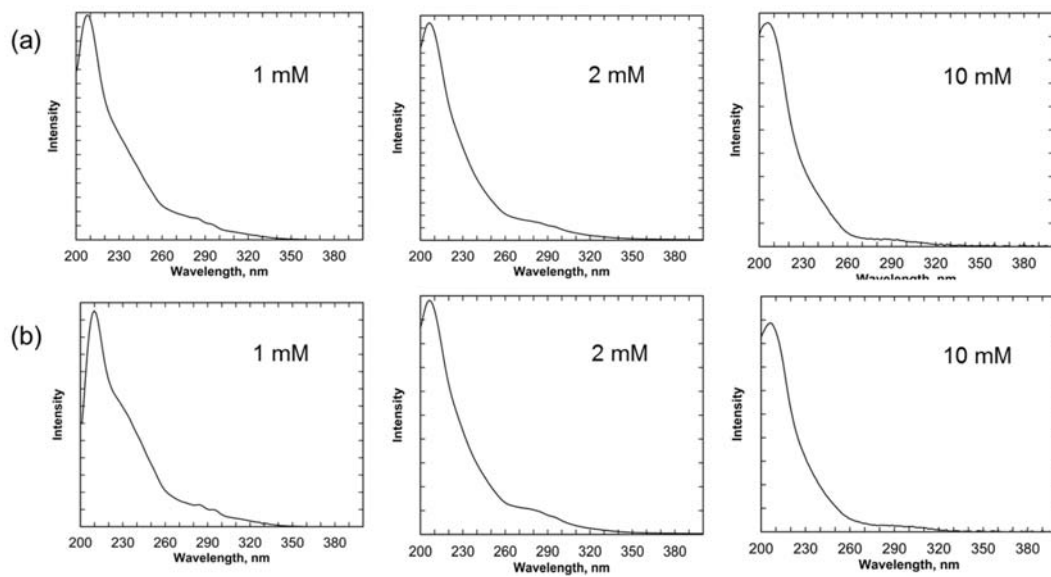


Figure S7.3. DAD generated UV spectra for the LMWA peak at 60 min for SW

(a) and CIP (b).

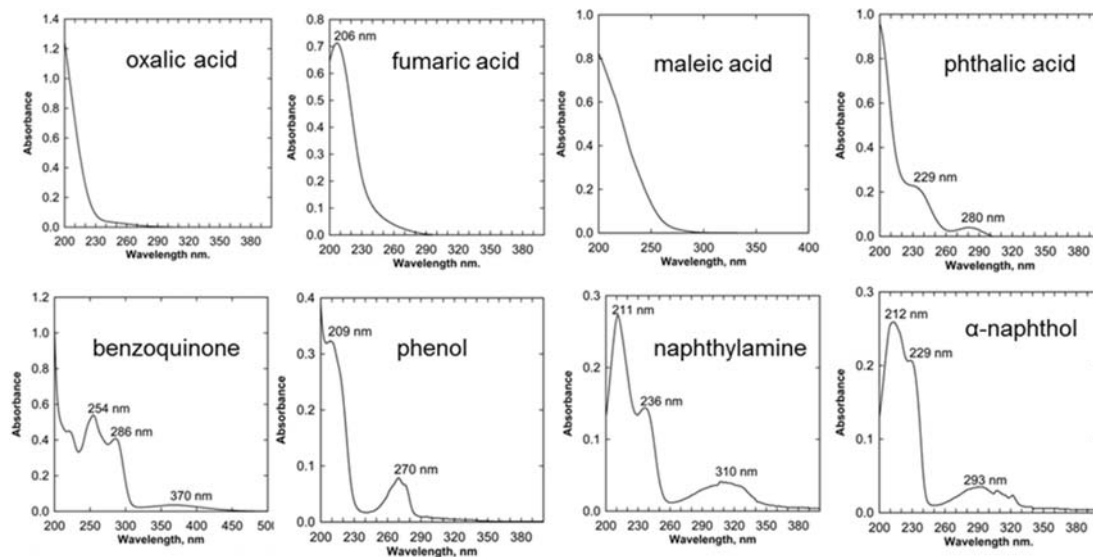


Figure S7.4. UV spectra for relevant chemicals

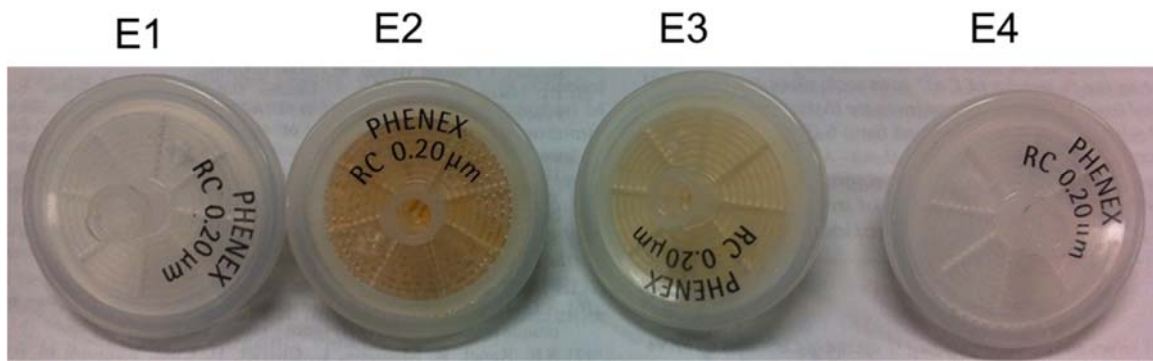


Figure S7.5. Syringe filter colouration after filtering reacting solutions from the different mode of PS addition as presented in Section 7.3.2.

## Chapter 8

### **Degradation of azo dye orange G by thermally activated persulphate: practical and theoretical implications\***

#### **Abstract**

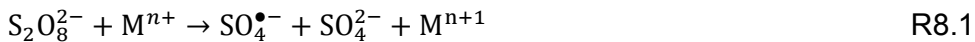
Thermally activated persulphate (TAPS) degradation process, although recognised as an effective means for pollutant degradation, is challenged by the high cost of energy. In this work, it is shown that waste heat from industries such as textile dyeing is adequate for the rapid degradation and mineralisation of orange G solution, a well-studied azo dye, in the absence or presence of high concentration of inorganic salts relevant to the textile industry. Azo dyes are known for their non-biodegradability and their direct or potential carcinogenicity. The study, for the first time, highlights the important role of radical kinetic energy in determining the rate and effectiveness of TAPS mineralisation of pollutants. One effect of the kinetic energy of radicals is the existence of an optimal mineralisation temperature range. For uncatalysed persulphate activation, the optimal temperature range is identified as 80 °C - 90 °C and is expectedly independent of the target pollutant. Also presented are new insights on a number of themes relevant to radical oxidation such as: inhibition and enhancement of decomposition and mineralisation by background ion; radical scavengers selection and reaction quenching assessment.

#### **8.1. Introduction**

Since the 1980s when advanced oxidation process (AOP) were first proposed for drinking water treatment [1, 2], activated persulphate (PS) AOP has been attracting significant amount of research interest for wastewater treatment. Application of PS-AOP is focused mainly on the treatment of wastewater contaminated by non-biodegradable or recalcitrant pollutants for reuse or before release into the environment. PS-AOP takes advantage of the high redox potential of the sulphate radicals ( $\text{SO}_4^{\bullet-}$ ) produced through a chemical or thermal cleavage of the O-O bond in PS or peroxymonosulphate [1, 3-5]. Chemical activation of PS for pollutant degradation has been the focus of several published

\*Under review for publication by Chemical Engineering Research and Design

reports since the last decade [6-10]. Mainly transition metal ions, commonly ferrous or ferric ion, are employed [8-11]. The general expression for transition metal activation of PS is given as R8.1 indicating the abstraction of an electron from the metal ion resulting in the production of one mole of  $\text{SO}_4^{\bullet-}$  for every mole of PS consumed [1].



The activation of PS by radiation, especially thermal energy, has also been a subject of significant research interest [3, 4, 12-14]. The general expression for radiation activation of PS is given as R8.2 showing a direct cleavage of the peroxide bond resulting in two moles of  $\text{SO}_4^{\bullet-}$  for every mole of PS activated [1].



It follows that radiation activation of PS yields stoichiometrically two times more  $\text{SO}_4^{\bullet-}$  than chemical activation for a given amount of PS [1, 13]. In addition, excess concentration of either PS or metal ion has been reported to result in rapid scavenging of the limited reactant amounting to poor pollutant degradation [9, 11, 12]. Metal activation of PS may also increase the concentration of dissolved metal or precipitates in the wastewater which may amount to a secondary water contamination necessitating further downstream treatment [1, 15]. In contrast, PS activation by irradiation does not additionally introduce foreign chemicals into the treated water other than PS nor does it consume PS except for the generation of  $\text{SO}_4^{\bullet-}$  for pollutant degradation. However, radiation as UV, sonication and heat can be energy intensive and therefore relatively expensive.

Nevertheless, since waste heat is discharged from many industrial activities, thermally activated PS (TAPS) is potentially a viable means for wastewater treatment in those industries. The textile industry, in particular, discharges substantial amount of heat with its dye-contaminated wastewater. Pulat et al. [16] published a summary of the typical heat content of the various operations involved in industrial textile dyeing as presented in Table 8.1. It can be seen that a number of operations produce wastewater with temperature close to 100 °C. The volumetric average temperature of the discharges listed in Table 8.1 is 71 °C. This is substantially high as most recent studies on thermal activation of PS

for various pollutants degradation were conducted at 70 °C or less [4, 12-14, 17-21]. Even temperatures as low as 40 °C for PS activation have been reported for effective pollutant degradation [18].

Table 8.1. Typical process parameters for industrial textile dyeing [16]

Dyeing operations	Operation time, min	Temperature, °C	Volume, L
<b>1. Bleaching</b>	30	96	5000
<b>2. Washing</b>	20	96	5000
<b>3. Acidification</b>	10	50	5000
<b>4. Dyeing</b>	60	96	5000
<b>5. Cold rinsing</b>	10	30	5000
<b>6. Washing</b>	20	90	5000
<b>7. Hot rinsing</b>	10	70	5000
<b>8. Finishing</b>	20	40	5000

Interestingly, the application of TAPS for degradation of textile industry wastewater containing recalcitrant dye is rare despite the considerable amount of dye contaminated wastewater annually produced by the textile industry [9]. In fact, on the basis of the volume generated and the composition, textile industry wastewater has been described as the most polluting of all industrial discharges [22]. Ghauch et al. [14] applied TAPS for the degradation of methylene blue and reported effective dye decolourisation and subsequent degradation of transformation products. Azo dyes, for which orange G (OG) is a well-known example [9, 11, 23-25], represent by far the most important category of dyes used in the textile industry [22]. This class of dyes constitute an environmental challenge due to their non-biodegradability and their direct or potential carcinogenicity and mutagenicity [9, 11, 22, 25]. Hence, research in the effective degradation of azo dyes has significant practical value for environmental sustainability. Another important feature of textile industry wastewater is the high concentration of inorganic salts [11, 22, 26, 27]. Consequently, understanding how the presence of high concentration of inorganic salts can influence the

degradation of azo dye is of practical relevance to the management of textile industry wastewater.

The aims of this work include the evaluation of TAPS for the degradation of OG under laboratory conditions relevant to the treatment of textile industry wastewater and a further elucidation of the nature and mechanism of TAPS degradation processes.

## 8.2. Experimental section

Details of chemicals used are provided in the Appendix. OG was dissolved in unbuffered water at a concentration of 0.1 mM. PS was used at a concentration of 10 mM or 1 mM. Unless otherwise stated, thermal activation of 10 mM and 1 mM PS solutions were scheduled at temperatures between 20 °C and 100 °C for batch degradation experiments. All kinetic experiments were performed in an oil bath whose temperature was kept uniform by overhead stirring while the reacting solution in a 30 ml glass flask immersed in the oil bath was stirred magnetically. All other experiments were performed in a temperature-controlled Thermo Scientific™ MaxQ™ 4450 Benchtop Orbital Shaker typically using 20 ml glass vials with 5 ml headspace. Experiments were performed at least as duplicates. Appropriate amount of OG with additives for each experiment were placed in a glass flask/vial and subjected to the required temperature while being stirred to assume the reaction temperature. Appropriate volume of PS from a 1 M stock solution was then added to start the reaction.

During the reactions, samples were taken at designated intervals from the reacting solutions or vials sacrificed depending on the quantity of samples required for specific analysis. Collected 1 ml aliquot samples were either transferred to 0.5 ml methanol for chemical quenching [7, 28] or they were transferred to an ice bath for thermal quenching [12, 19]. The effectiveness of the two common methods of radical reaction quenching were examined by transferring 1 ml aliquots at designated intervals to falcon tubes holding 0.5 ml methanol and to similar falcon tubes left empty but immersed in an ice bath. To determine the effects of the high concentration of dissolved salts, OG degradation experiments were conducted with 100 mM [11] of the following salts added separately [11, 26]: NaNO<sub>3</sub>, NaCl, NaHCO<sub>3</sub>, NaH<sub>2</sub>PO<sub>4</sub>, Na<sub>2</sub>SO<sub>4</sub>, CaCl<sub>2</sub>,

$\text{Mg}(\text{NO}_3)_2 \cdot 6\text{H}_2\text{O}$  and  $\text{Fe}(\text{NO}_3)_3 \cdot 9\text{H}_2\text{O}$ . Scavenging experiments were conducted with ascorbic acid, KI, pentanol-1 and propanol-1 at temperatures of 70 °C and 100 °C.

The rates of OG degradation were measured spectrophotometrically at the wavelength of 478 nm [11] using a Biochrom Libra S22 UV/Visible Spectrophotometer. High performance liquid chromatographic (HPLC) study of OG degradation was conducted using a Shimadzu Prominence-i LC 2030C Liquid Chromatograph. Details of the studies are provided in the Supplementary Material. TC values were determined using a Shimadzu TOC-V<sub>CSH</sub> Total Organic Carbon Analyzer. Sample for TC analysis were quenched in an ice bath. Error bars in the figures represents standard errors of at least two measurements.

### 8.3. Results and discussions

#### 8.3.1. Degradation kinetics

Semi-log fitted degradation trends of OG via TAPS at initial PS concentration ( $C_{PS,0}$ ) of 1 mM and 10 mM is shown in Figure S8.1 in the Appendix. The semi-log fittings assume a pseudo first order reaction kinetics and a constant PS concentration in consequence as follows:

$$\ln C_{OG,t}/C_{OG,0} = -k_{obs}t \quad 8.1$$

$$\frac{dC_{OG}}{dt} = -k_{obs}C_{OG} \quad 8.2$$

$$k_{obs} = kC_{PS} \quad 8.3$$

where  $C_{OG}$  and  $C_{PS}$  represents OG and PS concentration, respectively;  $t$  is reaction time in min; subscript t and 0 designate concentration at a given time and at the start of the reaction, respectively;  $k_{obs}$  and  $k$  represent the observed pseudo first order reaction constant and second order reaction constant, respectively, both expressed in  $\text{min}^{-1}$ . The obtained  $k_{obs}$  as a function of temperatures and  $C_{PS,0}$  are presented in Table 8.2.

Table 8.2. Pseudo first order reaction constants as a function of temperatures and  $C_{PS,0}$

Temperature (°C)	1 mM		$C_{PS,0}$	
	$k_{obs}$ (min <sup>-1</sup> )	R <sup>2</sup>	$k_{obs}$ (min <sup>-1</sup> )	R <sup>2</sup>
20	0.00011	0.919	0.00017	0.936
40	0.00037	0.993	0.0019	0.999
50	-	-	0.011	0.999
60	-	-	0.045	0.999
70	0.038	0.988	0.23	0.998
75	-	-	0.54	0.994
80	-	-	1.4	0.981
85	-	-	2.8	0.995
90	0.18	0.993	6.1	0.998
100	1.2	0.998	-	-

The exponential increase in  $k_{obs}$  with temperature suggests an Arrhenius type relationship [11, 29, 30]. The Arrhenius equation may be expressed as [29]:

$$k_{obs} = Ae^{-E_a/RT} \quad 8.4$$

where  $A$  is the frequency factor,  $E_a$  the apparent activation energy,  $R$  the ideal gas constant ( $8.314 \text{ Jmol}^{-1}\text{K}^{-1}$ ) and  $T$  temperature (K). Arrhenius plots [29] for the data given in Table 8.2 are presented in Figure 8.1. The Arrhenius plot at  $C_{PS,0} = 1 \text{ mM}$  shows a non-linear trend which suggest the reaction is influenced by another factor in addition to the strong temperature effect [30]. Considering that Equation 8.3 requires a constant PS concentration, it appears that  $C_{PS,0} = 1 \text{ mM}$ , with initial  $[\text{PS}]/[\text{pollutant}] = 10$ , was too low to meet this condition [14]. Arrhenius-type linear trends are typically obtained for initial  $[\text{PS}]/[\text{pollutant}] > 10$  [11, 13, 14, 21]. In consequence, it can be expected that when  $C_{PS,0} = 10 \text{ mM}$  ( $[\text{PS}]/[\text{pollutant}] = 100$ ), a more linear Arrhenius trend may be observed. This is seen to be the case as shown Figure 8.1.

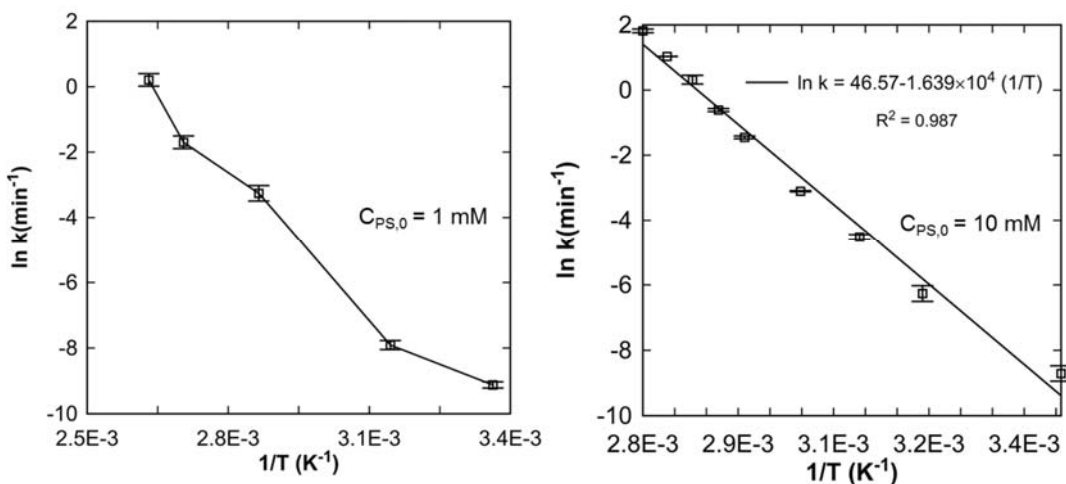


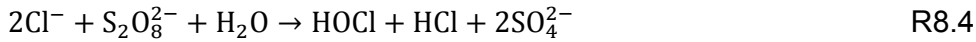
Figure 8.1. Arrhenius plot for  $C_{PS,0} = 1 \text{ mM}$  and  $10 \text{ mM}$

The apparent activation energy,  $E_a$ , obtained from the Arrhenius plot for  $C_{PS,0} = 10 \text{ mM}$  was  $136.3 \text{ kJmol}^{-1}$  which compares to the activation energy for the uncatalysed thermal rapture of the O-O bond in PS of  $140.2 \text{ kJmol}^{-1}$  [31]. Consequently, it may be said that OG and its degradation products have negligible effect on the cleavage of the O-O bond in PS. Hence, OG is a suitable probe to study the rupture of the O-O bond in PS.

### 8.3.2. Effects of ions on OG degradations by TAPS

The effects of various inorganic salts on the rate of OG degradation by TAPS are shown in Figure S8.2. The  $k_{obs}$  obtained from the assumption of pseudo first order reactions are presented in Table 8.3. It can be deduced that  $\text{SO}_4^{2-}$  and  $\text{H}_2\text{PO}_4^-$  showed a slight inhibiting effect on OG degradation (8% and 3%, respectively) while major inhibition of 38% was obtained from  $\text{HCO}_3^-$ . Bicarbonate inhibition of radical reactions is well recognised [11, 17, 21]. Both  $\text{Cl}^-$  and  $\text{NO}_3^-$  can be seen to improve the degradation of OG. Exponential improvement in dye decolourisation arising from  $\text{Cl}^-$  oxidisation to active chlorine species with rapid bleaching power has been previously reported [32]. Consequently, the observed 11%, 223% and 870% improvements in OG degradation in the presence of 100 mM NaCl, 100 mM  $\text{CaCl}_2$  and 200 mM NaCl, respectively, may be attributed to the bleaching effect of reactive chlorine [32]. Generation of reactive chlorine as

$\text{Cl}_2$  and HOCl from  $\text{Cl}^-$  by a peroxygen has been described by non-radical reactions [32] and may be simplified as follows:



Bleaching effect was not obtained when  $\text{Cl}^-$  was replaced by  $\text{NO}_3^-$  in reaction with a peroxygen [32], hence the 34% and 37% improvement in OG degradation due to  $\text{NaNO}_3$  and  $\text{Mg}(\text{NO}_3)_2$ , respectively, may be associated with the oxidising effect of the nitrate radical [33] produced as follows:



Improvement in OG decolourisation by the presence of  $\text{Cl}^-$  and  $\text{NO}_3^-$  as observed in this work is starkly opposed to the inhibition effects at similar ion concentration reported by Xu and Li [11] for  $\text{Fe}^{2+}/\text{PS}$  degradation of OG at 20 °C. The presence of  $\text{Fe}^{2+}$  as a ready source of electron may have influenced the overall reaction in the work by Xu and Li [11]. Additionally, the higher temperature for TAPS degradation may have resulted in more kinetically active radicals for enhanced OG degradation [34].

Table 8.3. Pseudo first order reaction constants for OG degradation in the presence of 100 mM (except where otherwise stated) of inorganic salts via TAPS at 70 °C and  $C_{PS,0} = 10$  mM

<b>Salt</b>	<b><math>k_{obs}</math></b>	<b>R<sup>2</sup></b>	<b>Inhibition</b>
	<b>min<sup>-1</sup></b>		<b>%</b>
<b>No additives</b>	0.0662	0.979	0
<b>NaHCO<sub>3</sub></b>	0.0414	0.962	38
<b>Na<sub>2</sub>SO<sub>4</sub></b>	0.0611	0.982	8
<b>NaH<sub>2</sub>PO<sub>4</sub></b>	0.0648	0.985	3
<b>NaCl</b>	0.0738	0.987	-11
<b>NaNO<sub>3</sub></b>	0.0893	0.998	-34
<b>Mg(NO<sub>3</sub>)<sub>2</sub></b>	0.0911	0.997	-37
<b>CaCl<sub>2</sub></b>	0.2149	0.987	-223
<b>NaCl (200 mM)</b>	0.6448	0.999	-870

### 8.3.3. Degradation mechanism

#### 8.3.3.1. Radical scavenging

Pollutant degradation by TAPS is frequently described as a radical reaction process. To verify a radical reaction, radical scavengers such as alcohol [28, 35], ascorbic acid [36], KI [36, 37] are usually added in excess. The effects of various radical scavengers on the rate of OG decolourisation are presented in Figure 8.2. In the presence of 4000 mM propanol-1, a steady decline in OG concentration can be seen but the  $k_{obs}$  was only 0.0038 min<sup>-1</sup>, representing 94% reduction in comparison with the degradation in the absence of propanol-1. Consequently, it can be said that OG degradation at 70 °C proceeded mainly by the radical mechanism.

Significant initial decolourisation was observed when 100 CaCl<sub>2</sub> was added despite the radical scavenging role of propanol-1. This outcome further supports the proposal that the presence of Cl<sup>-</sup> caused a non-radical bleaching of OG. Nevertheless, even when considering only the initial degradation trend, the  $k_{obs}$  obtained for CaCl<sub>2</sub>-enhanced decolourisation of OG in the presence of propanol-

$k_1$  was  $0.037 \text{ min}^{-1}$ . This rate constant indicates an 82% reduction when compared to the degradation without propanol-1. Furthermore, the decolourisation stalled after ~50% degradation of OG in the presence of propanol-1. These results point to an important role of the radical mechanism to the bleaching effect of Cl<sup>-</sup> contrary to the conclusion of Wang et al. [32]. Hence, the following simplified radical reaction is an important component in the production of reactive chlorine:



When propanol-1 was replaced by ascorbic acid as a scavenger, unique OG decolourisation behaviour was observed when reaction was quenched in methanol but not in an ice bath as shown in Figure 8.2b. The observation is described to some detail in the Appendix (S8.3). These results highlight the need for caution in the selection of radical scavengers for the study of reaction mechanism as well as the mechanism adopted for reactions quenching. Further study is required to evaluate how general is the PS/ascorbic acid/methanol reaction towards dye decolourisation and whether there are economic potentials in the reactions.

Figure 8.2c shows the scavenging role of propanol-1, pentanol-1 and KI on TAPS degradation of OG at 100 °C. 90% and 82% inhibition of OG degradation was observed when propanol-1 and pentanol-1, respectively, were present as scavengers while 99.9% inhibition was provided by KI confirming the radical nature of the reaction. The limited inhibition of the alcohols compared to KI may be attributed to rapid evaporation of propanol-1 at 100 °C (boiling point 97 °C) and the limited solubility of pentanol-1 in water (solubility 250 mmol/L).

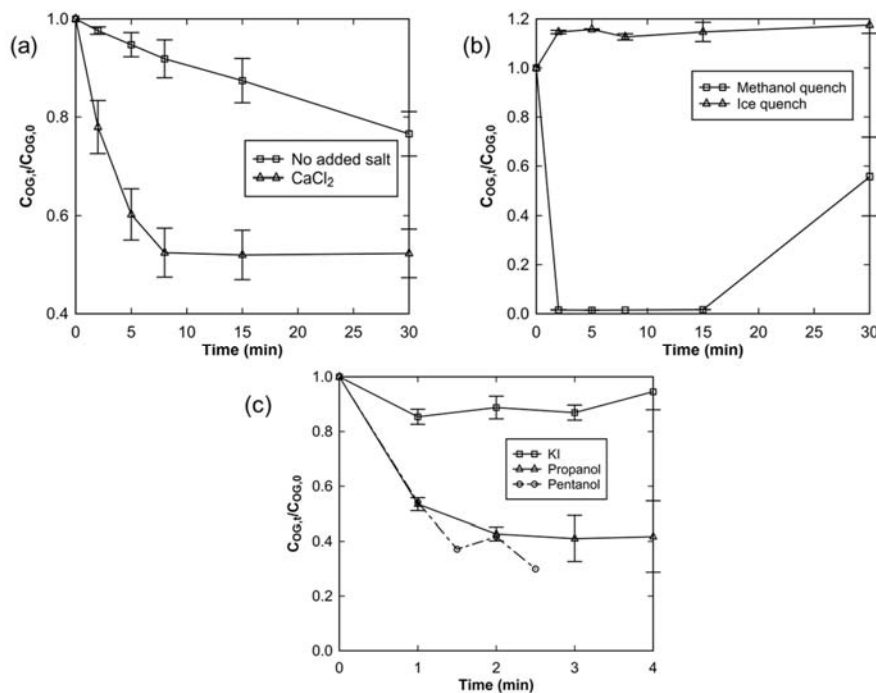


Figure 8.2. The effects of radical scavengers on TAPS degradation of 0.1 mM OG at 70 °C and 100 °C. Degradation trend at 70 °C for  $C_{PS,0} = 10$  mM with and without 100 mM  $\text{CaCl}_2$  in the presence of 4000 mM propanol-1 (a); at 70 °C for  $C_{PS,0} = 10$  mM in the presence of 100 mM ascorbic acid with sampled aliquots quenched either in methanol or in an ice bath (b); at 100 °C for  $C_{PS,0} = 1$  mM with either 100 mM KI, 8000 mM propanol-1 and 3000 mM of pentanol-1 added at start of reaction. OG concentration in the presence of KI measured chromatographically because solution colour interfered with the regular UV measurement. Degradation in the presence of pentanol-1 was not replicated.

### 8.3.3.2. Degradation pathway

The chromatograms for OG degradation at 70 °C, 90 °C and 100 °C for  $C_{PS,0} = 1$  mM is presented in Figure 8.3. The tentative identification of peaks is based on the retention times of known chemicals under identical chromatographic conditions as presented in Table S8.1. The peak labelled LMWA (low molecular weight acid) designate fumaric and/or oxalic acid. Consistent with the degradation rate analysis in Section 8.3.1, it can be seen that the rate of OG degradation and transformation to LMWA is strongly influenced by temperature. While practically no peak other than the LMWA can be observed in the 5 min chromatograms for the degradation experiments at 90 °C and 100 °C, a small

OG peak could be identified in the 8 min chromatograms for the OG degradation at 70 °C. Beside the rate of peak disappearance, it can also be observed that the number of chromatographic peaks is dependent on the temperature of degradation. Other than the OG and LMWA peaks, only three and five other peaks are distinguishable at 70 °C and 90 °C, respectively, while several more peaks were identified at 100 °C. Furthermore, degradation peaks other than the LMWA are more pronounced especially at 100 °C compared to the peaks observed at 70 °C. More rapid production of radicals at 100 °C compared to 70 °C may explain the faster degradation of OG accomplished within 5 min at 100 °C but which was not achieved after 8 min at 70 °C. However, the greater number of developed peaks at 100 °C compared to 70°C points to more energetic radicals able to attack the OG structure at more points to give more diversified intermediates.

The literature on radical reactions relevant to AOPs emphasise the role of the redox potentials of the radicals in the degradation of pollutants. However, the effects of the kinetic energy of radicals are not usually highlighted. Janzen [34] reported that the electron spin resonance (ESR) signal line for  $\text{SO}_2\cdot^-$  narrowed with increase in temperature which the author attributed to increased radical freedom of motion. The increased freedom of motion was correlated to increased decomposition reaction. Consequently, in addition to the redox potential of a radical, the kinetic energy, which is a function of temperature, may also be important in deciding its chemical behaviour [29]. Increasing kinetic energy derived from increasing temperature may allow the radical to overcome the activation energy barriers for more reactions [38] resulting in more diversified reaction products/intermediates as observed at 100 °C in this study.

Based on the chromatographic results, a simplified degradation pathway at 70 °C for OG, represented in a condensed structural form as  $\text{R}_2\text{-N=N-R}_1$ , may be expressed as [24, 38]:



where R may be one ring or two rings aryl structure. The aryl radicals formed would have reacted repeatedly with other radicals and molecules by abstraction and addition leaving behind few stable molecules until the formation of the LMWA [38, 39]. Consequently, the initial attack on the azo structure may be considered

the rate determining step in the transformation of OG to LMWA. This proposal would explain the dominance of the OG and LMWA peaks and the limited number of other peaks for the 70 °C reaction. On the other hand, the reaction at 100 °C can be said to be more complex in that radicals have enough energy to directly attack R<sub>1</sub>, R<sub>2</sub> and the linking azo bond [38]. These energetic attacks produced a number of stable molecules as well as radicals by bond fission and disproportionation [38] as follows:



However, the formed stable molecules were also rapidly attacked probably producing other stables molecules and radicals until the formation of LMWA. The reaction at 90 °C is mid-way between the reactions at 70 °C and 100 °C. Future work will attempt a development of the OG degradation pathways as a function of PS activation temperature.

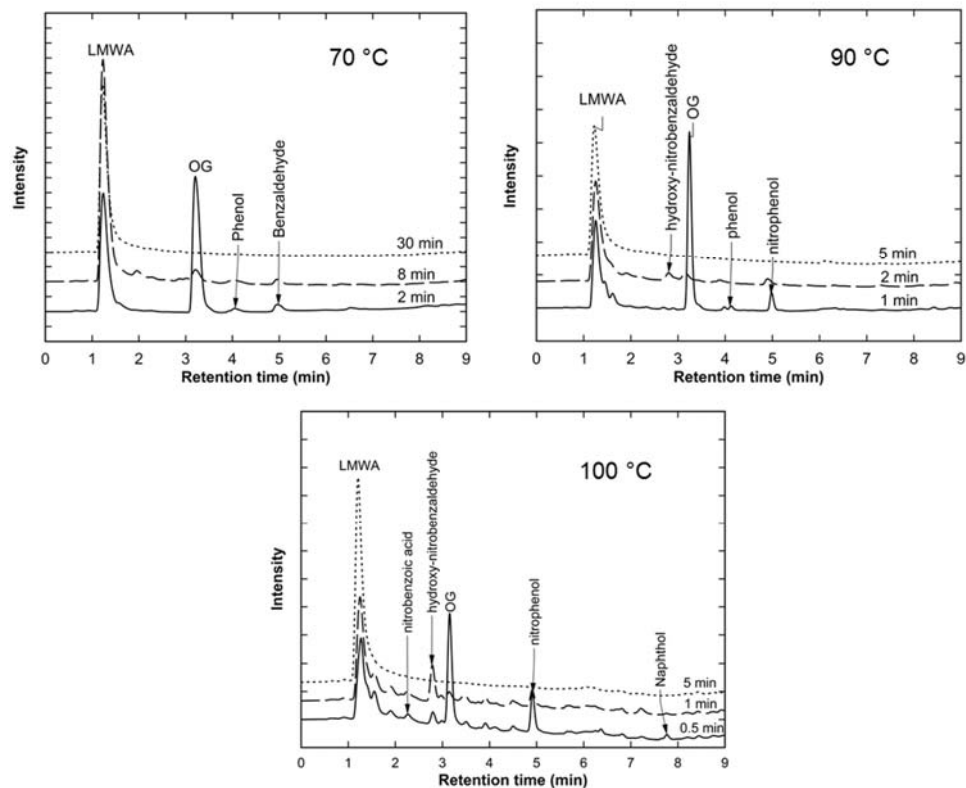


Figure 8.3. Chromatograms for 0.1 mM OG degradation at various temperature for  $C_{PS,0} = 1 \text{ Mm}$

### 8.3.3.3. Reaction quenching

Figure 8.4 shows the trend of absorbance decay with time for OG solutions under TAPS at 70 °C with quenching in either methanol (8000 mM) or an ice bath. It can be seen that quenching in an ice bath is as effective as quenching in methanol. Radical propagation is terminated in the presence of excess alcohol due to the formation of unreactive radicals incapable of maintaining the chain reaction [29, 40]. An explanation for radical termination in an ice bath is as follows. Compared to radical propagation reactions like abstraction and addition, radical terminating reactions like combination and disproportionation are highly exothermic [29, 38]. Combination of primary radicals may proceed with little or no energy of activation [38] and is independent of temperature [41]. Consequently, radical terminating reactions will dominate under low temperature conditions. It follows that ice bath quenching of radical reactions involve the production of non-radical chemical species from combination and disproportionation as the radicals become incapable of other reactions following diminished kinetic energy.

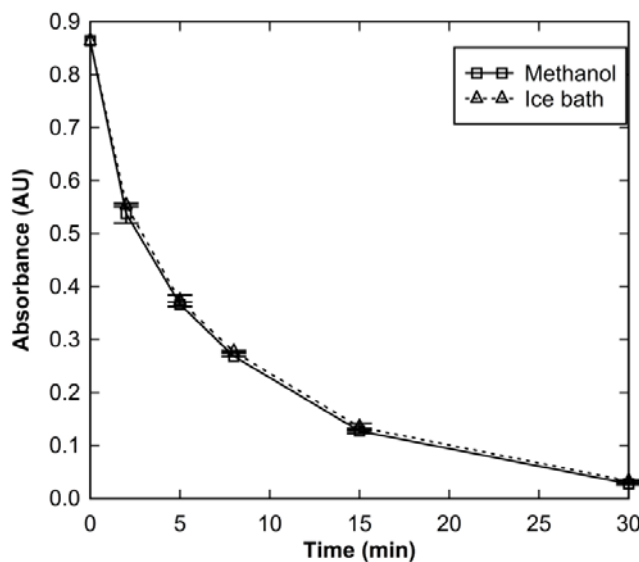


Figure 8.4. OG degradation for  $C_{PS,0} = 10 \text{ mM}$  at 70 °C with quenching in either methanol to give a solution with methanol concentration of 8000 mM or in an empty falcon tube immersed in an ice bath.

### 8.3.4. Mineralisation

The degree of pollutant mineralisation during TAPS degradation of OG was evaluated by measuring the percentage TC reduction. Figure 8.5a shows the proportion of TC removal achieved at the end of 1 h with reference to the original TC of the 0.1 mM OG solution. For both  $C_{PS,0} = 1 \text{ mM}$  and 10 mM and for a duration of 1 h, TC removal was poor for TAPS degradations of OG except at 90 °C and 100 °C. In fact > 90% TC reduction was recorded at 90 °C and 100 °C within 10 min when  $C_{PS,0} = 10 \text{ mM}$  highlighting the superior degradation potential of TAPS at those temperatures. For  $C_{PS,0} = 1 \text{ mM}$ , however, the mineralisation effectiveness was lower as TC reduction was only 55% and 44% at the end of 1 h for 90 °C and 100 °C reactions, respectively. It is interesting to note that mineralisation was more effective at 90 °C compared to 100 °C even after adjustment was made for evaporative loss at 100 °C considering that OG was more rapidly degraded at 100 °C than at 90 °C (Table 8.2). These results agree with the work of Goulden and Anthony [42] who studied PS mineralisation of nicotinic acid in solution between the temperatures of 90 °C and 130 °C and at varying PS concentration. The authors consistently reported the most effective mineralisation for the temperature of 90 °C. The optimisation of perfluorooctanoic acid mineralisation at 90 °C during PS degradation was also reported by Lee et al. [43]. Hori et al. studied perfluorooctanoic acid mineralisation at 80 °C and 150 °C. They reported better mineralisation at 80 °C compared to 150 °C. It appears then that mineralisation optimisation at 80 °C - 90 °C is general and could be considered the optimal condition for the operation of TAPS-AOP. However, further studies will be required to establish this generalisation. An explanation for the less effective mineralisation at 100 °C and higher temperatures may relate to the loss of active radicals as follows [19, 31, 44]:



It may be noted that the evolution of O<sub>2</sub> as described in R8.9 – R8.12 involve the breaking of O-H bond of water that has a bond-dissociation energy of 502 kJ mol<sup>-1</sup> [40]. The high bond-dissociation energy implies a high energy of activation [38]. Generally, as temperature increase, the fraction of chemical species with enough kinetic energy to overcome activation energy barriers for chemical reactions increase [29]. It appears that the fraction of radicals and ions with sufficient kinetic energy to break the O-H bond increased significantly at 100 °C compared to 90 °C resulting in the loss of mineralisation capacity at the former compared to the latter.

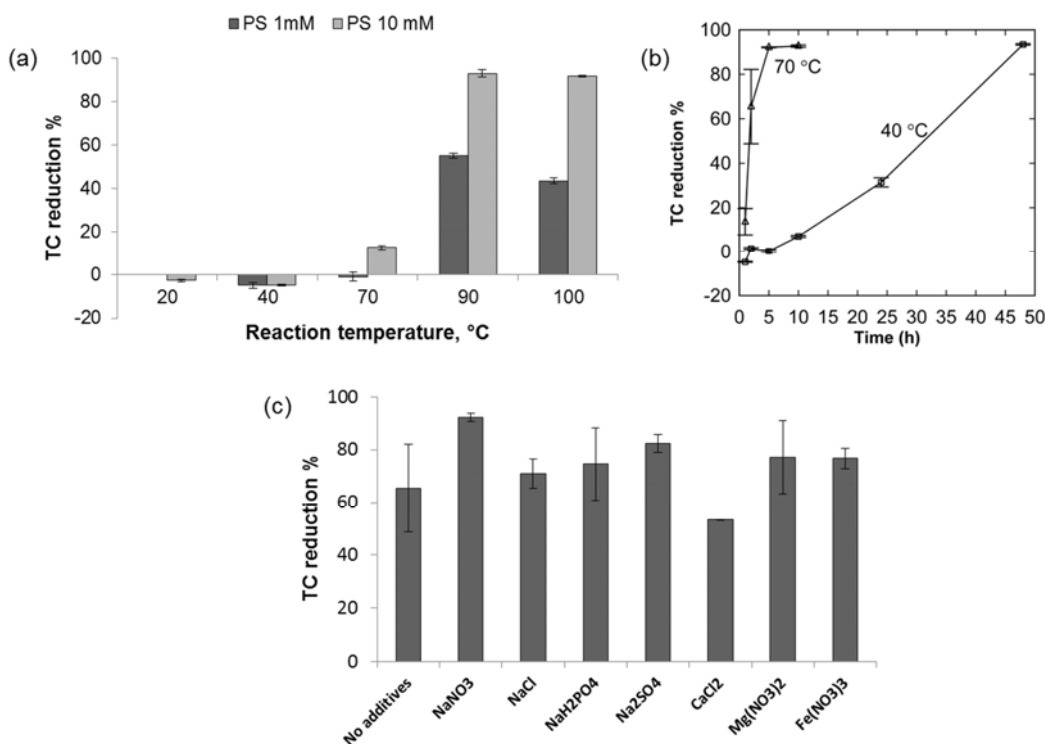


Figure 8.5. TC reduction for 0.1 mM OG with  $C_{PS,0} = 1$  mM and 10 mM for 1 h TAPS at 20 °C, 40 °C, 70 °C, 90 °C and 100 °C\* (a);  $C_{PS,0} = 10$  mM for 48 h TAPS at 40 °C and 70 °C (b); and  $C_{PS,0} = 10$  mM for 2 h TAPS with 100 mM added salt (c). \*TC reduction for 10 min is reported for  $C_{PS,0} = 10$  mM at 90 °C and 100 °C. Due to the evaporative loss of ~50% of water at 100 °C for the 1 h TAPS, the TC reduction reported for  $C_{PS,0} = 1$  mM at 100 °C were modified to account for fluid loss. TC reduction at 90 °C was not modified for fluid loss (evaporative loss was less significant).

Extending the degradation time as shown in Figure 8.5b revealed that the reduction in TC increased from 14% after 1 h to 65% after 2h for the 70 °C TAPS degradation process. For the 40 °C TAPS with limited thermal energy, only 1.5 % TC reduction was recorded after 2 h of degradation. The 70 °C TAPS achieved > 90% TC reduction after 5 h while the 40 °C TAPS attained > 90% TC reduction after 48 h. Evidently, in consideration of both Figures 8.5a and 8.5b, higher temperatures are more favourable for rapid OG mineralisation. Nevertheless, it is interesting to observe that even at the relatively low temperature of 40 °C, significant OG mineralisation can be achieved after 48 h.

The results of the effects of high salt concentrations on OG mineralisation by TAPS during 2 h experiments for  $C_{PS,0} = 10 \text{ mM}$  is shown in Figure 8.5c. It can be seen that the presence of  $\text{NO}_3^-$  tended to improve mineralisation especially for  $\text{NaNO}_3$  whose oxidising property is well known. On the other hand, the presence of  $\text{CaCl}_2$  can be seen to inhibit mineralisation despite the earlier rapid decolourisation observed. These results are consistent with the established effect of active chlorine on dye degradation where rapid dye decolourisation is associated with the formation of intermediates more resistant to mineralisation [32].

#### 8.4. Implications

This study indicates that the effective reactive potential of a radical, like other chemical species, is dependent on its inherent redox potential and its environment-influenced kinetic energy [29, 38, 40, 45, 46]. As the kinetic energy is reduced, the radical is less inclined to participate in chain-propagating reactions like H-atom and electron abstraction [38]. Consequently, radical terminating reactions such as combination prevail [41]. As kinetic energy is increased, the reaction become more diversified as activation energy barriers are readily overcome [29], producing intermediates that are more varied. Further increase in kinetic energy may increase ion/radical decomposition, impeding the chain reaction [42, 43]. This trend points to the existence of an optimal temperature condition for TAPS. In the absence of catalytic decomposition of PS, the generation and decomposition of  $\text{SO}_4^{\bullet-}$  follows a regular trend, which implies the optimal mineralisation temperature is independent of the target pollutant. Since 80 °C - 90 °C was found to be optimal for the mineralisation of OG (this study),

nicotinic acid [42], and perfluorooctanoic acid [43, 47], it may be said to be the optimal mineralisation temperature range for uncatalysed activation of PS subject to further experimental studies. Ironically, most recent research on TAPS were conducted  $\leq 70$  °C as mentioned in the introduction.

For the practical application of TAPS for the treatment of textile industry wastewater, it is interesting that temperature  $\geq 70$  °C are available as waste in the textile industry. At these temperatures, OG is rapidly transformed to LMWA within 30 min. Fast degradation of the azo bond but not the aromatic ring as reported in some previous studies [9, 11] may result in the persistence of toxic aromatic compounds in the treated dye solution which may constitute an environmental hazard [11, 22]. Based on whether textile industry waste streams are commingled or not, treatment at 80-90 °C (optimal temperatures), 70 °C and even at 40 °C are potential viable conditions.

Other than bicarbonate and chloride, the presence of high concentration of inorganic salts in the wastewater does not significantly affect dye decolourisation and mineralisation compared to  $\text{Fe}^{2+}$  activation of PS for OG degradation [11]. Consequently, since high salt concentrations are common features of dye-contaminated textile industry wastewater [11, 22, 26, 27], the TAPS process is uniquely situated for the treatment of such waste streams. Consequently, the TAPS process is potentially an effective means to resolve the wastewater challenge of the textile industry [22] without additional energy or chemical inputs other than the moderately cost PS [14] while treating water for reuse or safe disposal. Since actual textile industry wastewater more complex than the synthetic solutions studied in this work, future work would be aimed at evaluating OG degradation by TAPS within actual textile industry wastewater matrix.

### 8.5. Acknowledgement

The financial support provided by Victoria University to Ikechukwu A. Ike through the Victoria University International Postgraduate Research Scholarship is gratefully acknowledged. Sincere thanks to Dr Marlene Cran from Victoria University for her kind suggestions.

## References

- [1] Y. Deng, R. Zhao, Advanced Oxidation Processes (AOPs) in Wastewater Treatment, *Current Pollution Reports*, 1 (2015) 167-176.
- [2] R. Munter, Advanced oxidation processes - current status and prospects, *Proceedings of the Estonian Academy of Science. Chemistry*, 50 (2001) 59–80.
- [3] Y. Deng, C.M. Ezyske, Sulfate radical-advanced oxidation process (SR-AOP) for simultaneous removal of refractory organic contaminants and ammonia in landfill leachate, *Water Res.*, 45 (2011) 6189-6194.
- [4] C. Tan, N. Gao, Y. Deng, W. Rong, S. Zhou, N. Lu, Degradation of antipyrine by heat activated persulfate, *Separation and Purification Technology*, 109 (2013) 122-128.
- [5] X. Chen, M. Murugananthan, Y. Zhang, Degradation of p-Nitrophenol by thermally activated persulfate in soil system, *Chemical Engineering Journal*, 283 (2016) 1357-1365.
- [6] P. Devi, U. Das, A.K. Dalai, In-situ chemical oxidation: Principle and applications of peroxide and persulfate treatments in wastewater systems, *The Science of the total environment*, 571 (2016) 643-657.
- [7] J. Deng, Y. Shao, N. Gao, Y. Deng, C. Tan, S. Zhou, Zero-valent iron/persulfate(Fe0/PS) oxidation acetaminophen in water, *International Journal of Environmental Science and Technology*, 11 (2013) 881-890.
- [8] S.H. Do, Y.J. Kwon, S.H. Kong, Effect of metal oxides on the reactivity of persulfate/Fe(II) in the remediation of diesel-contaminated soil and sand, *J Hazard Mater*, 182 (2010) 933-936.
- [9] S. Rodriguez, L. Vasquez, D. Costa, A. Romero, A. Santos, Oxidation of Orange G by persulfate activated by Fe(II), Fe(III) and zero valent iron (ZVI), *Chemosphere*, 101 (2014) 86-92.
- [10] Y. Wu, R. Prulho, M. Brigante, W. Dong, K. Hanna, G. Mailhot, Activation of persulfate by Fe(III) species: Implications for 4-tert-butylphenol degradation, *J Hazard Mater*, 322 (2017) 380-386.

- [11] X.-R. Xu, X.-Z. Li, Degradation of azo dye Orange G in aqueous solutions by persulfate with ferrous ion, *Separation and Purification Technology*, 72 (2010) 105-111.
- [12] A. Ghauch, A.M. Tuqan, Oxidation of bisoprolol in heated persulfate/H<sub>2</sub>O systems: Kinetics and products, *Chemical Engineering Journal*, 183 (2012) 162-171.
- [13] A. Ghauch, A.M. Tuqan, N. Kibbi, Ibuprofen removal by heated persulfate in aqueous solution: A kinetics study, *Chemical Engineering Journal*, 197 (2012) 483-492.
- [14] A. Ghauch, A.M. Tuqan, N. Kibbi, S. Geryes, Methylene blue discoloration by heated persulfate in aqueous solution, *Chemical Engineering Journal*, 213 (2012) 259-271.
- [15] K.-M. Vuori, Direct and indirect effect of iron on river ecosystems, *Annales Zoologici Fennici*, 32 (1995) 317-329.
- [16] E. Pulat, A.B. Etemoglu, M. Can, Waste-heat recovery potential in Turkish textile industry: Case study for city of Bursa, *Renewable and Sustainable Energy Reviews*, 13 (2009) 663-672.
- [17] C. Tan, N. Gao, Y. Deng, N. An, J. Deng, Heat-activated persulfate oxidation of diuron in water, *Chemical Engineering Journal*, 203 (2012) 294-300.
- [18] D. Deng, L. Peng, M. Guan, Y. Kang, Impact of activation methods on persulfate oxidation of methyl tert-butyl ether, *J Hazard Mater*, 264 (2014) 521-528.
- [19] C. Liang, H.-W. Su, Identification of sulfate and hydroxyl radicals in thermally activated persulfate, *Industrial & Engineering Chemistry*, 48 (2009) 5558–5562.
- [20] D. Zhao, X. Liao, X. Yan, S.G. Huling, T. Chai, H. Tao, Effect and mechanism of persulfate activated by different methods for PAHs removal in soil, *J Hazard Mater*, 254-255 (2013) 228-235.
- [21] K.-C. Huang, R.A. Couttenye, G.E. Hoag, Kinetics of heat-assisted persulfate oxidation of methyl tert-butyl ether (MTBE), *Chemosphere*, 49 (2002) 413–420.
- [22] F.M. Drumond Chequer, G.A.R. de Oliveira, E.R. Anastacio Ferraz, J. Carvalho, M.V. Boldrin Zanoni, D.P. de Oliveir, *Textile Dyes: Dyeing Process and Environmental Impact*, in: *Eco-Friendly Textile Dyeing and Finishing*, InTech, 2013.

- [23] A.C. Mounguengui Steeve, Biodegradation of Reactive Blue 4 and Orange G by Pycnoporus sanguineus Strain Isolated in Gabon, *Journal of Bioremediation & Biodegradation*, 04 (2013).
- [24] H. Lachheb, E. Puzenata, A.M.K. Houas, E. Elaloui, C. Guillard, J.-M. Herrmann, Photocatalytic degradation of various types of dyes (Alizarin S, Crocein Orange G, Methyl Red, Congo Red, Methylene Blue) in water by UV-irradiated titania, *Applied Catalysis B: Environmental*, 39 (2002) 75-90.
- [25] J. Madhavan, F. Grieser, M. Ashokkumar, Degradation of orange-G by advanced oxidation processes, *Ultrasonics sonochemistry*, 17 (2010) 338-343.
- [26] C.M. Carliell, S.J. Barclay, C. Shaw, A.D. Wheatley, C.A. Buckley, The Effect of Salts Used in Textile Dyeing on Microbial Decolourisation of a Reactive Azo Dye, *Environmental Technology*, 19 (1998) 1133-1137.
- [27] J.-b. Guo, J.-t. Zhou, D. Wang, J. Wang, H. Yu, Z.-y. Song, Decolorization of azo dyes with high salt concentration by salt-tolerant mixed cultures under anaerobic conditions, *Journal of Environmental Sciences*, 17 (2005) 984-988.
- [28] G.P. Anipsitakis, D.D. Dionysiou, Radical generation by the interaction of transition metals with common oxidants, *Environmental Science & Technology*, 38 (2004) 3705-3712.
- [29] C.K. Law, *Combustion physics*, Cambridge University Press, Cambridge, 2006.
- [30] T.W. Swaddle, Inorganic chemistry, in: An industrial and environmental perspective, Elsevier Science, 1997.
- [31] I.M. Kolthoff, I.K. Miller, The chemistry of persulfate. I. The kinetics and mechanism of the decomposition of the persulfate ion in aqueous medium, *journal of American Chemical Society*, 73 (1951) 3055–3059.
- [32] Z. Wang, R. Yuan, Y. Guo, L. Xu, J. Liu, Effects of chloride ions on bleaching of azo dyes by Co<sup>2+</sup>/oxone reagent: kinetic analysis, *J Hazard Mater*, 190 (2011) 1083-1087.
- [33] R.P. Wayne, I. Barnes, P. Biggs, J.P. Burrows, C.E. Canosa-Mas, J. Hjorth, G. Le Bras, G.K. Moortgat, D. Perner, G. Poulet, G. Restelli, H. Sidebottom, The nitrate radical: physics, chemistry, and the atmosphere, *Atmospheric Environment. Part A. General Topics*, 25 (1991) 1-203.
- [34] E.G. Janzen, Electron spin resonance study of the SO<sub>2</sub>·- formation in the thermal decomposition of sodium dithionite, sodium and potassium metabisulfite,

and sodium Hydrogen Sulfite, *journal of Physical Chemistry*, 76 (1972) 157–162-152.

[35] H. Li, J. Wan, Y. Ma, M. Huang, Y. Wang, Y. Chen, New insights into the role of zero-valent iron surface oxidation layers in persulfate oxidation of dibutyl phthalate solutions, *Chemical Engineering Journal*, 250 (2014) 137-147.

[36] Z. Huang, H. Bao, Y. Yao, W. Lu, W. Chen, Novel green activation processes and mechanism of peroxymonosulfate based on supported cobalt phthalocyanine catalyst, *Applied Catalysis B: Environmental* 154–155 (2014) 36–43.

[37] D. Perner, R.H. Schuler, Hydrogen iodide as a radical scavenger in the radiolysis of hydrocarbons1, *Journal of Physical Chemistry*, 70 (1966) 2224–2232.

[38] C.J.M. Stirling, Radicals in organic chemistry, Oldbourne Press, London, 1965.

[39] A. Matilainen, M. Sillanpaa, Removal of natural organic matter from drinking water by advanced oxidation processes, *Chemosphere*, 80 (2010) 351-365.

[40] N. Uri, Inorganic free radicals in solution, *Chemical Review*, 50 (1952) 375–454.

[41] J.A. Walker, W. Tsang, Single-pulse shock tube studies on the thermal decomposition of n-butyl phenyl ether, n-pentylbenzene, and phenotole and the heat of formation of phenoxy and benzyl radicals, *Journal of Physical Chemistry*, 94 (1990) 3324-3327.

[42] P.D. Goulden, D.H.J. Anthony, Kinetics of uncatalyzed peroxydisulfate oxidation of organic material in fresh water, *Analytical Chemistry*, 50 (2002) 953-958.

[43] Y.C. Lee, S.L. Lo, P.T. Chiueh, D.G. Chang, Efficient decomposition of perfluorocarboxylic acids in aqueous solution using microwave-induced persulfate, *Water Res*, 43 (2009) 2811-2816.

[44] J. Kronholm, P. Jyske, M.-L. Riekkola, Oxidation efficiencies of potassium persulfate and hydrogen peroxide in pressurized hot water with and without preheating, *Industrial & Engineering Chemistry Research* 39 (2000) 2207-2213.

[45] J.L. Ferry, M.A. Fox, Temperature effects on the kinetics of carbonate radical reactions in near-critical and supercritical water, *Journal of physical Chemistry A*, 103 (1999 ) 3438-3441.

- [46] A.M. Dean, Predictions of pressure and temperature effects upon radical addition and recombination reactions, *The Journal of Physical Chemistry*, 89 (1985) 4600-4608.
- [47] H. Hori, Y. Nagaoka, M. Murayama, S. Kutsuna, Efficient Decomposition of Perfluorocarboxylic Acids and Alternative Fluorochemical Surfactants in Hot Water, *Environmental Science & Technology*, 42 (2008) 7438–7443.

## Appendix

### S8.1 Chemicals

Chemicals used for the experiment include OG, sodium salt, from Sigma, Na<sub>2</sub>S<sub>2</sub>O<sub>8</sub> (PS) ( $\geq$  99%) from BDH, NaNO<sub>3</sub> from BDH, NaCl from Merck, NaHCO<sub>3</sub> from Merck, NaH<sub>2</sub>PO<sub>4</sub> from Merck, Na<sub>2</sub>SO<sub>4</sub> from BDH, CaCl<sub>2</sub> from Sigma Aldrich, Mg(NO<sub>3</sub>)<sub>2</sub>.6H<sub>2</sub>O from Merck and Fe(NO<sub>3</sub>)<sub>3</sub>.9H<sub>2</sub>O from BDH. Others include ascorbic acid from Sigma, methanol (99.9%) from HoneyWell, propanol-1 (99%) from BDH, pentanol-1 (99%) from BDH and potassium iodide (KI) ( $\geq$  99.5%) from Rowe Scientific. MilliQ™ water used throughout the experiment was obtained from a MerckMillipore Water Purification System.

### S8.2 High performance liquid chromatography

High performance liquid chromatographic (HPLC) study of OG degradation was conducted using a Shimadzu Prominence-i LC 2030C Liquid Chromatograph with a UV detector at 280 nm. The column used was a Kinetex C18 5 $\mu$  100 Å, size 100 x 4.6 mm protected with a guard column and maintained at 25 °C throughout the analysis. Binary solvent linear gradient flow at 0.8 ml/min was employed in which solvent A, methanol, was increased from 30% to 90% in 10 min, maintained at 90% for 2.5 min and then rapidly decreased to 30% in 0.3 min. At this composition (A 30%), the column was equilibrated for 7.3 min. Solvent B was 50 mM ammonium phosphate at a pH of 6.8.

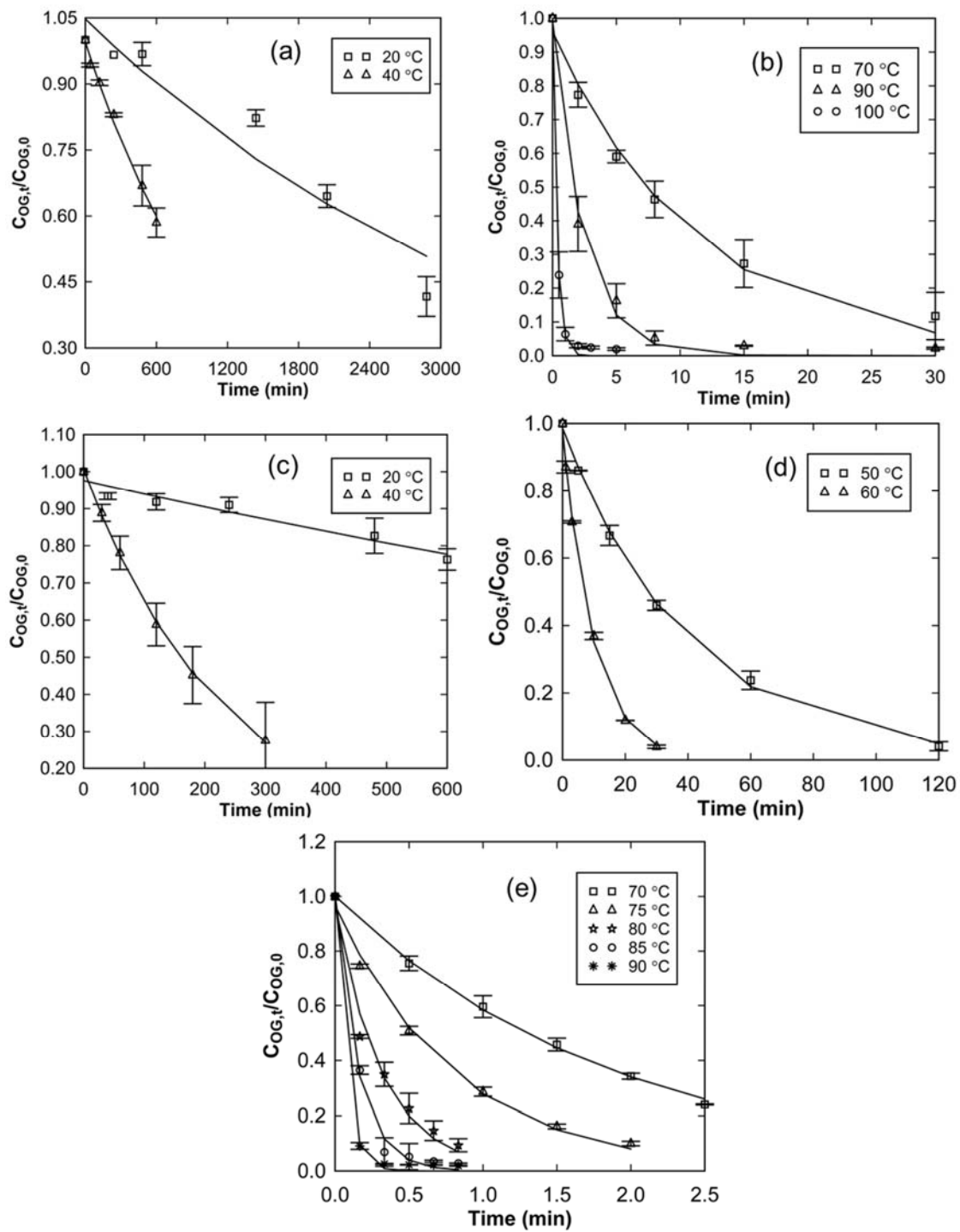


Figure S8.1. Rate of OG degradation for  $C_{PS,0} = 1 \text{ mM}$  (a) and (b);  $C_{PS,0} = 10 \text{ mM}$  (c), (d) and (e). Trends fitted with semilog curves.

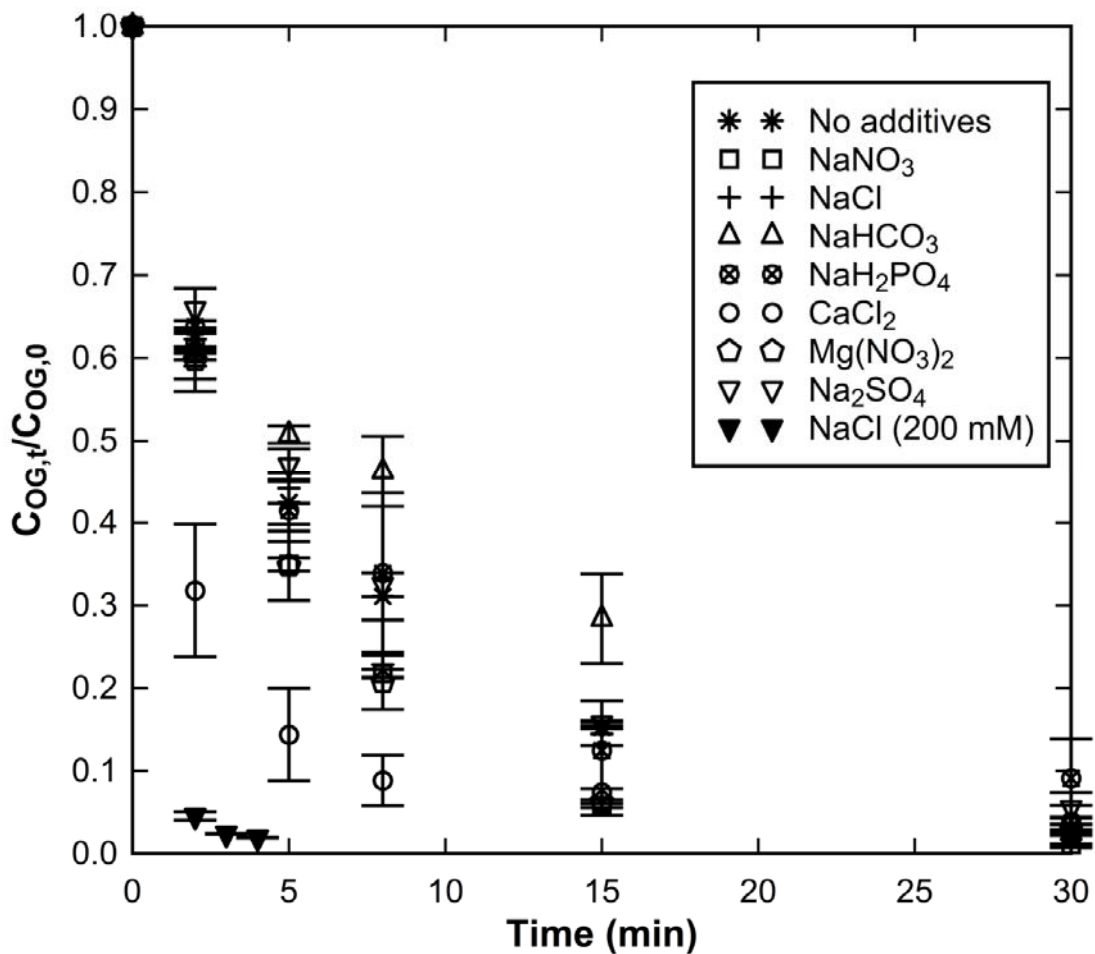


Figure S8.2. Effect of 100 mM (except where otherwise stated) salt concentrations on the rate of 0.1 mM OG degradation.  $C_{\text{PS},0} = 10 \text{ mM}$ ; temperature = 24 °C.

### S8.3 Ascorbic acid as radical scavenger

The use of ascorbic acid as a radical scavenger resulted in unique OG decolourisation behaviour. While the reacting PS/ascorbic acid system at 70 °C was visually similar to the PS/propanol system at 70 °C, it was observed that aliquot samples taken from the former into methanol containers to quench the reaction were decolourised on mixing with methanol after a few min (Figure 2b). The only exception was the aliquot sampled at 30 min that was not decolourised even after several hours in methanol. The same decolourisation effect was observed when the PS/ascorbic acid system were

subjected to a 40 °C reaction environment except that the decolourisation was faster and complete even for aliquots taken at 30 min (data not shown). Complete decolourisation of OG at all sampling time was also observed for a room temperature PS/ascorbic acid system but at a much slower rate compared to the 70 °C and 40 °C systems. In the absence of PS, no decolourisation of OG was observed by ascorbic acid. When aliquots taken from the PS/ascorbic acid system at 70 °C were quenched in an ice bath as shown in Figure 2b, practically no degradation was observed in 30 min.

Table S8.1. Retention times for known chemicals

<b>Chemicals</b>	<b>Retention time, min</b>
Fumaric acid	1.24
Oxalic acid	1.26
4-aminobenzoic acid	1.30
Pthalic anhydride	1.30
Pthalic acid	1.31
Maleic acid	1.33
3-hydroxybenzoic acid	1.33
2-Furoic acid	1.33
Hydroquinone	1.73
Resorcinol	2.20
Benzoquinone	2.24
Salicylic acid	2.32
4-nitrobenzoic acid	2.33
2-hydroxy-5-nitrobenzaldehyde	2.82
Orcinol	3.07
Orange G	3.21
Aniline	3.24
2,4, Dinitrophenol	3.39
4-Nitroaniline	3.82
Phenol	4.11
3,5 Dinitrosalicylic acid	4.81
Benzaldehyde	4.95
2-nitrophenol	4.95
1-hydroxy-2-naphthoic acid	5.53
Acetophenone	5.61
Nitrobenzene	6.21
2-nitroso-1-naphthol	6.27
Naphthylamine	6.64
$\alpha$ -Naphthol	7.68
2-hydroxy-1-naphthaldehyde	8.00
Bisphenol A	8.12

## Chapter 9

### **Activation of persulphate for effective humic acid degradation at waste heat temperature \***

#### **Abstract**

Humic acid (HA) as a major constituent of natural organic matter (NOM) in raw water presents major challenges to drinking water production including membrane fouling and serving as a precursor for the production of disinfection by products (DBPs). This study demonstrates the feasibility of HA degradation by heat-activated persulphate (PS) mainly at a low waste heat temperature of 40 °C, but also at 60 °C and 90 °C in which ~70% TOC loss was achieved within 168 h, 24 h and 1 h, respectively. The use of waste heat for water treatment eliminates reliance on electricity, which is a requirement for common advanced oxidation processes. Heat-activated PS treatment of synthetic raw water at 40 °C was also shown to significantly reduce ultrafiltration membrane fouling. Low concentration of chloride ( $\leq 0.9$  mM) accelerated PS degradation of HA but the promotion was lost at higher concentration ( $\geq 9$  mM). HA spiked into tap water was degraded by PS even at 25 °C suggesting activation by trace minerals present within regulatory limits. These results represent a potential overall sustainable improvement in the production of safe drinking water.

#### **9.1. Introduction**

Natural water used for drinking water supplies usually contains varying amounts of natural organic matter (NOM). NOM in raw water are typically composed of hydrophobic components such as humic acid (HA) and hydrophilic components such as carbohydrates [1]. The hydrophobic NOM are credited as the main precursor for the production of disinfection by products (DBPs) and they are recognised as major contributor to the fouling of filtration membranes [1, 2]. Increasing attention is been paid to the use of advanced oxidation processes (AOPs) for the degradation of NOM and other recalcitrant pollutants in water to improve conventional water treatment systems [1, 3].

\*Accepted for publication by ACS Sustainable Chemistry & Engineering

The most important AOPs applied to the production of potable water include UV-photolysis, ozonation and heterogeneous photocatalysis [1]. Hydrogen peroxide as a ready source of the hydroxyl radical ( $\cdot\text{OH}$ ) usually play a crucial role in the effectiveness of these AOPs in the degradation of NOM and other micropollutants[1]. Although processes that employ the sulphate radical ( $\text{SO}_4^{\bullet-}$ ) have surged in importance in recent decades as a viable means to purify water, they have been evaluated primarily for the degradation of micropollutants and recalcitrant organic compounds in wastewater [4]. The application of  $\text{SO}_4^{\bullet-}$  for the degradation of NOM, with the production of potable water in view, is not common. Nevertheless,  $\text{SO}_4^{\bullet-}$  produced through the activation of persulphate (PS) has many properties that could enhance the practical and economic viability of water treatment for drinking water production using AOP. Some of these properties include the relative stability of PS and  $\text{SO}_4^{\bullet-}$  compared to  $\text{H}_2\text{O}_2$  and  $\cdot\text{OH}$  [5], a limited tendency of  $\text{SO}_4^{\bullet-}$  to form bromate compared to  $\text{O}_3$  [6], moderate cost, and the ease of transportation, handling and storage of PS [5].

It is also worthy of note that most recent studies of  $\text{SO}_4^{\bullet-}$  AOPs, of relevance to the production of potable water, have tended to focus on UV activation of PS [7, 8]. UV activation is known to be an effective technique for pollutant degradation with the added benefit that the electromagnetic radiation itself also contributes to the degradation processes [9]. However, the energy implications for the treatment of large volume of water with *high-grade* electrical energy in the face of rising energy costs has an unfavourable impact on the water-energy nexus and overall environmental sustainability [10, 11]. It should be noted that the three common AOPs applied to drinking water production - UV-photolysis, ozonation and heterogeneous photocatalysis – also depend on onsite electricity for the generation of UV and/or  $\text{O}_3$  [12]. Consequently, they are themselves adverse to the water-energy nexus as they use up significant amount of high quality energy to purify water [10, 13].

Sustainable AOPs for potable water production using *low-grade* energy may be developed by harnessing the significant amount of waste heat produced from many industrial processes with discharges commonly available between 60 - 120 °C [14, 15]. Although PS activation is limited at 20 °C, it has been shown that PS

activated at 40 °C can effectively degrade water pollutants [16]. Interestingly, a number of recent publications have shown that waste heat from industrial processes can readily be harnessed to produce utility heating > 40 °C [15, 17]. In fact, a hydronic fluid temperature of 43 °C has been considered to be the lower limit for common utility application [15] while cooling water may be routinely heated to 45 °C during normal industrial processes [14]. Furthermore, even after efficient heat recovery, industrial waste heat at temperature of ~40 °C are common [18]. Hence, there is great potential for the development of cost-effective and environmental-friendly PS-AOP operating at ~40 °C, if drinking water systems were to be safely coupled to industrial waste heat streams. In practice, combining waste heat at 40 °C with higher temperature waste heats will potentially provide for effective treatment in reasonable time. Similar systems may also be deployed on a domestic scale harnessing household waste heat [19], especially in locations with a decentralised potable water supply.

It should be emphasised that many industrial activities consume significant amount of water for cooling and other applications [20, 21]. This is particularly the case for thermoelectric power generation where cooling water availability is a strong factor in selecting operation location and where water discharges may constitute both thermal and chemical pollution to the receiving water bodies. For inland locations, significant investment cost may be incurred in the construction and operation of cooling towers [20, 21]. By re-designing processes, waste heat removed by cooling water or supplied by hot exhaust gas or derived from other operations or a combination of these options may be employed for the activation of PS for the treatment of water that is already available for cooling. The PS-treated water can be reused so that the heat is recycled or the heat is dissipated during conventional distribution or further treatment to potable standard hence avoiding the thermal pollution of aquatic environments by industrial low-grade heat. This scheme will simultaneously result in energy-neutral potable water production and the elimination of thermal pollution of aquatic environments that would have being the case if warm water are discharged. This will potentially reduce or eliminate the need for industrial cooling towers. In effect, waste heat activation of PS for water treatment may significantly improve the operational

water-energy nexus as power generation, rather than reducing the amount of fresh water available for potable use, becomes a means for treating fresh water for industrial or domestic applications.

This work reports the feasibility of HA degradation as a representative NOM in synthetic raw water using PS, mainly thermally activated at 40 °C. Temperatures of 60 °C and 90 °C were also evaluated. These temperatures fall within the common waste-heat discharge temperature range of ≤ 120 °C [14, 15].

## 9.2. Materials and methods

Chemicals used for the experiment include Fluka humic acid (FHA), 53680, sodium persulphate (PS) from BDH, sodium chloride from Merck, calcium chloride from Sigma Aldrich, sodium carbonate from Merck, sodium dihydrogen phosphate from Merck and disodium hydrogen phosphate from BDH. MilliQ™ water used throughout the experiment was obtained from a MerckMillipore Water Purification System.

A HA stock solution was produced by magnetically stirring 1 g of FHA in 1 L of MilliQ water overnight. The solution was filtered through Adventec Grade 2 filter paper to remove undissolved particles and, thereafter, stored at 4 °C. Two synthetic raw water samples were made up containing 4 mg/L of HA representing typical organic load water for AOP or 15 mg/L of HA representing high organic load water for AOP [12]. HA was added to a 10 mM background ionic strength solution composed of 7 mM NaCl and 1 mM CaCl<sub>2</sub> [2]. Batch experiments were conducted with 0.25 mM (60 mg/L) of PS added to the 4 mg/L HA synthetic water. The solution was stirred in an orbital shaker set at a temperature 40 °C except where otherwise stated. The degradation of the 15 mg/L HA synthetic water at 40 °C with and without 1 mM (238 mg/L) of added PS was also evaluated. The fouling potential of the heat-activated PS treated and untreated 15 mg/L HA synthetic raw water during membrane ultrafiltration was evaluated using a laboratory scale crossflow rig. The membrane used for this study was a low fouling PVDF membrane with a narrow distribution of small pores (2.5 - 25 nm) and a relatively smooth selective surface produced by ultrasonication. Details of

the membrane synthesis and properties were recently published [22]. The membrane filtration experiment involved initial membrane compression by the filtration of MilliQ water with a transmembrane pressure (TMP) of 30 kPa for 10 min. This was followed by the filtration of the 10 mM ionic strength salt solution without added HA to determine the clean water flux of the membrane ( $J_0$ ) at a TMP of 20 kPa for 20 min. The feed flux ( $J$ ) of the synthetic raw water with degraded or freshly added HA was conducted at a TMP of 20 kPa for 2 h.

A Shimadzu UV-1800 UV spectrophotometer was used to analyse collected samples for UV absorption at 254 nm ( $UV_{254}$ ). Spectral scans between the wavelength of 200 nm and 600 nm were collected. Total organic carbon (TOC) was measured using a Shimadzu TOC-V<sub>CSH</sub> Total Organic Carbon Analyzer while excitation-emission-matrix (EEM) fluorescence spectra were collected using a Horiba Scientific Aqualog-UV-800-C. High performance liquid chromatography (HPLC) was conducted using a Shimadzu Prominence-i LC 2030C Liquid Chromatograph with UV detector at 280 nm. The column used was a Kinetex C18 5 $\mu$  100 Å, size 100 x 4.6 mm, maintained at 25 °C and preceded by a column guard. Binary solvent linear gradient flow at 0.8 mL/min was employed in which the concentration of solvent A, methanol, was increased from 30% to 90% in 10 min, maintained at 90% for 2.50 min and then rapidly decreased to 30% in 0.30 min. At this composition (A 30%), the column was equilibrated for 7.30 min. Solvent B was 50 mM ammonium phosphate at a pH of 6.8. The pH of solutions was measured using Hanna H1 2211 pH/ORP Meter. Error bars presented are standard errors of duplicate experiments.

### 9.3. Results and discussions

The result of the degradation of the 4 mg/L HA synthetic raw water is given in Figure 9.1 showing the trends of  $UV_{254}$  and the specific UV absorbance (SUVA), i.e.  $SUVA = UV_{254}/TOC$ . SUVA is often considered a measure of the aromaticity of NOM in raw water [23]. It can be seen that the activation of PS at 40 °C achieved significant reduction in  $UV_{254}$  (~60%) over a period of 72 h. This shows that HA in water can be degraded by PS activated at the relatively low temperature of 40 °C at which waste heat has limited application [15] but may still

present significant disposal challenges [20, 21]. Typically, AOPs achieve faster  $\text{UV}_{254}$  removal than TOC, which reflect the fact that NOM in raw water is sequentially oxidised to molecules with limited UV absorption before eventual mineralisation [9, 24]. Based on energy considerations, significant removal of  $\text{UV}_{254}$  but limited TOC reduction is often acceptable, as both membrane fouling and DBPs formation potential have been directly correlated to raw water  $\text{UV}_{254}$  [2, 9]. It can be seen that the trend of SUVA follows roughly that of  $\text{UV}_{254}$  but not perfectly as SUVA is also affected by variations in TOC. In fact, like  $\text{UV}_{254}$ , ~60% overall reduction in SUVA was achieved after 72 h. The SUVA result may be interpreted to mean that 60% of the aromaticity of the HA was degraded in 72 h and, with respect to the corresponding  $\text{UV}_{254}$  reduction (~60%), the overall TOC value was not significantly changed within this period. Consequently, the degradation proceeded by a preferential oxidations of the aromatic structures of HA [9].

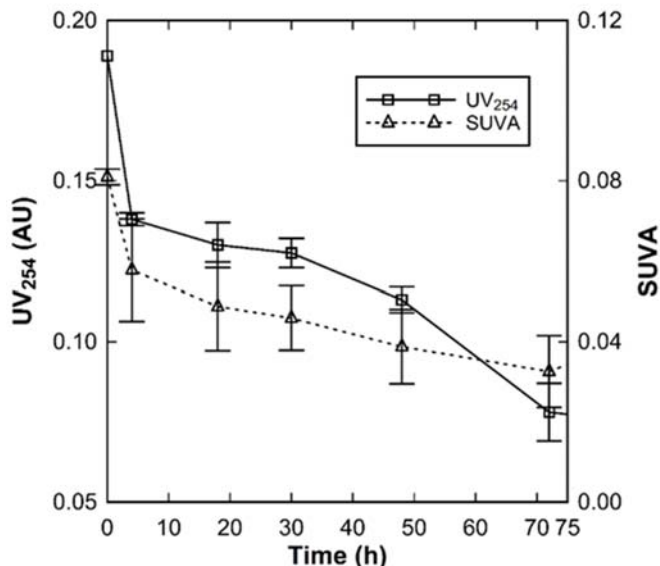


Figure 9.1. 4 mg/L HA synthetic raw water ( $[\text{Cl}^-] = 9 \text{ mM}$ ) degradation by 0.25 mM PS activated by heat at 40 °C as evaluated by  $\text{UV}_{254}$  and SUVA.

The HA degradation as measured by EEM fluorescence spectra is presented in Figure 9.2. The EEM fluorescence spectroscopy is a particularly sensitive and reliable technique to measure the presence and nature of HA in water and other matrices due to HA multi-chromophoric property [25-27]. However, the feature of the EEM spectra is dependent both on the chemical properties of the HA as well as on its concentration [25, 27]. Consequently, the spectral changes that are presented in Figure 9.2 may indicate both changes in HA concentration and chemical properties. The complete absence of any HA spectral feature at 168 h is an indication of the complete degradation of the HA in the water sample. The limits of the fluorescence spectra in 0 h was about 400 nm on the excitation wavelength axis and 610 nm on the emission wavelength axis. At 72 h, the limits of the spectra was roughly 350 nm and 520 nm on the excitation and emission wavelength axes respectively with much attenuated areal cover that disappeared completely at 168 h. Fluorescence signal at longer wavelength have been associated with high degree of aromatic polycondensation and high molecular weight. Signals at shorter wavelength have been linked with the presence of aliphatic species and low degree of aromatic polycondensation [28]. Consequently, the degradation of HA proceeded with the decrease in polycondensation and molecular weight. These modifications of the fluorescence spectra in Figure 9.2 with time mirror the measured reduction in UV<sub>254</sub> and SUVA in Figure 9.1, further confirming the preferential oxidation of the aromatic structures of HA.

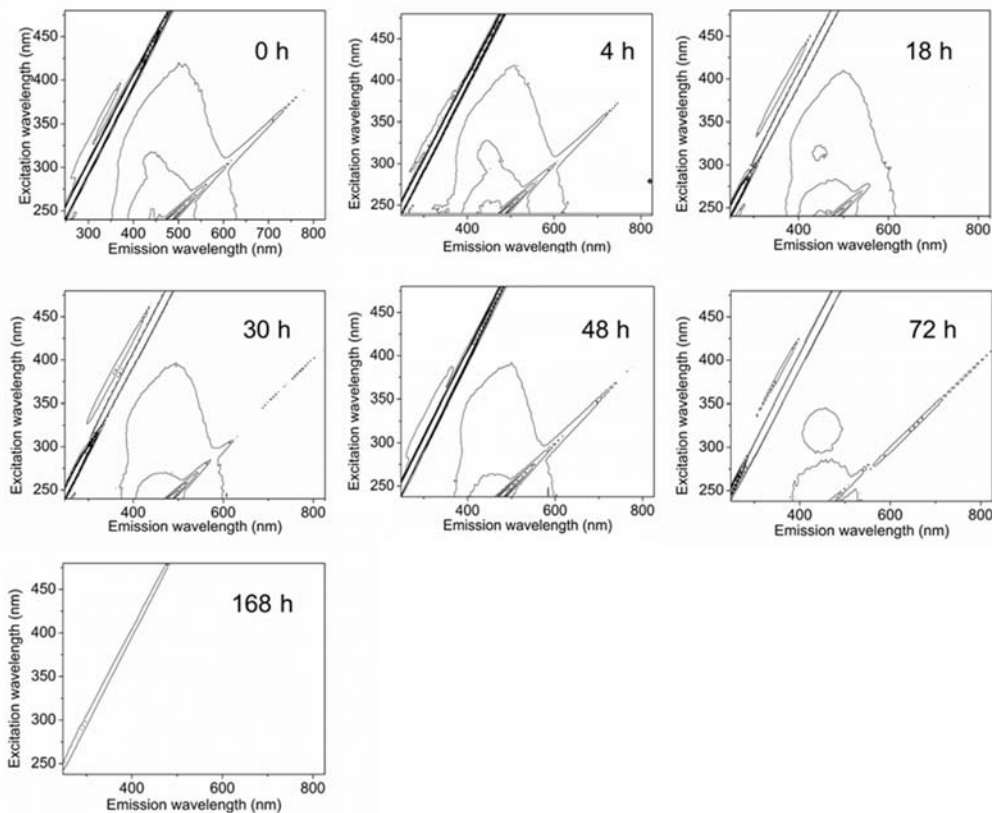


Figure 9.2. EEM contours for the degradation of 4 mg/L HA synthetic raw water ( $[Cl^-] = 9$  mM) by 0.25 mM PS thermally activated at 40 °C.

Further analysis of the degradation process by heat-activated PS at 40 °C is presented as a UV spectral scan between wavelengths 200 nm and 600 nm as shown in Figure 9.3a. As may be seen in Figure 9.3a at 0 h, the UV spectra shows an approximate exponential decay in intensity with increasing wavelength typical of HA [29]. HA is known to show such featureless absorption decay profile [27] due to its extended conjugated aromatic network. The partial degradation of HA have been reported to result in the formation of intermediates with aromatic and non-aromatic speciation [30, 31]. Comparing the spectral profile at 168 h with the profile of some aromatic and non-aromatic compounds given in Figure S9.1 in the Appendix, it can be seen that aromatic structures in HA were completely destroyed in the course of the AOP. The spectral pattern in Figure 9.3a suggests that the main degradation product at the end of 168 h are non-aromatic

compounds (see Figure S9.1). It may be said with greater confidence that the residual UV<sub>254</sub> absorbance is not due to the presence of HA but to its non-aromatic degradation product.

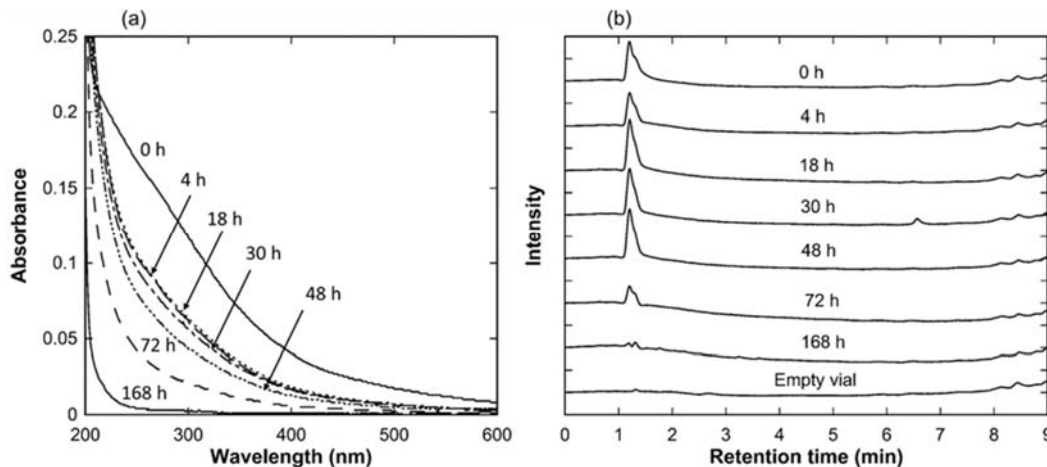


Figure 9.3. UV-visible spectral profile (a) and chromatograms (b) for 4 mg/L HA acid synthetic raw water ( $[Cl^-] = 9$  mM) degradation products; initial PS concentration 0.25 mM; reaction temperature 40 °C.

The results of the chromatographic analyses for samples taken at specific intervals during the thermally activated PS-AOP are presented in Figure 9.3b. Although categorised as hydrophobic [1], HA eluted quickly in the course of the chromatographic analysis suggesting limited interaction with the chromatographic column. As may be seen in Table S9.1, hydrophobic compounds with single or double benzene ring have longer retention times compared to more hydrophilic and often more oxidised molecules. An interesting feature of Figure 9.3b is that besides the HA peak, no other peak was observed except the possible aromatic peak at 6.6 min developed on the 30 h chromatogram. However, this peak was short-lived as it disappeared before the next sampling time. This result indicate that the AOP in this study produces limited amount of stable intermediates implying efficient degradation of HA. The two small residual peak after 168 h of degradation at 1.2 min and 1.3 min are

considered to be low molecular weight hydrophilic acids rather than remnant HA based on the UV-visible spectra of Figure 9.3a and EEM spectra of Figure 9.2.

Although significant  $\text{UV}_{254}$  removal with limited TOC loss can be an acceptable water treatment option [2, 9, 32], however, whenever feasible, substantial TOC removal is desirable to ensure that degradation products with high DBP formation potential are eliminated [9, 32, 33]. The TOC loss for 4 mg/L HA solutions degraded by 0.25 mM PS activated at relevant waste heat temperatures of 40 °C, 60 °C and 90 °C are shown in Figure 9.4. It can be seen that ~70% TOC loss was achieved after 168 h (7 d), 24 h and 1 h for PS activated at 40 °C, 60 °C and 90 °C, respectively, which suggests an exponential increase in mineralisation with increasing temperature consistent with the Arrhenius straight-line characteristic of PS activation [34, 35]. Operating at 90 °C provides fast mineralisation of HA comparable to results from conventional photocatalytic mineralisation of HA [2] while operating at 40 °C resulted in a relatively slow mineralisation due to the limited PS activation at lower temperatures.

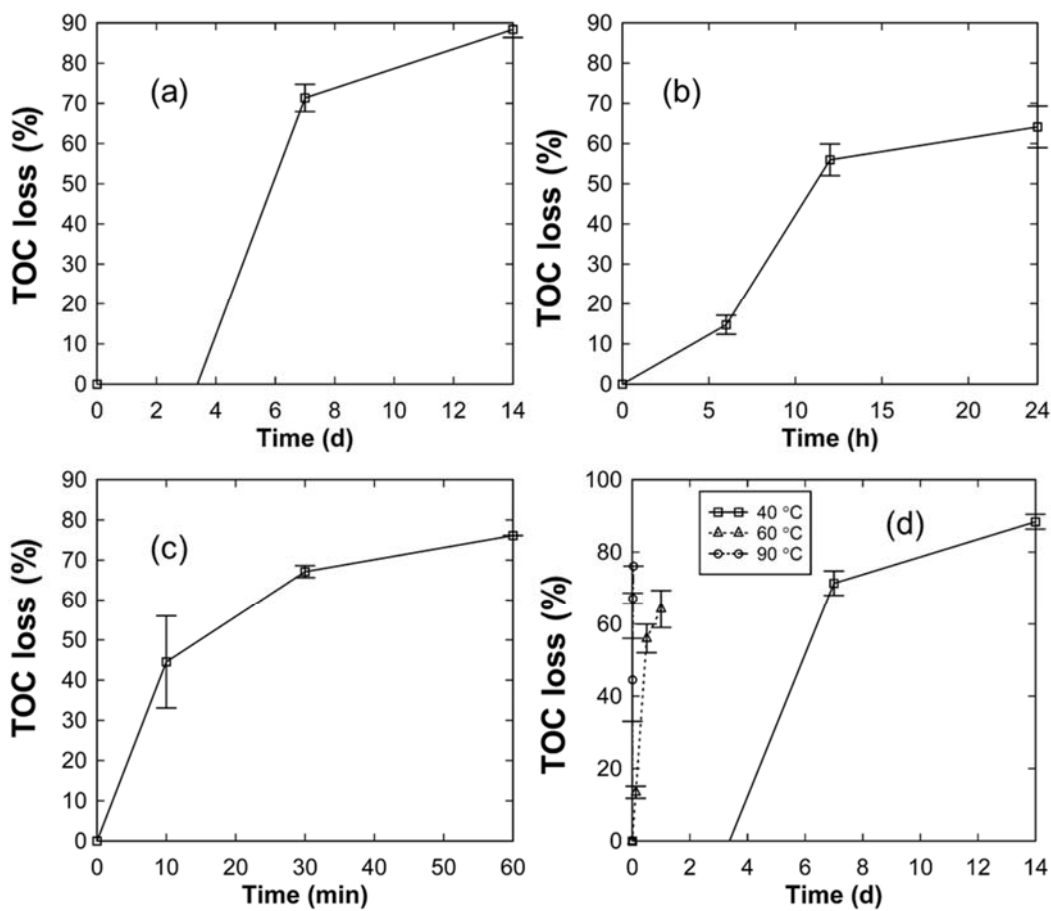


Figure 9.4. TOC loss for 4 mg/L HA synthetic raw water ( $[Cl^-] = 9\text{ mM}$ ) degradation by 0.25 mM PS activated thermally at 40 °C (a), 60 °C (b) and 90 °C (c). TOC loss at different temperatures plotted on the same horizontal axis (d).

The degradation of 15 mg/L HA synthetic raw water at 40 °C measured as reduction in TOC is presented in Figure 9.5a. Even with the increased PS concentration of 1 mM, it can be seen that a longer reaction time is required to significantly mineralise the organic substance load in the raw water. At the end of 336 h, ~90% mineralisation has been achieved. As may be expected, merely subjecting HA to a temperature of 40 °C does not result in degradation without added PS as the TOC remained practically unchanged for the 0 mM PS case in Figure 9.5a.

The normalised flux ( $J/J_0$ ) profile for the membrane filtration of the untreated 15 mg/L HA raw water is presented in Figure 9.5b alongside the flux profile after treatment with 1 mM PS thermally activated at 40 °C for 336 h. The result showed significant reduction in the normalised flux for the untreated raw water in the course of the 2h experiment indicating membrane fouling by HA while much less membrane fouling was experienced after HA degradation by heat-activated PS. The rapid fouling by HA observed for the untreated raw water was probably enhanced by the presence of calcium ion which is known to increase the following tendency of NOM [2]. As can be seen in Figure S9.2, without added PS, no improvement in fouling reduction was achieved by merely subjecting the raw water to a 40 °C environment for 336 h consistent with the practically zero reduction in TOC as shown in Figure 9.5a. As membrane fouling is a major challenge in the treatment of natural surface water [36], heat-activated PS treatment at 40 °C is a potential technique to significantly reduce the problem of fouling and improve process performance.

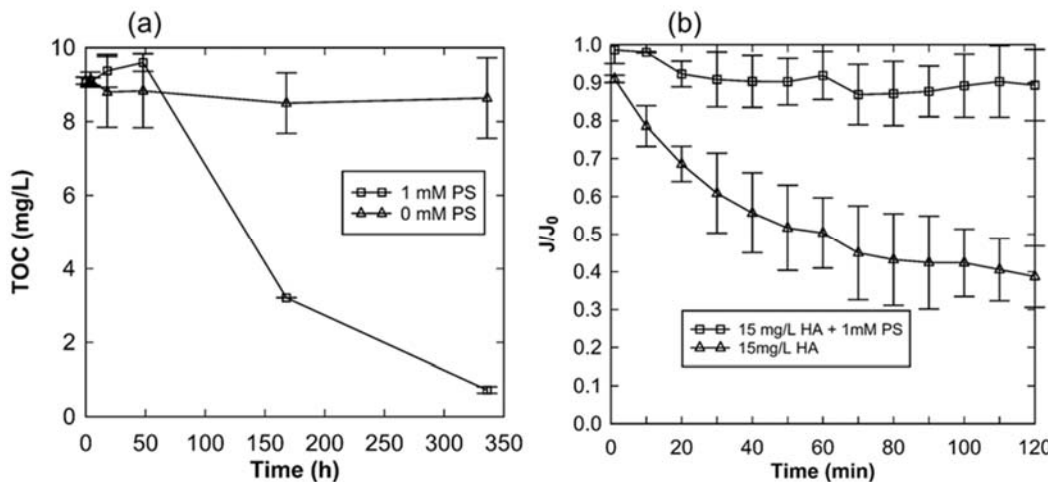


Figure 9.5. Degradation and flux profile. (a) Degradation of 15 mg/L HA synthetic raw water ( $[Cl^-] = 9$  mM) by 1 mM PS activated thermally at 40 °C. Normalised flux profile for the filtration of untreated 15 mg/L HA synthetic raw water ( $[Cl^-] = 9$  mM) compared to the filtration of treated raw water. Treatment condition: 1 mM PS activated at 40 °C for 336 h.

The loss in TOC for the treated 15 mg/L HA synthetic raw water after ultrafiltration was 90% while the corresponding TOC loss for the untreated raw water was 60%. Although a 60% reduction in TOC was achieved by the ultrafiltration of the untreated raw water, the EEM spectra of the filtrates (Figure 9.6) show that HA passed through the membrane. The passage of HA through ultrafiltration membrane is not surprising as the hydrodynamic radii of HA have been given [37] to range between 2.2 and 6.4 nm while the pore size in ultrafiltration membranes range between 10 nm and 100 nm [38]. In fact, except for the activated PS treated water, there is little difference in the EEM spectra between the original raw water and the water after ultrafiltration without prior PS degradation. Since ultrafiltration is a favoured technology for the production of drinking water [3], it is easy to see that significant amount of HA may bypass the treatment process into potable water distribution channels. The presence of HA in the filtrate constitute a significant risk of production of halomethanes and other DBPs upon chlorination [9, 39]. No HA was detected in the filtrate following the heat-activated PS treatment of the raw water. Consequently, for this case alone (heat-activated PS treatment) with practically complete removal of HA and significant TOC reduction (~90%), is chlorination of the membrane permeate safe as the potential for DBPs production is significantly decreased [9, 39]. However further work is required to measure DBPs formation to quantify the benefits.

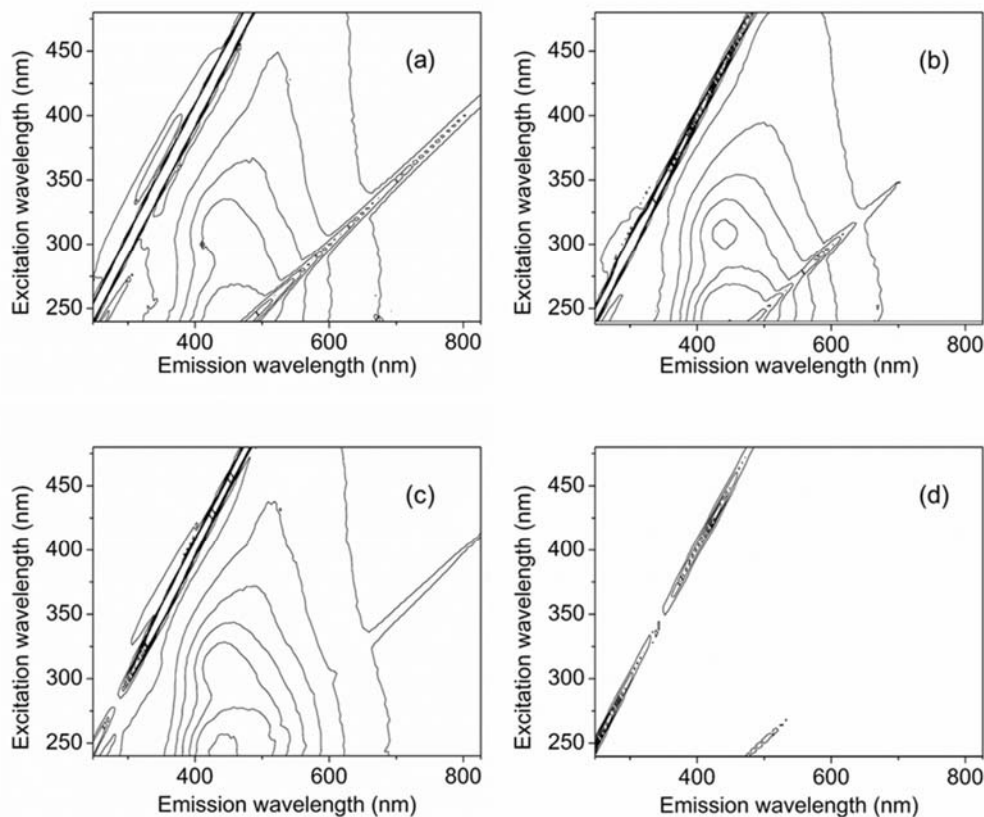


Figure 9.6. EEM spectra for HA 15 mg/L synthetic raw water ( $[Cl^-] = 9\text{ mM}$ ) (a); ultrafiltration permeate with raw water as feed (b); filtrate with raw water stirred at  $40^\circ\text{C}$  for 336 h as feed (c); filtrate with raw water degraded by 1 mM PS heat-activated at  $40^\circ\text{C}$  for 336 h as feed (d).

Figure 9.7 shows the effect of water chemistry on the degradation of HA by PS. For phosphate buffered, 9 mM  $Cl^-$  solutions (Figure 9.7a), a neutral pH provided for a slightly more effective degradation of HA compared to acidic condition. Experiments performed under basic conditions in the presence of phosphate buffer were not reliable due to particle precipitation interfering with  $UV_{254}$ . Phosphate buffer (10 mM) was added to stabilise the pH of solutions at initial conditions [40]. The lower degradation of HA under acidic conditions may be due to  $H^+$  catalysed unsymmetrical degradation of PS (R9.1) [41] or to the significantly

reduced conversion of  $\text{SO}_4^{\bullet-}$  to the kinetically fast  $\cdot\text{OH}$  arising from the lower concentration of  $\text{OH}^-$  (R9.2) [42].

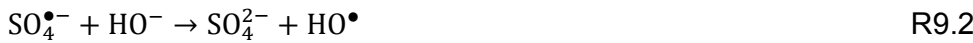
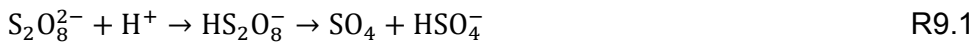


Figure 9.7b presents the effect of pH on the rate of HA degradation in the absence of  $\text{Cl}^-$ . The degradation of HA was most effective under neutral, unbuffered condition. This shows that the acidic environment is less suitable for HA degradation by heat-activated PS. It also highlights the scavenging effect of the phosphate ion on the oxidising radicals. However, in the absence of  $\text{Cl}^-$ , the buffered neutral solution does not appear to support fast HA degradation when compared to the acidic solutions. This observation might suggest that  $\text{Cl}^-$  have some effects on the efficiency of HA degradation.

The significant effect of  $\text{Cl}^-$  on the rate of HA degradation is clearly shown in Figure 9.7c for PS activated at 40 °C. The least degradation was observed for the solution with zero concentration of  $\text{Cl}^-$  while the solution with the highest  $\text{Cl}^-$  of 9 mM supported a slightly better HA degradation. However, relatively fast degradation of HA that achieved > 70%  $\text{UV}_{254}$  reduction in less than 30 h was observed for solutions with  $\text{Cl}^-$  concentrations of 0.9 and 0.09 mM. The  $\text{Cl}^-$  concentration in natural fresh water may range from 0.024 mM to 1.5 mM [40] which are closer to 0.09 and 0.9 mM  $\text{Cl}^-$  concentrations than to the  $\text{Cl}^-$  concentration of 9 mM used more extensively in this study. Hence, 9 mM  $\text{Cl}^-$  concentration represent a more challenging water matrix to HA degradation than natural fresh water. From the results presented in Figure 9.7c, it may be said that small amount of  $\text{Cl}^-$  promoted the degradation of HA while the benefit was lost at higher  $\text{Cl}^-$  concentration. Lutze et al [40] showed that  $\text{Cl}^-$  can transform  $\text{SO}_4^{\bullet-}$  into  $\cdot\text{OH}$  with suppressed formation of chlorate at  $\text{pH} > 5$  according to the following series of reactions.





Excess Cl<sup>-</sup> scavenge Cl<sup>•</sup> produced from R9.3 as follows thereby diminishing the degradation of the target substrate [40]:



The possible reaction between Cl<sup>•</sup> and HA during PS-AOP poses the risk of the formation of chlorinated degradation products like other water treatment options [33]. However, since the dominant oxidative species in solution can be controlled by pH adjustment for a given Cl<sup>-</sup> concentration [40], the reaction between Cl<sup>•</sup> and the target substrate may be minimised through process optimisation [40]. Alternatively, significant mineralisation should be targeted.

Figure 9.7d shows the effect of 2 mM CO<sub>3</sub><sup>2-</sup> on the degradation of HA. Radicals in solution are known to be significantly scavenged by CO<sub>3</sub><sup>2-</sup> [40]. The scavenging effect of CO<sub>3</sub><sup>2-</sup> may be associated with the poor removal of HA for the original 2 mM CO<sub>3</sub><sup>2-</sup> solution with a pH of 10.7. However, it can be seen that for the acidified solution with pH adjusted to 8, appreciable reduction in UV<sub>254</sub> (degradation of HA) was observed. This suggests that the scavenging effect of CO<sub>3</sub><sup>2-</sup> was significantly diminished following acidification. It is possible that the reduced pH resulted in the protonation of some CO<sub>3</sub><sup>2-</sup> leading to their evolution as CO<sub>2</sub>. Hence, it may be said that the stable concentration of CO<sub>3</sub><sup>2-</sup> at the pH relevant to drinking water treatment may show limited scavenging effect towards PS.

The degradation of HA spiked into tap water is presented in Figure 9.7e. The chemical analysis for the tap water is given in Table S9.2 showing a Cl<sup>-</sup> concentration of 0.37 mM and equivalent CaCO<sub>3</sub> concentration of 0.2 mM. A relatively fast degradation of HA is observed attaining ~70% UV<sub>254</sub> reduction in 24 h for initial pH of 7 and 10. The fast degradation may be attributed to the radical shuttling effect of Cl<sup>-</sup> with limited scavenging due to the low Cl<sup>-</sup> concentration. The trace metals present in the tap water sample (all within acceptable regulatory

limits) may have facilitated the activation of PS [43] for HA degradation. Figure 9.7f presents the degradation of HA spiked into different matrices with PS activated at 25 °C. At the low temperature of the test, no reduction in UV<sub>254</sub> was observed for MilliQ water and 9 mM Cl<sup>-</sup> matrices whereas ~70% reduction in UV<sub>254</sub> was observed after 72 h for the tap water matrix suggesting possible catalytic activation of PS attributable to the ions present in the tap water. The observed fast degradation of HA in tap water is a strong incentive for the adoption of PS-treatment of water for potable water production. Few publications have demonstrated that organic molecules and substrates associated with HA may activate PS [44-46]. However, the observation that practically no HA degradation was recorded after about 100 h for the 9 mM Cl<sup>-</sup> water matrix used extensively in this study as well as for the MilliQ water matrix shows that organic activators associated with HA are not important under the conditions of this work.

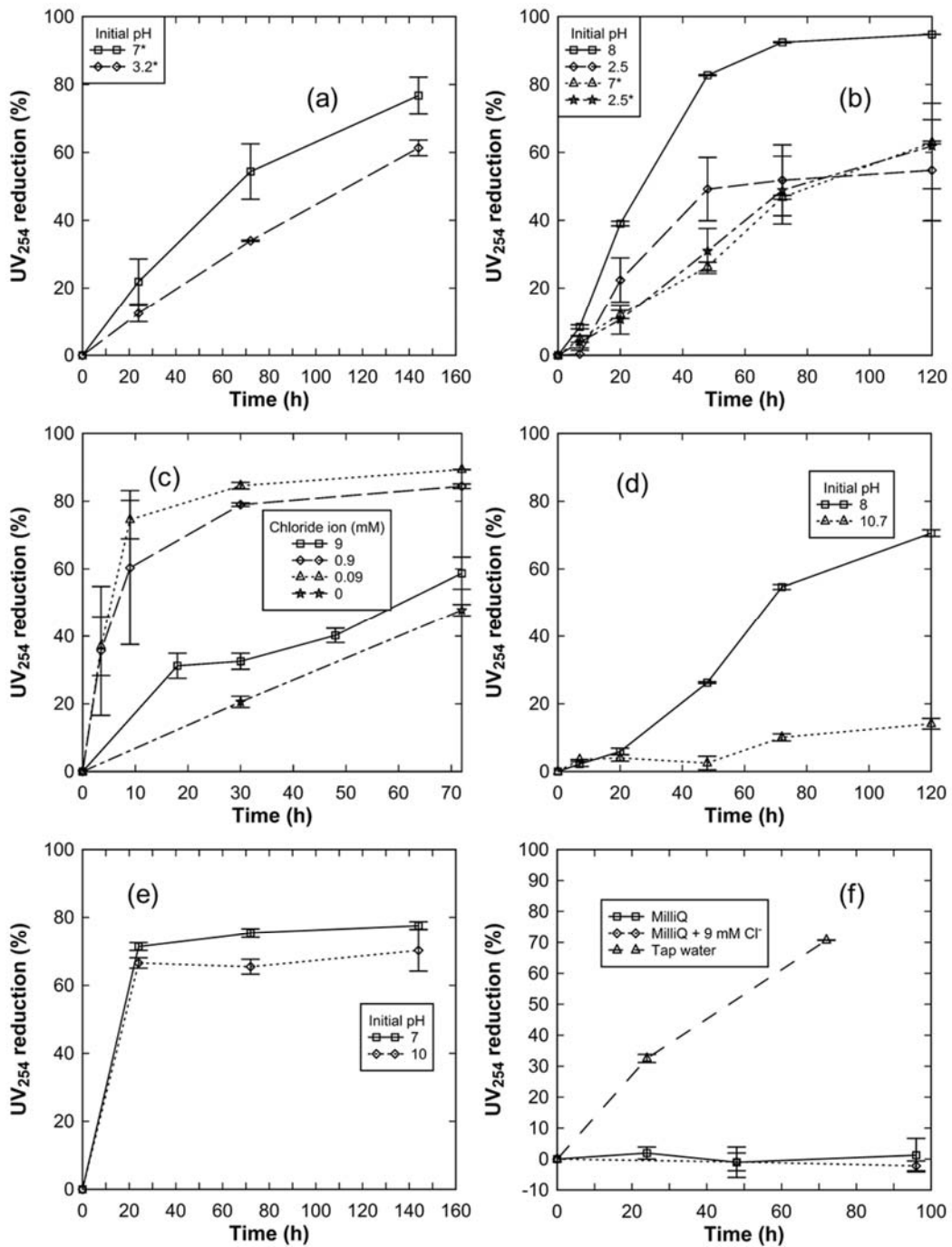


Figure 9.7. The effects of water chemistry on the degradation of 4 mg/L HA solution spiked into (a) 9 mM chloride solution, (b) MilliQ water, (c) different chloride concentration solutions, (d) originally 2 mM CO<sub>3</sub><sup>2-</sup> solution and (e) tap water<sup>^</sup> by 0.25 mM PS activated at 40 °C. (f) 0.25 mM PS activation at 25 °C for different matrices. \*Solutions phosphate buffered (10 mM). <sup>^</sup>Tap water chemical analysis presented in Table S9.2

The results of this study has shown that HA may be degraded by PS activated at common waste heat temperatures. Significant UV<sub>254</sub> reduction and TOC removal could be achieved over a period comparable to conventional water treatment processes depending on the chemistry of the raw water and the temperature of the available waste heat. The results raises the possibility of treating raw water in the future by harnessing waste heat from industrial and domestic processes thereby significantly reducing the cost of water treatment while opening up significant inland water resources for industrial cooling [47]. Previous studies [48, 49] has shown that activated PS effectively disinfects water, an outcome that is critically advantageous for both potable water production [50] and waste heat removal [20, 21].

Further studies are required to test the treatment effectiveness of PS activated at relevant waste heat temperature using real raw water as well as quantifying the DBPs reduction achieved. It should be noted that a PS-AOP implies the addition of sulphate into the water being treated. Precisely, the treatment of raw water with 0.25 mM or 1 mM PS as reported in this study amounts to the addition of the equivalent of 70 mg/L or 280 mg/L of Na<sub>2</sub>SO<sub>4</sub>, respectively, to the treated water. These values amount to 20% or 80%, respectively, of the thirst threshold for Na<sub>2</sub>SO<sub>4</sub> in drinking water which has been given as 350 mg/L [51]. However, a much higher sulphate concentration in water, up to 600 mg/L, has been reported to be tolerable [51] and even at a high concentration of 1200 mg/L, sulphate has not been convincingly associated with any harmful health consequences [52]. Nevertheless, if the source water is already rich in sulphate, the additional sulphate arising from PS treatment may be undesirable. The primarily aesthetic demerit of additional sulphate [53] should be weighed against the potentially significant and far-reaching benefits of water treatment using PS activated by waste-heat. The potential benefits include energy-neutral water treatment, more efficient water utilisation for domestic and industrial applications, reduction of thermal pollution of water bodies, elimination of industrial cooling towers and their attendant cost and pollution.

#### 9.4. Acknowledgment

The financial support provided by Victoria University to Ikechukwu A. Ike through the Victoria University International Postgraduate Research Scholarship is gratefully acknowledged.

#### References

- [1] A. Matilainen, M. Sillanpaa, Removal of natural organic matter from drinking water by advanced oxidation processes, *Chemosphere*, 80 (2010) 351-365.
- [2] X. Huang, M. Leal, Q. Li, Degradation of natural organic matter by TiO<sub>2</sub> photocatalytic oxidation and its effect on fouling of low-pressure membranes, *Water Res*, 42 (2008) 1142-1150.
- [3] W. Gao, H. Liang, J. Ma, M. Han, Z.-l. Chen, Z.-s. Han, G.-b. Li, Membrane fouling control in ultrafiltration technology for drinking water production: A review, *Desalination*, 272 (2011) 1-8.
- [4] P. Devi, U. Das, A.K. Dalai, In-situ chemical oxidation: Principle and applications of peroxide and persulfate treatments in wastewater systems, *The Science of the total environment*, 571 (2016) 643-657.
- [5] D. Deng, L. Peng, M. Guan, Y. Kang, Impact of activation methods on persulfate oxidation of methyl tert-butyl ether, *J Hazard Mater*, 264 (2014) 521-528.
- [6] H.V. Lutze, R. Bakkour, N. Kerlin, C. von Sonntag, T.C. Schmidt, Formation of bromate in sulfate radical based oxidation: mechanistic aspects and suppression by dissolved organic matter, *Water Res*, 53 (2014) 370-377.
- [7] W. Chu, D. Li, N. Gao, M.R. Templeton, C. Tan, Y. Gao, The control of emerging haloacetamide DBP precursors with UV/persulfate treatment, *Water Res*, 72 (2015) 340-348.
- [8] D. An, P. Westerhoff, M. Zheng, M. Wu, Y. Yang, C.A. Chiu, UV-activated persulfate oxidation and regeneration of NOM-Saturated granular activated carbon, *Water Res*, 73 (2015) 304-310.

- [9] R. Toor, M. Mohseni, UV-H<sub>2</sub>O<sub>2</sub> based AOP and its integration with biological activated carbon treatment for DBP reduction in drinking water, *Chemosphere*, 66 (2007) 2087-2095.
- [10] B.R. Scanlon, B.L. Ruddell, P.M. Reed, R.I. Hook, C. Zheng, V.C. Tidwell, S. Siebert, The food-energy-water nexus: Transforming science for society, *Water Resources Research*, 53 (2017) 3550-3556.
- [11] N. Vakilifard, M. Anda, P.A. Bahri, G. Ho, The role of water-energy nexus in optimising water supply systems – review of techniques and approaches, *Renewable and Sustainable Energy Reviews*, 82 (2018) 1424-1432.
- [12] R. Andreozzi, V. Caprio, A. Insola, R. Marotta, Advanced oxidation processes (AOP) for water purification and recovery, *Catalysis Today*, 53 (1999) 51–59.
- [13] G. Huang, Y. Zhou, T. Wang, I.V. Timoshkin, M.P. Wilson, S.J. MacGregor, M.J. Given, Statistical Analysis of Pulsed Microdischarges and Ozone Generation in Dielectric Barrier Discharges, *IEEE Transactions on Plasma Science*, 44 (2016) 2111-2120.
- [14] A.B. Little, S. Garimella, Comparative assessment of alternative cycles for waste heat recovery and upgrade, *Energy*, 36 (2011) 4492-4504.
- [15] S. Garimella, Low-grade waste heat recovery for simultaneous chilled and hot water generation, *Applied Thermal Engineering*, 42 (2012) 191-198.
- [16] B.-T. Zhang, Y. Zhang, Y. Teng, M. Fan, Sulfate radical and its application in decontamination technologies, *Critical Reviews in Environmental Science and Technology*, 45 (2015) 1756-1800.
- [17] M.Z. Stijepovic, P. Linke, Optimal waste heat recovery and reuse in industrial zones, *Energy* 36 (2011) 4019-4031.
- [18] N. Dow, S. Gray, J.-d. Li, J. Zhang, E. Ostarcevic, A. Liubinas, P. Atherton, G. Roeszler, A. Gibbs, M. Duke, Pilot trial of membrane distillation driven by low grade waste heat: membrane fouling and energy assessment, *Desalination*, 391 (2016) 30-42.
- [19] M. Ramadan, T. Iemenand, M. Khaled, Recovering heat from hot drain water—Experimental evaluation, parametric analysis and new calculation procedure, *Energy and Buildings*, 128 (2016) 575-582.
- [20] Aquaprox, Treatment of cooling water, Springer-Verlag Berlin Heidelberg, Germany, 2009.

- [21] S. Rajagopal, H.A. Jenner, V.P. Venugopalan, Operational and environmental consequences of large industrial cooling water systems, in, Springer Science+Business Media, USA, 2012.
- [22] I.A. Ike, J. Zhang, A. Groth, J.D. Orbell, M. Duke, Effects of dissolution conditions on the properties of PVDF ultrafiltration membranes, Ultrasonics sonochemistry, 39 (2017) 716-726.
- [23] L. Fan, J.L. Harris, F.A. Roddick, N.A. Booker, Influence of the characteristics of natural organic matter on the fouling of microfiltration membranes, Water Research, 35 (2001) 4455 - 4463.
- [24] J.R. Bolton, S.R. Cater, Homogeneous photodegradation of pollutants in contaminated water. An introduction, in: G. Helz, R. Zepp, D. Crosby (Eds.) Surface and Aquatic Photochemistry, CRC Press Boca Raton, 1994.
- [25] P. Fu, F. Wu, C. Liu, Fluorescence excitation-emission matrix characterization of a commercial humic acid, Chinese Journal of Geochemistry, 23 (2004) 309-318.
- [26] M.M. Sierra, M. Giovanelà, E. Parlanti, E.J. Soriano-Sierra, Fluorescence fingerprint of fulvic and humic acids from varied origins as viewed by single-scan and excitation/emission matrix techniques, Chemosphere, 58 (2005) 715-733.
- [27] B.J.H. Matthews, A.C. Jones, N.K. Theodorou, A.W. Tudhope, Excitation-emission-matrix fluorescence spectroscopy applied to humic acid bands in coral reefs, Marine Chemistry, 55 (1996) 317-332.
- [28] L. Bach, E.R. Garbelini, S. Stets, P. Peralta-Zamora, A. Emmel, Experimental design as a tool for studying trihalomethanes formation parameters during water chlorination, Microchemical Journal, 123 (2015) 252-258.
- [29] K. Kumada, Absorption spectra of humic acids, Soil Science and Plant Nutrition, 1 (1955) 29-30.
- [30] F. Martin, F.J. Gonzalez-Vila, Persulfate oxidation of humic acids extracted from three different soils, Soil Biology and Biochemistry, 16 (1984) 207-210.
- [31] M. Schnitzer, M.I.O. de Serra, The chemical degradation of a humic acid, Canadian Journal of Chemistry, 51 (1973) 1554-1566.
- [32] H. Gallard, U. von Gunten, Chlorination of natural organic matter: kinetics of chlorination and of THM formation, Water Research, 36 (2002) 65–74.

- [33] C. Wenhai, C. Tengfei, D. Erdeng, Y. Deng, G. Yingqing, G. Naiyun, Increased formation of halomethanes during chlorination of chloramphenicol in drinking water by UV irradiation, persulfate oxidation, and combined UV/persulfate pre-treatments, *Ecotoxicology and Environmental Safety*, 124 (2016) 147–154.
- [34] A. Ghauch, A.M. Tuqan, N. Kibbi, Ibuprofen removal by heated persulfate in aqueous solution: A kinetics study, *Chemical Engineering Journal*, 197 (2012) 483-492.
- [35] C. Tan, N. Gao, Y. Deng, N. An, J. Deng, Heat-activated persulfate oxidation of diuron in water, *Chemical Engineering Journal*, 203 (2012) 294-300.
- [36] M.B. Stewart, D.T. Myat, R.J. Michael, S.R. Gray, J.D. Orbell, A structural basis for the amphiphilic character of alginates –Implications for membrane fouling, *Carbohydrate Polymers* 164 (2017) 162–169.
- [37] M. Kawahigashi, H. Sumida, K. Yamamoto, Size and shape of soil humic acids estimated by viscosity and molecular weight, *Journal of colloid and interface science*, 284 (2005) 463-469.
- [38] H.T. Madsen, Membrane filtration in water treatment – removal of micropollutants, in: *Chemistry of advanced environmental purification processes of water - fundamentals and applications*, Elsevier, The Netherlands, 2014, pp. 199–248.
- [39] A. Chin, P.R. Berube, Removal of disinfection by-product precursors with ozone-UV advanced oxidation process, *Water Res*, 39 (2005) 2136-2144.
- [40] H.V. Lutze, N. Kerlin, T.C. Schmidt, Sulfate radical-based water treatment in presence of chloride: Formation of chlorate, inter-conversion of sulfate radicals into hydroxyl radicals and influence of bicarbonate, *Water Research*, 72 (2015 ) 349-360.
- [41] I.M. Kolthoff, I.K. Miller, The chemistry of persulfate. I. The kinetics and mechanism of the decomposition of the persulfate ion in aqueous medium, *journal of American Chemical Society*, 73 (1951) 3055–3059.
- [42] O.S. Furman, A.L. Teel, R.J. Watts, Mechanism of Base Activation of Persulfate, *Environmental Science & Technology*, (2010) 6423–6428.

- [43] G.P. Anipsitakis, D.D. Dionysiou, Radical generation by the interaction of transition metals with common oxidants, *Environmental Science & Technology*, 38 (2004) 3705-3712.
- [44] G. Fang, J. Gao, D.D. Dionysiou, C. Liu, D. Zhou, Activation of persulfate by quinones: free radical reactions and implication for the degradation of PCBs, *Environmental Science & Technology*, 47 (2013) 4605-4611.
- [45] M. Ahmad, A.L. Teel, R.J. Watts, Mechanism of persulfate activation by phenols, *Environ Sci Technol*, 47 (2013) 5864-5871.
- [46] A.M. Ocampo, Persulfate Activation by Organic Compounds, in: Department of Civil and Environmental Engineering, Washington State University, 2009.
- [47] I.A. Ike, K. Linden, J.D. Orbell, M. Duke, Critical review of the science and sustainability of persulphate advanced oxidation processes, *Chemical Engineering Journal*, 338 (2018) 651-669.
- [48] S. Ahn, T.D. Peterson, J. Righter, D.M. Miles, P.G. Tratnyek, Disinfection of ballast water with iron activated persulfate, *Environ Sci Technol*, 47 (2013) 11717-11725.
- [49] D. Xia, Y. Li, G. Huang, R. Yin, T. An, G. Li, H. Zhao, A. Lu, P.K. Wong, Activation of persulfates by natural magnetic pyrrhotite for water disinfection: Efficiency, mechanisms, and stability, *Water Res*, 112 (2017) 236-247.
- [50] C. Binnie, M. Kimber, *Basic Water Treatment*, in, ICE Publishing, London, 2013.
- [51] WHO, Sulfate in drinking-water, in: Background document for development of WHO Guidelines for Drinking-water Quality, World Health Organization, [http://www.who.int/water\\_sanitation\\_health/dwq/chemicals/sulfate.pdf](http://www.who.int/water_sanitation_health/dwq/chemicals/sulfate.pdf)
- 2004.
- [52] L.C. Backer, E. Esteban, C.H. Rubin, S. Kieszak, M.A. Mcgeehin, Assessing acute diarrhea from sulfate in drinking water *Journal - American Water Works Association*, 93 (2001) 76-84.
- [53] D. Salari, A. Niaezi, S. Aber, M.H. Rasoulifard, The photooxidative destruction of C.I. Basic Yellow 2 using UV/S<sub>2</sub>O<sub>8</sub>(2-) process in a rectangular continuous photoreactor, *J Hazard Mater*, 166 (2009) 61-66.

## Appendix

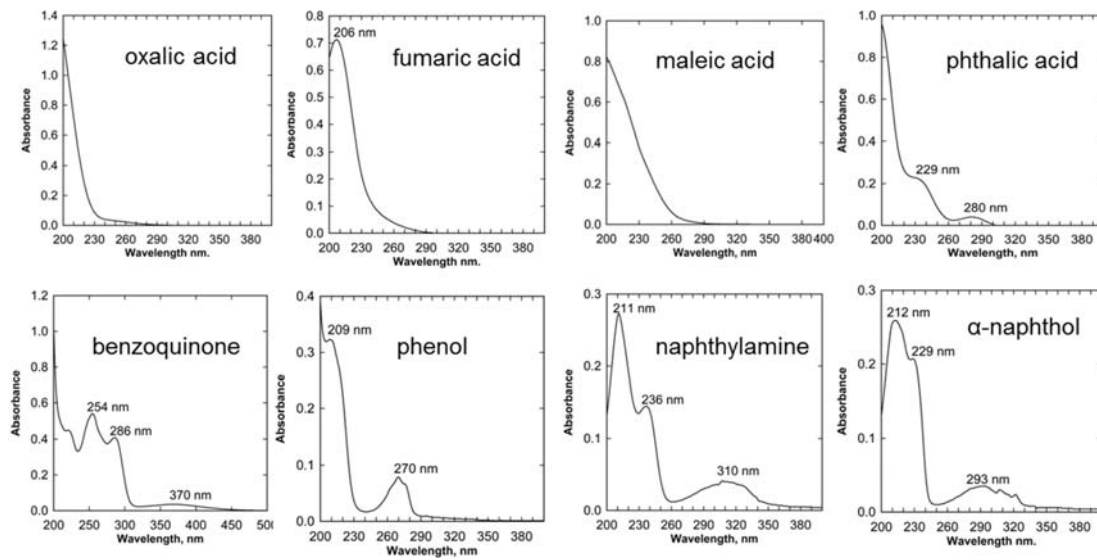


Figure S9.1. UV spectra for selected organic compounds

Table S9.1. Retention times for selected chemicals

<b>Chemicals</b>	<b>Retention time, min</b>
Fumaric acid	1.24
Oxalic acid	1.26
4-aminobenzoic acid	1.30
Pthalic anhydride	1.30
Pthalic acid	1.31
Maleic acid	1.33
3-hydroxybenzoic acid	1.33
2-Furoic acid	1.33
Hydroquinone	1.73
Resorcinol	2.20
Benzoquinone	2.24
Salicylic acid	2.32
4-nitrobenzoic acid	2.33
2-hydroxy-5-nitrobenzaldehyde	2.82
Orcinol	3.07
Aniline	3.24
4-Nitroaniline	3.82
Phenol	4.11
3,5 Dinitrosalicylic acid	4.81
Benzaldehyde	4.95
2-nitrophenol	4.95
1-hydroxy-2-naphthoic acid	5.53
Acetophenone	5.61
2-nitroso-1-naphthol	6.27
Naphthylamine	6.64
$\alpha$ -Naphthol	7.68
2-hydroxy-1-naphthaldehyde	8.00
Bisphenol A	8.12

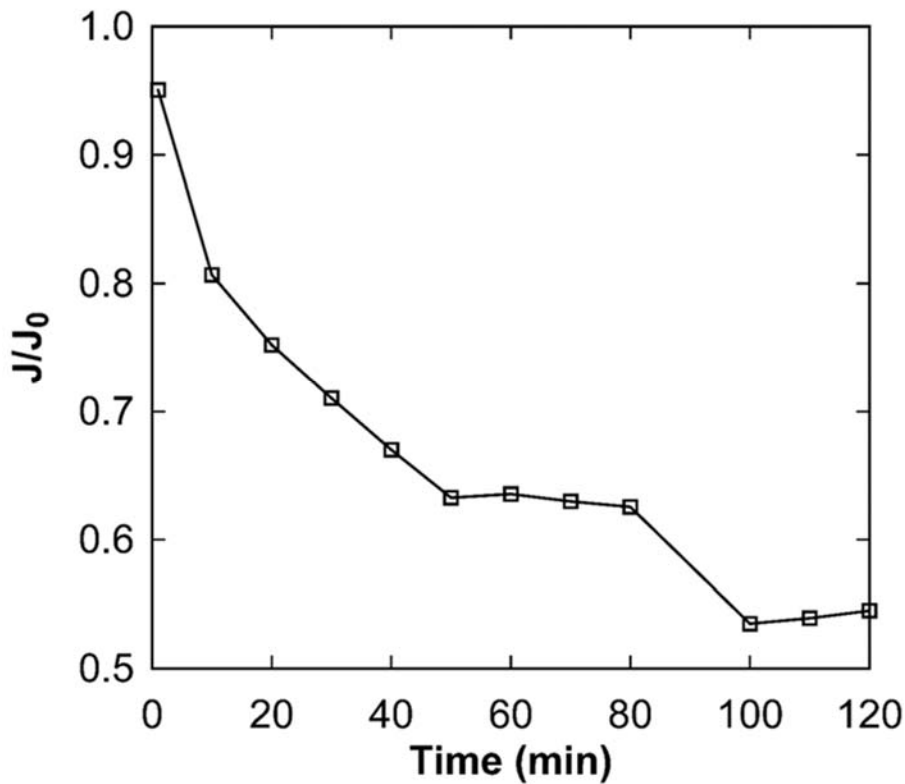


Figure S9.2. Normalised flux profile for raw water after treatment at 40 °C for 336 h without added PS. Data for single experiment reported.

Table S9.2. Tap water chemical analysis\*

Ion	Average (mg/L)
Aluminium (acid soluble)	0.02
Arsenic	<0.001
Cadmium	<0.002
Calcium	5.2
Chloride	13
Chromium	<0.001
Copper	0.003
Hardness (as CaCO <sub>3</sub> )	20
Iron	0.03
Lead	<0.001
Magnesium	1.6
Manganese	0.003
Mercury	<0.0001
Nitrate (NO <sub>3</sub> )	0.62
Potassium	0.9
Silica (SiO <sub>2</sub> )	2.7
Sodium	6.7
Sulphate	4.2
Zinc	0.004

\*City West Water, Drinking Water Quality Report 2016,  
[https://www.citywestwater.com.au/documents/water\\_quality\\_report\\_2016\\_web.pdf](https://www.citywestwater.com.au/documents/water_quality_report_2016_web.pdf)

## Chapter 10

### **General conclusion and future research**

#### 10.1 General conclusion

The future of human societies and the environment in which these societies operate are dependent on cost-effective and sustainable water treatment systems. This study has provided in-depth investigations into aspects of two of the highly effective modern water treatment technologies: membrane filtration processes and advanced oxidation processes. Membrane filtration processes are fairly advanced and consequently, a two-way research programme was proposed: continual search for novel concepts and techniques on the frontier of the field such as is provided by nanotechnology and re-evaluation of established procedures and routines for unexplored opportunities.

Nanotechnology is considered a promising field of frontier research for the resolution of the fouling and permeability-selectivity tradeoff challenge of membrane filtrations as presented in Chapter two. For practical incorporation of nanoparticles into membranes, aggregation remains a major problem especially regarding attempts to produce functional membrane composites. An assessment of the impact of routine membrane preparatory steps on promoting hydrophilic nanoparticle dispersion in a hydrophobic polymeric membrane was reported in Chapter three. The study focused on the impact of ultrasonication and the addition of a hydrophilic polymer. Results showed that hydrophilic nanoparticle dispersion in a hydrophobic polymeric matrix is promoted by ultrasonication as expected but also by the addition of a hydrophilic polymer. Other significant conceptual insights on the functional properties of polymeric membranes including the development and modification of porosity, crystallinity and thermal stability were identified and discussed. For instance, it was shown that the common opinion that hydrophilic polymers are “pore formers” was misleading. The principal function of hydrophilic polymers added to a hydrophobic membrane is to connect the pores developed during phase inversion. Instead, hydrophilic polymers may be more appropriately known as “pore connectors”. This new insights will potentially guide future membrane development and optimisation efforts.

Further investigation of routine membrane preparatory steps considered the effects of polymer dissolution conditions. The results presented in Chapter four showed that the commonly over-looked membrane-making step of polymer dissolution had immense impact on the properties of the final membrane. Significant fouling resistance benefit was derived from dissolving PVDF by ultrasonication compared to conventional stirring procedures. Other properties that could be tailored by modifying dissolution condition include porosity, permeability, thermal and mechanical stability. It was shown that the changes in permeability, fouling resistance, thermal and mechanical stability were linked to the membrane porosity. From this, it may be concluded that a procedure as ordinary as polymer dissolution could be a powerful design tool for controlling the properties of membranes for different applications. The overriding implication of these results is that developmental opportunities exist even in procedures that have become routine in membrane research. Exploration of these opportunities will potentially extend the functionalities and adaptability of future membranes.

The synergy between membrane filtration and advanced oxidation processes has been demonstrated and are heralded to become more important in the future especially regarding increased adoption of wastewater reuse. However, studies on the more novel combined membrane filtration and sulphate-radical-based AOPs are uncommon. To close this gap and to provide more options for effective and sustainable surface and subsurface water treatment, a critical review of sulphate-radical-based AOPs was undertaken (Chapter five) with specific focus on the commercially important persulphate oxidant. This review provided new insights for some important observations in the emerging field of persulphate AOPs, proposed several modifications to published reaction mechanisms and made several suggestions for further studies in the field. Overall, it was established that significant research opportunities exist in PS-AOPs and there are much potential for practical applications.

Among the several techniques for persulphate activation, iron based catalysis has attracted significant attention. Persulphate activation by zerovalent iron nanoparticles stabilised by phosphonic acid was employed for the degradation of a model water pollutant. The results from the study presented in Chapter six showed that the problem of zerovalent iron nanoparticle passivation towards

persulphate due to surface oxidation could be mitigated by phosphonic acid stabilisation. The functional properties of the stabilised nanoparticles were shown to be considerably influenced by the nature of the stabilising nanoparticles. The use of a low molecular weight chelator (ATMP) resulted in nanoparticles that were practically stable in water in the absence of persulphate but rapidly activated persulphate when present, achieving fast pollutant degradation and detoxification. These unique characteristics might be employed for rapid detoxification of contaminants, for example in a case of emergency pollution remediation. A much larger molecular weight chelator (HTPMP) showed oxidative properties to the target pollutant, orange G, in the presence or absence of persulphate. Hence, this nanoparticle might be used for pollutant degradation with or without persulphate.

To transition from laboratory studies to field application of zerovalent iron activation of persulphate, adequate access to affordable zerovalent iron particles is a requirement. Steel wool and carbonyl iron powder are relatively cheap, commercially available samples of zerovalent iron. In this study (Chapter seven), it was shown that steel wool and carbonyl iron powder are practically free of surface oxidation layers and so provide unpassivated zerovalent iron surfaces for persulphate activation. Rapid activation of persulphate resulting in the degradation of four target pollutants: orange G, salicylic acid, phenol and 1-naphthylamine in the presence or absence of methanol were observed without any prior modification of the iron samples. The addition of methanol mimics the presence of industrial solvents and/or feedstuff in real industrial wastewater. From the results, it was concluded that both steel wool and carbonyl iron powder are suitable for the activation of persulphate for practical wastewater treatment.

The study on steel wool activation of persulphate showed that the commercial material was more effective than the more popular ionic iron in activating persulphate. It was also shown that methanol had no effect on the nature of the degradation products but reduced the rate of degradation of the target pollutants. The alcohol had more retarding effect on the degradation of an aromatic pollutant relatively resistant to oxidation such as salicylic acid due to the presence of an electron-withdrawing group compared to a pollutant such as 1-naphthylamine that has an electron-donating group. The azo bond in orange G was found to

constitute a structural weakness leading to a comparatively more effective degradation of the aromatic moieties. It was further revealed that the gradual addition of persulphate achieves more effective pollutant degradation and mineralisation than sudden addition (except for salicylic acid) and always with less consumption of PS. These results are important for the development of affordable and effective schemes for the treatment of industrial wastewater.

The effectiveness of heat-activated persulphate oxidation of synthetic dye wastewater under conditions relevant to the textile industry was demonstrated in Chapter eight. One important implication of the results of this study for wastewater management in the textile industry is that the waste heat typically associated with the wastewater provides enough energy to drive the treatment. Consequently, the cost of persulphate is the primary operating cost that may be incurred. Since many other industries produce significant amount of waste heat, waste heat activated persulphate AOPs may play important role in resolving industrial wastewater treatment challenges in the future. This study also highlighted the unique effect of radical kinetic energy in determining the efficiency of pollutant mineralisation. Apart from the theoretical implications, greater awareness of the impact of radical kinetic energy in AOPs may provide for better process control and optimisation.

For drinking water production, NOM degradation by persulphate activated thermally, mainly at a low temperature of 40 °C but also at 60 °C and 90 °C in which ~70% TOC loss was achieved within 168 h, 24 h and 1 h, respectively, was demonstrated in Chapter nine. The practical implications of this study is that NOM and micropollutants in drinking water which may constitute a health hazard in themselves or serve as a precursor for DBPs could be readily removed by persulphate activated at waste heat temperature. It was shown that without persulphate pretreatment, not only was membrane filtration of the NOM containing synthetic raw water considerably challenged by fouling, the permeate from the UF process was found to contain significant amount of NOM. The presence of NOM in treated drinking water poses a risk of generation of DBPs upon chlorination. Both membrane fouling reduction and removal of NOM in the UF permeate was achieved by activated-persulphate pretreatment. This result shows that the quality of the product and the cost-effectiveness of a membrane

filtration process may benefit from PS-AOP integration. The study advances the exciting possibility that the power generation problem of waste heat disposal may be resolved in the production of treated/drinking water.

In summary, while further research in developing novel techniques and materials and optimising their applications is expected to continue to advance the maturing field of membrane filtration, re-evaluation of common practices is a promising route to further progress in the field. Careful re-assessment of the impact of established membrane preparatory steps can provide more control for the design of functional and adaptable membranes. The nascent field of persulphate AOP provide significant opportunities for cost-effective and sustainable treatment of surface and subsurface water for drinking water production, domestic and industrial waste management and abatement of environmental pollution. It also holds much promise for improving the performance of MFPs. Centralised production of persulphate using renewable hydrothermal energy and the harnessing of waste heat, reusable catalysts, cheap sources of iron and environmental activators could secure a sustainable future of abundance of good quality water and healthy ecological balance. The results from the researches reported in this work is directly applicable in the membrane industry for low-cost production of functional membranes and for remedying the elusive problem of membrane fouling. Manufacturing and environmental engineering industries stand to benefit from the research outcome in this work with regard to the development of more effective wastewater treatment and contamination remediation schemes using persulphate activated effectively at relatively low cost. The outcome from this study will potentially revolutionise both the drinking water and power generation industry.

## 10.2. Future research

The work in this thesis has opened up many opportunities for research in the development of MFPS and persulphate AOPs and their integration. These opportunities have been highlighted throughout the thesis so that only a brief summary of some key points can be attempted here. The significant effect of dissolution conditions and the effect of hydrophilic polymer addition were evaluated on the hydrophobic PVDF membrane. Further study is required to

confirm the generality of the results obtained and to test if unique modifications are obtainable using different combinations of additives, base polymer and preparatory steps. The observed strong influence of porosity on the functional properties of PVDF membranes achieved by dissolution modification calls for further research to more fully understand and harness the impact of porosity/pore size distribution and how this property could be conveniently modified. Fundamental research on the speculated polymer chains unfolding and entanglement may be valuable in controlling the structure and performance of polymeric membranes.

More research on persulphate AOPs integration with MFPs is recommended. The uncertainties surrounding the effectiveness of Ag(I) activation of persulphate for contaminant degradation calls for further studies. Also important is a fuller understanding of Fe(III) activation of persulphate and the sulphate radical reactions with the hydroxyl ions. These investigations have significant theoretical benefits in furthering the science of radical reactions as well as many potential benefits for water treatment and disinfection applications. An overall appraisal of industrial and domestic waste heat production with the view of establishing the accessibility of this form of energy to practical persulphate activation is proposed. This study will potentially assist in the development of sustainable full-scale waste management and water treatment systems producing high quality industrial and potable water at low cost. More research in developing reusable persulphate catalysts based on nanocarbon materials, novel transition metal compounds including large surface area iron (hydro) oxides is suggested. The feasibility of non-chlorine disinfection based on persulphate activated by waste heat or spontaneously activated to limit the occurrence of halogenated DBPs in potable water is proposed for investigation. Metal ions that may occur in drinking water within acceptable limits may play crucial role in persulphate activation under this scheme. The potential benefit of this system compared to established non-chlorine disinfection like UV irradiation is that residual protection against reinfection is available. Furthermore, the residual disinfection benefit of persulphate may outlast that of chlorine due to the non-volatile nature of the former. This study should be accompanied by a thorough clinical assessment of the acceptable intake of persulphate and whether planned destruction similar to

ozone disinfection is required. A quantitative evaluation of a waste management and water treatment economy based on centralised production of persulphate using sustainable hydrothermal energy and effective distribution may provide a valuable blueprint for future sustainability efforts.